GEODYNAMIC EVOLUTION AND PETROGENESIS OF THE NEOARCHAEAN FRANCISTOWN GRANITE-GREENSTONE COMPLEX IN NE BOTSWANA, SW MARGIN OF THE ZIMBABWE CRATON

ZIBISANI BAGAI

GEODYNAMIC EVOLUTION AND PETROGENESIS OF THE NEOARCHAEAN FRANCISTOWN GRANITE-GREENSTONE COMPLEX IN NE BOTSWANA, SW MARGIN OF THE ZIMBABWE CRATON

ZIBISANI BAGAI

Thesis submitted in fulfillment of the requirements for the degree of Doctor of Philosophy

Department of Geological Sciences

University of Cape Town

August, 2008

University of Cape Town

Declaration

The content of this thesis is original work of the author and has not previously been submitted for a degree at any university. The work of other people is acknowledged by reference.

Zibisani Bagai
Department of Geological Sciences
University of Cape Town
August, 2008

THIS THESIS IS DEDICATED TO THE FOLLOWING PEOPLE WHO PASSED AWAY DURING THE COURSE OF THIS STUDY;

MY MUM MRS AGNES BAGAI

MY SISTER SIBONGILE BAGAI

CO-SUPERVISOR PROF HENRI KAMPUNZU

TABLE OF CONTENTS

PART I – OBSERVATIONS

CHAPTER 3: PETROGRAPHY

CHAPTER 4: GEOCHRONOLOGY

PART II – INTERPRETATION

CHAPTER 9: PETROGENESIS OF THE MAFIC AND FELSIC LAVAS OF THE GREENSTONE BELTS

CHAPTER 10: PETROGENESIS OF THE GRANITOIDS

CHAPTER 11: PETROGENESIS OF THE SANUKITOID DIORITE

CHAPTER 12: SYNTHESIS AND CONCLUSION FOR THE EVOLUTION OF THE FRANCISTOWN GRANITE-GREENSTONE COMPLEX

ABSTRACT

The Archaean Francistown Granite-Greenstone Complex in NE Botswana is an integral part of the southwestern margin of the Zimbabwe Craton. It includes a suite of geochemically diverse Neoarchaean granitoids and mafic dominated-supracrustal assemblages. All the supracrustal rocks and mafic intrusions have undergone greenschist to lower amphibolite facies metamorphism, but most mafic intrusions have preserved original igneous textures. The Francistown Granite-Greenstone Complex likely represents an arc complex that developed along an active continental margin in the Neoarchaean.

This thesis presents new geological, geochemical and geochronological data with which to evaluate the crustal evolution of the NE Botswana, and with which to formulate a geodynamic model for better understanding of the Archaean crustal growth flanking the southwestern margin of the Zimbabwe Craton.

The Francistown Granite-Greenstone Complex comprises two main granite-greenstone terrains that have been assumed to date to be age-equivalents: (1) The Tati granite-greenstone terrain is dominated by tonalite-trondhjemite granitoids with subordinate quartz monzonite, trondhjemite, monzogranite, metagabbros and sanukitoid diorite, all spatially associated with mafic volcanics that are intercalated with minor felsic lavas; (2) The Vumba granite-greenstone terrain is composed of tonalite, granodiorite, quartz monzonite and granite plutonism associated with mafic and felsic lavas as well as subordinate ultramafic rocks.

More than 200 rock samples collected from the Francistown Granite-Greenstone Complex were evaluated in this study. One hundred and twenty of these samples were collected from rocks within the Vumba granite-greenstone area and the remainder sampled from the Tati granite-greenstone terrain. Major and trace element data from the volcanics and various plutonic rocks from the Francistown Granite-Greenstone Complex are presented, as are Nd, Sr and Pb isotope data for a selection of samples. These radiogenic isotope ratios are commonly used in geochemistry as petrogenetic tracers, yielding information about time-integrated elemental fractionation through processes of melting, magma mixing, crystallization, metamorphism, and metasomatism. U-Pb zircon SHRIMP data from selected rock units, as well as limited O isotope data from the gabbro, diorite and granitoids, are also presented. Geochronologic data constrain the sequence of magmatic events. Oxygen isotopes provide a way to distinguish between rocks formed in equilibrium with the mantle and those which formed from melting of continental crust, or through a combination of both.

The Archaean rocks of the Francistown Granite-Greenstone Complex in NE Botswana record a magmatic evolutionary history of ~100 Ma. The new U-Pb dates on magmatic zircons from the volcanic and plutonic rocks reveal that the Francistown Granite-Greenstone Complex formed between 2740 and 2640 Ma, and that there is a time gap of ~40 Ma between the formation of the Tati and the Vumba greenstone belts. The Tati greenstone belt formed at ~2740 Ma whilst development of the Vumba greenstone belt occurred circa 2700 Ma. Subsequent magmatism of granitoids in the two greenstone belts displays contrasting spectra of emplacement ages. Geochemical analyses of the mafic lavas in the Tati and Vumba greenstone belts show the

presence of both calc-alkaline and tholeiitic series. Various tectonic models applied to deduce the environment of deposition for the mafic lavas best reflect back-arc settings. The associated contemporaneous felsic lavas exhibit calc-alkaline affinities and Archaean adakites geochemical characteristics, consistent with a subduction zone setting. The greenstone belts of the Francistown Granite-Greenstone Complex appear to represent ancient subduction back-arc basin settings similar to those of modern subduction zone back-arc marginal basins in the western Pacific Ocean. REE modelling indicates that the mafic lavas of the Tati and Vumba greenstone belts formed through partial melting of a spinel lherzolite source. The felsic components require mafic sources and partial melting under high pressure conditions with a garnet bearing restite to explain their origin. REE modelling and HFSE ratios reveal that the mafic and ultramafic intrusions have a common origin with the mafic lavas. Petrographic analysis of the mafic intrusions reveals cumulate and doleritic textures; this is consistent with the intrusions as feeders to the mafic lavas. The samples with doleritic texture exhibit similar geochemical characteristics to those of the mafic lavas, providing further evidence that they are cogenetic.

The granitoids in the Francistown Granite-Greenstone Complex display geochemical affinity with volcanic arc granites. They are calc-alkaline, metaluminous to weakly peraluminous and I-type in nature. The Vumba granitoids exhibit coherent linear trends on Harker diagrams, which is suggestive of a common petrogenetic bond. Moreover, the tonalite, granodiorite and quartz monzonite in the Vumba terrain are penecontemporaneous. However, the quartz monzonite displays distinct geochemical characteristics from those of the tonalite and granodiorite units, in that it contains high Mg#, Ni, Cr and positive initial εNd values. This implies involvement of a mantle component in the genesis of the quartz monzonite. However, oxygen isotope analyses of quartz from the quartz monzonite yield non-mantle values. REE modelling indicates that the origin of the quartz monzonite cannot be explained by partial melting of a mafic source alone. It requires a mixture of mantle and mafic crustal components. The tonalite and granodiorite display geochemical features of adakites, and REE modelling indicates that their origin can be explained by partial melting a mafic source with a garnetiferous amphibolite restite containing about 10% modal garnet. The monzogranite, which marked the final magmatic event in the Vumba terrain, is texturally and compositionally heterogeneous, and possesses geochemical characteristics of both the quartz monzonite and the tonalite-granodiorite. These observations can be explained by partial melting a pre-existing crust comprising a quartz monzonite-tonalite-granodiorite composition.

By contrasts, the granitoids in the Tati granite-greenstone terrain do not show any coherent linear trends on Harker diagrams. They exhibit four episodes of granitoid magmatism of which three episodes involved tonalite-trondhjemite magmatism. The first episode, which is coeval with the deposition of supracrustal rocks in the greenstone belt, generated voluminous tonalite-trondhjemite plutons. These are confined to the northeastern margin of the greenstone belt. Petrogenetic analysis of these tonalite-trondhjemites indicates that they were formed by partial melting a mafic source at high pressure leaving an eclogitic restite. Nd isotope data reveals that their source was a juvenile crust less than 200 Ma. The second episode of magmatism which occurred at ~2715 Ma generated high-Mg diorite, trondhjemite and monzogranite rocks. Although the three rock units are coeval and spatially associated, they are not co-genetic. Petrogenetic analyses indicate that the diorite was generated from a heterogeneously enriched spinel lherzolite source, whereas monzogranite and trondhjemite are products of partially melted hydrous basaltic crust outside stability fields of garnet. Oxygen isotope data support a crustal origin for the trondhjemite and

monzogranite and a non-mantle origin for the diorite that can be explained by involvement of metasomatic fluids. Nonetheless, the three rock units are believed to be linked to a common heat source. The third episode of magmatism generated tonalite-trondhjemite dykes that intruded the mafic intrusions. On the basis of REE modelling these felsic dykes were generated from a partial melt of a mafic source within the stability field of garnet and with a residue containing less than 10% modal garnet. The final episode of granitoid magmatism in the Tati granite-greenstone terrain took place ~2670 Ma ago, and produced a large volume of tonalite-trondhjemite plutons confined to the southwestern margin of the greenstone belt. REE modelling indicates partial melting of a mafic source (leaving a residue with > 25% modal garnet) for the origin of these tonalite-trondhjemite plutons. The tonalite-trondhjemite displays positive εNd values that are consistent with a source with less than 200 Ma.

Based on petrological, geochronological, geochemical and isotopic data of all the studied rocks in the Tati and Vumba granite-greenstone terrains, petrogenetic models and tectonomagmatic environments for each rock unit has been established. Integration of the petrogenetic models and information on tectonomagmatic environments, coupled with geochronological data, was vital for the construction of the geodynamic models for the Tati and Vumba granite-greenstone terrains.

Geochronological data from this study clearly dismiss the notion that the Vumba and Tati granite-greenstone terrains are contemporaneous, even though they both suggest a subduction tectonic setting for their origins. The new results, in conjunction with previously published data from the Vumba granite-greenstone terrain, reveal distinct differences in the magmatic histories of the Tati and Vumba terrains. Also evident from this study is that the two terrains do not share a late tectonic history. Nevertheless, the ranges of Sr, Nd and Pb isotopic data from the mafic lavas of the two greenstone belts, overlap such that they cannot be distinguished on the basis of isotopic composition. It appears that the Tati and Vumba mafic lavas were derived from similar or perhaps identical mantle source material. However, the subtle differences in Nd isotopic composition that do exist between the Tati and Vumba mafic lavas, appear to reflect varying proportions of crustal involvement during their formation. These observations argue for a tectonic setting along a similar evolving convergent continental margin. This work therefore reveals that the Francistown Granite-Greenstone Complex has a more complex crustal growth history along the southwest margin of the Zimbabwe Craton than previously envisaged.

ACKNOWLEDGEMENTS

The journey to attain my PhD was a long and bumpy one indeed. It was like climbing Mount Everest. On many occasions I felt like giving up. Thanks to my supervisors, Prof A.P. le Roex and the late Prof. A.B. Kampunzu, and the USHEPiA staff who were always there to comfort and encourage me during those trying times. It was characterized by loads of family misfortune through out. At one time I stayed out of the study programme for almost five months. Indeed the old saying is true: when the going gets tough, the tough get going. What I learned from that experience was not to quit when faced with an insurmountable obstacle. I learnt that no matter how difficult things are you still have to go on and if you fall you must pick yourself up, dust yourself off and soldier on. Perseverance is the key to success. Nelson Mandela once said: "The greatest glory in living lies not in never falling, but in rising every time we fall." I believe that if you have the desire and passion to do something, and if it's God's will, you will achieve it despite the difficult circumstances. As humans, we continually put limits on our capabilities for no reason at all!

I gratefully acknowledge the considerable constructive discussions and comments provided by the two professors who supervised this study: Professor Maarten de Wit and Professor Anton le Roex. I'm really thankful to Professor Maarten de Wit for accepting to co-supervise this study at a late stage after the untimely death of Professor Henri Kampunzu. I have enjoyed his provocative questions that always stimulate critical thinking.

I also gratefully acknowledge the financial support provided by the USHEPiA through the University of Botswana. The aim of USHEPiA is to establish research collaboration between the University of Cape Town and some African universities including University of Botswana, in addition to capacity building at the partner universities. I'm thankful to all USHEPiA staff members for putting in place the necessary logistics for the success of this study.

Geochronological and geochemical data constitute the core of the thesis. Therefore, different people involved in acquisition of the high quality and reliable data achieved in this study are greatly acknowledged. They are Professor Dave Reid for XRF analyses, Dr. Andreas Späth for ICP-MS

analyses, Shereen Govender for Sr, Nd and Pb isotope analyses, Dr. Richard Armstrong for U-Pb geochronology analyses, and Professor Chris Harris for O stable isotope analyses.

Many thanks go to the department of Council for Geosciences at Pretoria for allowing me to use their zircon mineral separation facility free of charge and Mr. Elijah Nkosi for sharing his long experience in zircon separation with me. I'm also thankful to Mr. David Wilson for the thin section preparation. Mr. Ernest Stout is thanked for assisting with sample preparation for geochemical analyses.

I wish to thank my family at large, brothers and nephews for the moral support and encouragement they provided through out this study. To my daughter (*Unaswi*) and son (*Wetsho*), many thanks for bearing my long absence from home. Zillion thanks to my fiancé, Ketty for her indulgence and vital moral support as well as needed love during the extended time intervals of separation.

Finally, but not least I'm thankful to my colleagues and friends: Albertina, Dylan, Mxolisi, Robert, Tshifi, Tim, Eugene, Folefoc, James and Megane for their solidarity. I extend my gratitude to all the USHEPiA fellows that I have shared moments of loneliness and isolation from our families.

LIST OF FIGURES

illustrating effects of subduction (s), crustal assimilation (c), mantle (m) and fractionation (f). Abbreviations: TH-Tholeiite; CA-calc alkaline.

Fig. 9.5: Plot of εNd (t) versus Th_N/Nb_N (chondrite normalizing values are from Wood et al., 1979) for mafic lavas from the Tati and Vumba greenstone belts to illustrate probable sources of contamination. The diagram is after Sandeman et al. (2006).

Fig. 9.6: Ni against Zr log-log diagram for the (a) Tati mafic lavas and the (b) Vumba mafic lavas. Theoretical Rayleigh fractionation vectors modelled for crystallization of individual minerals and mineral assemblages are indicated.

Fig: 9.7: Plot of mafic lavas from the Tati greenstone belt on diagrams: (a) La/Sm versus La, (b) Sm/Yb versus Sm and (c) Sm/Yb versus La/Sm showing melt curves obtained using the non-modal batch melting equation of Shaw (2006). Black, blue and magenta coloured curves correspond to DMM, PM and mantle source similar to the Phoenix gabbro composition, respectively. The ticks on each curve correspond to degrees of partial melting for a given source mantle. Depleted mid ocean ridge basalt mantle (DMM) source composition is from McKenzie and O'Nions (1991). Primitive mantle (PM) composition is from Sun and McDonough (1989).

Fig. 9.8: Plot of mafic lavas from the Vumba greenstone belt on diagrams: (a) La/Sm versus La, (b) Sm/Yb versus Sm and (c) Sm/Yb versus La/Sm showing melt curves obtained using non-modal batch melting equation of Shaw (2006). Black and blue coloured melting curves correspond to DMM and PM sources, respectively. The ticks on each curve correspond to degrees of partial melting for a given source mantle. Depleted mid ocean ridge basalt mantle (DMM) source composition is from McKenzie and O'Nions (1991). Primitive mantle (PM) composition is from Sun and McDonough (1989).

Fig. 9.9: Plot of the mafic lavas from (a) Tati and (b) Vumba greenstone belts on the Ce/Nb versus Th/Nb diagram (after Saunders et al., 1988), which shows the various mantle components as follows: depleted MORB mantle (DMM)-source of mid ocean ridge basalt; residual slab component (RSC); and subduction derived component (SDC). The following fields are shown for comparison: normal ocean ridge basalt (N-MORB), enriched mid ocean ridge basalt (E-MORB), ocean island basalt (OIB), primordial mantle (PM), Broken Ridge Ocean Plateau (BROP), Back Arc Basin Basalts (BABB)from Marianas Trough, Iceland plume basalts, basalts from the Sea of Japan and Marianas arc basalts. The fields were adopted from Kerrich et al. (1999), Polat et al., 1999 and Sandeman et al. (2006).

Fig. 9.10: Plots of REE patterns of adakites from the (a) Tati and (b) Vumba greenstone belts compared with the average Cenozoic adakites (from Drummond et al., 1996) and Neoarchaean adakites from the Wawa and Birch-Uchi greenstone belts in Superior province. The data for the Birch-Uchi and Wawa greenstone belts are from Hollings and Kerrich, 2000; Polat and Kerrich, 2001, respectively.

Fig. 9.11: Plots of REE patterns of adakites from the (a) Tati and (b) Vumba greenstone belts compared with the Neoarchaean adakites from the Wutai greenstone belt in North China Craton. The data for the Wutai greenstone belts are from Wang et al. (2004).

LIST OF TABLES

CHAPTER 1

Introduction

1.0 Background of study

Despite numerous studies on the composition and structure of Archaean crust, many contentious issues remain. Some of the contentious issues include the mechanisms of initial extraction of primitive crust from the mantle and the processes by which this crust was converted into the first continental crust (Puchtel et al., 1995), the mechanism and rate of formation of cratonic lithospheric mantle keels underlying the Archaean crust, genetic relationship between the cratonic lithospheric keels and their overlying crustal sections (Davis et al., 2003), the volatile content of the mantle during the Archaean (Burke, 1997; de Wit, 1998), the temperature of the Archaean mantle (Abbott et al., 1994), the nature of the atmosphere (Burke, 1997), the amount and effects of more radioactive heat production (de Wit, 1998), the formation of first oceans and the nature of their depth (de Wit and Hynes, 1995), type of tectonic regime during the Archaean (Hamilton, 1998; de Wit, 1998), and rate of crustal accumulation and recycling (e.g. Puchtel et al., 1995; Bowring and Williams, 1999). Recently, geochemical studies on ancient detrital zircons have unraveled evidence of existence of at least some continental crust and surface water on the Earth by 4.4 Ga ago (e.g. Wilde et al., 2001; Mojzsis et al., 2001) less than 200 Ma since the formation of Earth (4.6 Ga). This is consistent with the initial epsilon Nd (ε_{Nd}) values as high as +3.5 in 3.8 to 4.0 Ga rocks from the Acasta gneiss and Greenland (Table 1.1). These high positive epsilon Nd values suggest that melt extraction from the mantle had occurred for a significant period prior to 4.0 Ga. Indeed crustal evolution has a long and complex geologic history.

To date the oldest known exposures of ancient continental crust on Earth are the 4.03 Ga granitoid gneisses (Goodwin, 1996; Bowring and Williams, 1999; Mojzsis et al., 2001; Wilde et al., 2001). Granite-greenstone terrains are among the most ancient fragments of the Archaean Earth's crust which constitute about 7.5% of the aerial extent of present continental crust (de Wit and Ashwal, 1997). The current knowledge on the early Earth's evolution and Archaean tectonics has emanated from the investigations of Archaean granite-greenstone terranes (e.g. Sandeman et al., 2004). These ancient crustal fragments provide direct evidence for the processes and results of early Earth evolution (Bowring and Williams, 1999). Several models

have been proposed for the origin of Archaean granite-greenstone terranes, however, such models have generated extensive debate regarding the extent to which modern tectonics are applicable to early Earth history. Proposed models range from oceanic to continental basins, island arcs to marginal basins, ocean ridge to plume-related oceanic plateaus, and accretionary to vertical tectonics (e.g. de Wit and Ashwal, 1997; Hamilton, 1998; Smithies et al., 2005; Condie, 2005a).

In Archaean terranes, mafic and felsic lavas are invariably found in close association with granitoids of tonalite-trondhjemite-granodiorite (TTG) composition. However, the temporal and genetic relationship between the lavas and TTGs has been one of the contentious issues in discussions about Archaean crustal growth. The area in NE Botswana has a classic example of an Archaean granite-greenstone complex, and is therefore a good site for studying Archaean crustal growth processes.

Table 1.1: Summary table of epsilon values recorded from some of the oldest known rocks on Earth.

Rock	Location	Age (Ga)	εNd (T)	Reference
Tonalitic gneiss	Acasta gneiss	4.0	3.5	Bowring and Housh, 1995
Amphibolitic gneiss	Acasta gneiss	4.0	-4.8	Bowring and Housh, 1995
Granitic gneiss	Acasta gneiss	3.94	3.6	Bowring and Housh, 1995
Pillow basalt	Greenland	3.81	2.6	Blichert-Toft et al. (1999)
Pillow basalt	Greenland	3.81	3.0	Frei and Jensen (2003)
Pillow basalt	Greenland	3.81	2.5	Frei and Jensen (2003)

The thermal regime of the Archaean mantle has been the subject of extensive debate. Most of the data on Archaean mantle temperature have come from Archaean komatiite studies (e.g. Nisbet and Fowler, 1983; McKenzie, 1984; Nisbet et al., 1993). Komatiites are extrusive ultramafic rocks found in Archaean greenstone belts and have been used to calculate the highest magma eruption temperatures in the Archaean (Nisbet et al., 1993).

Some workers have argued that komatiites were generated at hotspots hence cannot be used to calculate normal Archaean mantle temperature (e.g. Campbell et al., 1989; Abbott et al., 1994). However, Parman et al. (2004) presented a model demonstrating the possible generation of komatiites in Archaean subduction zones. These authors suggest that the melting regime during the Archaean was higher than the Phanerozoic by 100 °C, and it took place at greater depth. This debate on Archaean thermal regime is complicated by the uncertainty of the water content

of the Archaean mantle. There is the contention that high volatile content in the upper mantle would lower its potential temperature (e.g. Smith and Lewis, 1999).

The debate about Archaean tectonics and geodynamics is centered around two principal schools of thought. One school of thought strongly believes that modern type plate tectonics only started in the Proterozoic era, and prior to that mantle plume processes dominated (e.g. Hamilton, 1998; Goodwin, 1996; Park, 1997; Stern, 2002; Condie, 2005b). The other school contends that there is substantial geological evidence to support the existence of modern type of plate tectonics during the Archaean (e.g. Kroner, 1991; Windley, 1995; Condie, 1997; Percival, 1997; de Wit, 1998; Windley, 1998; Komiya et al., 1999; Kampunzu et al., 2003; Manya, 2004; Srivastava et al., 2004; Wang et al., 2004; Martin et al., 2005; Smithies et al., 2005; Sandeman et al., 2006). However, these latter workers acknowledge that the rate of plate tectonic processes during the Archaean may have been different from modern plate tectonic processes, perhaps due to high heat production in the upper mantle emanating from high abundance of radiogenic elements at that time. Thus, according to these workers the differences between Archaean and modern plate tectonics occurring are largely differences of degree not of style. On the other hand the critics of plate tectonics in early Earth argue that high heat production during the Archaean implies that Archaean lithosphere must have been hotter, less rigid and more buoyant, preventing plate tectonics in the modern style (e.g. Hamilton, 1998; Condie, 2005b).

Other important gray areas about the Archaean Earth include the volume of water at the surface and the effects of high heat produced by abundant radioactive elements (Burke, 1998; Abbott et al., 1994). The rate of radiogenic heat production at the end of Archaean was 1.6 to 2.8 times the present day heat production rate (Pollack, 1997). Whilst the high content of radioactive elements during early Earth history generated more heat in the mantle, the responses to that heat are still a contentious issue. According to Abbott et al. (1994) there are five processes that are responsible for controlling the heat flow from the interior of the Earth. The processes include radioactive heat production, the transport of heat across the core-mantle boundary, heat transport by convection in the mantle, crustal formation, and the conductive cooling of the lithosphere. The first two processes add heat to the mantle while the remaining three processes remove it. Despite the uncertainty of the effects of high heat production, some studies (Nisbet and Fowler, 1983; Davies, 1993; Karsten et al., 1996) envisage that high heat production

caused more vigorous mantle convection, faster spreading rates along mid-ocean ridges and greater volumetric production of oceanic lithosphere.

1.1 Cratons

Most Archaean crust is preserved within cratons. Archaean cratons are defined as pre-2.5 Ga complex fragments of continental lithosphere that has attained and maintained long-term stability (Bleeker, 2003). Most cratons are bounded by rift margins or Proterozoic collision belts which led to some workers to suggest that they are fragments of larger ancestral landmasses (e.g. Williams et al., 1991) called supercratons. For instance the Kaapvaal craton is proposed to have been connected to the Pilbara craton of Western Australia in a Vaalbara supercraton (Cheney, 1996) whereas the Zimbabwe craton is identified as a Slave-like craton which was prossibly a nearest neighbour to the Slave craton in the Neoarchaean supercraton termed Sclavia (Bleeker, 2003). One of the defining features of Archaean cratons is the presence of a thick lithospheric mantle keel, termed tectosphere, which commonly extends to the diamond stability field (Wyman and Kerrich, 2002). The tectosphere is characterised by high P-wave velocities, low geothermal gradient and chemically depleted composition (Davis et al., 2003). Thus long term stability of a craton is commonly attributed to the insulating effects of a thick, non-convecting, relatively cool and compositionally depleted and buoyant mantle keel beneath (Ballard and Pollack, 1987). It has been realized that lithospheric mantle keel thickness can vary by upto 200 km within and between cratons (e.g. Fouch et al., 2004; de Wit et al., 2004; Jones et al., 2003). The presence of mantle keels helps to preserve ancient continental crust such as Archaean granite-greenstone terrains. However, the timing and mechanism of development of lithospheric keels that characterise cratons is still a matter of debate (e.g. King, 2006). Most proposed models in development of cratonic keels implicate the formation of greenstone belts as the cause of depleted buoyant residue that subsequently ascend diapirically to form Archaean cratonic roots (e.g. Wyman and Kerrich, 2002; Parman et al., 2004; Manikyamba et al., 2004). Alternative models imply that the lithospheric keel attachment to the base of crustal lithosphere was synchronous with crust formation. These are models which envisage voluminous mantle plume activity to generate an ocean plateau-like crust floating on a depleted, buoyant and unsubductable subcontinental lithospheric mantle. Thus studies of ancient greenstone belts and their host cratons are essential in understanding the early Earth processes such as cratonisation, origin and evolution of the Archaean continent. Diamond studies have

shown that formation of diamond in Archaean cratonic mantle is episodic, and that episodicity applies to the formation and stabilization of the cratonic mantle (e.g. Shirey et al., 2003).

The geological record has revealed that cratons are the hosts of the Archaean granite-greenstone terrains and the debates on the origin and evolution of the cratons mirror those of granite-greenstone terrains. For instance there is great variation in the postulated rates of formation and evolution of individual cratons and greenstone belts. For example U-Pb geochronology has revealed that the Superior craton of Canada formed within time span of 500 Ma, with the majority of crustal formation including its famous greenstone belt, the Abitibi belt, in less than 100 Ma. In contrast, the Kaapvaal craton of Southern Africa developed over a longer period spanning about 1000 Ma (de Wit et al., 1992) with its Barberton greenstone belt documenting a polyphase tectonic evolutionary history spanning about 500 Ma (de Ronde and de Wit, 1994).

The southern Africa Archaean continental crust is made up of the Kaapvaal and the Zimbabwe cratons which are joined along the Limpopo orogenic belt. The two cratons collided along the Limpopo orogeny in the Neoarchaean (de Wit et al., 1992), but still share little tectonic history. Some workers argue that the two cratons appear radically different and probably did not collide until 2.0 Ga, which is the age of a high-grade metamorphic event in the Limpopo belt (Holzer et al., 1998). These authors contend that there is no evidence of shared tectonic history prior to 2.0 Ga. Some of the arguments raised are that the Transvaal Supergroup and the Bushveld Complex have no expression in the Zimbabwe craton and, vice versa, the craton-wide ca. 2600 Ma Chilimanzi Suite and 2574 Ma Great Dyke do not cross the high-grade Limpopo orogenic belt into the Kaapvaal craton.

1.1.1 Kaapvaal Craton evolution

The Kaapvaal craton which formed and stabilized between 3.7 and 2.7 Ga, is an aggregate of crustal blocks welded by accretionary processes (de Wit et al., 1992; Carlson et al., 1996; Smith et al., 2004). These crustal blocks have been labeled the Swaziland, Witwatersrand, Kimberley, Pietersburg and Kalahari blocks (see Fig. 1.1). The oldest rock formation dates occur in the Swaziland block which is in the southeastern block of the Kaapvaal craton. This southeastern portion of the Kaapvaal craton formed the nucleus of the craton, and it hosts the c.3.7 Ga Ancient Gneiss Complex and the famous Barberton Greenstone belt. Recent studies have

indicated different amalgamation periods between the blocks. The Swaziland and the Witwatersrand blocks were joined at c.3.23 Ga (de Ronde and de Wit, 1994) and by c.3 Ga this eastern block was already stabilized to support the deposition of the extensive sedimentary basins such as the Witwatersrand Supergroup in the centre of the craton and the Pongola Supergroup in the southeast. The collision time between the eastern block (merged Swaziland and Witwatersrand blocks) and the western Kimberley block falls between 2.92 and 2.76 Ga (de Wit and Tinker, 2004). These two blocks amalgamated along shallow west-dipping thrust zones (de Wit and Tinker, 2004), not along the Colesberg magnetic lineament as proposed elsewhere (e.g. Schmitz et al., 2004). The collision between the northern Pietersburg block and the eastern block occurred between 2.93 and 2.88 Ga (de Wit et al., 1992). Silver et al. (2004) suggest that the collisions of both the Kimberley and Pietersburg blocks with the eastern block imparted some mechanical anisotropy to the mantle that were subsequently reactivated by younger Neoarchaean collision events resulting in some of the major magmatic events experienced by the craton. Such an example is the Ventersdorp magmatic event. The crust beneath the central Kaapvaal Craton is thinner (de Wit and Tinker, 2004), like crust that has been severely extended subsequent to accretion (e.g. Mortimer et al., 2002). Ventersdorp tectonism at ca. 2.7 Ga caused significant extension of the Kaapvaal crust. Seismic data from the central and western blocks of the Kaapvaal Craton exhibit earlier tectonic structures, indicative of compressional tectonism, preserved below the Moho (de Wit and Tinker, 2004). This has been interpreted as an indication of involvement of mantle material in accretion processes.

Seismic studies have revealed that the Kaapvaal craton is underlain by a thick (250 to 300km) lithospheric mantle keel (James et al., 2001; Stankiewicz et al., 2002; Fouch et al., 2004). However, the mechanism of the formation of this mantle keel is still a matter of debate. The ideas emerging from this debate include the following models which are not mutually exclusive: (1) Depleted mantle residues that formed in response to komatiite formation in Archaean subduction environment (Parman et al., 2004), (2) A two-step lithospheric mantle keel creation model as suggested by diamond researchers (e.g. Richardson et al., 1984; Shirey et al., 2003, 2004). The first step was mantle depletion below early continental nuclei due to high degree melting events that occurred in the Mesoarchaean. This step is associated with the oldest harzburgitic diamond formation. The second step involves subduction-accretion events that took place in the Neoarchaean resulting in amalgamation of cratonic blocks and further depletion of

the mantle and subsequent craton stabilization. The prevalent Neoarchaean eclogitic diamonds formation is suggested to have been an integral part of this second step.

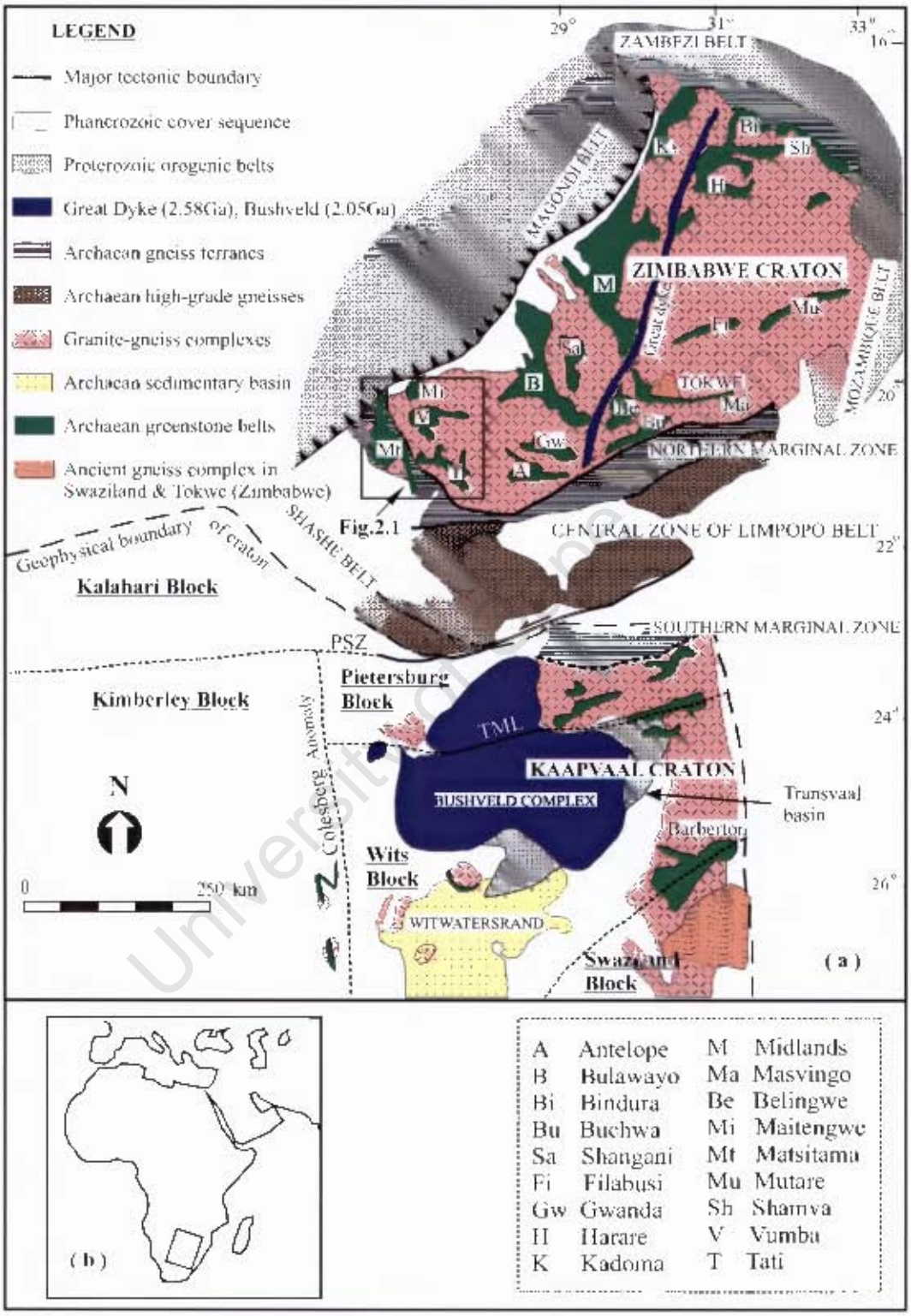

Fig. 1.1: (a) Map showing the main geological units of southern Africa cratons and adjacent Proterozoic belts (modified after Bagai et al., 2002; Eglington and Armstrong, 2004), names of the Zimbabwe and Botswana greenstone belts are given in inset. (b) Location of the southern Africa cratons in Africa.

1.1.2 Zimbabwe Craton evolution

The Zimbabwe craton has a long and complex geotectonic evolutionary history with a time span of at least 1000 Ma (Dirks and Jelsma, 2002; Jelsma and Dirks, 2002). Unlike the Kaapvaal very little is known about the Zimbabwe craton's lithospheric mantle, whose seismic thickness varies between 225 and 250 km (Silver et al., 2004). Re-Os studies have established that some of its lithospheric mantle was separated from the asthenosphere at least 3.8 Ga ago (Nägler et al., 1997). Previous studies have established that the evolution of Zimbabwe craton involved successive accretion and magmatic phases (e.g. Wilson et al., 1995; Jelsma and Dirks, 2002; Dirks and Jelsma, 2002; Hofmann et al., 2003; Prendergast, 2004) each encompassed the deposition of volcano-sedimentary sequence and the emplacement of granitoids (Hofmann et al., 2003). The early cratonic nuclei (the Tokwe block) in the central Zimbabwe craton formed between 3.57 and 3.35 Ga through lateral accretion of greenstones of the Sebakwean Group and tonalitic to trondhjemitic gneiss complexes (Wilson et al., 1995; Dirks and Jelsma, 2002). These gneisses and the Sebakwean greenstones were intruded by the 3.38 Ga Mushandike granite and 3.35 Ga Mont d'Or' granite, which possibly marked the stabilization of a Sebakwe proto-craton. Some workers (e.g. Kusky, 1998; Horstwood et al., 1999) interpret the sporadic Mesoarchaean U-Pb zircon dates within the Zimbabwe craton as evidence for an extensive old crustal block underlying a large area of the craton. Alternatively, Jelsma et al. (1996) considered them as older crustal nuclei against which newly formed crust accreted. However, it is also possible that the sporadic Mesoarchaean ages represent isolated continental fragments which were subsequently accreted.

The stabilization of the Sebakwe proto-craton was followed by clastic sedimentation along the western and southern margins between 3.10 and 2.95 Ga (Dirks and Jelsma, 2002). The stratigraphy comprises a transgressive sequence of conglomerates, sandstones, siltstones, shales, chert and ironstone. Detrital zircons from these sedimentary units give dates ranging between 3.81 and 3.06 Ga (Dodson et al., 1988; Dirks and Jelsma, 2002), which implies the existence of older crust than the Tokwe block but not necessarily preserved in Zimbabwe. A comprehensive geochronological spatial data base from Jelsma and Dirks (2002) demonstrates that magmatism started along the western margin of the Sebakwe proto-craton and produced the 2.90 to 2.88 Ga Belingwean Supergroup greenstones (Wilson et al., 1995) followed by the Lower Bulawayan Supergroup greenstones between 2.83 and 2.79 Ga. Tonalite-trondhjemite-granodiorite (TTG) granitoids aged between 2.98 and 2.75 Ga intruded the proto-craton and

Lower Bulawayan greenstones, and have been interpreted as the plutonic equivalents of the Belingwean Supergroup and Lower Bulawayan Supergroup felsic volcanics (Wilson et at., 1995; Jelsma et al., 1996). These intrusions have been named the Chingezi suite (Wilson et al., 1995).

The most voluminous greenstone successions in the Zimbabwe craton were formed between 2.75 and 2.65 Ga (e.g. Jelsma and Dirks, 2002). These greenstone successions are sub-divided into c.2.75 Ga Upper Bulawayan and the c.2.65 Ga Shamvaian volcano-sedimentary greenstone belt sequences (Jelsma et al., 1996; Hofmann et al., 2003). Notably, there are two distinctly different greenstone successions recognized within the Upper Bulawayan Group (Wilson, 1981; Jelsma and Dirks, 2002). The first succession has been associated with rift or back-arc settings and is confined to the eastern part of the craton. Examples of such greenstone successions are the Belingwe, Filabusi, Shangani, Shurugwi and Gweru all located in the central to eastern part of the Zimbabwe craton (Fig. 1.1). In the Belingwe area, the Upper Bulawayan succession is located between the 3.57 to 3.35 Ga proto-craton and c.2.9 to 2.8 Ga Lower Greenstone crustal segments trending north-northeast to south-southwest. Here a basal sedimentary succession is overlain by thick pile of ultramafic and mafic volcanics which have been dated at 2.69 Ga. However, the contact between the sedimentary succession and the volcanic pile is a high-strain zone and has been interpreted differently by different workers. For instance Blenkinsop et al. (1993) interpreted it as conformable but accommodating layer parallel slip during deformation of the belt. On the other hand Kusky and Kidd (1992) described it as a detachment surface that accommodated obduction of an oceanic plateau.

The second type of greenstone succession of the Upper Bulawayan Supergroup comprises a chain of greenstone belts along a ~700 km long northeast-southwest trend, which have been interpreted as a calc-alkaline volcanic arc that developed in the northwestern margin of the 3.57 to 2.75 Ga continent between 2.72 Ga and 2.68 Ga (Jelsma and Dirks, 2002). This 700 km long chain of greenstone belts extends from the Vumba greenstone belt in Botswana in the southwestern to the Mount Darwin greenstone belt in Zimbabwe in the northeastern of the craton (Fig. 1.1). These greenstone successions comprise on average 35% andesite, 15% rhyodacite, 30% basalt, 2% komatiites and 18% sedimentary rocks (Jelsma and Dirks, 2002). Both types of greenstone belts are associated with felsic intrusions ranging in age from 2.72 to 2.68 Ga which has been referred to as the Sesombi suites (Wilson et al., 1995). A younger phase of volcanism between 2.65 and 2.64 Ga is superimposed on the c.2.7 Ga Upper

Bulawayan Group and it has been interpreted as a late subduction-related magmatic event (Jelsma and Dirks, 2002). This event has been reported in the NE part of the craton (Harare greenstone belt), where felsic volcanism has been dated at 2.65 Ga (Jelsma et al., 1996) and is associated with the emplacement of late-tectonic tonalites and granodiorites dated at 2.65 Ga (Wilson et al., 1995). In contrast, in the southwestern part of the craton (Vumba greenstone belt) only late-tectonic monzogranite was emplaced at 2.65 Ga (Bagai et al., 2002).

Pan-cratonic emplacement of granodiorites and monzogranites of the Wedza and Chilimanzi suites occurred at c.2.6 Ga (Dirks and Jelsma, 2002). Nevertheless, these magmatic events are absent in the southwestern margin of the Zimbabwe craton. Jelsma and Dirks (2002) interpreted the Chilimanzi suite as crustal melts induced by overthickening caused by accretion. However, Kampunzu et al. (2003) suggest that crustal melting was initiated by lithospheric delamination or subduction slab break-off. It is the Chilimanzi suite which marked the final stabilization of the Zimbabwe craton. The Great Dyke was intruded into this stabilized craton at 2.58 Ga (Horstwood et al., 1999) and its emplacement is believed to be controlled by a conjugate fault set related to the north-northwest to south-southeast crustal shortening during the Limpopo orogeny (Silver et al., 2004). It is suggested that the Great Dyke was emplaced through a pre-existing inherited zone of rheological weakness in the lithospheric mantle that possessed a north-northeast to south-southwest orientation, which was reactivated during the collision between the Limpopo Central and Northern Marginal Zones (Silver et al., 2004).

The structural deformation history of the Zimbabwe craton is complex, as reflected by preponderance of thrust faults, recumbent folding and shear zones bounding low strain zones (e.g. Dirks and Jelsma, 2002). Thrust zones have significant implications for reconstructing the stratigraphy of the greenstone successions of the craton. They prompt the suggestion that some greenstone sequences are allochthonous and may have formed in unrelated tectonomagmatic environments. Anastomosing layer-parallel shear zones associated with east-west trending lineation (e.g. Dirks and Jelsma, 2002) are a common feature in the Zimbabwe craton. Dirks and Jelsma (2002) noted that the distribution of the main shear zones centred on the greenstone sequences tends to define a blocky pattern of bounded nappes that trend northeast and northwest and to lesser extent north and south. These blocks of nappes are arranged in an overlapping "fish-scale" like morphology with east dipping thrusts migrating westward (Fig. 1.2). It is believed that these patterns that are also parallel to the orientation of subduction related

greenstone successions, and base-metal mineralization (Dirks and Jelsma, 2002). All of these features developed between 2.68 and 2.60 Ga (Jelsma and Dirks, 2000). The interpretation of this tectonic pattern is contentious: some workers attributed it to late strike-slip faults originating in already stabilized craton (e.g. Treloar and Blenkinsop, 1995; Herrington, 1995), while others relate the pattern to Archaean lithospheric structures to have originated in a brittle upper mantle (e.g. Dirks and Jelsma, 2002).

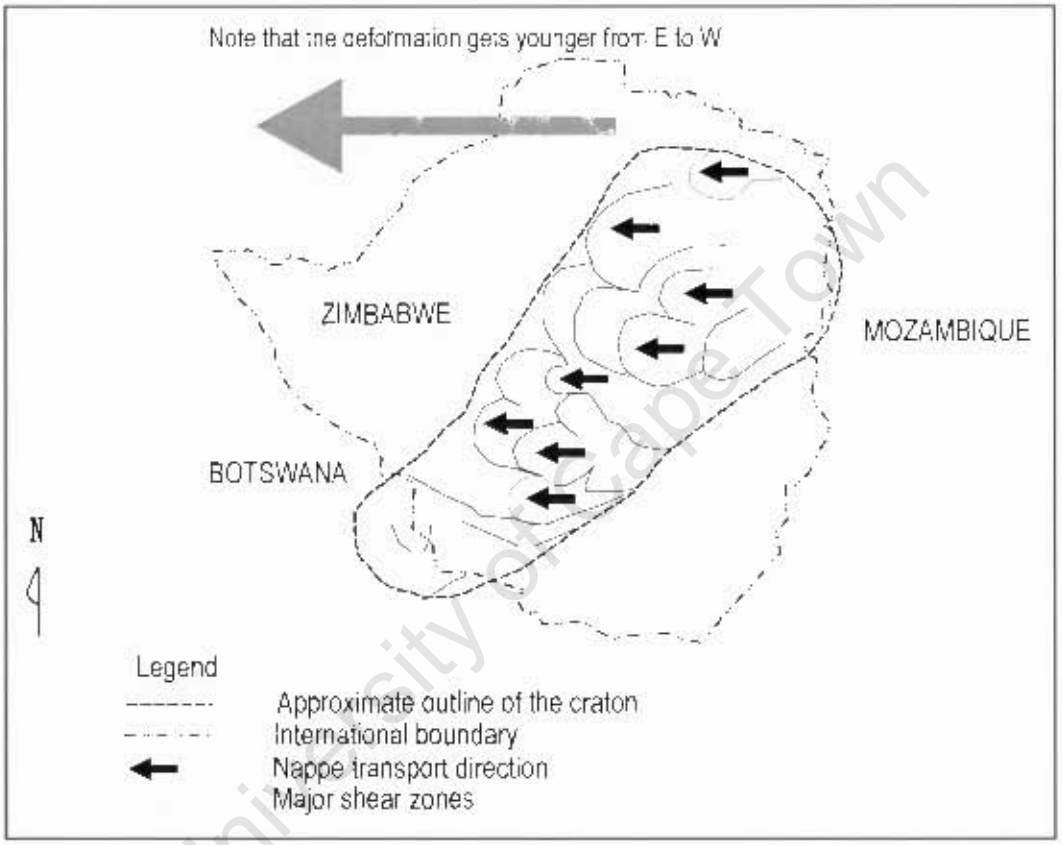

Fig. 1.2: A schematic diagram to illustrate the blocky "fish-scale like" pattern and westward thrusting of nappes (2.68 – 2.60 Ga) in the Zimbabwe craton (after Dirks and Jelsma, 2002).

1.2 Archaean Granite-Greenstone terrains

Archaean granite-greenstone terrains are the crustal component of the cratons. Much of the current understanding of the early Earth's evolution history has emanated from systematic investigations of the Archaean granite-greenstone terranes (Sandeman et al., 2004b). Nevertheless, the origin and formation of the Archaean granite-greenstone terrains around the world continue to be debated with regard to the roles of subduction, plume magmatism, rifting, and autochthonous versus allochthonous development (e.g. Polat, 1999; de Wit, 1998; Smithies

et al., 2005). To date no single tectonic model for their evolution exists (Burke, 1997; Hofmann et al., 2003). Instead, geoscientists agree to disagree on a single model for the origin of greenstone belts and granite-greenstone terrains. There is now a growing realization that some of the greenstone belts are composites of different terranes (Burke, 1997). The controversies are partly caused by structural complexities, which obliterate the nature of granite-greenstone contacts, complicating tectonic interpretations. In addition, the petrogenetic relationships between volcanic and plutonic components, which are often found in close spatial association in Archaean granite-greenstone terranes, have not yet been clarified satisfactorily. This study attempts to determine the petrogenetic relationship between such a diversity of igneous rocks found closely associated in space within the Francistown Granite-Greenstone Complex.

Understanding the mechanism and details of the various petrogenetic processes that were involved in the formation of Archaean granite-greenstone complexes would provide better insight into the evolution of the cratons and the original recycling of continents during early Earth history. The area in northeastern Botswana has rock assemblage of Archaean age that offer an opportunity to evaluate the tectonic processes occurring on the margins of the Zimbabwe Craton. Essentially, greenstone belts contain some of the oldest preserved mafic lavas derived from the Earth's mantle, and therefore provide a window into Archaean mantle compositions and mantle-crust evolutionary processes (Vennemann and Smith, 1999).

1.3 Justification of the study

This study sets out to examine the geochemistry of the Neoarchaean Francistown Granite-Greenstone Complex (FGGC) in northeastern Botswana that constitutes the southwestern margin of the Zimbabwe craton. To date there has been only limited and fragmented work on the Francistown Granite-Greenstone Complex, and in general these studies have been restricted to specific areas or selected rock units in a specific area of the complex. Examples of such recent work include the study of major and trace element geochemistry of plutonic rocks from Francistown by Kampunzu et al. (2003), the study of Sr and Nd isotope systematics of Francistown plutonic rocks by Zhai et al. (2006), U-Pb single zircon geochronology of granitoids in the Vumba granite-greenstone terrane by Bagai et al. (2002), the geochronological and geochemical investigation of the Vumba granite-greenstone terrane by Bagai (2000), and the structural architecture of Archaean terranes in northeastern Botswana by McCourt et al. (2004). In contrast, this study has been designed to obtain an overall synthesis of a large area of the

Francistown Granite-Greenstone Complex. The study has generated a wide range of new types of data, not acquired in previous studies.

Despite several detailed studies in the Francistown Granite-Greenstone Complex, the overall structure and geodynamic evolution of the complex are still poorly understood. For instance the extent and nature of petrogenetic relationships between the greenstone volcanics, the voluminous TTG type granitoids, mafic intrusions and the post-kinematic high-K granite suite of the Francistown Granite-Greenstone Complex, are poorly documented and analysed. The focus of this study is on the geodynamic and petrogenetic aspects engaging geochemical, isotope, petrological, geochronological data and field observations of the main rock assemblages of the Francistown Granite-Greenstone Complex.

The Zimbabwe craton, being a granite-greenstone composite type of craton, means the understanding of its origin from initial discrete terranes to a stable craton rests on among other factors understanding the crustal development of its constituent granite-greenstone terranes. The present study area is located along the craton margin contiguous to the Limpopo-Shashe orogenic belt, which renders it a good site to investigate the geotectonic relationship between the Archaean orogenic belt and the Zimbabwe craton. The results should enhance our knowledge on the Neoarchaean geology, crustal growth and cratonisation processes of the southwestern section of the Zimbabwe craton. From an economic perspective, it is worth mentioning that granite-greenstone terranes of the world host major ore deposits such as Au, Cu, Ni, PGE and Cr (Evans, 1993; Herrington, 1995; Herrington et al., 1997). Currently, two Cu-Ni deposits and one gold deposit are being mined in the study area. According to Whalen et al. (2004), Archaean low-Al TTGs, like the TTGs around the Francistown area (e.g. Kampunzu et al., 2003), have been documented to form small synvolcanic intrusions that underlie over 90% of known Precambrian volcanogenic massive sulfide deposits and have been linked genetically either as heat source and/or metal source to volcanogenic massive sulphides formation.

1.4 Objectives of the study

The primary objective of this study is to reconstruct a well-constrained geodynamic evolution model for the Neoarchaean Francistown Granite-Greenstone Complex. In order to achieve this, the most important issue to be resolved is the chronological sequence of magmatic events that produced the various rock assemblages of the Francistown Granite-Greenstone Complex and

establish the petrogenetic implications of the temporal relationships. This is attempted through U-Pb dating of zircons using the sensitive high-resolution ion microprobe (SHRIMP). A second objective is to test field relationships against petrogenetic relationship. The third objective is to determine possible constraints that can be placed on the sources of the parental melts of the various magmatic rocks within the Francistown Granite-Greenstone Complex.

1.5 Methodology

Field observations, geochronological, petrological, isotope systematics and geochemical analyses of diverse magmatic rocks of the Francistown Granite-Greenstone Complex were integrated to reconstruct the geodynamic evolution model for the complex. However, integrating different types of data from a wide variety of rocks is far from trivial. Different analytical approaches were employed in this study to achieve the project objectives.

1.5.1 Analyses

Petrography: Provides significant textural features and modal composition of rocks that can give insight into the magmatic evolutionary history and post crystallization history. In this study, 80 samples were thin sectioned and petrographically examined under the microscope.

Geochronology: Yields significant information on the age profile of the complex by constraining the period of magmatic events and the sequence in which they occurred, thus unraveling the magmatic evolutionary history of the igneous complex. Published geochronological data on Francistown Granite-Greenstone Complex were compiled and combined with the new age data generated in this study. The sensitive high resolution ion microprobe (SHRIMP) technique was used to date the zircons separated from 16 samples obtained from a variety of rock units within the Tati granite-greenstone terrain and surrounding areas.

***Bulk rock geochemistry*:** Constitutes major and trace element data. Major element data yield information on petrological processes that played a role in the magmatic history such as assimilation and fractional crystallization. Studying the distribution of certain trace elements in igneous rocks can yield important clues about the rock's origin and evolution. Trace elements do not give rise to characteristic minerals, but their behaviour can be modelled to provide historical information about the source magma as well as tectono-magmatic environment. Major element data was generated for all the samples using XRF spectrometry. .Trace element analyses on a

subset of representative samples were completed using ICP-MS. A major challenge with the geochemical study of Archaean volcanic sequences is to account for the effects of post-magmatic alteration on the primary composition of the volcanic rocks, otherwise the interpretation based on chemical parameters may be quite invalid. In order to mitigate against secondary alteration effects, various geochemical criteria were undertaken to test and detect the type and degree of alteration prior to any interpretation.

***Isotope geochemistry*:** Three radiogenic isotope systems and one stable light isotope system were employed. Radiogenic isotopes of Sr, Nd and Pb were analysed in whole-rock samples using a Finnigan-MAT261 thermal ionization mass spectrometer (TIMS) in the Radiogenic Isotope Facility in the Department of Geological Sciences, University of Cape Town. Oxygen stable isotope data was measured in quartz mineral separates from granitoids, whole-rock for some granitoids, and pyroxene mineral in case of gabbroic and dioritic rocks using a Thermo Finnigan Delta ^{Plus}XP mass spectrometer housed in the Archaeology Department, University of Cape Town. Radiogenic isotope ratios are commonly used in geochemistry as petrogenetic tracers, yielding information on time-integrated elemental fractionation through processes of melting, crystallization, metamorphism, metasomatism, and contamination (Davidson et al., 2007). Radiogenic isotopic ratios of Sr, Nd and Pb are not fractionated by processes of melting and crystallization (Dickin, 2005) and have thus become a commonly used tool for fingerprinting source contributions in magma suites. Nd is a rare earth element (REE) which may be more resistant to disturbances resulting from fluid-rock interactions and low-grade metamorphism, compared with Sr. Pb isotopes are useful in investigating intracrustal processes. Oxygen isotopes provide a way of distinguishing between rocks formed in equilibrium with the mantle and those which formed from the continental crust (Criss, 1999). Therefore, they are a valuable indicator of surface processes and a useful tracer of rocks that have been emplaced in the Earth's crust.

CHAPTER 2

Geological Setting and Sampling

2.0 Introduction

The geological framework of northeastern Botswana is dominated by Archaean crust that forms part of the Zimbabwe craton and the Limpopo orogenic belt (e.g. McCourt et al., 2004; Carney et al., 1994). The Zimbabwe craton is an oval NE trending (Fig. 2.1a) Archaean granitoid-greenstone terrain, c. 800 km long and up to 500 km wide (Prendergast, 2004; Jelsma and Dirks, 2000) largely confined to Zimbabwe with extension into NE Botswana (Key et al., 1976; Blenkinsop et al., 1997; Jelsma and Dirks, 2002). According to Carney et al. (1994) the sector of the Zimbabwe craton in Botswana occupies an area of about 60 000 km^2, about 15% of the entire craton.

2.1 Geology of NE Botswana

The geology of the northeastern Botswana is composed of distinct Archaean crustal complexes that were amalgamated during the Neoarchaean in response to accretionary processes (McCourt et al., 2004). The complexes include the Francistown Granite-Greenstone Complex, the Matsitama-Motloutse Complex and the Phikwe Complex (Fig. 2.1). The Francistown Granite-Greenstone Complex is regarded as a continental-margin (volcanic arc) that developed between 2.75 and 2.60 Ga (Kampunzu et al., 2003; Bagai et al., 2002). This complex constitutes the southwestern margin of the Zimbabwe craton in Botswana (Fig. 2.1). The metamorphic assemblages in the supracrustal rocks of the Francistown Granite-Greenstone Complex are predominantly at greenschist facies (McCourt et al., 2004; Coward and James, 1974). The Matsitama-Motloutse Complex is an accretionary assemblage, characterised by continental margin-type supracrustal rocks, and is in thrust contact with the Francistown Granite-Greenstone Complex along the Shashe shear zone (Fig. 2.1). According to McCourt et al. (2004) the supracrustal assemblage of the Matsitama-Motloutse Complex is younger than 2661 and older than 2647 Ma. Based on detrital zircon ages from the metasedimentary rocks that dominate the Matsitama-Motloutse Complex, it is suggested that the sediments were derived from the Francistown Granite-Greenstone Complex and its

hinterland (McCourt et al., 2004). The Phikwe Complex, which is part of the Limpopo Central Zone, is in contact with the Matsitama-Motloutse Complex along the Mogogaphate shear zone (Fig. 2.1). This complex is a high-grade metamorphic terrane (granulite facies) dominated by Neoarchaean granitoid magmatism (Kroner et al., 1999).

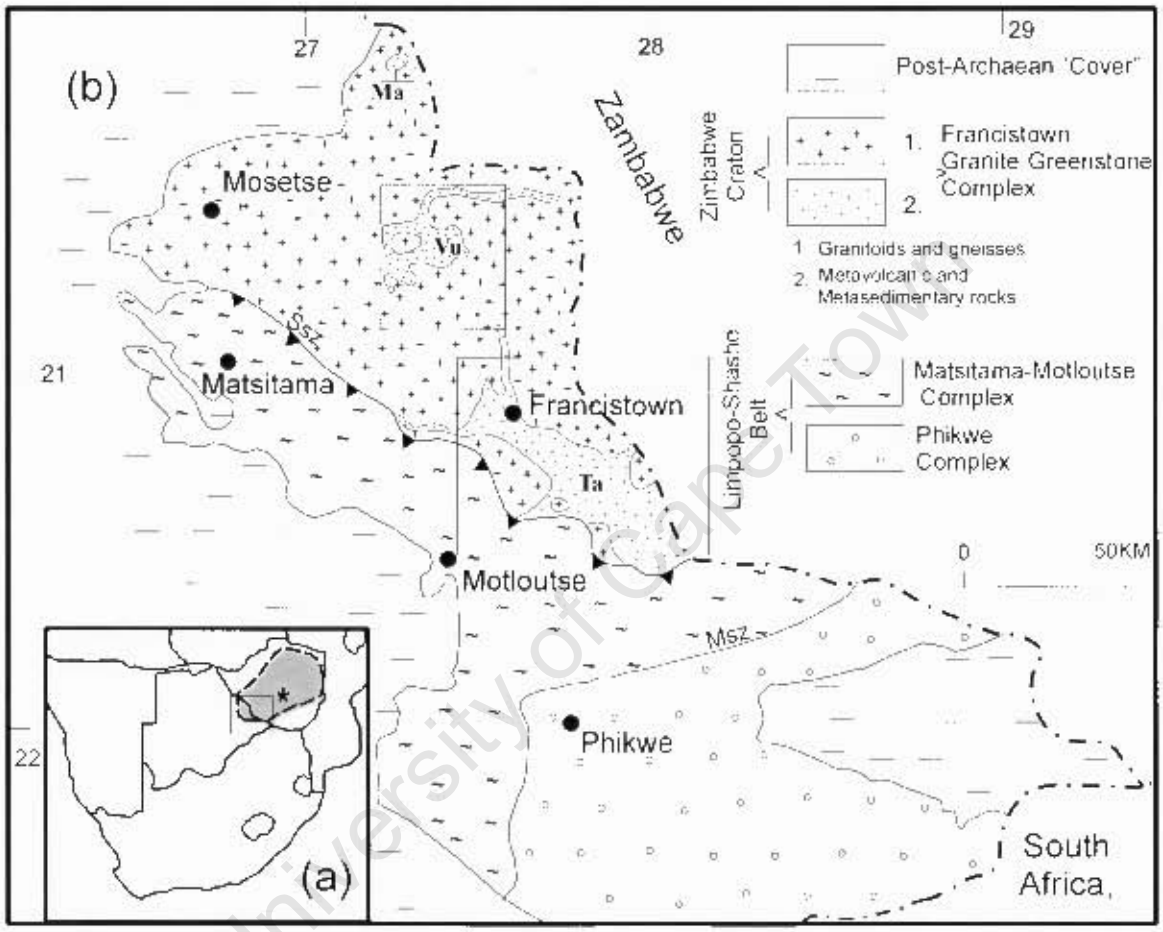

Fig. 2.1: (a) Locality map showing the position of the study area within the Zimbabwe craton; (b) The geology of the NE Botswana (after McCourt et al., 2004). Boxes highlight the three granite-greenstone terrains in the Francistown Granite-Greenstone Complex. Abbreviations: Ma-Maitengwe; Ta-Tati; Vu-Vumba; Msz-Mogogaphate shear zone; Ssz-Shashe shear zone ▼ ▼ ▼ .

On the basis of gravity data Ranganai et al. (2002) suggested that the Limpopo and Shashe belts belong to a single orogenic belt. According to these workers the Matsitama-Motloutse Complex is part of the north marginal zone of the Shashe section of the Limpopo-Shashe belt. This suggestion is compatible with the similarity in the zircon ages of the Neoarchaean in the Francistown Granite-Greenstone Complex, Matsitama-Motloutse Complex and the Phikwe Complex of the Limpopo belt (e.g. McCourt et al., 2004; Bagai et al., 2002; Kroner et al., 1999).

2.1.1 Geological setting of the Francistown Granite-Greenstone Complex

The Francistown Granite-Greenstone Complex is a composite granitoid-greenstone terrane comprising three individual greenstone belts associated with voluminous granitoid suites, minor mafic intrusions and wide distribution of gneisses. The greenstone terrains comprise metavolcanic and metasedimentary sequences at lower greenschist to lower amphibolite facies metamorphism (Key et al., 1976; Carney et al., 1994; McCourt et al., 2004). They also contain serpentinite and rare metapyroxenite. These greenstone sequences have been correlated to the Upper Bulawayan greenstone successions in Zimbabwe (e.g. Key et al., 1976).

The supracrustal rocks in the Francistown Granite-Greenstone Complex have been divided into three greenstone sequences, identified as the Maitengwe, the Vumba and the Tati greenstone belts (Fig. 2.1b; Key et al., 1976; Carney et al., 1994). The Maitengwe greenstone belt forms a tiny sequence underlain predominantly by banded ironstones in which magnetite-cummingtonite layers alternate with chert (Litherland, 1975). This banded iron formation is overlain by the Maitengwe Ultramafic Formation which comprises ultramafic schist associated with amphibolite, serpentinite and marble (Litherland, 1975; Carney et al., 1994). In terms of aerial size, the Maitengwe greenstone sequence covers small area of about 100 km^2 and it has been omitted from the current study. The focus is on the Tati and Vumba greenstone sequences that cover about 2100 km^2 and 1100 km^2, respectively. The two greenstone sequences display several lithological similarities which caused some workers to suggest that the two volcanic successions may be dismembered parts of an originally consanguineous supracrustal sequence (e.g. Litherland, 1975; Key, 1976). So far there is no tangible evidence to substantiate the above suggestion. A schematic stratigraphic column of the Tati and Vumba greenstone sequences is presented in Fig.2.2.

The Tati greenstone sequence has an overall length of about 70 km with a general northwest trend and has a maximum width of 30 km. It is subdivided from base to top into Lady-Mary, Penhalonga and Selkirk Formations (Key, 1976; Johnson, 1986; Carney et al., 1994). The Lady-Mary Formation is dominated by mafic lavas intercalated with minor felsic lavas and chemical sedimentary rocks. Minor ultramafic schist and concordant serpentinite horizons are recognizable in the southeastern part of the unit (Johnson, 1986). Pillow structures are preserved locally, which suggest that at least part of the formation is extrusive and was deposited under water (Fig. 2.3). The overlying

Penhalonga Formation predominately comprises andesitic lavas interbedded with metasediments. In most areas this formation comprises a uniform thickness of intermediate volcanics associated with shallow water sedimentary rocks. By contrast, the central area of the Penhalonga Formation consists of a thicker succession (~10 000 m) of interlayered andesitic lavas and interbedded fine-grained metasediments (Key, 1976). The existence of the Selkirk Formation is controversial. According to Key (1976) the Selkirk Formation occurs as a thick wedge-shaped formation dominated by a felsic succession at the top of the Tati belt sequence. However, mapping and petrographic study by Siegfried (1999) suggested that much of the area that Key (1976) believe is underlain by Selkirk Formation is actually underlain by tonalite-trondhjemite gneiss. This view is supported by this study because no outcrop of a felsic volcanic rock was observed during the field work in that specific area, except a few low-lying outcrops of granitoids resembling the tonalite-trondhjemite from the Sekukwe Pluton. Similar observations were made by Jackson (1981) who concluded that there seem to be no Selkirk Formation.

The geology of the Vumba greenstone belt has been described by several previous workers (e.g. Litherland, 1975; Rammlmair, 1986; Mosigi, 1987; Ludtke et al., 1989; Carney et al., 1994; Bagai, 2000). The Vumba greenstone sequence is subdivided in chronological order into the Sebina Ultramafic Formation, Vumba Mixed Volcanic Formation, Vumba Lower Felsic Formation, Vumba Lower Mafic Formation, Vumba Upper Felsic Formation and Vumba Upper Mafic Formation (Litherland, 1975; Carney et al., 1994; Fig. 2.2). The basal Sebina Ultramafic Formation contains poorly exposed talc-chlorite schist intercalated with amphibolite (Litherland, 1975). The widely distributed overlying Vumba Mixed Volcanic Formation predominately comprises mafic lavas, minor ultramafic schist and intrusives, felsic lavas, pyroclastics and metasediments. This formation hosts the serpentinite and metapyroxenite units that form rows of kopjes in the Vumba area. Litherland (1975) described these rows of kopjes of ultramafic rocks as syn-tectonic sills. Rammlmair (1986) remapped these rows of kopjes and interpreted them as flows at the base of volcanic sequence, i.e. an integral part of the Vumba volcanic sequence. In contrast, Ludtke et al. (1989) interpreted the ultramafic kopje rows as dykes and compared them to the Mashaba Complex in Zimbabwe. The Lower Vumba Felsic Formation contains felsic lavas, minor mafic lavas, chemical sediments and argillites (Litherland, 1975). The overlying Lower Vumba Mafic Formation is dominated by mafic lavas with minor felsic lavas, whereas the Upper Vumba Felsic Formation contains subordinate

aluminous schist in addition to felsic lavas. The top-most Upper Vumba Mafic Formation comprises predominately mafic lavas. The entire sequence was interpreted by Litherland (1975) as a submarine volcanic pile with a gradual trend towards acid volcanicity with intermittent clastic and chemical sedimentation.

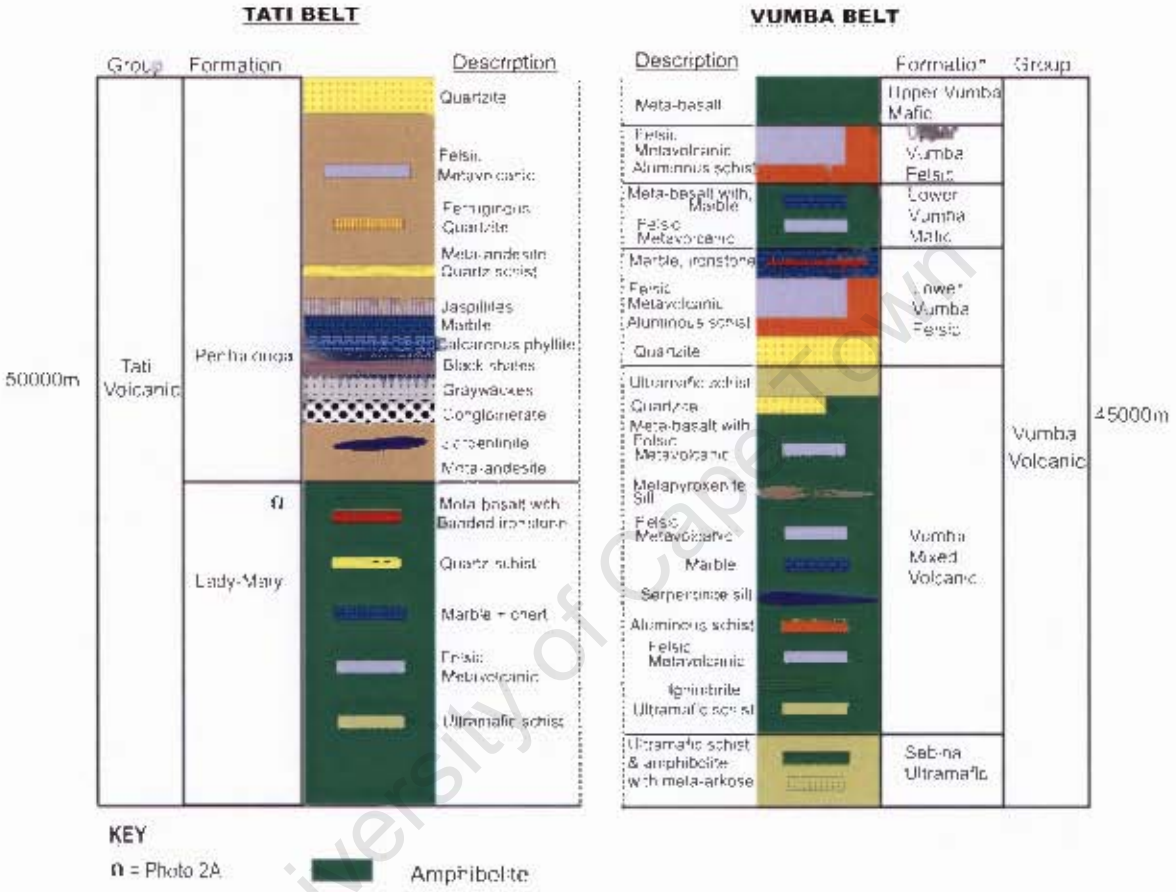

Fig. 2.2: Schematic stratigraphy of the Vumba and the Tati Volcanic Groups (modified from Key, 1976; Litherland, 1975; BGR, 1989; Carney et al., 1994; Siegfried, 1999)

Supracrustal rocks in the Francistown Granite-Greenstone Complex are associated with complexes of granitoid gneisses and massive granitoids. The massive granitoids vary in composition from quartz monzonite, monzogranite, granodiorite, trondhjemite to tonalite (e.g. Kampunzu et al., 2003; Bagai et al., 2002; Bagai, 2000; Carney et al., 1994; Ludtke et al., 1989; Litherland, 1975). Gabbro and diorite intrusions are less common. About one third of the Francistown Granite-Greenstone Complex is underlain by migmatitic to banded paragneisses (Crockett et al., 1974). Due to the poor level of exposure combined with high grade metamorphism (Key, 1976) and poor outcrop

conditions, the so-called paragneisses are poorly documented and they were given little or no attention in many previous investigations. They mainly outcrop in the river channels. The origin of these paragneisses is not well understood. Nevertheless, some previous workers (e.g. Key, 1976; Litherland, 1975) have advocated that strongly metamorphosed original supracrustal members of the Vumba, Tati and Maitengwe greenstone sequences, dominated by felsic metavolcanics and metasediments, represent the protolith for the paragneisses. They correlated these paragneisses to the paragneisses within the Limpopo-Shashe belt. According to Key (1976) the so-called anatectites represent local melting that occurred during the migmatisation event. Like previous studies, little attention is paid to the paragneisses in the current investigation. The reason is that the unit, whilst widely distributed, is very poorly exposed. To collect a representative number of good quality samples of the unit would mean spending considerable time hunting for outcrops over a large area. However, one sample GEOZB-1a from this unit was collected for geochronology in order to shed some light on the controversial age relationship of the paragneiss unit and the spatial associated granitoids in the area.

Fig. 2.3: Deformed pillow structures from the mafic lavas of Lady Mary Formation within the Tati greenstone belt, approximately at Ω in the stratigraphic column shown in Fig. 2.2.

The Maitengwe greenstone sequence is intruded by tonalitic and quartz monzonitic plutons (Litherland, 1975). In the Tati terrain the greenstone sequence has been intruded by quartz monzonite, monzogranite, trondhjemite, tonalite-trondhjemite, diorite and gabbro suites. The spatial relations of the quartz monzonite and tonalite-trondhjemite in the Tati terrain caused previous workers (Key, 1976; Litherland, 1975) to suggest that the latter has intruded the former to form ring-complexes. The monzogranite tends to occur in the form of dykes, and it cuts the rest of the granitoid types. Trondhjemite forms massive linear kopjes parallel to the trend of the Tati greenstone belt. It intrudes the top sequence of the Tati greenstone belt and the diorite unit. Lack of pervasive northwest-southeast solid state fabrics, in the trondhjemite led previous workers (e.g. Kampunzu et al., 2004; Key, 1976) to suggest that it post-dates the southwestern tonalite-trondhjemite plutons which are characterised by a strong NW-SE fabric. The tonalite-trondhjemite unit lying southwest of the Tati greenstone belt includes the Tati Pluton and its satellites, the Airport and South Tati Tonalite-Trondhjemite (Fig. 2.4). These are mainly foliated to banded grey gneisses with the main fabric trending parallel to the trend of the Tati belt. The tonalite-trondhjemite unit exposed in the northeast of the Tati belt includes the Sekukwe, the Mphoeng and the Matsiloje Plutons (Fig. 2.4). According to Kampunzu et al. (2003) metamorphism is of low grade in the northeastern tonalite-trondhjemite unit, as evidenced by local preservation of igneous foliation.

The diorite and gabbro intrusions are confined to the Tati area. Additionally, the dioritic rocks outcrop around the city of Francistown in the form of low kopjes (Fig. 2.4). The field age relationship with the neighbouring tonalite-trondhjemite unit of the Sekukwe pluton is unexposed. The gabbro forms two separate intrusions, which have been named the Selkirk and Phoenix gabbros. These gabbros are mineralized with Ni-Cu sulphides and are currently being mined for these commodities. The mineralization at Phoenix and Selkirk gabbros occurs largely in the form of massive and disseminated sulphides, respectively (Johnson, 1986). It is suggested that the massive sulphides in the Phoenix gabbro were generated from magmatic disseminated sulphides in the host rock by a heating event linked to the granitic to pegmatitic dykes that have intruded the gabbro (Johnson, 1986). It is probable that the dykes are related to the trondhjemite unit which intruded the central part of the Tati greenstone belt sequence. The age relationship between the gabbro and diorite is yet to be established. Key (1976) presumed that the gabbro intrusions are penecontemporaneous with the lavas of the Penhalonga Formation, which would imply that they are actually older than the

tonalite-trondhjemite unit. In contrast, Kampunzu et al. (2003) contend that the gabbros and diorite are younger than the tonalite-trondhjemite unit. Recently, Zhai et al. (2006) using Sm-Nd isochron dates argued that the tonalite-trondhjemite, diorite and the gabbro units are contemporaneous. However, the large errors associated with the Sm-Nd isochron dates (Zhai et al., 2006) render this data inconclusive. The geochronology of the Tati and Vumba terrains is discussed in the following chapter with the presentation of new U-Pb zircon dates.

Plutonism in the Vumba granite-greenstone terrain comprises quartz monzonitic, tonalitic, granodioritic and monzogranitic granitoids. The quartz monzonite forms a cluster of kopjes named the Kalakamati quartz monzonite, which display a strong foliation defined by biotite and hornblende. The tonalite unit occurs in the form of clusters of kopjes on the western to northern part of the Vumba belt and it has been named Maebe tonalite (Bagai et al., 2002). Its limit on the western contact is poorly defined due to the Kalahari cover. Unlike the quartz monzonite, the tonalite unit displays a weak foliation. The granodiorite unit comprises isolated bodies, which vary in dimension from pluton to stock size. The plutons of granodiorite include the Kalakamati and the Mashawe that have circular and oval shapes, respectively. The Kalakamati pluton intrudes the quartz monzonite unit and is therefore younger. The Mashawe pluton is conspicuously foliated whereas the Kalakamati pluton exhibits a weak foliation. The Vumba stock forms one kopje intruding the volcanic sequence of the Vumba greenstone belt. Some previous studies (Litherland, 1975) identified both the Sechele and the Vumba stocks as granite and equated them to the post-kinematic Domboshaba Granite (Fig. 2.4). However, it emerged during the fieldwork conducted for this study that the Vumba and Sechele stock are both foliated and the foliation attitude is similar to that recorded in the Kalakamati pluton. Additionally, petrographic analyses (Bagai, 2000), revealed that the stocks are granodioritic in composition. Monzogranite in the Vumba area is represented by the Domboshaba Granite which is a texturally heterogeneous intrusion. It intrudes the Kalakamati quartz monzonite and the granodiorite of the Kalakamati pluton. The Domboshaba Granite is made up of two phases that previous workers referred to as inner and outer granite (Litherland, 1975). The inner granite phase is coarse-grained and pink in colour whereas the outer granite is medium-grained and light pink. The contact between the two sections of the granite is gradational.

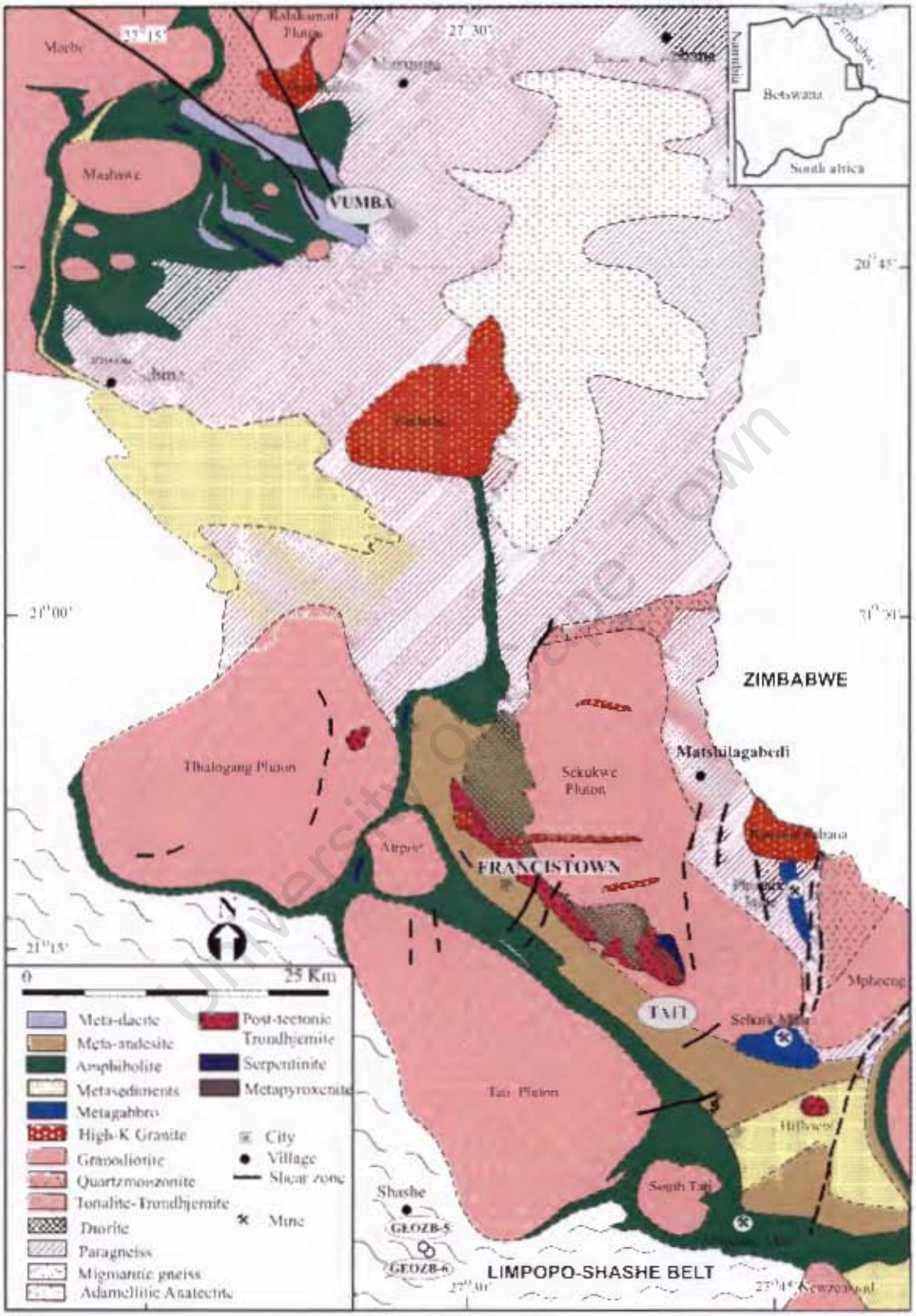

Fig. 2.4: Geology of the Vumba and Tati terrains of the Francistown Granite-Greenstone Complex (modified after Crockett et al., 1974).

2.2 Sampling

Exposure in the Francistown Granite-Greenstone Complex in general is very poor and most of the contacts between different rock units are unexposed. Sampling was conducted randomly, therefore, and obvious signs of alteration and/or veining were avoided. Additionally, sampling close to geological contacts was avoided as a precautionary measure against sampling non-representative samples. A global position system (GPS) was used during sampling to record the coordinates of each sample position. Sampling was conducted only in the Tati granite-greenstone terrane. Samples from the Vumba area were obtained from a previous study (Bagai, 2000). Because geochemical sampling of plutonic rocks in the Tati area was conducted previously (Kampunzu et al., 2003), only representative sampling in this area was undertaken for the current investigation. Table 2.1 gives a summary of sampled units, while Fig. 2.5 shows the general localities of the samples. The coordinates of the sample positions are presented in Appendix A. A summary of the samples gathered from the Vumba granite-greenstone terrain is presented in Table 2.2 and the general localities are shown in Fig. 2.6.

Table 2.1: Summary of samples collected in the Tati granite-greenstone terrain.

Rock units	No. of samples	Sample numbers
Quartz Monzonite	5	ZBT1 to ZBT5
Monzogranite	4	ZBT6 to ZBT9
Trondhjemite	7	ZBT10 to ZBT16
Diorite	10	ZBT17 to ZBT26
Tonalite-trondhjemite (Tati Pluton)	7	ZBT28 to ZBT34
Gabbro-Phoenix Mine : Tonalitic dyke	2	ZBT35 to ZBT36
: Gabbro	4	ZBT37 to ZBT40 & ZBT81
Lady-Marry Formation : Felsic lavas	5	ZBT41 to ZBT45
: Mafic lavas	17	ZBT46 to ZBT62
Gabbro (Selkirk Mine)	14	ZBT63 to ZBT76
Tonalite-trondhjemite (Sekukwe Pluton)	4	ZBT77 to ZBT80
TOTAL	**80**	

Table 2.2: Summary of samples collected previously in the Vumba granite-greenstone terrain (Bagai, 2000).

Rock Units	No. of Samples	Sample numbers
Quartz Monzonite	7	ZBV82-88
Monzogranite (Domboshaba)	9	ZBV69-77
Granodiorite: Vumba stock	1	ZBV78
: Sechele stock	3	ZBV79 -81
: Kalakamati Pluton	3	ZBV20, ZBV96-97
: Mashawe Pluton	5	ZBV89-92 & ZBV95
Tonalite (Maebe)	22	ZBV09-10, ZBV93-94 & ZBV131-149
Vumba Mixed Volcanic: Felsic lavas	11	ZBV53, ZBV160 -168
: Mafic lavas	19	ZBV13, ZBV23, ZBV197-199, ZBV200-217
: Serpentinite	6	ZBV02, ZBV05-06, ZBV08, ZBV191-192
: Metapyroxenite	6	ZBV39, ZBV43, ZBV193-196
Vumba Lower Felsic Formation: Felsic lavas	8	ZBV169-178
Vumba Lower Mafic Formation: Mafic lavas	6	ZBV183-188
Vumba Upper Felsic Formation: Felsic lavas	9	ZBV153 -159, ZBV218-219
Vumba Upper Mafic Formation: Mafic lavas	4	ZBV179-182
Porphyritic quartz diorite	4	ZBV44, ZBV150-152
TOTAL	**120**	

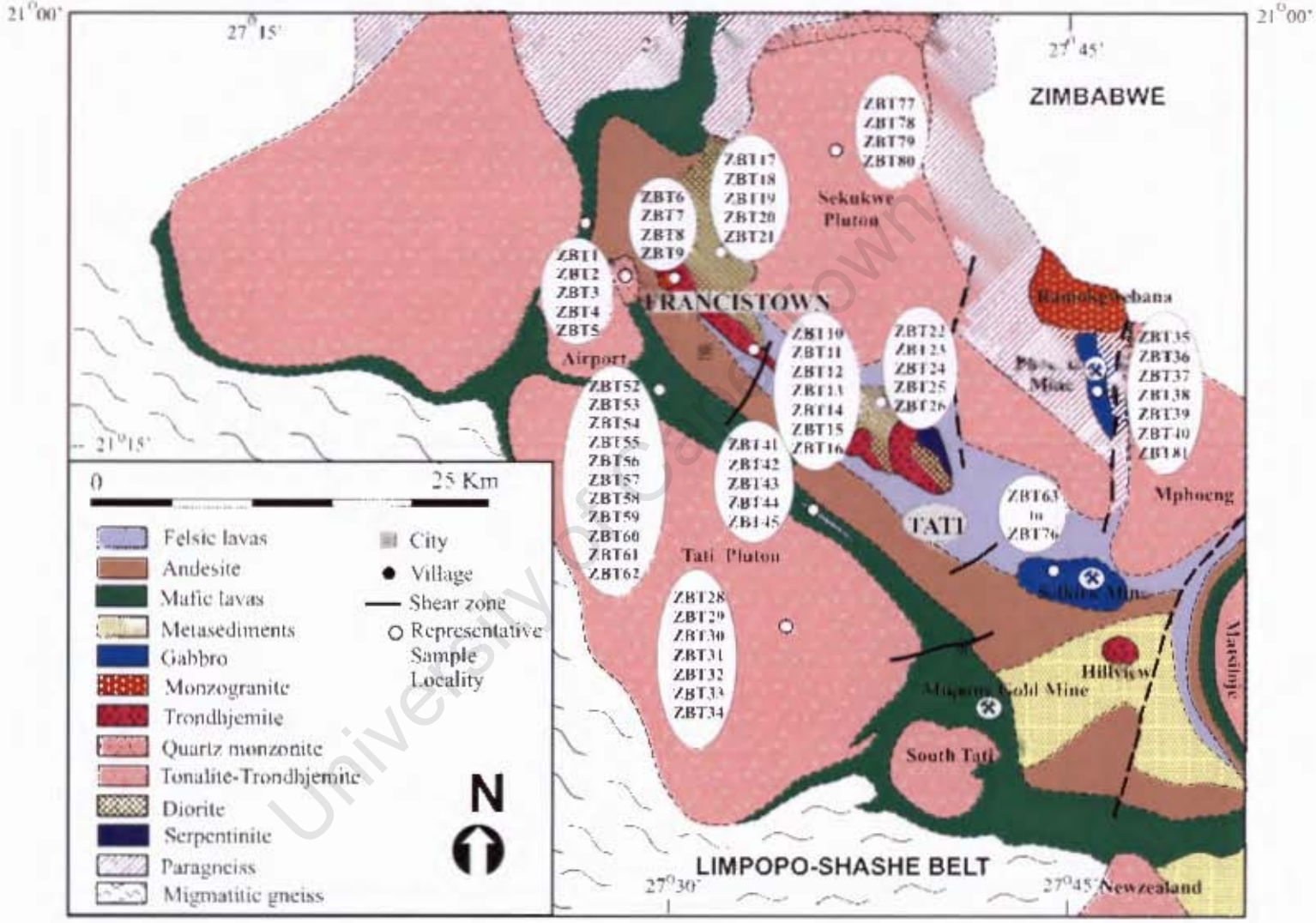

Fig. 2.5: Geolog c map and general sampling loca ities 'n the Tati granite-greenstone terrain (geology modified after Key, '976; S egfried, 1999).

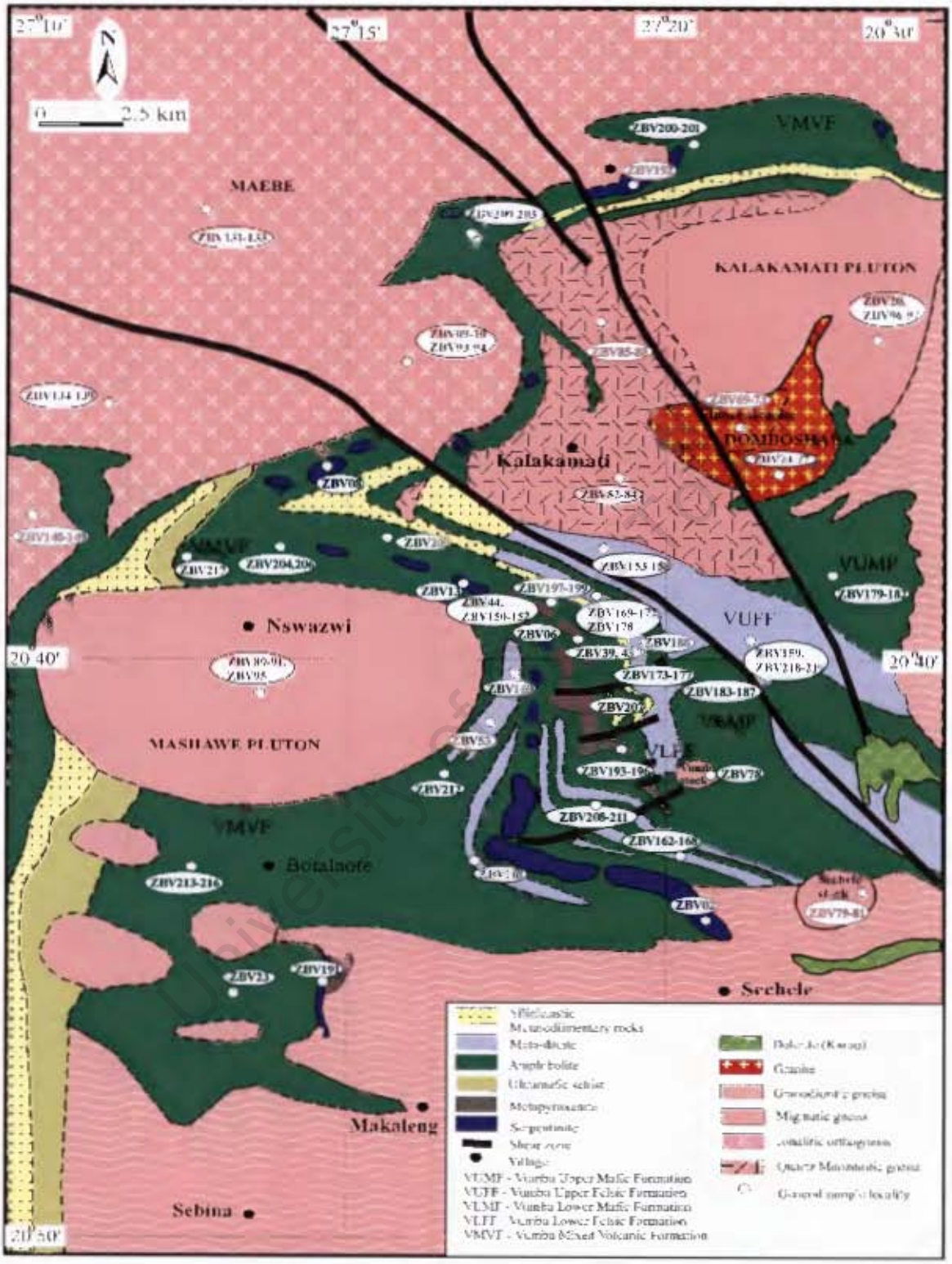

Fig. 2.6: Geologic map and general sampling localities in the Vumba granite-greenstone terrain (geology modified after Litherland, 1975).

CHAPTER 3

Petrography

3.0 Introduction

A summary of the main petrographic features of the rock units within the Francistown Granite-Greenstone Complex is presented in the following sections. Detailed petrographic descriptions of all samples from the Tati granite-greenstone terrain are presented in section A of appendix B. The International Union of Geological Sciences (IUGS) nomenclature (Le Maitre et al., 2002) is followed throughout in allocating rock names. Modal mineralogy was determined by visual estimate, and modal contents should be taken as approximations. A summary of petrographic descriptions for samples from the Vumba granite-greenstone terrain are from a previous study (Bagai, 2000) and are included for comparison purpose.

3.1 Mafic lavas

The mafic lavas within the Francistown Granite-Greenstone Complex have been variably deformed at low to medium grade metamorphism. This has generally overprinted the primary mineralogy and textures.

3.1.1 Tati mafic lavas

In hand specimen the mafic lavas from the Tati greenstone belt generally have a fine- to medium-grained basaltic appearance. They are massive to foliated aphanitic lavas with grey to greenish-grey colour. The mafic lavas show various types of textures including granular, granoblastic, porphyroblastic and schistose, and textures do not correlate with geographic location. The primary mineralogy has been overprinted under upper greenschist to lower amphibolite facies conditions, reflected by the prevalence of clinoamphibole, chlorite and epidote ± biotite ± muscovite ± calcite paragenesis. The samples that show porphyroblastic textures contain anhedral clinoamphibole porphyroblasts poikilitically enclosing fine xenomorphic quartz crystals set in a matrix composed of recrystallised plagioclase, hornblende and sporadic quartz. Plagioclase lacks twinning. The modal abundances of amphibole and plagioclase are on the order of 80% and 20%, respectively. Fe-Ti

oxides are a common accessory phase with an even distribution. Many of the relatively coarse-grained samples exhibit prismatic, skeletal and anhedral clinoamphibole grains that have pseudomorphed augitic clinopyroxenes. These grains are clouded with tiny inclusions of quartz (Fig. 3.1), and they are locally associated with a mosaic of simple twinned plagioclase laths, secondary calcite and relatively high proportion of Fe-Ti oxides. Locally, plagioclase laths show a range of crystal sizes, and are partially to wholly enclosed within the clinoamphibole. This resembles an inherited sub-ophitic to ophitic texture (Fig. 3.2). Plagioclase composition varies from laboradoritic to bytownitic. Quartz is an accessory mineral.

Schistose samples are fine-grained with the major constituent mineral assemblage aligned in a preferred orientation (Fig. 3.3). Clinoamphibole occurs in high modal proportions of (~80%), with lesser untwinned plagioclase (~10%) and quartz (10%). Fe-Ti oxides (<5%) are commonly associated with the clinoamphibole. Samples that display fine granular texture contain primary igneous augitic clinopyroxene, plagioclase and Fe-Ti oxides with clinopyroxene altered to a variable degree to clinoamphibole. Plagioclase feldspars form thin blades with simple twinning and random orientation (Fig. 3.4).

3.1.2 Vumba mafic lavas

The mafic lavas in the Vumba greenstone belt were previously described by Bagai (2000). They vary significantly in terms of grain size and mineralogical composition. Fine grained mafic lavas are the most prevalent and exhibit a variety of recrystallisation textures essentially comprising quartz, plagioclase and hornblende meeting at triple point junctions with interfacial angles of around 120º. This type of mafic volcanic rock is characterized by polygonal equigranoblastic, porphyroblastic and schistose textures. Most plagioclase crystals which have been examined for their An content yielded andesinic to labradoritic composition. Fe-Ti oxides and sphene are the common accessory phases. The medium grained mafic lavas are sparsely distributed and they possess ubiquitous skeletal augite poikilitically enclosing plagioclase crystals associated with hornblende and sporadic quartz. The texture resembles an inherited sub-ophitic and ophitic texture. Augite locally alters to hornblende while plagioclase is mildly sericitised. The modal content of plagioclase ranges between 30 and 35%, whereas the mafic phases (hornblende and augite) vary from 60 to 65%. Calcite occurs as a secondary mineral. Sphene and Fe-Ti oxides occur in accessory proportions.

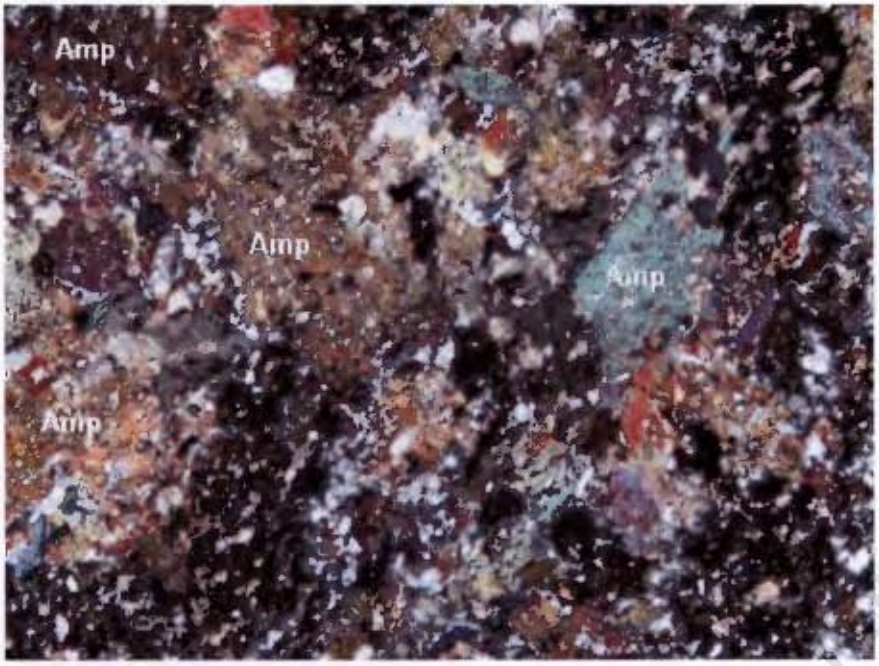

Fig.3.1: Photomicrograph taken under cross-polars showing a cluster of anhedral prismatic and skeleta clinoamph bole grains clouded with fine inclusions of quartz. Field of view (FOV) = 2.3mm. Sample ZBT54.

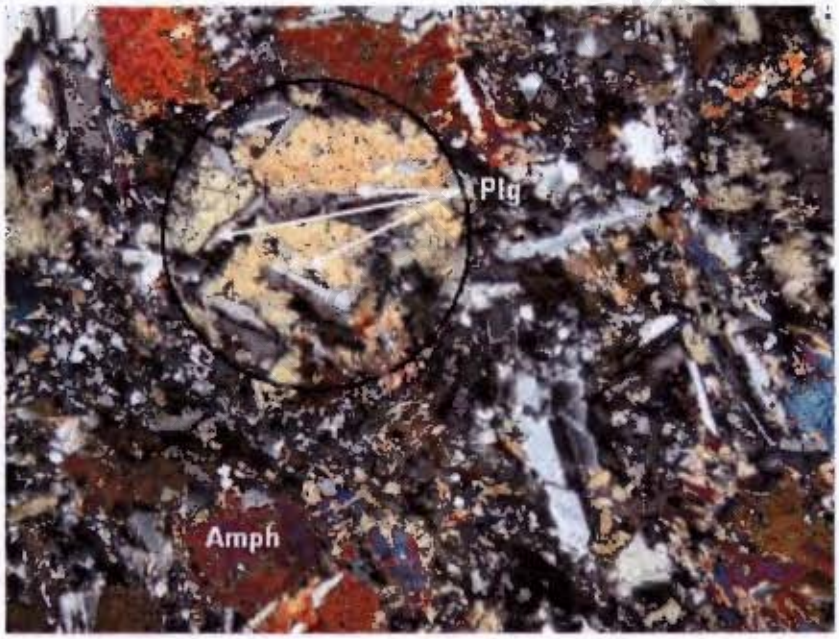

Fig. 3.2: Photomicrograph taken under cross-polars showing remnant ophitic textures as displayed by mafic volcanic rocks of the Tati greenstone belt. FOV = 2.3mm. Sample ZBT55

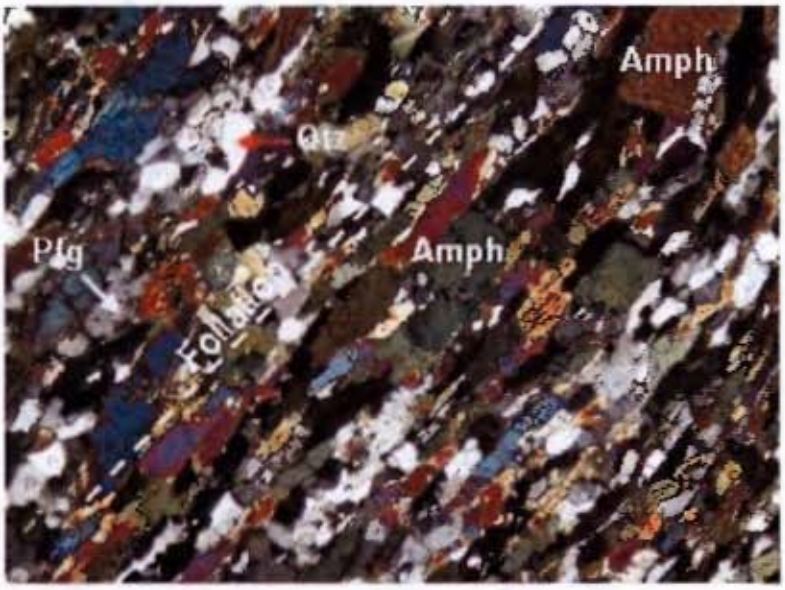

Fig. 3.3: Photomicrograph taken under cross-polars of a foliated mafic volcanic rock from the Tati greenstone belt. Clinoamphibole, untwinned plagioclase and quartz are aligned in a preferred direction. FOV = 2.3mm. Sample ZBT51

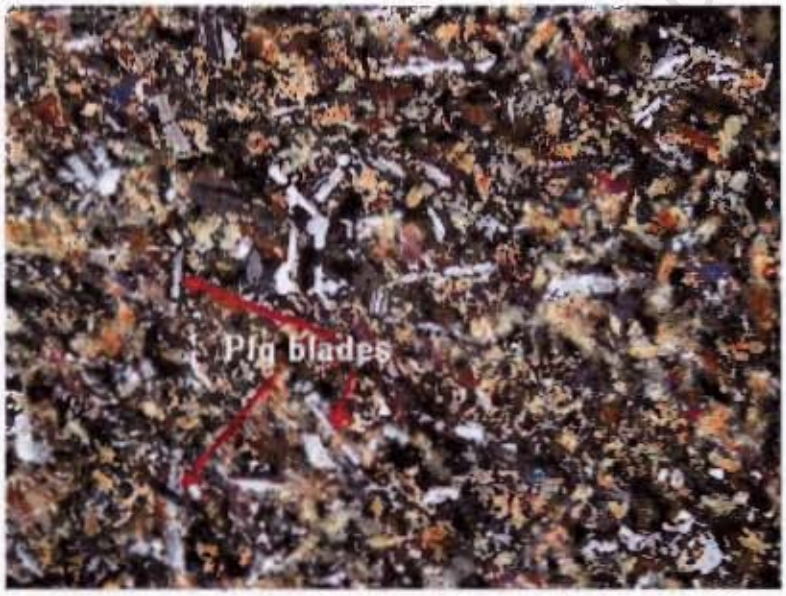

Fig. 3.4: Photomicrograph taken under cross-polars of a fine-grained mafic volcanic rock from the Tati greenstone belt showing an ophitic-like texture composed of randomly oriented simple twinned plagioclase associated with augitic clinopyroxene partially altered to hornblende. FOV=2.3mm. Sample ZBT57.

3.2 Felsic lavas

Felsic lavas exposed in the Tati area are variably deformed under conditions of low to medium grade metamorphism.

3.2.1 Tati Felsic lavas

In hand specimen the felsic lavas are aphanitic, massive and light grey. They show untwinned feldspars interlocked with quartz grains in a polygonal granoblastic texture (Fig. 3.5) in thin section. The modal estimate of combined feldspar and quartz is about 80%. Acicular to tabular biotite and hornblende crystals constitute the mafic phases and show a preferred orientation. Locally there is abundant acicular muscovite defining foliation together with anhedral tabular biotite (Fig. 3.6). Biotite (~10%) is more abundant than hornblende (~3%). Muscovite (~5%) and calcite (~2%) occur as secondary phases. Epidote and Fe-oxide constitute accessory phases.

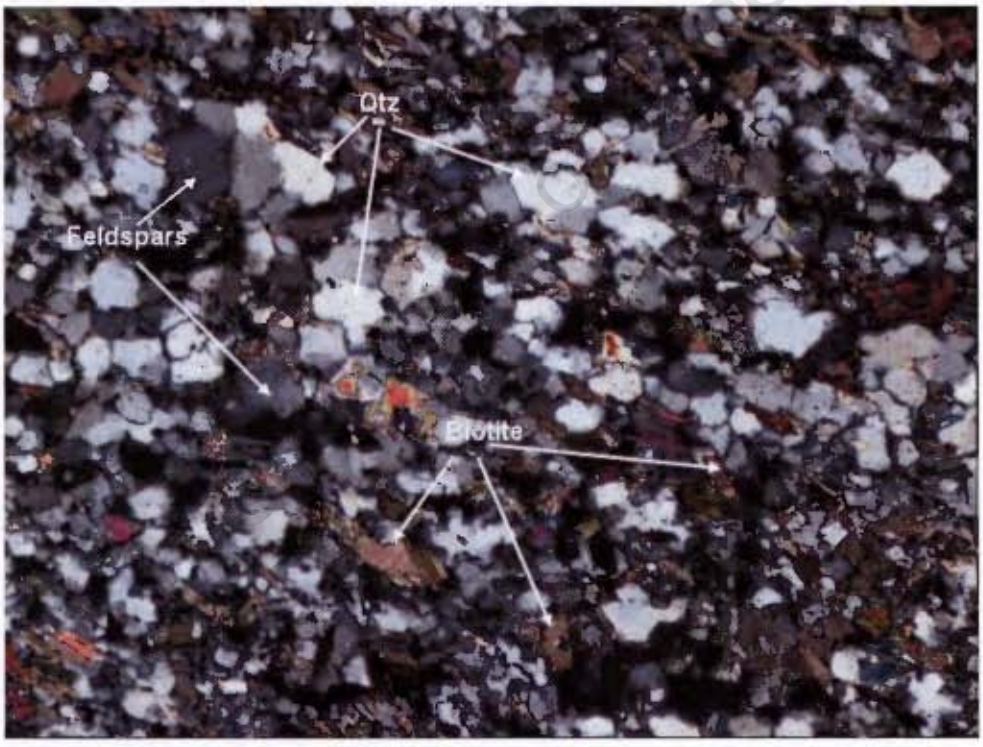

Fig. 3.5: Photomicrograph taken under cross-polars of a felsic volcanic rock from the Tati greenstone belt showing a polygonal granoblastic texture. Biotite defines a widely spaced foliation. FVO = 2.3mm. Sample ZBT43

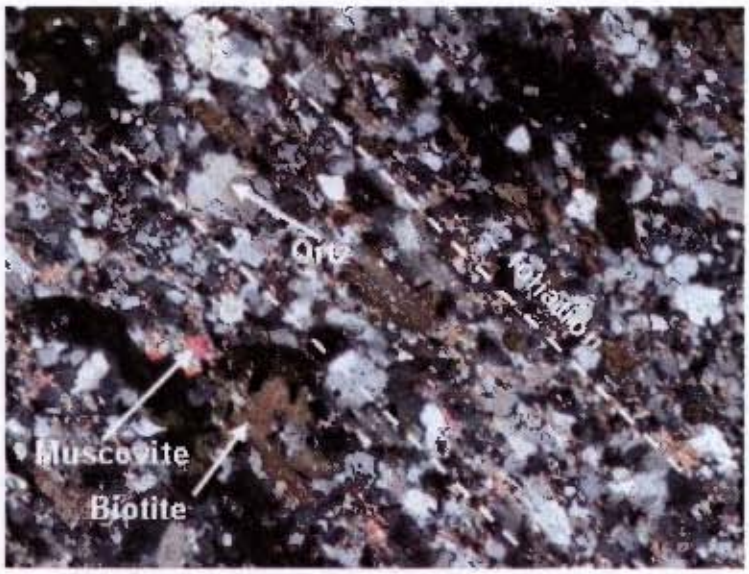

Fig. 3.6: Photomicrograph taken under cross-polars of a foliated felsic volcanic rock from the Tati greenstone belt displaying acicular muscovite and anhedral tabular biotite in a preferred orientation. FVO=2.3mm. Sample ZBT45

3.2.2 Vumba felsic lavas

The Vumba greenstone belt felsic volcanic rocks appear to be more pale-coloured than the Tati belt counterparts in hand specimen. Under the microscope they display two types of textures ranging from fine equigranoblastic to porphyroblastic. They are characterized by fine quartz and feldspar crystals associated variably with biotite and muscovite. In some instances fragmented or skeletal hornblende dominates over the micas. Porphyroblastic textures are defined by relatively coarse grains of quartz that form aggregates within the groundmass of quartz and feldspars. Micas and amphibole make up 5 to 10% of the rock. Calcite is present as a secondary phase and Fe-Ti oxides are accessory minerals.

3.3 Vumba serpentinite and metapyroxenite

The serpentinites are fine to medium grained, massive, pale grey-green to black in fresh hand specimen. Primary texture and mineralogy have been obliterated by metamorphism. Nonetheless, some thin sections of serpentinite samples preserved subhedral and fine rounded olivine crystals pseudomorphed by serpentine. Other minerals in association with the serpentine are tremolite, chlorite, magnetite and calcite. The state of alteration precludes any detailed petrographic analysis.

Metapyroxenite samples are greenish grey, massive, medium-grained and homogeneous in hand specimen. In thin section, they exhibit augite and diopside crystals intermingled with anhedral scarce plagioclase. Coarse clinopyroxene crystals are skeletal and altered to actinolite. Fine crystals of clinopyroxene display chaotic distribution while coarse crystals show a preferred orientation. Locally, plagioclase crystals are poikilitically enclosed within the coarse clinopyroxenes. Carbonate and quartz occurs as common secondary phases.

3.4 Metagabbros

The Selkirk and Phoenix metagabbros are densely mineralized in places with pyrite, phyrrhotite and chalcopyrite. Both the gabbro intrusions have been deformed to greenschist facies metamorphism but most samples display remnant igneous textures. On the basis of these textures, the gabbros have been classified as meta-gabbros (metamorphosed but original igneous textures preserved).

3.4.1 Selkirk metagabbro

The Selkirk metagabbro is medium to fine-grained, massive and pale green to grayish green in colour. Fourteen thin sections from the Selkirk metagabbro were petrographically investigated. Despite being fresh looking in hand specimen, most of the thin sections revealed that the gabbro is mildly to extensively hydrothermally altered, which is possibly linked to its mineralization (Fig. 3.7). The state of the alteration restricts detailed petrographic analysis of the unit. Phases commonly observed within the altered domains are plagioclase and clinopyroxene with minor quartz and secondary epidote, chlorite, calcite, tremolite, serpentine and abundance of opaque minerals. In some samples the alteration is too extensive to identify individual phases. Furthermore, locally the metagabbro is thoroughly carbonated as reflected by the presence of up to 50% secondary calcite (Fig. 3.8). Despite the alteration, the Selkirk metagabbro exhibits locally preserved doleritic (Fig. 3.9) and granular textures (Fig. 3.10). The granular texture is dominated by clinoamphibole grains which have pseudomorphed primary clinopyroxene. Replacement of original pyroxene crystals by amphiboles without any change in original igneous textures is suggestive of isochemical changes. Previous investigations (e.g. Johnson, 1986) described some troctolitic gabbro within the Selkirk metagabbro, but this has not been confirmed by this study.

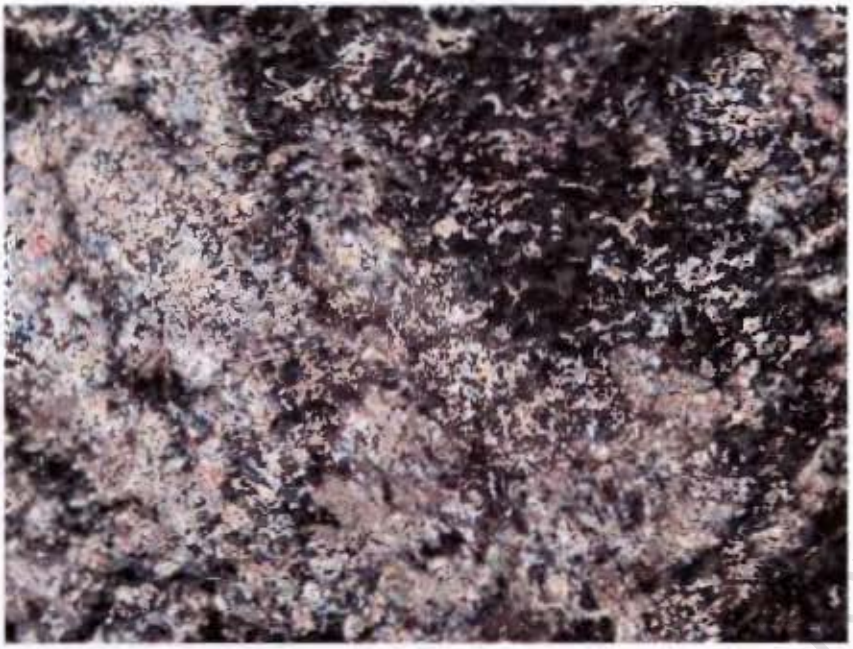

Fig. 3.7: Photomicrograph taken under cross-polars of a thin section from the Selkirk metagabbro illustrating the degree of (hydrothermal) alteration. FOV=2.3 mm. Sample ZBT63.

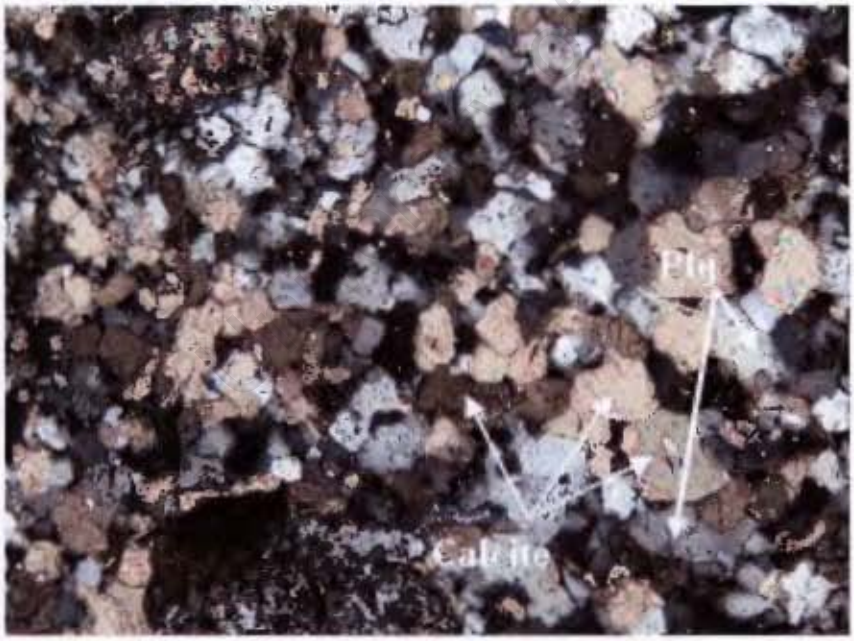

Fig. 3.8: Photomicrograph taken under cross-polars of a thin section from the Selkirk metagabbro illustrating the degree of carbonitisation in local areas. FOV=2.3 mm. Sample ZBT69.

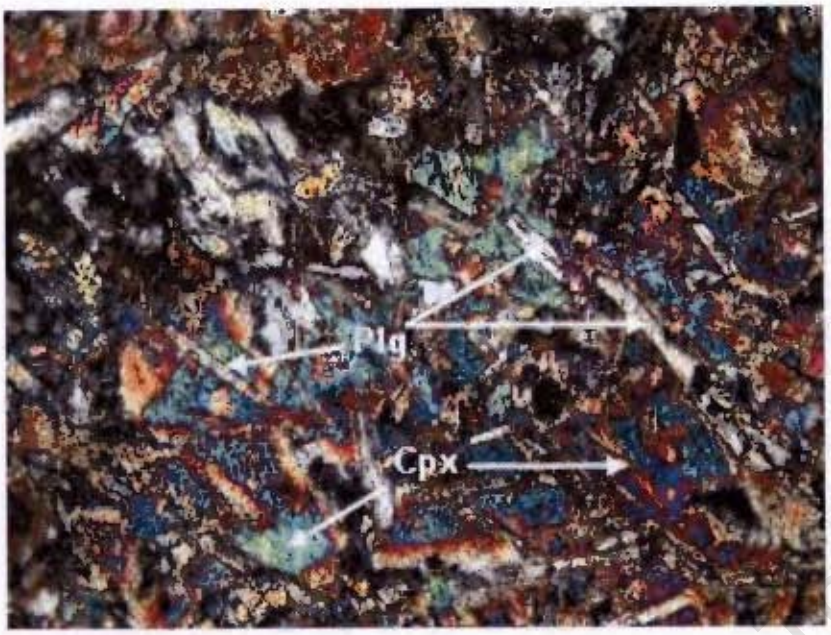

Fig. 3.9: Photomicrograph taken under cross-polars of a thin section from the Selkirk metagabbro illustrating the poikilitic texture constituted by partially altered plagioclase thin blades and clinopyroxene. FOV=2.3 mm. Sample ZBT71.

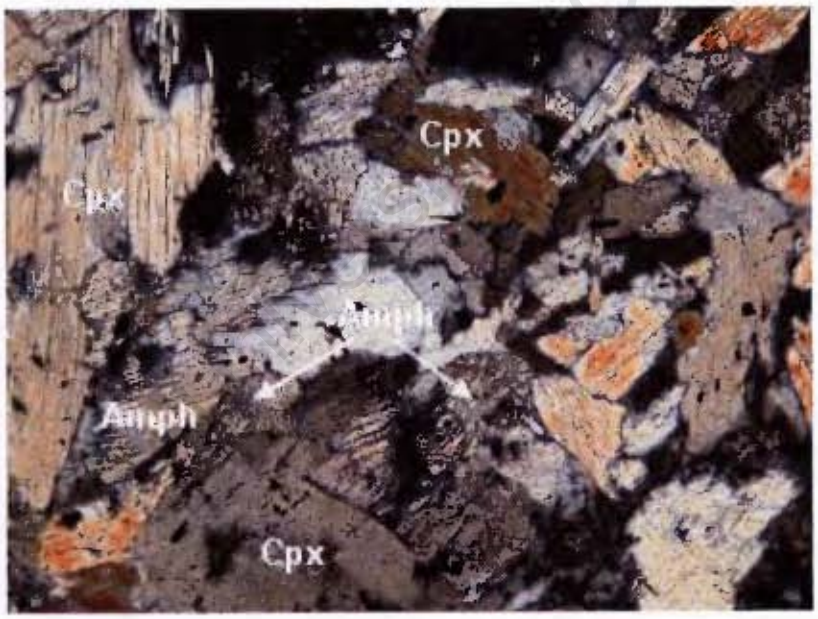

Fig. 3.10: Photomicrograph taken under cross-polars of a thin section from the Selkirk metagabbro illustrating the granular texture dominated by clinopyroxene and clinoamphibole. FOV=2.3 mm. Sample ZBT74.

3.4.2 Phoenix metagabbro

Samples of gabbroic rock from the Phoenix mine are medium-grained, massive, homogeneous and dark grey in hand specimen. They mostly display cumulate texture composed of euhedral to subhedral plagioclases and xenomorphic augitic clinopyroxene which has been partially to completely replaced by clinoamphibole. Plagioclase exhibits albite, Carlsbad and combined albite-Carlsbad twinning with variable grain sizes that range from 0.5mm to 4mm in length. The composition of plagioclase ranges from labradoritic to bytownitic. Altered clinopyroxene grain sizes vary between 1mm and 4mm long and up to 3mm wide. The gabbro has been variably amphibolitised and it commonly displays the following assemblages in the alteration product: hornblende, chlorite, epidote and calcite. In spite of the alteration, primary magmatic textures such as ophitic and sub-ophitic textures are recognizable (Fig. 3.11) where clinopyroxene wholly to partially enclose plagioclase laths. The Phoenix metagabbro is compositionally leucogabbroic (Fig. 3.12) to melagabbroic. Leucogabbro is dominated by plagioclase while melagabbro contains prevalent altered clinopyroxene. Primary clinoamphibole occurs sporadically within the clinopyroxene dominated samples. Quartz, secondary muscovite, calcite, epidote and chlorite are present in accessory amount. Opaque minerals are common in the Phoenix gabbro.

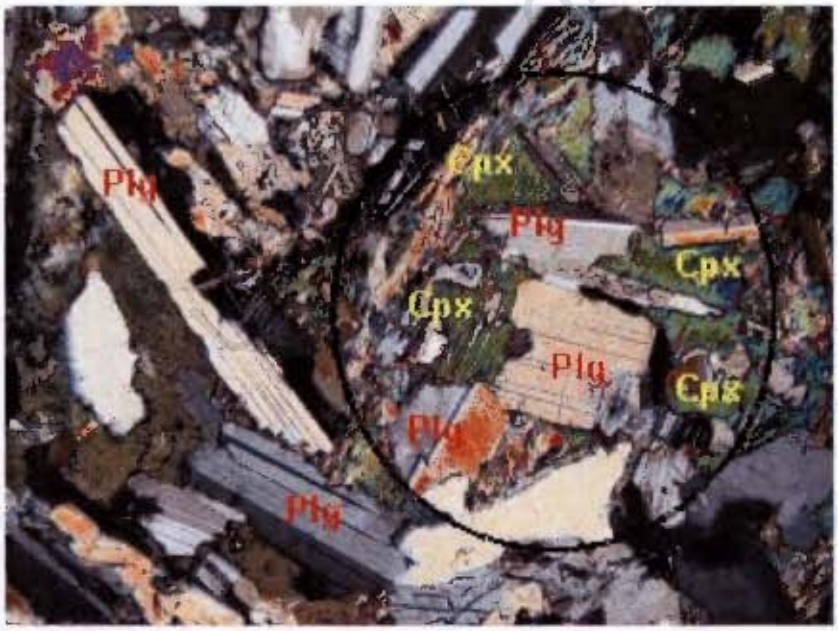

Fig. 3.11: Photomicrograph taken under cross-polars of a thin section from the Phoenix metagabbro illustrating the sub-ophitic texture. FOV=2.3 mm. Sample ZBT39.

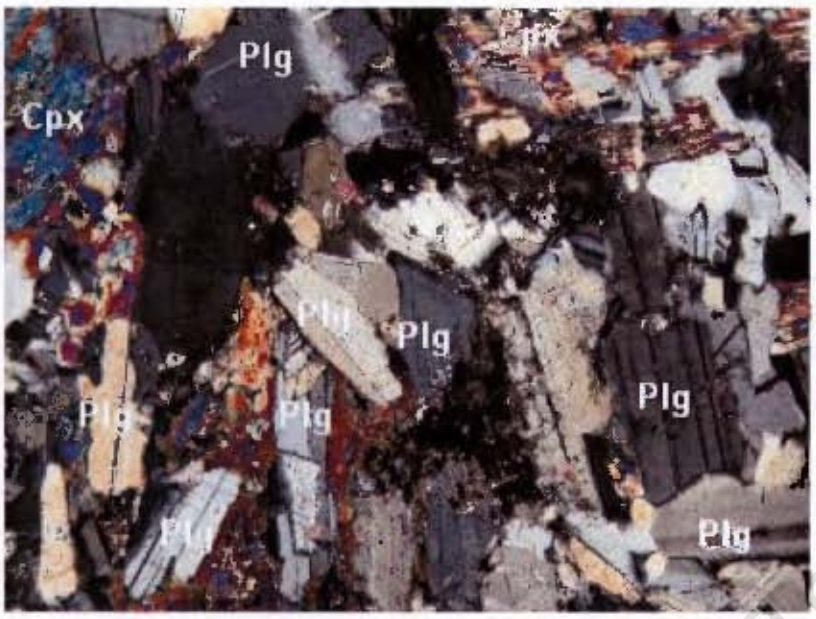

Fig. 3.12: Photomicrograph taken under cross-polars of a thin section from the Phoenix metagabbro illustrating the cumulus texture dominated by plagioclase. FOV=2.3 mm. Sample ZBT81

3.5 Diorite

The diorite is medium-grained, homogeneous, massive and grey with a spotted appearance imparted by the granular texture of amphibole/pyroxene and plagioclase. There are two types of diorite in the Tati granite-greenstone terrain. The first type includes samples which are composed of plagioclase, equant orthopyroxene, prismatic clinopyroxene, clinoamphibole and quartz as essential phases. The distribution of these essential phases is uneven, and some samples being dominated by plagioclase (Fig. 3.13) and others pyroxene (Fig. 3.14). On average the modal proportions of plagioclase, orthopyroxene, clinopyroxene, amphibole and quartz are 55%, 8%, 30%, 5% and 2%, respectively. The phases display smooth and regular grain contacts. Locally, clinopyroxene crystals exhibit mild alteration to clinoamphibole. Plagioclase appears euhedral to subhedral with albite, Carlsbad and combined albite-Carlsbad twinning. Orthopyroxene is equant (0.6 mm) and sub rounded with a thin alteration rim around the margin. The second type of diorite encompasses samples that are devoid of orthopyroxene but dominated by clinopyroxene and clinoamphibole which make up to 55% of the rock. Proportions of clinopyroxene to clinoamphibole are variable with clinoamphibole being predominant and pseudomorphing the clinopyroxene in most areas. Plagioclase and quartz constitute 43% and 2%, respectively. The mineral assemblage shows a general preferred orientation.

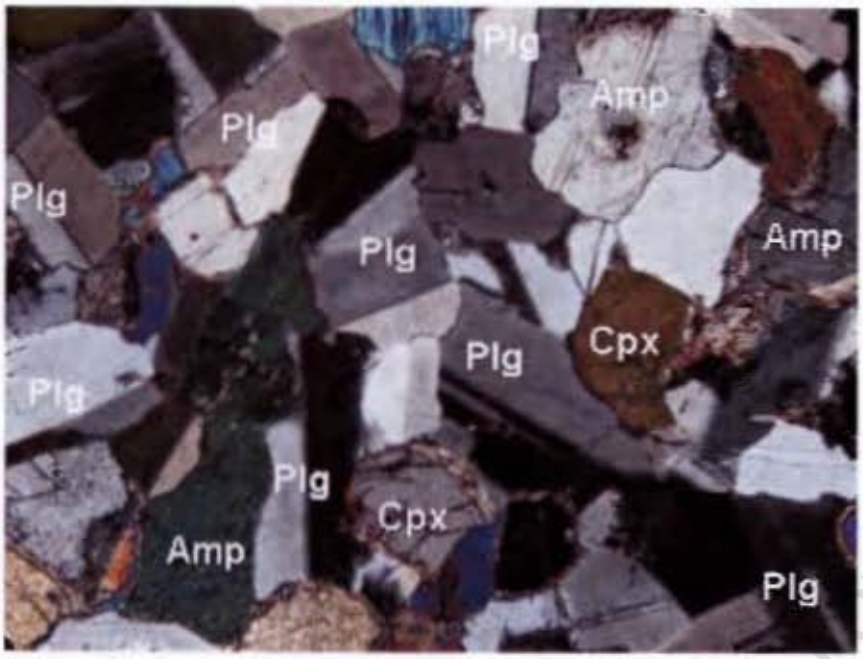

Fig. 3.13: Photomicrograph taken under cross-polars of a thin section from the diorite unit illustrating the granular texture dominated by plagioclase. FOV=2.3 mm. Sample ZBT21.

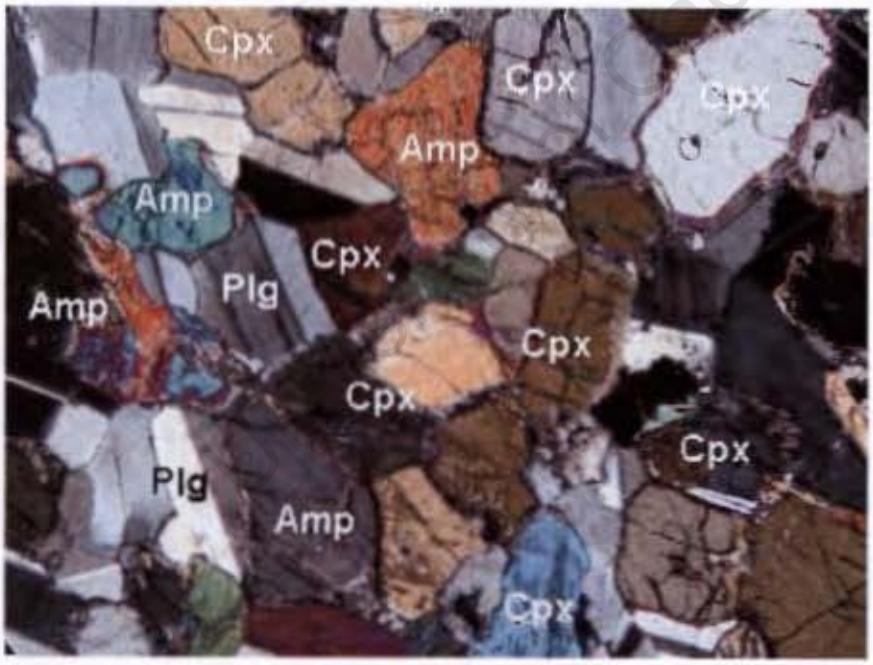

Fig. 3.14: Photomicrograph taken under cross-polars of a thin section from the diorite unit illustrating the pyroxene dominated granular texture. FOV=2.3 mm. Sample ZBT24.

3.6 Granitoids

3.6.1 Quartz monzonite

Quartz monzonite forms the least common granitoid in the Francistown Granite-Greenstone Complex. In the field it appears medium-grained, grey, foliated and homogeneous with conspicuous white feldspars, black hornblende, biotite and scarce quartz. This unit occurs contiguous to the tonalite-trondhjemite suite in the Tati granite-greenstone terrain. The samples display a microgranoblastic to granoblastic polygonal texture and have on average 45% alkali feldspars, 20% plagioclase, 15% quartz and 25% mafic phases. Feldspars and quartz are interlocked, commonly displaying straight contact boundaries, indicative of recrystallisation. Petrographically, it is a biotite-hornblende quartz monzonite gneiss. Alkali feldspars occur as anhedral orthoclase, microcline and perthite, with variable grain-size from 0.1mm to 2.5mm. Plagioclase forms mildly sericitised subhedral, multiple twinned, laths with a similar grain size to the alkali feldspar. Phenocryst-like feldspars are characteristic and cause the rock porphyritic (Fig. 3.15). The mafic phases are hornblende, biotite and epidote with the average proportions of 15%, 8% and 2%, respectively. These mafic phases tend to show uneven distribution as reflected in local aggregates of hornblende, biotite and epidote. Hornblende locally displays a poikilitic texture riddled with quartz inclusions. Quartz forms fine weakly strained grains despite conspicuous foliation, which is consistent with recrystallisation. Memyrkite is ubiquitous in the quartz monzonite. Accessory phases include apatite, muscovite, zircon and sphene.

Quartz monzonite in the Vumba granite-greenstone terrain displays a similar field appearance to the quartz monzonite outcropping in the Tati terrain, forming a relatively large single body that has been mapped as the Kalakamati Monzonite (Litherland, 1975: Fig.2.4). It has a medium to coarse grained texture, composed of the following mineral assemblage: perthitic microcline, plagioclase, quartz, hornblende and biotite. The average modal proportions are 50%, 20%, 10%, 15% and 5%, respectively. Hornblende occurs as anhedral skeletal crystals poikilitically enclosing fine grains of quartz. Biotite displays fine- to medium-sized grains with anhedral habits. Myrmekite and microperthite textures are common in the Kalakamati Monzonite. Apatite, zircon and Fe-Ti oxide are ubiquitous accessory phases.

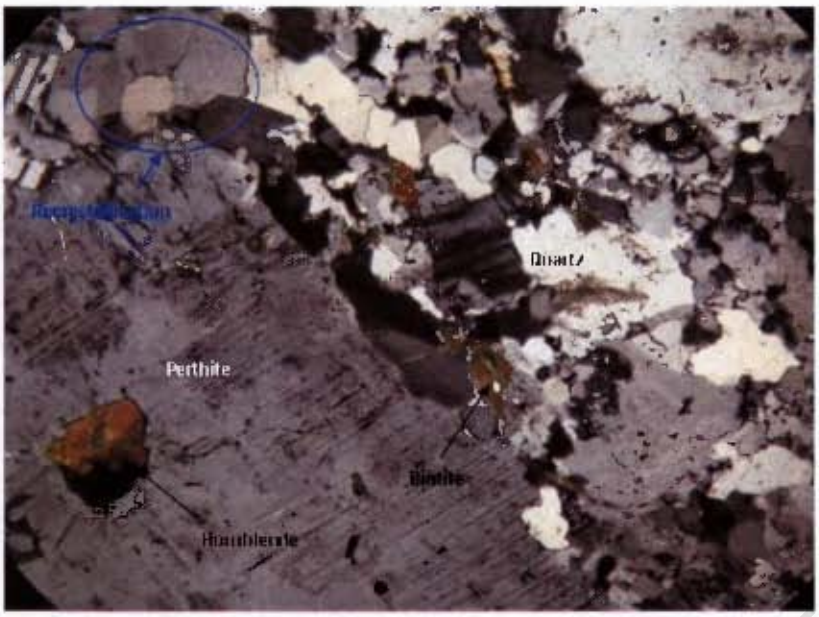

Fig. 3.15: Photomicrograph taken under cross-polars of a thin section from the quartz monzonite unit illustrating the porphyritic texture defined by feldspar phenocryst in a matrix of fine grains of recrystallised quartz and feldspars. FOV = 2.3 mm. Sample ZBT1

3.6.2 Monzogranite

The granite suite outcrops as intrusions of variable size and as dykes, generally trending east-west in the Francistown Granite-Greenstone Complex. It is more common and more widely distributed than the quartz monzonite. The granite in the Tati terrain has pinkish red colour, spotted with silver grey quartz aggregates in the field (Fig. 3.16). It is medium-grained, homogeneous and massive, with sporadic green tint possibly chlorite. The feldspars are extensively sericitised despite fresh looking hand specimens. The rock is granular with common granophyric texture (Fig. 3.17). Compositionally, it is a hornblende monzogranite composed of about 50% orthoclase, 10% plagioclase, 35% quartz and 5% hornblende which has completely altered to chlorite and Fe-Ti oxides. Feldspar and quartz grain sizes range between 1 mm and 2.5 mm, while fine amorphous aggregates of chlorite and Fe-Ti oxides occur along their boundaries. Some quartz grains are fractured and strained with undulatory extinction.

In the Vumba terrain the monzogranite exhibits two different facies, one medium to coarse grained, massive, granular and pink in colour, while the other is medium to fine grained and pale pink. Both are monzogranite and composed of sericitised plagioclase, quartz with undulose extinction and microcline which commonly occur as microperthite. The coarser granite contains lower modal

content of chloritised biotite as the mafic phase, whereas the finer granite has both chloritised biotite and hornblende. Granophyric textures are common in this unit. Zircon, apatite, muscovite and Fe-Ti oxides are the common accessory phases in both facies.

Fig.3.16: A field photograph of a monzogranite outcrop in the Tati granite-greenstone terrain illustrating its field appearance.

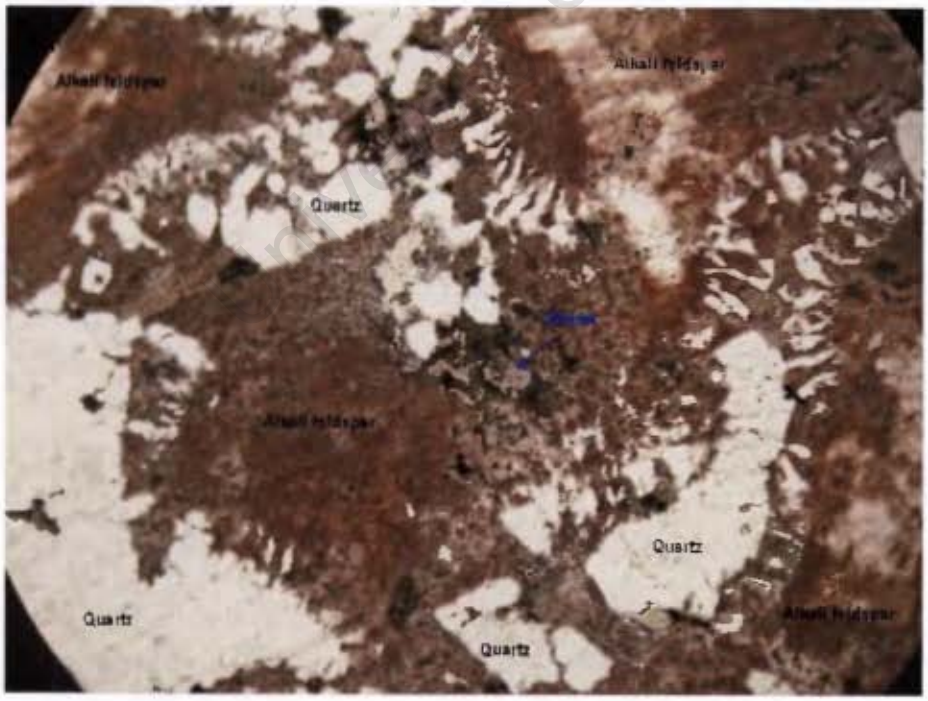

Fig.3.17: Photomicrograph of a thin section from the monzogranite under plain polarized light showing granophyric texture with highly altered alkali feldspars. FOV=2.3 mm. Sample ZBT6

3.6.3 Trondhjemite

The trondhjemite unit is dull grey, massive, homogeneous and medium-grained. Conspicuous minerals in a hand specimen include cream to white feldspars, biotite and smoky quartz which, makes it visually different from other granitoids in the area. Texturally, it is granular with a wide variation of grain size from 1mm to 4mm. It is compositionally a muscovite-biotite trondhjemite with variable amount of secondary calcite. The rock contains about 35% plagioclase, 10% alkali feldspar, 35% quartz, 10% biotite, 7% muscovite and up to 3% calcite. Epidote and Fe-Ti oxides are accessory phases. Hornblende is absent. Biotite and muscovite form very fine anhedral crystals (< 0.1 mm) randomly included within feldspars or aggregates of biotite with irregular shape (Fig. 3.18). Plagioclase forms subhedral, twinned grains which have slightly altered to sericite and epidote. The composition of the plagioclase is oligoclase. Alkali feldspars occur mainly as orthoclase, sporadic microcline and rare perthite. Quartz is present as anhedral clear grains with sutured boundaries. In local places quartz forms segregates of equant grains with fine sericitised feldspar filling interstitial spaces. Quartz grains are highly strained and cracked, with wavy extinction, indicating mild deformation.

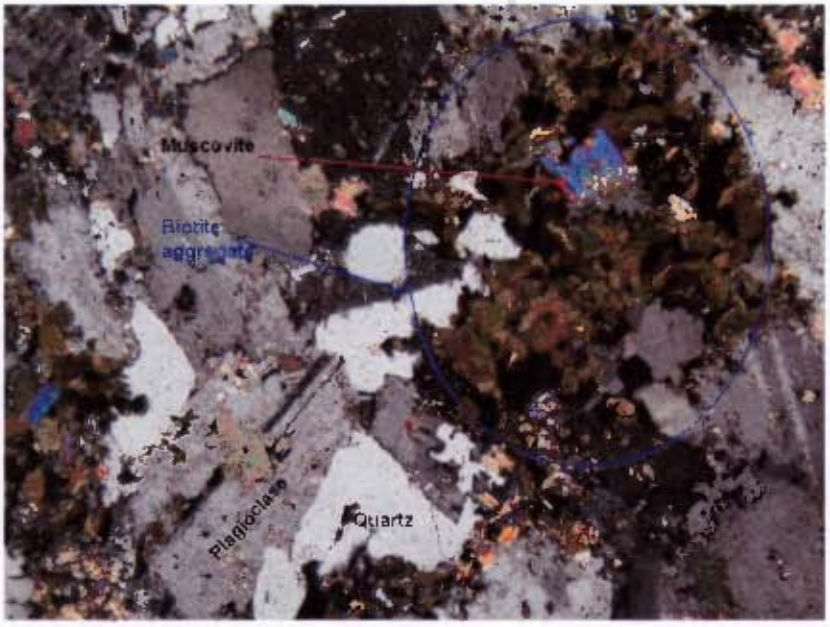

Fig. 3.18: Photomicrograph taken under cross-polars of a thin section from the trondhjemite unit showing characteristic texture of biotite (aggregates) in this unit. FOV = 2.3 mm. Sample ZBT 12.

3.6.4 Tonalite

Tonalite forms the Maebe granitoid in the Vumba granite-greenstone terrain (Fig.2.5). It is medium-grained with medium-grey colour. Both in hand specimen and thin section it displays conspicuous preferred orientation of mafic phases. The Maebe tonalite consists of sericitised plagioclase, fine microcline, quartz, biotite and hornblende as essential phases. The modal abundance of hornblende and biotite is about 10% with hornblende being the most abundant. In most instances, anhedral coarse quartz grains are set in a mosaic of fine equant quartz that has completely recrystallised. Zircon, apatite, Fe-Ti oxides and epidote are the accessory phases. It is compositionally, biotite-hornblende tonalite.

3.6.5 Granodiorite

Granodiorite bodies are distributed within the Vumba granite-greenstone terrain in a range of sizes from large plutons (e.g. Mashawe pluton) to numerous small stocks (e.g. Vumba and Sechele stocks, Fig. 2.5). The granodiorites exhibit some variations in terms of texture and mineral features from one body to another. The Mashawe pluton is leucocratic, medium-grained, light grey and well-foliated. Samples from this pluton consist mainly of mildly sericitised plagioclase, perthitic alkali-feldspar and abundant anhedral strained quartz that is characterized by serrated grain boundaries. Biotite is the only mafic phase present and its modal proportion is less than 5%. The Mashawe pluton is compositionally a leucocratic biotite granodiorite.

The Kalakamati pluton is medium-grey, medium-grained and displays weak foliation. The samples from this pluton mostly exhibit a porphyritic texture both in hand specimen and thin section. Phenocrysts of alkali-feldspar, which constitute 4 to 6% of the rock by volume, poikilitically enclose quartz, biotite and plagioclase. Myrmekitic texture is a common feature. Locally chloritised biotite and hornblende comprise the mafic phases. Their modal proportion ranges between 5% and 10%. Accessory phases include zircon, apatite and Fe-Ti oxides.

The stock size bodies are variably and weakly foliated, homogeneous and pale grey in colour. The Vumba and Sechele stocks are massive and are equated with the Domboshaba granite in age. This implies that they are younger than the Mashawe and the Kalakamati granodiorites. The

Vumba stock is mainly composed of sericitised plagioclase, aggregates of quartz, alkali-feldspar, biotite and scarce hornblende. The Sechele stock is a porphyritic granodiorite containing alkali-feldspar phenocrysts which poikilitically enclose fine crystals of plagioclase, biotite and quartz. Hornblende is rare. Zircon, apatite and Fe-Ti oxide are common accessory minerals in both the stock bodies.

3.6.6 Massive and gneissose tonalite-trondhjemite

The tonalite-trondhjemite (TT) intrusions flanking the Tati greenstone belt in the southwestern and western margins are foliated to banded grey gneisses. Unlike the southwestern tonalite-trondhjemite intrusions, the western TT is non-banded and its foliation trends NE-SW, in contrast to the NW-SE foliation in the southwest TT (Fig.3.19). The intensity of the tectonic fabric increases towards the boundary with the Limpopo-Shashe belt. The banding is at centimeter scale and is defined by alternating well-foliated biotite-rich bands and granular quartz-feldspar bands (Fig. 3.20). The quartz-feldspar bands are composed of plagioclase, alkali feldspar, quartz and minor biotite with secondary muscovite and accessory zircon and Fe-Ti oxides. The proportions of alkali feldspar and plagioclase are variable resulting in granitic to tonalitic composition. The leucocratic bands of the banded gneisses exhibit recrystallisation and annealing textures (Fig. 3.21) under the microscope. The common mineral assemblage for the biotite-rich (melanocratic) layers of the banded gneisses is biotite, plagioclase, alkali feldspar and quartz. Their modal abundances are 25%, 35%, 10% and 30% respectively. The heterogeneous gneisses display a granular texture with the following essential minerals; Plagioclase, alkali feldspar, biotite and quartz. Plagioclase forms about 40% of the rock, and shows a wide range of grain size (0.5 – 2 mm). The alkali feldspar proportion varies between 15 and 20%, and it occurs mainly as orthoclase and sporadic microcline. Biotite exhibits anhedral habit and fine grain size ranging from 0.2 to 0.8 mm. Its modal content ranges from 5 to 8%. Quartz grain sizes range from 0.08 mm to 2 mm and they are highly strained and locally stretched in a preferred direction. The proportion of quartz is about 30%. Myrmekitic texture is ubiquitous. Common accessory phases include muscovite, calcite and epidote.

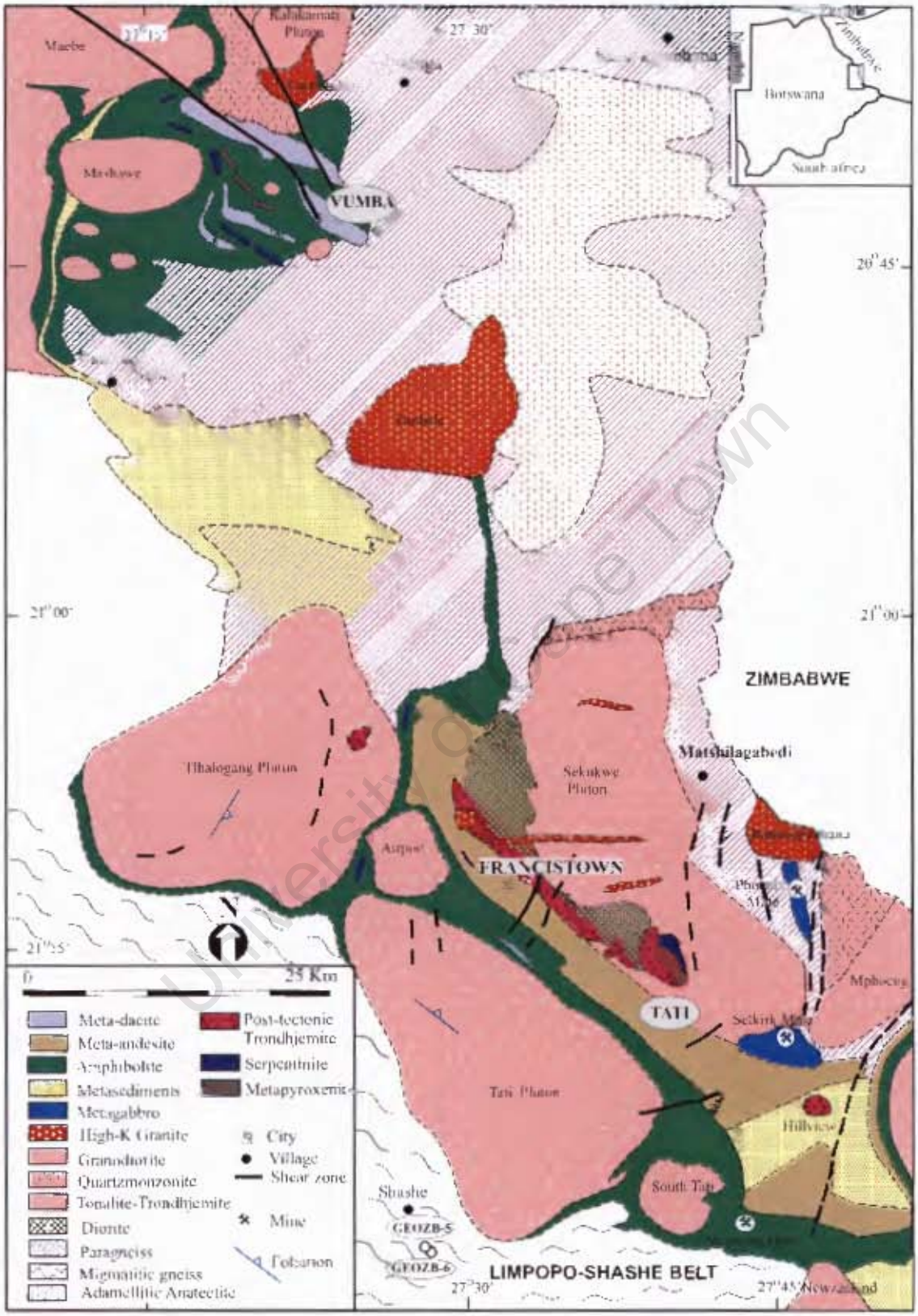

Fig. 3.19: Geological map of the Francistown Arc Complex illustrating the foliation trends of the tonalite-trondhjemite.

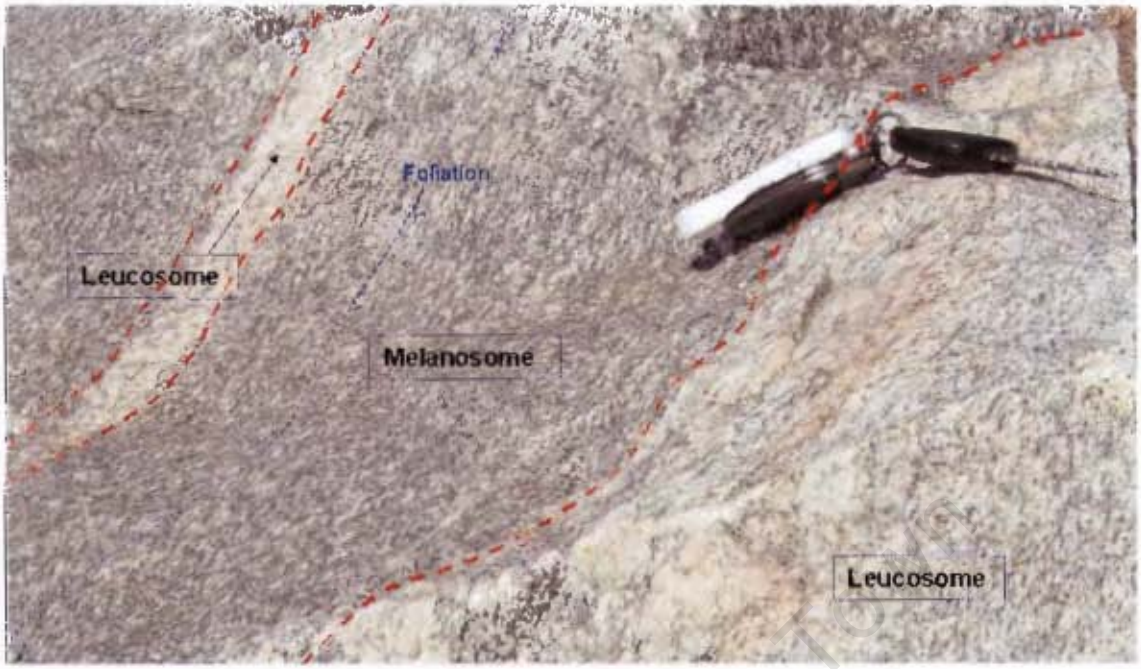

Fig. 3.20: Field photograph of the banded tonalite-trondhjemite gneiss from the Tati pluton illustrating the banding and foliation

The Sekukwe Pluton is massive, homogeneous and leucocratic, with a phaneritic medium-grained granular texture made of grayish white feldspars and clear quartz. No recognizable mafic phase is present in hand specimen. The Sekukwe Pluton is compositionally a leucocratic trondhjemite-tonalite composed of about 60% anhedral plagioclase, 10% alkali feldspar and 30% allotriomorphic quartz. Sericitisation of feldspars is mild to extensive. Biotite, muscovite, calcite, chlorite and Fe-Ti oxide are present in accessory amount. Rare very fine amorphous biotite crystals that are mostly chloritised straddle the boundaries between feldspars and quartz crystals. Plagioclase is mildly altered to sericite, and myrmekite is common along grain margin (Fig. 3.21). Alkali feldspar occurs as subhedral orthoclase with similar grain size to the plagioclase. Quartz forms 1 to 6 mm anhedral and fractured grains with normal extinction, irregular shape and smooth grain boundaries.

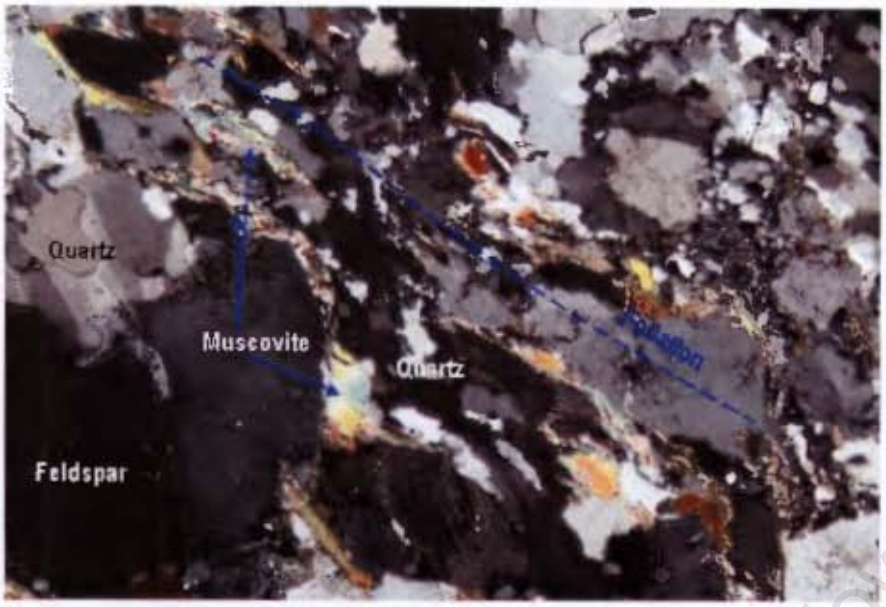

Fig. 3.21: Photomicrograph taken under cross-polars of a thin section from the Tati pluton tonalite-trondhjemite illustrating the deformation and annealing texture. FOV = 2.3 mm. Sample ZBT32.

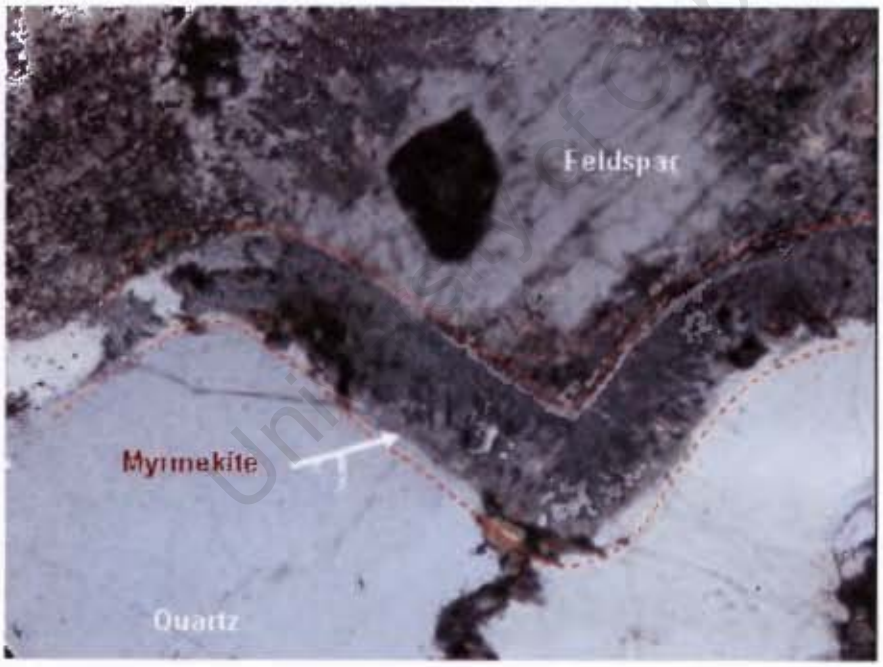

Fig. 3.22 Photomicrograph taken under cross-polars of a thin section from Sekukwe Pluton illustrating a rim of myrmekite between feldspars and quartz grains, which is a unique feature of this pluton. FOV = 1.5 mm.

CHAPTER 4

GEOCHRONOLOGY

4.0 Introduction

Poor exposure and hence the absence of definitive field relationships render the chronological order of geological events in the Francistown Granite-Greenstone Complex and Limpopo-Shashe area speculative and controversial. In this study new U-Pb zircon dates for volcanic, plutonic and metasedimentary rocks from the Francistown Granite-Greenstone Complex and the Limpopo-Shashe orogeny (c.f. McCourt et al., 2004) were determined on 16 samples in order to establish an absolute time frame for the volcanic and plutonic magmatic activities, as well as major deformation events, within the Neoarchaean Francistown Granite-Greenstone Complex. This provides the first detailed geochronological framework for the crustal development of the Francistown Granite-Greenstone Complex. Sampled rock units and localities of the geochronology samples are indicated in Figure 4.1. Petrological descriptions, sampling rationale and dates for these samples are discussed below. This chapter concludes by combining the U-Pb zircon ages from this study with the recently published U-Pb zircon ages from the contiguous Vumba terrain, which forms part of the Francistown Granite-Greenstone Complex. The combined data from the two terranes of the Francistown Granite-Greenstone Complex are collectively evaluated and discussed in the context of a geochronological magmatic history of the Complex.

4.1 Background

U-Pb zircon geochronology has, over the past two decades, revolutionized the investigation of Archaean geology (Blake et al., 2004), which is mostly characterised by polymetamorphism and a complex geotectonic evolutionary history. This emanates from the fact that zircon is a refractory mineral whose internal structure and U-Pb signatures are rarely entirely perturbed even at highest grades of metamorphism (Cavosie et al., 2005; Jamal, 2005; Gribble and Hall, 1992). For instance, no known rocks on Earth are older than the 4.0 Ga Acasta gneiss in Canada, yet evidence of older rocks (4403 ± 8 Ma) is provided by detrital zircon grains in metasedimentary rocks from Western

Australia (Cavosie et al., 2005; Condie, 2005a; Wilde et al., 2001). Additionally, zircon has a high blocking temperature of 750 °C to 800 °C (Heaman and Ludden, 1991), which renders it useful for recording magmatic and high-grade metamorphic events. With the application of the Scanning High Resolution Ion-Microprobe (SHRIMP) technique, it is possible to unravel the geological history of complex zircon grains, since a number of analyses can be made on a single zircon crystal. Zircon grains from Archaean terranes often possess complex structures due to multiple thermal events that can cause growth and/or recrystallisation of the zircon grains (e.g. Bowring and Williams, 1999). However, with the high resolution of the SHRIMP technique, a record of multi-stage thermal history of a rock unit preserved in the micron-scale zonation of individual zircon grains can be revealed. The disadvantage of the SHRIMP technique is that it is very expensive and time consuming.

Numerous previous studies have revealed the power of zircon U-Pb geochronology in exposing the ages and rates of ancient geological processes in areas with poorly exposed rocks and structural complexities (e.g. Bowring and Williams, 1999). Many studies have applied zircon U-Pb geochronology, amongst other things, to unravel the duration of Archaean granite-greenstone development (e.g. Ellington and Armstrong, 2004; Mapeo et al., 2004), the rate of basin evolution (e.g. Ayer et al., 2002) and Archaean mafic-felsic volcanic successions, for resolving fundamental questions about geotectonic evolution. Furthermore, zircon U-Pb geochronology can be coupled with other geological studies to provide insights into the rates of geological processes and secular changes over the course of Earth history. For instance, zircon U-Pb geochronology has been coupled with paleomagnetic studies to investigate continental drift rates in the Archaean (e.g. Blake et al., 2004). Additionally, zircon geochronology has been coupled with isotopic data to distinguish terrains of continental recycling from terrains of juvenile mantle origin in studies of crustal evolution in many Archaean granite-greenstone terrains (e.g. Käpyaho et al., 2006).

The mineral zircon contains U and Th whose presence is attributed to isomorphous replacement of Zr^{+4} by U^{+4} and Th^{+4} (Faure, 1986). Pb is excluded from zircon during crystallization because of its large radius and low charge. Hence, zircon contains very little Pb at the time of formation and has very high U/Pb and Th/Pb ratios. Uranium has two radioactive isotopes, U^{238} and U^{235} that decay naturally to give rise to ^{206}Pb and ^{207}Pb, respectively (Faure, 1998). Thus, radioactive decay of U to Pb gives rise to two independent geochronometers that should give concordant dates in situations

where zircon remained closed to U and all its daughter isotopes. In most cases the two U-Pb dates obtained for a single zircon do not agree precisely and this gives rise to discordance with respect to concordia curve. A concordia curve (Wetherill, 1956), represents the locus of present day $^{206}Pb/^{238}U$ and $^{207}Pb/^{235}U$ ratios for closed U-Pb systems of all ages and has been widely used as a reference in studies of U-Pb systems in zircon (e.g. Stacey and Kramer, 1975). Analyses of cogenetic zircon grains that have remained closed to U and all its daughters should plot on the concordia curve. Such analyses are said to be concordant. However, in most cases zircon crystals lose varying proportions of their radiogenic Pb subsequent to their crystallization due to factors such as metamorphism, alteration and metamictization (radiation damage due to U and Th decay). As a result, zircon grains commonly record discordant dates that plot as collinear data points off the concordia curve. Discordia often occurs thereafter, as a result of polyphase tectono-magmatic events particularly in polyphase terranes such as Archaean granite-greenstone complexes. This emanates from a mixture of analyses on inherited, overgrowth and magmatic zircon grains. A regression line through the collinear data points of zircon analyses intercept the concordia curve. The collinearity of the zircon analyses near the upper intercept is usually interpreted to indicate an initial concordance followed by Pb loss, in which case the upper intercept provides the date of primary zircon crystallization. The existence of discordance in zircon populations is common and allows multiple geochronological interpretations. For instance, more than one zircon populations can occur in a sample resulting in more than one upper intersection with the concordia curve.

It is worth-mentioning that the age of zircon is not necessarily identical to the age of the host rock, because zircon is a refractory mineral with the potential to survive high temperatures during partial melting of protoliths of the host rocks (e.g. Rubatto and Herman, 2003). This phenomenon is called zircon inheritance. Inheritance is generally reflected in the variation of $^{207}Pb/^{206}Pb$ dates from different grains within a zircon population of the same sample. Generally, inherited zircon grains have cores that represent zircon fragments around which later zircon has nucleated and grown. Often such zircon grains display structureless cores. Magmatic zircon grains are commonly euhedrally zoned, an indication that they crystallized from a melt. However, magmatic zircon grains can develop overgrowths, or recrystallize due to subsequent thermal events. Therefore, the interpretation of zircon dates requires the distinction between magmatic, overgrowths, recrystallised and inherited zircon (xenocryst). Overgrowths are commonly recognized by an unconformable

relationship to the magmatic zoning because it usually follows a period of partial resorption. Recrystallisation is an in situ process that modifies the structure and chemistry of magmatic zircon grains. Thus, close examination of the morphology and internal structures of individual zircon grains can enable the distinction between different types of zircon grains (e.g. Pidgeon, 1992; Bowring and Williams, 1999). However, recrystallised zircon grains at times can be difficult to distinguish from magmatic zircon grains using structural features alone. Therefore, it warrants other criteria. The Th/U ratio is often used as a geochemical tool to distinguish between magmatically derived and metamorphically grown zircon (e.g. Bowring and Williams, 1999; Katongo et al., 2004; Davis et al., 2004). For instance igneous zircon grains from a wide range of rock types have present day Th/U ratios that typically vary from 0.2 to 1.0, whereas both subsolidus zircon overgrowths and new zircon grains grown under metamorphic conditions commonly possess distinctly lower Th/U values that range between 0.1 and << 0.05 (Maas et al., 1992; Bowring and Williams, 1999). The examination of the external morphology and internal structure of zircon cannot be achieved by conventional petrographic method because there is little geological information revealed and the internal structure of zircon is barely visible in thin section. Instead cathodoluminescence (CL) imaging technique better reveals the complex and varied internal zonation of zircon grains necessary for the distinction between magmatic and non-magmatic zircon types. CL imaging has been applied in this study to aid the selection of areas for U-Th-Pb isotopic analyses using SHRIMP, in addition to highlighting the internal structures of zircon crystals for chronologic interpretation. Results of U-Pb zircon isotopic analyses from this study are presented in Tables 4.1 to 4.10. CL images of zircon populations and the concordia diagrams are depicted in Figs. 4.2 to 4.30.

4.2 Zircon mineral separation

The zircon separation was conducted at the Council for Geosciences in Pretoria by the author. Zircon minerals were liberated from rock samples by conventional crushing and mineral separation techniques. Firstly, samples were pulverized in two stages to a final grain size in the 10 to 200 micron range using a jaw crusher followed by a disk mill. The sample powders were then passed over a Wilfley Table to obtain heavy mineral concentrates. At this stage the sample sizes were reduced by 90 to 95%. The dry heavy mineral separates were spread on a clean white A4 sheet of paper and then a hand magnet covered with plastic transparent paper was hovered above the sample to remove most magnetic particles, such as magnetite and iron particles from the steel

crushing plates. The next stage involved transfer of the sample concentrates to a Frantz Isodynamic separator to remove micas, amphiboles, pyroxenes, garnets, etc. from the concentrates. The Frantz side tilt was set at 5 degrees and the current adjusted gradually from 0.1 to 0.5 Am. Further mineral separation was accomplished first with the heavy liquid bromoform, to remove feldspars and quartz, followed by the heavy liquid methylene iodide, to remove apatite. For most felsic igneous rocks, a relatively pure concentrate of zircon grains was obtained at this stage. A final Frantz separation was performed to isolate zircon grains based on slight differences in paramagnetism by gradually reducing the side tilt in 2 degree increments to zero degrees at 1.8 Am. Most often the best quality zircon grains devoid of fractures, inclusions, alteration and other imperfections were found in the least magnetic Frantz (i.e. non-magnetic at 0 degree side tilt) split. In certain samples zircon grains could not be separated perfectly from other minerals, and therefore the zircon grains had to be hand-picked under a binocular microscope. During all stages of mineral separation, stringent cleaning procedures were adopted to ensure that there was minimal chance for cross-sample laboratory contamination. The zircon concentrates were sent to the Australian National University geochronology laboratory for analyses.

4.3 Analytical technique: U-Pb SHRIMP Geochronology

The zircon grains were analysed using the SHRIMP II (Sensitive High Mass Resolution Ion Microprobe) at the Research School of Earth Science (RSES) of the Australian National University (ANU) by Dr. Richard Armstrong. Firstly, the zircon grains were mounted in epoxy together with the zircon standard AS3 (Duluth Complex gabbroic anorthosite) and the RSES standard SL13. The grains were then sectioned approximately in half, and polished. Microphotographs were taken under both transmitted and reflected light to help identify fractures and inclusions, as well as to guide ion probing. Cathodoluminescence imaging on a SEM (Scanning Electron Microscope) was carried out prior to the analyses to aid in the selection of the best target areas for the analyses. The mount surface was cleaned, and gold-coated to facilitate an electrical potential of the mount as required for fixed and optimal extraction of secondary electrons (e.g. Claoue-Long, et al., 1995). The zircon grains were analysed for U-Th-Pb using the SHRIMP II. Detailed procedure for the analysis of zircon grains using SHRIMP are described in Compston et al. (1984). A 2-4 nA primary beam of negative oxygen ions was focused on a probe spot 15-30 µm diameter. The sputtered secondary electrons were analysed at mass resolution of 5500 to eliminate all significant isobaric interference.

The SHRIMP data have been reduced as described by Compton et al., (1992) and Williams and Claesson (1987). U-Pb in the unknowns were normalized to a ^{206}*Pb/^{238}U value of 0.1859 (equivalent to an age of 1099 Ma) for AS3. The determination U and Th concentration was made relative to those measured in the SL13 standard (572 Ma).

Dates were calculated using the radiometric ^{207}Pb/^{206}Pb ratios, with the correction for common Pb made using the measured ^{204}Pb and the appropriate common Pb composition assuming the model of Cumming and Richards (1975). U/Pb dates for zircon rims were calculated from their radiogenic ^{206}*Pb/^{238}U ratios, with a correction for common Pb made using the measured ^{207}Pb/^{206}Pb and ^{238}U/^{206}Pb based on the concordance procedure following Tera and Wasserburg (1972) and as described in Compston et al. (1992). Uncertainties in the isotopic ratios and dates in the data tables (and in the error bars in the plotted data) are reported at 95% confidence limits, with all statistical analyses and calculations done using the software Isoplot/Ex (Ludwig, 2003).

4.4 U-Pb zircon analyses

4.4.1 Paragneiss: *Sample GEOZB-1a*

This sample is from a widespread paragneiss unit underlying the eastern part of the Francistown Granite-Greenstone Complex. Previous workers (e.g. Litherland, 1975; Key, 1976; Carney et al., 1994) have suggested that the paragneiss unit post-dates the widely distributed tonalite-trondhjemite plutons within the Francistown Granite-Greenstone Complex. However, these workers indicated that the precursor of the paragneiss was part of the greenstone supracrustal sequences, which they presumed pre-dated the emplacement of the tonalite-trondhjemite plutons. This is rather paradoxical. According to Litherland (1975) and Key (1976) a regional tectonothermal event that reached the upper amphibolite facies converted part of the greenstone successions into the paragneiss unit. Their argument is that this thermal event affected the tonalite-trondhjemite, tonalite and granodiorite units in the Francistown Granite-Greenstone Complex, therefore the thermal event is younger. By selecting a sample from this unit I aimed at obtaining both the age of the tectonothermal event and the protolith or provenance of the protolith. The sample selected for U-Pb geochronology was sampled about 20 km east of the city of Francistown within Matshelagabedi village (Fig. 4.1). It is a medium to coarse-grained felsic non-banded gneiss composed of 65% feldspar and 20% quartz that form a granoblastic texture with 5% biotite as the mafic constituent.

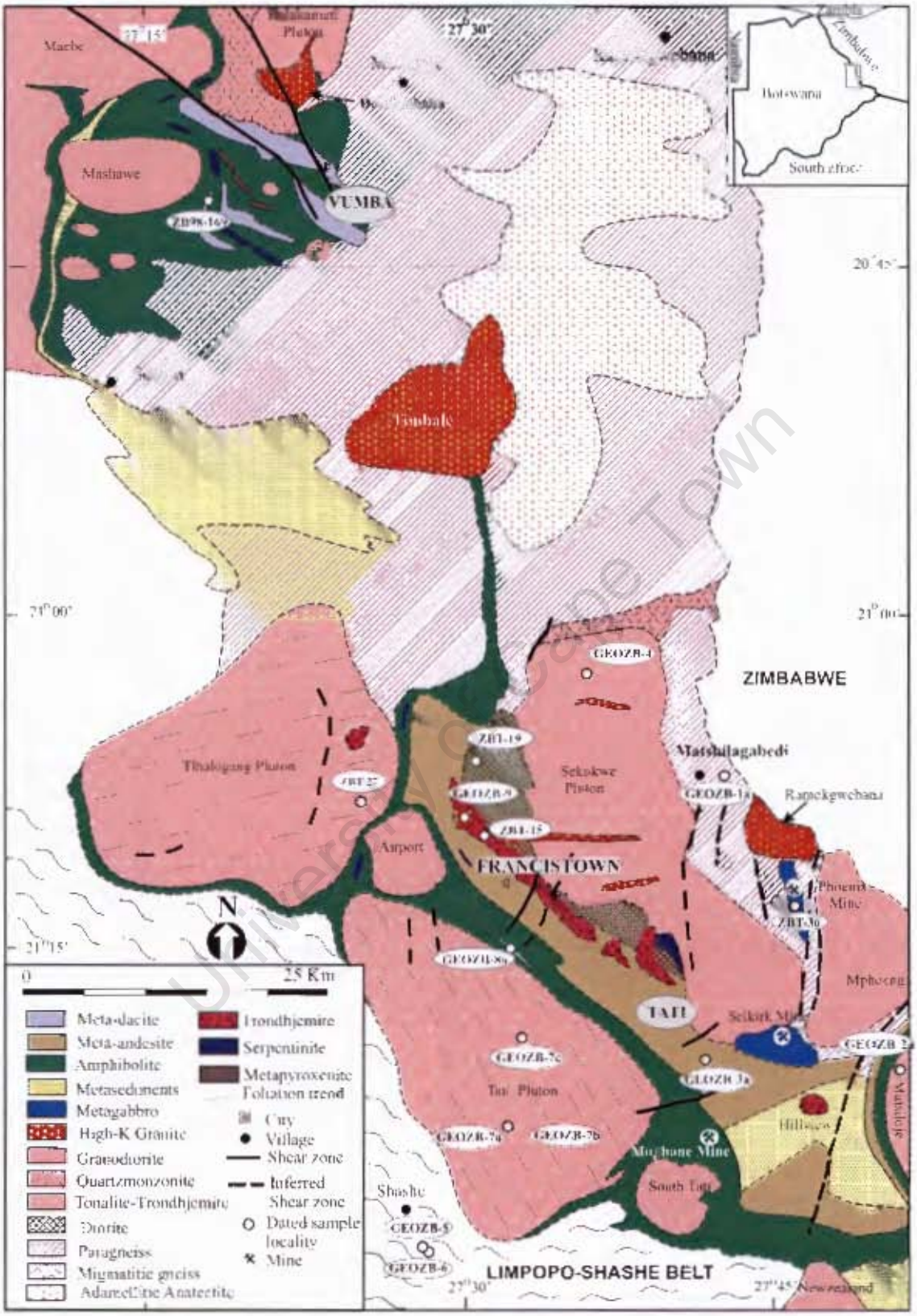

Fig. 4.1: Geological map showing the sample localities for U-Pb zircon dating

The zircon grains display prismatic habit with variable sizes (≥100 µm in length). Cathodoluminescence imaging revealed that the zircon grains are metamict and extensively altered (Fig. 4.2). The grains consist mostly of turbid centers surrounded by relatively clear mantle of overgrowth, which is damaged by alteration and partly by fractures. Nonetheless, fifteen analyses were obtained from fourteen zircon grains. All the analysed spots are from the overgrowth domain because it is least altered compared to the core. The zircon grains contain between 0.67 and 6.37% common Pb and variable contents of U and Th in the range of 730 to 2011 ppm and 63 to 607 ppm, respectively (Table 4.1). The Th/U ratio ranges between 0.32 and 0.05, which is typical for non-magmatic zircon grains. Despite attempts to date only the least altered areas, the data are highly discordant which renders the calculation of a precise or accurate date impossible. However, a regression of all data points, except data point # 6.1, gave an upper intercept date of 2755 ± 100 Ma and a lower intercept of 593 ± 120 Ma with a large scatter (MSWD = 4.9; Fig. 4.3). The upper intercept date is interpreted as the approximate age of the high grade regional metamorphic event that lead to the formation of the paragneiss

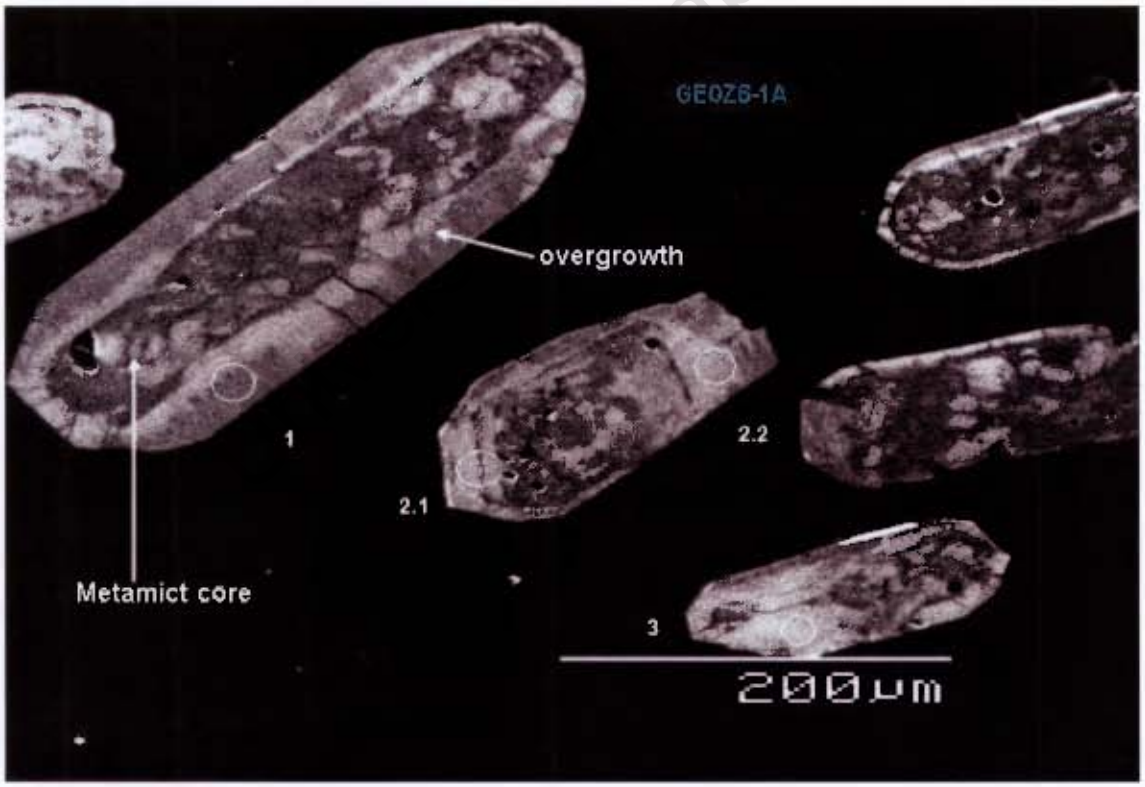

Fig. 4.2: CL images of some zircon grains extracted from the paragneiss sample GE0ZB-1a presented to illustrate the quality of the zircon grains and analysed spots. Note the ubiquitous mantle (envelope) of clear zircon overgrowth on anhedral metamict (altered) cores. No metamict core was analysed.

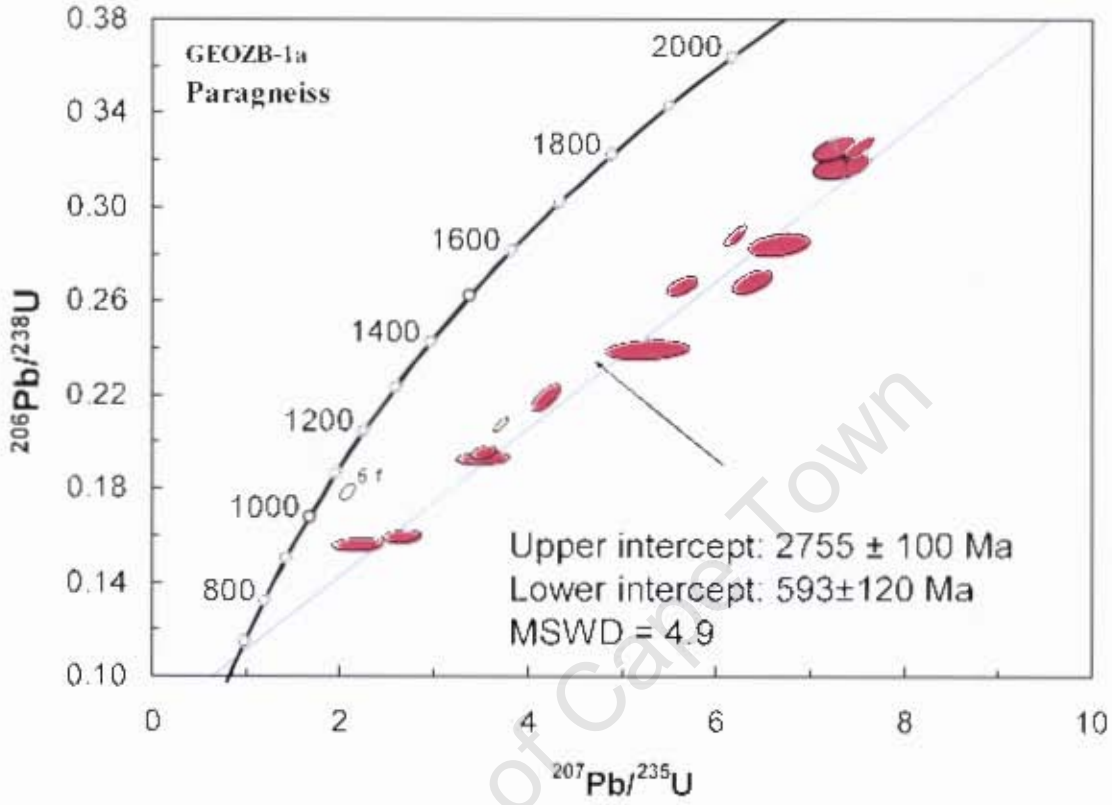

Fig. 4.3: U-Pb concordia plot of SHRIMP data for zircon grains from the paragneiss unit sample GEOZB-1a within the Tati granite-greenstone terrain. Only the overgrowths of the zircon grains were analysed.

Table 4.1: U-Th-Pb isotopic compositions of zircon grains from the paragneiss unit sample GEOZB-1a.

Concentration						Radiogenic ratios						Age [Ma]				
Grain Spot	% $^{206}Pb_c$	U (ppm)	Th (ppm)	Th/U	$^{206}Pb^*$ (ppm)	(1) $^{207}Pb^*/^{206}Pb^*$	±%	(1) $^{207}Pb^*/^{235}U$	±%	(1) $^{206}Pb^*/^{238}U$	±%	(1) $^{206}Pb/^{238}U$ Age		(1) $^{207}Pb/^{206}Pb$ Age		% Discordant
1.1	3.11	749	95	0.13	211	0.1709	2.3	7.47	2.6	0.317	1.2	1775	±18	2566	± 39	31
2.1	6.37	2011	607	0.30	284	0.1119	7.3	2.37	7.4	0.154	1.2	923	±10	1830	±130	50
2.2	1.72	1320	136	0.10	251	0.145	1.6	4.36	2.4	0.2178	1.8	1270	±20	2288	± 28	44
3.1	0.67	848	79	0.09	151	0.1373	0.77	3.888	1.3	0.2054	1.1	1204	±12	2193	± 13	45
4.1	1.61	819	117	0.14	190	0.158	1.4	5.79	1.8	0.2657	1.1	1519	±14	2434	± 24	38
5.1	6.20	756	107	0.14	165	0.165	5.3	5.42	5.4	0.2384	1.2	1378	±15	2507	± 89	45
6.1	1.45	1596	85	0.05	246	0.0943	1.9	2.295	2.3	0.1765	1.2	1048	±12	1514	± 36	31
7.1	3.91	704	185	0.26	178	0.1744	3	6.81	3.2	0.2833	1.1	1608	±16	2600	± 50	38
8.1	5.52	1099	94	0.09	191	0.1407	5	3.71	5.1	0.1912	1.1	1128	±12	2235	± 86	50
9.1	0.70	841	111	0.13	208	0.1605	0.73	6.346	1.3	0.2867	1.1	1625	±15	2461	± 12	34
10.1	0.90	773	78	0.10	217	0.1711	0.9	7.65	1.4	0.3245	1.1	1811	±17	2568	± 15	29
11.1	1.80	818	110	0.13	232	0.1656	1.7	7.4	2	0.3241	1.1	1810	±17	2514	± 29	28
12.1	2.27	730	233	0.32	172	0.1768	1.8	6.52	2.2	0.2676	1.3	1529	±18	2623	± 29	42
13.1	4.61	1517	290	0.19	215	0.1314	4.6	2.85	4.8	0.1575	1.1	943.1	± 9.9	2117	± 81	55
14.1	2.35	1161	63	0.05	198	0.1389	2.2	3.705	2.4	0.1935	1.1	1140	±11	2213	± 38	48

Uncertainties in ages are reported at the 2 sigma confidence level.

% $^{206}Pb_c$ denotes the percentage of ^{206}Pb that is common Pb.

$^{206}Pb^*$ indicates the portion of radiogenic Pb.

(1) Common Pb corrected using measured ^{204}Pb

4.4.2 Tonalite-trondhjemite plutonism NE Tati greenstone belt

Samples GEOZB-2a and GEOZB-4

Two samples, GEOZB-2a and GEOZB-4, were collected from the Matsiloje and the Sekukwe plutons, respectively. These plutons form the major constituents of the tonalite-trondhjemite units flanking the northeastern and eastern sections of the Tati greenstone belt. The Sekukwe and Matsiloje plutons are presumed to be coeval and time-equivalents of the tonalite-trondhjemite plutons outcropping along the southwestern and western side of the Tati greenstone belt (e.g. Key, 1976; Kampunzu et al., 2003; Zhai et al., 2006). The two samples selected for U-Pb zircon geochronology were processed in order to constrain the age of the plutonic activity along the northeastern part of the Tati greenstone belt and to test correlations with the already dated plutonism in the Vumba terrain.

Sample GEOZB-2a, from the Matsiloje pluton, is a medium-grained, pale-grey, homogeneous, weakly foliated biotite tonalite-trondhjemite. Zircon grains extracted from this sample were fragmented, extremely altered and metamict. Small grains generally display subhedral and prismatic habit. Most of the grains display a relatively bright cathodoluminescence (representative of lower U, Th and less alteration) core, surrounded by structureless and highly altered dark brown overgrowths (Fig. 4.4). In some cases the alteration can be seen to break up and disrupt the original zoning patterns. Six analyses were carried out on 6 different zircon grains. The concentrations of U and Th in these grains range from 275 to 1865 ppm and 72 to 958 ppm, respectively, resulting in Th/U ratios in the range of 0.12 to 0.55 (Table 4.2). This broad range of Th/U ratio suggests that the zircon grains are a mixture of non-magmatic and magmatic origins. There is only one analysis (#8.2), which yielded a relatively higher Th/U ratio (0.55), comparable with that of magmatic zircon grains. Additionally, the zircon grain #8 exhibit oscillatory zoning, which is indicative of a magmatic origin. No accurate magmatic date could be obtained from these zircon grains due to the combined problems of severe alteration and possible inheritance. Analyses of the low-U cores are also discordant and appear to be heterogeneous. Analysis # 8.2 (Table 4.2) gave a near-concordant minimum $^{207}Pb/^{206}Pb$ date of 2911 ± 5.5 Ma, and analysis # 9.3 a near-concordant minimum date of 2647 ± 30 Ma. The date of 2911 ± 5.5 Ma is interpreted as an inherited age from the protolith to the Matsiloje tonalite-trondhjemite rather than of emplacement. The date of 2647 ± 30 Ma is interpreted as a metamorphic age. Nonetheless, linear regression of all the six analyses on a concordia

diagram yielded an upper intercept date of 2876 ± 160 Ma and a lower intercept of 967 ± 250 Ma (MSWD = 17; Fig. 4.5).

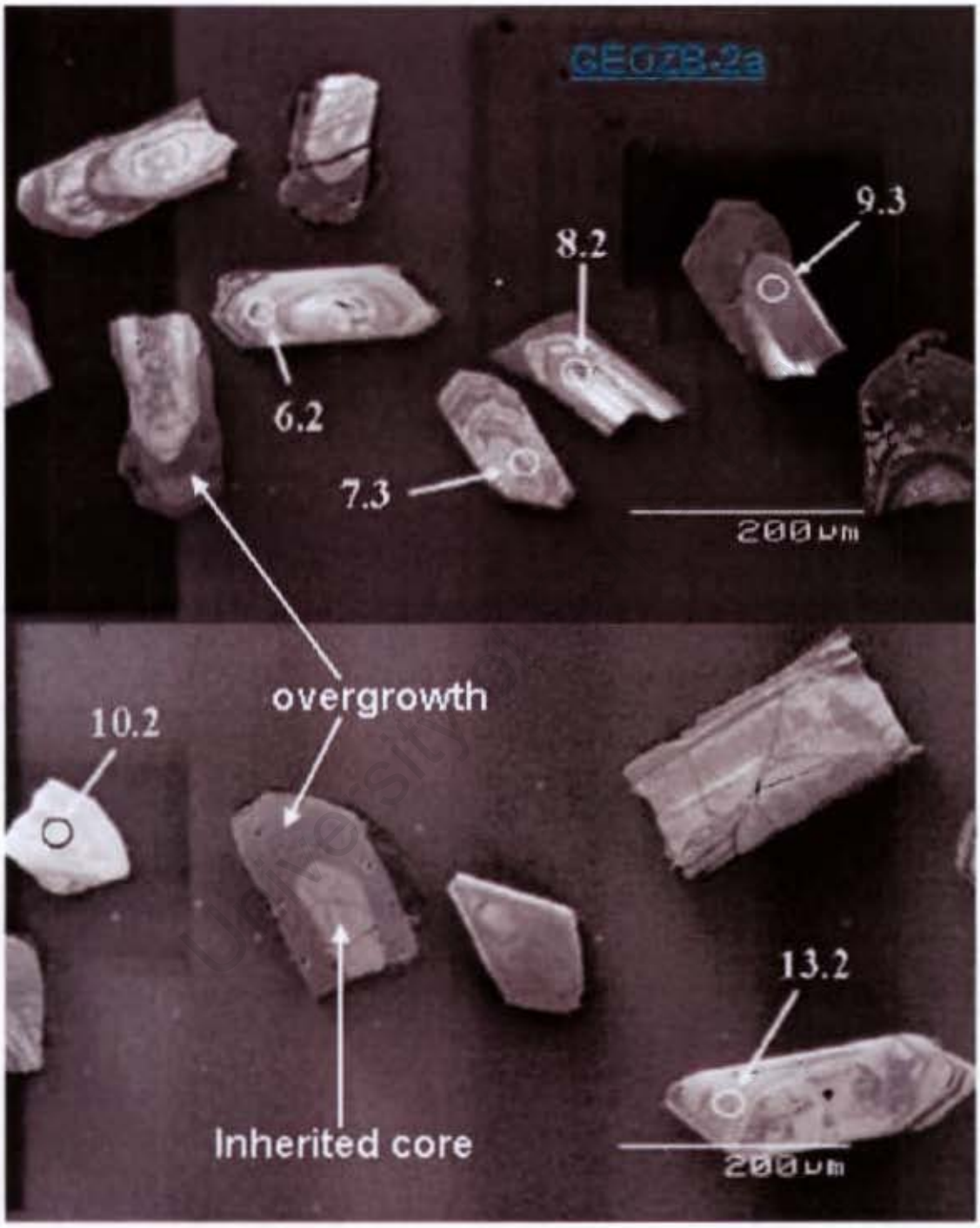

Fig. 4.4: CL images of all the zircon grains from the Matsiloe Pluton sample GEOZB-2a showing the quality of zircon grains and the analysed spots. Note the zircon grain #6 with good magmatic-like zoning that recorded a date of 2911 ± 5.5 Ma. Also note the overgrowths around structureless cores in some grains.

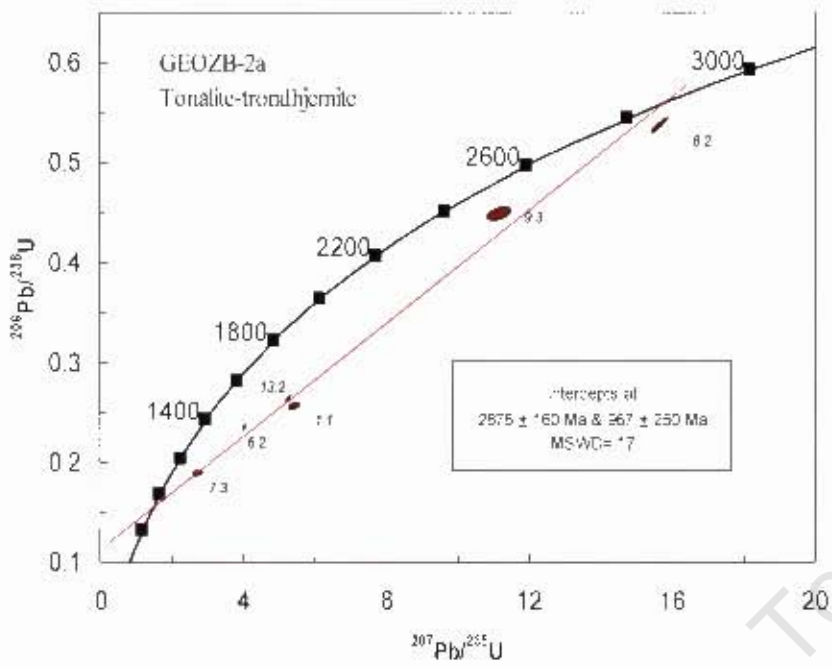

Fig. 4.5: U-Pb concordia plot of SHRIMP data for zircon grains from the Matsiloje Pluton sample GEOZB-2a, a tonalite-trondhjemite granitoid in the eastern Tati greenstone belt.

Sample GEOZB-4 was collected from the Sekukwe pluton (see Fig. 4.1). This is a large massive, medium-grained, leucocratic, homogeneous, granular trondhjemite/tonalite intrusion. The sample yielded 31 zircon grains that are brown, and vary in form from elongate forms with long pyramidal terminations to more stubby grains. Most grains show good magmatic zoning (Fig. 4.6) but there is a range in cathodoluminescence brightness reflecting the broad range in U and Th concentrations measured. The zircon grains yielded a wide range of U and Th concentrations that vary from 81 to 1735 ppm and 29 to 1071 ppm, respectively (Table 4.2). As a result Th/U ratios vary broadly between 0.13 and 0.79 indicating both signatures of non-magmatic and magmatic zircon grains. Some zircon grains are clearly altered and metamict as they are high in common Pb and discordant. A total of 44 analyses were done on 30 grains and the results are presented in Table 4.2. Regression of all the data gives an upper intercept date of 2732 ± 24 Ma (MSWD = 26; Fig. 4.7a). However, a group of analyses plot along the concordia and give a weighted mean $^{207}Pb/^{206}Pb$ date of 2732.7 ± 4.4 Ma (MSWD = 1.06; Fig. 4.7b), which is interpreted as the best estimate of magmatic age of the Sekukwe tonalite-trondhjemite pluton. A few analyses (grains # 22.1, 31.1) give a near concordant $^{207}Pb/^{206}Pb$ date of 2673 ± 4.5 Ma, but a non-magmatic zircon Th/U ratio. This date is therefore interpreted as the age of metamorphism.

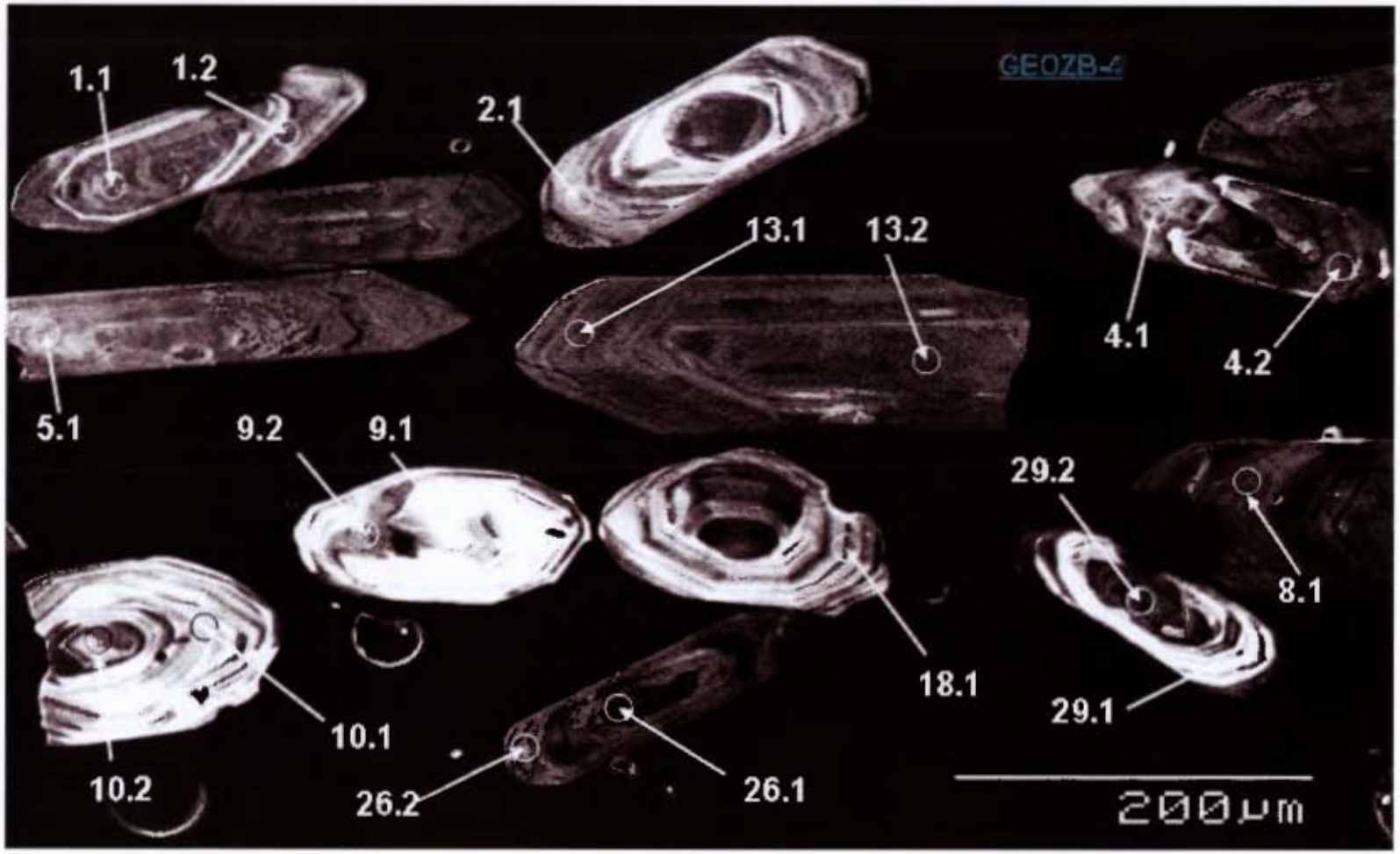

Fig. 4.6: C_ images of some zircon grains extracted from the Sekukwe pluton sample GEOZB-4 showing euhedral to subhedral prismatic habit and good magmatic zoning. White circles denote analysed spots. The magmatic age of this pluton is 2732 Ma, with a metamorphic overprint of 2673 Ma.

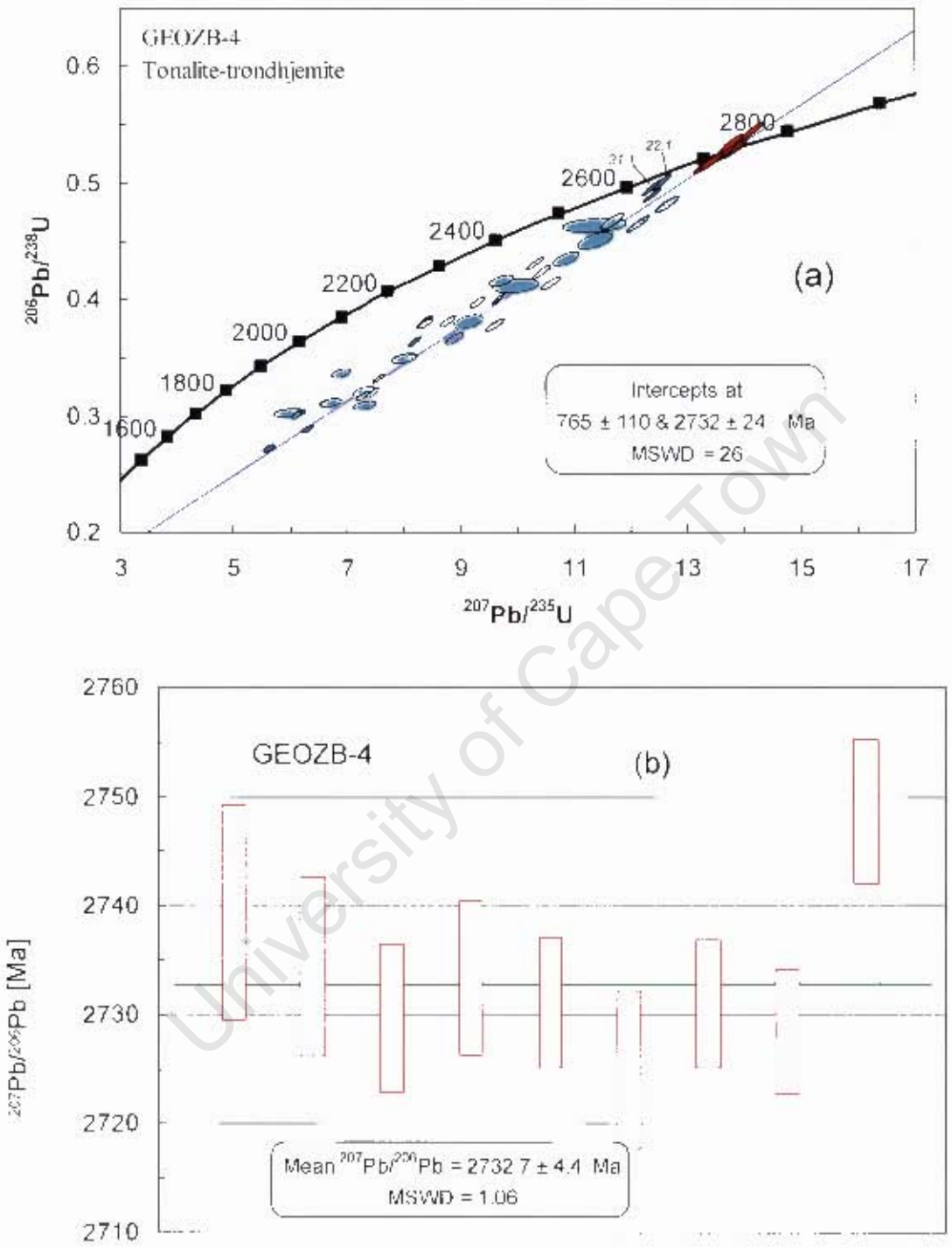

Fig. 4.7: U-Pb concordia plot of SHRIMP data for zircon grains from the (a) Sekukwe Pluton sample GEOZB-4, which is a tonalite-trondhjemite granitoid in the northeastern Tati greenstone belt. Red ellipses represent concordant analyses while the blue ellipses show discordant data. (b) Weighted average mean $^{207}Pb/^{206}Pb$ date for 9 concordant data plots. Confidence limit for error ellipses is 1σ.

Table 4.2: U-Th-Pb isotopic compositions of zircon grains from samples of the NE tonalite-trondhjemite plutons in the Tati granite-greenstone terrane.

Concentration						Radiogenic ratios						Age [Ma]				
Grain Spot	% $^{206}Pb_c$	U (ppm)	Th (ppm)	Th/U	$^{206}Pb^*$ (ppm)	(1) $^{207}Pb^*/^{206}Pb^*$	±%	(1) $^{207}Pb^*/^{235}U$	±%	(1) $^{206}Pb^*/^{238}U$	±%	(1) $^{206}Pb/^{238}U$ Age		(1) $^{207}Pb/^{206}Pb$ Age		% Discordant
GEOZB-2a: Matsiloje Pluton																
6.2	0.15	1068	130	0.12	213	0.12185	0.46	3.899	0.95	0.2320	0.83	1,345	±10	1,983.5	± 8.2	32
7.3	3.06	1865	958	0.51	307	0.1010	3.7	2.584	3.8	0.1856	0.88	1,097.7	± 8.9	1,642	±69	33
8.2	0.19	335	185	0.55	155	0.21070	0.34	15.63	0.98	0.5381	0.92	2,776	±21	2,911.0	± 5.5	5
9.3	2.32	272	86	0.32	107	0.1794	1.8	11.10	2.0	0.4487	0.97	2,389	±19	2,647	±30	10
10.2	1.73	598	72	0.12	133	0.1517	1.7	5.32	1.9	0.2544	0.94	1,461	±12	2,366	±29	38
13.2	0.20	1043	143	0.14	235	0.14284	0.36	5.155	0.91	0.2618	0.83	1,499	±11	2,261.9	± 6.2	34
GEOZB-4: Sekukwe Pluton																
1.1	0.08	81	34	0.42	36.6	0.1897	0.60	13.78	1.3	0.5271	1.1	2,729	±24	2,739.3	± 9.9	0
1.2	0.01	108	49	0.45	49.0	0.19003	0.41	13.73	1.1	0.5267	10	2,728	±22	2,734.3	± 8.2	0
2.1	0.68	735	240	0.33	241	0.16172	0.58	8.437	1.0	0.3784	0.85	2,069	±15	2,473.7	± 9.8	16
3.1	0.20	134	66	0.49	55.3	0.19127	0.51	12.65	1.1	0.4798	1.0	2,526	±21	2,753.1	± 8.4	8
3.2	0.07	140	61	0.44	63.2	0.18927	0.37	13.67	1.0	0.5259	0.94	2,724	±21	2,729.5	± 6.8	0
4.1	0.37	928	694	0.75	264	0.16816	0.40	7.642	0.92	0.3296	0.83	1,836	±13	2,539.5	± 6.8	28
4.2	0.21	882	525	0.59	303	0.17723	0.27	9.729	0.85	0.3985	0.80	2,162	±15	2,625.5	± 4.8	18
5.1	0.44	811	223	0.28	222	0.17219	0.45	7.523	0.96	0.3169	0.85	1,774	±13	2,579.1	± 7.5	31
6.1	0.51	1022	474	0.46	334	0.16976	0.43	8.854	0.94	0.3783	0.83	2,068	±15	2,555.2	± 7.2	19
7.1	0.54	967	476	0.49	301	0.16620	0.46	8.270	0.95	0.3609	0.84	1,986	±14	2,519.8	± 7.7	21
8.1	0.47	578	243	0.42	156	0.17046	0.55	7.371	1.0	0.3136	0.90	1,759	±14	2,562.1	± 9.2	31
9.1	0.17	146	61	0.42	65.3	0.18897	0.43	13.58	1.1	0.5212	0.98	2,704	±22	2,733.2	± 7.1	1
9.2	0.02	166	64	0.39	73.5	0.18933	0.33	13.43	0.99	0.5162	0.92	2,683	±20	2,730.9	± 6.0	2
10.1	0.03	113	43	0.38	50.0	0.18800	0.44	13.32	1.1	0.5138	1.0	2,673	±22	2,724.8	± 7.2	2
10.2	--	147	55	0.38	68.4	0.18935	0.34	14.12	1.0	0.5427	0.94	2,795	±21	2,730.8	± 5.9	-2
11.1	0.33	178	84	0.47	57.7	0.1867	0.57	9.67	1.1	0.3756	0.98	2,056	±17	2,713.1	± 9.4	24
11.2	0.51	230	37	0.16	92.5	0.1824	0.62	11.70	1.1	0.4653	0.97	2,463	±20	2,675	±10	8
12.1	0.39	926	314	0.34	343	0.17513	0.35	10.362	0.90	0.4291	0.83	2,302	±16	2,607.3	± 5.8	12
12.2	0.58	653	140	0.21	223	0.17193	0.48	9.348	0.97	0.3949	0.81	2,146	±15	2,573.9	± 9.0	17

Uncertainties in ages are reported at the 2 sigma confidence level. % $^{206}Pb_c$ denotes the percentage of ^{206}Pb that is common Pb. $^{206}Pb^*$ indicates the portion of radiogenic Pb.

Table 4.2: Continued

Concentration						Radiogenic ratios						Age [Ma]				
Grain Spot	% $^{206}Pb_c$	U (ppm)	Th (ppm)	Th/U	$^{206}Pb^*$ (ppm)	(1) $^{207}Pb^*/^{206}Pb^*$	±%	(1) $^{207}Pb^*/^{235}U$	±%	(1) $^{206}Pb^*/^{238}U$	±%	(1) $^{206}Pb/^{238}U$ Age		(1) $^{207}Pb/^{206}Pb$ Age		% Discordant
13.1	1.46	650	169	0.26	180	0.1689	1.7	7.40	1.9	0.3176	0.88	1,778	±14	2,547	±29	30
13.2	0.80	793	275	0.35	197	0.1626	0.66	6.392	1.1	0.2857	0.80	1,620	±12	2,480	±12	35
14.1	0.80	355	281	0.79	112	0.1786	0.74	8.96	1.2	0.3640	0.93	2,001	±16	2,640	±12	24
14.2	0.15	173	91	0.53	61.3	0.1871	0.54	10.64	1.1	0.4125	0.99	2,226	±19	2,716.6	± 8.8	18
14.3	0.87	216	92	0.42	81.1	0.1836	0.90	10.92	1.4	0.4330	0.90	2,319	±18	2,679	±17	13
15.1	0.18	313	57	0.18	113	0.18000	0.44	10.47	1.0	0.4219	0.91	2,269	±17	2,652.9	± 7.2	14
15.2	2.82	533	102	0.19	194	0.1779	2.2	10.02	2.7	0.4099	0.93	2,214	±17	2,633	±37	16
16.1	1.43	154	40	0.26	60.4	0.1843	1.4	11.41	1.7	0.4488	1.0	2,390	±21	2,692	±23	11
17.1	3.54	1427	873	0.61	381	0.1474	3.0	6.09	3.1	0.2997	0.87	1,690	±13	2,316	±51	27
18.1	0.03	195	122	0.63	77.4	0.19020	0.38	12.14	1.0	0.4630	0.96	2,453	±20	2,743.9	± 6.3	11
19.1	1.90	417	162	0.39	139	0.1766	1.4	9.19	1.9	0.3787	1.0	2,070	±18	2,616	±27	21
20.1	1.56	1580	1071	0.68	462	0.1518	1.3	6.98	1.6	0.3341	0.80	1,858	±13	2,363	±24	21
21.1	1.86	631	84	0.13	170	0.1753	1.4	7.39	1.8	0.3068	0.83	1,725	±13	2,604	±26	34
22.1	--	178	29	0.16	76.5	0.18303	0.32	12.55	0.97	0.4988	0.91	2,609	±19	2,675.3	± 5.5	2
23.1	1.80	832	301	0.36	225	0.1603	1.4	6.80	1.8	0.3084	0.82	1,733	±12	2,455	±27	29
25.1	3.74	485	124	0.26	202	0.1796	2.7	11.38	3.2	0.4617	0.88	2,447	±18	2,642	±51	7
26.1	0.71	1059	496	0.47	273	0.15116	0.62	6.200	1.1	0.2980	0.80	1,681	±12	2,359	±11	29
26.2	1.94	362	127	0.35	111	0.1699	1.5	8.09	1.9	0.3466	0.87	1,918	±14	2,557	±25	25
27.1	1.35	821	349	0.42	297	0.1715	1.0	9.77	1.4	0.4140	0.82	2,233	±15	2,572	±17	13
28.1	0.15	527	340	0.65	221	0.18470	0.23	12.40	0.86	0.4877	0.82	2,561	±17	2,695.5	± 3.8	5
28.2	0.83	755	363	0.48	176	0.1545	0.82	5.717	1.2	0.2690	0.82	1,536	±11	2,396	±14	36
29.1	0.01	159	104	0.65	73.0	0.18839	0.35	13.79	1.0	0.5327	0.94	2,753	±21	2,728.2	± 5.7	-1
29.2	--	124	58	0.46	56.3	0.19074	0.40	13.77	1.1	0.5262	0.98	2,725	±22	2,748.5	± 6.6	1
30.1	0.76	1735	603	0.35	568	0.16253	0.58	8.448	1.0	0.3774	0.79	2,064	±14	2,482.2	± 9.8	17
31.1	0.01	350	74	0.21	149	0.18204	0.24	12.38	0.89	0.4940	0.85	2,588	±18	2,671.6	± 4.0	3

4.4.3 Tonalite-trondhjemite plutonism SW Tati greenstone belt:

Samples GEOZB-7A, GEOZB-7B, GEOZB-7C and ZBTF-27.

The Tlhalogang and Tati plutons are the main bodies of the tonalite-trondhjemite units flanking the western and southwestern part of the Tati greenstone belt, respectively (Fig. 4.1). These plutons display a penetrative deformational fabric that has been linked to the collision with the Limpopo-Shashe belt (e.g. McCourt et al., 2004; Kampunzu et al., 2003). However, the deformation fabric in the Tlhalogang pluton is different from the trend in the Limpopo-Shashe belt. The Tlhalogang pluton displays a deformation fabric trending SW – NE direction, while the deformation fabric for the Tati pluton trends NW-SE parallel to the trend of the Tati greenstone belt. The Tati pluton is an oval-shaped heterogeneous intrusive body with local banding on centimeter scale defined by alternating well-foliated biotite-rich (melanocratic) bands and granular quartz-feldspar rich (leucocratic) bands. The leucocratic bands (leucosome) are represented by sample GEOZB-7A, which is a medium-grained granular granite with low modal proportion of biotite.

Zircon grains extracted from sample GEOZB-7A were variable in shape and size (100 – 300 µm length). They display subhedral to anhedral habit and dark pink to red colour. Some grains are chunky whereas others tend to be more prismatic and they all have pronounced oscillatory zoning suggesting magmatic origin (Fig. 4.8). The central parts of the grains generally comprise bright cathodoluminescence (low U) areas surrounded by dark cathodoluminescence growth. Thirty-five analyses of 27 zircon grains were obtained from this sample (Table 4.3). Twenty-three analyses were of the cores while the remaining analyses were of the rims overgrowths. The dark cathodoluminescence areas are metamict and produced discordant data. In some cases the outer zones appear to cross-cut the inner growth zones and it is tempting on the basis of this evidence to suggest that these are inherited cores surrounded by later magmatic or metamorphic origin. In other cases the rims and cores appear to be part of a continuous, albeit changing growth phase. The cores of the grains contain between 60 and 600 ppm U and have relatively high Th/U ratios of >0.4. In contrast, the rims contain between 800 to 2415 ppm U and have low Th/U ratios mostly less than 0.15 (Table 4.3), which suggests a metamorphic origin. Regression of all data gives an upper intercept date of 2668 ± 24 Ma with a large MSWD of 34 (Fig. 4.9a). The oldest group (N=14) of concordant and near-concordant data is interpreted as a magmatic age of 2670 ± 10 Ma (MSWD = 1.5). This is interpreted as the magmatic age of the protolith to the leucosome. The 14 analyses that

produced this age are identified to allow the reader to evaluate the relative numbers of core and rim analyses. A few discrete grains may represent another zircon population (see Table 4.3). Regression of these few data points gives 2639.7 ± 7.9 Ma (MSWD = 0.089; Fig. 4.9b). This apparent younger date represents growth during high grade metamorphism at about 2639.7 ± 7.9 Ma, and is interpreted to date leucosome formation (result of high grade metamorphism).

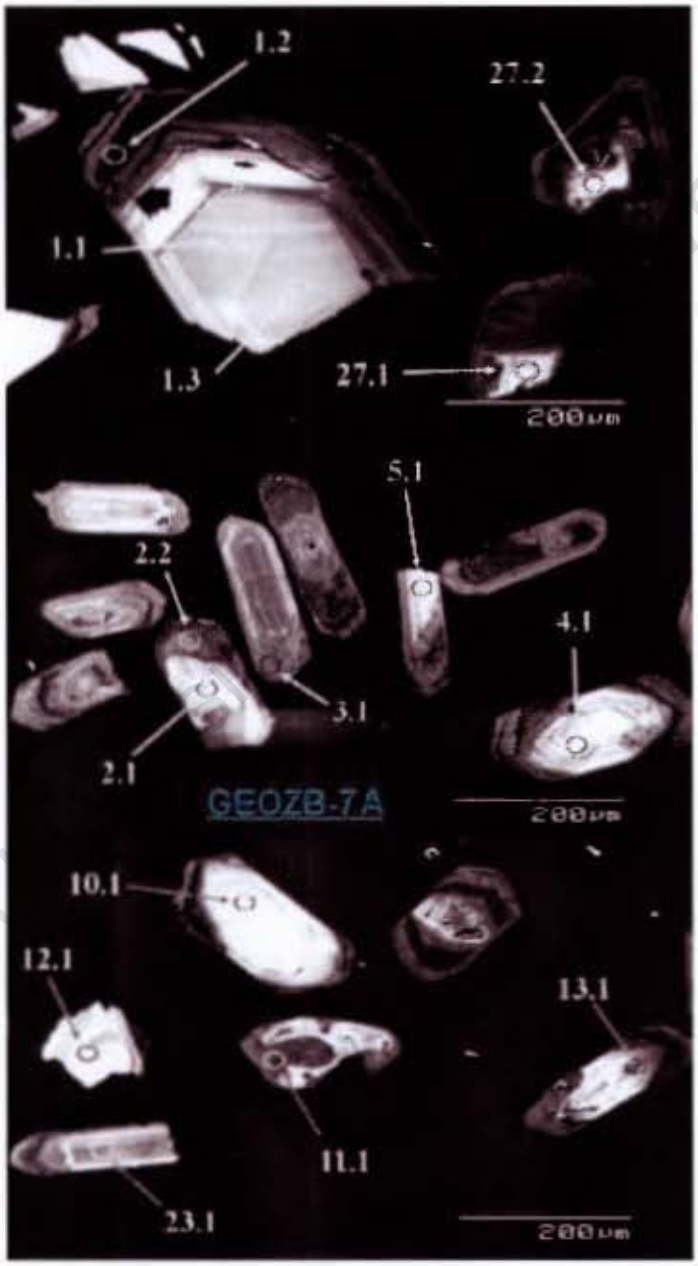

Fig. 4.8: CL images of some of the zircon grains extracted from leucosome sample GEOZB-7A in the Tati Pluton. Note some multi-domain grains (e.g. # 4) with euhedral and oscillatory zoned centers mantled by overgrowths. Numbers refer to the spots at which the analyses were taken. The magmatic age of this pluton is 2670 Ma, with a metamorphic overprint of 2640 Ma

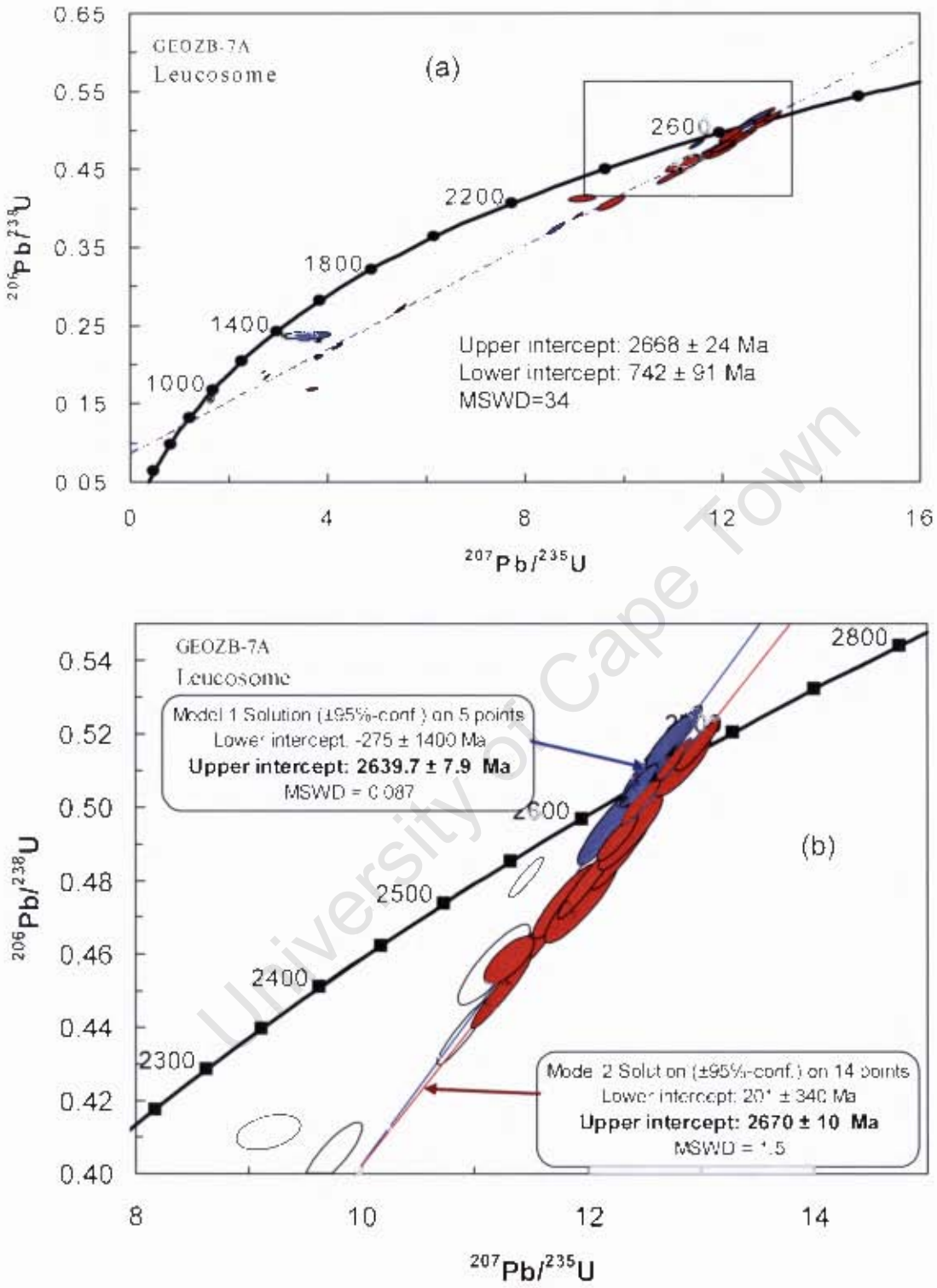

Fig. 4.9. (a) U-Pb concordia plot of SHRIMP data for zircon grains from the leucosome sample GEOZB-7A from the Tati Putor which is a tonalite-trondhjemite unit in the southwestern Tati greenstone belt. (b) Plot of enlarged area in the box. Blue ellipses represent a young zircon population, whereas red ellipses are for the older zircon population. Unfilled error ellipses were excluded in the calculation of the dates. Confidence limit for error ellipses is 1σ.

Sample GEOZB-7B was taken from a melanocratic band in the Tati Pluton and it is a biotite-rich tonalite. This sample yielded poor quality zircon grains that are highly metamict (particularly at the tips), subhedral to anhedral, prismatic and pale brown to colorless. The zircon grains have variable size from 100 to 300 µm long and have poorly preserved concentric zoning (Fig. 4.10a). Some grains display structureless cores surrounded with thick overgrowth. Sixteen analyses from 15 zircon grains were obtained from this sample. The observed U concentrations are between 66 and 6595 ppm (Table 4.3). The Th/U ratios vary from 0.05 to 1.09 with many grains exhibiting a Th/U ratio of more than 0.5. Analyses of the high-U rims are characterised by low Th/U ratios and they are highly discordant and scattered. This is indicative of metamorphic disturbance. Nevertheless, analyses of the low-U areas, which might include inherited cores, show a short discordia trend with an upper intercept date of 2684 ± 22 Ma (MSWD = 0.45; Fig. 4.11a). The low-U areas have Th/U ratios more than 0.5. Therefore, the date of 2684 ± 22 Ma is interpreted to be the magmatic age of the pluton. Noteworthy is the observation that this age is within margin of error of the age of 2670 ± 10 Ma recorded in the leucosome sample, which was interpreted as the magmatic age of the pluton.

Sample GEOZB-7C was collected from the grey gneiss (non-banded) section of the Tati pluton. It is a medium-grained foliated grey tonalite/trondhjemite with xenomorphic feldspars, quartz and biotite as essential phases. This sample yielded zircon grains that are brown, euhedral to subhedral with some crystals showing chisel-shaped terminations. Cathodoluminescence imaging shows central areas are weakly zoned and these are surrounded by stronger oscillatory zoned margin (Fig. 4.10b). Some structural cores are seen in a few grains through cathodoluminescence imaging, but no firm evidence of inheritance is seen in the analytical data. If there is inheritance then these xenocrysts are probably not much older than the magmatic population of zircon grains. Twenty-nine analyses of 22 zircon grains were obtained from this sample. The grains contain Th/U ratios between 0.47 and 1.33, which is typical for magmatic zircon grains. The data shows some discordance, especially on high-U margins, but a weighted mean $^{207}Pb/^{206}Pb$ date on a group of data straddling the concordia gives 2672.9 ± 2.8 Ma (MSWD = 1.3; Fig. 4.11b-c), which is interpreted to be the magmatic age of the Tati pluton. This age is within error of the ages of 2670 ± 10 Ma and 2684 ± 22 Ma obtained from samples GEOZB-7A and GEOZB-7B, respectively. These two samples are from highly deformed section characterised by strong foliation and metamorphic banding. Therefore, geochronological data reveal that the Tati pluton was emplaced around 2670 Ma and subsequently

affected by a metamorphic event around 2640 Ma resulting in partial melting of some sections of the pluton particularly towards the margin with the Limpopo-Shashe belt.

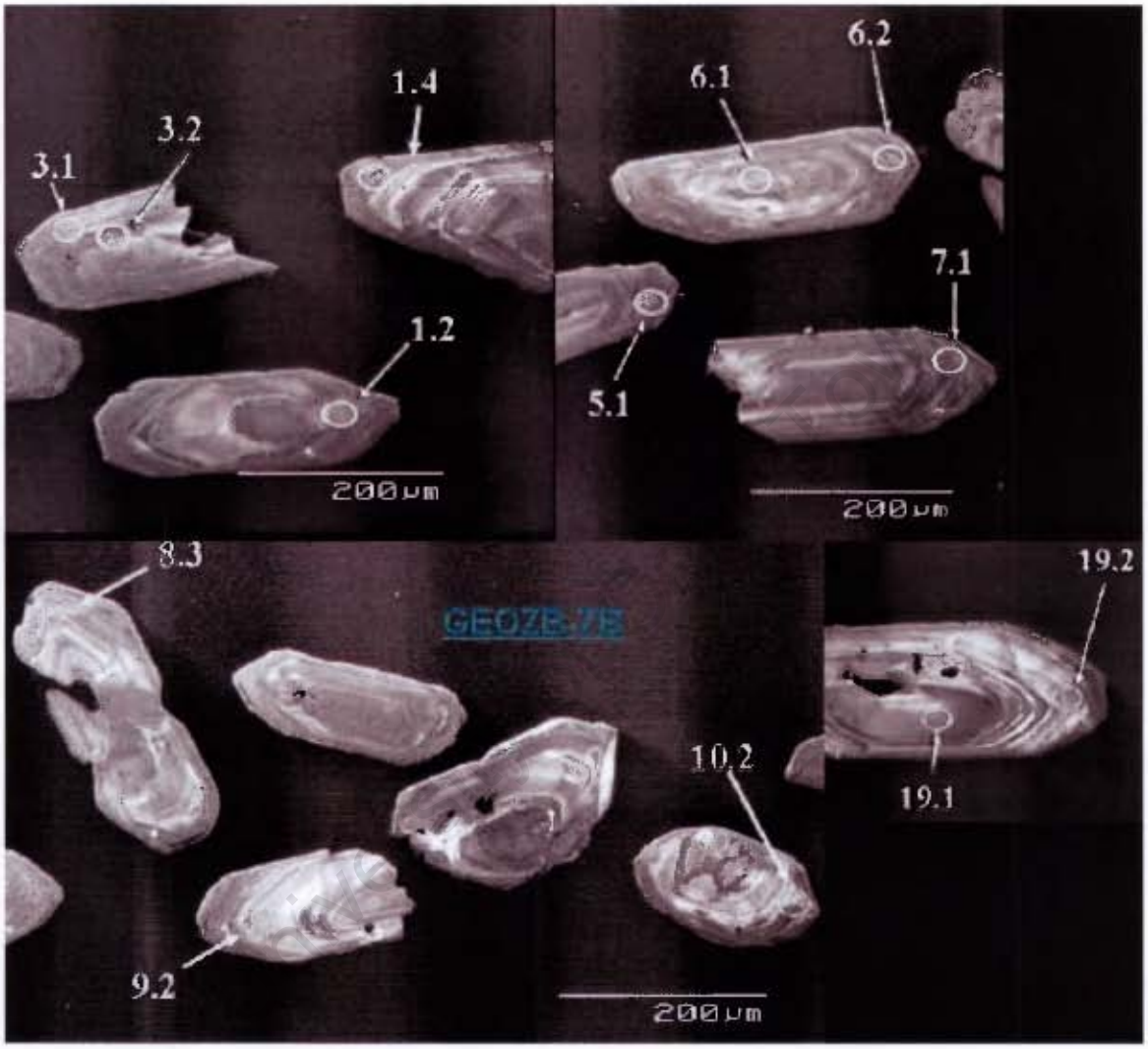

Fig. 4.10a: CL images for some zircon grains extracted from the samples GEOZB-7B from the Tati Pluton. Note the magmatic-like zoning and the analysed spots (white circles) indicated by white arrows. The magmatic age of this pluton is 2684 ± 22 Ma.

Fig. 4.10b: C. images of some selected zircon grains from the sample GEOZB-7C from the Tati Pluton to illustrate their quality, and some analysed spots (black circles). Note the euhedral centers with magmatic zoning and very altered metamorphic rims. The magmatic age of this pluton is 2672.9 ± 2.8 Ma.

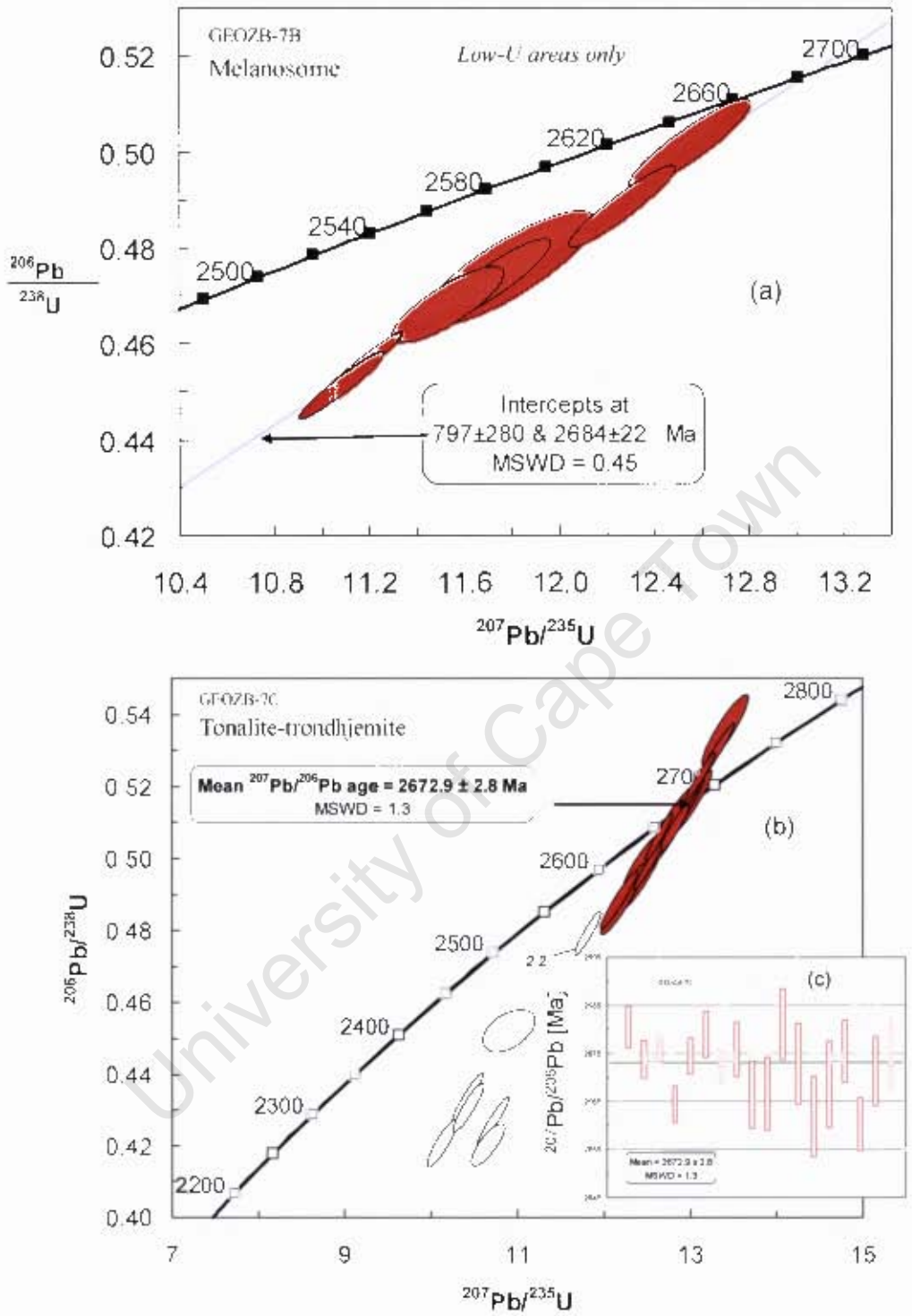

Fig. 4.11. U-Pb concordia plot of SHRIMP data for zircon grains from the (a) Melanosome sample GEOZB-7B (only low-U analyses plotted) and (b) Tonalite-trondhjemite sample GEOZB-7C from the Tati Pluton. The discordant analyses are represented here by unfilled error ellipses that are not included in the calculated $^{207}Pb/^{206}Pb$ date. (c) Inset illustrates the weighted average mean $^{207}Pb/^{206}Pb$ date. Confidence limit for error ellipses is 1σ.

Sample ZBT-27

The Tlhalogang pluton, from which sample ZBT-27 was collected, forms a large semi-circular and homogeneous body located 2 km northwest of the Tati pluton (Fig. 4.1). The selected sample for U-Pb geochronology is medium grained, strongly foliated, light-grey tonalite with anhedral quartz, feldspars and biotite. The sample yielded mostly metamict zircon grains that are generally subhedral and brown with diffuse oscillatory zoning suggesting magmatic origin. Most grains are prismatic and elongated (≤ 200 μm in length). Representative zircon grains from sample ZBT-27 are shown in Fig. 4.12. Lack of sharply defined zoning is probably a result of the alteration seen in these zircon grains. Rare bright cathodoluminescence patches cross-cutting the original zoning were also observed. These are likely metamorphic in origin.

Forty analyses from 26 zircon grains were obtained from this sample. The zircon grains yielded broad ranges in U (76-1643 ppm) and Th (15-3096 ppm) concentrations. Th/U ratios vary from 0.10 to 1.88 suggesting that the zircon grains are of mixed origin. Most of the data are highly discordant (indicative of Pb-loss) and the zircon grains have elevated common Pb, suggesting significant alteration. For the calculation of a date only a small group of data for zircon grains with the least discordance was used. These analyses give a weighted mean $^{207}Pb/^{206}Pb$ date of 2651.1 ± 3.4 Ma (MSWD = 1.13; Fig. 4.13). All these analyses were measured from the rims of a few subhedral to euhedral grains, which are most likely recrystallised zircon grains hence, recording a metamorphic age. In view of the state of deformation of rocks of the Tlhalogang pluton and lack of another zircon population dated younger than the 2651.1 ± 3.4 Ma, I interpret this date to be a metamorphic age. Analyses from cores of the zircon grains give a range in apparent dates with the two most near-concordant analyses giving minimum $^{207}Pb/^{206}Pb$ dates of 2739 ± 7.2 Ma and 2718 ± 12 Ma (see analyses #4.2 and #6.1, Table 4.3). These dates are interpreted to be magmatic ages from zircon grains that survived the deformation event. The dates are similar to the age of the Sekukwe Pluton described earlier. Based on the above arguments the $^{207}Pb/^{206}Pb$ date of 2739 ± 7.2 Ma is interpreted as the magmatic emplacement age of the Tlhalogang tonalite-trondhjemite pluton. This interpretation is tested in section 4.4.5, where zircon grains from a trondhjemite that intrude the Tlhalogang pluton (Fig. 4.1) are analysed. The zircon analyses from this trondhjemite give a magmatic age of around 2715 Ma, which is consistent with my interpretation here.

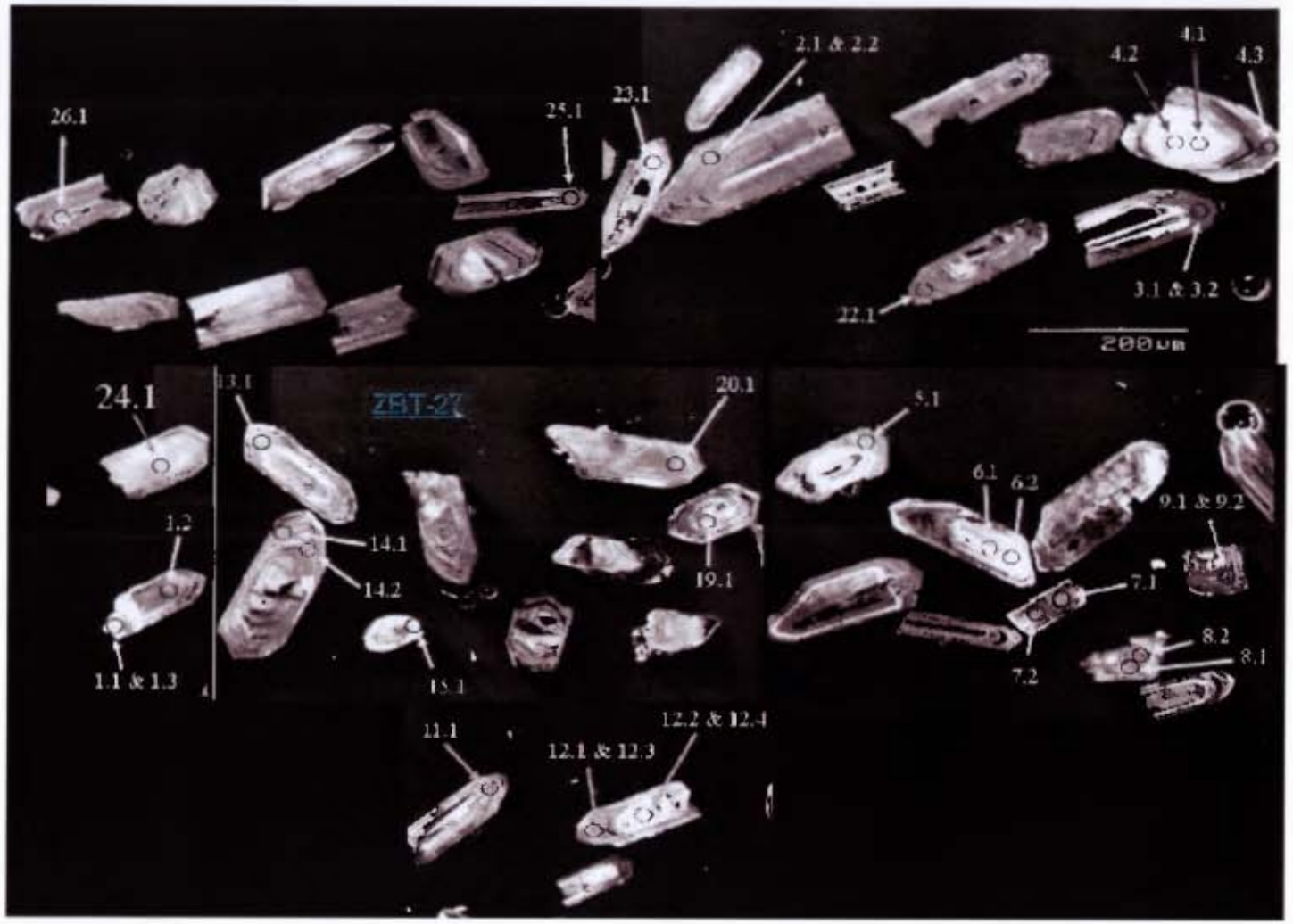

Fig. 4.12: CL images of zircon grains from the Thalegang pluton sample ZBT-27 illustrating the quality of zircon grains and analysed spots (black circles). Note that most of the analysed spots are on the rim of the grains. The magmatic age of this pluton is 2739 ± 7.2 Ma, with a metamorphic overprint of 2651.1 ± 3.4 Ma.

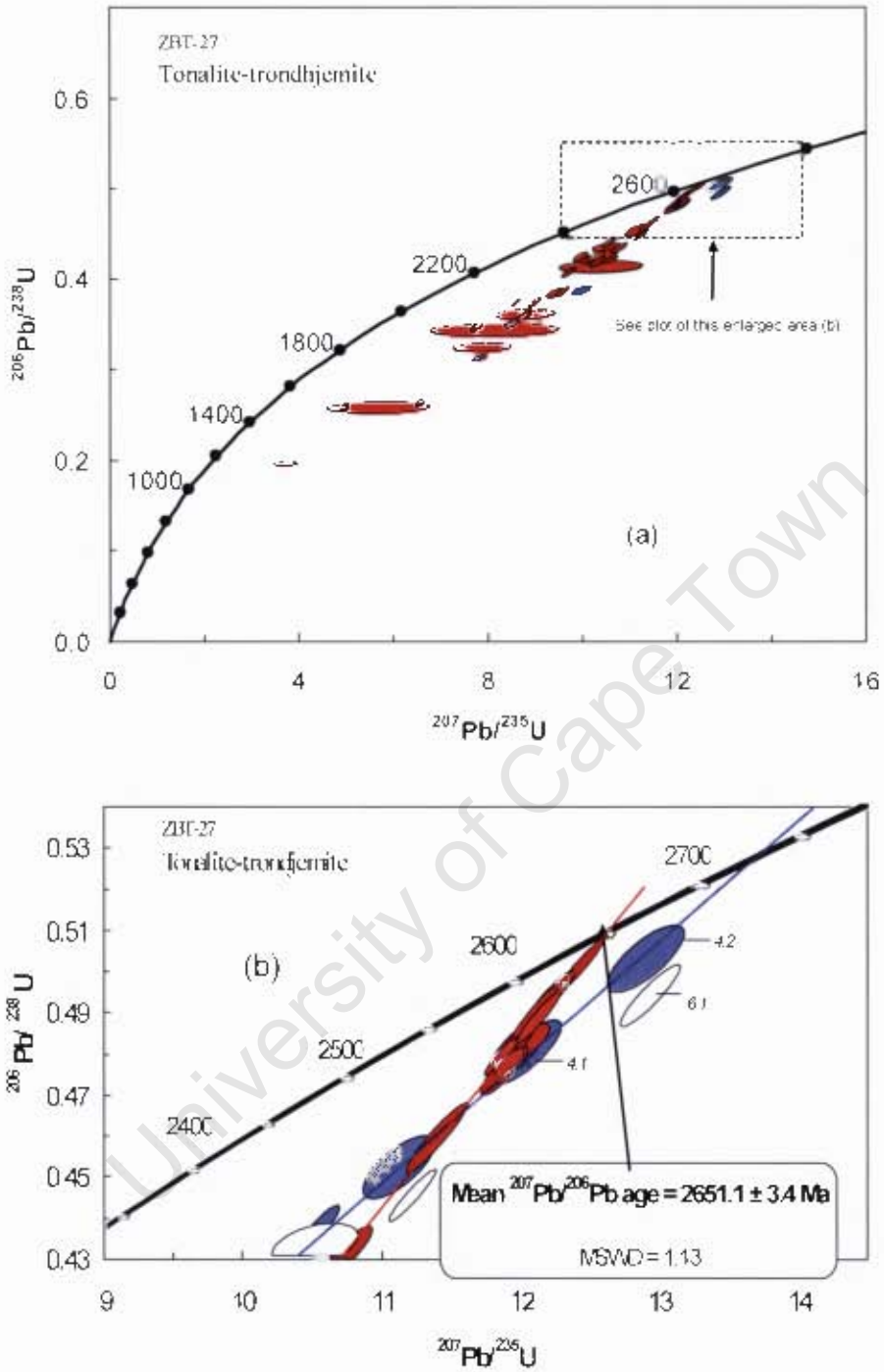

Fig. 4.13 U-Pb concordia plot of SHRIMP data for (a) all analyses of zircon grains from sample ZBT-27 from Thalabgang Pluton. (b) concordant analyses (red ellipses) used in the calculation of $^{207}Pb/^{206}Pb$ date. Blue ellipses correspond to cores for same zircon population. Unfilled ellipses represent analyses excluded from the calculation of the dates. Confidence limit for error ellipses is 1σ

Table 4.3: U-Th-Pb isotopic compositions and age calculation of zircon grains from samples of the Tati and Tlhalogang tonalite-trondhjemite plutons.

Concentration						Radiogenic ratios						Age [Ma]				
Grain Spot	% $^{206}Pb_c$	U (ppm)	Th (ppm)	Th/U	$^{206}Pb^*$ (ppm)	(1) $^{207}Pb^*/^{206}Pb^*$	±%	(1) $^{207}Pb^*/^{235}U$	±%	(1) $^{206}Pb^*/^{238}U$	±%	(1) $^{206}Pb/^{238}U$ Age		(1) $^{207}Pb/^{206}Pb$ Age		% Discordant
GEOZB-7a: Tati Pluton: Leucosome																
1.1c	0.01	118	61	0.52	47.2	0.18060	0.52	11.55	1.5	0.4638	1.4	2,456	±29	2,658.4	± 8.6	8
1.2r	0.21	2376	364	0.15	319	0.08284	0.47	1.779	1.4	0.1557	1.3	933	±11	1,265.5	± 9.2	26
1.3c	0.01	141	74	0.53	62.4	0.18210	0.38	12.97	0.96	0.5164	0.89	2,684	±19	2,672.1	± 6.3	0
2.1c	0.40	60	23	0.39	23.6	0.1772	0.94	11.17	1.8	0.4572	1.6	2,427	±32	2,627	± 16	8
2.2r	4.27	1533	239	0.16	327	0.1125	8.3	3.69	8.4	0.2378	1.6	1,375	±20	1,840	±150	25
3.1r	0.57	949	467	0.49	183	0.1395	0.76	4.295	1.5	0.2233	1.3	1,299	±15	2,221	± 13	42
4.1c	0.06	151	49	0.32	56.9	0.18026	0.49	10.91	1.5	0.4389	1.4	2,346	±27	2,655.3	± 8.2	12
5.1c	0.23	158	86	0.54	55.1	0.1747	0.93	9.75	1.8	0.4050	1.5	2,192	±28	2,603	± 16	16
6.1c	0.39	118	74	0.63	48.1	0.1805	0.68	11.80	1.6	0.4743	1.4	2,502	±29	2,657	± 11	6
7.1c	--	163	143	0.88	62.9	0.18131	0.45	11.24	1.5	0.4498	1.5	2,394	±30	2,664.9	± 7.5	10
8.1c	0.00	61	19	0.31	25.9	0.1790	0.68	12.23	1.7	0.4955	1.5	2,595	±33	2,643	± 11	2
8.2r	0.26	2412	180	0.07	383	0.11350	0.54	2.887	1.4	0.1845	1.2	1,091	±13	1,856.2	± 9.7	41
9.1c	0.00	119	62	0.52	49.0	0.18261	0.50	12.11	1.5	0.4809	1.4	2,531	±30	2,676.7	± 8.2	5
9.3c	0.01	99	43	0.43	44.4	0.17860	0.46	12.80	1.0	0.5198	0.94	2,698	±21	2,640.0	± 7.6	-2
10.1c	0.19	59	19	0.33	23.9	0.1827	0.82	11.94	1.8	0.4741	1.6	2,502	±32	2,677	± 14	7
11.1r	0.07	898	100	0.11	209	0.14898	0.38	5.565	1.3	0.2709	1.3	1,545	±17	2,334.3	± 6.4	34
12.1c	0.01	145	50	0.34	60.6	0.18305	0.45	12.30	1.4	0.4875	1.4	2,560	±29	2,680.7	± 7.4	5
13.1c	0.25	244	164	0.67	107	0.17828	0.52	12.58	1.5	0.5117	1.4	2,664	±31	2,636.9	± 8.6	-1
14.1r	0.46	187	56	0.30	60.1	0.1681	0.65	8.64	1.5	0.3727	1.4	2,042	±24	2,539	± 11	20
14.2r	0.17	149	50	0.34	66.3	0.17813	0.45	12.71	1.0	0.5177	0.92	2,689	±20	2,635.5	± 7.5	-2
15.1c	0.02	311	132	0.42	128	0.18138	0.43	11.98	1.4	0.4790	1.3	2,523	±28	2,665.5	± 7.1	5
15.2c	0.14	611	361	0.59	204	0.16939	0.26	9.082	0.78	0.3889	0.73	2,118	±13	2,551.6	± 4.3	17
16.1c	0.06	160	119	0.74	67.7	0.1822	0.62	12.37	1.5	0.4926	1.4	2,582	±29	2,673	± 10	3
17.2r	0.51	1070	34	0.03	194	0.1361	0.79	3.931	1.3	0.2095	1.1	1,226	±12	2,178	±14	44
18.1c	--	61	20	0.32	26.7	0.1823	0.62	12.84	1.3	0.5110	1.1	2,661	±24	2,673	±10	0
19.1c	2.40	505	278	0.55	183	0.1618	1.9	9.18	2.0	0.4114	0.76	2,221	±14	2,474	±32	10

Uncertainties in ages are reported at the 2 sigma confidence level. % $^{206}Pb_c$ denotes the percentage of ^{206}Pb that is common Pb. $^{206}Pb^*$ indicates the portion of radiogenic Pb. (1) Common Pb corrected using measured ^{204}Pb.

Table 4.3: Continued

Concentration						Radiogenic ratios						Age [Ma]				
Grain Spot	% $^{206}Pb_c$	U (ppm)	Th (ppm)	Th/U	$^{206}Pb^*$ (ppm)	(1) $^{207}Pb^*/^{206}Pb^*$	±%	(1) $^{207}Pb^*/^{235}U$	±%	(1) $^{206}Pb^*/^{238}U$	±%	(1) $^{206}Pb/^{238}U$ Age		(1) $^{207}Pb/^{206}Pb$ Age		% Discordant
21.1r	0.45	1560	54	0.03	308	0.12453	0.54	3.930	0.89	0.2289	0.70	1,328.6	± 8.4	2,022.1	± 9.6	34
21.2c	0.27	175	68	0.39	74.0	0.18095	0.44	12.26	0.96	0.4914	0.85	2,577	±18	2,661.6	± 7.3	3
22.1r	0.14	944	71	0.08	171	0.13371	0.43	3.876	0.83	0.2102	0.71	1,230.0	± 8.0	2,147.3	± 7.5	43
23.1c	--	271	246	0.91	119	0.18051	0.29	12.75	0.84	0.5121	0.79	2,666	±17	2,657.6	± 4.8	0
24.1r	0.19	295	69	0.23	122	0.17287	0.33	11.458	0.84	0.4807	0.78	2,530	±16	2,585.6	± 5.6	2
25.1r	0.31	1999	227	0.11	329	0.10832	0.47	2.848	0.84	0.1907	0.70	1,125.0	± 7.2	1,771.3	± 8.6	36
26.1c	0.22	243	104	0.43	105	0.18034	0.39	12.46	0.90	0.5012	0.81	2,619	±17	2,656.0	± 6.5	1
26.2r	0.28	291	119	0.41	127	0.17857	0.36	12.45	0.86	0.5058	0.78	2,639	±17	2,639.6	± 6.1	0
27.1c	1.37	146	122	0.84	21.4	0.1632	1.6	3.793	1.8	0.1685	0.94	1,004.0	± 8.7	2,489	±26	60
27.2c	0.86	118	37	0.31	46.8	0.1790	0.86	11.31	1.3	0.4582	0.92	2,432	±19	2,643	±14	8
GEOZB-7b: Tati Pluton: Melanosome																
1.1	0.84	2221	111	0.05	630	0.14218	0.3	6.404	0.79	0.3268	0.73	1823	±12	2253.1	± 5.2	19
2.1	2.15	3230	271	0.08	1170	0.1486	1.1	8.39	1.3	0.4099	0.76	2214	±14	2328	±18	5
2.2	0.32	6595	1271	0.19	1880	0.15236	0.24	6.932	0.76	0.3301	0.72	1839	±12	2372.2	± 4.1	22
3.1	5.78	686	319	0.47	248	0.1546	1.2	8.33	1.7	0.3923	1.2	2134	±22	2391	±20	11
4.1	1.12	1630	200	0.12	386	0.14417	0.28	5.412	1	0.2723	0.99	1552	±14	2277.9	± 4.9	32
4.2	0.09	189	71	0.37	79.6	0.18199	0.42	12.26	1.2	0.4886	1.1	2565	±24	2671.1	± 6.9	4
5.1	0.10	103	55	0.54	44.4	0.1814	0.57	12.54	1.4	0.5016	1.2	2621	±27	2665.4	± 9.4	2
6.1	1.15	643	343	0.53	236	0.15864	0.47	9.23	1.1	0.4222	1	2270	±20	2441.2	± 7.9	7
7.1	0.70	66	25	0.38	27.1	0.1797	1.1	11.79	2	0.4758	1.7	2509	±35	2650	±18	5
8.1	0.05	578	112	0.19	226	0.17777	0.27	11.16	1.1	0.4554	1	2419	±21	2632.2	± 4.4	8
10.1	0.13	788	15	0.02	306	0.17804	0.31	11.08	1.1	0.4514	1	2402	±20	2634.7	± 5.2	9
11.1	0.40	2655	907	0.34	782	0.15341	0.22	7.226	1	0.3416	0.99	1895	±16	2384.3	± 3.8	21
12.1	4.11	642	699	1.09	235	0.164	1.2	9.24	1.6	0.4087	1.1	2209	±21	2497	±20	12
13.1	0.06	687	568	0.83	219	0.16902	0.43	8.651	1.1	0.3712	1	2035	±18	2547.9	± 7.2	20
14.1	1.62	263	187	0.71	108	0.1786	0.78	11.53	1.4	0.4682	1.1	2476	±23	2640	±13	6
15.1	0.18	148	98	0.67	60.1	0.1796	0.59	11.73	1.3	0.4736	1.2	2499	±24	2649.2	± 9.8	6
15.2	0.11	522	234	0.45	181	0.16826	0.3	9.36	1.1	0.4036	1.1	2185	±20	2540.4	± 5.1	14

Table 4.3: Continued

Concentration						Radiogenic ratios						Age [Ma]				
Grain Spot	% $^{206}Pb_c$	U (ppm)	Th (ppm)	Th/U	$^{206}Pb^*$ (ppm)	(1) $^{207}Pb^*/^{206}Pb^*$	±%	(1) $^{207}Pb^*/^{235}U$	±%	(1) $^{206}Pb^*/^{238}U$	±%	(1) $^{206}Pb/^{238}U$ Age		(1) $^{207}Pb/^{206}Pb$ Age		% Discordant
GEOZB-7c: Tati Pluton: Tonalite-Trondhjemite																
1.2	0.43	522	557	1.07	194	0.17553	0.47	10.42	1.1	0.4305	1.0	2,308	±20	2,611.1	± 7.9	12
2.1	0.05	218	118	0.54	94.7	0.18305	0.27	12.76	0.95	0.5057	0.91	2,638	±20	2,680.7	± 4.5	2
2.2	0.27	504	245	0.49	208	0.17877	0.33	11.81	0.90	0.4791	0.84	2,523	±18	2,641.5	± 5.4	4
3.1	0.02	258	179	0.70	117	0.18228	0.25	13.27	1.1	0.5280	1.1	2,733	±25	2,673.8	± 4.1	-2
3.2	0.05	323	236	0.73	142	0.18251	0.35	12.92	1.2	0.5134	1.1	2,671	±24	2,675.8	± 5.9	0
4.1	0.15	623	297	0.48	146	0.13696	0.63	5.132	1.0	0.2717	0.82	1,550	±11	2,189	±11	29
5.1	0.02	567	409	0.72	252	0.18252	0.17	13.01	0.96	0.5169	0.94	2,686	±21	2,675.9	± 2.7	0
6.1	0.39	208	110	0.53	75.2	0.1838	0.71	10.64	1.2	0.4201	0.92	2,261	±18	2,687	±12	16
6.2	2.22	463	422	0.91	184	0.1746	1.6	10.89	1.8	0.4521	0.86	2,405	±17	2,603	±27	8
7.1	0.66	457	277	0.61	130	0.1686	0.60	7.67	2.0	0.3299	1.9	1,838	±30	2,543.4	±10.0	28
8.3	0.22	300	190	0.63	126	0.18144	0.44	12.25	1.2	0.4898	1.1	2,570	±24	2,666.1	± 7.3	4
9.2	0.28	295	180	0.61	124	0.18146	0.48	12.18	1.2	0.4869	1.1	2,557	±23	2,666.2	± 7.9	4
10.2	0.07	347	202	0.58	151	0.18122	0.24	12.63	0.88	0.5055	0.85	2,637	±18	2,664.0	± 4.0	1
11.1	0.05	265	354	1.33	113	0.18237	0.23	12.50	0.89	0.4973	0.85	2,602	±18	2,674.5	± 3.9	3
12.1	0.19	219	130	0.59	95.8	0.18288	0.30	12.81	0.92	0.5079	0.87	2,647	±19	2,679.1	± 5.0	1
13.1	0.04	303	143	0.47	136	0.18211	0.21	13.11	0.87	0.5222	0.84	2,709	±19	2,672.2	± 3.5	-1
13.2	0.01	395	117	0.30	145	0.18192	0.35	10.70	1.1	0.4267	1.1	2,291	±20	2,670.4	± 5.8	14
14.1	0.01	1128	194	0.17	85.4	0.18256	0.23	2.218	0.86	0.08811	0.82	544.3	± 4.3	2,676.2	± 3.8	80
15.1	0.87	1116	623	0.56	282	0.1515	1.6	6.08	1.9	0.2911	1.0	1,647	±15	2,363	±26	30
15.2	0.04	313	297	0.95	135	0.18199	0.45	12.58	1.2	0.5014	1.1	2,620	±24	2,671.1	± 7.5	2
16.1	0.02	208	156	0.75	92.3	0.18312	0.46	13.01	1.2	0.5152	1.2	2,679	±25	2,681.3	± 7.7	0
17.1	0.29	339	330	0.97	150	0.18217	0.53	12.85	1.2	0.5117	1.1	2,664	±24	2,672.7	± 8.8	0
18.1	0.12	279	222	0.80	120	0.18092	0.53	12.43	1.2	0.4984	1.1	2,607	±24	2,661.3	± 8.7	2
19.1	--	143	102	0.71	65.8	0.1817	0.57	13.40	1.4	0.5349	1.2	2,762	±28	2,668.3	± 9.4	-4
19.2	0.05	292	158	0.54	98.1	0.1820	0.63	9.80	1.3	0.3908	1.1	2,126	±20	2,671	±10	20
20.1	0.07	597	303	0.51	222	0.17456	0.36	10.42	1.1	0.4331	1.0	2,320	±20	2,601.9	± 6.0	11
20.2	0.37	554	76	0.14	201	0.17446	0.55	10.12	1.2	0.4206	1.0	2,263	±20	2,600.9	± 9.2	13
21.1	0.02	319	241	0.76	140	0.18247	0.41	12.82	1.2	0.5097	1.1	2,655	±24	2,675.4	± 6.7	1
21.2	0.00	475	332	0.70	199	0.18075	0.34	12.17	1.1	0.4882	1.1	2,563	±23	2,659.7	± 5.7	4
22.1	0.05	259	230	0.89	110	0.18239	0.47	12.43	1.3	0.4944	1.2	2,590	±25	2,674.7	± 7.8	3

Table 4.3: Continued

Concentration						Radiogenic ratios						Age [Ma]				
Grain Spot	% $^{206}Pb_c$	U (ppm)	Th (ppm)	Th/U	$^{206}Pb^*$ (ppm)	(1) $^{207}Pb^*/^{206}Pb^*$	±%	(1) $^{207}Pb^*/^{235}U$	±%	(1) $^{206}Pb^*/^{238}U$	±%	(1) $^{206}Pb/^{238}U$ Age		(1) $^{207}Pb/^{206}Pb$ Age		% Discordant
ZBTF-27: Tlhalogang Pluton																
1.1	0.85	106	15	0.15	41.4	0.1781	1.1	11.11	1.5	0.4523	1.1	2,405	±22	2,635	± 17	9
1.2	0.60	895	1024	1.14	267	0.1633	0.63	7.732	1.1	0.3439	0.85	1,905	±14	2,490	± 11	23
1.3	0.72	203	34	0.17	74.4	0.1767	0.79	10.24	1.3	0.4219	0.90	2,269	±17	2,622	± 13	13
2.1	0.27	502	100	0.20	187	0.1802	0.56	10.73	1.1	0.4318	0.92	2,314	±18	2,654.9	± 9.2	13
2.2	0.23	515	100	0.19	217	0.17994	0.27	12.10	0.87	0.4884	0.82	2,564	±17	2,652.3	± 4.4	3
3.1	0.22	327	170	0.52	129	0.17951	0.41	11.37	1.3	0.4593	1.2	2,436	±24	2,648.4	± 6.8	8
3.2	0.15	563	271	0.48	233	0.17937	0.23	11.86	0.85	0.4803	0.82	2,529	±17	2,647.1	± 3.8	4
4.1c	0.54	135	16	0.12	55.9	0.1817	0.81	12.02	1.3	0.4800	1.1	2,527	±22	2,668	± 13	5
4.2c	0.53	76	21	0.27	33.1	0.1872	0.75	12.88	1.4	0.5026	1.1	2,625	±23	2,718	± 12	3
4.3	0.26	382	72	0.19	163	0.17956	0.32	12.20	0.91	0.4936	0.84	2,586	±18	2,648.8	± 5.2	2
5.1	0.48	632	149	0.24	221	0.17330	0.48	9.675	1.0	0.4049	0.91	2,192	±17	2,589.7	± 8.0	15
6.1c	0.19	196	152	0.77	83.4	0.18964	0.44	12.91	1.1	0.4936	1.0	2,586	±21	2,739.1	± 7.2	6
6.2c	1.09	150	64	0.43	50.2	0.1881	0.91	9.94	1.4	0.3852	0.94	2,100	±17	2,726	± 15	23
7.1	0.06	344	40	0.12	132	0.18234	0.32	11.20	1.0	0.4454	0.95	2,375	±19	2,674.3	± 5.3	11
7.2	--	320	33	0.10	135	0.17929	0.26	12.09	0.88	0.4897	0.84	2,570	±18	2,646.3	± 4.3	3
8.1	0.47	550	105	0.19	177	0.17474	0.52	8.954	1.1	0.3716	0.92	2,037	±16	2,603.6	± 8.6	22
8.2	0.40	591	106	0.18	224	0.17463	0.37	10.522	0.91	0.4377	0.82	2,340	±16	2,602.5	± 6.1	10
9.1	0.44	468	117	0.25	168	0.17953	0.48	10.29	1.0	0.4158	0.93	2,242	±18	2,648.5	± 7.9	15
9.2	0.25	549	128	0.23	228	0.17980	0.44	11.93	0.93	0.4817	0.82	2,535	±17	2,651.1	± 7.2	4
10.1	13.09	799	239	0.30	202	0.161	12	5.67	12	0.2556	1.6	1,467	±21	2,464	±210	40
11.1	0.03	639	242	0.38	204	0.16690	0.35	8.537	0.97	0.3710	0.91	2,034	±16	2,526.8	± 5.8	20
12.1	6.80	502	139	0.28	149	0.1769	5.1	7.85	5.3	0.3220	1.2	1,800	±19	2,624	± 85	31
12.2c	0.85	193	24	0.13	58.3	0.1767	0.93	8.51	1.4	0.3492	1.0	1,931	±17	2,623	± 16	26
12.3	5.48	561	107	0.19	185	0.1780	4.0	8.76	4.7	0.3590	0.98	1,977	±17	2,634	± 67	25
12.4c	0.91	205	31	0.15	55.4	0.1824	0.82	7.77	1.3	0.3106	0.91	1,744	±14	2,675	± 14	35
13.1	0.75	533	172	0.32	165	0.1772	0.66	8.723	1.1	0.3570	0.92	1,968	±16	2,627	± 11	25
14.1	5.86	366	81	0.22	137	0.183	5.6	10.36	5.7	0.4116	1.1	2,222	±22	2,676	± 92	17

Table 4.3: Continued

Concentration						Radiogenic ratios						Age [Ma]				
Grain Spot	% $^{206}Pb_c$	U (ppm)	Th (ppm)	Th/U	$^{206}Pb^*$ (ppm)	(1) $^{207}Pb^*/^{206}Pb^*$	±%	(1) $^{207}Pb^*/^{235}U$	±%	(1) $^{206}Pb^*/^{238}U$	±%	(1) $^{206}Pb/^{238}U$ Age		(1) $^{207}Pb/^{206}Pb$ Age		% Discordant
14.2	12.03	536	133	0.25	184	0.174	9.5	8.10	11	0.3412	1.4	1,892	±22	2,597	±160	27
15.1	0.48	1643	3096	1.88	106	0.0576	1.8	0.591	2.0	0.07442	0.99	462.7	± 4.4	515	± 39	10
16.1	0.02	378	52	0.14	162	0.18006	0.24	12.41	0.88	0.5005	0.84	2,616	±18	2,653.5	± 3.9	1
16.2	3.11	1212	326	0.27	275	0.1362	3.0	4.77	3.3	0.2548	0.83	1,463	±11	2,180	± 52	33
17.1	0.82	723	198	0.27	265	0.1708	0.63	9.92	1.1	0.4221	0.81	2,270	±15	2,566	± 10	12
18.1	0.60	935	284	0.30	390	0.18116	0.54	12.01	0.99	0.4813	0.80	2,533	±17	2,663.5	± 8.9	5
19.1	1.06	199	66	0.33	66.4	0.1790	0.88	9.39	1.4	0.3820	0.91	2,086	±16	2,644	± 15	21
20.1	1.94	928	252	0.27	347	0.1785	1.4	10.43	1.8	0.4247	0.81	2,282	±16	2,639	± 23	14
21.1	0.71	331	38	0.12	75.0	0.1821	0.68	6.532	1.2	0.2611	0.86	1,496	±11	2,672	± 11	44
22.1	4.21	1359	299	0.22	237	0.1390	4.0	3.69	4.4	0.1934	0.97	1,140	±10	2,214	± 69	49
23.1	2.44	238	49	0.21	88.4	0.1787	2.2	10.30	2.6	0.4200	0.94	2,260	±18	2,640	± 37	14
24.1c	0.28	419	67	0.16	139	0.18086	0.49	9.548	1.0	0.3836	0.84	2,093	±15	2,660.8	± 8.1	21
25.1	0.47	414	165	0.40	170	0.18115	0.43	11.86	0.96	0.4757	0.83	2,509	±17	2,663.5	± 7.1	6
26.1	2.11	628	291	0.46	240	0.1765	1.6	10.49	1.9	0.4325	0.83	2,317	±16	2,620	± 26	12

4.4.4 Greenstone lavas: *Samples GEOZB-3a, GEOZB-8a and ZB98-169*

Three samples of lavas were selected from the greenstone sequence of the Francistown Granite-Greenstone Complex in order to try and constrain the depositional ages of both the Vumba and the Tati volcanic rocks. Sample GEOZB-3a was collected from a porphyritic meta-andesite of the Penhalonga Formation within the Tati greenstone belt. This formation is interpreted to overlie the mafic lava-dominated Lady Mary Formation (e.g. Carney et al., 1994). Key (1976) suggested that the andesitic lavas and mafic lavas in the Tati greenstone belt are co-magmatic, hence coeval. The selected sample is porphyritic, pale-green, schistose and fine to medium-grained with rounded translucent quartz grains up to 1cm across, set within a fine grained andesitic matrix. This sample produced a large number of fresh zircon grains. The general population of zircon grains is subhedral to anhedral with oblate to rounded form (Fig. 4.14). Cathodoluminescence imaging of sectioned grains shows very well-developed oscillatory zoning, consistent with an igneous origin. No inherited cores were observed. Sixteen analyses were obtained from zircon grains of this sample. Concentrations of U and Th in these grains are low with restricted ranges of 103-173 ppm and 43-94 ppm, respectively (Table 4.4). The Th/U ratios vary from 0.35 to 0.65, which is consistent with a magmatic origin for the zircon grains. On a concordia plot (Fig. 4.15a), the data yielded an upper intercept date of 2736.8 ± 3.5 Ma (MSWD = 0.80). The data gives a weighted mean $^{207}Pb/^{206}Pb$ date of 2737 ± 3.2 Ma (MSWD = 0.80; Fig. 4.15b) that is interpreted as the magmatic age of the andesitic lavas.

Sample GEOZB-8a is a sample from felsic lavas intercalated with the mafic lava-dominated Lady Mary Formation in the Tati greenstone belt. It is a massive, homogeneous, whitish-grey rock, with a dacitic composition. The sample yielded only 8 zircon grains from which 10 analyses were obtained. The contents of U and Th are variable with ranges of 196-899 ppm and 67-395 ppm respectively (Table 4.4). Th/U ratios of the zircon grains vary from 0.31 and 0.46, suggests mildly disturbed magmatic zircon grains. The zircon grains are small in size (80-180 μm) and anhedral with rare subhedral habits. Cathodoluminescence imaging shows oscillatory zoning suggesting magmatic origin. Apart from one analysis, all the data are discordant to different degrees. Regression of all data gives an upper intercept date of 2735 ± 30 Ma (MSWD = 12; Fig. 4.15c) that is interpreted to be the magmatic age of the felsic lavas. The high uncertainty and MSWD of 12 reflects the scatter

of the data about the discordia. This age is similar, within error, with the age of the andesitic lavas (2737 + 3.2 Ma) of the Tati greenstone belt.

Sample ZB98-169 was taken from felsic lavas that form lenses interbedded with mafic lavas in the Vumba greenstone succession (Fig. 4.1). It is homogeneous, fine-grained, whitish-grey, massive and dacitic in composition. The sample was collected from a felsic layer intercalated with the mafic lavas of the Vumba Mixed Volcanic Formation, which in turn is suspected to be an extension of the Lady Mary Formation of the Tati belt (Key, 1976; Litherland, 1975). Therefore, the U-Pb zircon dates from the felsic lavas interlayered with the Lady Mary and the Vumba Mixed Volcanic Formations constrain the deposition and would confirm or dismiss the envisaged link between the two formations and/or greenstone belts.

The sample ZB98-169 yielded light brown zircon grains that are subhedral to anhedral with strongly developed oscillatory compositional zoning in most grains, typical for magmatic zircon. The zircon grains are mostly equant with ≤200 µm diameter (Fig. 4.18). Twenty analyses from 19 zircon grains were obtained from this sample. The Th/U ratios vary from 0.23 to 1.05, with many grains having a Th/U ratio > 0.5 (Table 4.4). The U concentrations are between 119 and 647 ppm. Analyses of the zircon grains produced a mixture of concordant to near-concordant and highly discordant data. The highly discordant data display some scatter suggesting significant alteration, hence Pb loss. A discordia fitted to all the analyses yielded upper and lower intercept dates of 2695.5 ± 6.6 Ma and 709 ± 150 Ma respectively (MSWD = 0.97; Fig. 4.19). Ignoring the discordant analyses and considering only the concordant and near-concordant data, a weighted mean $^{207}Pb/^{206}Pb$ date of 2695.7 ± 5.9 Ma was obtained (MSWD = 0.75; Fig. 4.19 inset). This date of 2695.7 ± 5.9 Ma is interpreted as the magmatic age of the felsic lavas in the Vumba greenstone belt. This age is nearly 40 million years younger than that of the Lady Mary Formation (2735 ± 30 Ma). This does not support stratigraphic link between the Vumba Mixed Volcanic and Lady Mary Formations, and therefore the suggested correlations between the two greenstone belts are not reliable.

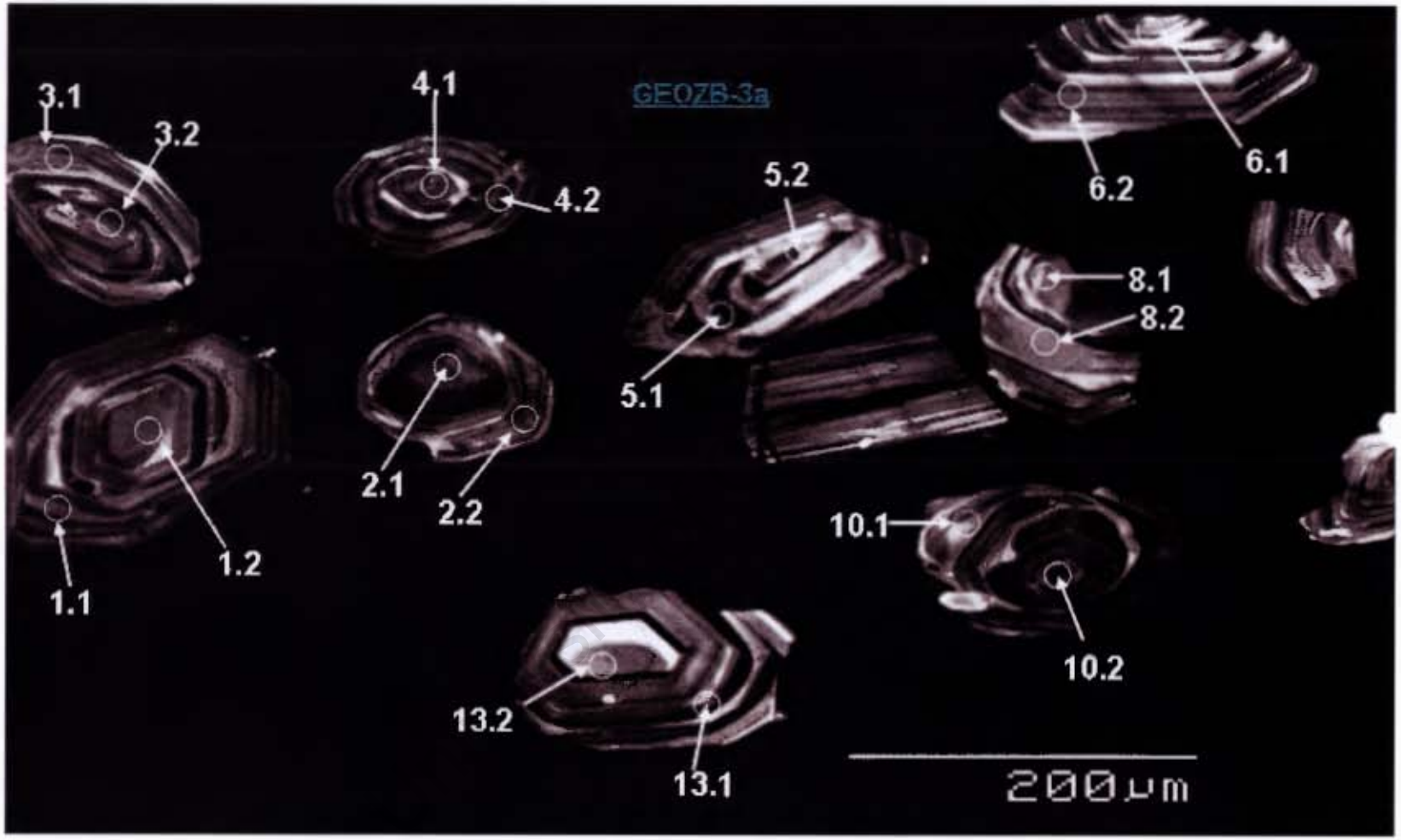

Fig. 4.14: C_ images of zircon grains from the andesitic lavas (sample GEOZB-3a) that overly the mafic lavas of the Lady Mary formation in the Tati greenstone belt. Note the well-developed oscillatory zoning indicating magmatic origin. Also note lack of metamorphic rims or overgrowths. Analysed spots are denoted by white circles. The magmatic age of this andesitic lavas is 2737 Ma

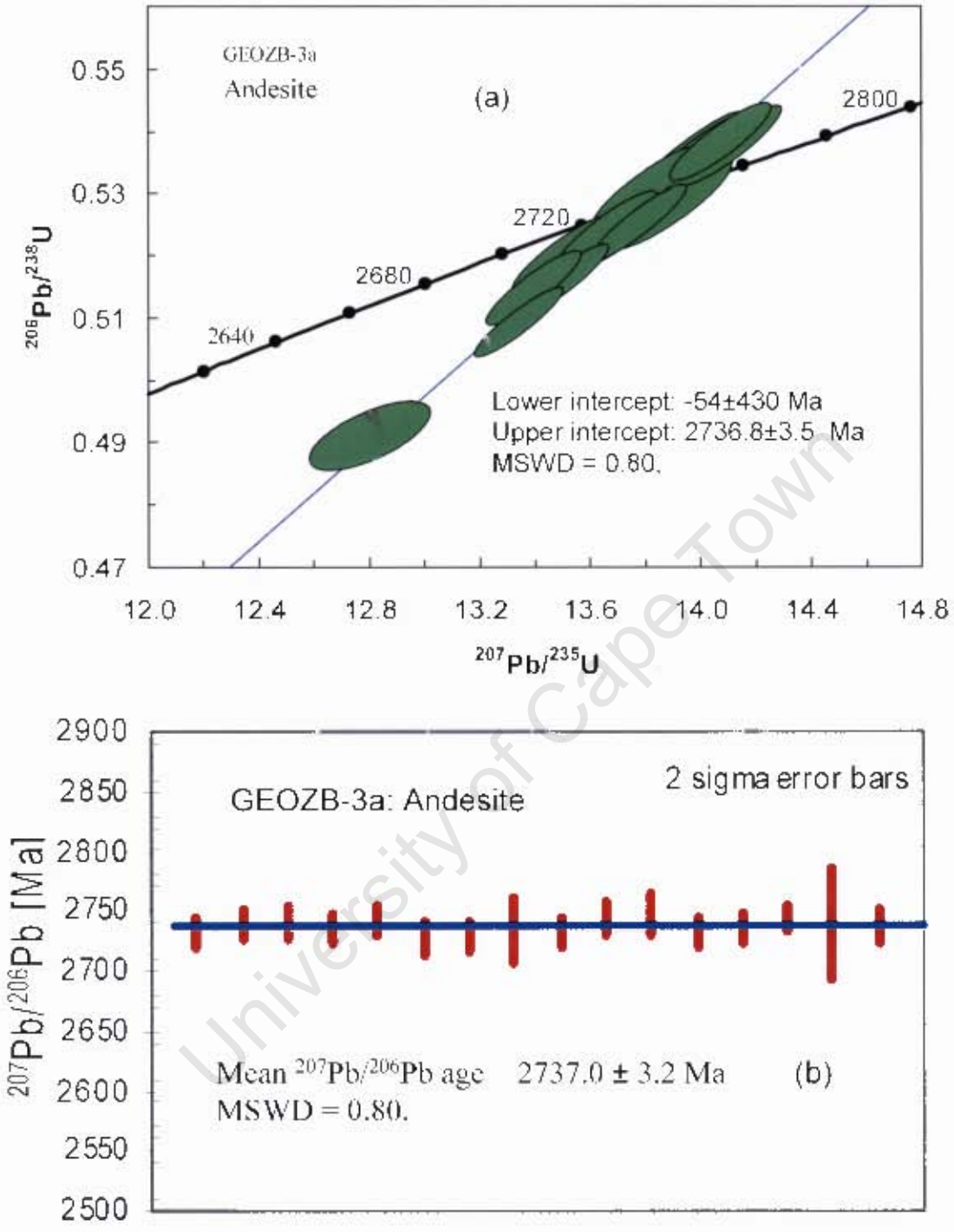

Fig. 4.15: U-Pb concordia plot of SHRIMP data for zircon grains from the (a) Andesite sample GEOZB-3a from the Tati greenstone belt; (b) weighted average $^{207}Pb/^{206}Pb$ dates.

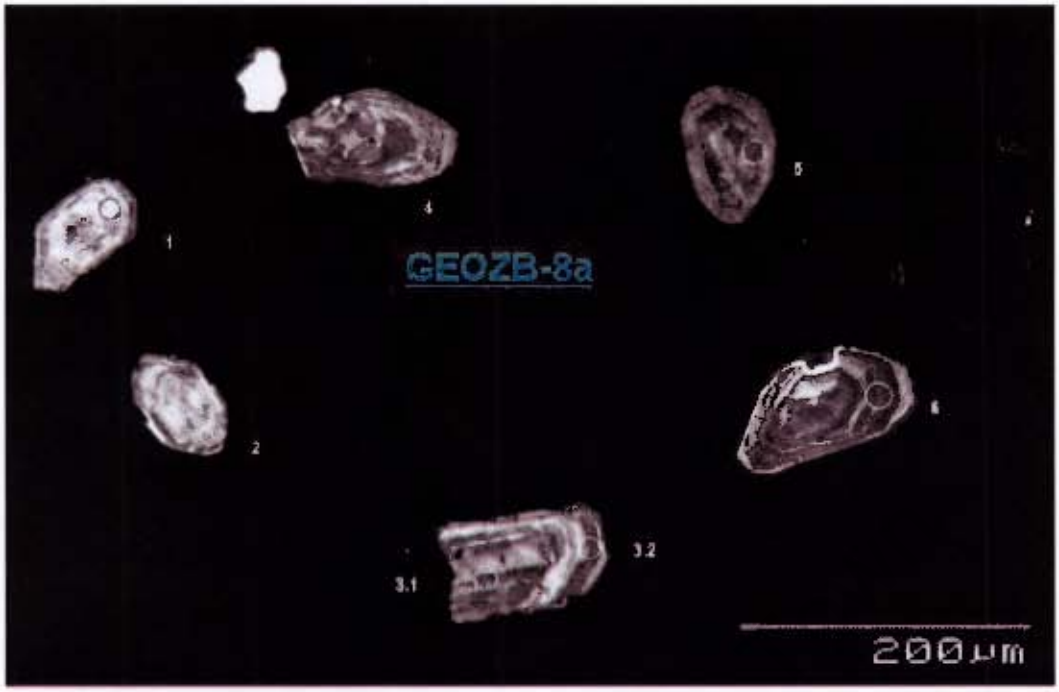

Fig. 4.16: CL images of zircon grains from the dacitic lavas (sample GEOZB-8a) intercalated with the mafic lavas of the Lady Mary Formation in the Tati greenstone belt. Note the oscillatory zoning indicative of a magmatic origin. The magmatic age of this dacitic lava is 2735 Ma.

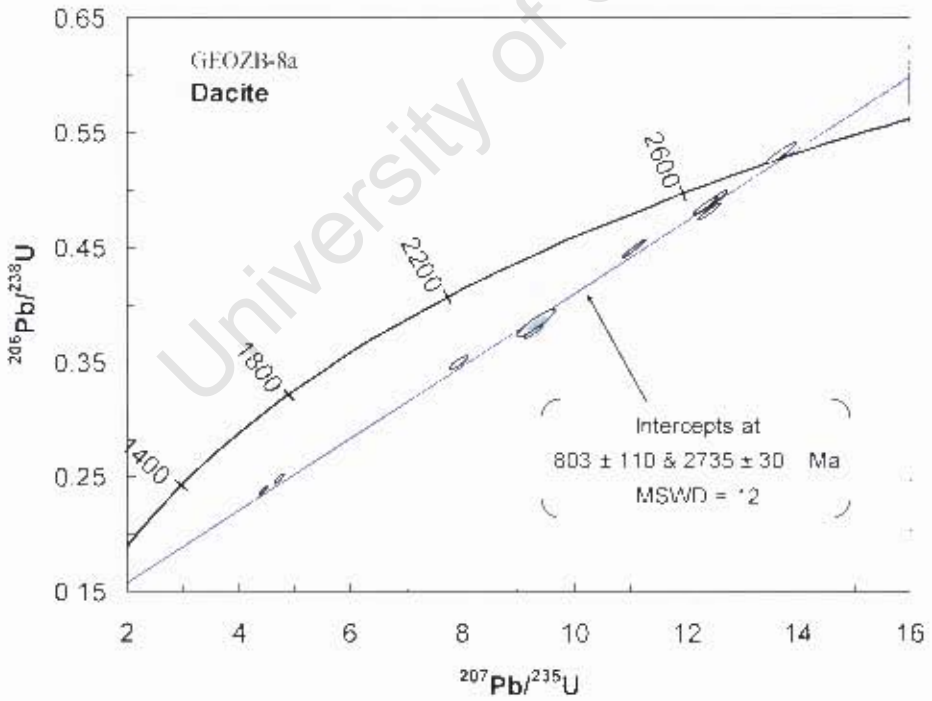

Fig. 4.17 U-Pb concordia plot of SHRIMP data for zircon grains from the dacite sample GEOZB-8a from thin lenses intercalated with tholeiitic basalt in the Tati greenstone belt.

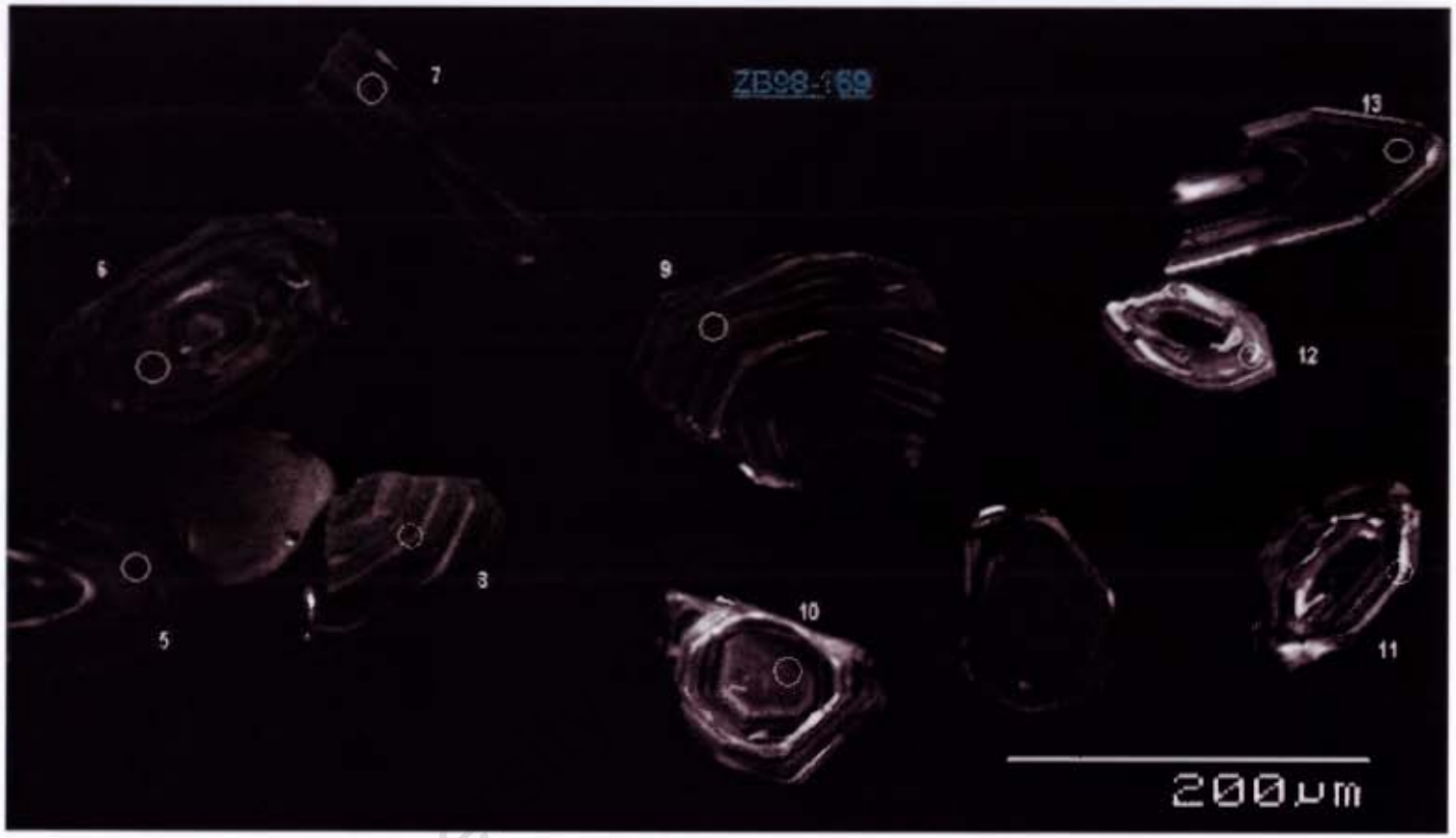

Fig. 4.18: CL images of zircon grains from the dacitic lavas (sample ZB98-169) interca aled with the mafic lavas of the Vumba Mixed Volcanic Formation in the Vumba greenstone belt showing subhedral and equant habit. The zircon grains show wel-developed oscil atory zoning, ind cative of a magmatic origin. Note the absence of metamorphic rims. The magmatic age of this dacitic lava is 2695 Ma

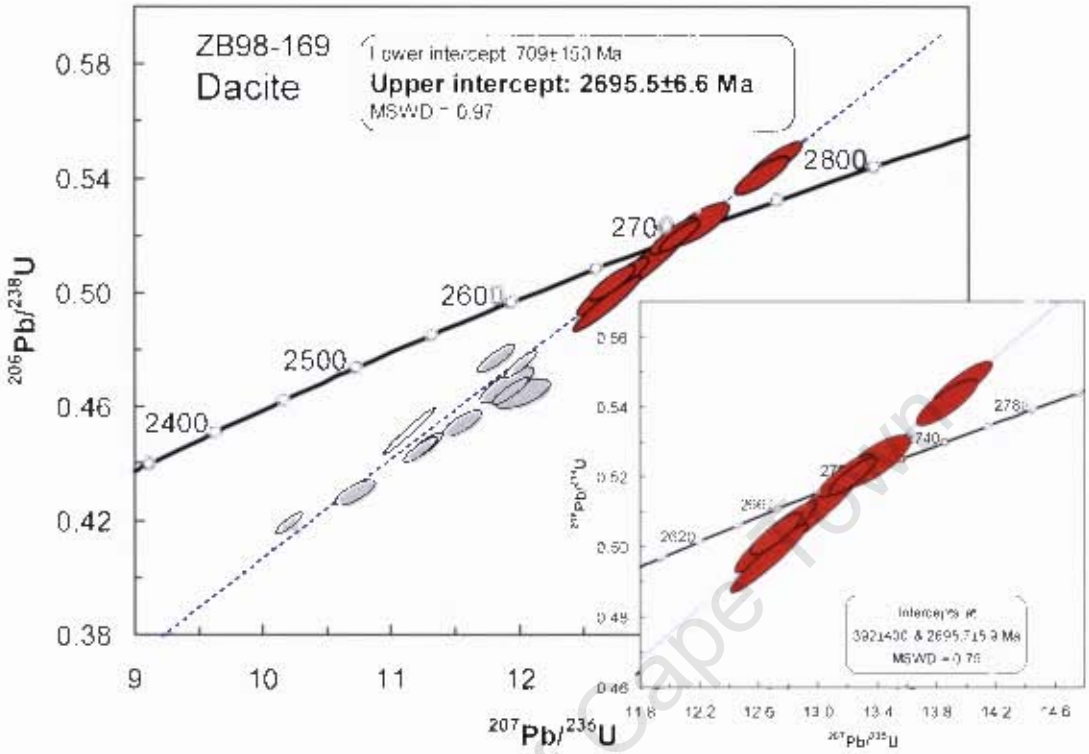

Fig. 4.19 U-Pb concordia plot of SHRIMP data for zircon grains from the dacite sample ZB98-169 from felsic lenses interbedded with tholeiitic basalt in the Vumba greenstone belt. Gray ellipses represent discordant analyses while the red ones stand for near-concordant analyses that were used for the calculation of the dacite age. Inset shows only the near-concordant analyses. Confidence limit for error ellipses is 1σ.

Table 4.4: U-Th-Pb isotopic compositions of zircon grains and age calculations from samples of meta-volcanic rocks in the Tati and Vumba greenstone belts.

Concentration						Radiogenic ratios						Age [Ma]				
Grain Spot	% $^{206}Pb_c$	U (ppm)	Th (ppm)	Th/U	$^{206}Pb^*$ (ppm)	(1) $^{207}Pb^*/^{206}Pb^*$	±%	(1) $^{207}Pb^*/^{235}U$	±%	(1) $^{206}Pb^*/^{238}U$	±%	(1) $^{206}Pb/^{238}U$ Age		(1) $^{207}Pb/^{206}Pb$ Age		% Discordant
Tati Andesitic lava (GEOZB-3a): Tati greenstone belt																
1.2	--	160	70	0.44	70.7	0.18970	0.34	13.49	0.84	0.5158	0.77	2,681	± 17	2,739.6	± 5.7	2
2.2	--	121	47	0.39	54.5	0.18975	0.42	13.71	0.90	0.5239	0.79	2,716	± 18	2,740.0	± 7.0	1
3.2	0.05	125	53	0.42	56.3	0.18935	0.37	13.71	1.0	0.5253	0.96	2,722	± 21	2,736.6	± 6.0	1
4.2	0.06	173	92	0.54	75.6	0.19001	0.31	13.34	0.80	0.5092	0.73	2,653	± 16	2,742.2	± 5.2	3
5.2	0.14	105	57	0.54	47.2	0.18831	0.42	13.51	0.92	0.5202	0.82	2,700	± 18	2,727.4	± 6.9	1
6.2	0.01	103	43	0.41	46.9	0.18846	0.39	13.80	0.90	0.5310	0.81	2,746	± 18	2,728.8	± 6.4	-1
8.2	1.04	166	92	0.55	70.9	0.1891	0.82	12.80	1.1	0.4910	0.75	2,575	± 16	2,734	±14	6
10.2	0.04	116	55	0.48	53.4	0.19020	0.38	14.10	0.88	0.5378	0.80	2,774	± 18	2,743.9	± 6.2	-1
13.2	0.10	65	23	0.35	29.4	0.1906	0.53	13.88	1.1	0.5284	0.93	2,735	± 21	2,747.2	± 8.7	0
14.2	0.03	130	59	0.45	59.8	0.18871	0.36	13.93	1.0	0.5353	0.98	2,764	± 22	2,731.0	± 5.9	-1
15.2	0.07	115	47	0.41	53.2	0.18924	0.41	14.01	0.91	0.5367	0.81	2,770	± 18	2,735.6	± 6.7	-1
16.2	0.02	158	69	0.44	71.2	0.19012	0.33	13.77	0.83	0.5254	0.76	2,722	± 17	2,743.2	± 5.4	1
17.2	0.36	156	94	0.60	63.7	0.1897	1.4	12.40	6.5	0.474	6.3	2,501	±130	2,739	±23	9
19.1	--	161	81	0.50	71.3	0.18875	0.38	13.40	0.85	0.5147	0.76	2,677	± 17	2,731.3	± 6.2	2
20.1	0.09	115	75	0.65	52.0	0.18896	0.38	13.66	0.88	0.5241	0.79	2,717	± 18	2,733.1	± 6.3	1
21.1	0.20	141	52	0.37	65.5	0.18949	0.40	14.07	0.87	0.5385	0.77	2,777	± 17	2,737.7	± 6.6	-1
Dacite (GEOZB-8a): Tati greenstone belt																
1.1	0.86	378	130	0.34	126	0.1764	0.92	9.32	2.4	0.3833	2.2	2,092	±39	2,619	±16	20
2.1	0.11	804	47	0.06	164	0.13683	0.44	4.466	1.1	0.2367	1.1	1,370	±13	2,187.4	± 7.7	37
3.1	0.09	544	248	0.46	209	0.17958	0.29	11.07	1.3	0.4473	1.2	2,383	±24	2,648.8	± 4.8	10
3.2	0.13	353	163	0.46	114	0.17933	0.37	9.27	1.2	0.3749	1.1	2,053	±19	2,646.5	± 6.3	22
4.1	0.04	376	128	0.34	158	0.18510	0.37	12.47	1.4	0.4886	1.3	2,565	±28	2,699.0	± 6.2	5
5.1	0.09	899	319	0.35	191	0.13912	0.63	4.742	1.2	0.2472	1.1	1,424	±13	2,216	±11	36
6.1	0.02	323	103	0.32	135	0.18448	0.35	12.34	1.2	0.4852	1.1	2,550	±23	2,693.6	± 5.8	5
7.1	0.06	404	157	0.39	167	0.18744	0.31	12.40	1.1	0.4800	1.1	2,527	±23	2,719.7	± 5.2	7
7.2	0.01	196	60	0.31	89.5	0.18735	0.41	13.71	1.2	0.5307	1.2	2,744	±26	2,719.1	± 6.8	-1
8.1	0.43	853	395	0.46	257	0.1654	0.66	7.96	1.4	0.3492	1.2	1,931	±20	2,511	±11	23

Uncertainties in ages are reported at the 2 sigma confidence level. % $^{206}Pb_c$ denotes the percentage of ^{206}Pb that is common Pb. $^{206}Pb^*$ indicates the portion of radiogenic Pb. (1) Common Pb corrected using measured ^{204}Pb.

Table 4.4: Continued

Concentration						Radiogenic ratios						Age [Ma]				
Grain Spot	% $^{206}Pb_c$	U (ppm)	Th (ppm)	Th/U	$^{206}Pb^*$ (ppm)	(1) $^{207}Pb^*/^{206}Pb^*$	±%	(1) $^{207}Pb^*/^{235}U$	±%	(1) $^{206}Pb^*/^{238}U$	±%	(1) $^{206}Pb/^{238}U$ Age		(1) $^{207}Pb/^{206}Pb$ Age		% Discordant
Dacite (ZB98-169): Vumba greenstone belt																
1.1	0.03	119	65	0.54	55.7	0.18558	0.49	13.97	0.98	0.5458	0.84	2808	± 19	2703.4	± 8.1	-4
2.1	0.12	126	70	0.55	58.8	0.18598	0.54	13.87	0.98	0.5409	0.82	2787	± 19	2706.9	± 8.8	-3
3.1	0.08	249	261	1.05	111	0.18468	0.39	13.23	0.8	0.5196	0.7	2698	± 15	2695.4	± 6.4	0
4.1	0.09	304	262	0.86	119	0.18467	0.54	11.54	0.88	0.4534	0.69	2410	± 14	2695.3	± 8.9	11
5.1	0.03	491	114	0.23	176	0.17684	0.34	10.195	0.69	0.4181	0.6	2252	± 11	2623.5	± 5.6	14
6.1	--	257	120	0.47	103	0.18575	0.37	11.914	0.8	0.4652	0.71	2462	± 14	2704.9	± 6.1	9
7.1	0.03	414	311	0.75	169	0.18329	0.31	11.996	0.71	0.4747	0.64	2504	± 13	2682.8	± 5.2	7
8.1	0.11	303	101	0.33	116	0.1831	0.37	11.213	0.77	0.4442	0.67	2369	± 13	2681.1	± 6.1	12
9.1	0.05	266	143	0.54	102	0.18331	0.44	11.252	0.83	0.4452	0.7	2374	± 14	2683	± 7.3	12
10.1	0.04	129	97	0.75	58.1	0.1853	0.74	13.38	1.2	0.5238	0.94	2715	±21	2701	±12	-1
11.1	0.09	174	126	0.72	69.6	0.1876	0.89	12.01	1.2	0.4642	0.79	2458	± 16	2722	± 15	10
12.1	0.21	119	84	0.71	47.8	0.1847	0.69	11.89	1.1	0.467	0.92	2470	± 19	2695	± 11	8
13.1	0.09	249	141	0.57	102	0.17973	0.42	11.807	0.82	0.4765	0.7	2512	± 15	2650.4	± 7	5
14.1	0.21	246	181	0.74	90.9	0.181	0.61	10.71	0.93	0.4289	0.71	2301	± 14	2662	± 10	14
15.1	0.05	148	71	0.48	64.2	0.18327	0.46	12.71	0.92	0.5031	0.8	2627	± 17	2682.7	± 7.7	2
16.1	0.07	144	65	0.45	64.5	0.18396	0.46	13.18	0.92	0.5197	0.8	2698	± 18	2688.9	± 7.6	0
17.1	0.13	222	110	0.49	94.9	0.18520	0.42	12.66	1.4	0.4960	1.3	2,596	±28	2,700.0	±7.0	4
18.1	0.12	204	113	0.55	89.7	0.1846	0.57	12.99	1.7	0.5102	1.6	2,658	±35	2,694.6	±9.4	1
19.1	0.13	172	71	0.42	74.1	0.18353	0.54	12.71	1.4	0.5022	1.3	2,623	±29	2,685.0	±8.9	2
19.2	0.05	647	216	0.33	251	0.17904	0.24	11.13	1.2	0.4509	1.2	2,399	±24	2,644.0	±4.0	9

4.4.5 Trondhjemite: *Sample ZBT-15*

Sample ZBT-15 was selected from the trondhjemite unit exposed in the vicinity of the city of Francistown (Fig. 4.1). Because of the absence of any conspicuous deformation fabric in this unit, it is regarded post-tectonic and envisaged to be younger than the greenstone belt and the variably deformed tonalite-trondhjemite granitoids flanking the southwestern and northeastern margins of the Tati greenstone belt (e.g. Key, 1976; Kampunzu et al., 2003). It is a dull grey, massive, medium-grained granular biotite trondhjemite. It contains 30% quartz, 45% plagioclase, 10% microcline, 10% biotite and 5% muscovite, with calcite and epidote as minor phases. The trondhjemite unit is spatially associated with the diorite unit but their field age relation is unexposed. However, Key (1976) reported angular blocks of dioritic composition within the trondhjemite, which suggest that the trondhjemite intruded into the diorite. This observation was verified by this study where small dioritic xenoliths were observed within the trondhjemite towards the margin with the diorite (Fig. 4.20). By selecting a sample from this unit for U-Pb dating, I aimed at resolving the chronological order of plutonism in the Tati granite-greenstone terrain and a minimum age of the greenstone belt.

Zircon grains extracted from sample ZBT-15 form a subhedral population of brown to dark pink grains that mostly have ≤200 µm length. These grains show weakly-zoned to unzoned central area surrounded by increasingly more U-enriched outer growth (Fig. 4.21). Seventeen analyses were obtained from the zircon population of 20 grains. The zircon grains have Th/U ratios of 0.38 to 0.66 and U concentrations of between 133 and 292 ppm (Table 4.5), which is consistent with the characteristics of magmatic zircon grains. Many grains have apparent cores, however the ages of these cores are indistinguishable from that measured for the general magmatic population and thus a single date is defined. Linear regression of all the analyses on a concordia diagram (Fig. 4.22a) yielded an upper intercept age of 2714.3 ± 2.8 Ma and a lower intercept of 358 ± 140 Ma (MSWD = 0.62). Apart from two analyses (# 17.1 and 19.1; Table 4.5), all the remaining 15 data plots with a few % of discordance gave a weighted mean $^{207}Pb/^{206}Pb$ date of 2715.2 ± 2.7 Ma (MSWD = 0.70; Fig. 4.22b), which is interpreted to be the magmatic age of the trondhjemite unit. This age confirms that the date 2739 ± 7.2 Ma interpreted as the age of Tlhalogang pluton is appropriate. In Fig. 4.1 a small plug of the trondhjemite unit protrudes within the Tlhalogang pluton. The field relationship between the trondhjemite unit and the Sekukwe does not allow evaluation of any relative age

relation between the two rock sequences because of lack of continuous outcrops (see Fig. 4.1). The trondhjemite is intrusive into the andesitic volcanics of the Tati greenstone belt. The trondhjemite age is consistent with the ages of the felsic and andesitic volcanics of the Tati belt, which are relatively older

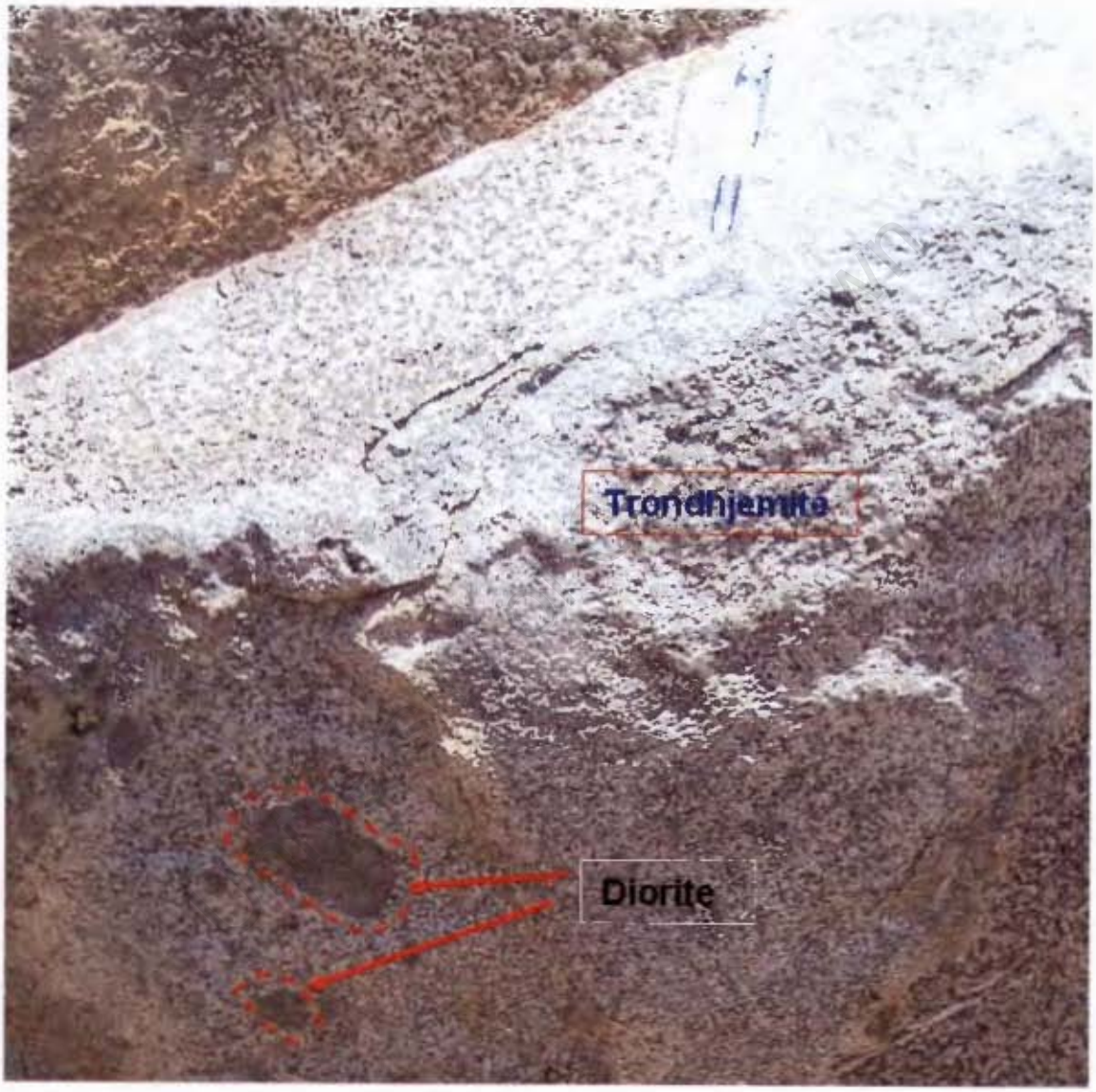

Fig. 4.20: A field photograph showing dioritic xenoliths within the trondhjemite unit. This indicates that the trondhjemite intruded the diorite unit hence should record a younger age than the diorite.

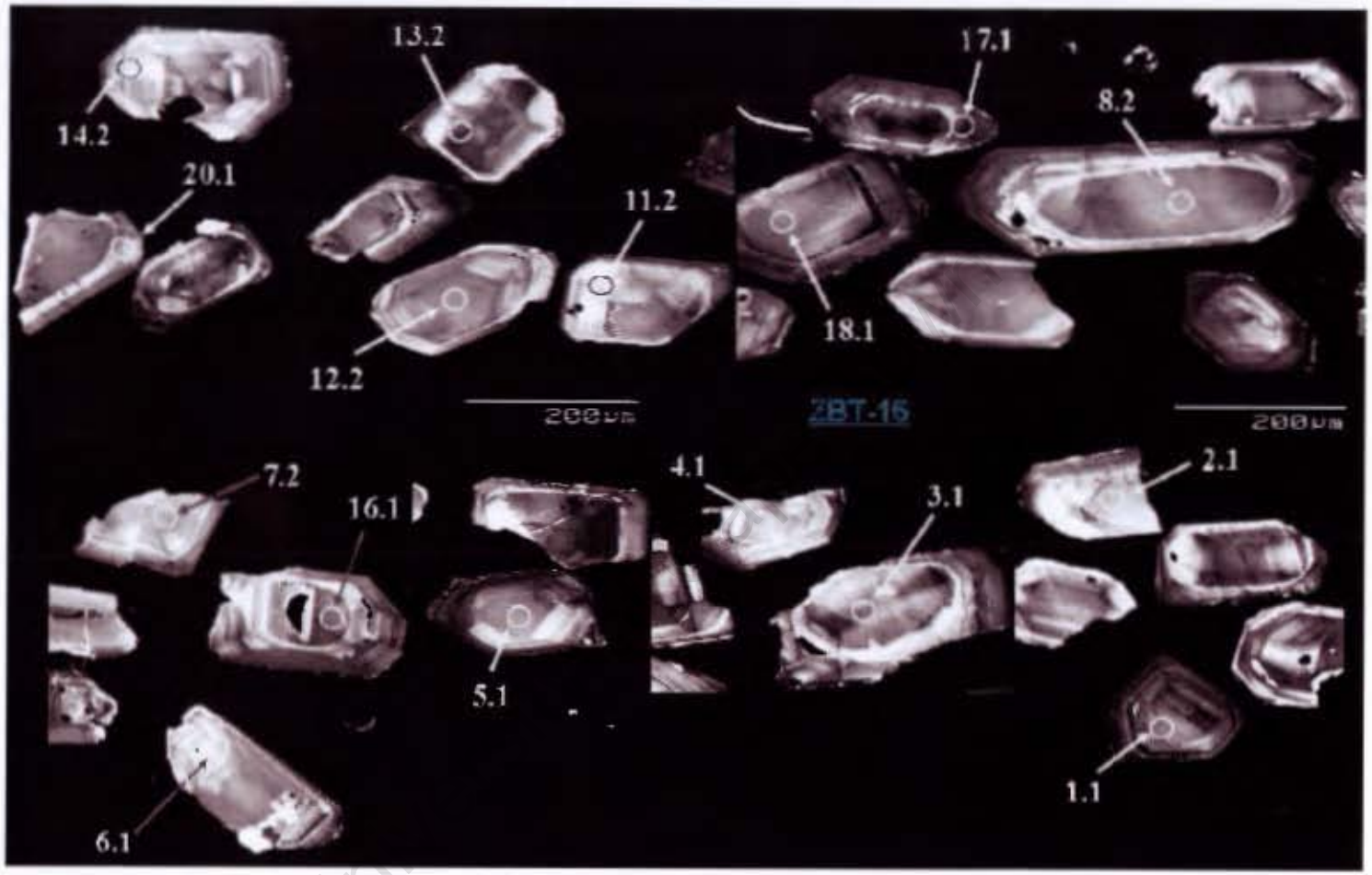

Fig. 4.21: CL images of zircon grains from the trondhjemite (sample ZBT-15). Note the non-metamict quality of zircon grains and the absence of inherited cores. Also note the oscillatory zoning, indicative of magmatic origin. Analysed spots are denoted by white circles. The magmatic age of this trondhjemite is 2715 Ma.

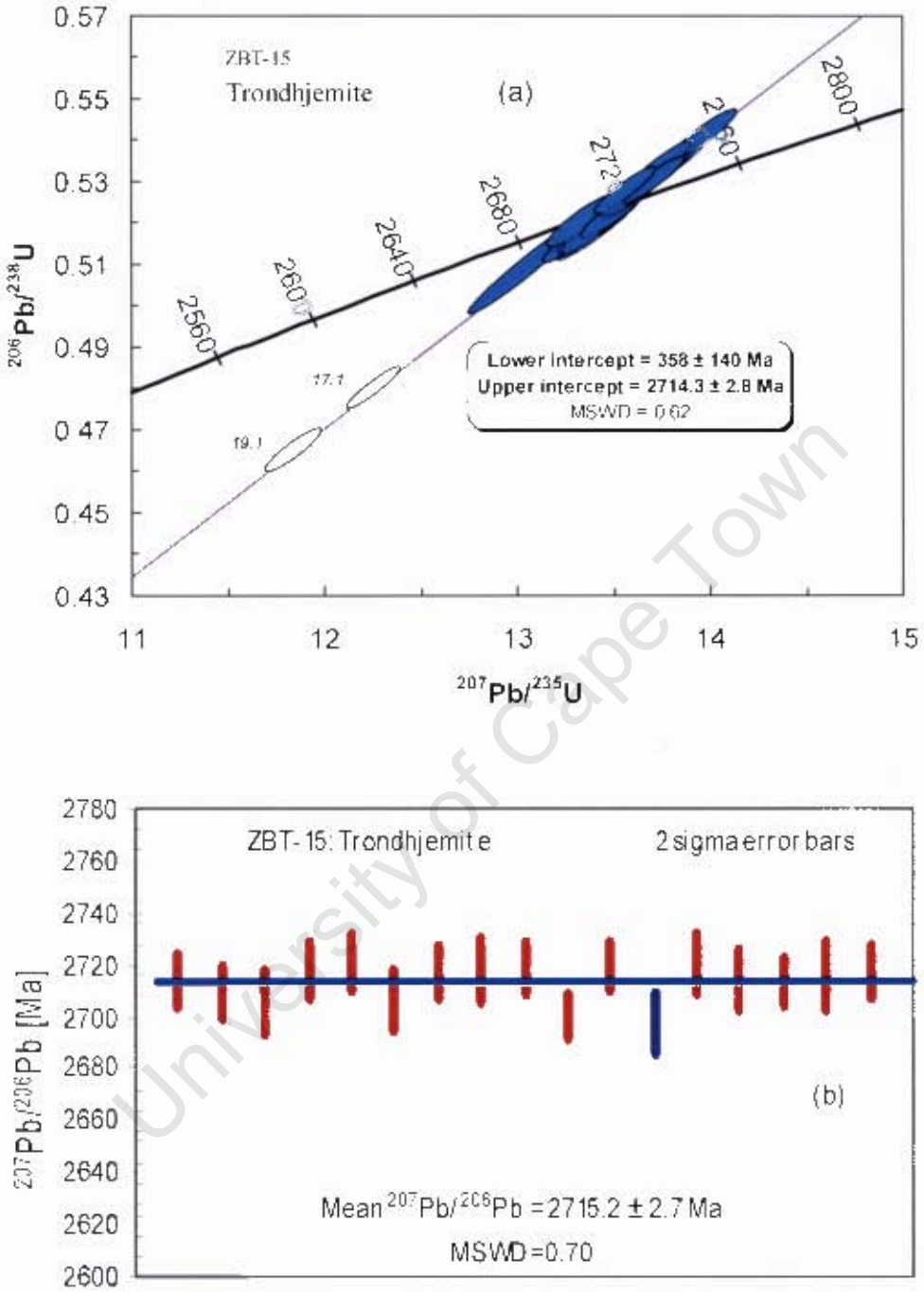

Fig. 4.22: (a) U-Pb concordia plot of SHRIMP data of zircon grains from the trondhjemite unit sample ZBT-15. The discordant analyses #17.1 and 19.1 (represented here by unfilled error ellipses) were not included in the calculated $^{207}Pb/^{206}Pb$ date. (b) Weighted average mean $^{207}Pb/^{206}Pb$ date for the concordant analyses. Confidence limit for error ellipses is 1σ.

Table 4.5: U-Th-Pb isotopic compositions of zircon grains and age calculations from Trondhjemite sample ZBTF-15 from the Tati granite-greenstone terrain.

Concentration						Radiogenic ratios						Age [Ma]				
Grain Spot	% $^{206}Pb_c$	U (ppm)	Th (ppm)	Th/U	$^{206}Pb^*$ (ppm)	(1) $^{207}Pb^*/^{206}Pb^*$	±%	(1) $^{207}Pb^*/^{235}U$	±%	(1) $^{206}Pb^*/^{238}U$	±%	(1) $^{206}Pb/^{238}U$ Age		(1) $^{207}Pb/^{206}Pb$ Age		% Discordant
Trondhjemite (ZBTF-15)																
1.1	0.01	193	84	0.43	88.0	0.18678	0.30	13.67	0.79	0.5309	0.73	2,745	±16	2,714.0	±5.0	-1
2.1	0.05	225	122	0.54	102	0.18630	0.29	13.56	0.78	0.5278	0.72	2,732	±16	2,709.8	±4.9	-1
3.1	0.05	122	60	0.49	54.8	0.18583	0.39	13.34	0.89	0.5205	0.80	2,701	±18	2,705.6	±6.5	0
4.1	--	153	64	0.42	68.4	0.18724	0.34	13.41	0.96	0.5195	0.90	2,697	±20	2,718.0	±5.6	1
5.1	0.02	147	70	0.47	65.7	0.18757	0.35	13.43	1.1	0.5193	1.0	2,696	±23	2,720.9	±5.7	1
6.1	0.00	200	75	0.38	90.5	0.18707	0.30	13.60	0.79	0.5271	0.73	2,729	±16	2,716.6	±5.0	0
7.2	0.02	172	76	0.44	78.6	0.18718	0.37	13.71	0.84	0.5312	0.75	2,747	±17	2,717.5	±6.1	-1
8.2	--	174	98	0.56	78.8	0.18729	0.32	13.62	0.82	0.5272	0.75	2,730	±17	2,718.5	±5.3	0
11.2	0.01	159	60	0.38	71.1	0.18747	0.34	13.50	0.83	0.5222	0.76	2,709	±17	2,720.1	±5.6	0
12.2	0.01	164	93	0.57	72.9	0.18678	0.33	13.34	1.0	0.5179	0.96	2,690	±21	2,714.0	±5.5	1
13.2	0.01	218	104	0.48	99.8	0.18664	0.29	13.74	0.78	0.5341	0.72	2,759	±16	2,712.8	±4.8	-2
14.2	--	133	52	0.39	61.0	0.18699	0.40	13.79	0.88	0.5350	0.78	2,762	±18	2,715.9	±6.7	-2
16.1	0.16	177	100	0.56	77.5	0.18588	0.36	13.06	1.5	0.5094	1.5	2,654	±33	2,706.1	±5.9	2
17.1	0.05	292	194	0.66	121	0.18518	0.26	12.260	0.74	0.4801	0.69	2,528	±14	2,699.9	±4.3	6
18.1	--	221	118	0.54	100.0	0.18742	0.28	13.70	0.77	0.5302	0.72	2,742	±16	2,719.6	±4.7	-1
19.1	0.04	194	85	0.44	77.4	0.18483	0.34	11.849	0.82	0.4649	0.74	2,461	±15	2,696.7	±5.6	9
20.1	0.05	196	94	0.48	91.0	0.18707	0.31	13.96	0.80	0.5414	0.74	2,789	±17	2,716.6	±5.1	-3

Uncertainties in ages are reported at the 2 sigma confidence level. % $^{206}Pb_c$ denotes the percentage of ^{206}Pb that is common Pb. $^{206}Pb^*$ indicates the portion of radiogenic Pb. (1) Common Pb corrected using measured ^{204}Pb.

4.4.6 Diorite Unit: *Sample ZBT-19*

A geochronological sample ZBT-19 collected from a diorite unit north of the city of Francistown (Fig. 4.1) exhibits grey colour, granular texture and medium grain size. The diorite unit exhibits no conspicuous evidence of deformation and is flanked by the trondhjemite unit. However, there is no exposed contact to define the age relationship between the two units. Petrographically, it contains hornblende, andesine plagioclase, clinopyroxene, minor quartz and secondary chlorite. The diorite, like the trondhjemite unit, intruded the volcanic sequence of the Tati greenstone belt. Its age relations with the surrounding granitoids have been contentious. Kampunzu et al. (2003) suggested that the diorite is relatively younger than the tonalite-trondhjemite units within the Tati granite-greenstone terrain. Recently, Zhai et al. (2006) presented poorly constrained Sm-Nd ages indicating that the diorite and tonalite-trondhjemite units are contemporaneous. The U-Pb date from this sample can potentially resolve the uncertainties in these age relationships.

Zircon grains from the sample ZBT-19 are translucent with mostly anhedral habit. They are variable in size up to ca. 400 µm long. The zircon grains are generally fragmented and show only occasional facets. Internally, they show broad oscillatory zoning (Fig. 4.23). Some of the zircon grains exhibit post-crystallization recrystallisation and growth as evidenced by bright cathodoluminescence zircon growth fillings along microfractures (see grain #6 in Fig. 4.23). However, these infillings are too small to analyze. Zircon grains from the diorite sample have moderate U concentrations (61 -405 ppm) and high Th/U ratios (0.5-1.84), which suggest an igneous origin. Isotopic data was obtained from 18 grains (Table 4.6). Apart from two analyses (#8.1 and #13.1; Table 4.6) all data are near concordant. Analysis #13.1 has relatively high U and Th contents of 900 and 1670 ppm respectively and is grossly discordant with Pb-loss indicated at about 1.0 – 1.1 Ga. On a concordia diagram (Fig. 4.24a) all the analyses define upper and lower intercept dates of 2717.8 ± 7.2 Ma and 1063 ± 62 Ma, respectively (MSWD = 2.8). The near-concordant analyses give a weighted mean $^{207}Pb/^{206}Pb$ date of 2715.9 ± 2.5 Ma (MSWD = 1.13; Fig. 4.24b). This date is interpreted as the magmatic age of the diorite. This is within error of the age of the trondhjemite (2714 – 2715 Ma), which in turn implies that the diorite and trondhjemite units are contemporaneous, and both are younger than the Tlhalogang and Sekukwe plutons, but older than the Tati pluton.

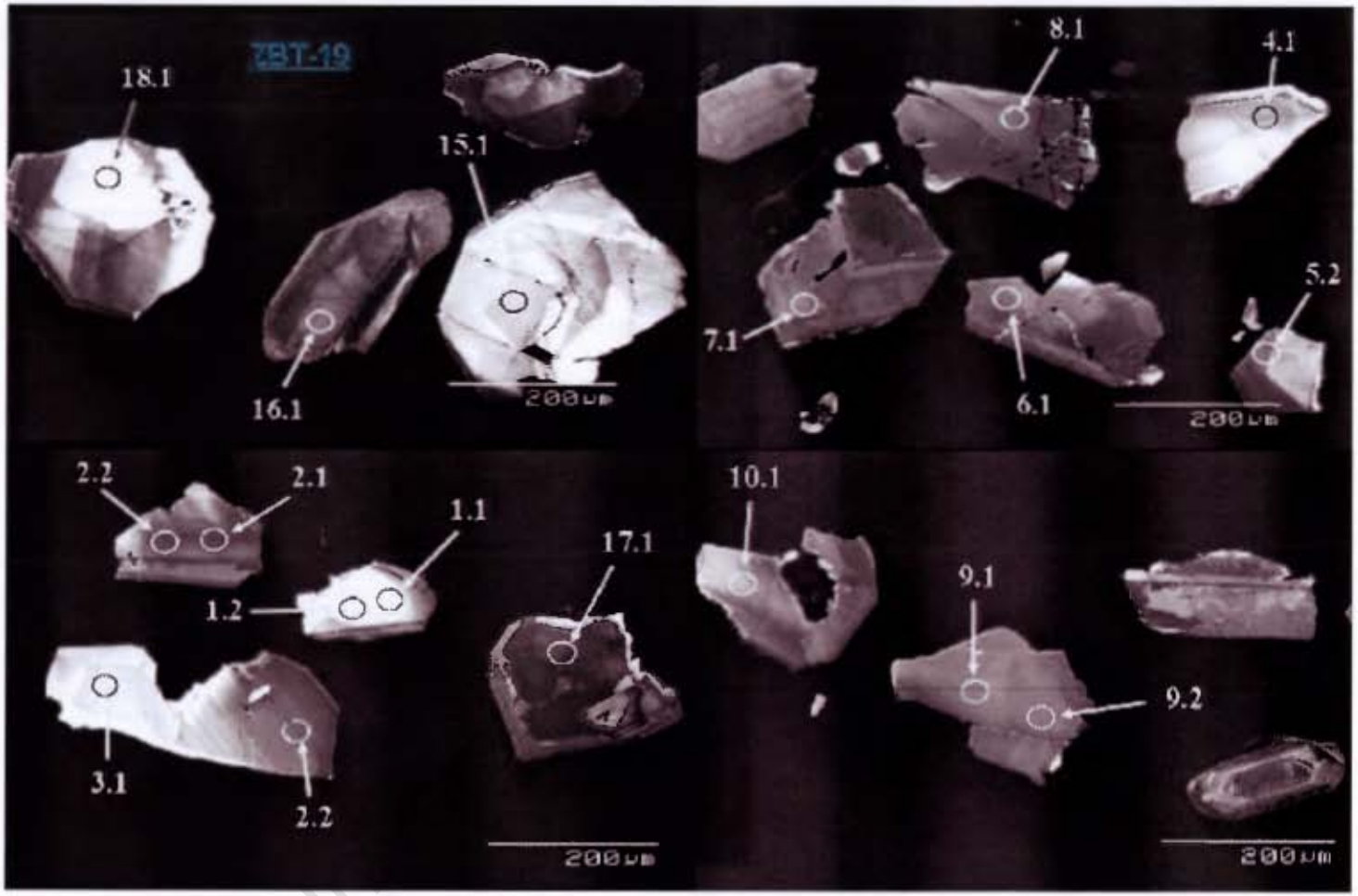

Fig. 4.23: CL images of zircon grains from the diorite (sample ZBT-19). Note the anhedral habit of zircon grains and complex zoning indicative of igneous origin. Analysed spots are denoted by white circles and in some areas the circles are black. The magmatic age of this diorite is 2715 Ma

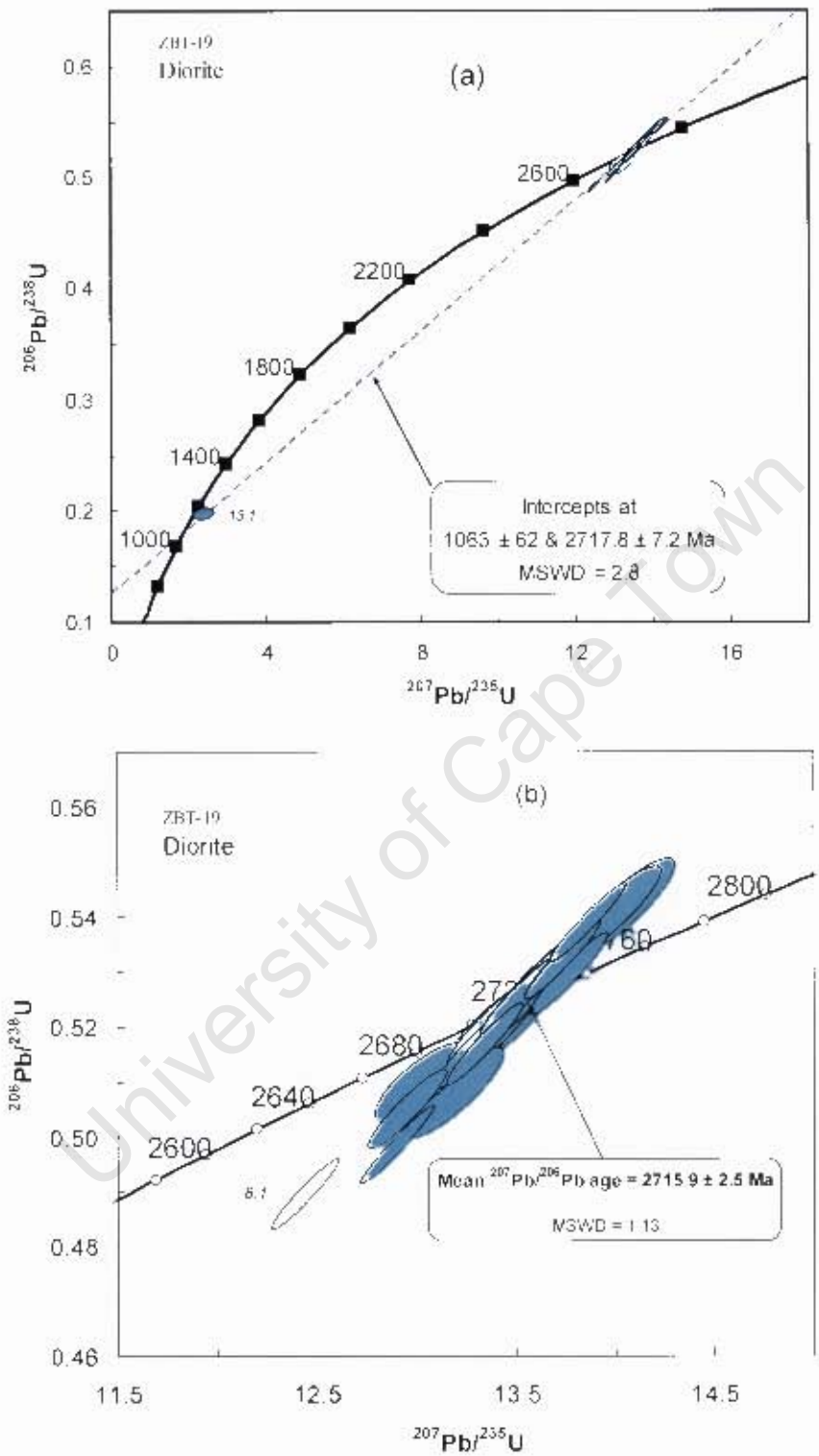

Fig. 4.24: (a) U-Pb concordia plot of all SHRIMP data for zircon grains from the diorite sample ZBT-19 intruding the Tati greenstone belt; (b) Concordia plot for near-concordant analyses used to calculate weighted mean $^{207}Pb/^{206}Pb$ age of ZBT-19. Unfilled error ellipse excluded in weighted mean age. Confidence limit for error ellipses is 1σ

Table 4.6: U-Th-Pb isotopic compositions of zircon grains and age calculations from Diorite sample ZBT-19 intruding the Tati greenstone belt.

Concentration						Radiogenic ratios						Age [Ma]				
Grain Spot	% $^{206}Pb_c$	U (ppm)	Th (ppm)	Th/U	$^{206}Pb^*$ (ppm)	(1) $^{207}Pb^*/^{206}Pb^*$	±%	(1) $^{207}Pb^*/^{235}U$	±%	(1) $^{206}Pb^*/^{238}U$	±%	(1) $^{206}Pb/^{238}U$ Age		(1) $^{207}Pb/^{206}Pb$ Age		% Discordant
Diorite (ZBTF-19)																
1.1	0.03	64	44	0.70	27.9	0.1881	0.61	13.19	1.2	0.5083	1.1	2,649	±23	2,726	± 10	3
1.2	0.00	76	50	0.66	34.0	0.1870	0.66	13.43	1.4	0.5211	1.3	2,704	±28	2,716	±11	0
2.1	0.02	280	320	1.14	120	0.18763	0.22	12.90	0.97	0.4986	0.94	2,608	±20	2,721.5	± 3.6	4
2.2	0.00	330	352	1.07	145	0.1852	0.71	13.02	1.2	0.5100	0.93	2,657	±20	2,700	±12	2
3.1	0.03	89	42	0.47	39.7	0.18630	0.53	13.36	1.1	0.5202	0.99	2,700	±22	2,709.7	± 8.8	0
3.2	0.02	276	256	0.93	125	0.18654	0.35	13.60	1.0	0.5286	0.95	2,736	±21	2,711.9	± 5.8	-1
4.1	--	151	76	0.50	68.9	0.18850	0.29	13.77	0.96	0.5296	0.91	2,740	±20	2,729.1	± 4.8	0
5.2	0.02	129	73	0.57	57.3	0.18691	0.50	13.38	1.2	0.5191	1.1	2,695	±24	2,715.1	± 8.3	1
6.1	0.02	201	213	1.06	92.0	0.18715	0.26	13.74	0.92	0.5323	0.88	2,751	±20	2,717.3	± 4.3	-1
7.1	0.04	149	98	0.66	66.9	0.18720	0.31	13.54	0.99	0.5245	0.94	2,718	±21	2,717.8	± 5.0	0
8.1	0.04	247	160	0.65	104	0.18416	0.25	12.44	0.90	0.4898	0.87	2,570	±18	2,690.7	± 4.2	4
9.1	0.02	224	142	0.63	104	0.18651	0.24	13.86	0.91	0.5389	0.87	2,779	±20	2,711.7	± 3.9	-2
9.2	0.00	252	144	0.57	113	0.18613	0.36	13.36	1.0	0.5204	0.96	2,701	±21	2,708.2	± 5.9	0
10.1	0.02	136	78	0.57	61.5	0.18653	0.33	13.59	0.98	0.5286	0.92	2,736	±21	2,711.8	± 5.4	-1
11.2	0.00	287	297	1.03	127	0.18674	0.34	13.29	1.0	0.5161	0.94	2,682	±21	2,713.6	± 5.6	1
12.1	0.02	104	85	0.82	48.2	0.18755	0.51	13.99	1.1	0.5411	0.97	2,788	±22	2,720.8	± 8.5	-2
13.1	3.70	906	1670	1.84	158	0.0870	6.8	2.35	7.1	0.1955	1.9	1,151	±20	1,361	±130	15
14.2	0.00	277	181	0.65	120	0.18592	0.37	12.95	1.0	0.5051	0.94	2,636	±20	2,706.4	± 6.1	3
15.1	--	61	38	0.62	28.4	0.1878	0.61	14.03	1.3	0.5415	1.1	2,790	±25	2,723	± 10	-2
16.1	0.03	126	84	0.67	56.7	0.18658	0.33	13.52	0.98	0.5255	0.93	2,723	±21	2,712.2	± 5.4	0
17.1	0.00	405	334	0.83	180	0.18714	0.29	13.34	0.97	0.5169	0.93	2,686	±20	2,717.2	± 4.7	1
18.1	0.00	72	42	0.59	31.7	0.1868	0.67	13.18	1.5	0.5117	1.3	2,664	±28	2,714	±11	2

Uncertainties in ages are reported at the 2 sigma confidence level. % $^{206}Pb_c$ denotes the percentage of ^{206}Pb that is common Pb. $^{206}Pb^*$ indicates the portion of radiogenic Pb. (1) Common Pb corrected using measured ^{204}Pb.

4.4.7 Tonalite-trondhjemite dyke at Phoenix mine*: Sample ZBT-36*

Sample ZBT-36 was collected from tonalite-trondhjemite dykes exposed in the Phoenix mine, located 26 Km east of Francistown (Fig. 4.1). These dykes intruded into the gabbro body that is mined for Cu-Ni ore. It has been suggested by Johnson (1986), that the dykes, which he misidentified as granite dykes, are responsible for the massive sulphides mineralization in this gabbro. Another mineralized gabbro body occurs 11 kilometers south of the Phoenix gabbro. This gabbro named the Selkirk gabbro (e.g. Key, 1976), exhibits disseminated type of sulphides mineralization, but there are no associated tonalite-trondhjemite dykes. Key (1976) suggested that the Selkirk gabbro is penecontemporaneous with the volcanic rocks of the Tati greenstone belt. Sample ZBT-36 is light-grey, medium-grained, massive, homogenous and granular. Its modal composition comprises 10% microcline, 30% quartz, 60% albatic plagioclase and accessory biotite and zircon, which is a leucocratic tonalite/trondhjemite. The sample was selected in order to constrain the minimum age of the gabbro emplacement, since it is difficult to date gabbros using the U-Pb zircon technique. In addition the age of the dykes has the potential to link them with other magmatic events in the study area, which would enhance the understanding of the area's magmatic history.

This sample yielded a simple population of zircon grains with signs of various degrees of Pb losses (metamict). The zircon grains are generally subhedral with prismatic habit. Despite the alteration state of most of the grains, some internal zoning indicative of magmatic origin is still discernable (Fig. 4.25). Twenty-six analyses from 23 zircon grains were obtained from the sample ZBT-36. Zircon grains from this sample have variable Th/U ratios from 0.005 to 0.53, with many grains possessing a Th/U ratio of approximately 0.4 (Table 4.7). The U concentrations range between 176 and 1351 ppm. The data form a scattered population about a discordia with an upper intercept date of 2699 ± 26 Ma with MSWD of 58 indicating large scatter (Fig. 4.26a). When considering only the concordant and near-concordant analyses, the upper intercept gives $^{207}Pb/^{206}Pb$ date of 2703.5 ± 4.1 Ma (MSWD=0.78; Fig. 4.26b), which is interpreted as the magmatic age of the tonalite-trondhjemite dyke and provide a minimum age for the Phoenix Gabbro.

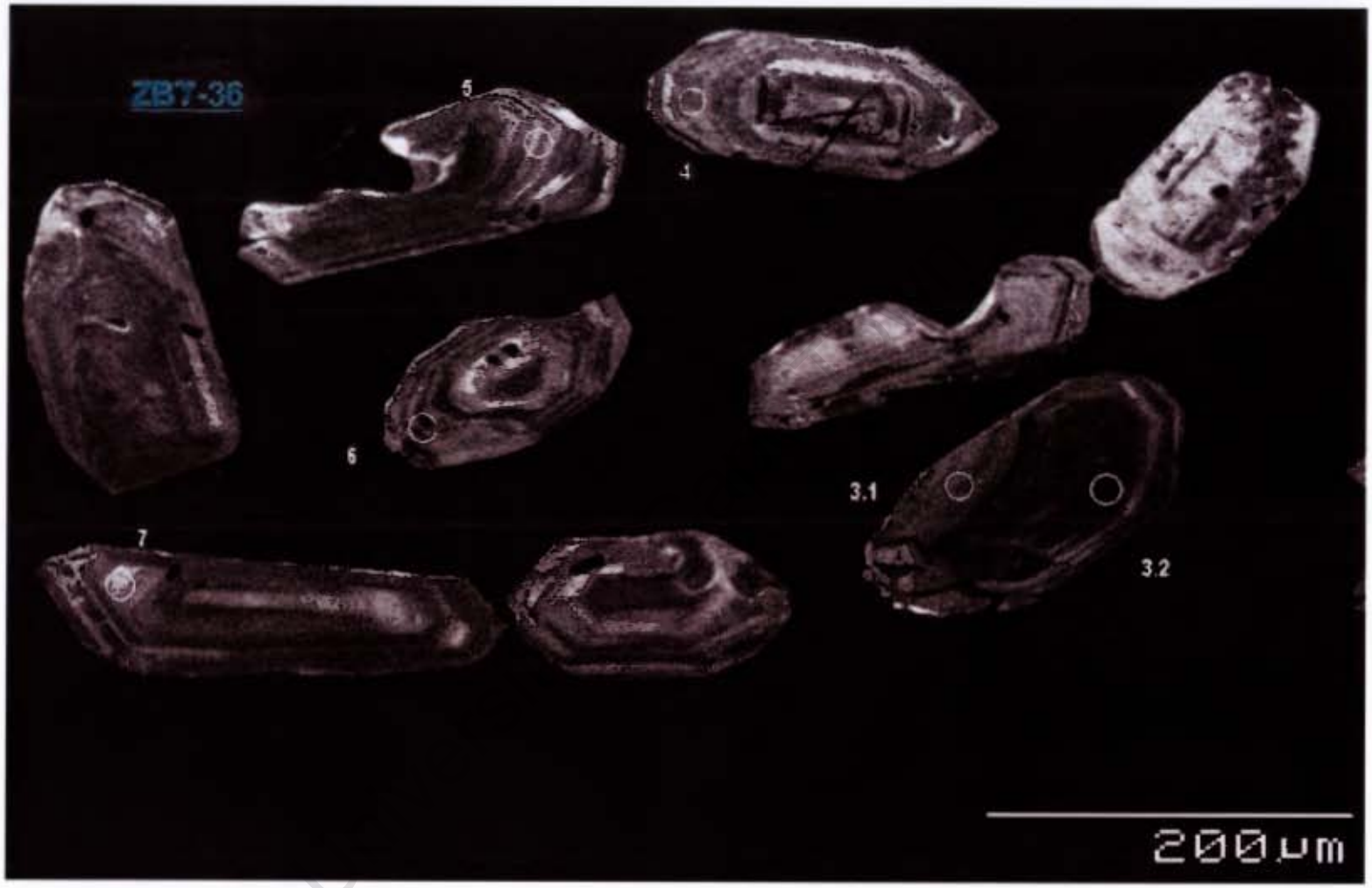

Fig. 4.25: CL images of representative zircon grains from the tonalite-trondhjemite dyke that cuts the Phoenix gabbro (sample ZBT-36). Note the oscillatory zoning indicative of magmatic origin despite alteration state. Also note lack of inheritance and metamorphic rims. The magmatic age of this tonalite-trondhjemite dyke is 2703 Ma.

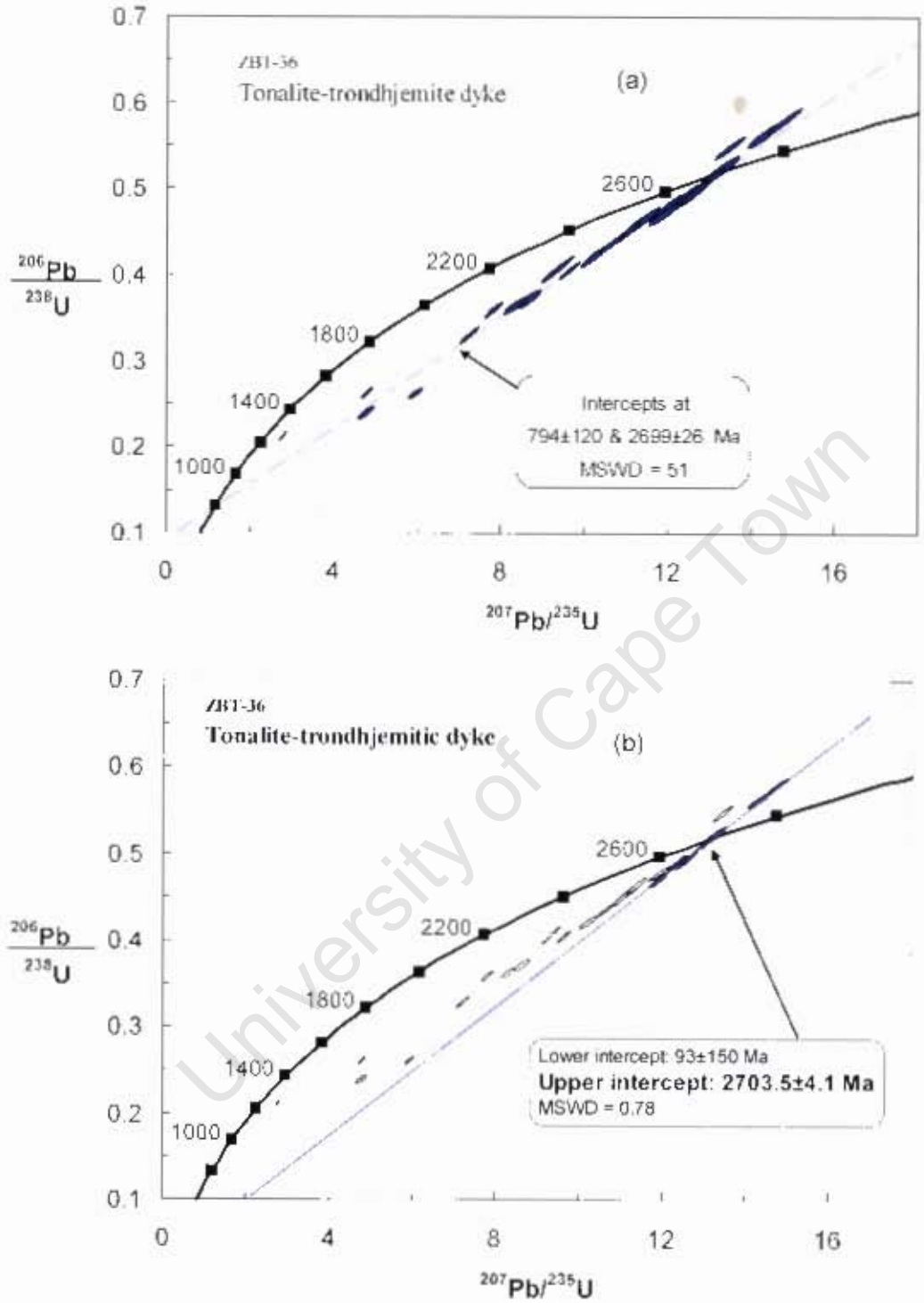

Fig. 4.26: U-Pb concordia plot of SHRIMP data for zircon grains from the tonalite-trondhjemite dyke sample ZBT-36; (a) all the 28 analyses were included on the discordia line regression; (b) only 9 concordant and near-concordant analyses (blue ellipses) were included on the discordia line regression. Confidence limit for error ellipses is 1σ.

Table 4.7: U-Th-Pb isotopic compositions of zircon grains and age calculations from tonalite-trondhjemite dyke sample ZBT-36 from the Phoenix Mine in the Tati terrain.

Concentration						Radiogenic ratios						Age [Ma]				
Grain Spot	% $^{206}Pb_c$	U (ppm)	Th (ppm)	Th/U	$^{206}Pb^*$ (ppm)	(1) $^{207}Pb^*/^{206}Pb^*$	±%	(1) $^{207}Pb^*/^{235}U$	±%	(1) $^{206}Pb^*/^{238}U$	±%	(1) $^{206}Pb/^{238}U$ Age		(1) $^{207}Pb/^{206}Pb$ Age		% Discordant
Tonalite-trondhjemite dyke intruding the Gabbro at Phoenix Mine (ZBT-36)																
1.1	0.23	1351	6	0.005	242	0.0984	0.38	2.822	1.1	0.208	1	1218	±12	1594	± 7.2	24
1.2	0.05	176	83	0.47	78.9	0.18563	0.49	13.33	1.3	0.5206	1.2	2702	±26	2703.8	± 8	0
2.1	0.04	289	112	0.39	143	0.18609	0.28	14.82	1.1	0.5776	1.1	2939	±25	2707.9	± 4.6	-9
3.1	0.16	810	49	0.06	180	0.1353	0.48	4.831	1.2	0.2589	1.1	1484	±15	2167.9	± 8.4	32
3.2	0.03	298	120	0.40	127	0.186	0.32	12.69	1.1	0.4949	1.1	2592	±23	2707.1	± 5.3	4
4.1	0.28	469	175	0.37	146	0.16815	0.58	8.37	1.4	0.3608	1.2	1986	±21	2539.3	± 9.8	22
5.1	0.04	193	59	0.30	93.2	0.18566	0.43	14.35	1.2	0.5606	1.1	2869	±26	2704.1	± 7	-6
6.1	0.98	1067	474	0.44	218	0.1478	0.82	4.811	1.7	0.2361	1.4	1366	±18	2320	±14	41
7.1	0.09	213	75	0.35	95	0.18498	0.38	13.26	1.4	0.5198	1.4	2698	±30	2698	± 6.2	0
8.1	0.04	729	288	0.39	272	0.17852	0.33	10.7	1.2	0.4347	1.1	2327	±22	2639.2	± 5.4	12
9.1	0.00	289	140	0.49	126	0.18573	0.33	13.04	1.1	0.5091	1.1	2653	±24	2704.7	± 5.5	2
9.2	0.06	566	173	0.31	159	0.16146	0.39	7.262	1.4	0.3262	1.3	1820	±21	2471	± 6.6	26
10.1	0.08	262	119	0.45	101	0.17915	0.38	11.03	1.2	0.4466	1.1	2380	±22	2645	± 6.3	10
11.1	0.09	200	61	0.30	80.3	0.18509	0.43	11.93	1.3	0.4676	1.2	2473	±25	2699	± 7.1	8
12.1	0.08	748	193	0.26	230	0.15954	0.42	7.848	1.2	0.3568	1.2	1967	±20	2450.8	± 7	20
13.1	0.05	347	132	0.38	125	0.17769	0.48	10.28	1.3	0.4194	1.2	2258	±24	2631.4	± 8	14
14.1	0.09	352	88	0.25	122	0.16842	0.35	9.38	1.7	0.404	1.6	2187	±31	2542	± 5.8	14
15.1	0.02	513	207	0.40	177	0.17456	0.28	9.68	1.1	0.4021	1.1	2179	±20	2601.8	± 4.7	16
16.1	0.27	857	453	0.53	191	0.16814	0.52	5.99	1.2	0.2584	1.1	1481	±14	2539.2	± 8.8	42
17.1	0.75	667	199	0.30	315	0.1793	0.28	13.5	1.1	0.5459	1.1	2808	±24	2646.4	± 4.7	-6
18.1	0.12	226	80	0.36	95.2	0.18607	0.41	12.57	1.4	0.4899	1.3	2570	±28	2707.6	± 6.8	5
19.1	0.03	288	120	0.42	118	0.18241	0.36	11.97	1.3	0.476	1.3	2510	±27	2674.9	± 5.9	6
20.1	0.21	223	65	0.29	88.6	0.17954	0.44	11.43	1.4	0.4619	1.3	2448	±27	2648.4	± 7.2	8
21.1	0.05	258	91	0.35	108	0.18419	0.39	12.4	1.4	0.4885	1.3	2564	±28	2690.9	± 6.5	5
22.1	0.08	208	104	0.50	81.6	0.17929	0.48	11.28	1.4	0.4562	1.3	2423	±27	2646.2	± 7.9	8
23.1	0.04	635	249	0.39	202	0.1705	0.64	8.68	1.4	0.3693	1.2	2026	±21	2563	±11	21

Uncertainties in ages are reported at the 2 sigma confidence level. % $^{206}Pb_c$ denotes the percentage of ^{206}Pb that is common Pb. $^{206}Pb^*$ indicates the portion of radiogenic Pb. (1) Common Pb corrected using measured ^{204}Pb.

4.4.8 Monzogranite: *Samples GEOZB-9*

The monzogranite generally occurs as undeformed small stocks and dykes intruding the greenstone succession and other granitoids in the Tati granite-greenstone terrane. The dykes have a preferred direction with an azimuth of about 100º. Noteworthy, is the observation that the monzogranite is confined mainly to the NE of the Tati greenstone belt. The monzogranite unit is considered the youngest (Key, 1976; Kampunzu et al., 2003; Zhai et al., 2006) magmatic event in the Tati granite-greenstone terrane. Some investigators link it to the craton wide monzogranite of the Chilimanzi suite in Zimbabwe, which was emplaced ca 2600 Ma ago (e.g. Kampunzu et al., 2003). Zhai et al. (2006) dated the monzogranite using Sm-Nd method and obtained a poorly constrained age of 2.59 ± 0.40 Ga. Key (1976) considered the monzogranite dykes as different from the monzogranite plutons such as the Ramokgwebana and Timbale Granites (Fig. 4.1). He observed that the monzogranite dykes have the same strike as the Karoo dolerite dykes and suggested that they may be Mesozoic in age. A sample was selected for U-Pb dating from the small stock of the monzogranite outcrop in order to establish the true age of this monzogranite unit.

The sample GEOZB-9 was collected from a small kopje of monzogranite located 5 Km north of the Francistown city centre (Fig. 4.1). The rock is granular, massive, homogenous, medium-grained biotite bearing monzogranite. This sample yielded a population of zircon grains that are clear with subhedral to anhedral forms. The zircon grains show no obvious overgrowth or evidence of inheritance (Fig. 4.27). Generally, the grains are equant and ≤100 µm in size. Oscillatory zoning is conspicuous, which is taken to indicate an igneous origin of these zircon grains. Twenty analyses from 18 zircon grains were obtained from this sample. Contents of U and Th range from 157 to 313 ppm and 80 to 218 ppm, respectively, resulting in Th/U ratios in the range of 0.55 to 0.75, typical for magmatic zircon (Table 4.8). All the analyses were close to concordant except analysis #5.1, which is significantly discordant. On the concordia diagram, linear regression of all data points yielded an upper intercept age of 2719.9 ± 8.4 Ma (MSWD = 1.4; Fig. 4.28a). The near-concordant analyses define a population with the weighted mean $^{207}Pb/^{206}Pb$ date of 2716.1 ± 3.7 Ma (MSWD = 1.18; Fig. 4.28b), which is interpreted as the magmatic age of the monzogranite. Within the errors, this age is indistinguishable from the ages of the trondhjemite (2715 ± 2.7 Ma) and diorite (2715.9 ± 2.5 Ma) units within the same area. The fact that the monzogranitic dykes cut the two other units, this implies some comagmatic affinity of these rock units.

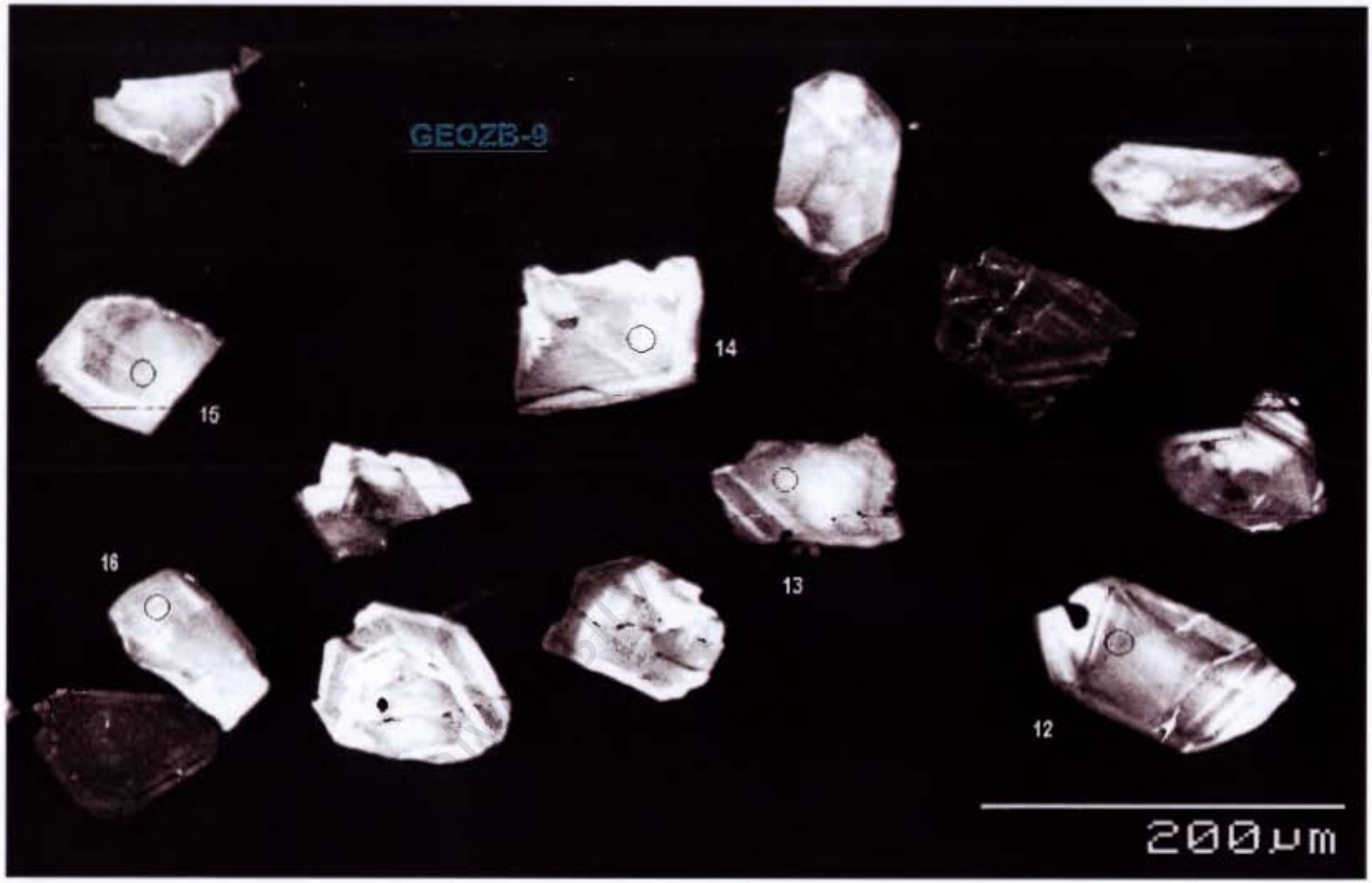

Fig. 4.27: CL images of a subset of zircon grains from the monzogranite sample GECZB-9. Note the clarity of zircon grains and complex zoning indicative of magmatic origin. Also note the evident lack of inherited cores and metamorphic overgrowth. Analysed spots are denoted by black circles. The magmatic age of this monzogranite is 2716 Ma.

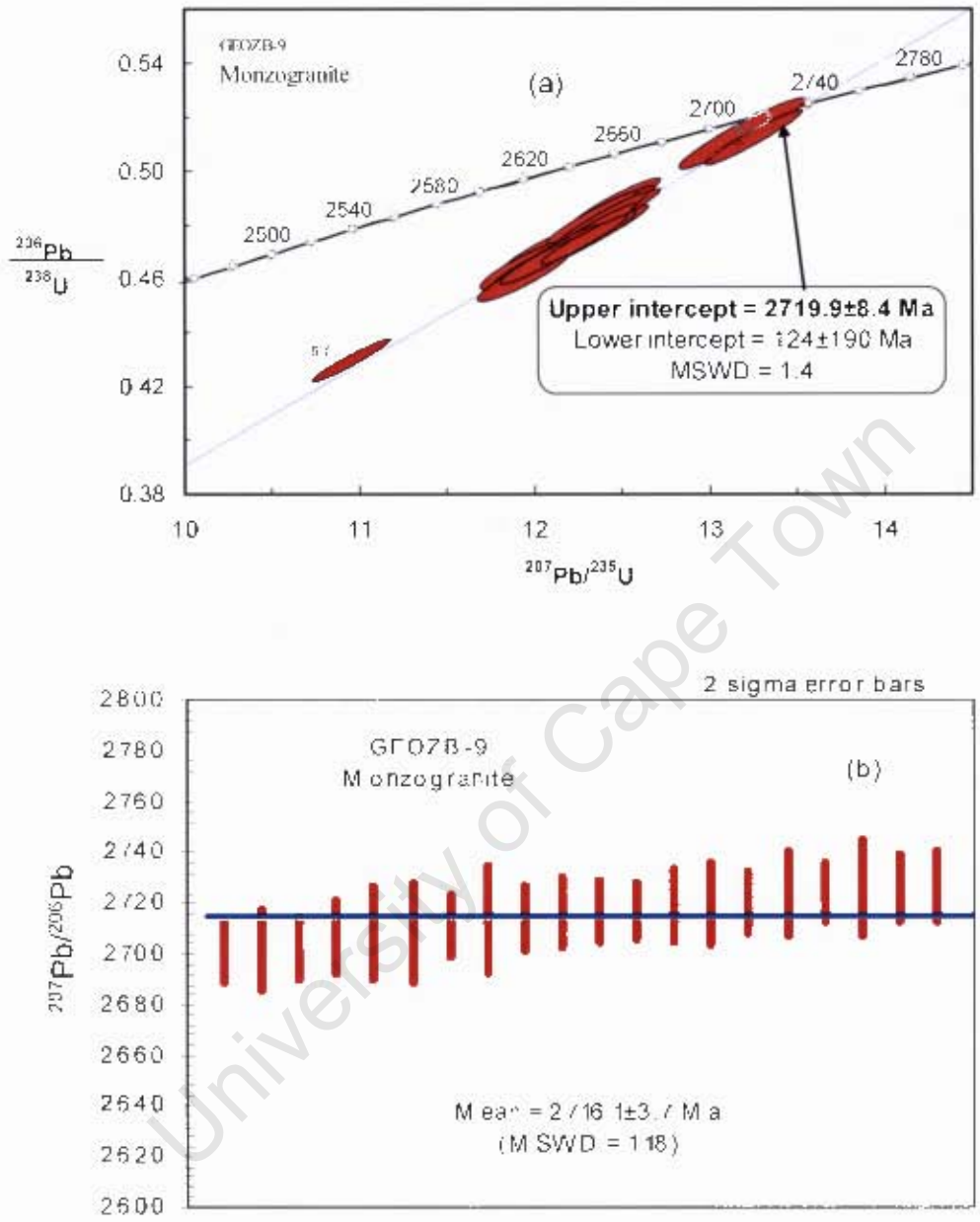

Fig. 4.28: (a) U-Pb concordia plot of all SHRIMP data for zircon grains from the Monzogranite sample GEOZB-9; (b) Weighted average mean $^{207}Pb/^{206}Pb$ age calculated from near concordant analyses. Confidence limit for error ellipses is 1σ.

Table 4.8: U-Th-Pb isotopic compositions of zircon grains and age calculations from monzogranite sample GEOZB-9 in the Tati granite-greenstone terrain

Concentration						Radiogenic ratios						Age [Ma]				
Grain Spot	% $^{206}Pb_c$	U (ppm)	Th (ppm)	Th/U	$^{206}Pb^*$ (ppm)	(1) $^{207}Pb^*/^{206}Pb^*$	±%	(1) $^{207}Pb^*/^{235}U$	±%	(1) $^{206}Pb^*/^{238}U$	±%	(1) $^{206}Pb/^{238}U$ Age		(1) $^{207}Pb/^{206}Pb$ Age		% Discordant
Monzogranite (GEOZB-9)																
1.1	0.04	198	109	0.55	81.3	0.18823	0.43	12.38	1.4	0.477	1.4	2514	±28	2726.7	± 7	8
1.2	0.07	240	142	0.59	106	0.18749	0.38	13.24	1.4	0.5124	1.3	2667	±29	2720.3	± 6.3	2
2.1	0.09	224	129	0.58	89.3	0.1867	0.64	11.96	1.5	0.4644	1.3	2459	±27	2713	±11	9
3.1	0.04	276	172	0.62	114	0.18713	0.34	12.33	1.3	0.478	1.3	2519	±27	2717.1	± 5.6	7
4.1	0.04	292	201	0.69	117	0.18734	0.43	12.05	1.4	0.4664	1.3	2468	±27	2718.9	± 7.2	9
5.1	0.05	313	218	0.70	115	0.18527	0.37	10.95	1.3	0.4285	1.3	2299	±25	2700.7	± 6.1	15
6.1	0.11	204	125	0.61	83.9	0.18703	0.43	12.33	1.4	0.4783	1.3	2520	±28	2716.2	± 7.1	7
7.1	0.06	179	102	0.57	72.5	0.1861	0.59	12.08	1.5	0.4709	1.4	2487	±28	2708	± 9.8	8
8.1	0.01	318	204	0.64	130	0.18795	0.36	12.28	1.3	0.4737	1.3	2500	±27	2724.3	± 5.9	8
9.1	0.10	233	141	0.61	97	0.18597	0.43	12.41	1.4	0.4841	1.3	2545	±28	2706.8	± 7.1	6
10.1	0.07	292	179	0.61	119	0.18786	0.51	12.31	1.4	0.4753	1.3	2507	±27	2723.5	± 8.4	8
10.2	0.10	157	80	0.51	69.5	0.1861	0.56	13.18	1.8	0.5136	1.7	2672	±37	2708	± 9.3	1
11.1	0.08	225	134	0.60	88.8	0.1881	0.58	11.93	1.5	0.4601	1.3	2440	±27	2725.6	± 9.6	10
12.1	0.06	274	175	0.64	113	0.18648	0.37	12.38	1.4	0.4816	1.3	2534	±27	2711.3	± 6	7
13.1	0.04	221	129	0.59	90.1	0.18816	0.41	12.3	1.4	0.4741	1.3	2501	±28	2726.1	± 6.8	8
14.1	0.05	194	109	0.56	77.4	0.18742	0.50	12.02	1.4	0.465	1.4	2462	±28	2719.7	± 8.3	9
15.1	0.03	294	187	0.64	122	0.18679	0.39	12.46	1.4	0.4837	1.3	2544	±27	2714.1	± 6.5	6
16.1	0.00	265	162	0.61	110	0.18543	0.38	12.32	1.4	0.482	1.3	2536	±27	2702	± 6.2	6
17.1	0.04	262	195	0.75	106	0.18711	0.38	12.12	1.4	0.47	1.3	2483	±27	2716.9	± 6.2	9
18.1	0.10	229	139	0.60	96.1	0.18538	0.50	12.45	1.4	0.487	1.3	2558	±28	2701.6	± 8.3	5

Uncertainties in ages are reported at the 2 sigma confidence level. % $^{206}Pb_c$ denotes the percentage of ^{206}Pb that is common Pb. $^{206}Pb^*$ indicates the portion of radiogenic Pb. (1) Common Pb corrected using measured ^{204}Pb.

4.4.9 Shashe gneiss: *Samples GEOZB-5 and GEOZB-6*

The Shashe gneiss unit is exposed to the southwestern area of the Tati greenstone belt. It contains a variety of lithologies amongst them migmatitic gneiss and granitic augen gneiss (Key, 1976). This unit occurs within the Motloutse-Matsitama Complex, which is part of the Limpopo-Shashe orogenic belt (McCourt et al., 2004). The migmatisation is more pronounced towards the Tati granite-greenstone terrain and it has been interpreted as the transition zone between the Zimbabwe craton and the Limpopo-Shashe orogenic belt by Key (1976). He suggests that the Shashe gneiss is older than the Tati greenstone belt. In contrast, McCourt et al. (2004) argue that the Tati greenstone belt is older and it was the source of the sedimentary rocks within the Motloutse-Matsitama Complex. These authors believe the Limpopo-Shashe Belt was accreted to the Tati granite-greenstone terrain between 2661 and 2647 Ma. They interpreted the migmatised zone as the Shashe shear zone, delineating the contact between the two terrains. The leucosomes in the migmatite occur mostly as veins with diffuse and irregular borders with the melanosomes. The leucosome is interpreted to have formed during anatexis linked to the collision between the Limpopo-Shashe Belt and Francistown Granite-Greenstone Complex. Thus, the ages from the Shashe gneiss and the Tati pluton will provide key information on geotectonic relationship between the Limpopo-Shashe orogeny and the Francistown Granite-Greenstone Complex. Kampunzu et al. (2003) believe that the plutonic rocks in the Tati granite-greenstone terrain and coeval igneous rocks in the Zimbabwe craton and Limpopo-Shashe Belt represent a single accretionary system that includes a continental magmatic arc within the Zimbabwe craton and an accretionary sedimentary and volcanic/plutonic assemblage within the southward-convex Limpopo-Shashe Belt. However, others content that the Limpopo-Shashe Belt is due to collision of the Francistown Granite-Greenstone Complex (Zimbabwe Craton) with the Kaapvaal Craton around 2650 Ma (e.g. Percival et al., 1997).

Jelsma and Dirks (2002) envisage a northeast to southwest oriented magmatic arc related to southeast directed subduction below the proto-Zimbabwe craton for the evolution of the granite-greenstone terrains along the northwest margin of the Zimbabwe Craton, which include the Francistown Granite-Greenstone Complex. This differs with the model of Kampunzu et al. (2003) that suggests an Andes-type convergent margin along the southern and southwestern margins of the proto-Zimbabwe craton.

Sample GEOZB-5 was sampled from a felsic vein (leucosome) of the migmatite. It is a cream-white, granular rock with fine quartz crystals sandwiched between medium-grained orthoclase and perthite. Biotite, zircon and sphene are the accessory phases. The sample yielded zircon grains that are light brown, subhedral, oscillatory zoned and sometimes with radial fracturing presumably caused by volume expansion of metamict interiors. Thirty analyses of 19 zircon grains were obtained from sample GEOZB-5. Majority of the zircon grains contain 200 to 600 ppm U, although grains with higher U contents (1484 ppm) were also present (Table 4.9). The Th/U ratios are between 0.05 and 1.21 with many grains having a Th/U ratio of more than 0.5. A group of analyses form a near-concordant population with a weighted mean $^{207}Pb/^{206}Pb$ date of 2629.4 ± 3.2 Ma (MSWD = 0.95). Nevertheless, there are a number of analyses which are very discordant. When all the analyses are plotted on a concordia diagram, an upper intercept date of 2640 ± 22 Ma is obtained (Fig. 4.29). The near-concordant population of zircon grains with weighted mean $^{207}Pb/^{206}Pb$ date of 2629.4 ± 3.2 Ma is interpreted to date leucosome formation and partial melting of host rock.

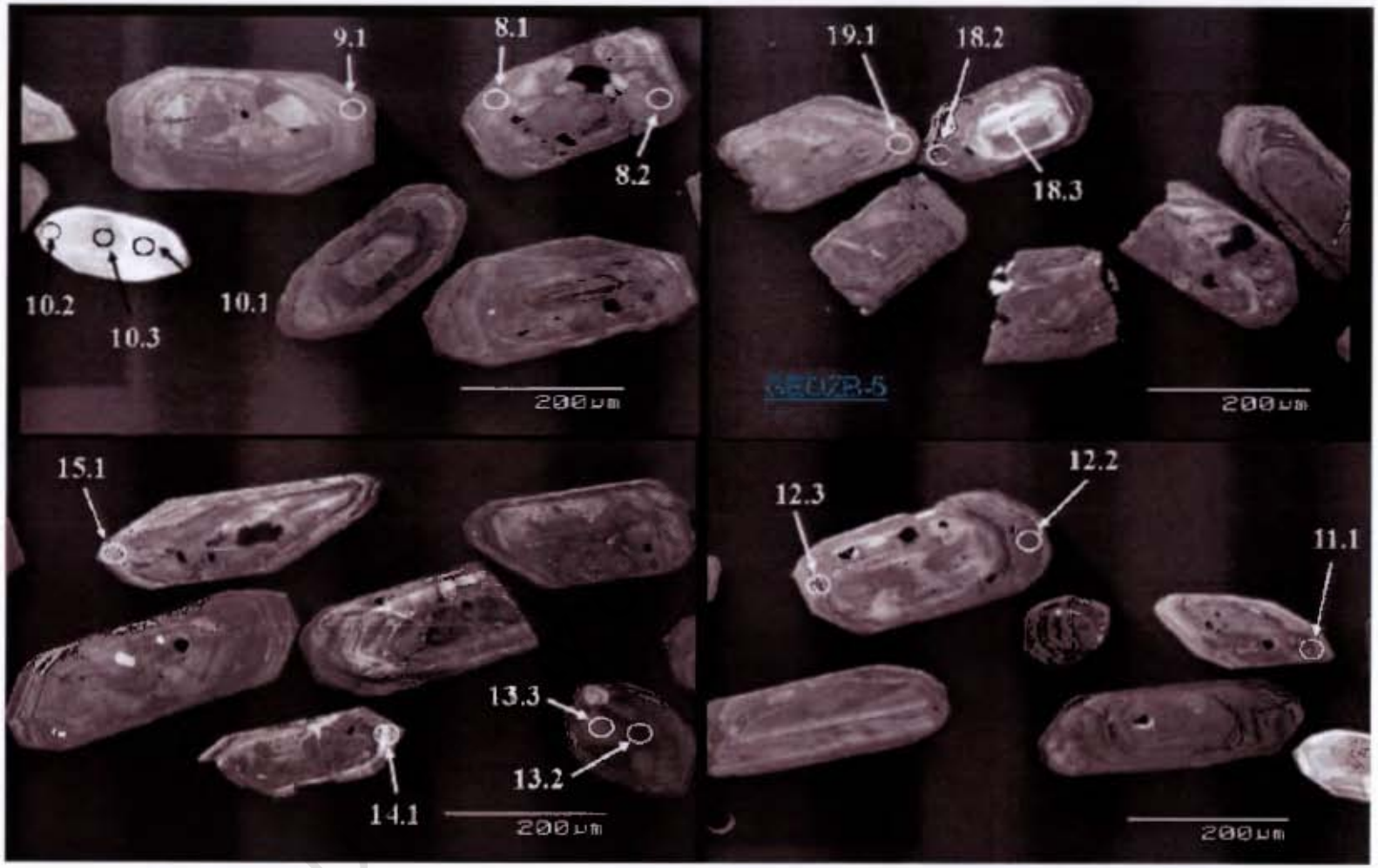

Fig. 4.29: CL images of zircon grains from the leucosome sample GEOZB-5 collected from the migmatised Shashe gneiss within the Limpopo-Shashe Belt. Note the oscillatory zoning in most grains indicative of magmatic origin. The analysed spots are illustrated by white circles. The magmatic age of the leucosome is 2630 Ma

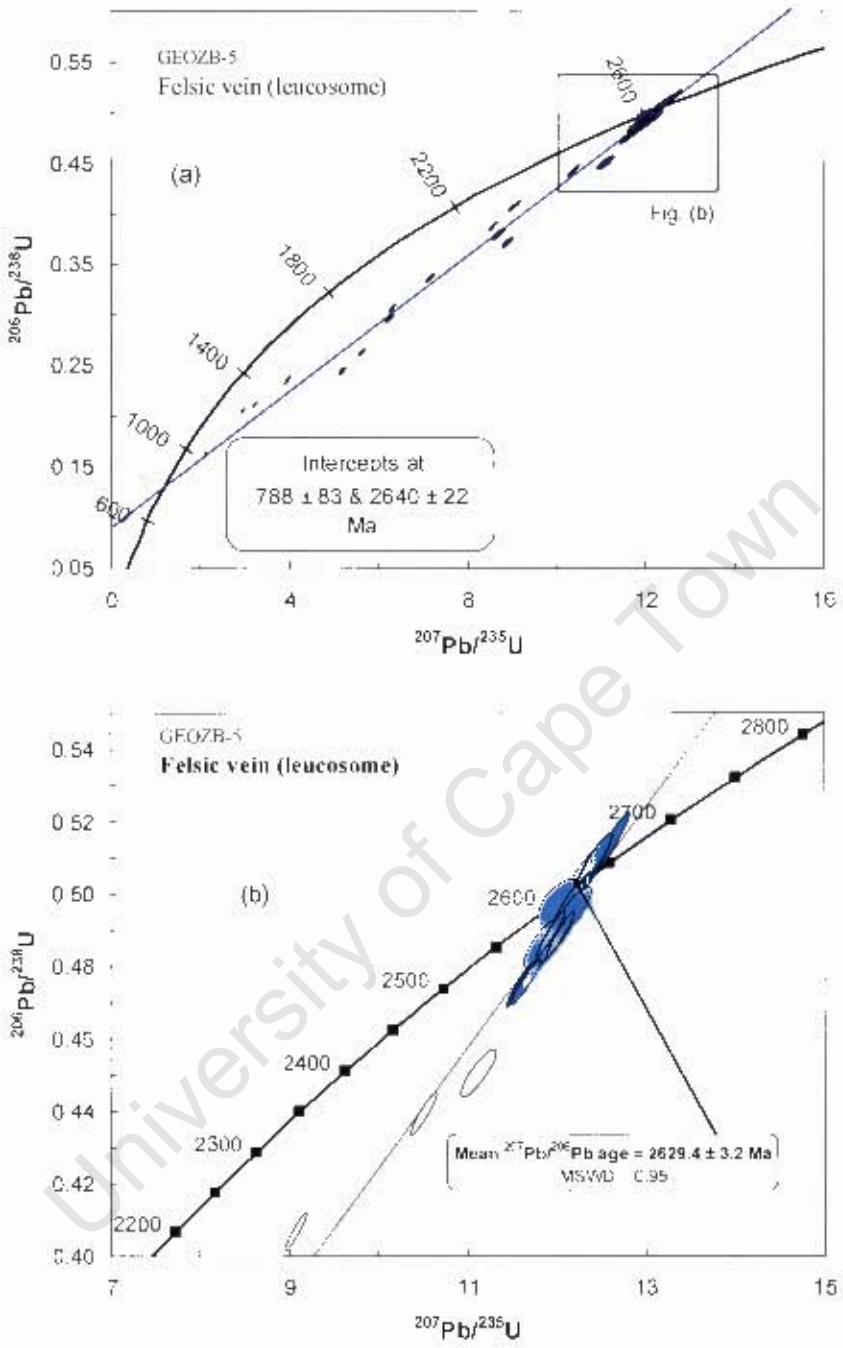

Fig. 4.30: U-Pb concordia plot of SHRIMP data for zircon grains from the leucosome (partial melt) sample GEOZB-5, taken in the Limpopo-Shashe Belt: (a) Plot of all the analyses, (b) Plot of only near-concordant analyses that were included in the calculation of the weighted mean $^{207}Pb/^{206}Pb$ date. Unfilled ellipses represent discordant analyses excluded from the calculation of the $^{207}Pb/^{206}Pb$ date. Confidence limit for error ellipses is 1σ.

Table 4.9: U-Th-Pb isotopic compositions of zircon grains and age calculations from leucosome sample GEOZB-5 within the Limpopo-Shashe Belt

Concentration						Radiogenic ratios						Age [Ma]				
Grain Spot	% $^{206}Pb_c$	U (ppm)	Th (ppm)	Th/U	$^{206}Pb^*$ (ppm)	(1) $^{207}Pb^*/^{206}Pb^*$	±%	(1) $^{207}Pb^*/^{235}U$	±%	(1) $^{206}Pb^*/^{238}U$	±%	(1) $^{206}Pb/^{238}U$ Age		(1) $^{207}Pb/^{206}Pb$ Age		% Discordant
1.1	0.02	207	113	0.55	84.3	0.17681	0.29	11.57	0.94	0.4744	0.89	2,503	±19	2,623.2	± 4.8	5
2.1	0.16	503	285	0.57	126	0.15449	0.41	6.217	0.95	0.2919	0.86	1,651	±12	2,396.1	± 7.1	31
3.1	0.04	152	109	0.72	66.8	0.17775	0.37	12.57	1.3	0.5129	1.2	2,669	±27	2,631.9	± 6.2	-1
3.2	0.07	342	89	0.26	108	0.17460	0.54	8.874	1.0	0.3687	0.87	2,023	±15	2,602.1	± 8.9	22
3.3	0.04	208	93	0.45	91.0	0.17686	0.44	12.41	1.1	0.5090	10	2,652	±22	2,623.7	± 7.4	-1
4.1	0.06	248	257	1.04	101	0.17764	0.33	11.63	0.94	0.4748	0.88	2,505	±18	2,630.9	± 5.4	5
5.1	0.58	1484	662	0.45	307	0.15513	0.58	5.120	1.0	0.2395	0.82	1,384	±10	2,403	±11	42
6.1	0.14	874	45	0.05	119	0.09339	0.39	2.031	0.99	0.1577	0.91	944.0	± 8.0	1,495.8	± 7.5	37
7.1	0.23	906	121	0.13	161	0.11085	0.37	3.148	0.94	0.2060	0.86	1,207.4	± 9.5	1,813.2	± 6.9	33
7.2	0.06	234	207	0.88	98.4	0.17862	0.27	12.03	0.92	0.4884	0.87	2,564	±19	2,640.0	± 4.5	3
7.3	0.04	264	221	0.84	112	0.17694	0.40	12.10	1.0	0.4961	0.97	2,597	±21	2,624.4	± 6.6	1
8.1	0.04	237	163	0.69	98.0	0.17779	0.26	11.81	0.93	0.4819	0.89	2,536	±19	2,632.3	± 4.4	4
8.2	0.12	526	370	0.70	199	0.17058	0.32	10.362	0.94	0.4406	0.89	2,353	±17	2,563.4	± 5.4	8
9.1	0.16	829	168	0.20	216	0.14956	0.35	6.249	0.93	0.3031	0.85	1,707	±13	2,340.7	± 6.1	27
10.1	0.07	106	74	0.70	45.6	0.17737	0.39	12.17	1.1	0.4978	1.0	2,604	±22	2,628.3	± 6.6	1
10.2	0.06	99	62	0.62	38.2	0.1790	0.58	11.10	1.2	0.4496	10	2,394	±20	2,644.0	± 9.7	9
10.3	0.01	146	92	0.63	61.2	0.17748	0.53	11.91	1.5	0.4866	1.4	2,556	±29	2,629.5	± 8.8	3
11.1	0.30	829	868	1.05	185	0.15616	0.41	5.569	0.93	0.2587	0.83	1,483	±11	2,414.2	± 7.3	39
12.2	1.42	323	236	0.73	140	0.1757	1.0	12.03	1.5	0.4973	0.88	2,602	±19	2,611	±19	0
12.3	0.09	685	357	0.52	239	0.16161	0.29	9.036	0.92	0.4055	0.87	2,194	±16	2,472.6	± 4.9	11
13.2	0.06	303	298	0.98	127	0.17700	0.26	11.91	0.90	0.4882	0.86	2,563	±18	2,624.9	± 4.4	2
13.3	0.02	260	316	1.21	113	0.1767	0.64	12.28	1.4	0.5041	1.2	2,631	±26	2,622	±11	0
14.1	0.32	122	62	0.51	39.8	0.16640	0.56	8.655	1.1	0.3773	0.96	2,064	±17	2,521.3	± 9.6	18
15.1	0.21	943	265	0.28	188	0.12205	0.45	3.887	1.2	0.2310	1.1	1,340	±13	1,986.2	± 8.2	33
16.1	0.39	1137	111	0.10	197	0.10446	0.54	2.886	0.99	0.2004	0.82	1,177.5	± 8.9	1,705	±10	31
17.1	0.12	201	124	0.62	85.6	0.1784	0.60	12.16	1.1	0.4947	0.91	2,591	±19	2,637	±10	2
17.2	0.48	323	99	0.30	136	0.1764	0.72	11.81	1.2	0.4855	0.94	2,551	±20	2,620	±12	3
18.2	0.15	708	399	0.56	234	0.16126	0.23	8.552	0.86	0.3847	0.83	2,098	±15	2,468.7	± 3.9	15
18.3	0.03	118	104	0.88	49.7	0.1780	0.58	11.99	1.3	0.4886	1.2	2,565	±25	2,634.6	± 9.7	3
19.1	0.08	593	545	0.92	170	0.15493	0.45	7.122	1.0	0.3334	0.94	1,855	±15	2,401.0	± 7.7	23

Uncertainties in ages are reported at the 2 sigma confidence level. % $^{206}Pb_c$ denotes the percentage of ^{206}Pb that is common Pb. $^{206}Pb^*$ indicates the portion of radiogenic Pb.

Granitic augen gneiss (GEOZB-6)

Sample GEOZB-6 was collected from a granitic augen gneiss outcrop within the Shashe river bed. It is medium to coarse-grained, foliated biotite-rich rock with anhedral quartz and alkali feldspars. The zircon grains from this sample are light brown in colour. They form a population of mostly euhedral to subhedral prismatic zircon grains that vary in length from 180 to 250 µm. Cathodoluminescence imaging of the zircon grains has revealed well-developed oscillatory zoning suggesting a magmatic origin. Thirty-five analyses were conducted on 25 zircon grains (Table 4.10). U concentrations of the range 58 to 1825 ppm were recorded from the zircon grains of sample GEOZB-6. Th/U ratios broadly vary between 0.01 and 1.58 (Table 4.10), which is consistent with a mixed zircon population of metamorphic and igneous origins. The data show a wide dispersion along a crude discordia indicating significant Pb-loss in many of the grains (Fig. 4.31a). Linear regression of all the analyses gives an upper intercept of 2639 ± 20 Ma and a lower intercept of 871 ± 72 Ma respectively (MSWD = 44; Fig. 4.30a). However, the best date was calculated from the 18 data points that plot as a coherent group near the concordia and has a weighted mean $^{207}Pb/^{206}Pb$ date of 2630 ± 4.7 Ma (MSWD = 1.4; Fig. 4.30b). This date is considered the magmatic age of the augen gneiss and overlaps in age with the leucosome from the migmatite.

In summary, the granitic augen gneiss and the main deformation fabric in Limpopo-Shashe Belt (Motloutse-Matsitama Complex) are syntectonic. The partial melts formed during the orogenic deformation possibly date the age of deformation at around 2630 Ma.

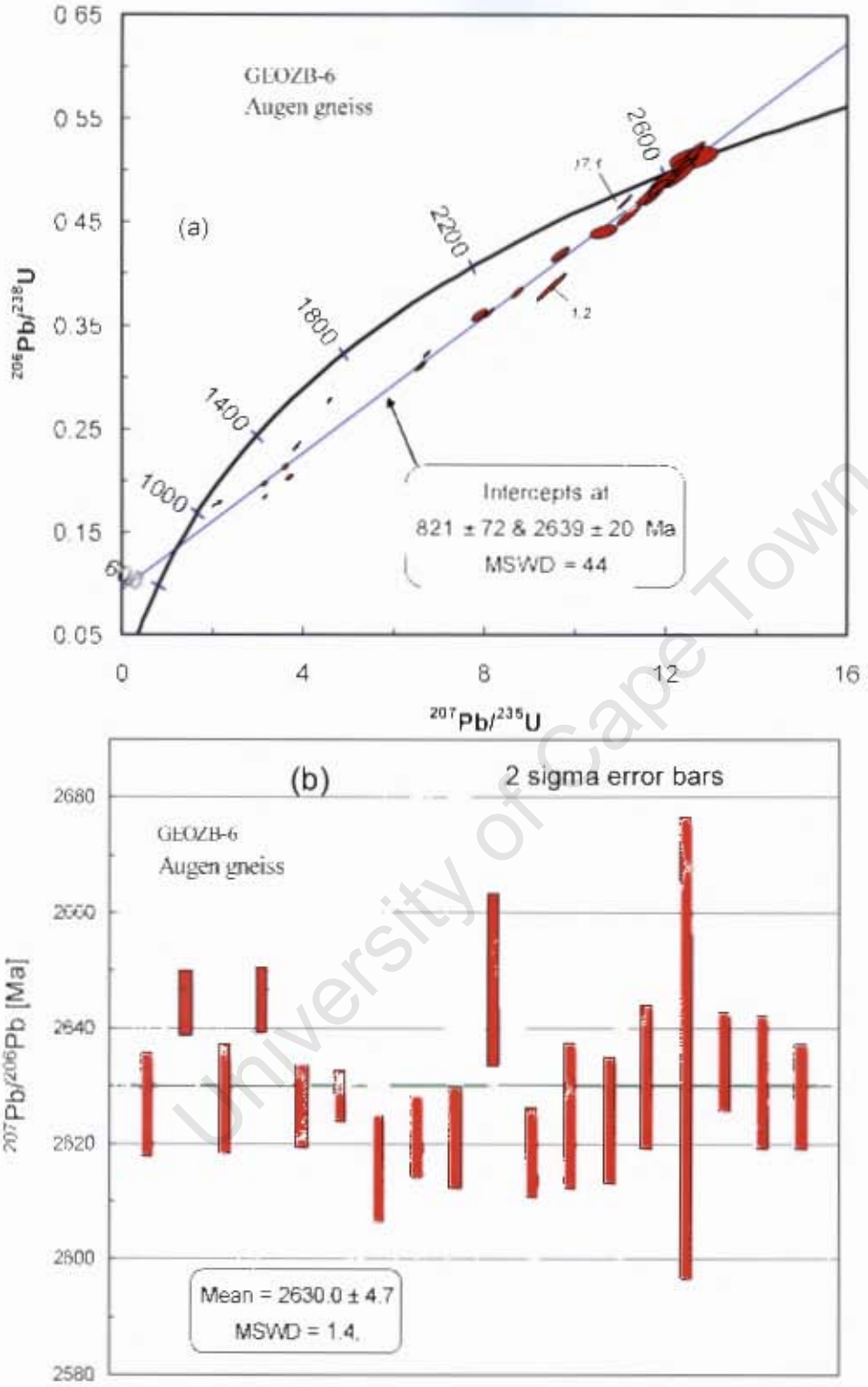

Fig. 4.31: Plots of U-Pb SHRIMP data for zircon grains from the granitic augen gneiss sample GEOZB-6, sampled within the Limpopo-Shashe Belt near the collision zone. (a) Concordia plot of all the analyses showing intercept ages; (b) Weighted average mean $^{207}Pb/^{206}Pb$ age calculated from near concordant analyses. Confidence limit for error ellipses is 1σ.

Table 4.10: U-Th-Pb isotopic compositions of zircon grains and age calculations from augen granitic gneiss sample GEOZB-6 within the Limpopo-Shashe Belt

Concentration						Radiogenic ratios						Age [Ma]				
Grain Spot	% $^{206}Pb_c$	U (ppm)	Th (ppm)	Th/U	$^{206}Pb^*$ (ppm)	(1) $^{207}Pb^*/^{206}Pb^*$	±%	(1) $^{207}Pb^*/^{235}U$	±%	(1) $^{206}Pb^*/^{238}U$	±%	(1) $^{206}Pb/^{238}U$ Age		(1) $^{207}Pb/^{206}Pb$ Age		% Discordant
GEOZB-6: Augen gneiss																
1.1	0.24	384	111	0.29	126	0.16620	0.44	8.728	0.96	0.3809	0.86	2,080	±15	2,519.8	± 7.3	17
1.2	0.14	348	421	1.21	115	0.17809	0.49	9.46	2.4	0.3854	2.3	2,102	±42	2,635.2	± 8.1	20
2.1	0.11	84	40	0.48	32.8	0.17715	0.54	11.14	1.5	0.4561	1.4	2,422	±27	2,626.4	± 8.9	8
2.2	0.43	1034	28	0.03	246	0.12029	0.50	4.566	0.96	0.2753	0.81	1,568	±11	1,960.5	± 9.0	20
2.3	0.06	127	69	0.54	55.2	0.1776	0.70	12.39	1.5	0.5060	1.3	2,639	±29	2,630	±12	0
3.1	0.34	684	210	0.31	182	0.15454	0.36	6.564	0.99	0.3081	0.92	1,731	±14	2,396.7	± 6.2	28
4.1	0.14	192	189	0.98	77.7	0.17905	0.34	11.64	0.96	0.4715	0.90	2,490	±19	2,644.1	± 5.6	6
4.2	0.04	214	202	0.94	93.0	0.17795	0.52	12.40	1.3	0.5052	1.2	2,636	±26	2,633.8	± 8.7	0
5.1	0.87	901	293	0.33	151	0.1177	1.1	3.146	1.4	0.1939	0.83	1,142.6	± 8.7	1,921	±20	41
6.1	1.91	147	151	1.03	56.5	0.1748	1.6	10.60	1.8	0.4400	0.94	2,351	±19	2,604	±26	10
6.2	2.88	158	152	0.96	71.5	0.1782	2.4	12.57	2.8	0.5116	1.3	2,663	±29	2,636	±40	-1
7.1	0.61	657	189	0.29	120	0.1240	1.1	3.600	1.4	0.2105	0.84	1,231.7	± 9.4	2,015	±19	39
8.1	0.10	58	25	0.43	24.1	0.1773	0.57	11.80	1.3	0.4827	1.1	2,539	±23	2,627.4	± 9.5	3
8.2	0.85	888	142	0.16	154	0.1338	0.97	3.690	1.3	0.2001	0.83	1,175.7	± 8.9	2,148	±17	45
9.1	0.08	489	205	0.42	152	0.16281	0.26	8.092	0.88	0.3605	0.84	1,984	±14	2,485.1	± 4.4	20
10.1	0.19	664	174	0.26	176	0.15531	0.28	6.613	0.87	0.3088	0.82	1,735	±13	2,405.3	± 4.7	28
11.2	0.02	147	231	1.58	59.8	0.17910	0.34	11.72	0.99	0.4746	0.93	2,504	±19	2,644.5	± 5.7	5
11.3	--	169	166	0.98	71.2	0.1777	0.76	12.00	1.6	0.4900	1.4	2,571	±29	2,631	±13	2
12.1	0.28	1203	14	0.01	179	0.08554	0.82	2.038	1.2	0.1728	0.82	1,027.4	± 7.8	1,328	±16	23

Uncertainties in ages are reported at the 2 sigma confidence level.

% $^{206}Pb_c$ denotes the percentage of ^{206}Pb that is common Pb.

$^{206}Pb^*$ indicates the portion of radiogenic Pb.

(1) Common Pb corrected using measured ^{204}Pb

Table 4.10: Continued

Concentration						Radiogenic ratios						Age [Ma]				
Grain Spot	% $^{206}Pb_c$	U (ppm)	Th (ppm)	Th/U	$^{206}Pb^*$ (ppm)	(1) $^{207}Pb^*/^{206}Pb^*$	±%	(1) $^{207}Pb^*/^{235}U$	±%	(1) $^{206}Pb^*/^{238}U$	±%	(1) $^{206}Pb/^{238}U$ Age		(1) $^{207}Pb/^{206}Pb$ Age		% Discordant
13.1	0.08	647	126	0.19	178	0.15228	0.31	6.714	0.89	0.3198	0.84	1,789	±13	2,371.7	± 5.2	25
14.1	0.03	187	160	0.86	82.6	0.17712	0.43	12.58	1.1	0.5151	0.97	2,678	±21	2,626.1	± 7.2	-2
14.2	0.37	226	247	1.09	92.5	0.1769	0.67	11.56	1.4	0.4741	1.2	2,502	±25	2,624	±11	5
15.1	0.19	846	302	0.36	168	0.12146	0.48	3.867	1.6	0.2309	1.5	1,339	±18	1,977.8	± 8.6	32
16.1	--	233	194	0.83	101	0.17731	0.26	12.32	0.94	0.5038	0.90	2,630	±19	2,627.9	± 4.4	0
17.1	0.05	514	293	0.57	207	0.17135	0.20	11.06	1.0	0.4682	1.0	2,476	±21	2,570.9	± 3.3	4
17.2	0.37	572	371	0.65	256	0.17626	0.47	12.61	1.2	0.5190	1.0	2,695	±23	2,618.0	± 7.9	-3
18.1	1.08	1564	26	0.02	238	0.0887	1.5	2.143	1.7	0.1751	0.81	1,040.4	± 7.8	1,399	±28	26
19.1	0.24	223	101	0.45	97.1	0.17600	0.55	12.28	1.0	0.5063	0.85	2,641	±19	2,615.2	± 9.4	-1
19.2	0.00	67	70	1.04	28.6	0.1795	0.90	12.26	1.8	0.4953	1.6	2,593	±34	2,648	±15	2
20.1	0.00	123	67	0.54	52.0	0.1770	0.76	11.98	1.6	0.4910	1.3	2,575	±29	2,625	±13	2
21.1	0.53	461	446	0.97	166	0.1675	0.63	9.65	1.3	0.4177	1.1	2,250	±21	2,533	±11	11
22.1	0.88	623	318	0.51	194	0.1590	0.93	7.86	1.4	0.3587	1.1	1,976	±18	2,445	±16	19
23.1	0.07	317	254	0.80	138	0.17655	0.42	12.31	1.2	0.5057	1.1	2,638	±24	2,620.7	± 7.0	-1
23.2	0.00	180	173	0.96	75.4	0.17730	0.56	11.92	1.3	0.4877	1.2	2,561	±26	2,627.8	± 9.2	3
24.1	0.03	179	195	1.09	74.2	0.17654	0.53	11.72	1.3	0.4817	1.2	2,535	±26	2,620.6	± 8.9	3
25.1	0.45	1825	423	0.23	285	0.12655	0.63	3.160	1.2	0.1811	0.98	1,072.9	± 9.7	2,051	±11	48

4.5 Discussion

4.5.1 Introduction

Collectively, the Tati and Vumba granite-greenstone terrains represent a significant area (~5500 km^2) of the Francistown Granite-Greenstone Complex, which in turn represents a significant region (~6050 km^2) of the Neoarchaean crustal extension to the SW margin of the Zimbabwe craton. However, until recently the geochronology data of the Francistown Granite-Greenstone Complex was inadequate to asses the regional timing of volcanism, plutonism and deformation and hence the evolution of the Complex. Based on the evaluation of combined new data from this study, and the previous data from Bagai et al. (2002), a new, more robust geochronological framework of the Francistown Granite-Greenstone Complex is presented below. A summary of U-Pb zircon ages from previous studies and the present studies is presented in Table 4.11.

4.5.2 Geochronological framework

A schematic summary diagram of all U-Pb zircon ages from the complex is shown in Figure 4.32 to illustrate the temporal variation in the occurrence of magmatic activities, and major metamorphic events associated with development of the Vumba and Tati granite-greenstone terrains. According to the available ages, volcanic and plutonic rocks in the Francistown Granite-Greenstone Complex formed between 2740 and 2640 Ma, a time period of over 100 million years. The spectra of rock ages in the Tati granite-greenstone terrain reveal clear contrasts with those from the Vumba granite-greenstone area (e.g. Bagai et al., 2002). For instance the rocks in the Tati area, specifically the felsic volcanic rocks of the Tati greenstone belt formed between 2740 and 2730 Ma, whilst those in the Vumba greenstone belt formed between 2700 and 2690 Ma. Similarly, the major granitoid intrusions in the Vumba belt are younger (2700-2680 Ma) than those flanking the Tati belt (ca. 2740-2700 Ma) except the Tati pluton (2670 Ma). Interestingly, the felsic and intermediate volcanic rocks in the Tati area are approximately equivalent in age to Tlhalogang and Sekukwe tonalite-trondhjemite units and may be the extrusive equivalents of these plutonic rocks. In contrast, tonalite and granodiorite units in Vumba do not have precise age equivalent extrusive in the Vumba greenstone belt.

The recognition of the close timing relationship between the felsic and volcanic sequences and granitoids is becoming common in many granite-greenstone terrains. It has been reported in

granite-greenstone terrains hosted by the Slave, Yilgarn, Pilbara and Kaapvaal Cratons (e.g. Ridley et al., 1997). In all these cases geochemical evidence shows that the felsic volcanic rocks are often genetically related to the granitoids. For instance in the Barberton Belt (Kaapvaal Craton) there is geochemical evidence for genetic relations between felsic sequences and both granitoids intruding and flanking the greenstone belt (de Wit et al., 1987). Felsic lavas that separate the Moodies and Fig Tree Groups are interpreted as extrusive equivalents of tonalite-trondhjemite plutons flanking the north-eastern margin of the Barberton Greenstone Belt whilst in the southern part of the greenstone belt, the Hooggenoeg Formation Dacites are the age equivalents of the Theespruit pluton (3460-3470 Ma) (e.g. the Kapapvalley tonalite; de Ronde et al., 1991). In the Pilbara Craton the dacitic to rhyolitic lavas have indistinguishable ages from those of the exposed batholiths, to which they are genetically linked (Ridley et al., 1997). The genetic relationships between the felsic volcanic rocks and granitoids that have indistinguishable ages in the Francistown Granite-Greenstone Complex will be evaluated in the synthesis of geodynamic model chapter.

The differences in emplacement ages between the two granite-greenstone terrains argue for different magmatic evolutionary histories (Table 4.11). Additionally, there is a recognizable compositional disparity in the rock assemblages between the Tati and Vumba granite-greenstone terrains suggesting different tectonomagmatic environments. For instance, the volcanic sequence in the Tati greenstone belt comprise abundant tholeiitic basalt and andesite with minor dacite whereas in the Vumba greenstone belt tholeiitic basalt is prevalent intercalated with moderate volume of dacite and deficient andesite. The plutonic rock assemblage of the Vumba granite-greenstone terrain is composed of tonalite, granodiorite, quartz monzonite and monzogranite (high-K granite) plutonism whereas tonalite-trondhjemite, gabbro, diorite, trondhjemite, quartz monzonite and monzogranite comprise the plutonic rock assemblage in the Tati granite-greenstone terrain.

Table 4.11: Summary of U-Pb zircon ages for igneous rocks from the Tati and Vumba granite-greenstone terrains of the Francistown Granite-Greenstone Complex.

Locality and field relation	Location	Rock type	Zircon Age ± 2σ error (Ma)	Interpretation	Reference
Paragneiss unit in Matshilagabedi village	Tati	Paragneiss	2755 ± 100	Metamorphic	This study
Penhalonga FM overlying mafic lavas of Lady Mary FM	Tati	Andesite	2737 ± 3.2	Magmatic	This study
Felsic layer intercalated with mafic lavas of Lady Mary FM	Tati	Dacite	2735 ± 30	Magmatic	This study
Mashoje pluton flanks the mafic lavas in the eastern margin.	Tati	Tonalite-trondhjemite	2911 ± 5	Inherited	This study
	"	"	2876 ± 160	Magmatic	This study
	"	"	2647 ± 30	Metamorphic	This study
Sekukwe pluton intruded the andesitic lavas of Penhalonga Formation in the NE.	Tati	Tonalite-trondhjemite	2732.7 ± 4.4	Magmatic	This study
	"	"	2673 ± 4.5	Metamorphic	This study
Felsic dykes intruded the gabbro at Phoenix Mine.	Tati	Tonalite-trondhjemite	2703.5 ± 4.1	Magmatic	This study
Central Tati pluton - The pluton flanks the mafic lavas in the SW margin	Tati	Leucosome from TT	2639.7 ± 7.9	Metamorphic	This study
	"	"	2670 ± 10	Magmatic	This study
Central Tati pluton.	Tati	Melanosome from TT	2684 ± 22	Magmatic	This study
Northeastern Tati pluton.	Tati	Tonalite-trondhjemite	2672.9 ± 2.8	Magmatic	This study
Tlhalogang pluton flanks the mafic lavas in the western side. A kopje of the trondhjemite is intruded into the Tlhalogang pluton.	Tati	Tonalite-trondhjemite	2739 ± 7.2	Magmatic	This study
	"	"	2651.1 ± 3.4	Metamorphic	This study
Central Tati is intruded andesitic lavas of Penhalonga FM.	Tati	Diorite	2715.9 ± 2.5	Magmatic	This study
Central Tati is contain xenoliths of diorite.	Tati	Trondhjemite	2715.2 ± 2.7	Magmatic	This study
Central Tati is intruded the trondhjemite & Sekukwe pluton.	Tati	Monzogranite	2716.1 ± 3.7	Magmatic	This study
Within the paragneiss near Sebina village.	Vumba	Amphibolitic xenolith	2733 ± 5	Inherited	Bagai et al.(2002)
Intruded the serpentinite ridge north of Mashawe pluton.	Vumba	Quartz diorite dyke	2696 ± 3.5	Magmatic	Bagai et al.(2002)
Felsic layer intercalated with mafic lavas of VMV Formation.	Vumba	Dacite	2695.9 ± 5.9	Magmatic	This study
Maebe Tonalite intruded the mafic lavas.	Vumba	Tonalite	2690 ± 4	Magmatic	Bagai et al.(2002)
	"	"	2669 ± 6	Metamorphic	Bagai et al.(2002)
Mashawe pluton intruded the mafic lavas.	Vumba	Granodiorite	2686 ± 6	Magmatic	Bagai et al.(2002)
	"	"	2673 ± 6	Metamorphic	Bagai et al.(2002)
Domboshaba Granite intruded granodiorite & quartz monzonite.	Vumba	Monzogranite	2647 ± 4	Magmatic	Bagai et al.(2002)
Shashe gneiss -migmatite outcrop in Shashe.	Limpopo-Shashe	Leucosome from migmatite	2629.4 ± 3.2	Partial melting	This study
Shashe gneiss exposed in the Shashe river bed.	Limpopo-Shashe	Augen granitic gneiss	2630 ± 4.7	Partial melting	This study

Abbreviations: FM-Formation; TT-tonalite-trondhjemite; VMV Vumba Mixed Volcanic

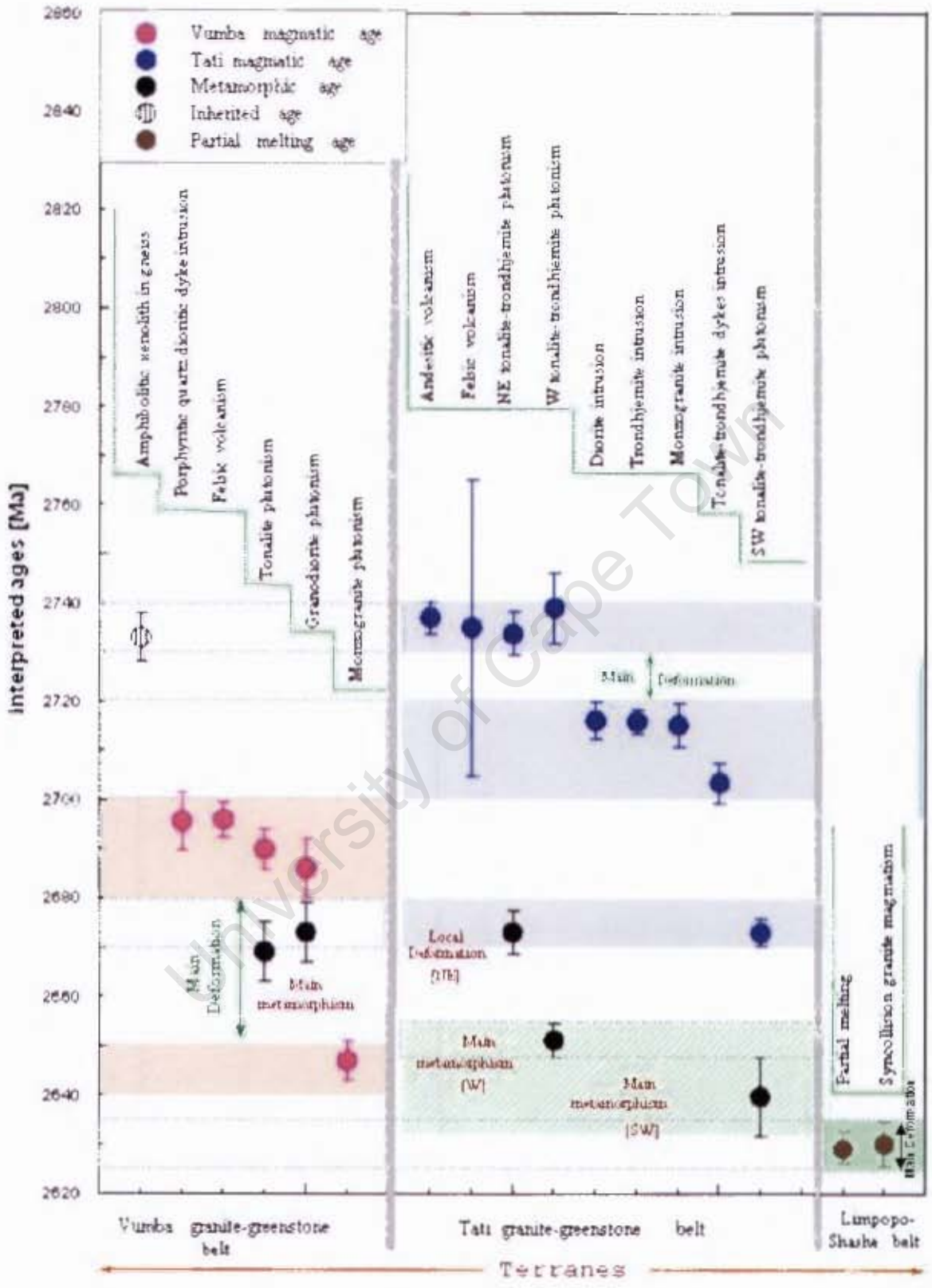

Fig. 4.32: A chronologic chart constructed using U-Pb zircon ages from the Francistown Granite-Greenstone Complex illustrating the sequence of magmatic and deformation events for the Tati and Vumba granite-greenstone terrains.

4.5.2.1 Magmatism and deformation in the Vumba granite-greenstone terrain

The ~2695 Ma age of the felsic lavas intercalated with the mafic lavas in the Vumba greenstone belt determined by this study warrant a review of the interpretation of the previous age of 2733 ± 5 Ma (Bagai et al., 2002) recorded from an amphibolitic gneiss xenolith in the Sebina gneiss that was interpreted as a minimum age for the deposition of the Vumba greenstone belt. The previous interpretation was made on the assumption that the amphibolitic xenolith was part of the mafic lavas of the Vumba greenstone belt since it appeared contiguous with the *unexposed* contact between the gneiss and the basal formation of the Vumba greenstone succession (Fig. 4.1). One possibility is that the xenolith is not related to the mafic lavas of the Vumba greenstone belt hence the age is for a different magmatic event. Another possibility is that the xenolith is part of the Vumba mafic volcanism but that the zircon grains are inherited. The later possibility seems more likely and hence favoured because it is rare to obtain magmatic zircon grains from mafic rocks. Many zircon grains recovered from the ancient mafic lavas elsewhere are inherited and also considered as strong evidence of interaction with older continental crust (e.g. Wilson et al., 1995; Kerrich et al., 1999). However, either interpretation complicates the understanding of the development of the Vumba granite-greenstone terrain. The host rock for the xenolith is a tonalitic gneiss, which Key (1976) and Litherland (1975) interpreted as paragneiss. A paragneiss normally contains enclaves in the form of restite or melanosome, and xenoliths are common features for intrusive rocks but not for supracrustal rocks. From the sharp boundary between the xenolith and the host gneiss, we can infer it is not an enclave (Fig. 4.33). This observation casts doubt on the interpretation of the gneiss by previous workers as a paragneiss. It is possible that the gneiss exposed at Sebina village is a migmatised orthogneiss, which intruded into the Vumba volcanic sequence and was then deformed together with it. If this re-interpretation is correct, then the 2733 ± 5 Ma zircon date implies that an older continental crust or crustal material existed before the deposition of the Vumba greenstone belt. It is of course also possible that it is part of a basement to the Vumba succession and that an unconformity exists that has not yet been recognized. However, a geochemical investigation on the gneiss is now required for verification of its origin. Interestingly, the age of 2733 ± 5 Ma is similar to the age of the Sekukwe and Tlhalogang plutons, both tonalite-trondhjemites plutons flanking the NE and W Tati greenstone belt, respectively.

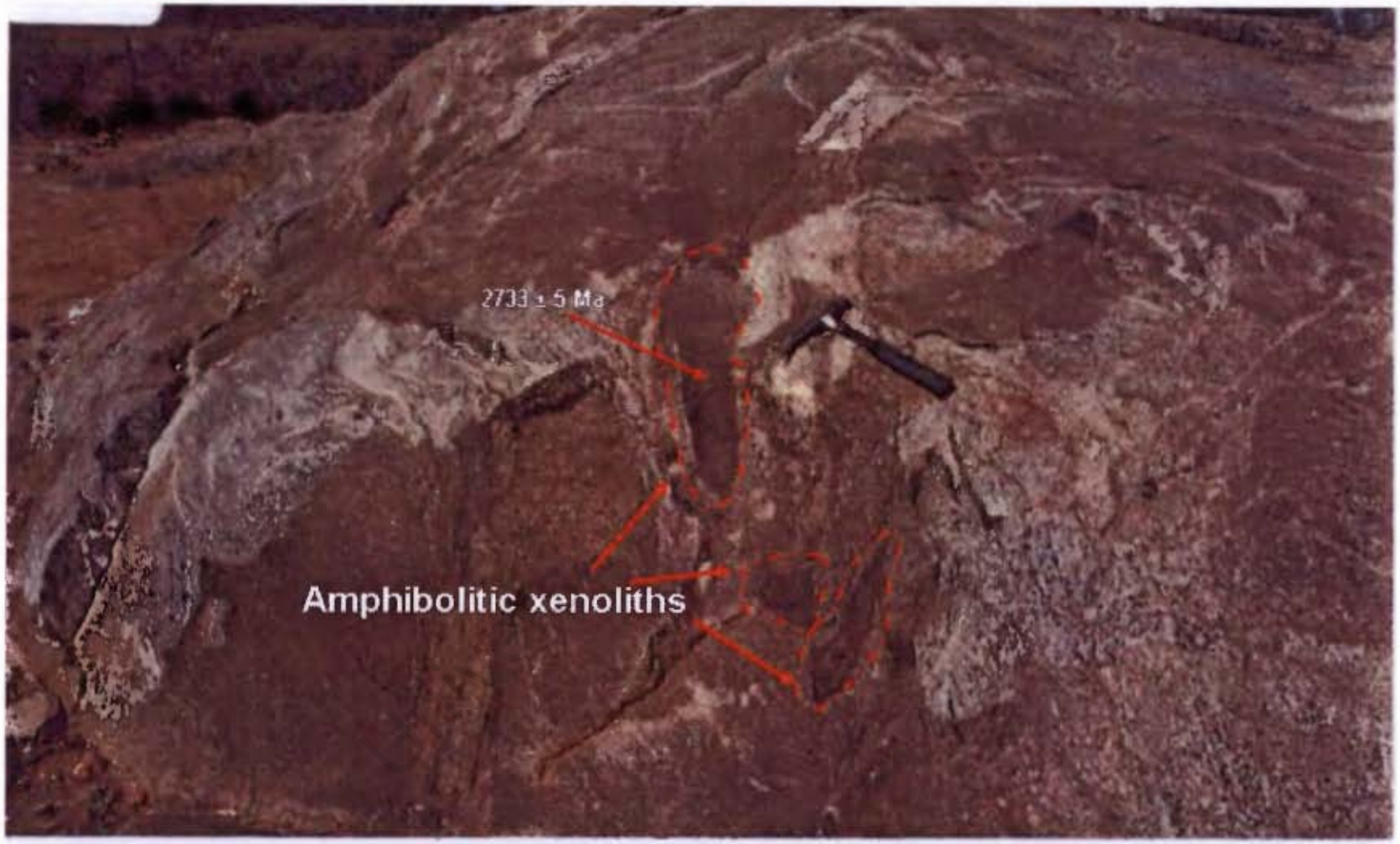

Fig. 4.33: A field photograph of a migmatised gneiss near Sebina village hosting amphibolitic xenoliths containing inherited zircon grains that are ~2733 million years old. The age of the gneiss is unknown

The earliest dated extrusive igneous rocks in the Vumba granite-greenstone is 2695.9 ± 5.9 Ma (Dacite) and 2696 ± 3.2 Ma (quartz porphyritic diorite, a minor intrusion). The quartz porphyritic diorite is considered a shallow intrusion equivalent to the dacite. The dacitic lava is intercalated with voluminous mafic lavas, which suggests that they are contemporaneous or penecontemporaneous. Volcanism in the Vumba terrain is closely followed by tonalitic plutonism, dated at 2690 ± 4 Ma (Bagai et al., 2002). However, the ages of the tonalite plutonism and volcanism are the same within margin of errors suggesting that the tonalite may be plutonic equivalent of the greenstone volcanics. The tonalite flanks the western margin of the Vumba greenstone belt. Subsequent granodioritic intrusions occurred at 2686 ± 6 Ma (Mashawe Pluton and related intrusions) within the greenstone belt, and farther away from it (e.g. the Kalakamati pluton). Although no absolute U-Pb age is available for the quartz monzonite unit, field relations indicate that it is older than the granodiorite but younger than mafic lavas. This implies that the quartz monzonite is approximately coeval with the tonalite. Thus the period between 2700 and 2680 Ma was a major episode of magmatic events that generated more than 90% of the igneous rocks in the Vumba granite-greenstone terrain. It is worth mentioning that the tonalite, quartz monzonite and granodiorite display variable deformation fabric. The fabric is more strongly developed in the quartz monzonite than in the other granitoids. The youngest magmatic event in the Vumba terrain took place at 2647 ± 5 Ma. This is defined by monzogranite plutonism which is devoid of any deformation fabric. The absence of deformation fabric in the monzogranite confirms that all the pervasive ductile deformation in the Vumba granite-greenstone terrain ceased prior to ca. 2650 Ma.

4.5.2.2 Magmatism and deformation in the Tati granite-greenstone terrain

The magmatic history of the Tati granite-greenstone terrain is more complex and comprises two magmatic episodes, both different in age to those recorded in the Vumba terrain. This is the main distinction between the two terrains (Fig. 4.32). The first episode of magmatic events in the Tati area, comprising both volcanism and plutonism, took place between 2740 Ma and 2730 Ma. So it is possible that the Vumba rocks were deposited on rocks that are associated with Magmatism that generated the Tati terrain. The volcanism generated mafic through intermediate to felsic lavas, during the formation of the Tati greenstone belt. At this time the Vumba greenstone belt did not exist. The synvolcanic plutonism produced tonalite-trondhjemite plutons that flank the northeastern and western margins of the Tati greenstone belt (hereafter referred to as NE tonalite-trondhjemite

and W tonalite-trondhjemite). These plutons include the Sekukwe, Mphoeng and Matsiloje as NE tonalite-trondhjemites (Fig. 4.36). The W tonalite-trondhjemite is represented by the Tlhalogang pluton. The NE and W tonalite-trondhjemites differ in their state of deformation. Tectonic fabrics in the NE tonalite-trondhjemites is not very obvious, whereas the W tonalite-trondhjemite displays a very conspicuous foliation that trends NE-SW. In addition, the W tonalite-trondhjemite zircon dating records a metamorphic event at 2651 ± 3.4 Ma that possibly dates the formation of the strong NE-SW tectonic fabric. The new zircon data reveals that the NE tonalite-trondhjemite plutons and the associated marginal quartz monzonite, is probably coeval as originally suggested by Key (1976). Noteworthy, the NE tonalite-trondhjemite plutonism contain inherited zircon grains (2911 ± 5 Ma; sample GEOZB-2a) suggesting involvement of older crustal material in their genesis.

A subsequent magmatic event occurred between 2720 and 2710 Ma generating diorite, trondhjemite and monzogranite intrusions near simultaneously. These three contemporaneous intrusive rocks outcrop in close proximity and they display no obvious deformation fabrics. This is consistent with the quality of zircon grains extracted from the monzogranite, trondhjemite and diorite, which do not exhibit any evidence of metamorphism. Despite, contemporary ages, in the field the monzogranite forms dykes that cut diorite and trondhjemite intrusions indicating that it is likely penecontemporaneous with the two associated units. The outcrop patterns for the trondhjemite and diorite units are linear and run parallel to the trend of Tati greenstone belt but no contact between the two is exposed anywhere. However, small xenoliths of dioritic composition can be observed in the field, which indicate that the trondhjemite is relatively younger. In some places, particularly near the margin with the diorite, the trondhjemite and diorite form a hybrid rock (Fig. 4.34) that suggests the trondhjemite intruded the diorite while the diorite was still hot. This is consistent with the overlapping ages, given the uncertainties difference of 0.7 Ma (see Table 4.11 and Fig. 4.36). This confirms the comagmatic evolution. The occurrence of diorite and monzogranite in temporal association has been reported in some Archaean terranes elsewhere (e.g. Whalen et al., 2004). Moyen et al. (2001) also observed that diorite and monzogranite have a tendency to share a unique temporal relationship in all Archaean cratons where the later is emplaced shortly following the former.

A third episode of magmatic activities in the Tati area was minor, as represented minor tonalite-trondhjemite dykes intruding the gabbro unit at Phoenix mine. These were emplaced at 2703.5 ± 4.1 Ma, shortly after the intrusion of the diorite, trondhjemite and monzogranite. These dykes constrain the minimum age of the gabbro unit in the Tati terrain. This implies that the gabbro magmatism was part of either the second or first episode described above. Noteworthy is the observation that the tonalite-trondhjemite dykes possess no obvious deformation fabric yet the gabbro has been deformed. This suggests that the gabbro belongs to the first episode of magmatism that generated the mafic-felsic volcanic rocks of the Tati greenstone belt, and the first tonalite-trondhjemite plutons. This is in line with the suggestion of Key (1976) that the Selkirk gabbro, located 11 km south of the Phoenix gabbro, is contemporaneous with the mafic-andesitic volcanic sequence in the greenstone belt. The Selkirk gabbro is also deformed.

A final magmatic episode occurred at about 2673 Ma. This produced a chain of tonalite-trondhjemite plutons that mostly flank the southwestern margin of Tati greenstone belt (e.g. Tati pluton and its satellites, South Tati, Airport and New Zealand; Fig. 4.36). These tonalite-trondhjemite intrusions exhibit a strong deformation fabric and local tectonic banding, features that are absent in the tonalite-trondhjemite granitoids that occur elsewhere. This implies the deformation is diachronous yet older from N to S towards the Limpopo-Shashe Belt. This trend links the tectonic of the Tati granite-greenstone terrain with the Limpopo-Shashe Belt. The presence of deformation fabric that gradually intensifies towards the margin with the Limpopo-Shashe Belt further suggests geotectonic relationship between the Tati and Limpopo-Shashe Belt. Such trends are observed in the Vumba granite-greenstone terrain.

Geochronological data from this study has revealed that the final amalgamation between the Francistown Granite-Greenstone Complex (Zimbabwe Craton) and the Kaapvaal Craton took place at 2629.4 ± 3.2 Ma (sample GEOZB-5) resulting in formation of syntectonic granite (granitic augen gneiss) within the Limpopo-Shashe Belt and probably deformation of the southwestern plutons of the Zimbabwe Craton. However, it is worth mentioning that the deformation of the granitoids in the southwestern margin of the Zimbabwe craton could have been caused by Neoarchaean dynamo-metamorphism of the belt which was not related to the collision with the Kaapvaal craton (Holzer et al.,1999).

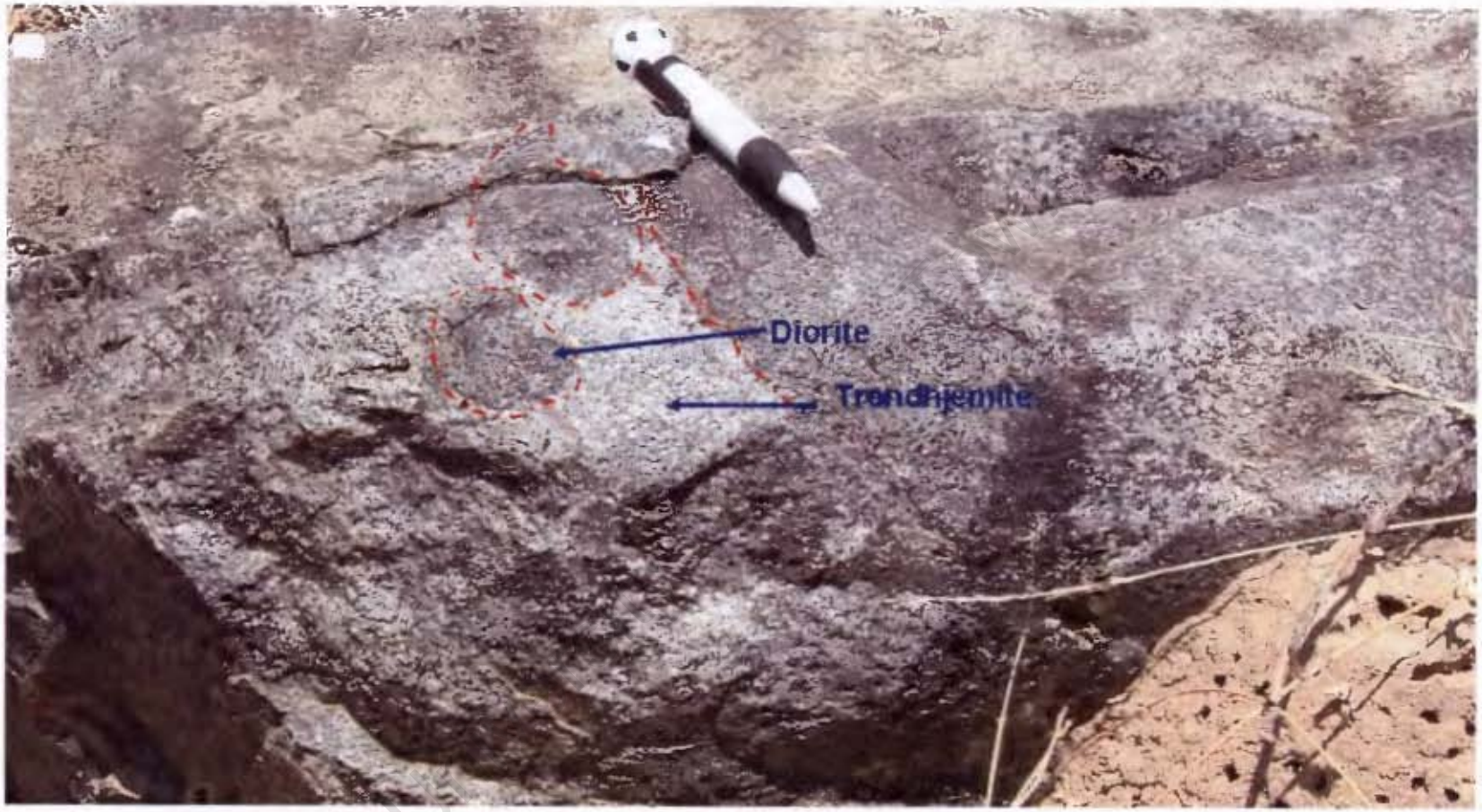

Fig. 4.34: A field photograph showing a hybrid rock composed of trondhjemite and diorite components. The picure was taken at the foot of a trondhjemite hill contiguous to the margin with the diorite about 3 km north of the Francistown city centre.

4.5.2.3 Deformation history of the Francistown Granite-Greenstone Complex

Previous studies reported a regional tectono-thermal event that affected the Francistown Granite-Greenstone Complex and which converted major part of the supracrustal rocks into high-grade paragneiss (e.g. Litherland, 1975; Key, 1976). Furthermore, the studies indicated that this event post-dated formation of the greenstone belt rocks and the emplacement of the tonalite-trondhjemite plutons in Tati and, tonalite and granodiorite plutons in Vumba in the Francistown Granite-Greenstone Complex. However, the present study reveals that the tonalite-granodiorite plutonism in the Vumba area is younger than the diorite, trondhjemite and monzogranite in the Tati terrain, all plutonic rocks that were previously regarded as post high-grade metamorphism in the Francistown Granite-Greenstone Complex (e.g. Key, 1976). The new data presented here therefore raises new questions about the origin and age of the paragneiss terrane in the Francistown Granite-Greenstone Complex. In addition the greenstone sequences are metamorphosed at lower grade (greenschist to lower amphibolite) than the paragneiss, despite their relatively older age. Petrography and the geochronological data for the older volcanic and plutonic rocks do not show any evidence of a metamorphic overprint as might be anticipated for rocks affected by a major tectono-thermal event. In this study a paragneiss sample collected within the Tati granite-greenstone terrain with the aim of constraining this regional tectono-thermal event yielded a poorly constrained U-Pb zircon date of 2755 ± 100 Ma, which is interpreted as a metamorphic age since all the analysed spots of the zircon grains are from their outer overgrowth rims (e.g. see Fig. 4.2). It is therefore suggested that a regional metamorphic event must have been older than any of the plutonism as well as volcanism in the Francistown Arc Complex. In view of the severity of this deformation event (see Fig. 4.35 for the deformation state of the paragneiss), it is highly likely that it would have caused some zircon disturbance in older rocks, which is not the case. Although, the NE and W tonalite-trondhjemites yielded zircon grains that show evidence of subsequent disturbance by metamorphic events, the ages obtained for the events are clearly different, indicating that they are possibly related to isolated events. Additionally, these metamorphic events are younger than the post-kinematic intrusions, which argue against them being regional high-grade metamorphic events. Since none of the samples analysed for geochronological information has revealed evidence of such an event, it is proposed that the deformation event which lead to formation of the paragneiss pre-dated the volcanism and plutonism events of the Francistown Granite-Greenstone Complex. Thus, the

paragneiss terrane probably constitutes the basement to the Francistown Granite-Greenstone Complex. However, this paragneiss unit needs further investigation.

The volcanic rocks and synvolcanic plutonic rocks in both the Vumba and Tati terrains are deformed to various degrees. In the Vumba granite-greenstone terrain the (last) deformation took place between 2686 Ma and 2647 Ma. The zircon grains from the Mashawe pluton (granodiorite) and Maebe tonalite record metamorphic ages of 2673 ± 6 and 2669 ± 6 Ma, respectively. These ages are equivalent, within margins of error, and are similar to the emplacement age (~2670 Ma) of the Tati pluton (SW tonalite-trondhjemite) in the Tati granite-greenstone terrain. The minimum age of deformation in the Vumba area is constrained by the post-kinematic monzogranite emplacement age of 2647 ± 5 Ma. In the Tati granite-greenstone, the diorite, trondhjemite and monzogranite plutons, which were all emplaced ca. 2716 Ma, are not deformed, thus providing a minimum age for deformation. However, the zircon grains from the Sekukwe Pluton (NE tonalite-trondhjemite) record a 2673 ± 4.5 Ma metamorphic age that corresponds to the metamorphic age in the Vumba area and the magmatic age of the SW tonalite-trondhjemite plutons. This event is interpreted as local metamorphic event confined to the NE of the Tati granite-greenstone terrain and the Vumba area because it did not apparently affect the ca. 2716 Ma intrusions. Another record of a local metamorphic event dated at 2651.1 ± 3.4 Ma is preserved in the Tlhalogang Pluton (W tonalite-trondhjemite). This age is within margins of error with the metamorphic age of 2647 ± 30 Ma recorded in the Matsiloje pluton. The SW tonalite-trondhjemite records a high-grade metamorphic event at 2639.9 ± 7.9 Ma, which resulted in partial melting of this unit. This period is broadly syngenetic with the 2630 ± 4.7 Ma migmatisation of the Shashe gneiss that is interpreted to be related to orogenesis in the Limpopo-Shashe Belt. This belt is a result of the collision between the Francistown Granite-Greenstone Complex (part of Zimbabwe craton) and Kaapvaal Craton. The metamorphic event is, therefore, attributed to final collision between the Francistown Granite-Greenstone Complex and the Kaapvaal craton. This is consistent with the fact that there is an increase in degree of deformation towards the Limpopo-Shashe Belt. In spite of the severity of the deformation, the impact of the orogeny is not recorded in the 2716 Ma diorite, trondhjemite and monzogranite suite that outcrop about 20 km NE of the collision zone. This remains a big enigma in the evolution history of the region. It is probable that the SW tonalite-trondhjemite plutons acted as a buffer zone, shielding the rest from further deformation.

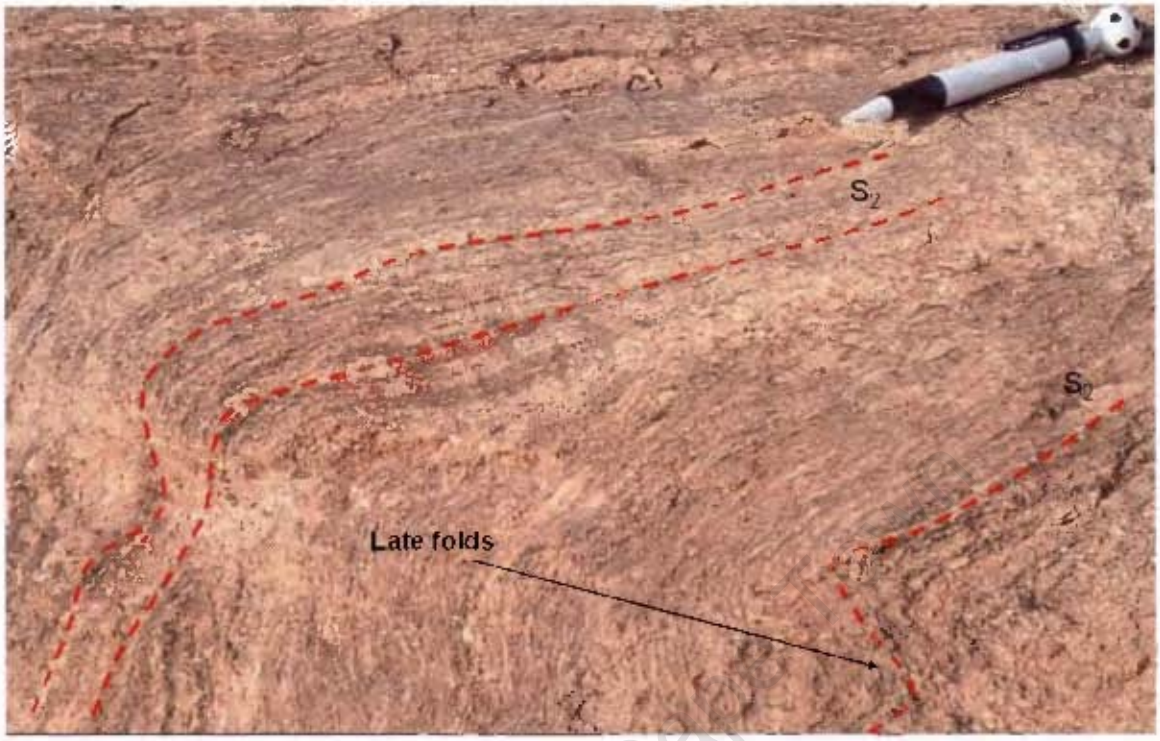

Fig. 4.35: A field photograph of a paragneiss unit in the Francistown Granite-Greenstone Complex. It was taken near Matshelagabedi village to illustrate the deformation state of the paragneiss unit. Note the S_2 migmatitic foliation that is folded by open kink-like structure.

4.5.3 Conclusion

The Archaean rocks of the Francistown Granite-Greenstone Complex in NE Botswana record a magmatic evolution over a period of ~100 Ma. The new results, in conjunction with previously published data from the Vumba granite-greenstone terrain, reveal distinct differences in the magmatic histories of the Tati and Vumba granite-greenstone terrains. The new data suggest that the two terrains of the Francistown Granite-Greenstone Complex developed independently and the supracrustal rocks (greenstone belts) differ in age by at least 30-40 million years after one another. Also evident from this data is that the two terrains do not share a late tectonic history. Thus, the previous suggested correlation of granitoids between the two terrains (e.g. Bagai et al., 2002; Kampunzu et al., 2003; McCourt et al., 2004; Zhai et al., 2006) is not supported by the geochronological data reported in this study. These differences are summarized in Fig. 4.36, which shows the geology of the Francistown Granite-Greenstone Complex together with the ages of the dated units. Magmatic events in the Vumba terrain show that it is younger than the Tati granite-greenstone terrain. A significant time gap of about 30-40 Ma exists between the initial magmatic

events of the two granite-greenstone terrains. Only the NE tonalite-trondhjemite plutons in the Tati terrain contain inherited zircon grains aged 2911 Ma. This is indicative of involvement of old crustal material in their generation. This may also be an indication that the paragneiss terrane acted as basement to the Tati terrain. This study therefore indicates that the Francistown Granite-Greenstone Complex has a more complex crustal growth history than previously envisaged.

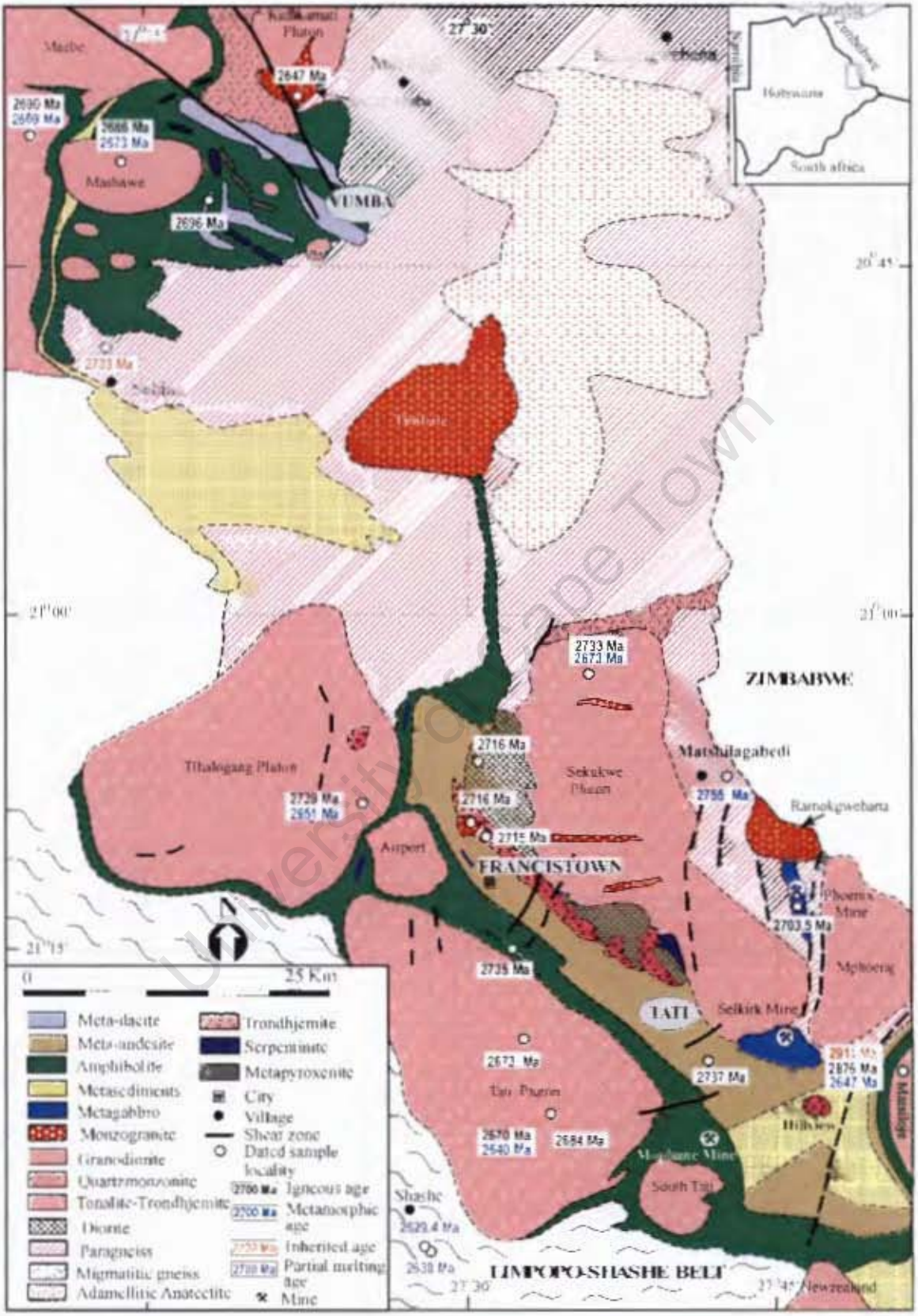

Fig. 4.36: Geological map showing the U-Pb zircon ages of rock units in the Francistown Granite-Greenstone Complex.

CHAPTER 5

MAJOR ELEMENT GEOCHEMISTRY

5.0 Introduction

In this chapter major element data from 80 samples collected from the mafic lavas, felsic lavas, gabbro, diorite and granitoids from the Tati granite-greenstone terrain are presented. The samples were analyzed using X-ray Fluorescence (XRF) spectrometry technique on fused glass discs in the Department of Geological Sciences at the University of Cape Town following the method of Willis (1999). Sample preparation, analytical procedures and precision are documented in Appendix A. Major element analyses of the 120 samples from the Vumba granite-greenstone terrain, which were conducted, in 2000, on fused glass discs at the Department of Geological Sciences at the University of Durham, England are shown in the background for comparison, and regional evaluation and analysis of the Francistown Granite-Greenstone Complex. These data from the Vumba terrain formed part of the MSc project which was completed in year 2000 by the author at the University of Durham.

The whole-rock major element compositions were calculated to 100% on a volatile-free basis before plotting. Values of 0.2 and 0.5 were adopted for calculation of Fe_2O_3/FeO ratio (e.g. Middlemost, 1989) of all the mafic and felsic samples, respectively. Major element compositions in Archaean rocks are commonly affected by post-magmatic processes such as supergene alteration, metamorphism and hydrothermal alteration. Thin section analyses of the Tati granite-greenstone terrain rocks indicate that they have undergone deformation and greenschist to lower amphibolite facies metamorphism (see chapter 3). Therefore, the effects of these processes need to be evaluated prior to any attempt to classify the rocks using standard major element variation diagrams.

5.1 Evaluation of major element mobility

The degree of alteration in ancient rocks is generally measured by the magnitude of the loss on ignition (LOI) values recorded by the samples. The samples analyzed in this study have yielded low to very high LOI values (0.16 to 10.05 wt.%) suggesting variable degree of alteration and thus opportunity for mobility of the elements. A summary of the LOI values recorded by all the analysed rock units is presented in Table 5.1. The Selkirk gabbro recorded the highest LOI values with an average of 4.95%. This is consistent with the thin section observations presented in chapter 3, which reveals a high degree of alteration within the samples of Selkirk Gabbro. The generally high values of LOI (Table 5.1) indicate that alteration is significant hence it cannot be ignored in this study. On this basis, all samples with LOI values greater than 3% were discarded. This screening procedure affected mostly analyses from the Selkirk Gabbro which were reduced from 14 to 8 analyses.

Table 5.1: Summary of LOI values for all rock units from the Tati granite-greenstone terrain analysed in this study.

	LOI %			
Rock unit	**Minimum**	**Maximum**	**Average**	**No. of Sample**
Mafic lavas	0.29	3.51	1.21	17
Felsic lavas	0.92	1.66	1.38	5
Selkirk Gabbro	2.11	10.05	4.95	14
Phoenix Gabbro	1.88	2.85	2.36	5
Diorite	0.21	1.36	0.91	10
Monzogranite	0.81	2.73	1.30	4
Trondhjemite	0.75	2.13	1.33	7
Tonalite-Trondhjemite (Sekukwe Pluton)	0.76	2.16	1.51	4
Tonalite-Trondhjemite (Tati Pluton)	0.16	0.34	0.31	7
Quartz monzonite	0.34	0.39	0.37	5
Tonalite-Trondhjemite dyke	0.61	1.06	0.84	2

Abbreviations: LOI-loss on ignition.

Further tests for post-magmatic modification of the major element compositions of volcanic rocks from the Tati granite-greenstone belt were carried out on the screened samples using different criterion. The major element concentrations of volcanic samples were plotted against the Na_2O/CaO ratio as index of alteration (Fig. A1 in appendix C). This criterion is used for studying

major element mobility of rock samples from greenschist facies metamorphic terrains (Pearce, 1996). Any correlation between the major element concentration and Na_2O/CaO ratio would suggest mobility of the major element due to metamorphism (Pearce, 1996). Another test adopted in this study is the correlation between major elements and LOI as index of alteration (Fig. A2 in appendix C). Similarly, any correlation between the major element concentration and the LOI would be suggestive of the element mobility due to supergene alteration (Rollinson, 1993).The plots of the major element concentrations of the volcanic rocks against LOI values and Na_2O/CaO ratios do not display any obvious correlations suggesting no major disturbance of the major element compositions by secondary processes in screened samples. A third test of major element mobility in volcanic samples applied in this study is simple the comparison of two classification schemes, one involving the major elements (total alkalis and silica; Fig. 5.1a) and the other based on ratios of relatively immobile trace elements (Zr/Ti and Nb/Y; Fig. 5.1b). According to this test there are no significant disparities between the two independent classification schemes suggesting a minimal effect of post-magmatic alteration in the volcanic rocks from the Tati greenstone belt. Thus standard variation diagrams may be used to obtain meaningful classification of the volcanic rocks.

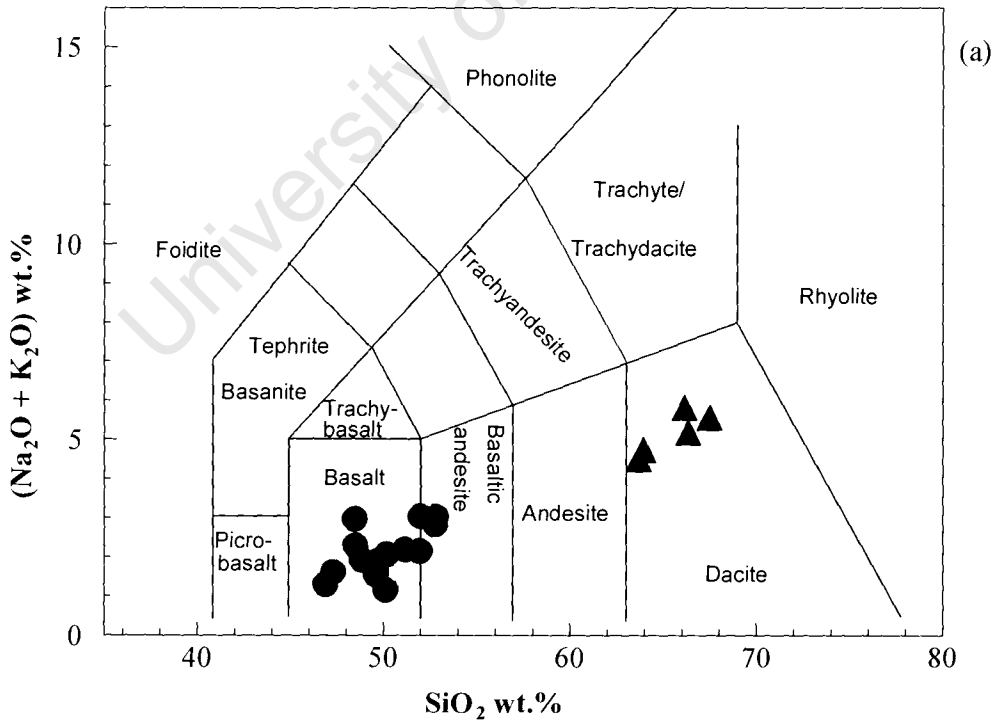

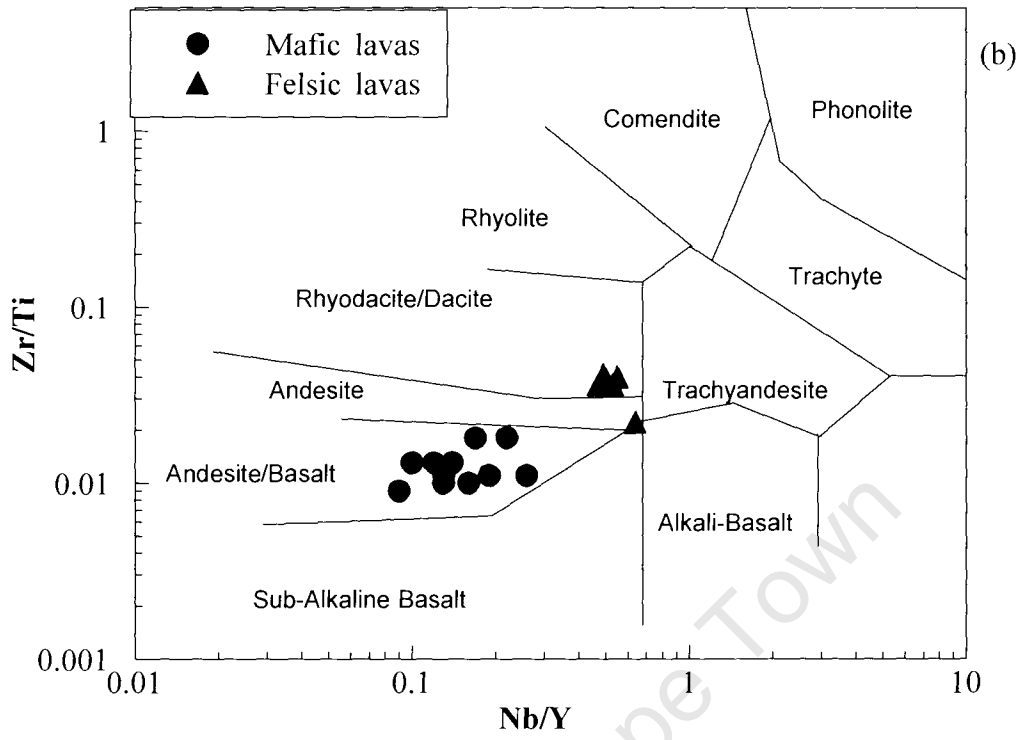

Fig. 5.1: Chemical classification of mafic rocks and felsic lavas from the Tati greenstone belt: (a) Chemical classification using the total alkalis versus silica (TAS) diagram of Le Maitre et al. (1989); (b) Chemical classification using immobile trace element ratios (Zr/Ti and Nb/Y) diagram of Winchester and Floyd (1977).

5.2 Mafic Lavas

The whole-rock major element data for the mafic lavas from the Tati greenstone belt are presented in Table 5.2. The content of SiO_2 in the mafic lavas from the Tati greenstone belt ranges from 44.83 to 52.82 wt.%, indicating a basic composition (Table 5.2). The Mg#s (atomic $Mg/[Mg+Fe^{2+}]$ with $Fe_2O_3/FeO = 0.2$) vary from 0.43 to 0.67 indicating that they are not primary melts. On a total alkalis silica (TAS) diagram of Le Maitre et al. (1989) presented as Fig. 5.2a, the majority of samples plot as basalt with a few extending into the field of basaltic andesite. All samples plot as tholeiitic basalts on Miyashiro's (1974) discrimination diagram (Fig.5.2b). On SiO_2 versus K_2O diagram (Fig.5.3), with subdivisions from Pecerillo and Taylor (1976) and Gill (1981), the mafic lavas from the Tati greenstone belt plot as low-K series basalts. The mafic lavas from the Tati greenstone belt are therefore interpreted as low-K tholeiitic basalts. The major element compositions of these lavas are compared with the composition of the mafic lavas from the Vumba greenstone belt (Bagai, 2000).

Table 5.2: Major element (wt.%) data for mafic lavas from the Tati greenstone belt. LOI = loss on ignition; Mg# = atomic Mg/(Mg + Fe^{2+}) with $Fe_2O_3/FeO = 0.2$.

Sample	ZBT-46	ZBT-47	ZBT-48	ZBT-49	ZBT-50	ZBT-51	ZBT-52	ZBT-53	ZBT-54	ZBT-55	ZBT-56	ZBT-57	ZBT-58	ZBT-59	ZBT-60	ZBT-61	ZBT-62
SiO_2	49.40	49.63	49.60	50.11	49.60	48.46	52.77	44.83	50.20	51.96	51.17	48.85	51.99	52.82	47.30	48.49	46.89
TiO_2	0.68	0.68	0.66	0.68	0.70	1.74	0.81	1.04	0.72	1.47	0.75	1.44	0.81	0.81	1.37	1.03	1.01
Al_2O_3	14.92	14.95	14.78	15.33	15.56	13.25	14.80	16.76	14.12	15.82	14.44	15.53	14.95	15.07	14.81	16.12	15.41
Fe_2O_3	10.11	10.30	10.18	10.06	10.49	16.38	10.78	12.53	10.21	10.03	10.68	13.34	10.79	10.55	11.42	12.36	12.64
MnO	0.18	0.17	0.16	0.17	0.19	0.27	0.18	0.19	0.21	0.21	0.20	0.24	0.18	0.18	0.31	0.17	0.25
MgO	8.82	8.48	8.61	6.34	6.60	5.88	6.18	8.99	6.29	5.10	6.52	5.80	6.07	5.99	3.63	6.57	7.80
CaO	12.70	12.44	12.98	13.49	12.96	9.53	10.06	12.54	12.29	11.58	11.41	12.33	10.22	9.98	14.56	11.52	11.51
Na_2O	1.68	1.74	1.47	1.00	1.34	2.74	2.64	1.71	1.92	2.00	2.04	1.71	2.85	2.83	1.43	2.15	1.23
K_2O	0.13	0.15	0.19	0.16	0.21	0.23	0.19	0.15	0.15	0.15	0.16	0.21	0.19	0.19	0.19	0.14	0.08
P_2O_5	0.06	0.08	0.06	0.06	0.07	0.15	0.09	0.09	0.09	0.14	0.09	0.13	0.09	0.09	0.13	0.09	0.09
LOI	0.67	0.71	0.63	1.88	1.77	0.52	1.08	0.65	3.05	0.99	2.12	0.45	1.15	0.91	3.57	0.77	2.43
Total	99.35	99.32	99.33	99.29	99.49	99.15	99.59	99.48	99.24	99.45	99.56	100.03	99.30	99.43	98.73	99.41	99.34
Mg#	0.67	0.66	0.66	0.60	0.60	0.46	0.57	0.63	0.59	0.54	0.59	0.50	0.57	0.57	0.43	0.54	0.59

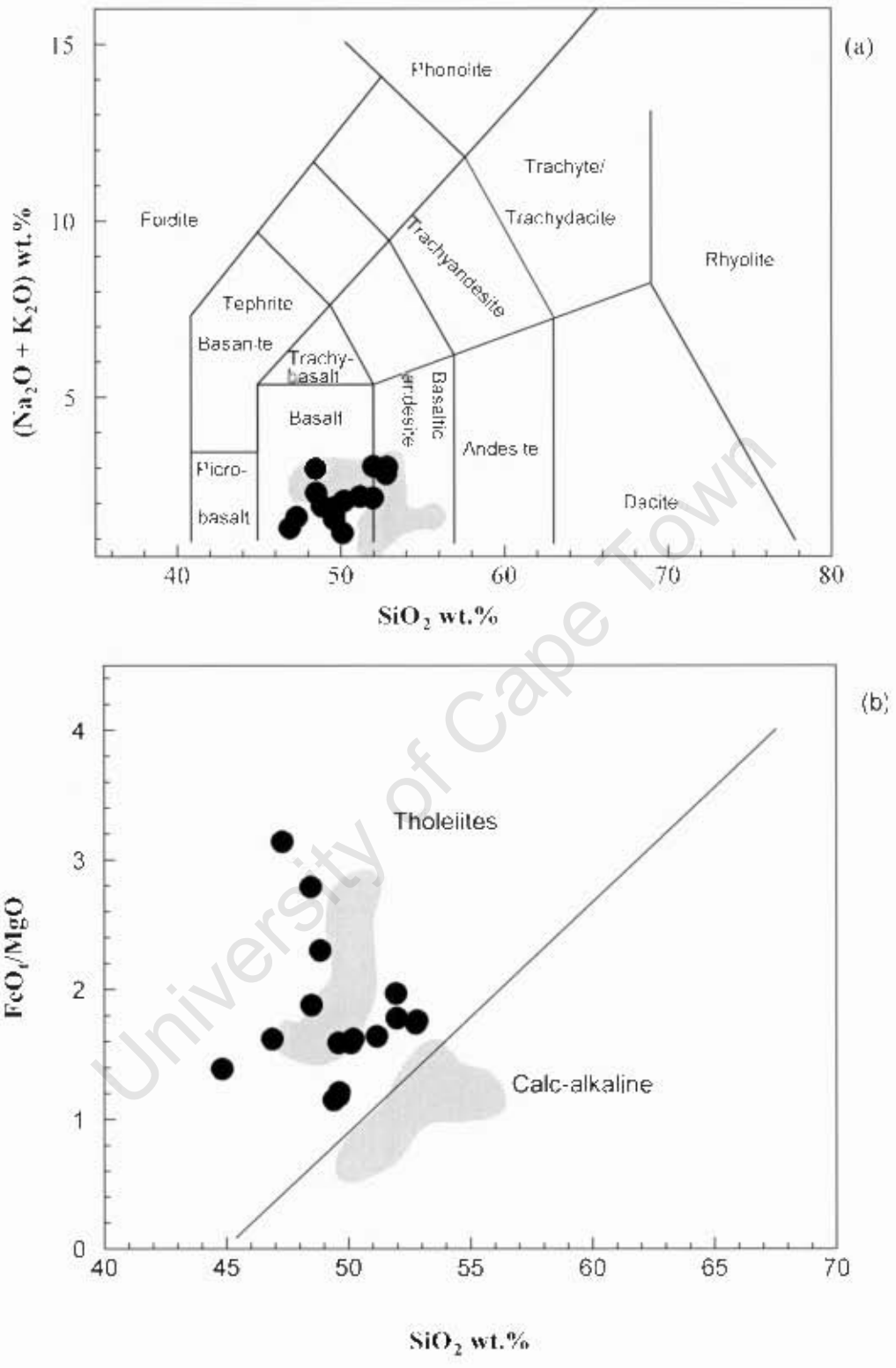

Fig. 5.2: Chemical classification for the mafic lavas from the two greenstone belts of the Francistown Granite-Greenstone Complex. (a) Plot of total alkalis versus SiO_2 (after Le maitre et al., 1989). (b) Discrimination diagram for tholeiitic versus calc-alkaline magma series, from Miyashiro (1974). The Vumba mafic lavas composition s displayed in pale grey fields for comparison.

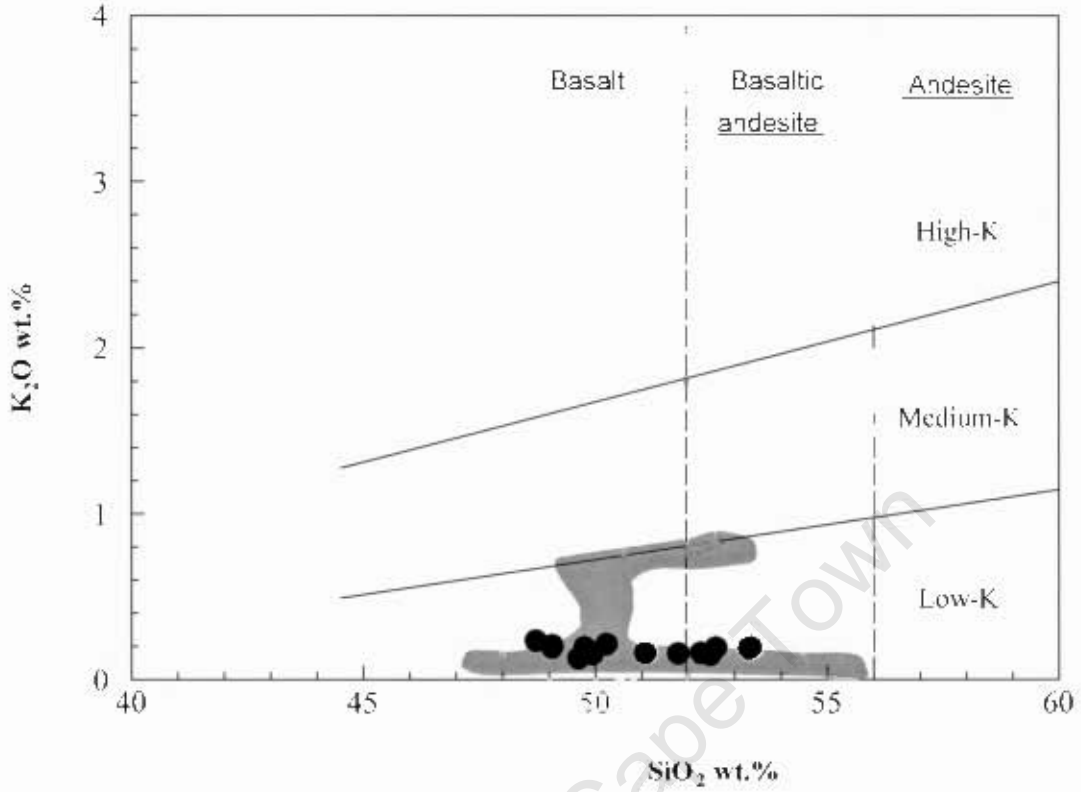

Fig. 5.3: Plot of the mafic lavas from the Tati greenstone belt of the Francistown Granite-Greenstone Complex in the K_2O versus SiO_2 diagram with fields drawn according to Peccerillo and Taylor (1976) and Gill (1981). The Vumba mafic lavas composition are displayed in pale grey field for comparison.

The major element compositional ranges are compared in Figure 5.4 relative to Mg#. It is evident that there are no significant differences between the mafic lavas from the Vumba and the Tati greenstone belts in terms of major element compositions. It is also evident that there is generally no well defined correlation between the major elements and Mg# except TiO_2, Fe_2O_3t and P_2O_5 which display decreasing trends with increasing Mg#. K_2O content of the Vumba greenstone mafic lavas defines three groups (Fig. 5.4g). One group which is indistinguishable from the mafic lavas from the Tati belt displays a negative correlation with Mg#. The second group defines a positive correlation with the Mg# and it has relatively high K_2O contents. It is stratigraphically confined to the Vumba Upper Mafic Formation, which is the topmost succession in the Vumba belt (Fig.2.5). The third group forms an outlier and is characterised by high Mg#. It is defined by gabbroic amphibolite samples, spatially limited to the outcrop adjacent to the metapyroxenite unit within the Vumba Mixed Volcanic Formation.

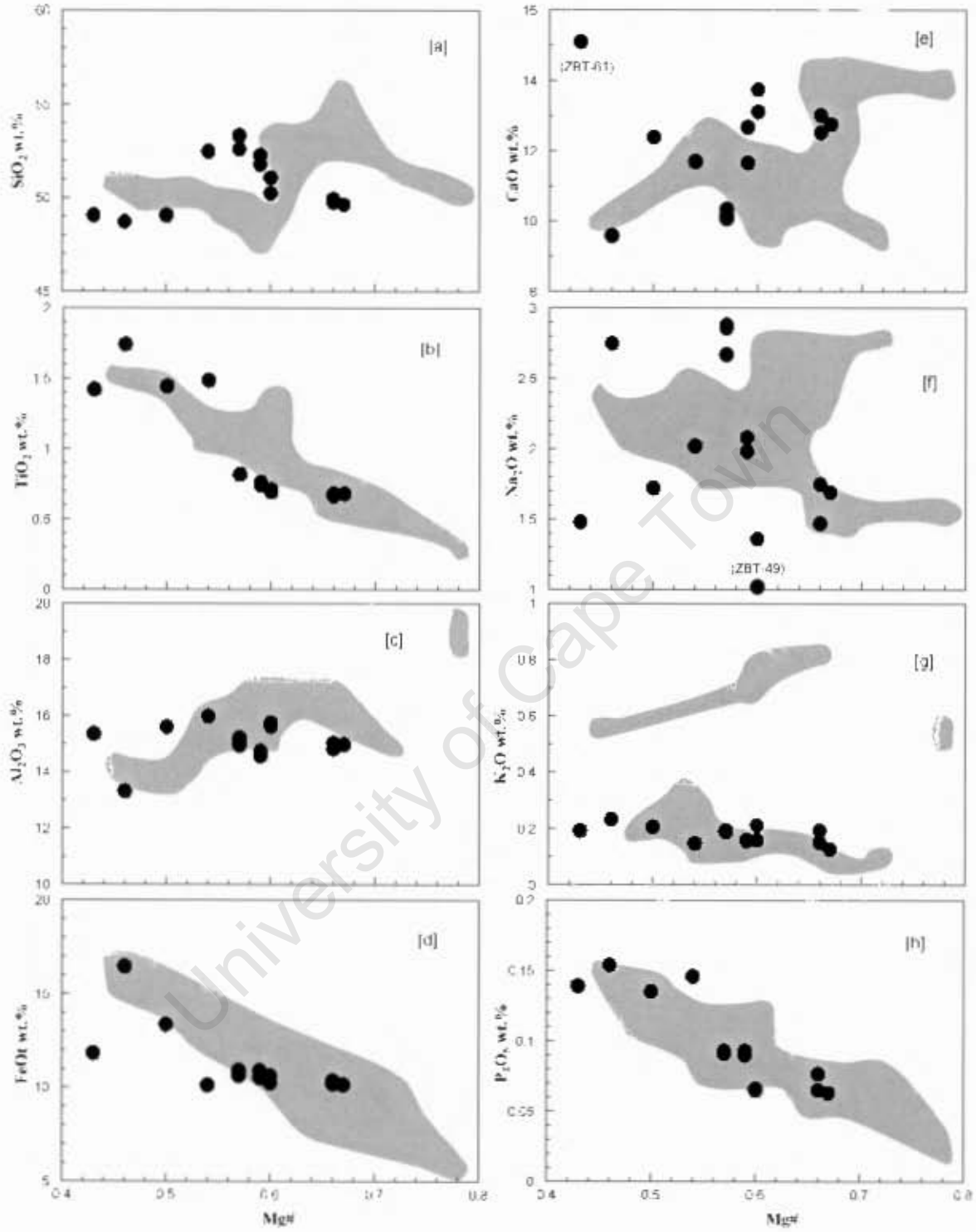

Fig. 5.4: Plots of major elements (wt.%) versus Mg# (atomic Mg/[Mg+Fe^{2+}]) for the mafic lavas from the Tati greenstone belt of the Francistown Granite-Greenstone Complex. The background for the mafic lavas from the Vumba greenstone belt is shown in pale gray fields for comparison.

Al_2O_3 is the only major element which displays a broad positive correlation against Mg# which is consistent with the involvement of feldspar during the differentiation of these mafic lavas. CaO and Na_2O exhibit the scattered, uncorrelated cloud of data in the variation diagrams.

5.3 Felsic lavas

This section concentrates on the major element characteristics, classification and major element variation diagrams of felsic lavas that are spatially associated with the previously mentioned mafic lavas. The whole rock major element data for the felsic volcanic rocks from the Tati greenstone belt are presented in Tables 5.3. The silica concentration of the felsic lavas from the Tati belt varies between 65 and 70% with the majority of the samples having silica composition between 63 and 68 wt.% (Table 5.3). The chemical classification of felsic lavas using the total alkalis versus silica (TAS) diagram of Le Maitre et al. (1989) is presented in Fig. 5.5a. Figure 5.5b shows K_2O versus SiO_2 contents of the felsic lavas compared with the compositional fields of Le Maitre et al. (1989) subdivisions which clearly demonstrate that the felsic lavas from the Tati greenstone belt are essentially medium-K dacites.

Table 5.3: Major element (wt.%) data for felsic lavas from the Tati greenstone belt. A/CNK = alumina saturation index calculated as Mol% $Al_2O_3/(CaO + Na_2O + K_2O)$. L.O.I= loss on ignition.

Samples	ZBT41	ZBT42	ZBT43	ZBT44	ZBT45
SiO_2	67.5	66.2	63.7	63.9	66.3
TiO_2	0.62	0.62	0.58	0.61	0.61
Al_2O_3	16.2	16.2	16.1	15.5	16.0
Fe_2O_3	2.85	3.98	5.86	5.81	5.08
MnO	0.10	0.11	0.13	0.17	0.11
MgO	0.82	1.05	1.26	1.54	1.11
CaO	4.51	3.96	5.49	5.68	4.17
Na_2O	2.78	3.43	2.84	2.75	3.11
K_2O	2.78	2.37	1.64	1.97	2.06
P_2O_5	0.15	0.15	0.15	0.16	0.15
L.O.I	1.56	1.33	1.65	1.74	0.97
Total	99.8	99.3	99.4	99.9	99.7
Mg#	0.44	0.42	0.37	0.42	0.37
A/CNK	1.02	1.05	0.98	0.91	1.07
K_2O/Na_2O	1.00	0.69	0.58	0.72	0.66

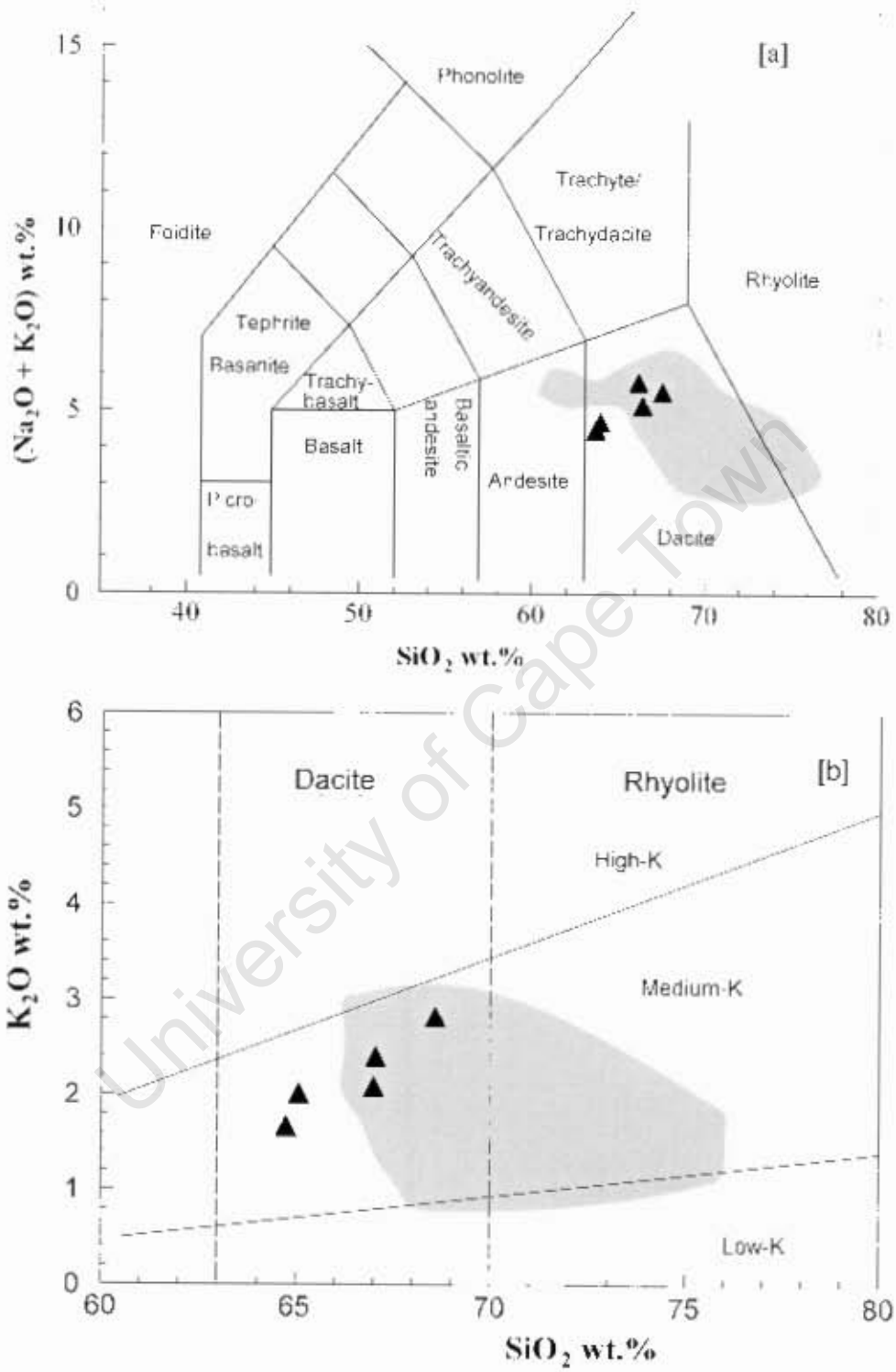

Fig. 5.5: Geochemical classification of the felsic lavas from the greenstone belts of the Francistown Granite-Greenstone Complex. (a) Chemical classification of felsic lavas using total alkalis versus silica diagram of Le Maitre et al. (1989); (b) K_2O versus SiO_2 classification diagram with subdivisions of Le Maitre et al. (1989). Pale gray = field for Vumba greenstone belt.

On most of the diagrams in Figure 5.6 there are no clearly defined correlations between the major elements and SiO_2 content except the MgO content which displays a negative correlation.

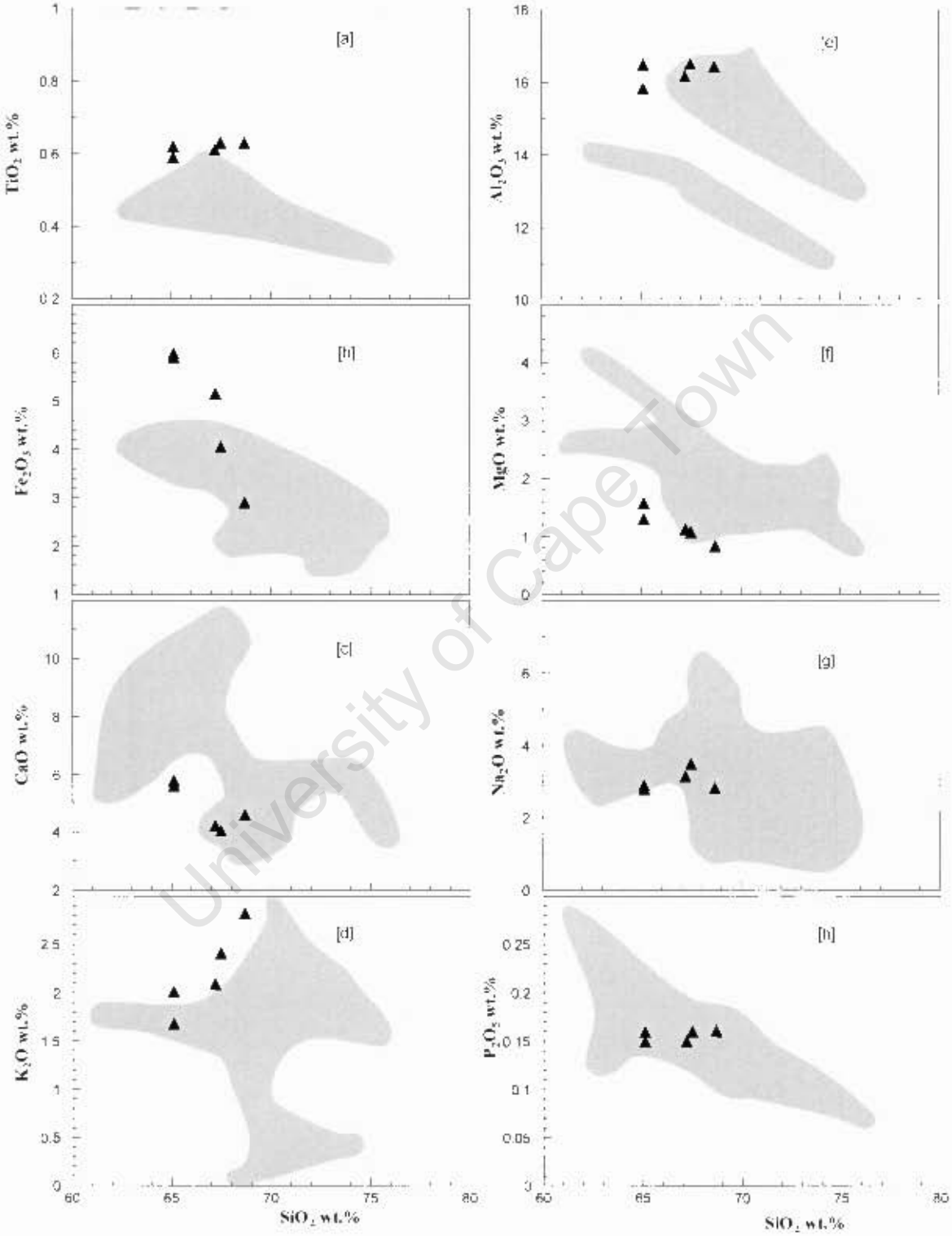

Fig. 5.6: Plot of major elements versus SiO_2 wt.% for the felsic lavas from the Tati greenstone belt of the Francistown Granite-Greenstone Complex. Pale gray = fields for Vumba greenstone belt.

The alumina saturation indices [mol% $Al_2O_3/(Na_2O + K_2O + CaO)$] for the Tati felsic lavas range from 0.97 to 1.07, which indicates metaluminous to peraluminous character (Chappell and White, 1992). According to Chappell and White (1992) igneous rocks with alumina saturation indices (ASI) less than 1.1 are derived from igneous or meta-igneous sources (I-type melts), whereas the igneous rocks possessing ASI > 1.1 are generated from metasedimentary sources, S-type melts.

5.4 Gabbro

Twenty representative samples from the gabbro unit were analysed for their major element composition; 5 samples coming from the Phoenix gabbro, and 15 from the Selkirk gabbro of which 8 were discarded because of high LOI values (> 5%). Results are reported in Table 5.6 whereas Fig. 5.7 presents variation diagrams of the major elements versus Mg#. In terms of SiO_2 content the Phoenix gabbro displays a narrow range between 42 and 46 wt.% (Table 5.4) which is indicative of an ultrabasic to basic composition. The samples are characterised by high MgO content (13.5 to 9.74 wt.%), relatively low FeO_{total} abundance and high Mg# (average 0.81), indicative of their primitive nature. However, gabbros are often partial cumulates.

The Selkirk gabbro exhibits a relatively wide variation of SiO_2 content, 42 to 49 wt.%, which is indicative of its ultrabasic to basic composition. In contrast to the Phoenix gabbro, the Selkirk gabbro is characterised by low values of Mg# (0.59 to 0.74; Table 5.4), high FeOt abundances (13.50 to 8.00 wt.%) and broad variation of MgO content (12.32 to 7.95 wt.%). In Figure 5.9 it is clear that the two gabbroic bodies are different in terms of the FeO_{total}, TiO_2 and to lesser extent P_2O_5 concentrations, with the Selkirk gabbro having higher values of these elements than the Phoenix gabbro. The Selkirk gabbro displays two distinct groups in terms of TiO_2 and P_2O_5 contents that show constant TiO_2 and P_2O_5 with increasing Mg#. Unfortunately, it is not possible to evaluate the spatial distribution of these samples because they were collected randomly in a mine shaft and there are no locality coordinates. It is worth-mentioning that some previous workers (e.g. Key, 1976) reported the presence of both troctolite and gabbro at the Selkirk site. The surface expression of the Selkirk gabbro is completely obliterated by the mining activities and this renders surface sampling very difficult.

Table 5.4: Major element data (wt.%) for the gabbros unit from the Tati granite-greenstone terrain of the Francistown Granite-Greenstone Complex. Mg# calculated assuming $Fe_2O_3/FeO = 0.2$.

Unit	Phoenix					Selkirk							
Sample	ZBT37	ZBT38	ZBT39	ZBT40	ZBT81	ZBT64	ZBT66	ZBT67	ZBT70	ZBT71	ZBT73	ZBT74	ZBT75
SiO_2	44.7	44.4	43.4	42.6	45.0	42.1	41.8	42.5	42.7	41.3	47.2	43.9	43.9
TiO_2	0.18	0.17	0.17	0.14	0.19	0.29	0.28	1.09	0.28	0.33	0.99	0.31	0.29
Al_2O_3	18.2	17.8	19.9	20.5	19.2	19.5	19.7	16.3	18.9	20.0	15.5	20.3	19.1
Fe_2O_3	7.50	7.15	6.96	7.14	5.82	10.1	10.1	12.4	9.65	11.0	12.2	8.57	10.2
MnO	0.11	0.11	0.10	0.10	0.10	0.13	0.13	0.32	0.14	0.24	0.25	0.15	0.13
MgO	13.0	13.5	12.5	12.7	9.74	9.97	9.56	7.88	10.63	9.70	7.78	9.24	10.28
CaO	11.0	12.6	12.7	12.1	14.6	12.5	11.1	12.6	11.2	11.3	11.6	11.7	10.8
Na_2O	1.31	1.14	1.31	1.13	1.34	0.41	0.65	1.99	0.46	0.70	1.69	0.99	0.66
K_2O	0.26	0.21	0.12	0.10	0.16	0.12	0.11	0.12	0.10	0.03	0.16	0.06	0.08
P_2O_5	0.02	0.01	0.02	0.01	0.01	0.03	0.02	0.11	0.02	0.03	0.08	0.02	0.02
L.O.I	2.7	2.06	2.33	2.85	1.88	3.39	3.90	4.22	4.04	3.90	2.11	3.92	3.70
Total	99.0	99.2	99.5	99.4	98.1	98.5	97.5	99.5	98.1	98.6	99.6	99.1	99.2
Mg#	0.80	0.82	0.81	0.81	0.80	0.70	0.69	0.60	0.72	0.67	0.60	0.72	0.70

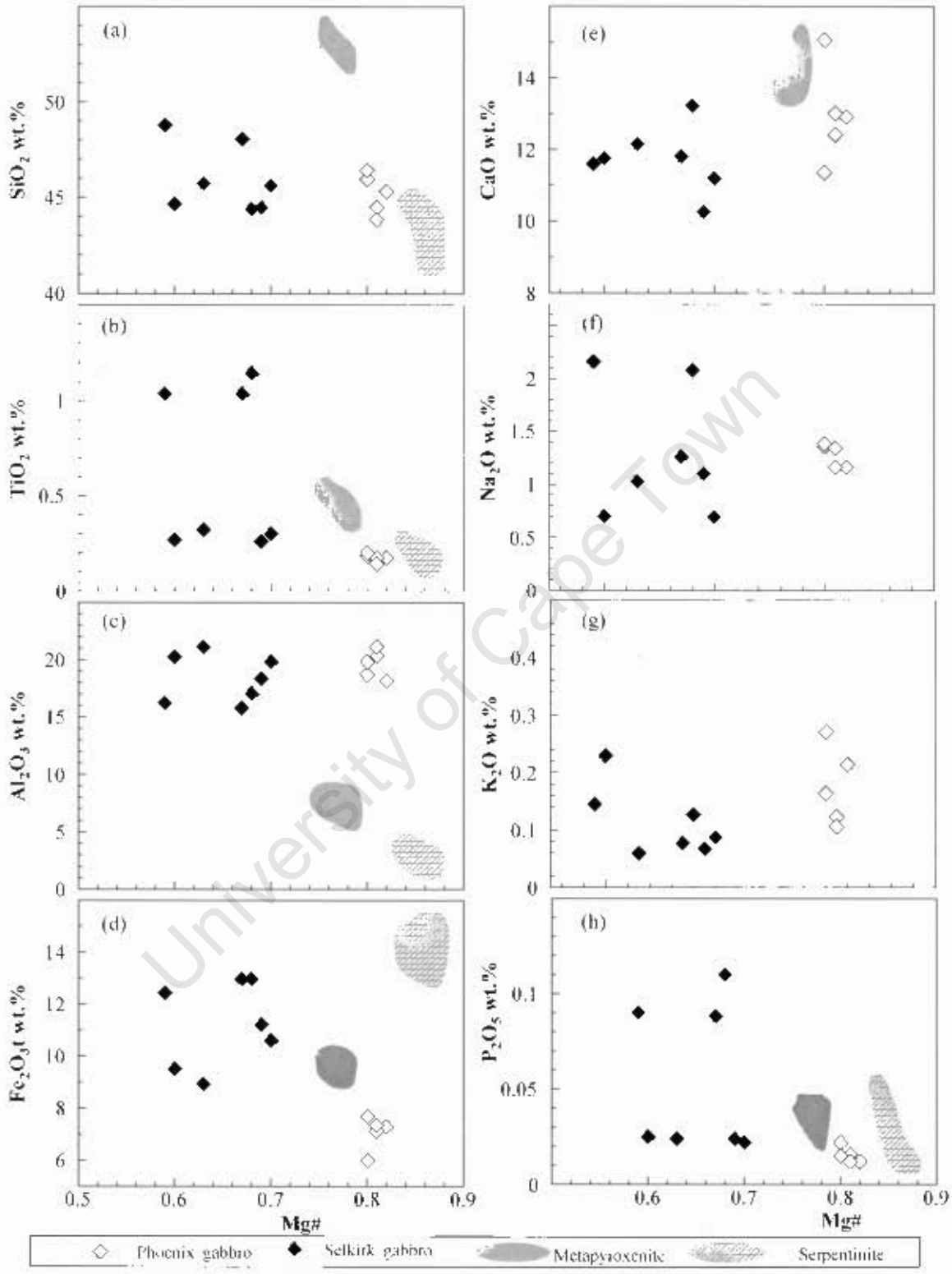

Fig. 5.7: Plots of major elements (wt.%) versus Mg# (atomic Mg/[Mg + Fe^{2+}]) for the gabbro unit from the Tati granite-greenstone terrain of the Francistown Granite-Greenstone Complex. Serpentinite and metapyroxenite from the Vumba greenstone belt are presented as pale fields on background for comparison.

5.5 Diorite

This section presents major element data from ten samples of a diorite unit that outcrop in the Tati granite-greenstone terrain. The diorite unit has intruded both the mafic and felsic lavas in the Tati greenstone belt. Whole-rock major element analyses for the dioritic unit are provided in Table 5.5. A previous investigation (Kampunzu et al., 2003) has described the diorite unit in the study area as an Archaean sanukitoid.

Table 5.5 Major element geochemistry (wt.%) of the diorite unit from the Tati granite-greenstone terrain. Mg# calculated assuming $Fe_2O_3/FeO = 0.2$.

Sample	ZBT17	ZBT18	ZBT19	ZBT20	ZBT21	ZBT22	ZBT23	ZBT24	ZBT25	ZBT26
SiO_2	50.8	50.3	50.8	49.3	50.3	49.0	49.1	49.7	49.4	49.1
TiO_2	0.39	0.37	0.35	0.29	0.29	0.16	0.12	0.16	0.18	0.19
Al_2O_3	15.8	15.7	16.8	16.3	15.5	17.2	18.1	16.5	17.9	17.4
Fe_2O_3	8.04	8.91	8.10	7.91	8.02	7.23	7.59	6.82	6.52	6.70
MnO	0.15	0.16	0.15	0.14	0.15	0.13	0.13	0.13	0.13	0.13
MgO	8.62	8.72	7.84	9.29	8.83	8.80	10.7	10.5	9.29	9.39
CaO	12.6	12.0	12.9	11.9	13.0	13.8	10.8	15.3	14.3	14.0
Na_2O	2.04	1.98	2.32	1.93	2.02	1.91	1.49	1.46	1.70	1.51
K_2O	0.54	0.43	0.29	0.46	0.32	0.17	0.10	0.05	0.07	0.11
P_2O_5	0.07	0.06	0.05	0.04	0.03	0.00	0.01	0.01	0.02	0.01
L.O.I	1.05	1.15	0.80	1.36	0.91	0.71	1.10	0.21	0.70	1.09
Total	100.1	99.7	100.4	99.0	99.4	99.1	99.3	100.8	100.2	99.6
Mg#	0.71	0.70	0.69	0.73	0.72	0.74	0.77	0.78	0.77	0.77

The diorite unit in the Francistown Granite-Greenstone Complex is basic with SiO_2 content ranging between 49 and 51 wt.% (Table 5.5). It is characterized by high MgO contents which range from 7.9 to 10.87 wt.% as well as high Mg# (0.69 to 0.78; Table 5.5). The values of Mg# of the diorite unit from the Francistown Granite-Greenstone Complex are similar to values recorded in the high-Mg andesites from the Japanese island arc (e.g. Stevenson et al., 1999). K_2O contents of the Francistown dioritic unit are very low (< 0.55 wt.%). On Figure 5.8 which is a variation diagram of K_2O plotted versus SiO_2 with discrimination boundaries from Gill (1981), the diorite samples plot in the low-K tholeiite field. On the major element variation diagrams presented in Figure 5.9, the diorite unit display linear trends showing broad negative correlations on the plots of SiO_2, TiO_2, FeO_t, Na_2O, K_2O and P_2O_5 versus Mg#, and positive correlations on plots of CaO and Al_2O_3 versus

Mg#. The major element variations of the dioritic unit are qualitatively consistent with an evolution dominated by olivine, clinopyroxene and feldspar fractionation. These trends will be discussed quantitatively in the petrogenesis chapter. Samples (ZBT17-21) obtained from the dioritic outcrops north of the city of Francistown are more evolved (relatively low Mg#) as compared to samples (ZBT22-26) collected from the southeastern outcrops (Fig. 2.4).

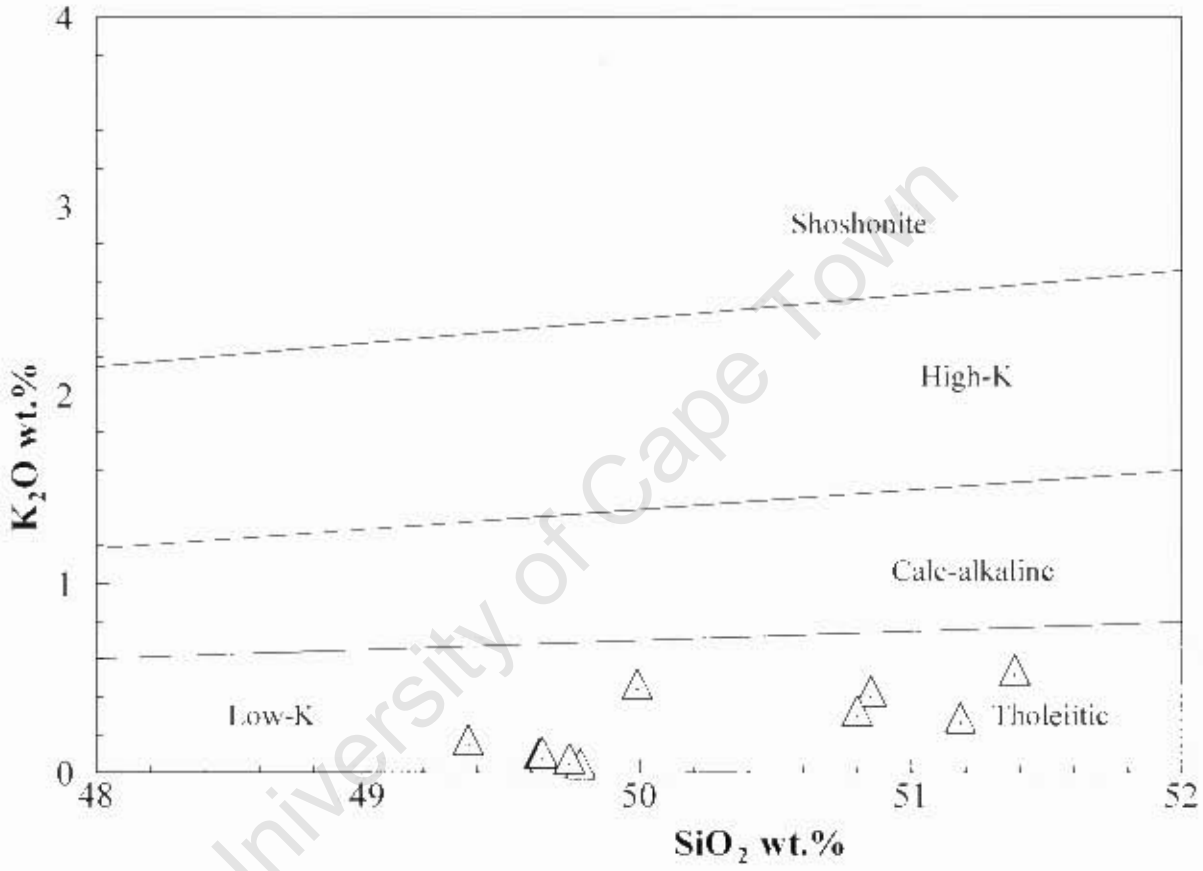

Fig. 5.8: Plot of K_2O vs. SiO_2 for the diorite unit from the Francistown Granite-Greenstone Complex with subdivisions based on K_2O contents from Gill (1981).

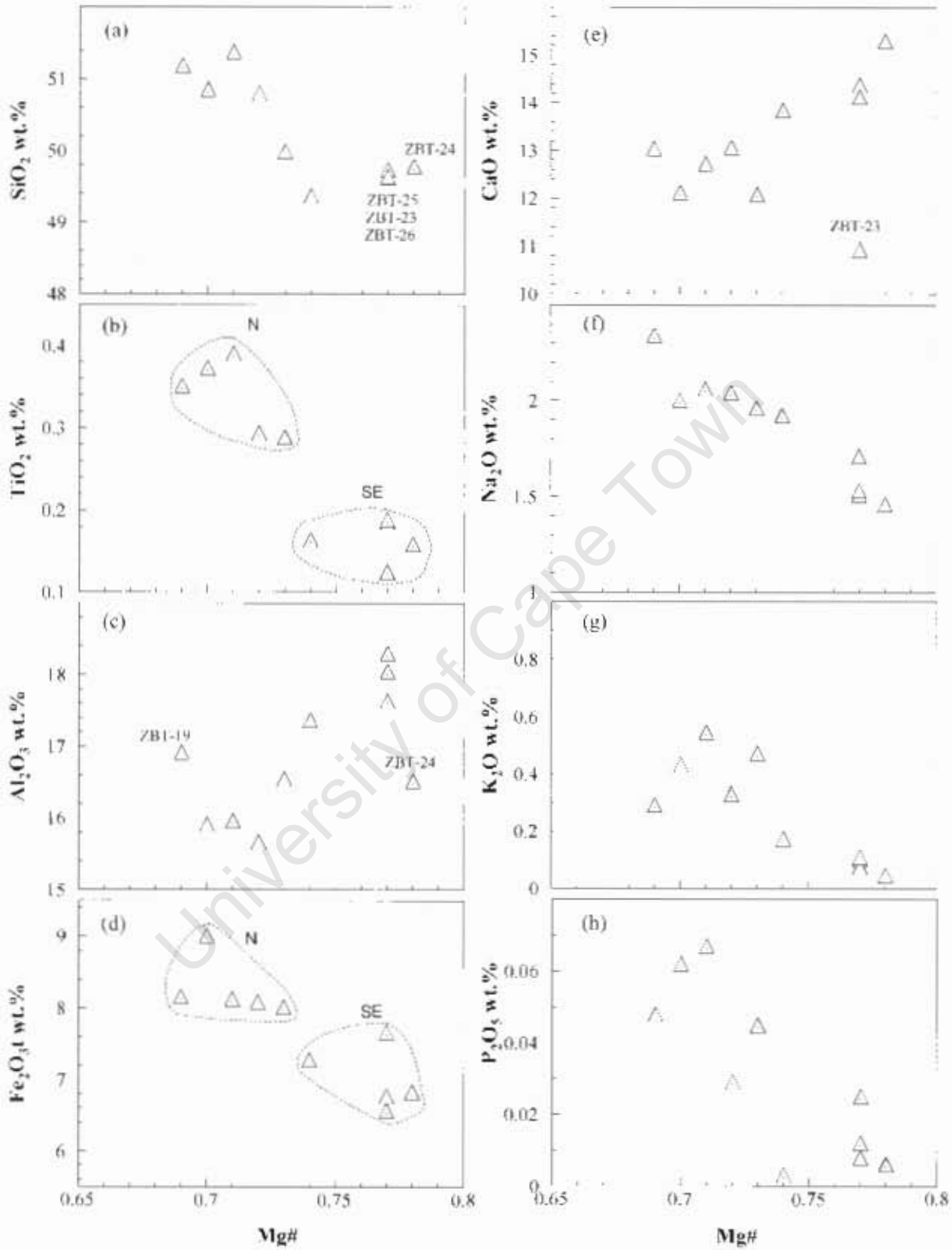

Fig. 5.9: Plots of major elements (wt.%) versus Mg# (atomic Mg/[Mg + Fe²⁺]) for the diorite unit from the Tati granite-greenstone terrain of the Francistown Granite-Greenstone Complex. N – Northern outcrop sample; SE-southeastern outcrop samples.

5.6 Granitoids

Twenty-nine samples of different types of granitoids from the Tati granite-greenstone terrain were analyzed and the data are presented in Table 5.6. Geochemical classification of the Tati granitoids based on their normative feldspar compositions is presented in Fig. 5.10. The heterogeneity of the Tati pluton is reflected in the normative feldspar proportions with samples plotting in the tonalite, trondhjemite and granite fields. The two samples from the felsic dykes that cut the Phoenix gabbro plot in the tonalite and trondhjemite fields, suggesting an association with the tonalite-trondhjemite unit. Samples from the quartz monzonite unit plot on the border between granodiorite and quartz monzonite fields. The monzogranites from the Tati terrain tends to straddle the boundary between the trondhjemite and granite fields. Harker diagrams for the Tati granitoids are presented as Fig. 5.11 with fields for granitoids from the Vumba granite-greenstone terrain shown on backgrounds for comparison.

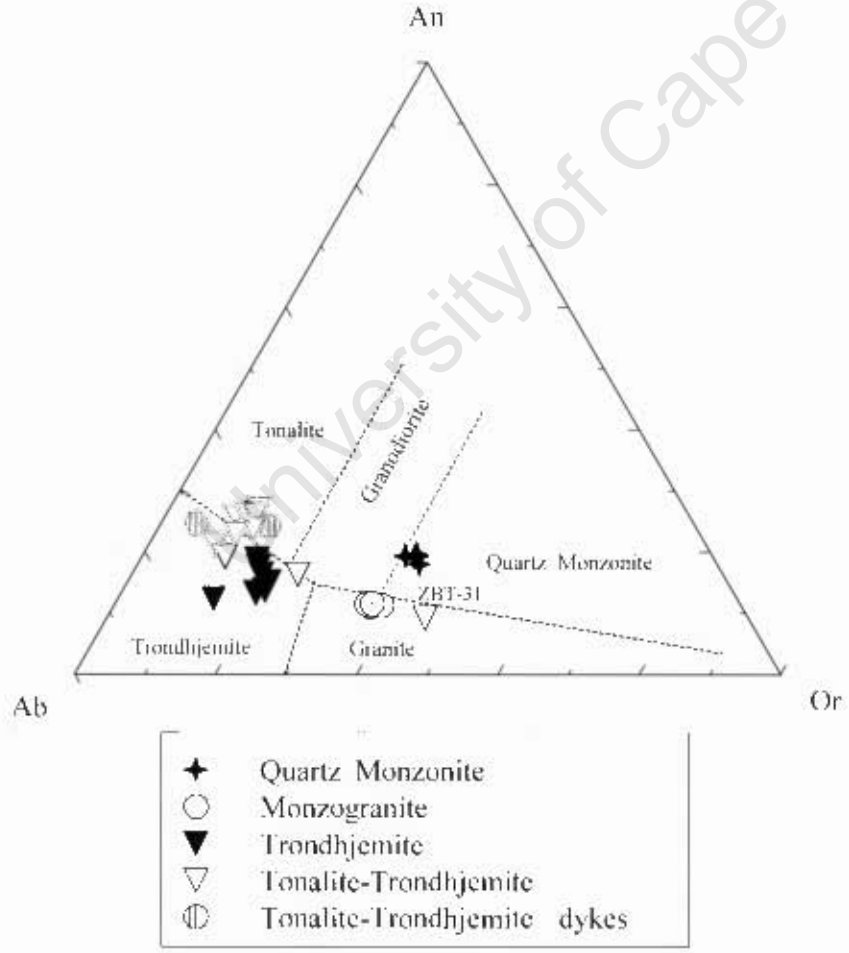

Fig. 5.10: Geochemical classification of the granitoids from the Tati granite-greenstone terrain.

Table 5.6: Major element (wt.%) data for representative samples of granitoids from the Tati granite-greenstone terrain. ASI-aluminum saturation index calculated as Mol% $Al_2O_3/(CaO + Na_2O + K_2O)$.

Unit	Quartz Monzonite					Monzogranite				Trondhjemite						
Sample	**ZBT1**	**ZBT2**	**ZBT3**	**ZBT4**	**ZBT5**	**ZBT6**	**ZBT7**	**ZBT8**	**ZBT9**	**ZBT10**	**ZBT11**	**ZBT12**	**ZBT13**	**ZBT14**	**ZBT15**	**ZBT16**
SiO_2	62.6	62.70	62.8	63.9	62.7	74.5	72.3	73.9	74.3	73.2	71.5	74.4	74.2	74.8	73.3	73.4
TiO_2	0.60	0.59	0.62	0.60	0.63	0.25	0.25	0.26	0.26	0.27	0.31	0.22	0.27	0.23	0.29	0.29
Al_2O_3	17.7	17.59	17.2	16.5	16.80	11.9	12.1	12.1	11.88	12.51	12.4	11.91	11.8	11.83	11.92	12.0
Fe_2O_3	4.18	4.12	4.38	4.25	4.48	4.36	4.41	4.51	4.69	4.09	4.65	3.68	4.23	3.54	4.57	4.37
MnO	0.05	0.05	0.06	0.05	0.06	0.09	0.09	0.09	0.10	0.08	0.06	0.05	0.06	0.05	0.06	0.05
MgO	1.92	1.79	1.89	1.73	1.95	0.10	0.13	0.11	0.06	0.25	0.18	0.11	0.19	0.18	0.20	0.17
CaO	3.48	3.49	3.64	3.50	3.73	1.47	1.45	1.48	1.54	1.87	2.25	1.70	2.08	1.37	2.01	1.98
Na_2O	4.26	4.18	4.21	4.25	4.29	2.07	1.69	1.85	4.38	3.95	4.35	4.31	4.03	4.69	4.43	4.21
K_2O	3.71	3.87	4.14	3.95	3.85	4.27	4.18	4.34	1.78	1.51	1.75	1.88	1.47	1.23	1.79	1.86
P_2O_5	0.30	0.29	0.32	0.30	0.32	0.02	0.03	0.03	0.03	0.04	0.05	0.02	0.03	0.03	0.05	0.04
L.O.I	0.39	0.38	0.34	0.35	0.37	0.82	2.73	0.81	0.82	1.55	2.13	1.57	1.33	1.20	0.75	0.76
Total	99.3	99.06	99.6	99.4	99.2	99.8	99.3	99.5	99.9	99.4	99.6	99.9	99.7	99.1	99.4	99.1
Mg#	0.51	0.50	0.49	0.48	0.50	0.05	0.06	0.05	0.03	0.12	0.08	0.06	0.08	0.08	0.13	0.08
ASI	1.02	1.01	0.96	0.94	0.94	0.99	1.06	1.02	1.02	0.95	0.95	0.97	0.99	1.02	0.92	0.95
K_2O/Na_2O	0.87	0.92	0.98	0.93	0.90	2.07	2.47	2.35	0.41	0.38	0.40	0.44	0.36	0.26	0.41	0.44

Unit	Tonalite-Trondhjemite (Tati Puton)							Tonalite-Trondhjemite Dyke		Tonalite-Trondhjemite (Sekukwe Pluton)			
Sample	**ZBT28**	**ZBT29**	**ZBT30**	**ZBT31**	**ZBT32**	**ZBT33**	**ZBT34**	**ZBT35**	**ZBT36**	**ZBT77**	**ZBT78**	**ZBT79**	**ZBT80**
SiO_2	69.1	71.3	74.6	74.3	71.8	69.7	69.5	72.3	75.7	65.9	71.1	67.8	69.5
TiO_2	0.35	0.27	0.08	0.12	0.29	0.35	0.36	0.20	0.23	0.20	0.14	0.18	0.17
Al_2O_3	16.0	15.13	14.16	13.6	15.2	15.62	15.8	14.5	12.6	17.4	15.71	17.3	16.2
Fe_2O_3	2.87	2.49	1.16	1.64	2.60	2.81	2.82	2.26	1.97	1.92	1.54	1.78	1.50
MnO	0.03	0.02	0.02	0.04	0.03	0.03	0.03	0.03	0.01	0.02	0.02	0.03	0.02
MgO	0.77	0.55	0.21	0.32	0.53	0.72	0.72	0.79	0.39	0.72	0.51	0.66	0.54
CaO	3.67	3.23	2.07	1.17	3.31	3.48	3.56	2.85	2.63	3.62	2.87	3.00	3.17
Na_2O	4.59	4.34	4.42	3.40	4.69	4.79	4.72	4.07	4.30	5.50	5.42	6.13	5.21
K_2O	1.39	1.14	2.47	4.80	1.05	1.33	1.40	1.49	0.44	1.70	1.04	1.50	1.31
P_2O_5	0.13	0.09	0.02	0.01	0.10	0.13	0.12	0.04	0.04	0.07	0.04	0.07	0.05
L.O.I	0.33	0.48	0.16	0.27	0.31	0.30	0.34	1.06	0.61	2.16	1.29	0.76	1.83
Total	99.2	99.0	99.3	99.7	99.9	99.3	99.3	99.7	99.0	99.2	99.7	99.3	99.4
Mg#	0.38	0.33	0.29	0.31	0.31	0.37	0.36	0.44	0.31	0.46	0.43	0.46	0.45
ASI	1.02	1.06	1.03	1.05	1.02	1.00	1.00	1.08	1.02	1.00	1.03	1.01	1.03
K_2O/Na_2O	0.30	0.26	0.56	1.41	0.22	0.28	0.30	0.37	0.10	0.31	0.19	0.24	0.25

The tonalite-trondhjemite unit, which is the most dominant and widely distributed, forms plutons of variable sizes both on the southwestern and northeastern part of the Tati greenstone belt (Fig. 4.1). The southwestern tonalite-trondhjemite plutons include the Tati Pluton which is the largest and is relatively well exposed. Based on the results from previous studies (e.g. Kampunzu et al., 2003), the Tati pluton is regarded a representative of the tonalite-trondhjemite granitoids flanking the SW margin of the Tati greenstone belt. The samples from the Tati pluton show a wide range of SiO_2 from 67 to 75 wt.% (Table 5.6) with two samples ZBT30 and ZBT31 having the highest values (74.6 and 74.3 wt.%, respectively). These two samples were sampled from leucocratic sections of locally banded outcrops which is a common feature in the southwestern tonalite-trondhjemite plutons. On Harker diagrams involving K_2O and CaO (Fig. 5.11c & d) the two samples deviate from the trends defined by other samples from the Tati pluton by having considerably lower CaO and higher K_2O. Nonetheless, the two samples plot with the other samples on variation diagrams involving the rest of the major elements (Fig. 5.11). Petrographic analyses (see petrography section) show that the two samples are tonalitic and granitic in composition, respectively.

The Sekukwe pluton is the largest tonalite-trondhjemite body flanking the northeast margin of the Tati greenstone belt (Fig. 2.3), and is SiO_2 rich (70 to 72 wt.%; Table 5.6). The samples display negative trends on Harker diagrams that involve CaO, Al_2O_3, Na_2O and K_2O, and they are indistinguishable from those of the Tati pluton. On Harker diagrams involving TiO_2, FeOt and P_2O_5 (Fig. 5.11a, b & h), the Sekukwe samples define a distinct group with elevated compositions.

The trondhjemite unit forms linear kopje outcrops parallel to the trend of the Tati greenstone belt located between the Tati and the Sekukwe plutons (Fig. 2.3). In contrast to the tonalite-trondhjemite unit, trondhjemite shows a lack of pervasive fabric. The trondhjemite unit is characterised by high SiO_2 abundance with narrow range from 73 to 76 wt.% (Table 5.6). Major elements show coherent negative trends on variation diagrams versus SiO_2, except Al_2O_3, Na_2O and MgO which display no correlation (Fig. 5.11). Although it is clear from the variation diagrams (Fig. 5.11) that this trondhjemite unit is chemically distinct from the tonalite-trondhjemite unit, it is noteworthy that its Al_2O_3 and FeOt concentrations (Table 5.6) are conspicuously low and high, respectively, in comparison with the tonalite-trondhjemite unit.

The monzogranite unit in the Tati granite-greenstone terrain mainly crops out in the form of east-trending dykes and a few kopjes. A relatively large outcrop is the Ramokgwebana Granite which occurs along the border between Botswana and Zimbabwe. Its aerial extent in Zimbabwe is unknown. Chemically, the monzogranite has high SiO_2 contents (72 to 75 wt.%; Table 5.6), which is similar to the range of silica recorded from the trondhjemite unit. All the analysed samples have yielded major element concentrations which are indistinguishable from those of the trondhjemite unit except the K_2O and Na_2O contents (see Fig. 5.11 and Table 5.6).

There are two samples which were sampled from a felsic dyke cutting the Phoenix gabbro. The samples have high SiO_2 abundance (72.3 to 75.7 wt.%; Table 5.6) and low K_2O contents. On Harker diagrams the two samples appear to fall on the same trends as the tonalite-trondhjemite units (Fig. 5.11).

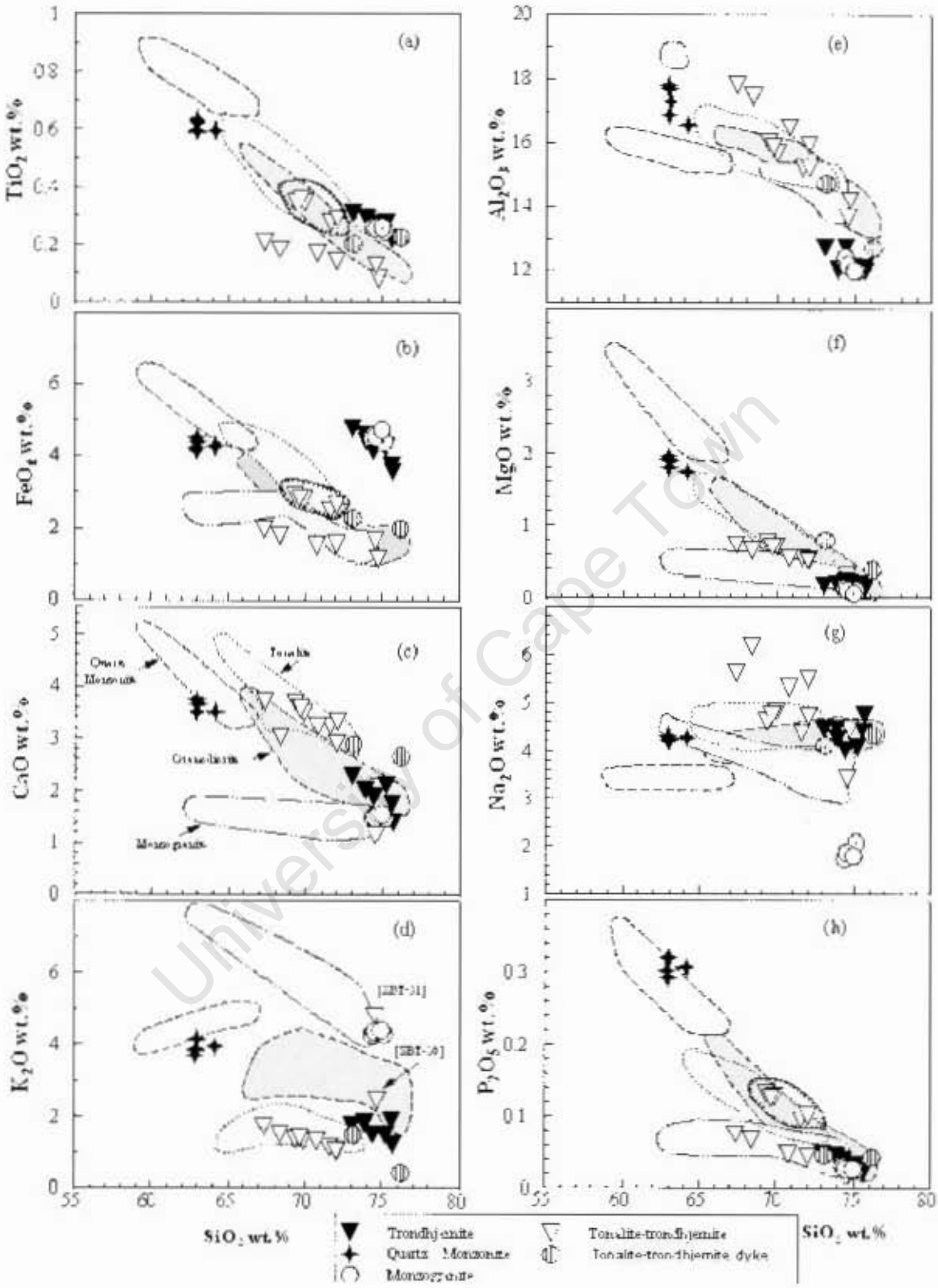

Fig. 5.11: Harker variation diagrams for the granitoids from the Tati granite-greenstone terrain.

5.6.1 Comparison of the Tati and Vumba granitoids' major element chemical characteristics

Figure 5.12 displays the differences and similarities in major element abundances between the granitoids from the Tati and Vumba terranes. Notably, the granitoids from the Vumba terrane exhibit coherent variation trends in most Harker diagrams which is a rare feature in the granitoids from the Tati granite-greenstone terrane. These variation trends suggest a common evolutionary relationship amongst the Vumba granitoids.

The quartz monzonite units overlap in all the major element contents except in Al_2O_3 and Na_2O where the Tati unit has higher abundances. Moreover, the quartz monzonite samples from the Vumba terrane are shoshonitic whereas those from the Tati area straddle the boundary between high-K and shoshonitic fields (Fig. 5.12 a-b). Furthermore, the quartz monzonite in the Vumba terrane is exclusively metaluminous while the Tati quartz monzonite varies from metaluminous to peraluminous (Fig. 5.13). However, the quartz monzonite unit from the two terranes are characterised by high Mg# (0.54 to 0.62) values corresponding to values recorded in Archaean sanukitoid suites (e.g. Shirey and Hanson, 1984; Stern and Hanson, 1991). Additionally, the quartz monzonite unit displays a calc-alkaline evolutionary trend (Fig. 5.12). Monzogranite units from the two terranes are distinct in terms of Na_2O, Al_2O_3 and FeOt abundances with the tati monzogranite possessing lower Na_2O, Al_2O_3 and higher FeOt than the monzogranite unit from the Vumba area. In terms of k-series, the monzogranite unit from the Vumba terrane displays high-K to shoshonitic affinity while the Tati monzogranite exhibits high-K character (Fig. 5.12 a-b). Both monzogranite units show a calc-alkaline evolutionary trend (5.12 c-d). The granodiorite unit which is confined to the Vumba terrane is mainly peraluminous accept the Vumba stock which is metaluminous. The latter displays medium-K to high-K affinity and a calc-alkaline to sodic evolutionary trend (Fig. 5.12). The Maebe tonalite from the Vumba terrane is medium-K and metaluminous to peraluminous (Fig. 5.13a) with a sodic evolutionary trend (Fig. 5.12a).

The trondhjemite unit within the Tati terrane shows mainly metaluminous to sparingly peraluminous characteristics (Fig. 5.13) and it is medium-K with a trondhjemitic evolutionary trend (Fig. 5.12 b, d). The wide spread tonalite-trondhjemite unit in the Tati area possesses peraluminous character and medium-K affinity, with a sodic evolutionary trend except one sample from the felsic section of the

banded Tati pluton which displays a medium-K calc-alkaline affinity (Fig. 5.12 b, d). The two samples from the tonalite-trondhjemitic dykes cutting the Phoenix gabbro are peraluminous and medium- to low-K affinity with a sodic evolutionary trend indistinguishable from the tonalite-trondhjemite unit (Fig. 5.12d).

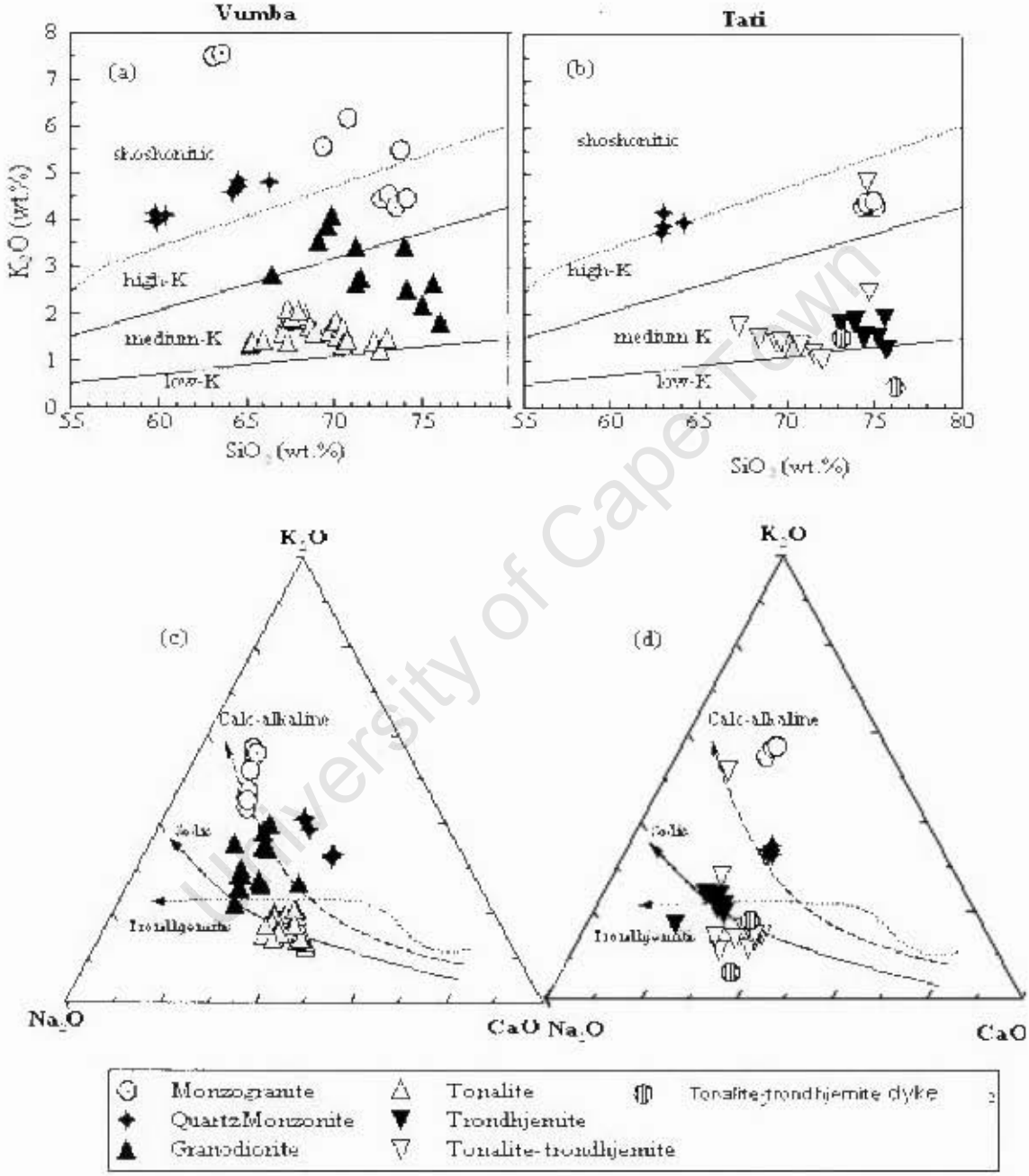

Fig. 5.12: (a-b) Plot of K_2O versus SiO_2 for granitoids from the Vumba and Tati terrains, subdivisions are based on K_2O content from Le Maitre (1989). (c-d) Plot of Na_2O-K_2O-CaO diagram with evolution trends after Hawkesworth and Lias (1994).

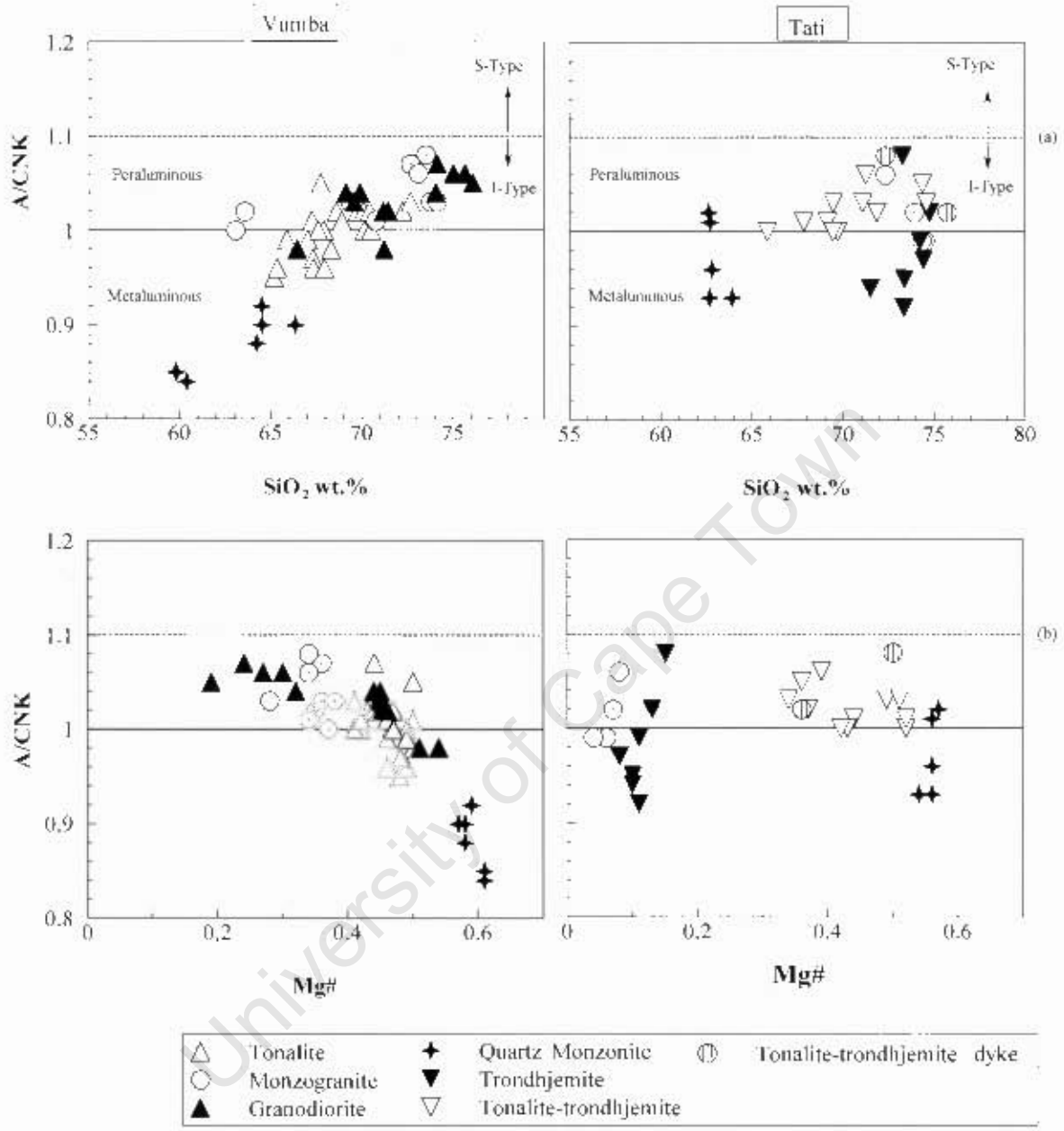

Fig. 5.13: Comparison of major elements based parameters for the granitoids from the Vumba and the Tati granite-greenstone terrains. (a) Plot of A/CNK (Mol% $Al_2O_3/[Na_2O + K_2O + CaO]$) versus SiO_2. (b) Plot of A/CNK versus Mg#.

5.7 Summary

The major element geochemistry of the mafic lavas from the Tati greenstone belt indicates that these lavas are mainly low-K, Fe-rich quartz tholeiites. However, there are occurrences of the sporadic existence of olivine tholeiites in the Tati greenstone belt. The mafic lavas from the Tati belt have low Mg# less than 0.68, indicating that they are not primary melts, whereas the lavas from the Vumba greenstone belt have Mg# values ranging from 0.48 to 0.78, suggesting a mixture of primary and non-primary melts. Chemical classification of the mafic lavas reveal that they vary from basalt to andesitic basalt.

The spatially associated felsic lavas from the Tati and Vumba greenstone belts exhibit calc-alkaline affinity and have medium-K affinity. Chemical classification indicates that the felsic lavas associated with the mafic lavas from the Tati greenstone belt are essentially dacitic. Moreover, the felsic lavas are metaluminous to slightly peraluminous with alumina saturation indices less than 1.1, which indicates that they are I-type melts.

Gabbroic units are represented by two bodies that exhibit compositional differences in terms of major elements, particularly FeOt and TiO_2. The Phoenix gabbro is characterised by high MgO content and high Mg# averaging 0.81, which are all indicators of cumulate rocks, as confirmed also by their textures. The Selkirk gabbro has low values of Mg# (0.59 to 0.74) and high FeOt abundances. Both gabbroic bodies show a low-K tholeiitic affinity. The diorite unit has high MgO abundances as well as high Mg# averaging 0.74, which is comparable to Mg# values recorded in high-Mg andesites from the Japanese island arc. It belongs to a low-K tholeiite magma series.

Granitoids in the Tati granite-greenstone terrain are metaluminous to slightly peraluminous. The quartz monzonite and monzogranite are mostly of high-K to slightly shoshonitic composition. Based on Na_2O-K_2O-CaO diagram with evolution trends after Hawkesworth and Luas (1994) they define a calc-alkaline trend. Additionally, the quartz monzonite is Al-rich whereas the monzogranite Al-poor. Tonalite-trondhjemite granitoids are high-Al, medium-K and define a sodic evolutionary trend. Trondhjemite is low-Al and medium-K in character with a trondhjemitic evolution trend.

CHAPTER 6

Trace element geochemistry

6.0 Introduction

This chapter focuses on the description of trace element variations and geochemical characteristics of the igneous rocks from the Tati granite-greenstone terrain of the Francistown Granite-Greenstone Complex, whose major element data has been documented in chapter 5. In this study, only the concentrations of a range of trace elements in these various rocks from the Tati granite-greenstone terrain were determined by inductively coupled plasma mass spectrometry (ICP-MS) and X-ray fluorescence spectrometry (XRF). Details of the sample preparation procedures and analytical techniques are presented in Appendix B. For comparison, the concentrations of selected trace elements were determined by both XRF and ICP-MS techniques. The correlation of trace element concentrations that were determined by both techniques, display high correlation coefficients (> 0.9), indicative of a good comparison in concentration values obtained by two different techniques (See appendix C for the correlation plots). However, Zr, Sc and Nb in some samples display poor correlation between the concentration values obtained by XRF and ICP-MS analytical methods. For these three elements the XRF concentration values are higher relative to the values obtained from ICP-MS analyses. This is probably due to incomplete dissolution of Zr, Sc and Nb bearing phases prior to ICP-MS analyses. Therefore, XRF Zr, Sc and Nb data have preferentially been used in this chapter, otherwise the concentration values obtained by ICP-MS technique were used for plotting the data. ICP-MS trace element data for the mafic metavolcanics, felsic metavolcanics, ultramafic intrusives and various felsic granitoids from the Vumba granite-greenstone terrain from previous study (Bagai, 2000) have been included in the data set for regional comparison purpose. Additionally, the data is re-interpreted in the context of the regional evolution of the entire Francistown Granite-Greenstone Complex, hence detailed interpretation, which was never done in the previous study, is involved.

6.1 Trace element mobility evaluation

Thin section analyses of the volcanic rocks of the Neoarchaean greenstone belts of the Francistown Granite-Greenstone Complex have revealed that these greenstone belts experienced deformation and greenschist to lower amphibolite facies metamorphism, which could potentially result in mobility of some elements. Additionally, the samples of volcanic rocks have yielded variable loss on ignition values up to 3.6 wt.% (but most samples have LOI < 2 wt.%) which is an indication of alteration processes that could potentially cause mobility of elements. Based on a large number of studies in Archaean greenstone belts it has been established that some elements are relatively mobile and others less so during alteration and metamorphism, the most vulnerable being the large ion lithophile elements (LILE) such as Ba, K, Rb, Sr and Cs. The high field strength elements (HFSE: Nb, Th, Ti, Ta, P, Hf, Zr, Y), rare earth elements (REE) and some transition metals (Cr, Ni, Co, V) are considered relatively immobile during low grade metamorphism and hydrothermal alteration (e.g. Winchester and Floyd, 1977; Jochum et al., 1991; Pearce, 1996; Kerrich et al., 1999; Polat et al., 1999; Manya, 2004). Nonetheless, it is imperative to test the mobility of trace elements when dealing with Archaean metamorphic terranes such as the Francistown Granite-Greenstone Complex in order to distinguish primary distribution of trace elements from the alteration-induced distribution.

In this study the trace element mobility test adopted is the one first used by Cann (1970) where the correlation matrix for all the elements that should behave incompatibly during mantle partial melting was examined. List of correlation matrices of trace elements determined from both mafic and felsic lavas collected from the Tati greenstone belt, gabbro and diorite are presented in Tables C1 to C5 of Appendix C. These correlation matrices were calculated by the Pearson product-moment coefficient of correlation. According to Pearce (1996) and Cann (1970), when the correlation coefficient for a pair of elements is high (e.g. >0.7 or < -0.7) the ratio of these elements is unlikely to have been changed by post-magmatic alteration processes. If the correlation coefficient is low it indicates that at least one of the elements has been disturbed (Rollinson, 1993). In Table C1 which presents the correlation coefficient of trace elements determined from the Tati mafic lavas, large ion lithophile elements (Rb, Cs, Sr and Ba), Pb, U, Sc, Hf, Nb and LREE (La, Ce, Pr, Nd) exhibit low correlation coefficient values (shaded values in Table C1 of Appendix C) indicating that their primary abundances probably have been disturbed. HFSE and LREE are expected to behave as

immobile elements under low grade metamorphic conditions similar to the ones experienced by the Tati greenstone belt. Ratios of REE and HFSE in greenstone volcanic rocks are not affected by losses and gain of major elements during secondary processes (Condie, 1994). Thus ratios of HFSE and LREE in mafic lavas from the Tati greenstone belt were evaluated in this study by plotting the ratios of Nb/Ce and Th/Ce both normalized to primitive mantle versus LOI values (Fig. 6.1) in order to establish whether the HFSE and LREE abundances are indeed alteration-affected. This technique has been applied in many greenstone belt studies (e.g. Kerrich et al., 1999; Hollings and Wyman, 1999; Manya, 2004) and has proved to be effective in distinguishing Th-Nb-LREE systematics that have been disturbed by hydrothermal alteration and metamorphism from the Th-Nb-LREE systematics affected by other petrological processes such as fractional crystallization, crustal contamination and heterogeneous source partial melting. As can be seen from Figure 6.1 the Nb/Ce_{pm} and Th/Ce_{pm} do not show any correlation with LOI which suggests that the distribution of Th-Nb-LREE concentrations in the Tati mafic lavas cannot be attributed to secondary processes such as hydrothermal alteration, weathering and metamorphism. Therefore, the low correlation coefficients displayed by HFSE and LREE must be due to petrological processes. Table C2 (Appendix C) list correlation matrices for trace elements calculated from the Tati felsic lavas. Correlation matrices for the gabbros are given in Tables C3 and C4 (Appendix C). LILE except Cs in Tati felsic lavas possess high correlation coefficient suggesting non-disturbance of primary concentration by secondary processes. Sc, Zr and Nb are trace elements which have recorded low correlation coefficients. However, the ratio of Zr/Nb does not reflect any significant correlation with LOI as anticipated for rocks which have their Zr and Nb concentrations disturbed by hydrothermal alteration or/and metamorphism. Therefore, their abundance should be due to igneous processes. For these reasons more emphases in this study is placed on REE and HFSE, particularly in metavolcanic rocks, gabbro and diorite. LILE and other elements that show signs of alteration are given less attention, and their interpretation is guided by information from the immobile elements.

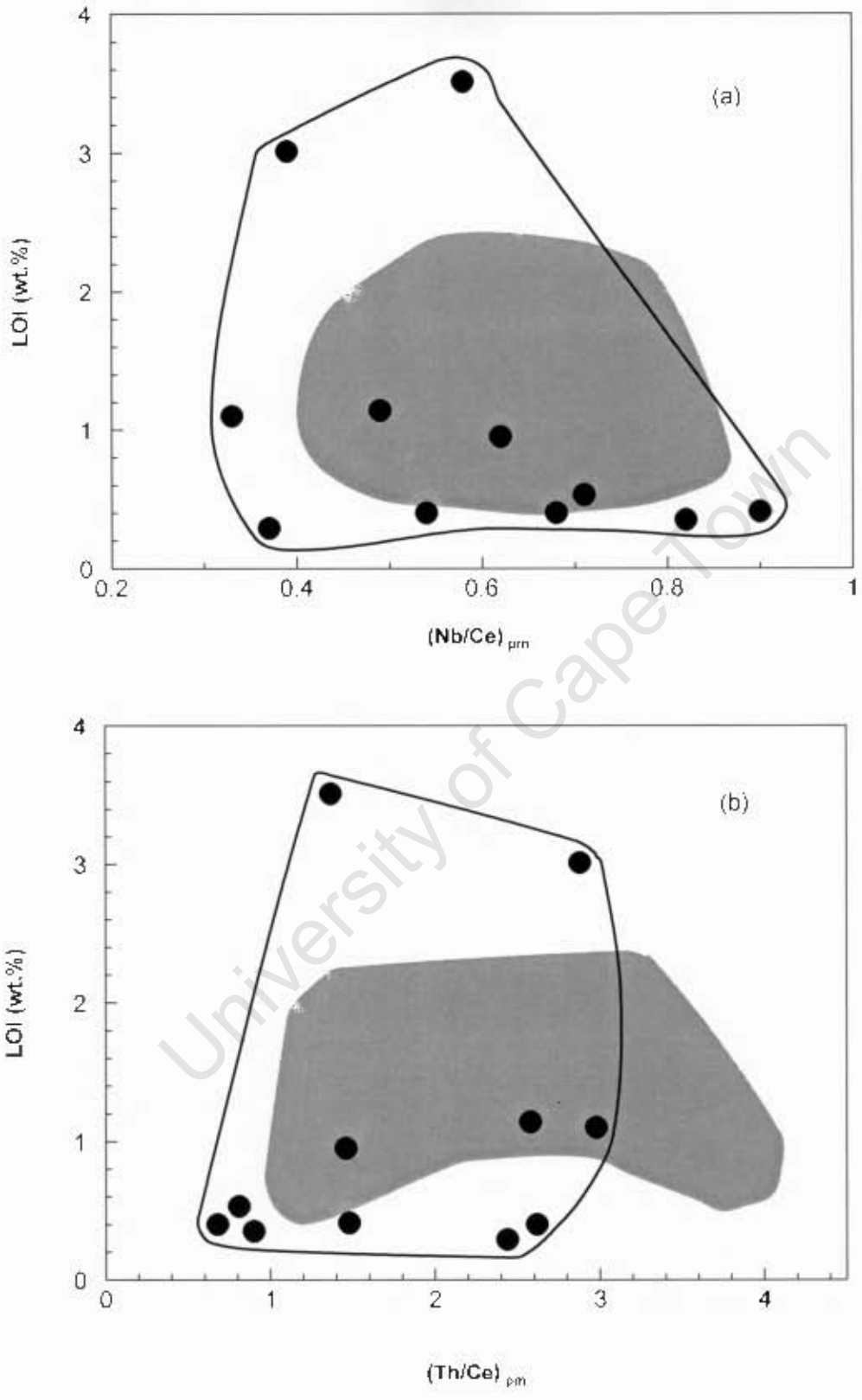

Fig. 6.1: Loss on ignition (LOI) versus Nb/Ce_{pm} (a) and Th/Ce_{pm} (b) for the Tat mafic lavas indicating that TH-Nb-Ce inter-element ratios do not correlate with alteration and metamorphism. The grey field represents Vumba mafic lavas. Pm = primitive mantle normalized.

6.2 Mafic lavas

Twelve samples of mafic lavas from the Tati greenstone belt have been analysed for their trace elements abundance and are presented in Table 6.1.

6.2.1 Compatible trace elements

Compatible trace element variations in the Tati mafic lavas are illustrated with respect to Mg# in Figure 6.2. The variation of trace elements from the Vumba mafic lavas are shown in the background for comparison. Vanadium shows similar behaviour in both the Tati and Vumba mafic lavas by having a broad range of abundance (128 to 388 ppm; Table 6.1) and defining a good negative correlation with Mg# (Fig. 6.2a). However, the samples from the Vumba mafic lavas define a better negative trend than the samples from the Tati mafic lavas. Chromium displays a similar behaviour in both samples from the two mafic lavas in terms of concentration range (41 – 460 ppm for Tati, Table 6.1) and positive correlation with Mg#, except sample ZBT61, which plot as an outlier in the variation diagram (Fig. 6.2b). The mafic lavas from the two greenstone belts exhibit overlapping Ni concentration ranges (Tati: Ni = 46 – 167 ppm, Table 6.1; Vumba: Ni = 35 – 264 ppm, Table B5 in Appendix B) with samples from the Vumba greenstone belt recording the broadest and highest values (Fig. 6.2c). Ni concentrations in the mafic lavas from the Tati greenstone belt define a mild positive correlation with Mg# similar to the Vumba mafic lavas. Similarly Co displays a great overlap in terms of its abundances in the mafic lavas from the two greenstone belts (Tati: Co = 35 – 58 ppm, Table 6.1). The Co abundance in the Tati mafic lavas shows a scattered relationship with the Mg# whereas in the Vumba samples it defines a decreasing trend with increasing Mg#. The Tati mafic lavas possess relatively higher abundance of Sc (37 – 52 ppm; Table 6.1) which defines a broad and steep negative trend against the Mg# (Fig. 6.2e) whilst mafic lavas from the Vumba greenstone belt have recorded restricted Sc abundance which displays a shallow poor negative trend versus Mg# (Fig. 6.2e). However, the trace element mobility test suggests that Sc has been slightly disturbed by secondary processes in the mafic lavas from the Tati greenstone belt. In summary, variation diagrams for the mafic lavas involving compatible elements versus Mg# as an index of differentiation indicate depletion of Cr and Ni accompanied by enrichment of V, Co and Sc. This qualitatively suggests the dominance of olivine fractionation over pyroxene. The trends will be dealt with quantitatively later in the petrogenesis chapter.

Table 6.1: Trace element analyses of the mafic lavas from the Tati greenstone belt. Zr* = XRF determined value.

Sample	ZBT-46	ZBT-48	ZBT-50	ZBT-51	ZBT-53	ZBT-54	ZBT-55	ZBT-57	ZBT-58	ZBT-60	ZBT-61	ZBT-62
Sc*	42.9	41.5	44.0	51.8	41.4	34.9	47.5	47.2	37.1	46.5	45.0	39.0
V	165	210	219	388	267	178	315	247	221	293	262	256
Cr	460	404	433	41.3	315	125	215	166	106	228	245	262
Co	35.0	44.6	48.8	47.3	49.9	39.8	54.3	40.0	46.5	57.8	43.5	44.9
Ni	112	147	160	46.5	169	57.5	87.9	69.7	61.4	87.8	78.9	145
Cu	16.2	66.0	72.7	94.6	86.3	12.9	95.6	89.6	41.9	117	59.4	44.4
Rb	0.70	3.50	1.82	2.02	1.67	1.27	0.51	0.56	0.86	1.50	1.34	1.13
Sr	92.4	90.6	72.5	170	168	124	122	86.3	127	118	137	141
Cs	0.10	0.41	0.10	0.05	0.28	0.23	0.06	0.04	0.16	0.24	0.13	0.06
Ba	23.0	43.8	73.6	79.7	34.1	14.4	40.9	32.7	23.0	34.5	19.8	21.8
Y	13.5	14.7	15.7	34.9	18.9	14.3	24.3	16.1	16.9	24.4	19.4	19.7
Zr*	53.0	52.0	54.1	113	64.7	79.3	102	92.0	87.6	88.1	57.2	60.3
Nb*	1.94	1.43	1.91	4.64	2.46	3.09	4.68	4.19	2.81	3.91	1.80	2.45
Hf	0.68	0.74	0.86	1.56	0.43	1.41	1.33	0.68	2.04	1.22	0.77	1.38
Ta	0.07	0.08	0.13	0.28	0.12	0.02	0.24	0.13	0.21	0.17	0.06	0.05
Pb	2.51	2.59	2.23	1.55	1.14	3.93	3.28	2.53	4.99	4.83	7.18	18.6
Th	1.11	1.12	1.21	0.60	0.29	2.71	1.30	0.82	3.06	1.12	0.32	0.20
U	0.21	0.25	0.26	0.13	0.07	0.76	0.35	0.23	0.87	0.32	0.09	0.06
La	4.20	4.13	4.27	4.71	3.29	9.40	7.77	4.72	10.2	7.20	3.02	2.57
Ce	8.89	9.56	9.79	14.0	9.00	19.6	18.7	11.6	21.4	16.9	8.30	7.47
Pr	1.25	1.25	1.30	2.23	1.37	2.29	2.52	1.56	2.54	2.27	1.29	1.18
Nd	6.10	6.08	6.34	12.5	7.50	10.2	12.2	7.63	11.2	11.2	7.04	6.58
Sm	1.70	1.71	1.79	4.10	2.40	2.36	3.34	2.11	2.66	3.13	2.23	2.14
Eu	0.63	0.62	0.63	1.33	0.85	0.69	1.16	0.74	0.83	1.04	0.87	0.82
Gd	2.19	2.27	2.39	5.61	3.23	2.69	4.17	2.69	3.07	3.87	3.05	3.07
Tb	0.37	0.38	0.41	0.93	0.53	0.43	0.68	0.45	0.49	0.65	0.52	0.51
Dy	2.48	2.73	2.88	6.31	3.59	2.70	4.68	3.07	3.20	4.42	3.57	3.59
Ho	0.53	0.58	0.60	1.33	0.76	0.57	0.98	0.64	0.67	0.94	0.75	0.77
Er	1.57	1.72	1.79	3.90	2.21	1.66	2.84	1.88	1.91	2.80	2.24	2.25
Tm	0.23	0.25	0.26	0.55	0.32	0.24	0.40	0.27	0.28	0.40	0.32	0.33
Yb	1.54	1.67	1.76	3.68	2.07	1.58	2.63	1.79	1.82	2.67	2.12	2.14
Lu	0.23	0.25	0.26	0.54	0.30	0.23	0.37	0.26	0.26	0.40	0.30	0.32
ΣREE	31.9	33.2	34.5	61.7	37.4	54.6	62.4	39.4	60.6	58.0	35.6	33.7
Th/Nb	0.57	0.78	0.63	0.13	0.12	0.88	0.28	0.20	1.09	0.29	0.18	0.08
Ce/Nb	4.58	6.69	5.12	3.02	3.66	6.35	3.99	2.76	7.63	4.33	4.61	3.05
Th/La	0.27	0.27	0.28	0.13	0.09	0.29	0.17	0.17	0.30	0.15	0.11	0.08
Ce/Yb	5.78	5.72	5.58	3.81	4.35	12.4	7.11	6.48	11.7	6.34	3.91	3.50
Th/Yb	0.73	0.67	0.69	0.16	0.14	1.71	0.50	0.46	1.68	0.42	0.15	0.09
Zr/Nb	27.3	36.3	28.3	24.3	26.3	25.6	21.7	21.9	31.2	22.5	31.8	24.6
Zr/Hf	77.6	70.4	62.9	72.3	150	56.2	76.4	136	43.0	72.0	74.0	43.8
Th/Ta	15.1	13.4	9.11	2.13	2.47	145	5.53	6.21	14.4	6.44	5.10	3.89
Ta/Yb	0.05	0.05	0.08	0.08	0.06	0.01	0.09	0.07	0.12	0.06	0.03	0.02
Ta/Nb	0.04	0.06	0.07	0.06	0.05	0.01	0.05	0.03	0.08	0.04	0.03	0.02
Th/Ce	0.13	0.12	0.12	0.04	0.03	0.14	0.07	0.07	0.14	0.07	0.04	0.03
La/Nb	2.17	2.89	2.23	1.02	1.34	3.04	1.66	1.13	3.64	1.84	1.68	1.05

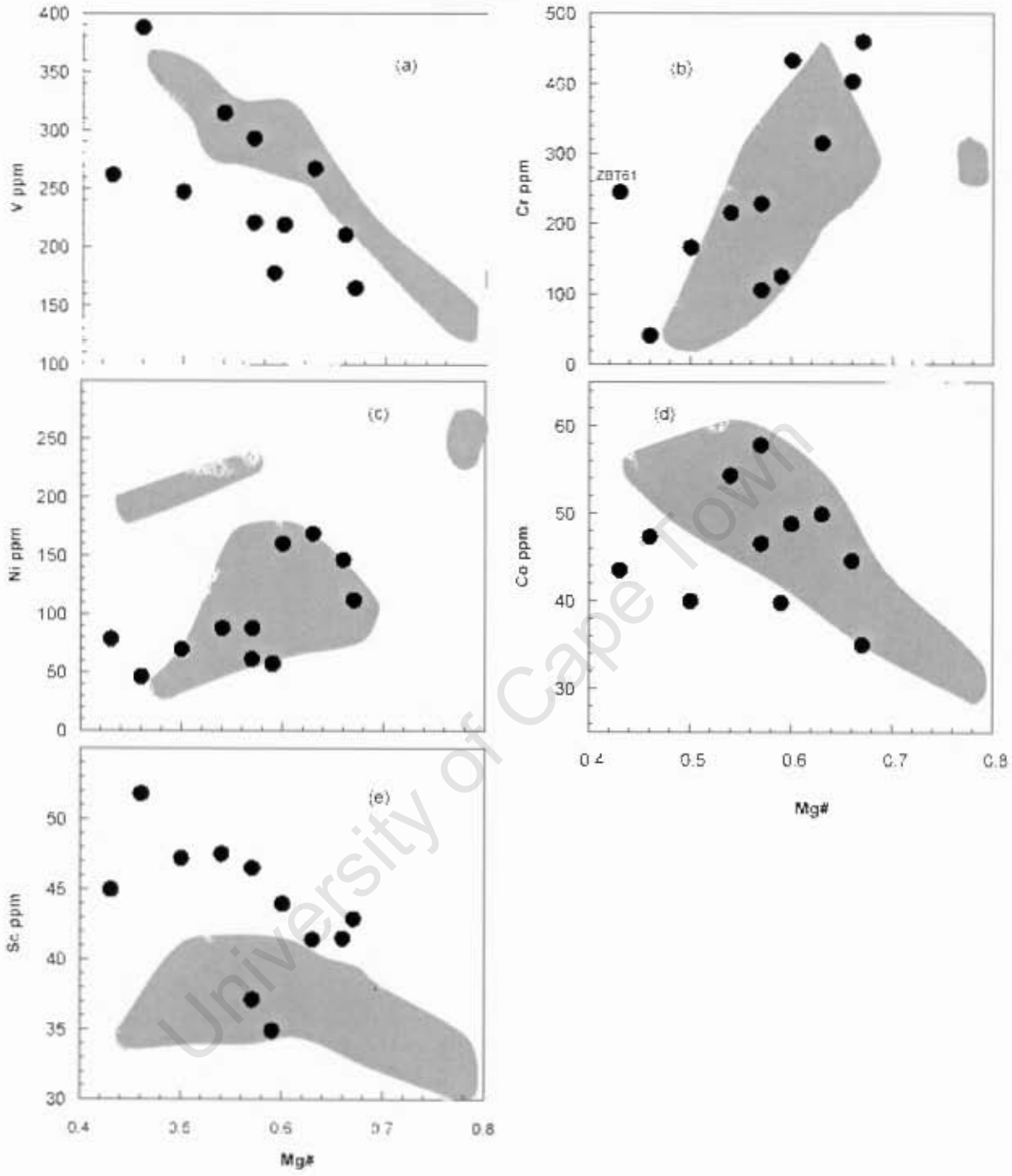

Fig. 6.2: Variation diagrams of selected compatible trace elements versus Mg# for the mafic metavolcanic samples from the Francistown Granite-Greenstone Complex. Grey field represent Vumba samples.

6.2.2 Incompatible trace elements

Incompatible trace element variation in the mafic lavas from the Tati greenstone belt is shown in Figure 6.3 with respect to Mg#. The HFS elements (Nb, Zr, Y and Th) show similar behaviour to

those of the Vumba mafic lavas, all displaying overlapping ranges in abundances and showing decreasing trends with increasing Mg# (Fig. 6.3A a-d). However, there are a few outliers from the Tati samples in all the variation diagrams involving Nb, Zr, Y and Th. The Hf concentration shows a scattered relationship with Mg# (Fig. 6.3Ae) in the samples from the Tati mafic lavas whereas in the samples from the Vumba greenstone belt it exhibits a negative correlation. A variation diagram involving La (LREE representative) shows a scattered correlation against Mg# (Fig. 6.3Af) for the mafic lavas. HFSE enrichment accompanies the depletion of Cr and Ni in the mafic lavas of both the greenstone belts.

The incompatible trace elements versus Zr display positive correlations with the Vumba samples showing tight correlations (Fig. 3B).

6.2.2.1 Rare earth element (REE) patterns

The REE characteristics of the Tati mafic lavas can be divided into sub-groups in which each sub-group has distinct and relatively uniform characteristics. This is readily apparent on the chondrite-normalized REE patterns for the mafic lavas presented in Figure 6.4. The mafic lavas from the Tati greenstone belt display three sub-groups of REE patterns like the mafic lavas from Vumba greenstone belt. However, the three sub-groups observed in the Tati mafic lavas resemble the two common sub-groups in the Vumba mafic lavas, presumably reflecting similar petrogenetic processes.

Sub-group 1 of the mafic lavas of the Tati greenstone belt displays mild enrichment in the light REE relative to the heavy REE hence fractionated REE patterns (La/Yb_N = 2.2-1.7). Additionally, the sub-group exhibits variable negative Eu anomalies (Eu/Eu* = 1.0 – 0.8) and overall REE abundances that range from 31.9 to 62.4 ppm (Table 6.1). This sub-group compares with the sub-group 1 of the mafic lavas of the Vumba greenstone belt, which exhibits fractionated REE profiles (La/Yb_N = 2.8 - 1.6; Fig. 6.4d) with variable Eu anomalies (Eu/Eu* = 1.1 - 0.8). Their overall REE abundances vary between 30.4 and 72.7ppm.

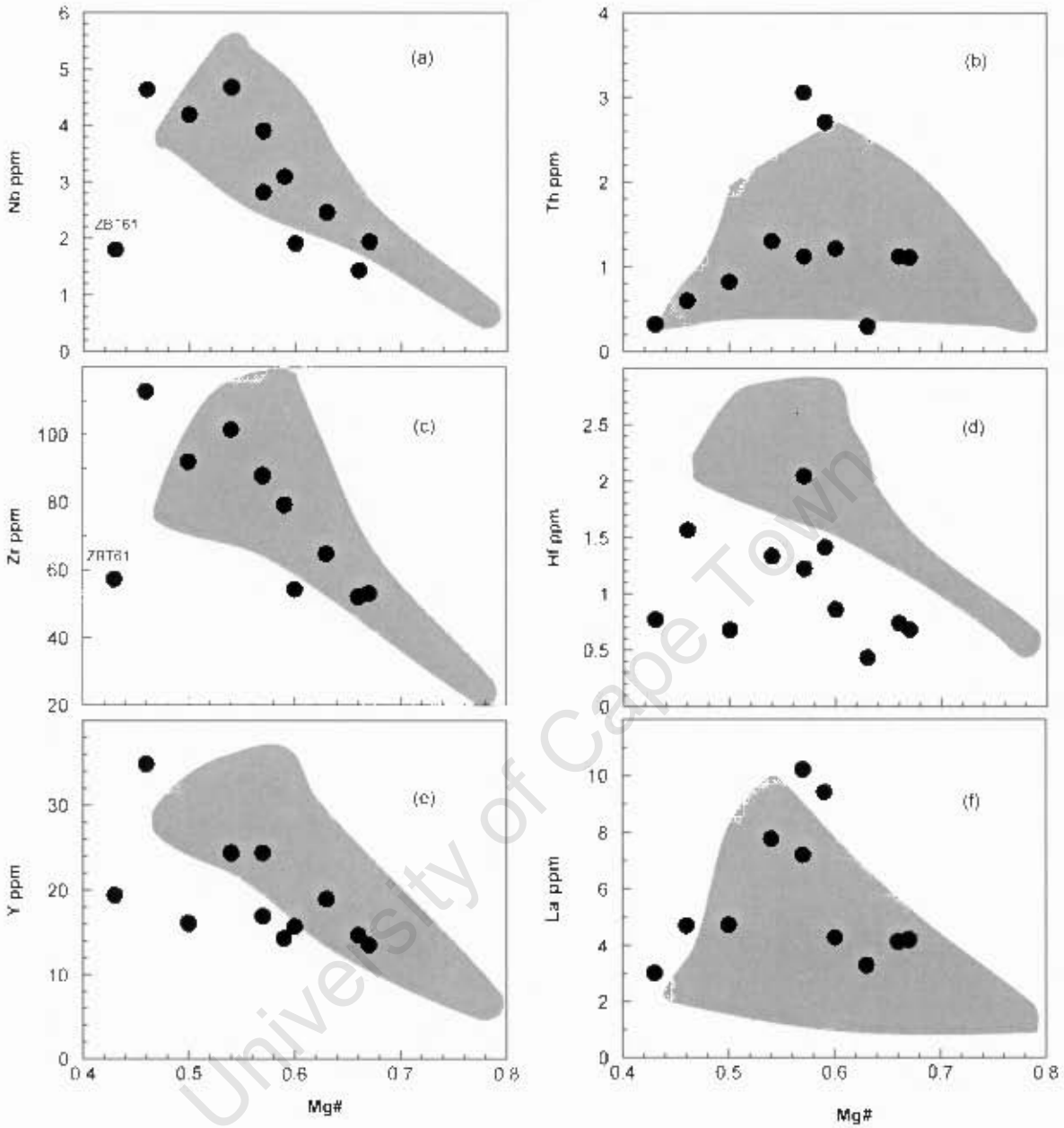

Fig. 6.3 A: Variation diagrams of selected incompatible trace elements versus Mg# for the mafic metavolcanic samples from the Francistown Granite-Greenstone Complex. Grey fields represent the Vumba samples.

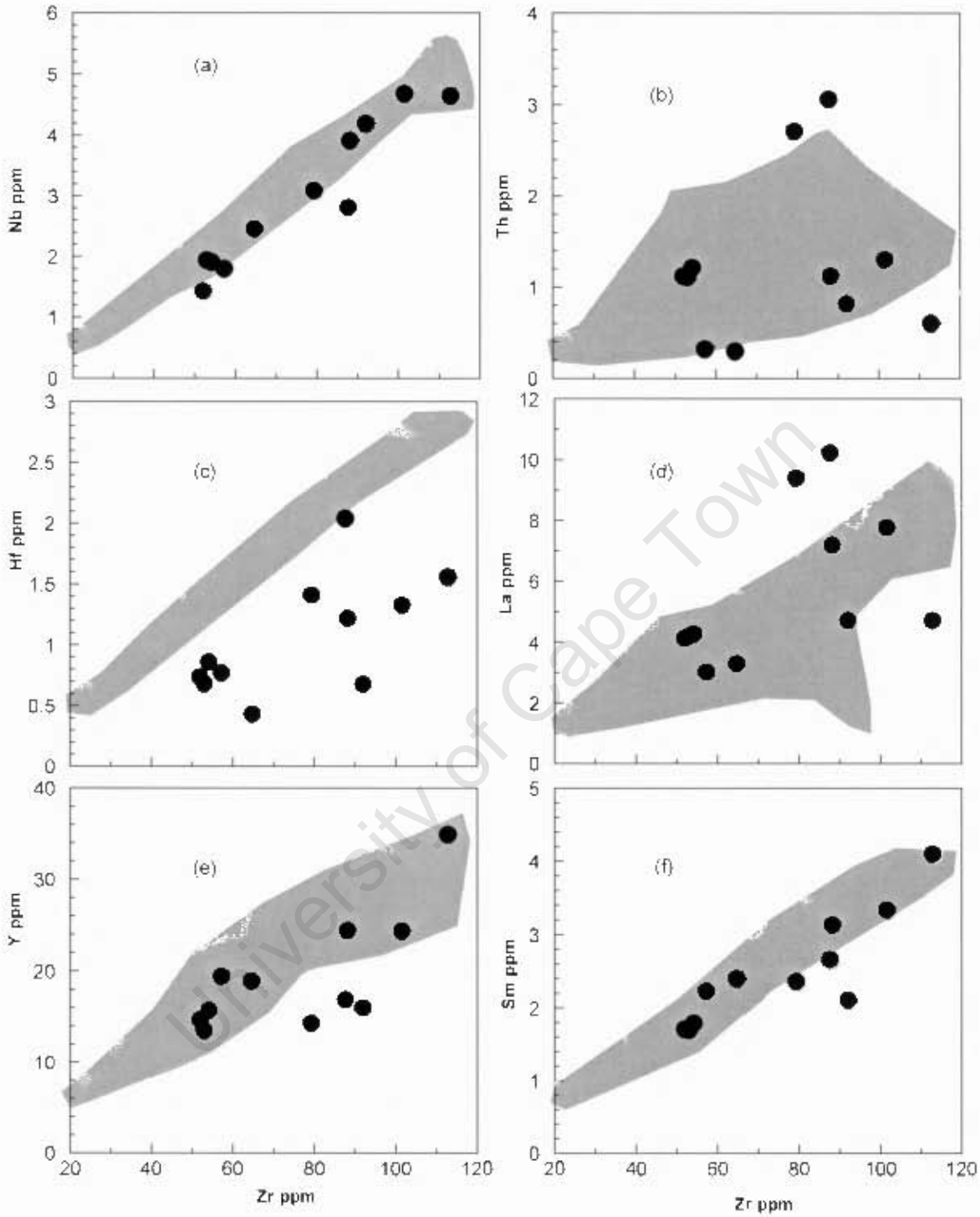

Fig. 6.3B: Variation diagrams of selected incompatible trace elements versus Zr for the mafic metavolcanic samples from the Francistown Granite-Greenstone Complex. Grey fields represent the Vumba samples.

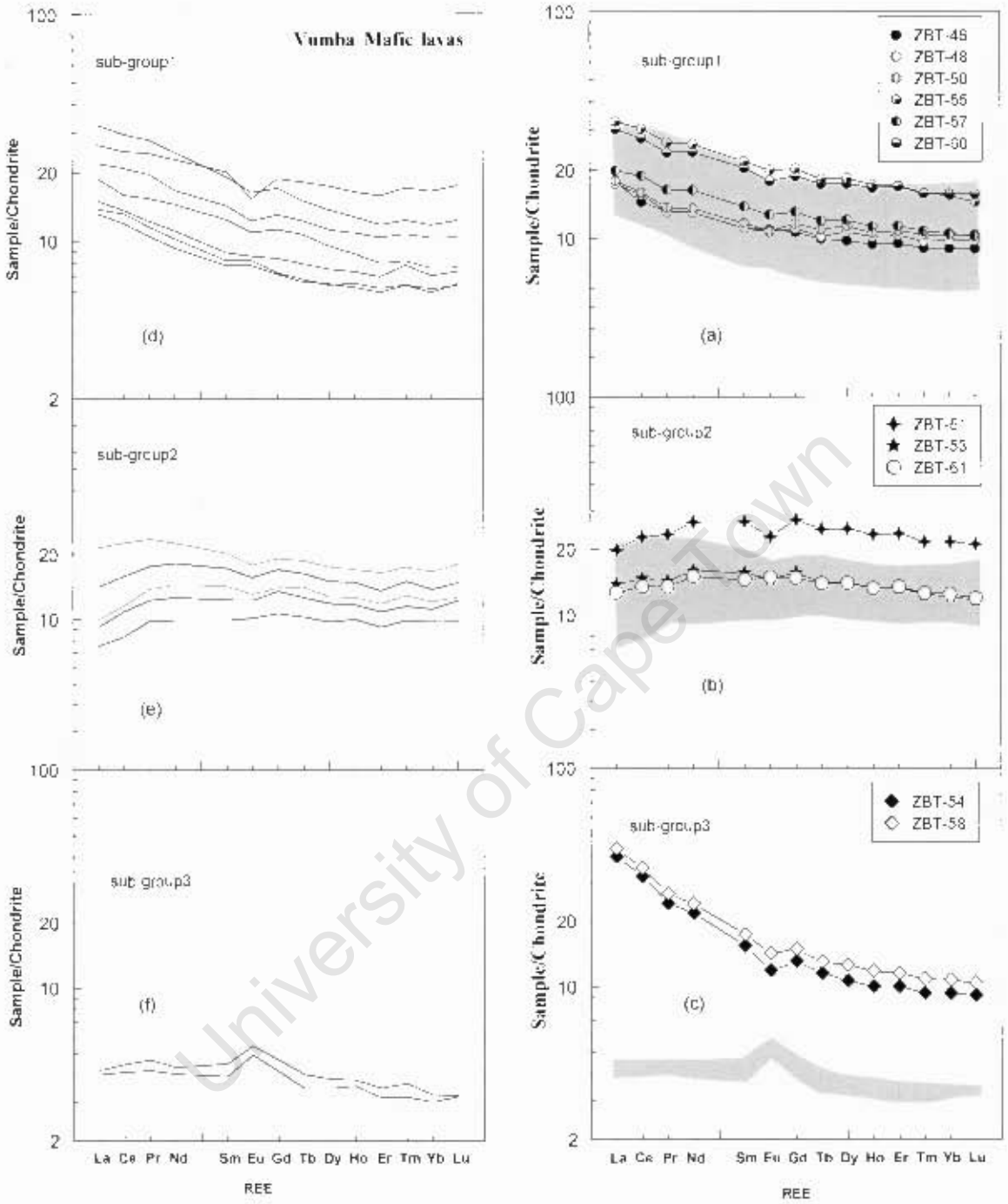

Fig. 6.4: Chondrite-normalized REE patterns for the mafic lavas from the Tati greenstone belt. Grey fields are mafic lavas from the Vumba greenstone belt (normalizing values after Sun and McDonough, 1989).

Sub-group 2 of the Tati mafic lavas, which is represented by relatively few samples, displays flat REE patterns (La/Yb_N = 1.14 – 0.92) with no to prominent negative Eu anomalies (Eu/Eu^* = 1.0 – 0.85). In addition the sub-group exhibits LREE depletion (La/Sm_N = 0.88 – 0.74). The overall REE abundances overlap those of the sub-group 1 mafic lavas (ΣREE = 33.7 – 61.4; Table 6.1). Sub-

group 2 mafic lavas resembles the sub-group 2 mafic lavas of the Vumba greenstone belt in the sense that they are both characterised by non-fractionated REE profiles with no to minor negative Eu anomalies (Eu/Eu* = 1.0 – 0.9; Fig. 6.4b,e). Furthermore, REE analyses of the Tati mafic lavas revealed a third less common sub-group (sub-group 3) which is characterised by prominent LREE enrichment and negative Eu anomalies. Though this sub-group resembles the sub-group 1, it possesses significant enrichment in LREE contents (Fig. 6.4c). The third sub-group from the Vumba mafic lavas exhibits flat REE patterns (La/Yb_N = 1.3) with prominent positive Eu anomalies (Eu/Eu* = 1.22 – 1.18) and low overall REE abundances (ΣREE = 12.8 – 13.9).

6.2.2.2 Multi-element profiles

The three distinct sub-groups within the Tati mafic lavas are also apparent on the primitive mantle-normalized multi-element profiles presented in Figure 6.5. Samples of the sub-group 1 mafic lavas display multi-element profiles with variable enrichment in large ion lithophile elements (LILE), flat REE, negative Nb, Ta, Hf, Sr, variable Ti, P and prominent positive Pb anomalies (Fig. 6.5a). Additionally, the profiles reflect Th enrichment with respect to light REE. In comparison, the sub-group 1 mafic lavas of the Vumba greenstone belt exhibits multi-element profiles with negative Nb, Ta, P, Ti and variable Sr anomalies (Fig. 6.5a). Moreover, the profiles reflect variable LILE enrichment as well as Th enrichment with respect to LREE.

Sub-group 2 Tati mafic lavas exhibits similar multi-element profiles to those of sub-group 1 but lack LILE enrichment, prominent Nb negative anomalies and Th enrichment with respect to LREE (Fig. 6.5b). The multi-element profiles of the sub-group 2 show prominent negative Hf, P and variable generally positive Sr anomalies. The multi-element profiles for the sub-group 3 mafic lavas resemble those of sub-group 1 to a large extent except they possess positive Zr anomalies and negative Ti & P anomalies. In comparison, the sub-group 1 mafic lavas of the Vumba belt resembles sub-group 3 of Tati mafic lavas in terms of multi-element profiles. It is worth mentioning that the Zr and Nb analyses for sample ZBT-53 by XRF and ICP-MS do not agree, which makes the Hf and Ta negative anomalies suspect (Fig. 6.5b).

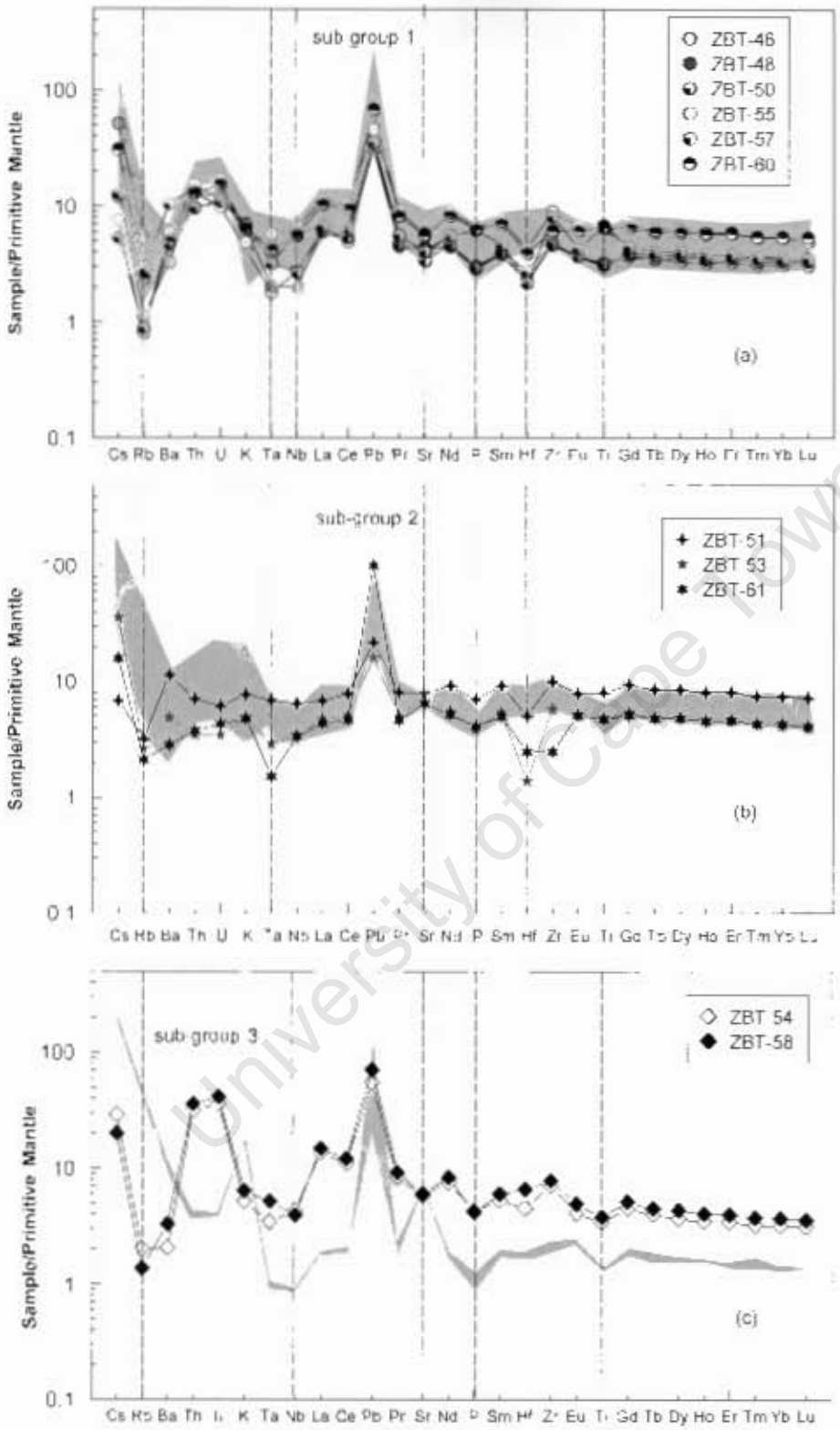

Fig. 6.5: Primitive mantle –normalized multi-element diagrams for the Tati mafic lavas (normalizing values after Sun and McDonough, 1989). (a) and (c) Sub-groups 1 & 3 mafic lavas with negative Nb anomalies; (b) Sub-group 2 mafic lavas with no negative Nb anomalies. Grey fields represent samples from the Vumba greenstone belt.

The sub-group 2 samples from both belts are comparable except that Vumba samples display a mixture of positive and negative Sr, P and Ti anomalies. The obvious difference is that the Tati sub-group is devoid of any Ti anomaly. The Vumba sub-group 3 profiles are comparable with those of sub-group 1 to some extent despite incomparable REE patterns. The profiles show negative Nb, P and Ti anomalies and Th enrichment with respect to LREE.

All the mafic lavas from the Vumba and Tati greenstone belts show a strong positive Pb anomaly, probably indicative of crustal contamination. However, it should be noted that modern arc volcanics that display no evidence of crustal contamination could also show large positive Pb anomalies due to subduction contamination.

6.3 Felsic lavas

Five representative samples of felsic lavas from the Tati greenstone belt have been analysed for trace element abundances and are compared to trace element analyses of 15 samples of felsic lavas from the Vumba greenstone belt available from a previous study (Bagai, 2000). The trace element analyses for the felsic lavas from the Tati belt are presented in Table 6.2.

6.3.1 Compatible trace elements

Compatible trace element variation within the felsic lavas from the Tati and the Vumba greenstone belts are presented in Figure 6.7 versus SiO_2 wt.% as index of differentiation. The compatible trace elements display scattered relationships with SiO_2 wt.% except V contents in the Vumba samples that show a negative trend, in line with amphibole fractionation. Nevertheless, the felsic lavas from the Tati greenstone belt are distinct from the Vumba felsic lavas in terms of compatible trace element abundances. Low Sc, high Cr, Ni, V and Co (Table 6.2) abundances characterise the Tati felsic lavas. Sample ZBT 41 is an outlier in terms of V (49.6 ppm), Ni (14.8 ppm) and Co (3.55 ppm) concentrations which are much lower than in other samples. The Vumba felsic lavas possess lower abundances and broader ranges of V, Cr, Ni and Co than the Tati felsic lavas. It is worth-noting that the Ni contents in the Tati felsic and mafic lavas partially overlap.

Table 6.2: Trace element analyses of the felsic lavas from the Tati greenstone belt. Zr* = XRF determined value.

Sample	ZBT-41	ZBT-42	ZBT-43	ZBT-44	ZBT-45
Sc*	16.8	17.8	15.8	14.7	14.5
V	49.6	93.6	91.8	95.2	93.2
Cr	102	105	104	97.3	105
Co	3.55	14.8	13.4	14.6	11.7
Ni	14.8	52.7	60.8	62.9	44.2
Cu	22.6	28.9	13.7	16.5	3.52
Rb	26.9	47.3	41.1	49.4	51.9
Sr	50.0	134	179	126	95.5
Cs	0.94	1.20	1.08	1.66	1.43
Ba	176	346	283	345	392
Y	5.20	11.1	12.3	13.1	11.5
Zr*	173	172	166	172	166
Nb*	6.45	6.44	5.85	6.01	6.30
Hf	1.88	3.52	3.14	2.64	3.12
Ta	0.09	0.48	0.48	0.51	0.50
Pb	4.26	7.27	9.45	8.20	7.10
Th	3.18	6.34	6.18	6.36	6.12
U	0.63	1.22	1.21	1.40	1.35
La	10.2	20.9	19.1	20.6	17.6
Ce	18.7	40.8	37.2	39.3	34.2
Pr	2.05	4.36	3.98	4.12	3.60
Nd	8.08	16.8	15.5	16.0	14.0
Sm	1.51	3.14	2.96	2.99	2.56
Eu	0.48	0.93	0.84	0.88	0.67
Gd	1.41	2.78	2.57	2.81	2.52
Tb	0.20	0.39	0.38	0.41	0.37
Dy	1.09	2.36	2.38	2.46	2.29
Ho	0.21	0.45	0.46	0.49	0.44
Er	0.60	1.22	1.27	1.42	1.23
Tm	0.08	0.17	0.18	0.20	0.17
Yb	0.55	1.15	1.19	1.34	1.16
Lu	0.08	0.16	0.17	0.18	0.17
ΣREE	45.19	95.64	88.21	93.16	81.01
Th/Nb	0.49	0.98	1.06	1.06	0.97
La/Nb	1.58	3.25	3.27	3.43	2.80
Ce/Nb	2.90	6.33	6.35	6.53	5.43
Ce/Pb	4.38	5.61	3.93	4.79	4.81
Th/Yb	5.82	5.53	5.21	4.76	5.28
Th/La	0.31	0.30	0.32	0.31	0.35
Zr/Nb	26.9	26.8	28.4	28.5	26.3
Zr/Hf	92.2	49.0	52.8	65.1	53.1
Ta/Hf	0.05	0.14	0.15	0.19	0.16

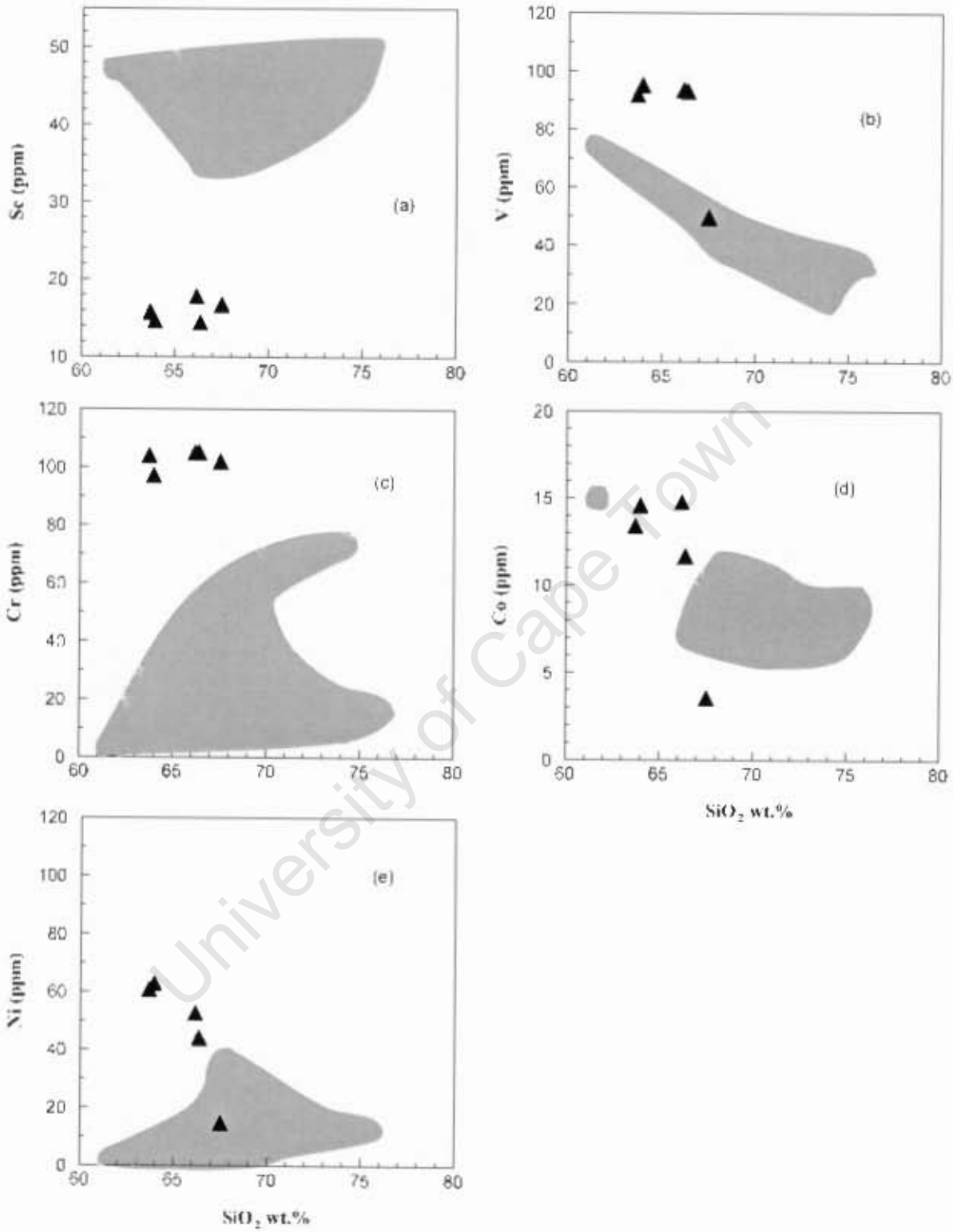

Fig. 6.6: Variation diagrams of selected compatible trace elements versus SiO_2 wt.% for felsic lavas from the Tati greenstone belt. Felsic lavas from the Vumba greenstone belt are shown in grey fields.

6.3.2 Incompatible trace elements

Incompatible trace elements variations in the felsic lavas are presented in Figure 6.7. Ba, a large ion lithophile element, Th and La (light rare earth element) exhibit a weak relationship with increasing SiO_2 wt.%, whereas Zr, Nb and Sr show a tight correlation.

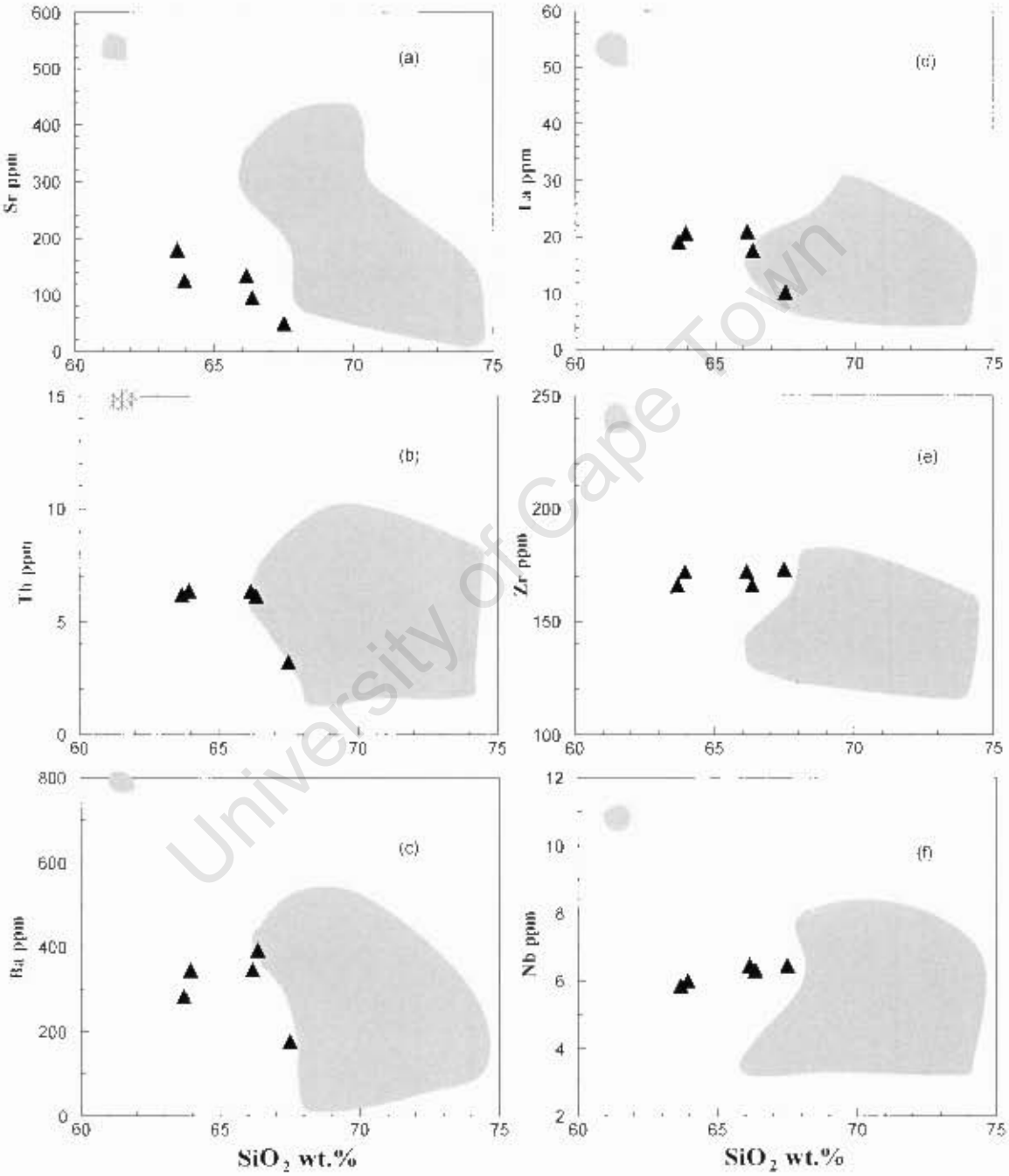

Fig. 6.7: Variation diagrams of selected incompatible trace elements versus SiO_2 wt.% for felsic lavas from the Tati greenstone belt. Vumba greenstone belt felsic lavas are shown as grey fields.

6.3.2.1 Rare earth element (REE) pattern

Chondrite normalized REE data for the felsic lavas from the two greenstone belts are presented in Figure 6.8. The Tati felsic lavas display fractionated REE patterns (La/Yb_N = 12.6 - 10.3; La/Sm_N = 4.34 - 4.07; Gd/Yb_N = 2.08 - 1.70) with negligible negative to no Eu anomalies (Eu/Eu^* = 1.0 - 0.9) except Sample ZBT 41, which has a pronounced negative anomaly (Eu/Eu^* = 0.8; Fig. 6.8). The overall REE abundances range from 45.2 to 95 6 ppm. In comparison, felsic lavas from the Vumba greenstone belt is characterised by fractionated REE patterns with variable Eu anomalies (Fig. 6.8). Additionally, the Vumba felsic lavas display a broad range of overall REE abundances. Overall the two felsic lavas are comparable in terms of REE characteristics.

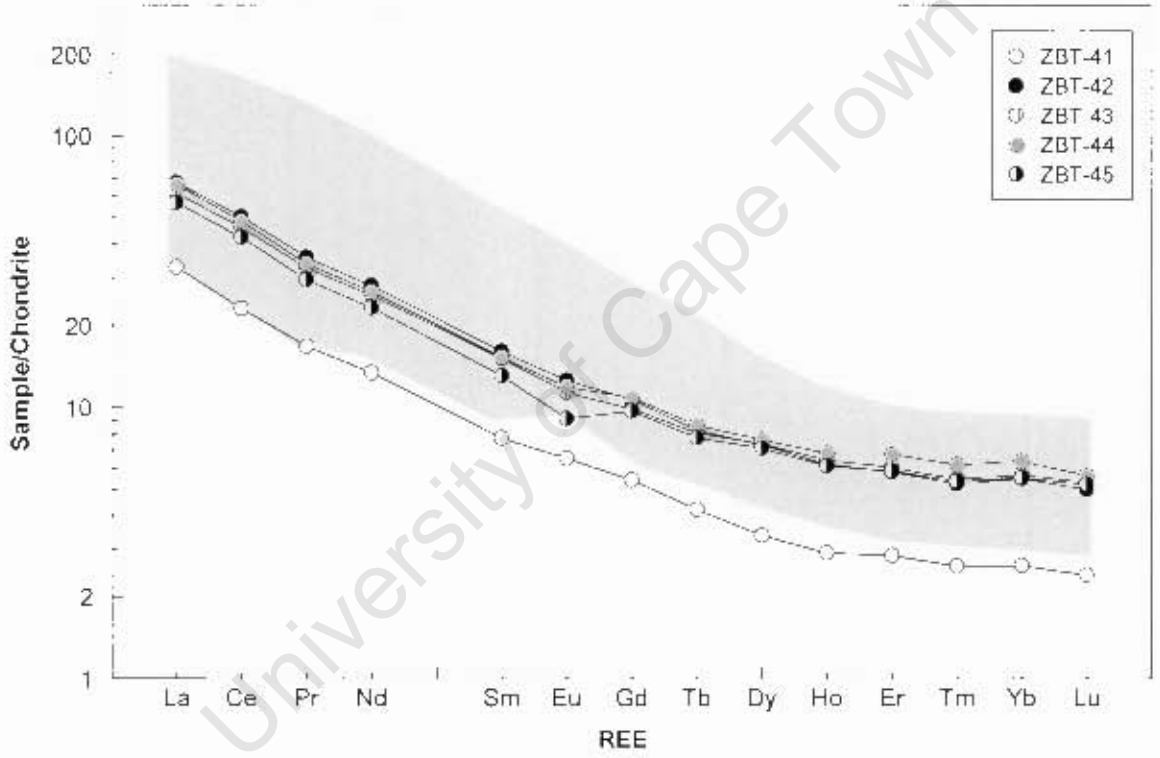

Fig. 6.8: Chondrite-normalized REE patterns for the felsic lavas from the Tati greenstone belt. Felsic lavas from the Vumba greenstone belt are shown as grey fields (normalizing values after Sun and McDonough, 1989).

6.3.2.2 Multi-element profiles

On primitive mantle normalized multielement plots, the felsic lavas from the Tati greenstone belt are characterised by negative Nb, Ta, Ti, Sm, P, Sr, Ba and positive Zr anomalies (Fig. 6.9). LILE in the multielement plot of the Tati felsic lavas show coherent patterns indicating that their primary abundance has been preserved. This is consistent with the results of the trace element mobility test

presented in section 6.1. Felsic lavas from the Vumba greenstone belts exhibit prominent negative Nb, P and Ti anomalies (Fig. 6.10). Additionally the multielement plots of the felsic lavas show negative Sm anomalies, positive Zr, Hf anomalies and variable negative and positive Sr anomalies. Notably, the felsic lavas from the Vumba area possess a deeper Ti trough than their Tati counterpart. Large ion lithophile elements (LILE) display chaotic patterns most likely due to alteration. Nonetheless, the multielement plots are LILE-enriched.

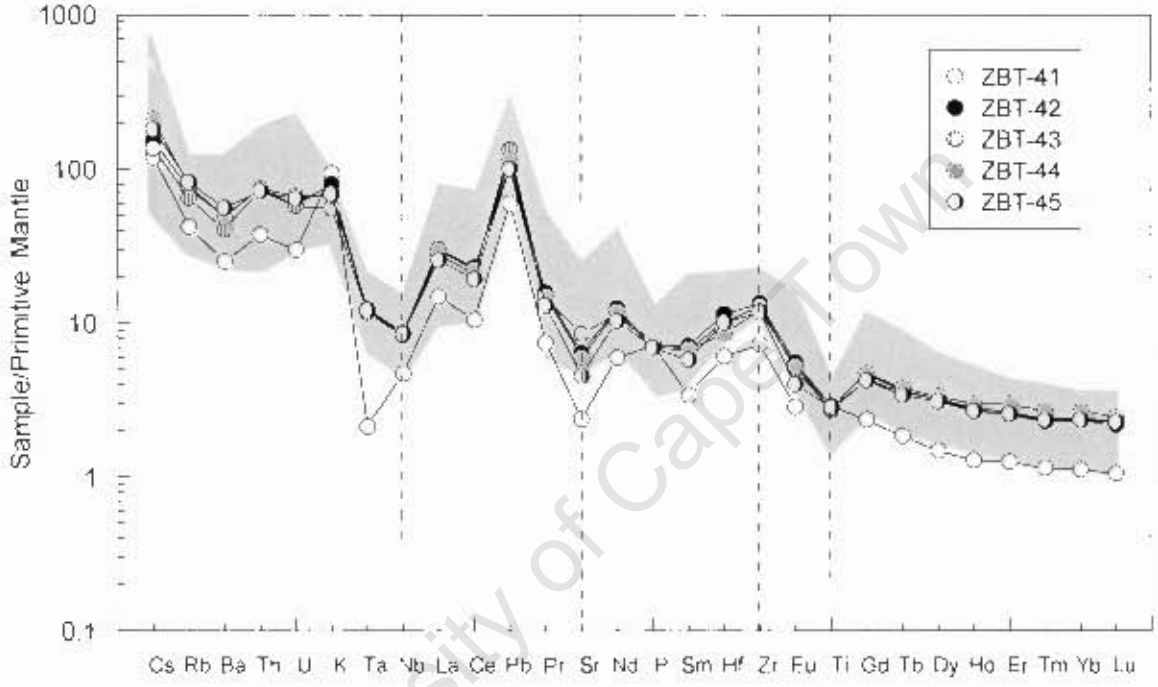

Fig. 6.9: Primitive mantle-normalized multi-element plots for felsic lavas from the Tati greenstone belt. Felsic lavas from the Vumba greenstone belt are shown as grey fields (normalizing values are from Sun and McDonough, 1989).

6.4 Gabbros

A total of eleven representative samples from the Phoenix (5) and Selkirk (6) gabbro intrusions were analysed for a range of trace elements. The analyses are reported in Table 6.3. The gabbro intrusions are compared with analyses of mafic lavas from the Tati greenstone belt and samples of ultramafic intrusives from the Vumba greenstone belt.

Table 6.3: Trace element analyses of the Phoenix and Selkirk Gabbro intrusions from the Tati granite-greenstone terrane. Zr* = XRF determined value. *N.d.* = not detected.

Unit	Phoenix - Gabbro					Selkirk - Gabbro					
Sample	ZBT-37	ZBT-38	ZBT-39	ZBT-40	ZBT-81	ZBT-63	ZBT-67	ZBT-71	ZBT-72	ZBT-73	ZBT-75
Sc*	17.4	24.8	17.9	12.7	32.19	39.0	40.5	19.3	15.5	39.0	19.1
V*	70.3	96.2	68.3	45.7	119	267	376	115	88.6	272	102
Cr*	755	1336	670	214	897	319	355	1051	578	321	1025
Co*	77.2	67.6	63.2	79.8	52.8	52.8	34.7	83.5	32.2	39.4	57.6
Ni	795	603	568	983	502	158	233	720	404	158	677
Cu	98.6	184	97.3	438	251	34.9	22.4	173	25.2	46.2	896
Rb	5.87	6.62	3.59	3.00	3.84	1.13	1.96	0.41	5.04	2.82	1.69
Sr	73.4	77.4	93.5	97.8	91.8	141	108	99.6	106	136	88.4
Cs	0.59	0.69	0.44	0.43	0.40	0.06	0.09	0.06	0.20	0.07	0.12
Ba	18.3	24.0	14.8	12.6	15.9	22.8	35.3	10.8	72.9	46.7	26.5
Y	2.97	3.81	3.49	2.64	4.09	20.8	19.9	7.00	5.26	19.5	5.32
Zr*	8.15	8.81	10.2	8.00	10.72	60.3	33.21	18.5	6.59	37.8	5.94
Nb	0.23	0.29	0.30	0.22	0.21	2.45	2.48	0.73	0.53	2.25	0.43
Hf	0.15	0.18	0.19	0.15	0.18	1.38	0.87	0.33	0.18	1.18	0.20
Ta	*n.d.*	0.01	0.01	*n.d.*	0.15	0.05	0.03	*n.d.*	*n.d.*	0.04	0.13
Pb	2.05	2.14	2.02	2.15	1.60	18.6	21.7	38.2	118	20.4	24.5
Th	0.05	0.05	0.06	0.04	0.06	0.20	0.22	0.11	0.09	0.19	0.07
U	0.02	0.02	0.02	0.01	0.02	0.06	0.06	0.07	0.03	0.06	0.03
La	0.51	0.47	0.50	0.45	0.47	2.57	3.10	1.36	0.95	2.58	1.05
Ce	1.33	1.25	1.32	1.19	1.21	7.47	8.87	3.36	2.35	7.46	2.41
Pr	0.19	0.18	0.18	0.16	0.19	1.18	1.35	0.48	0.35	1.17	0.33
Nd	1.00	1.08	1.11	0.95	1.05	6.58	7.57	2.56	1.85	6.68	1.76
Sm	0.32	0.39	0.39	0.30	0.34	2.14	2.47	0.77	0.58	2.15	0.60
Eu	0.20	0.21	0.20	0.18	0.18	0.82	0.88	0.37	0.30	0.78	0.29
Gd	0.47	0.53	0.52	0.40	0.48	3.07	3.28	1.08	0.79	3.02	0.83
Tb	0.08	0.10	0.09	0.07	0.09	0.51	0.58	0.18	0.14	0.51	0.15
Dy	0.55	0.67	0.62	0.50	0.57	3.59	3.83	1.30	0.96	3.57	0.97
Ho	0.12	0.15	0.13	0.10	0.12	0.77	0.81	0.26	0.21	0.75	0.22
Er	0.33	0.42	0.41	0.30	0.37	2.25	2.37	0.81	0.57	2.22	0.64
Tm	0.05	0.07	0.06	0.04	0.05	0.33	0.34	0.12	0.09	0.32	0.09
Yb	0.36	0.43	0.40	0.30	0.36	2.14	2.21	0.80	0.57	2.16	0.63
Lu	0.06	0.07	0.06	0.04	0.05	0.32	0.32	0.12	0.08	0.31	0.09
ΣREE	5.59	6.00	5.99	5.00	5.56	33.7	38.0	13.6	9.79	33.7	10.1
Th/Nb	0.21	0.18	0.19	0.18	0.28	0.08	0.09	0.16	0.16	0.08	0.17
Th/Yb	0.14	0.12	0.14	0.13	0.16	0.09	0.10	0.14	0.16	0.09	0.11
Zr/Nb	35.1	30.5	33.9	35.8	52.2	24.6	13.4	25.2	12.4	16.8	14.0
Zr/Yb	22.8	20.5	25.6	26.7	29.5	28.2	15.1	23.0	11.6	17.5	9.49
Zr/Hf	52.8	47.7	52.6	53.4	58.3	43.8	38.4	56.5	36.0	32.0	30.1
Th/La	0.10	0.11	0.11	0.09	0.12	0.08	0.07	0.08	0.09	0.07	0.07
Zr/Y	2.74	2.31	2.91	3.02	2.62	2.90	1.67	2.64	1.25	1.94	1.12
Ce/Nb	5.74	4.33	4.41	5.33	5.91	3.05	3.57	4.58	4.41	3.32	5.67
Sr/Y	24.69	20.30	26.77	36.99	22.42	6.81	5.44	14.23	20.19	6.99	16.60
Sr/Ce	55.05	61.92	70.62	82.30	75.69	18.94	12.21	29.62	45.22	18.26	36.66

6.4.1 Compatible trace elements

Compatible trace element abundances for the two gabbro intrusions are shown in Figure 6.10 where the fields for serpentinite, metapyroxenite and the mafic lavas are indicated in the background for comparison. The Phoenix gabbro is characterised by high and variable concentrations of the compatible trace elements (e.g. Ni = 568 to 983 ppm; Cr = 214 to 1336 ppm: Table 6.3). Sc and V abundances in the Phoenix gabbro and serpentinite overlap and are lower than the concentrations recorded from the metapyroxenite and the collective mafic lavas of the Tati and Vumba greenstone belts (Fig. 6.10). However, the concentrations of Cr, Co and Ni in the Phoenix gabbro are lower than in the serpentinite but higher than in the mafic lavas. The serpentinite samples possess very high concentrations of Cr, which suggests the prevalence of phases like chromite in their composition.

The Selkirk gabbro is characterised by variable concentrations of compatible trace elements that define two groups (Fig. 6.10). One group, comprising samples with relatively low Mg#, displays compatible trace element abundances that are indistinguishable from the mafic lavas whereas the second group, which comprises higher Mg# samples, possesses compatible trace element concentrations similar to the Phoenix gabbro.

6.4.2 Incompatible trace elements

In terms of incompatible trace element abundances, the Selkirk gabbro still maintains the two groups (Fig. 6.11) where group 1 exhibits higher abundances than group 2. Additionally, group 2 Selkirk gabbro shows overlapping incompatible trace element contents with the Phoenix gabbro and serpentinite. The incompatible trace element abundances in the Phoenix gabbro are low, with very narrow ranges (Table 6.3) comparable with those of the serpentinite (Fig. 6.11).

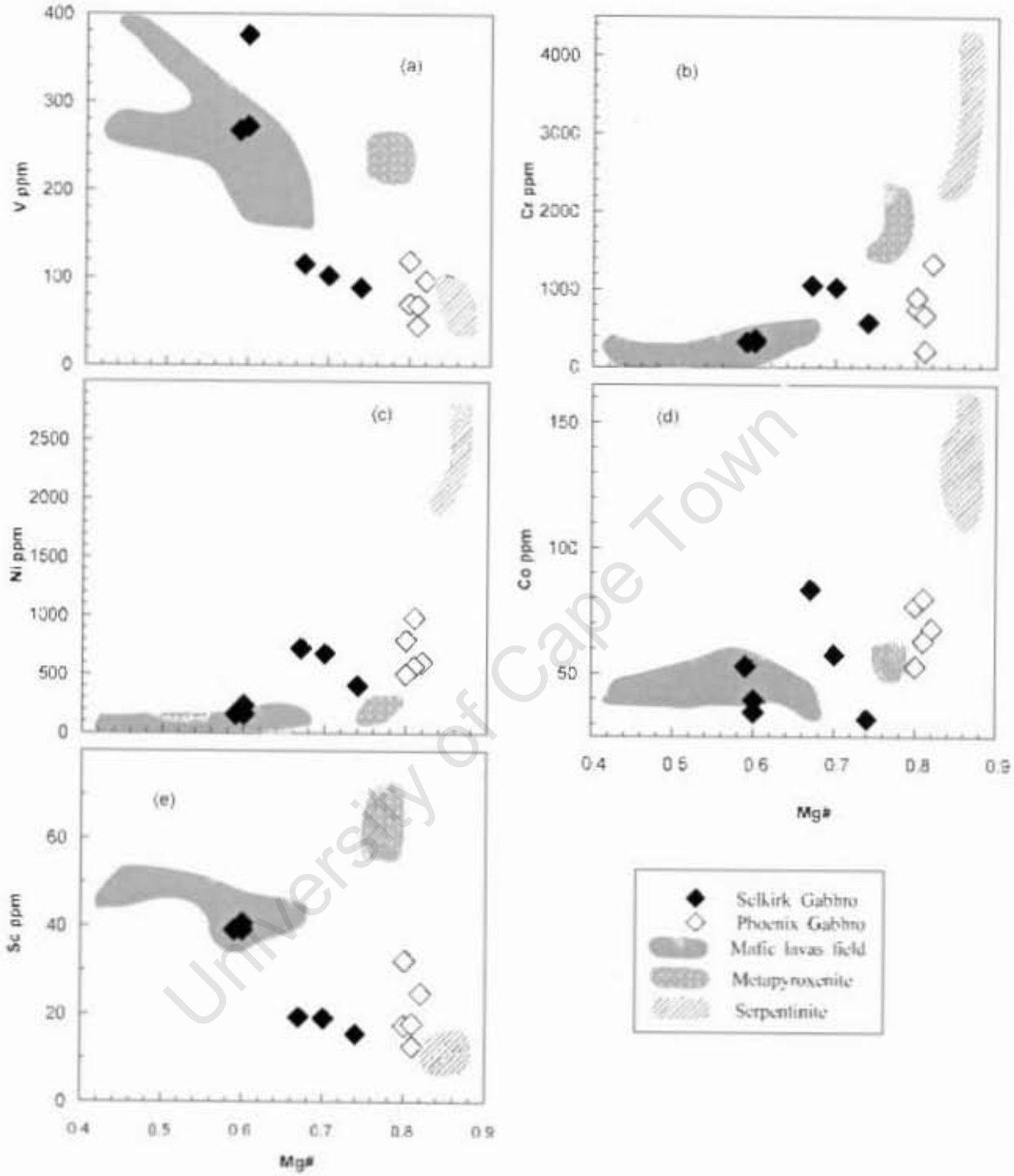

Fig. 6.10: Variation diagrams of selected compatible trace elements versus Mg# for Phoenix and Selkirk Gabbro intrusions from the Tati granite-greenstone terrain. Fields of serpentinite, metapyroxenite from the Vumba granite-greenstone terrain as well as the mafic lavas are shown as grey fields for comparison.

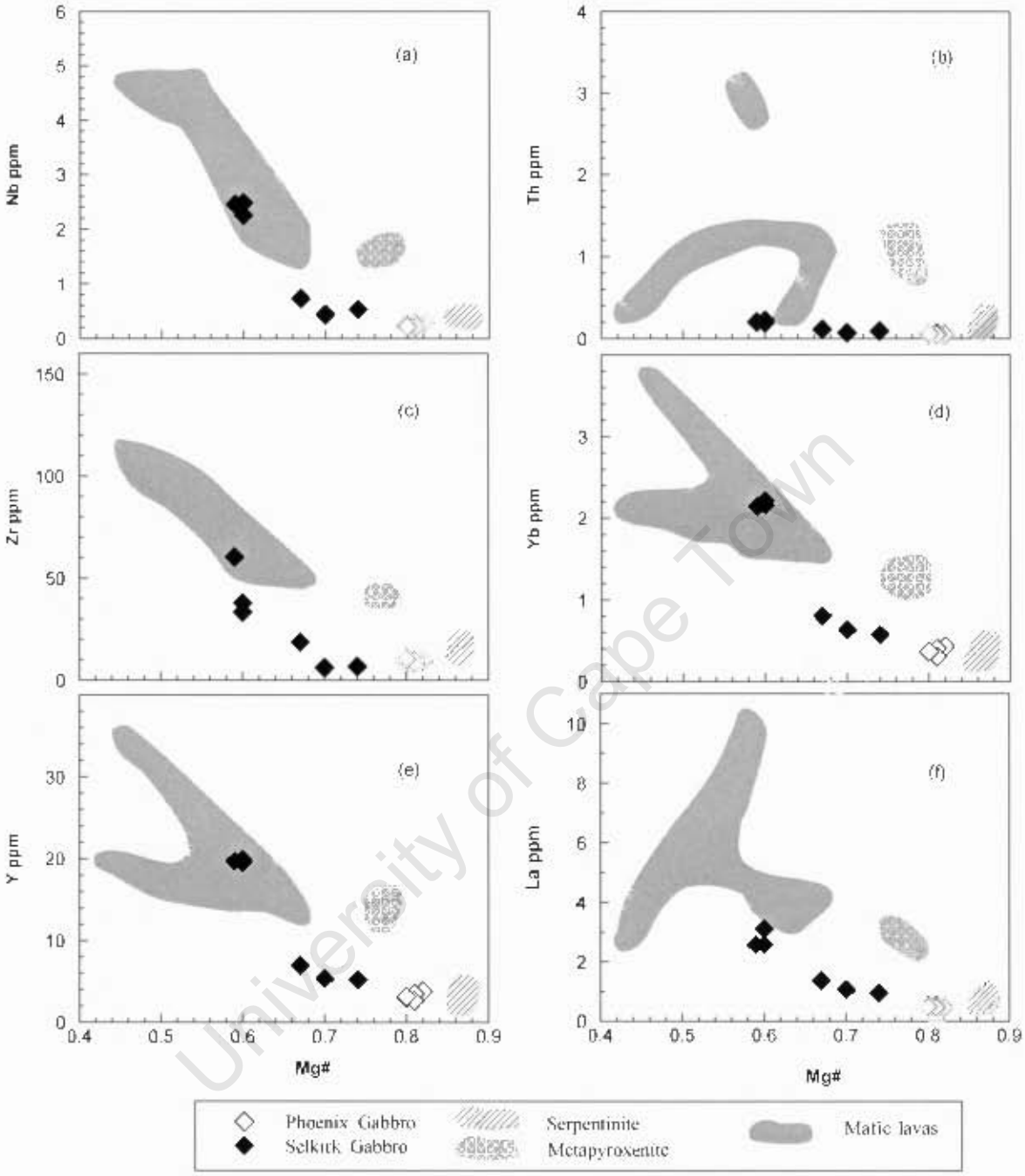

Fig. 6.11: Variation diagrams of selected incompatible trace elements versus Mg# for Phoenix and Selkirk Gabbro intrusions from the Tati granite-greenstone terrain. Fields of serpentinite, metapyroxenite from the Vumba granite-greenstone terrain as well as the mafic lavas are shown as grey fields for comparison.

6.4.2.1 Rare earth element (REE) patterns

Chondrite normalized REE plots for the Phoenix and Selkirk gabbros are presented in Figure 6.12. The Selkirk gabbro REE patterns maintain the two groups that were revealed by the compatible and incompatible trace element distributions (Fig. 6.12a). One group, the relatively low Mg# samples, is characterised by slightly LREE depleted REE patterns (La/Yb_N = 0.95 – 0.81; La/Sm_N = 0.79 – 0.76), negligible negative Eu (Eu/Eu* = 0.98 – 0.94) anomalies. Additionally, this group has higher total REE abundances (ΣREE = 38.0 – 33.7) than the second group (ΣREE = 13.6 – 9.79). The second group which is composed of high Mg# samples, possesses generally flat REE patterns (La/Yb_N = 1.14 – 1.13) with prominent positive Eu (Eu/Eu* = 1.35 -1.25) anomalies. The Phoenix gabbro displays REE patterns that are flat to slightly LREE depleted (La/Yb_N = 1.01 – 0.74; La/Sm_N = 1.00 – 0.77) with prominent positive Eu (Eu/Eu* = 1.64 – 1.28) anomalies consistent with significant plagioclase enrichment and low total REE abundances (ΣREE = 6.00 – 5.00; Table 6.3, Fig. 6.12b). The REE patterns for the serpentinite and metapyroxenite are presented in Figure 6.12 for comparison. However, the REE patterns of these ultramafic intrusives are flat with no Eu anomalies, except one sample of the serpentinite that has a negative Eu anomaly.

6.4.2.2 Multi-element profiles

Primitive mantle normalized multielement plots for the two gabbroic intrusions are presented in Figure 6.13. Two sub-groups of gabbros can be identified from the Selkirk samples that correspond to the two sub-groups already revealed by REE patterns. The first group which correspond to sub-group 1 of the REE patterns is characterised by weak negative Nb (Nb/La_{pm} = 0.86-0.80), and Th, positive Sr, and P, variable Zr and Hf anomalies (Fig.6.13a). The second sub-group displays prominent negative Nb (Nb/La_{pm} = 0.54-0.39), and Th, positive Sr, negative P, Zr, Hf and Ti anomalies. Both groups show similar coherent negative Rb anomalies. The REE abundances in the second group are almost equivalent to the composition of the primitive mantle whereas the first group possesses REE abundances that are about 4 times the primitive mantle composition. Primitive mantle normalized multi-element plots for the Phoenix gabbro exhibit conspicuous negative Th, Nb (Nb/La_{pm} = 0.59-0.43), positive Sr, negative P, Hf, positive Eu and negative Ti anomalies. Additionally, the Phoenix gabbro is depleted in HFSE and REE, and highly enriched in large ion lithophile elements (LILE) compared to the Selkirk gabbro. Furthermore, the HFSE and REE abundances of the Phoenix gabbro are lower than the primitive mantle composition. The multi-

element profiles for the ultramafic intrusives from the Vumba greenstone belt are presented in Figure 6.13 for comparison with gabbro intrusions from the Tati granite-greenstone terrain.

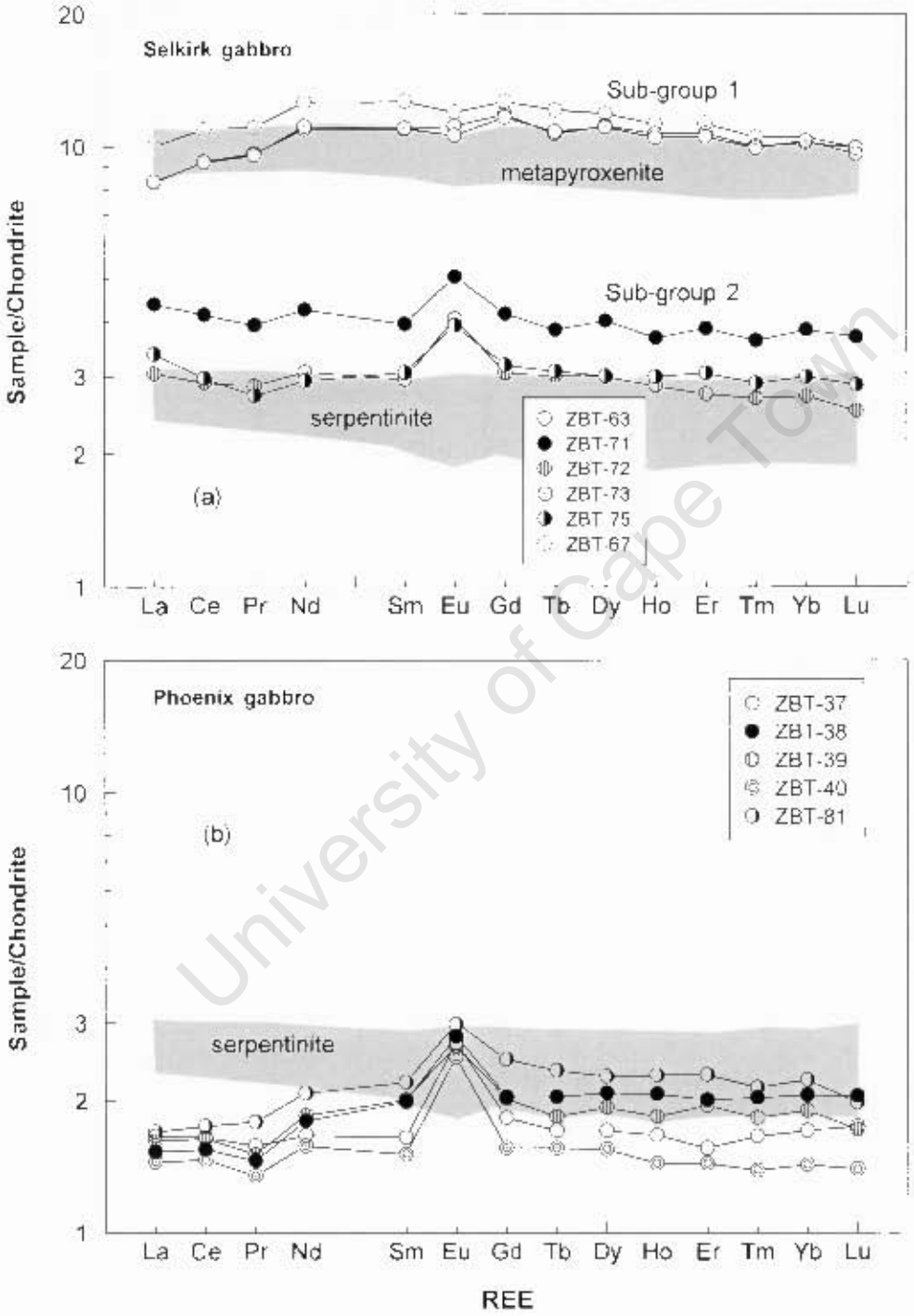

Fig. 6.12: Chondrite-normalized REE patterns for the gabbro intrusions in the Tati granite-greenstone terrain (normalizing values are after Sun and McDonough, 1989). (a) Selkirk Gabbro REE plot showing two sub-groups. (b) Phoenix Gabbro REE plots. Metapyroxenite and Serpentinite samples from the Vumba greenstone belt are shown as grey fields.

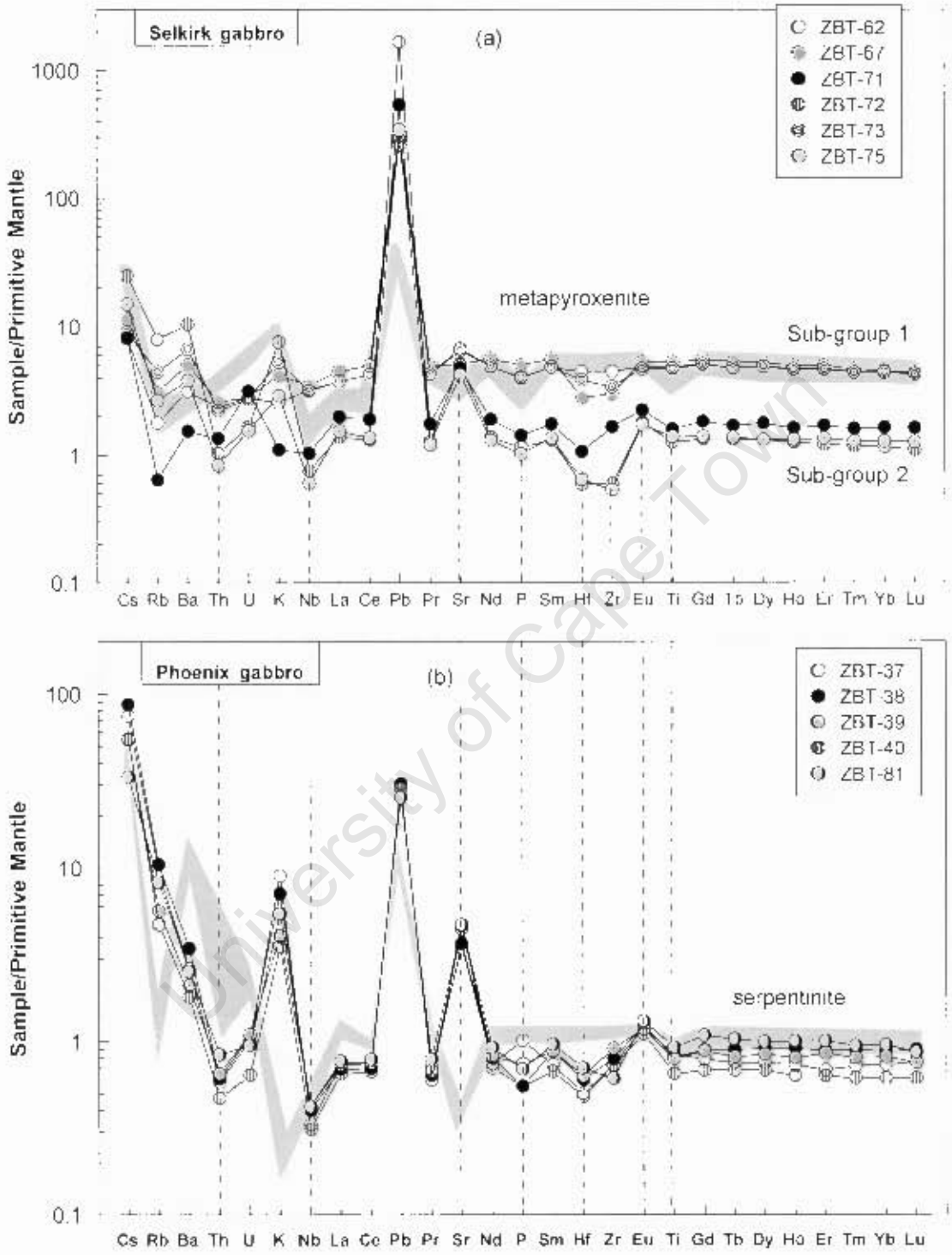

Fig. 6.13 Primitive mantle-normalized multi-element plots for the gabbroic intrusions from the Tati granite-greenstone terrain (normalizing values are from Sun and McDonough, 1989). (a) Selkirk Gabbro profiles defining two sub-groups. (b) Phoenix Gabbro profiles. Dashed lines highlight the significant anomalies. Metapyroxenite and Serpentinite samples from the Vumba greenstone belt are shown as grey fields.

6.5 Diorite

Ten representative samples of the diorite unit from the Tati granite-greenstone terrain were analyzed for a range of trace elements and the results are recorded in Table 6.4.

6.5.1. Compatible trace elements

Compatible trace element abundance variations within the diorite are presented in Figure 6.14. Fields for the Phoenix and Selkirk gabbro intrusions are indicated in the background for comparison purpose. Sc displays uniform distribution against Mg# except sample ZBT-23 which is an outlier with very low content (Sc = 28.7 ppm). V and Co show concentration ranges that vary negatively with the increase in Mg# (Table 6.4; Fig. 6.14b, d). However, samples ZBT-19 and ZBT-23 are outliers in the variation diagram of Co versus Mg#. Cr and Ni in the diorite exhibit broad concentration ranges (Table 6.4) that widely increase with increasing Mg# (Fig. 6.14c, e). The concentration of the compatible elements in the diorite rarely overlaps the concentration fields of the gabbro intrusions within the same area.

6.5.2. Incompatible trace elements

The diorite samples exhibit a wide range of incompatible trace element abundances (Fig. 6.15), which comprise two sub-groups, one exhibiting higher abundances of incompatible trace elements and the other having low contents similar to the Phoenix gabbro. Samples ZBT17 to ZBT21 possess higher concentration of Th, Zr, Y and La than samples ZBT22 to ZBT24 which are characterised by low abundances of the same elements (Table 6.4). The sub-group with low incompatible element content corresponds to samples with higher Mg# (Mg# ≥ 0.74).

Table 6.4: Trace element analyses of the diorite from the Tati granite-greenstone terrain. Zr* = XRF determined value. *N.d.* = not detected.

Sample	ZBT-17	ZBT-18	ZBT-19	ZBT-20	ZBT-21	ZBT-22	ZBT-23	ZBT-24	ZBT-25	ZBT-26
Sc*	53.6	49.8	47.5	45.0	50.7	52.2	28.7	47.0	47.1	48.8
V*	164	169	152	140	148	118	69.5	120	114	106
Cr*	61.1	126	117	137	96.5	45.3	174	186	168	232
Co*	49.9	52.4	45.5	49.6	51.2	50.8	52.8	47.1	45.0	47.0
Ni*	140	145	131	168	143	92	204	188	122	134
Cu	134	102	127	129	133	113	151	127	40.5	34.3
Rb	21.6	9.85	5.45	18.3	10.6	4.93	2.28	0.86	1.06	3.15
Sr	165	158	182	206	158	203	181	167	207	185
Cs	1.22	0.66	0.59	0.80	0.51	0.23	0.21	0.21	0.10	0.13
Ba	92.5	68.5	56.6	72.3	48.3	33.6	26.4	22.14	28.2	70.0
Y	7.99	8.49	7.82	6.81	7.26	4.03	1.88	3.78	3.01	3.27
Nb	1.50	1.28	1.44	0.68	0.97	0.06	0.13	0.01	1.07	0.14
Zr*	36.9	37.5	38.2	26.9	33.6	7.42	6.13	5.84	7.2	9.11
Hf	0.68	0.58	0.74	0.44	0.55	0.14	0.09	0.13	0.14	0.17
Ta	0.10	0.07	0.07	0.22	0.03	*n.d*	*n.d*	*n.d*	0.25	*n.d*
Pb	2.15	2.97	2.30	2.00	2.43	1.61	1.70	1.91	0.73	1.21
Th	0.94	0.90	0.97	0.59	0.69	0.06	0.10	0.02	0.08	0.12
U	0.27	0.26	0.27	0.17	0.20	0.02	0.03	0.01	0.03	0.03
La	4.26	4.63	4.50	3.91	3.68	1.17	1.06	0.87	0.96	1.12
Ce	9.26	10.3	9.78	8.34	7.98	2.64	2.00	2.01	2.10	2.42
Pr	1.16	1.26	1.18	1.01	0.97	0.34	0.21	0.29	0.28	0.31
Nd	5.16	5.71	5.24	4.57	4.45	1.83	1.01	1.55	1.41	1.59
Sm	1.26	1.33	1.21	1.09	1.05	0.51	0.21	0.47	0.41	0.42
Eu	0.47	0.51	0.52	0.45	0.45	0.34	0.24	0.30	0.29	0.28
Gd	1.34	1.53	1.36	1.24	1.22	0.67	0.25	0.63	0.51	0.57
Tb	0.22	0.23	0.22	0.20	0.20	0.10	0.04	0.10	0.08	0.09
Dy	1.47	1.62	1.47	1.25	1.34	0.73	0.32	0.71	0.55	0.60
Ho	0.30	0.34	0.31	0.27	0.28	0.16	0.07	0.15	0.12	0.13
Er	0.92	1.02	0.90	0.80	0.82	0.49	0.23	0.45	0.35	0.40
Tm	0.13	0.15	0.14	0.12	0.13	0.07	0.04	0.07	0.05	0.05
Yb	0.89	1.00	0.92	0.80	0.86	0.49	0.29	0.47	0.35	0.39
Lu	0.14	0.15	0.15	0.12	0.13	0.07	0.04	0.07	0.06	0.06
ΣREE	27.0	29.8	27.9	24.2	23.6	9.62	6.02	8.14	7.53	8.44
Th/Nb	0.63	0.70	0.67	0.88	0.71	0.96	0.81	2.14	0.07	0.85
Th/Yb	1.06	0.90	1.05	0.74	0.80	0.12	0.36	0.05	0.22	0.30
Zr/Nb	24.5	29.3	26.4	39.6	34.7	119	48.1	551	6.73	65.8
Zr/Yb	41.6	37.5	41.5	33.5	39.0	15.1	21.4	12.6	20.7	23.2
Zr/Hf	54.1	64.7	51.9	61.7	60.7	54.4	70.0	43.6	51.2	54.0
Th/La	0.22	0.19	0.22	0.15	0.19	0.05	0.10	0.03	0.08	0.10
Zr/Cr	0.60	0.30	0.33	0.20	0.35	0.16	0.04	0.03	0.04	0.04
Zr/Y	4.62	4.42	4.88	3.95	4.62	1.84	3.25	1.55	2.39	2.79
La/Nb	2.83	3.61	3.12	5.75	3.81	18.79	8.31	82.09	0.90	8.12
Sr/Ce	17.8	15.4	18.6	24.7	19.8	76.9	90.4	83.0	98.4	76.2
Sr/Y	20.6	18.6	23.3	30.2	21.7	50.5	95.9	44.2	68.6	56.4
Ce/Pb	4.30	3.45	4.25	4.17	3.28	1.64	1.17	1.05	2.87	2.01
Th/Ce	0.10	0.09	0.10	0.07	0.09	0.02	0.05	0.01	0.04	0.05

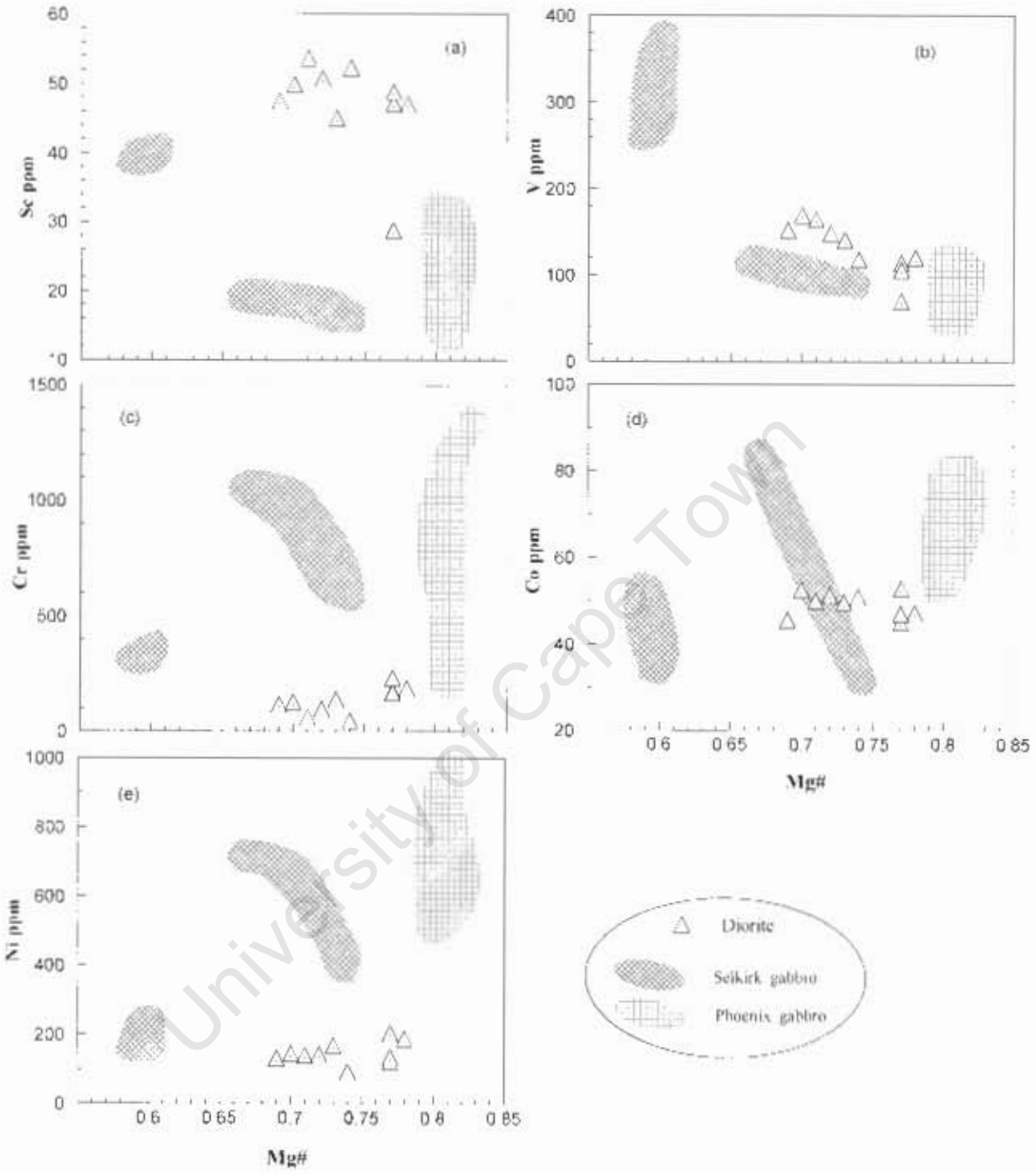

Fig. 6.14: Variation diagrams of selected compatible trace elements versus Mg# for the diorite from the Tati granite-greenstone terrain.

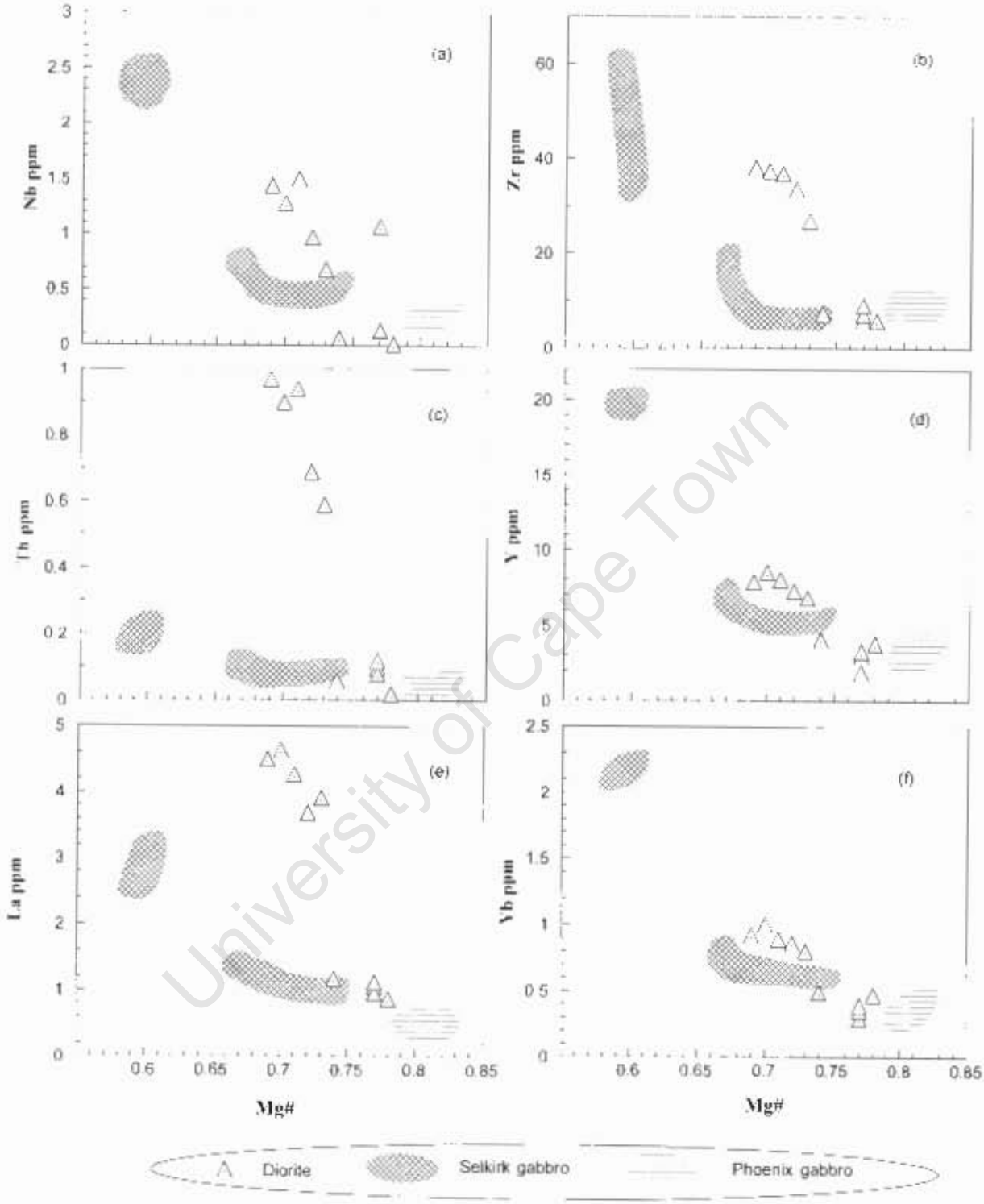

Fig. 6.15: Variation diagrams of selected incompatible trace elements versus Mg# for the diorite from the Tati granite-greenstone terrain.

6.5.2.1 *Rare earth element (REE) patterns*

The two sub-groups within the diorite samples are readily apparent in their chondrite-normalized REE patterns presented as Figure 6.16. The higher Mg# sub-group exhibits slightly fractionated REE patterns (La/Yb_N = 1.93-1.26) with prominent positive Eu anomalies (Eu/Eu^* =1.94-1.66) and overall low REE abundances (ΣREE = 9.62-6.02, Table 6.4). The other sub-group display REE patterns which are characterised by LREE enrichment (La/Yb_N = 3.28-2.88), modest positive Eu anomalies (Eu/Eu^* = 1.22-1.09) and relatively high overall REE abundances (ΣREE = 29.8-23.6; Table 6.4). It is worth noting that the sub-group of the diorite with non-fractionated REE pattern, is remarkable similar to the Phoenix Gabbro, sub-group 2 of the Selkirk Gabbro and the sub-group 3 of the Vumba mafic lavas in terms of their REE patterns which are generally flat with prominent positive Eu anomalies and overall low REE abundances.

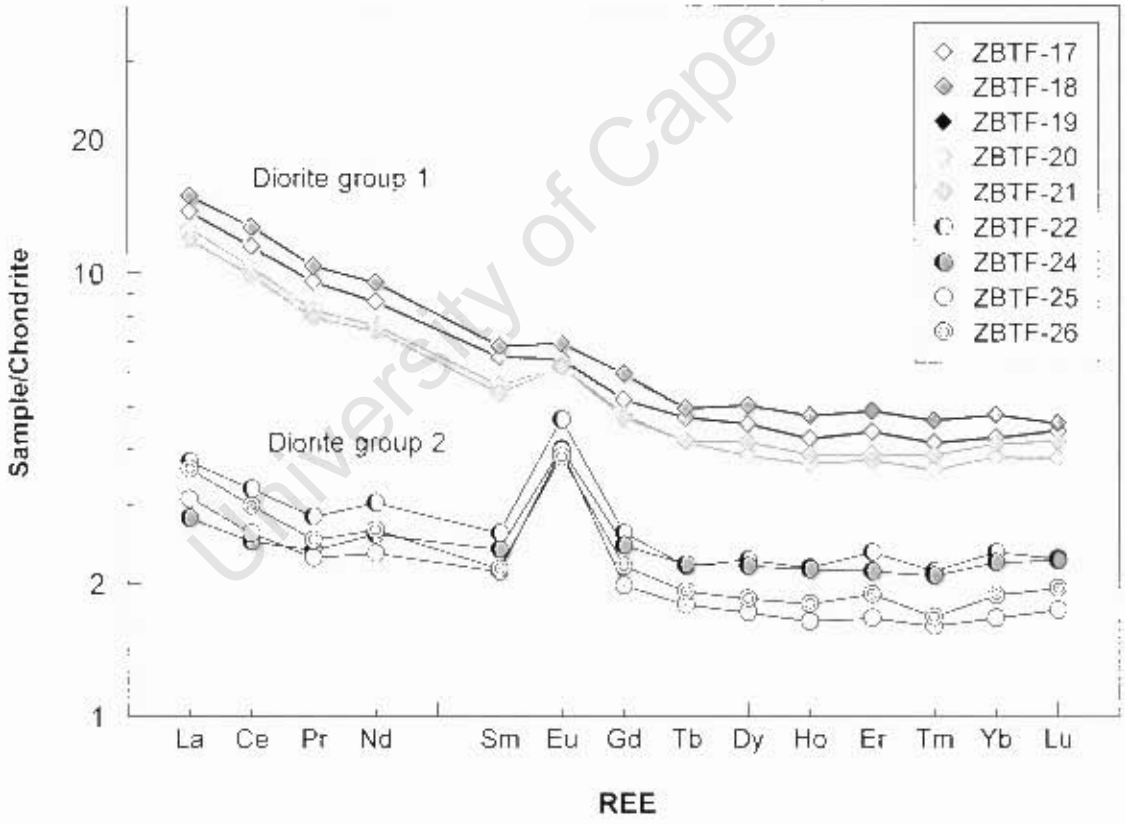

Fig. 6.16: Chondrite-normalized REE patterns for the diorite from the Tati granite-greenstone terrain (normalizing values are after Sun and McDonough, 1989).

6.5.2.2 *Multi-element profiles*

Primitive mantle-normalized multi-element profiles of the two sub-groups of the diorite samples are presented in Figure 6.17. The low Mg# sub-group exhibits multi-element profiles that are moderately fractionated with variable LILE, Th and LREE. Additionally, this sub-group's multi-element profiles exhibit prominent negative Nb, mild Ti, P and Hf anomalies, but have prominent positive Sr and Pb anomalies (Fig. 6.17a) The multi-element profiles of the other sub-group are characterised by Th depletion with respect to LREE, prominent negative Nb, P, Hf and Ti anomalies, but have prominent positive Sr and Eu anomalies indicative of plagioclase accumulation (Fig. 6.17b).

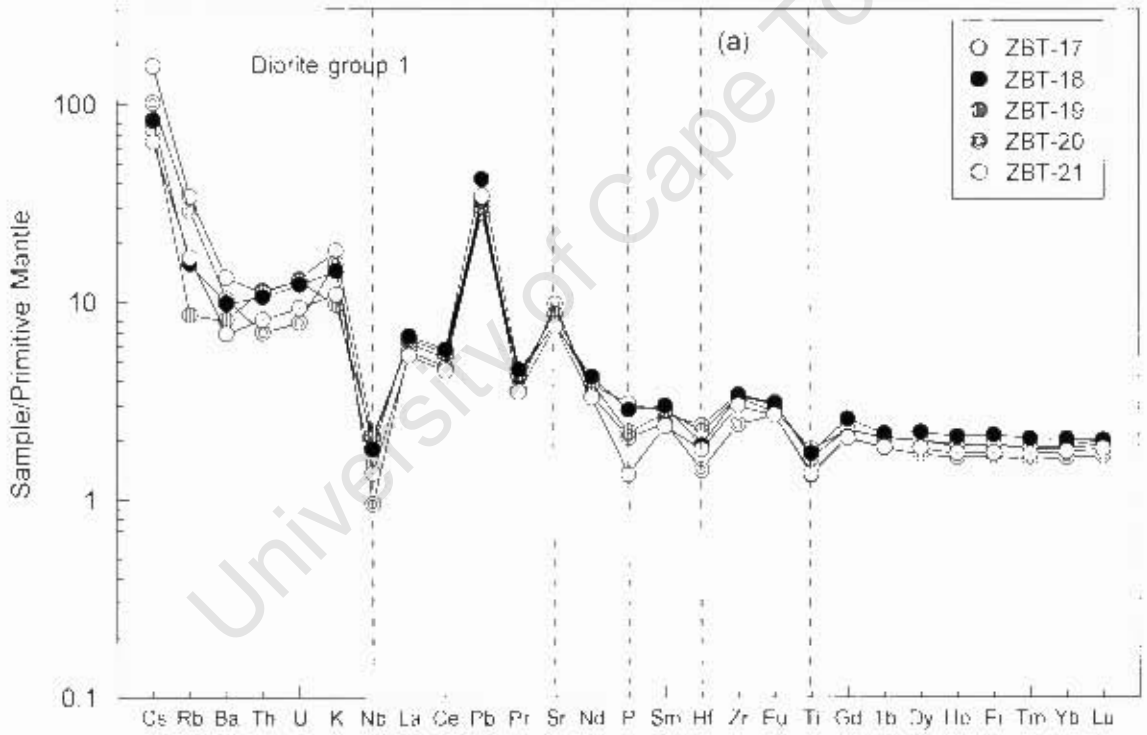

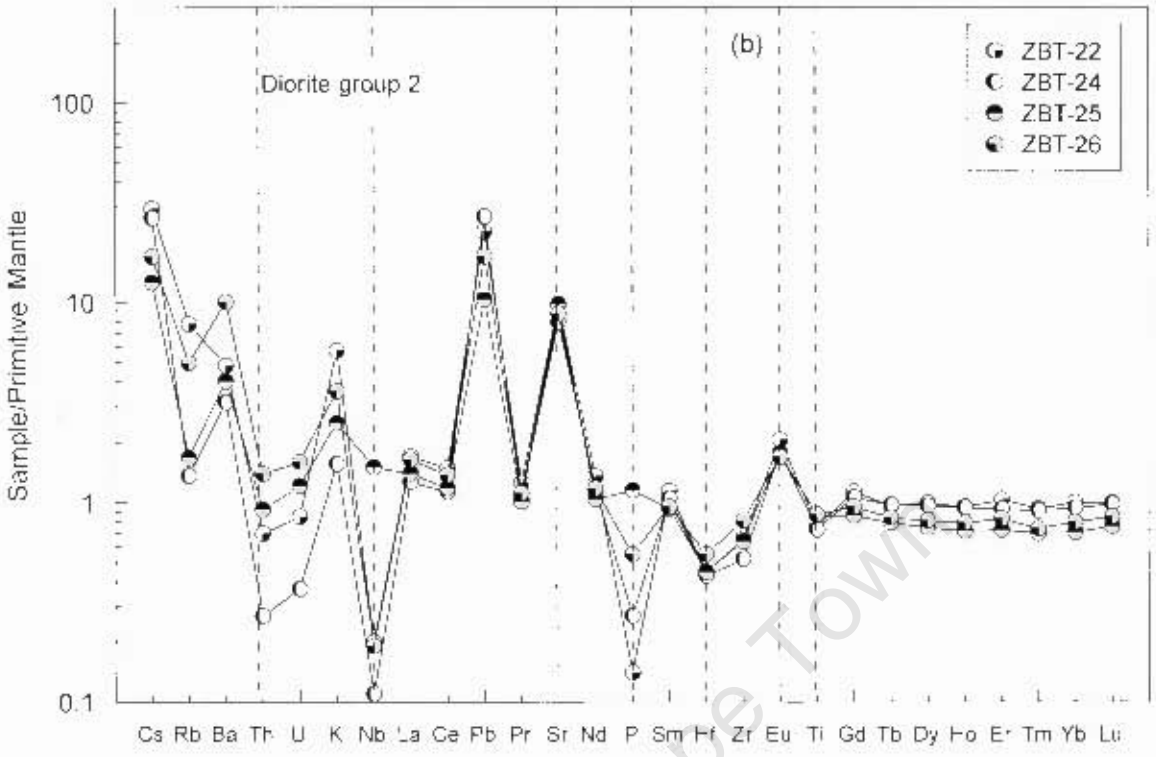

Fig. 6.17: Primitive mantle-normalized multi-element plots for the diorite from the Tati granite-greenstone terrain (normalizing values are from Sun and McDonough, 1989) (a) Sub-group 1 diorite profiles showing negative Nb, Sr, P, Hf and Ti anomalies. (b) Sub-group 2 diorite profiles exhibiting negative Nb, P, Hf, Ti, positive Eu, Sr anomalies and Th, U depletion with respect to LREE.

6.6 Granitoids

Trace element analyses from 29 representative samples of granitoids from the Tati granite-greenstone terrane were analysed for a range of trace elements and the analytical data are reported in Table 6.5.

6.6.1 Compatible trace elements

The compatible trace element variations within the Tati granitoids are shown in Figure 6.18 with backgrounds of the granitoids from the Vumba granite-greenstone terrain shown for comparison purpose. It evident from the variation diagrams that the Tati granitoids possess lower abundances of compatible trace elements than the granitoids outcropping in the neighbouring Vumba terrane (Fig. 6.18). The quartz monzonite unit in the Tati area shows relatively higher Ni (27.0 – 24.4 ppm), Cr (30.0 – 26.7 ppm), V (62.2 – 55.0 ppm) and Co (12.6 – 11.3 ppm) concentrations (Table 6.5) than the rest of the granitoids in that area. However, it can be seen from Figure 6.18 that the

abundances of compatible trace element concentrations are much lower than the abundances recorded in the quartz monzonite unit of the Vumba granite-greenstone terrain.

The samples of monzogranite unit from the Tati granite-greenstone terrain do not compare with the monzogranite of the Vumba granite-greenstone terrain in terms of the compatible trace element abundances. Contrary, they possess very low contents of V (2.33 – 1.93 ppm), Cr (12.4 – 6.59 ppm), Co (1.18 – 1.02 ppm), Ni (3.75 – 3.01 ppm) and Sc (10.4 – 9.94 ppm). The monzogranite from the Vumba terrain is characterised by variable Cr, high Sc, V and low Co concentrations.

The trondhjemite unit is indistinguishable from the tati monzogranite in terms of the compatible trace element abundances (Fig. 6.18 and Table 6.5). The two units are in turn distinct from the rest of the granitoids in the Tati terrain by exhibiting high Sc concentrations (Fig. 6.18).

Table 6.5: Trace element analyses of granitoids from the Tati granite-greenstone terrain. Sc* = XRF determined value; *b.d.l* = below detection limit.

Unit	Quartz monzonite					Monzogranite				Trondhjemite						
Sample	ZBT-1	ZBT-2	ZBT-3	ZBT-4	ZBT-5	ZBT-6	ZBT-7	ZBT-8	ZBT-9	ZBT-10	ZBT-11	ZBT-12	ZBT-13	ZBT-14	ZBT-15	ZBT-16
Sc *	6.92	6.81	7.32	6.68	7.11	10.3	9.94	10.4	10.2	10.8	14.2	8.97	10.3	8.73	9.28	9.64
V	56.0	55.0	55.7	56.8	62.2	1.93	2.33	2.08	2.06	2.88	3.06	1.96	3.63	3.38	3.09	3.52
Cr	32.8	26.7	26.9	27.3	30.0	6.59	7.67	6.96	12.4	6.12	5.52	11.0	7.36	7.51	12.1	6.90
Co	11.3	11.4	11.5	11.7	12.6	1.15	1.10	1.18	1.02	1.33	1.49	0.84	1.44	1.04	1.51	1.52
Ni	24.9	24.6	24.4	24.8	27.0	3.01	3.63	3.20	3.75	3.20	2.93	3.41	3.98	3.69	3.71	3.56
Cu	21.7	31.2	39.2	27.7	34.2	5.51	6.01	6.91	12.2	2.84	3.07	1.12	7.96	2.92	3.33	3.89
Rb	201	208	205	212	209	52.3	45.9	48.0	43.9	41.2	51.5	36.9	45.7	34.8	43.5	43.0
Sr	570	580	577	586	622	99.7	96.6	95.1	95.9	83.5	99.3	102	94.9	64.0	113	112
Cs	13.0	12.8	11.7	14.8	12.0	0.43	0.38	0.41	0.37	0.37	0.41	0.24	0.39	0.40	0.30	0.29
Ba	1091	1005	1001	1014	1045	750	777	804	802	685	615	1041	561	593	1057	983
Y	13.1	13.9	14.0	14.0	14.1	36.4	32.9	33.0	33.9	30.4	28.6	36.6	27.6	32.9	32.3	35.9
Zr *	254	249	257	245	238	326	311	307	316	284	271	319	265	301	290	253
Nb *	9.93	10.0	10.5	10.1	10.1	13.6	13.2	12.5	13.5	12.0	14.5	13.4	11.4	13.6	12.6	12.1
Hf	5.13	5.65	6.14	6.04	5.47	7.53	6.42	6.44	6.93	5.95	5.66	7.51	5.64	6.96	4.58	5.28
Ta	0.47	0.80	0.78	0.96	0.73	0.92	0.85	0.85	0.53	0.81	0.85	0.70	0.78	0.86	0.57	0.85
Pb	46.9	47.7	48.2	46.6	45.2	3.82	4.64	4.92	4.31	4.02	4.04	4.99	4.16	4.76	4.90	5.66
Th	46.5	45.4	47.0	41.7	41.8	11.3	9.16	9.49	10.1	9.19	9.57	12.0	8.67	11.3	10.8	10.9
U	7.66	16.9	9.16	15.3	17.2	3.20	2.63	2.71	2.94	2.33	2.12	3.32	2.17	2.69	2.37	2.46
La	73.9	68.3	73.7	72.4	68.5	36.1	28.3	30.2	39.2	34.0	34.9	21.6	30.5	58.0	35.7	48.4
Ce	148	136	145	142	136	73.1	57.2	61.0	82.2	68.4	71.9	47.7	61.3	111	73.9	95.6
Pr	14.7	14.1	14.8	14.6	14.3	7.92	6.26	6.67	8.79	7.78	8.01	5.53	6.75	11.4	7.89	10.5
Nd	54.5	52.6	55.3	54.3	53.2	31.6	25.4	26.7	35.3	31.3	32.0	24.0	27.1	42.2	31.7	40.6
Sm	8.19	7.88	8.13	8.03	7.91	6.14	5.04	5.21	7.21	5.98	6.11	5.46	5.24	7.04	6.26	7.12
Eu	1.79	1.66	1.66	1.68	1.68	1.16	0.99	1.03	1.41	1.23	1.43	1.03	1.04	1.16	1.41	1.27
Gd	5.77	5.24	5.27	5.29	5.16	6.30	5.33	5.40	7.11	5.78	5.81	6.02	5.09	6.43	6.28	6.60
Tb	0.68	0.60	0.62	0.60	0.60	0.98	0.87	0.87	1.07	0.90	0.87	1.00	0.78	0.98	0.97	0.99
Dy	2.90	3.10	3.19	3.16	3.10	6.59	5.91	5.89	6.39	5.78	5.62	6.42	5.13	6.33	6.01	6.59
Ho	0.50	0.53	0.53	0.53	0.51	1.36	1.25	1.23	1.33	1.18	1.12	1.40	1.06	1.27	1.26	1.36
Er	1.35	1.26	1.40	1.33	1.29	4.12	3.75	3.74	3.96	3.48	3.25	4.28	3.24	3.79	3.77	4.02
Tm	0.17	0.18	0.19	0.19	0.18	0.61	0.57	0.57	0.60	0.52	0.48	0.67	0.48	0.57	0.56	0.59
Yb	1.12	1.19	1.20	1.19	1.16	4.24	3.89	3.89	4.06	3.60	3.27	4.44	3.37	3.91	3.76	4.08
Lu	0.16	0.16	0.17	0.17	0.16	0.64	0.59	0.59	0.62	0.55	0.51	0.67	0.51	0.59	0.56	0.60
ΣREE	313	293	311	305	294	181	145	153	199	170	175	130	152	255	180	228
Zr/Hf	49.4	44.1	41.9	40.5	43.4	43.3	48.5	47.7	45.6	47.7	47.9	42.4	47.0	43.2	63.3	48.0
Sr/Y	43.7	41.8	41.1	41.7	44.1	2.74	2.94	2.89	2.83	2.75	3.47	2.80	3.44	1.94	3.50	3.11
Ba/Rb	5.44	4.84	4.89	4.77	5.00	14.4	16.9	16.8	18.3	16.6	11.9	28.2	12.3	17.1	24.3	22.9
Th/Nb	4.68	4.52	4.46	4.14	4.12	0.83	0.69	0.76	0.75	0.77	0.66	0.90	0.76	0.83	0.86	0.90
Ce/Pb	3.15	2.85	3.01	3.05	3.01	19.1	12.3	12.4	19.1	17.0	17.8	9.57	14.7	23.3	15.1	16.9
Th/La	0.63	0.67	0.64	0.58	0.61	0.31	0.32	0.31	0.26	0.27	0.27	0.56	0.28	0.19	0.30	0.22
Zr/Nb	25.5	24.8	24.4	24.3	23.5	23.9	23.6	24.5	23.5	23.8	18.8	23.8	23.2	22.2	23.0	21.0
Ta/Hf	0.092	0.09	0.14	0.13	0.16	0.13	0.12	0.13	0.13	0.08	0.14	0.15	0.09	0.14	0.12	0.12

Table 6.5: Continued

Unit	Tonalite-Trondhjemite (Tati pluton)							Felsic dykes-Phoenix		Tonalite-Trondhjemite (Sekukwe Pluton)			
Sample	ZBT-28	ZBT-29	ZBT-30	ZBT-31	ZBT-32	ZBT-33	ZBT-34	ZBT-35	ZBT-36	ZBT-77	ZBT-78	ZBT-79	ZBT-80
Sc *	3.60	2.76	2.14	2.86	3.49	3.43	3.67	3.82	3.67	3.49	2.79	3.44	3.36
V	22.6	12.3	7.10	4.56	9.86	19.0	17.2	14.0	11.9	18.2	13.2	15.0	14.2
Cr	10.2	8.96	7.32	6.28	6.31	10.3	15.0	10.4	13.3	8.40	13.6	8.39	8.26
Co	5.26	3.08	1.14	1.31	3.17	4.86	3.92	2.89	7.47	3.34	2.52	3.00	2.73
Ni	7.15	4.15	3.77	3.36	3.62	6.50	5.56	6.13	68.2	5.24	5.01	5.57	6.50
Cu	37.8	7.84	13.4	2.70	8.79	3.42	5.98	7.95	1078	16.2	1.09	11.5	10.0
Rb	55.0	42.0	45.6	139	69.9	69.9	42.8	40.2	11.0	51.9	33.9	38.3	42.0
Sr	305	284	204	108	264	266	151	133	119	397	381	484	414
Cs	1.73	1.38	0.46	1.77	3.58	3.43	1.63	1.12	0.53	0.61	0.70	0.44	0.54
Ba	484	414	1606	1086	266	465	219	497	273	328	332	481	271
Y	3.98	3.15	1.77	6.26	3.56	4.35	2.24	8.77	12.9	2.80	1.63	2.99	2.16
Zr *	292	222	55.4	83.2	234	295	287	149	202	110	88.0	105	102
Nb *	5.31	3.28	2.11	10.2	2.86	5.62	6.26	6.93	4.66	1.84	*b.d.l*	0.83	1.27
Hf	4.48	4.20	1.41	2.47	4.37	5.16	3.22	2.78	5.30	2.03	1.73	1.86	2.09
Ta	0.35	0.17	0.06	1.00	0.14	0.50	0.30	0.80	0.46	0.08	0.05	0.09	0.05
Pb	12.3	13.0	24.2	30.2	14.6	12.9	9.15	17.7	13.0	7.74	8.44	12.8	8.28
Th	3.02	9.62	3.26	9.82	9.37	3.32	1.27	18.6	13.1	0.61	0.39	1.02	1.85
U	1.84	0.85	1.16	4.00	0.99	2.54	1.62	6.31	3.05	0.46	0.59	0.55	0.36
La	11.1	29.7	9.30	20.8	28.6	12.3	4.59	28.9	25.2	2.15	2.41	5.42	11.9
Ce	19.9	49.2	16.4	39.7	48.3	22.6	10.1	47.4	47.3	3.90	4.41	9.65	23.7
Pr	2.04	4.57	1.67	4.12	4.62	2.28	0.81	4.31	4.96	0.45	0.47	1.11	2.55
Nd	7.65	16.3	5.97	15.2	16.5	8.46	3.09	14.8	19.4	2.07	2.06	4.58	10.0
Sm	1.26	2.35	0.74	2.58	2.32	1.42	0.62	2.54	3.51	0.56	0.51	0.79	1.45
Eu	0.61	0.75	0.46	0.47	0.68	0.59	0.30	0.63	0.81	0.35	0.37	0.38	0.41
Gd	1.04	1.72	0.63	1.94	1.48	1.11	0.55	2.26	2.96	0.66	0.46	0.82	0.84
Tb	0.14	0.19	0.08	0.24	0.16	0.14	0.08	0.32	0.41	0.09	0.06	0.10	0.09
Dy	0.72	0.72	0.38	1.27	0.77	0.79	0.43	1.71	2.48	0.50	0.32	0.55	0.47
Ho	0.14	0.12	0.06	0.21	0.13	0.15	0.08	0.31	0.47	0.10	0.06	0.10	0.08
Er	0.40	0.35	0.16	0.56	0.33	0.43	0.24	0.88	1.30	0.30	0.18	0.30	0.22
Tm	0.05	0.05	0.02	0.08	0.05	0.06	0.04	0.13	0.19	0.04	0.03	0.04	0.03
Yb	0.44	0.32	0.17	0.57	0.38	0.51	0.26	0.99	1.35	0.31	0.19	0.27	0.22
Lu	0.06	0.05	0.03	0.08	0.06	0.08	0.04	0.13	0.20	0.05	0.03	0.04	0.04
ΣREE	45.6	106	36.1	87.9	104	51.0	21.2	105	111	11.5	11.6	24.2	52.0
Zr/Hf	65.1	52.7	39.3	33.6	53.7	57.3	89.2	53.7	38.1	54.1	50.8	56.3	48.5
Sr/Y	76.6	90.2	115	17.3	74.4	61.2	67.4	15.2	9.28	142	234	162	191
Ba/Rb	8.79	9.85	35.2	7.80	3.80	6.66	5.10	12.4	24.8	6.32	9.79	12.6	6.45
Th/Nb	0.57	2.93	1.54	0.96	3.28	0.59	0.20	2.68	2.81	0.33	-	1.23	1.45
Ce/Pb	1.62	3.78	0.68	1.31	3.31	1.75	1.10	2.68	3.64	0.50	0.52	0.75	2.87
Th/La	0.27	0.32	0.35	0.47	0.33	0.27	0.28	0.64	0.52	0.29	0.16	0.19	0.16
Zr/Nb	54.9	67.6	26.2	8.14	81.9	52.5	45.9	21.5	43.3	59.8	-	126	79.9
Ta/Hf	0.08	0.08	0.04	0.04	0.40	0.03	0.10	0.09	0.29	0.09	0.04	0.03	0.05

Tonalite-trondhjemite samples from the Tati and the Sekukwe plutons are indistinguishable in terms of the compatible trace element abundances (Fig. 6.18 and Table 6.5). Nonetheless, they possess low abundances of compatible trace elements than the tonalite and granodiorite units of the Vumba granite-greenstone terrain. The tonalite-trondhjemite and the two samples from the tonalite-trondhjemite dykes cutting the Phoenix gabbro are comparable in terms of compatible trace element abundances. However, sample ZBT-36 of the felsic dyke is an outlier in terms of Ni and Co possessing higher values than the tonalite-trondhjemite samples. It is important to note that the granitoids in the Tati granite-greenstone terrain are chemically distinct from the spatial associated felsic lavas in terms of the compatible trace elements concentrations (Fig. 6.18).

6.6.2 Incompatible trace element

The distribution variation of incompatible trace elements in the granitoids of the Tati granite-greenstone terrain is presented in Figure 6.19 with the background of the granitoids from the Vumba area shown for comparison. It is apparent from the figure 6.19 that the selected incompatible trace element abundances from the tati granitoids display no correlation against SiO_2 wt.% as index of differentiation. The tati quartz monzonite unit has low Nb, Zr, Y and Yb than its Vumba counterpart (Fig. 6.19a,b,c,f). In terms of Th and La contents it greatly overlaps the Vumba quartz monzonite. The trondhjemite and monzogranite in the tati granite-greenstone terrain are characterised by high abundances of Y (36.6 – 27.6 ppm) and Yb (4.44 – 3.27 ppm) than any granitoid in the Francistown Granite-Greenstone Complex. Y and Yb are known to be very compatible in garnet.

The incompatible trace element distribution within the tonalite-trondhjemite samples from the Tati and the Sekukwe plutons display overlapping contents (Fig. 6.19), which overlap the abundances recorded in the tonalite unit from the Vumba granite-greenstone terrain. The samples from the tonalite-trondhjemite dykes are characterised by incompatible trace elements abundances overlapping those recorded from the felsic lavas from the Tati greenstone belt.

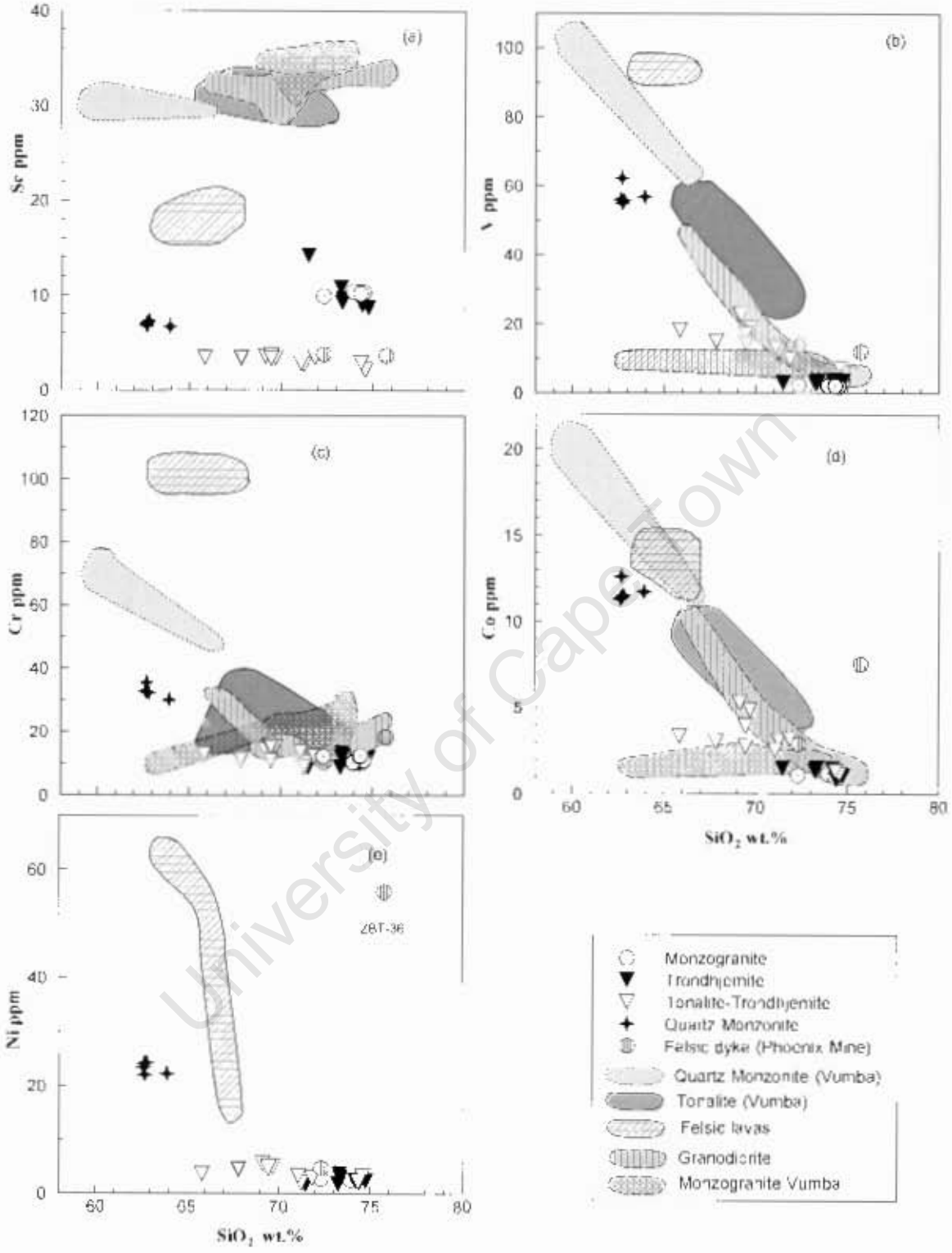

Fig. 6.18: Variation diagrams of selected compatible trace elements versus SiO_2 wt % for the granitoids from the Tati granite-greenstone terrain. Vumba granitoids are shown in background.

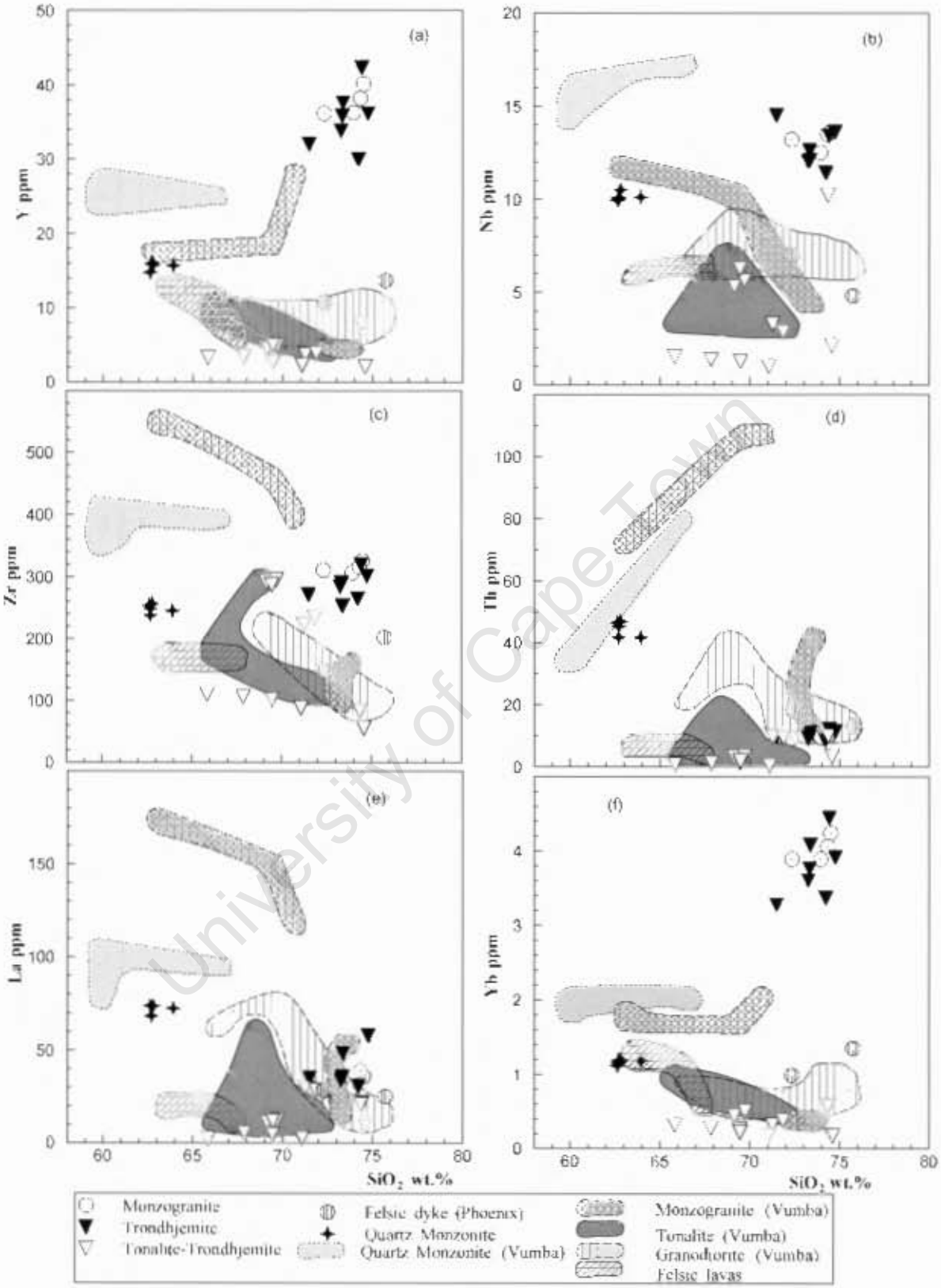

Fig.6.19: Variation diagrams of selected incompatible trace elements versus SiO_2 wt.% for the granitoids from the Tati granite-greenstone terrain. Vumba granitoids are indicated in the background

6.6.2.1 Rare earth element (REE) patterns

The chondrite-normalized REE patterns for the granitoid from the Tati granite-greenstone terrain are presented in Figure 6.20. The various granitoid samples exhibit variable fractionated REE profiles. The quartz monzonite samples display strongly fractionated REE patterns (La/Yb_N = 44.4-38.8) with negligible negative Eu anomalies (Eu/Eu* = 0.81-0.77) and fractionated HREE (Fig. 6.20a). Samples of the monzogranite exhibit moderately fractionated REE patterns (La/Yb_N = 6.51-4.91) with prominent negative Eu anomalies (Eu/Eu* = 0.60-0.57) and flat Heavy REE (Fig. 6.20b). Trondhjemite samples display fractionated REE patterns that are remarkably similar to those of the monzogranite. The REE patterns are moderately fractionated (La/Yb_N = 10.0-3.28) with conspicuous negative Eu anomalies (Eu/Eu* = 0.74-0.53) and non-fractionated HREE. This similarity presumably reflects some petrogenetic bond between the two granitoids. Samples of the tonalite-trondhjemite from the Sekukwe Pluton exhibit a wide range of REE profiles. The profiles define a continuous range in the degree of fractionation, a feature strongly highlighted by the variation in the LREE rather than HREE concentrations (Fig.6.20). The patterns are variably fractionated (La/Yb_N = 36.9-4.74), have prominent positive Eu anomalies (Eu/Eu* = 2.3-1.1), low HREE abundances and have concave HREE segments (Fig. 6.20). Samples of the tonalite-trondhjemite from the Tati Pluton exhibit REE patterns that resemble those of the Sekukwe Pluton. These patterns are fractionated (La/Yb_N = 61.9-12.1) with variable positive Eu anomalies (Eu/Eu* = 2.1-1.1) except sample ZBT31 that displays negative Eu anomaly, concave HREE section and low HREE abundances. The tonalite-trondhjemite dykes display REE patterns similar to the REE profiles of the quartz monzonite (Fig. 6.20). The patterns are fractionated (La/Yb_N = 19.8-12.6) with minor negative Eu anomalies (Eu/Eu* = 0.88-0.77).

The chondrite-normalized REE profiles for the granitoids from the Vumba granite-greenstone terrain are presented for comparison in Figure 6.21. The granitoids are generally characterised by strongly fractionated REE profiles with variable Eu anomalies and concave HREE segments. The monzogranite REE patterns from the Vumba do not compare with the REE profiles displayed by the Tati monzogranite. The profiles of the quartz monzonite samples from the two granite-greenstone terrains are comparable to some extent. However, the Tati quartz monzonite samples exhibit more

fractionated REE patterns than their Vumba counterpart. The REE patterns of the tonalite from the Vumba terrain resemble those of the tonalite-trondhjemite samples (Fig. 6.21f).

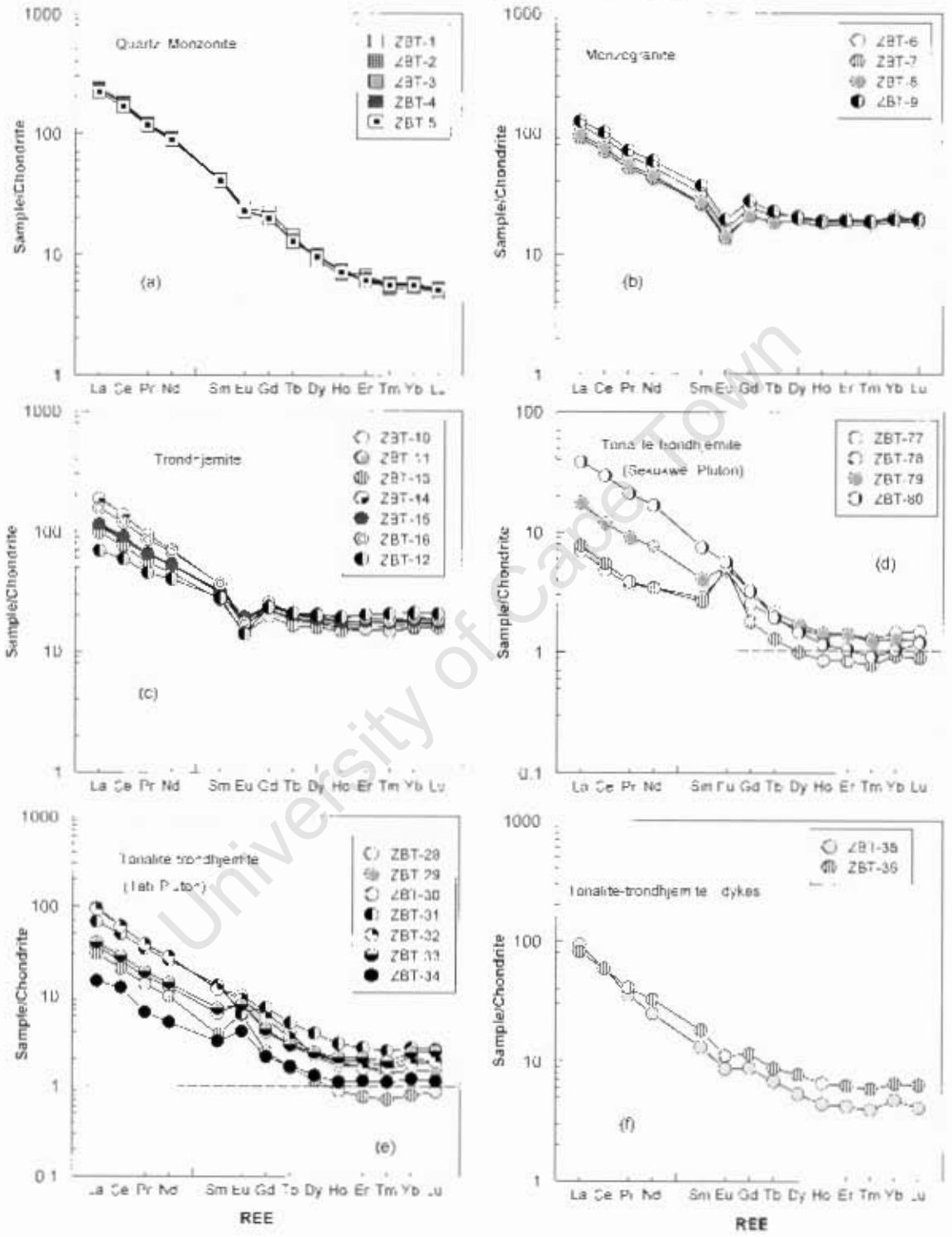

Fig. 6.20: Chondrite-normalized REE patterns for the granitoids from the Tati granite-greenstone terrain (normalizing values are after Sun and McDonough, 1989). Note differences in scale.

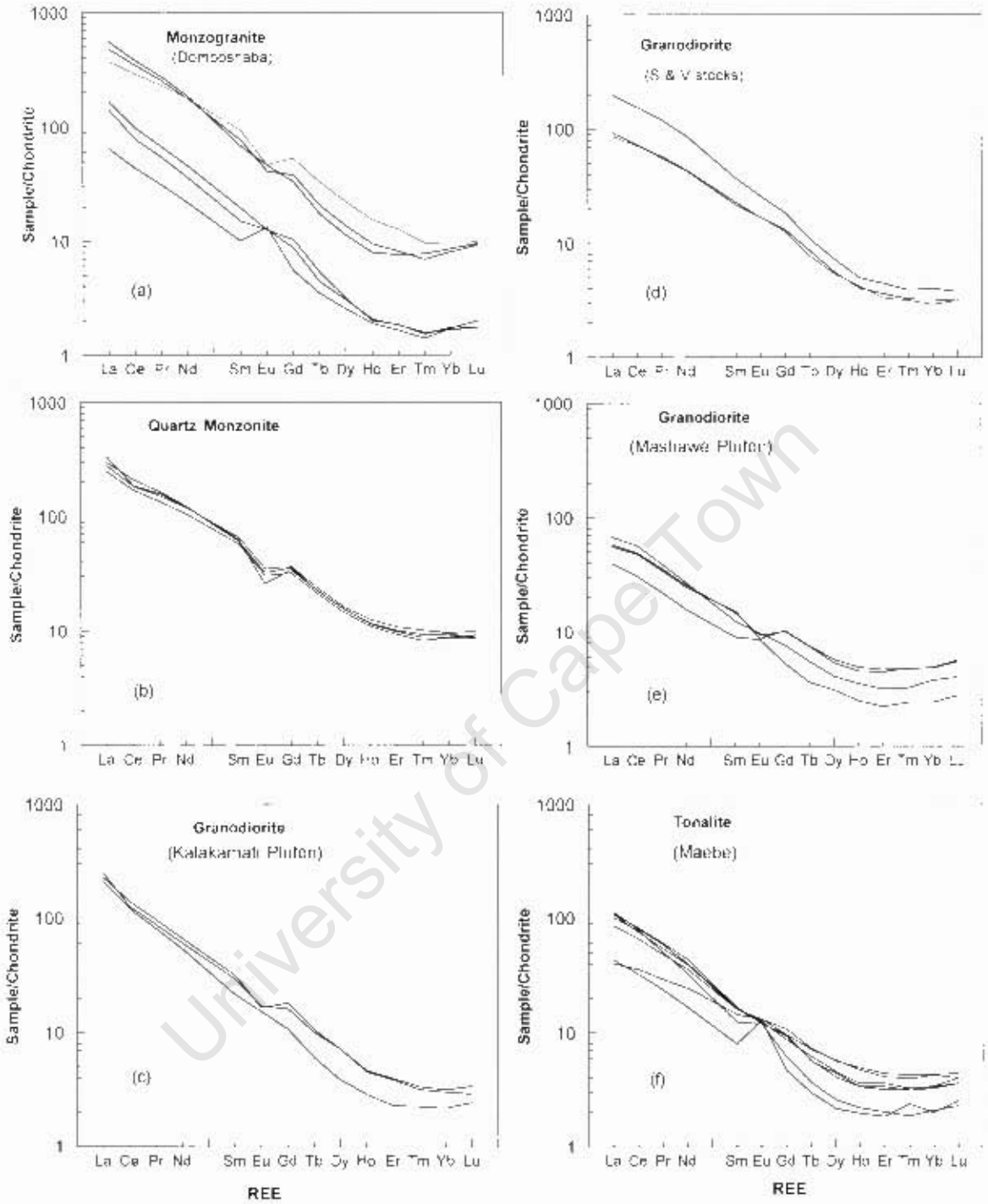

Fig. 6.21: Chondrite-normalized REE patterns for the granitoids from the Vumba granite-greenstone terrain (normalizing values are after Sun and McDonough, 1989) presented for comparison with the Tati granitoids.

6.6.2.2 Multi-element Profiles

The primitive mantle-normalized multi-element profiles for the Tati granitoids are given in Figure 6.22. Samples of the quartz monzonite exhibit coherent and fractionated multi-element profiles that have negative Nb, Ta, Ti, Sr, P and Ba anomalies as well as positive Pb anomalies (Fig. 6.22a). The monzogranite samples show coherent multi-element profiles that have prominent negative Ti, P, Sr, Ta and Nb anomalies (Fig. 6.22). Additionally, the profiles show flat HREE, minor positive Pb anomalies and less LILE enrichment (Fig. 6.22b). The samples of the tonalite-trondhjemite dykes display fractionated multi-element profiles characterised by negative Ti, P, Sr, Nb and positive Pb anomalies (Fig. 6.22c). The multi-element profiles for the trondhjemite samples resemble those of the monzogranite. Their profiles exhibit prominent negative Ti, P, Nb, Ta and Sr anomalies. Tonalite-trondhjemite samples from the Sekukwe and the Tati Plutons exhibit less coherent multi-element profiles characterised by negative Ti, Nb, Ta, variable Sm, P, Sr and prominent positive Pb anomalies. Additionally, the profiles reflect depletion of HREE with respect to primitive mantle composition. Notably, the Sekukwe tonalite-trondhjemite and some tonalite-trondhjemite samples from the Tati Pluton exhibit negative Th anomalies, a feature that is not observed in the profiles of the other granitoids in the area.

The multi-element profiles for the Vumba granitoids presented in Figure 6.23 for comparison, display coherent, fractionated and variable LILE enriched profiles. Samples of monzogranite from the Vumba area comprise two sub-groups which have multi-element profiles characterised by prominent negative Ta, Nb, Sr, P and Ti anomalies. Though the profiles of the monzogranite samples from the two terrains do not resemble each other, they are comparable in terms of the Ta, Nb, Sr, P and Ti negative anomalies. The quartz monzonite samples from the Vumba area have remarkably similar multi-element profiles to those of the Tati quartz monzonite. They display negative Ba, Ta, Nb, Sr, P and Ti anomalies (Fig. 6.23). Samples of the tonalite display multi-element profiles comparable to those of the tonalite-trondhjemite samples from the Tati granite-greenstone terrain. The profiles show negative Ti, P, Nb, Ta and variable Sr anomalies. Additionally, they exhibit variable Th and positive Pb anomalies. Multi element profiles from the granodiorite samples (Vumba area) are characterised by negative Ti, Nb, Ta, P and variable Sr anomalies.

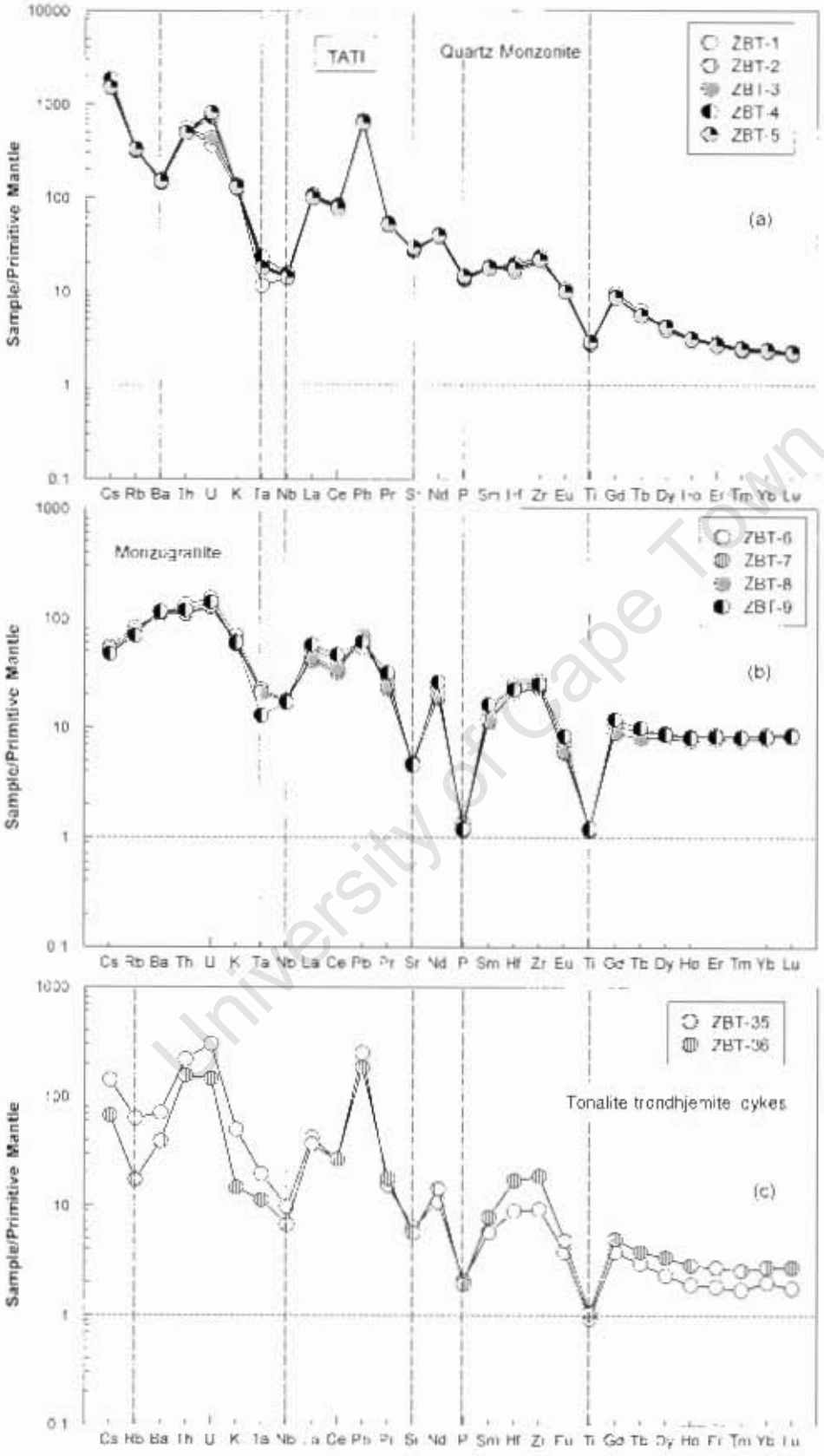

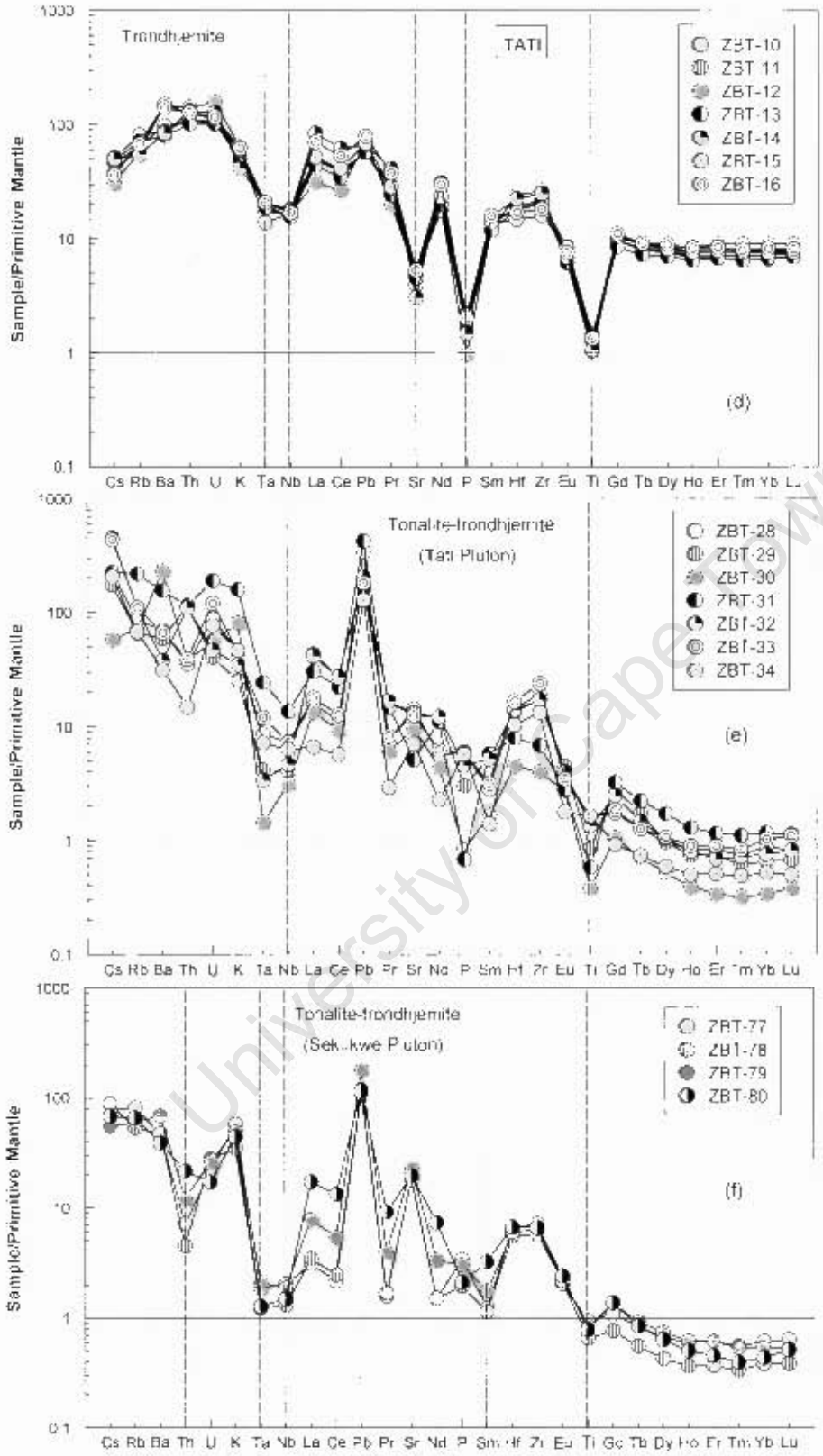

Fig. 6.22 Primitive mantle-normalized multi-element diagrams for the Tati granitoids (normalizing values after Sun and McDonough, 1989). (a) Quartz monzonite profiles; (b) Monzogranite profiles; (c) Tonalite-tronchjemite dykes profiles; (d) Tronchjemite profiles; (e) Tati Pluton profiles. (f) Sekukwe Pluton profiles.

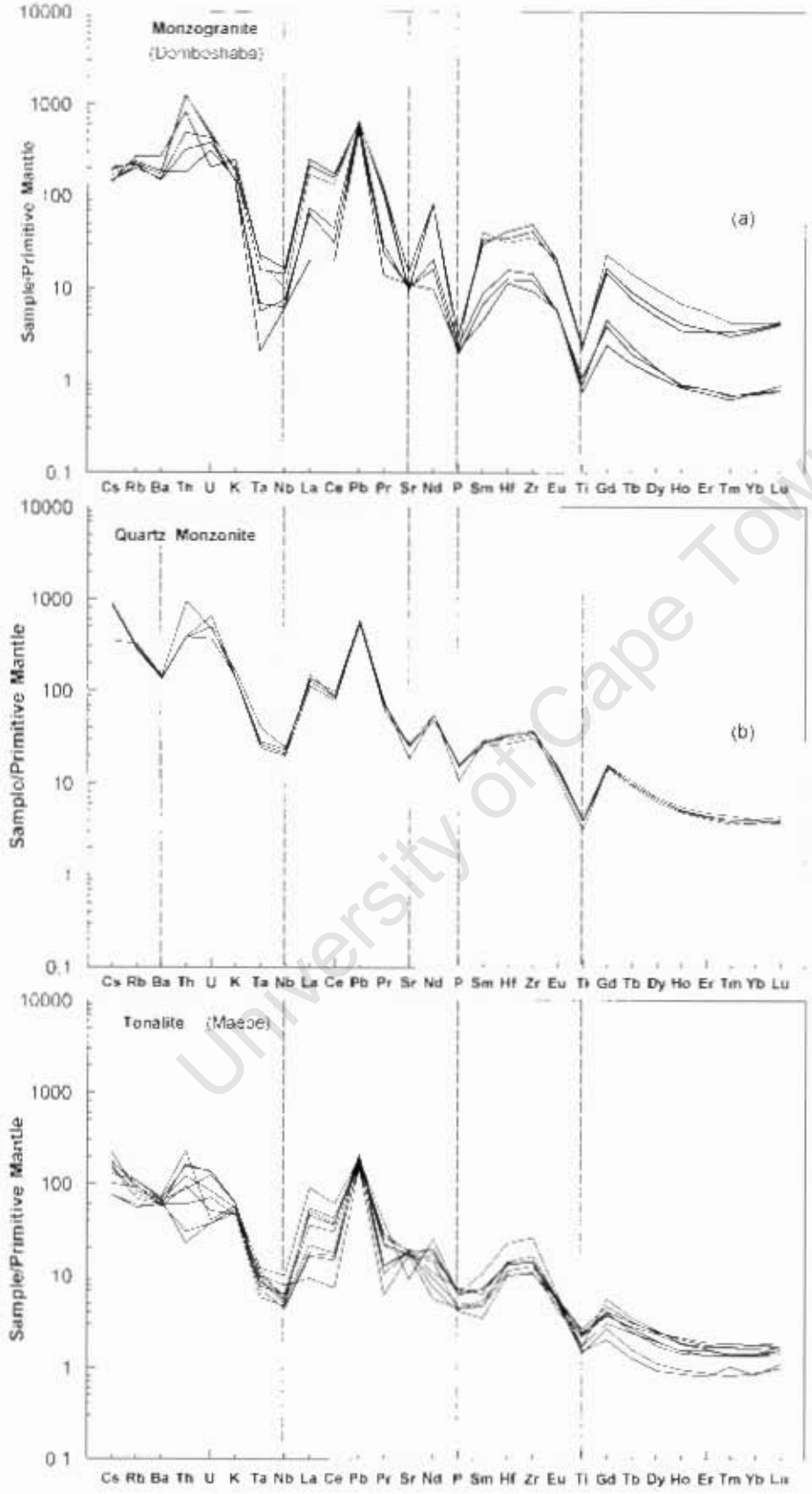

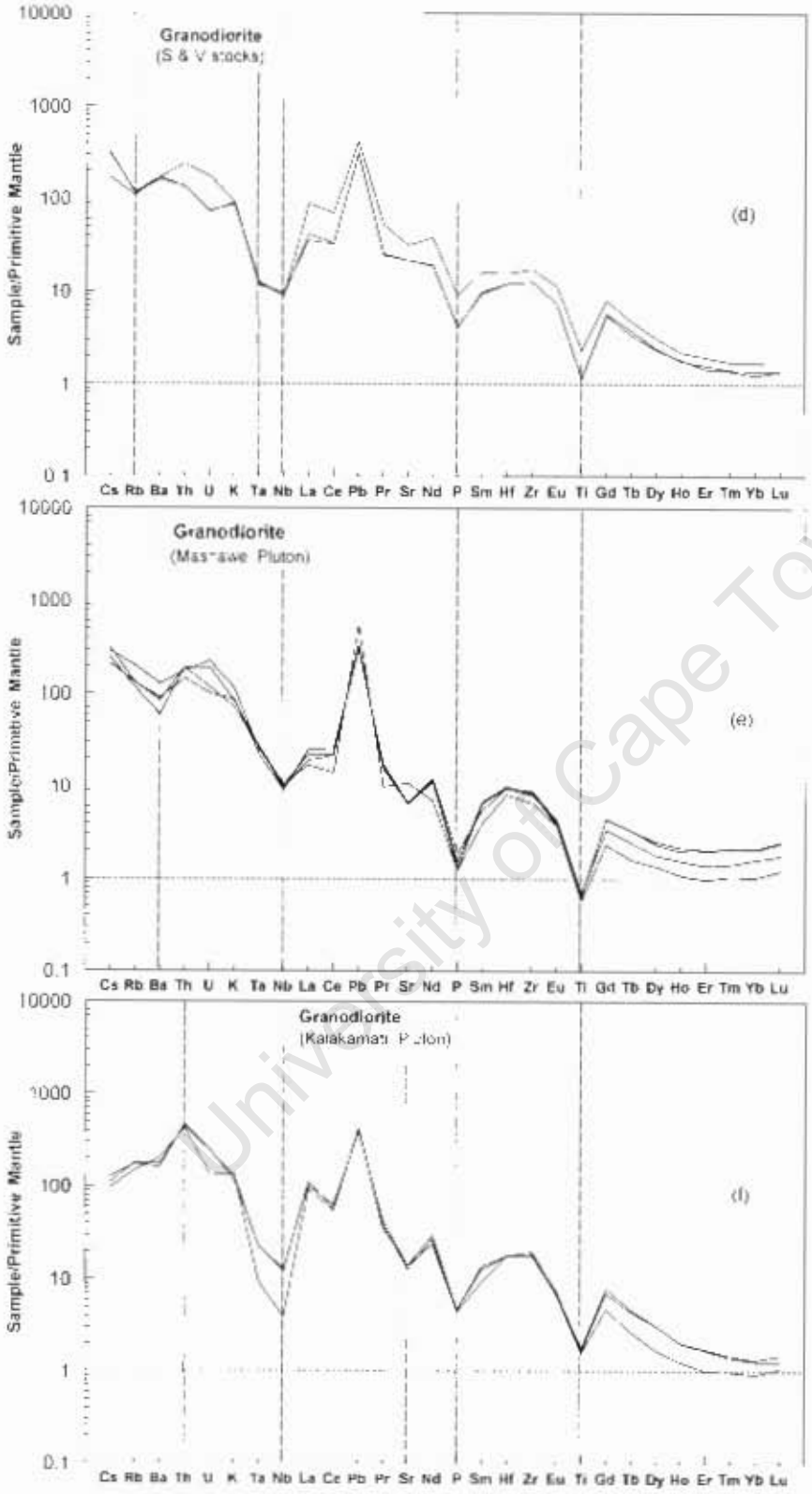

Fig. 6.23: Primitive mantle-normalized multi-element diagrams for the Vumba granitoids (normalizing values after Sun and McDonough, 1989) presented for comparison with the Tati granitoids.

6.10 Summary

Rare earth element characteristics of the mafic lavas from the Tati greenstone belt define three distinct sub-groups. One subgroup exhibits mildly LREE-enriched patterns and pronounced negative Nb-Ta, Sr, P, Hf and Ti anomalies in their primitive-mantle normalized multi-element plots. The second subgroup samples possess flat REE patterns with minor negative Eu anomalies and display multi-element profiles with less pronounced negative Nb and Ti anomalies. The third subgroup is LREE enriched and displays multi-element profiles with negative Rb, Ta-Nb, Sr, P and Ti anomalies. Felsic lavas in the Tati greenstone belt are characterised by high Cr, Co and Ni contents. Their multi-element profiles are enriched in LIL elements and show Nb, Sr and Ti negative anomalies.

The Phoenix gabbro contains lower incompatible element abundances than the Tati mafic lavas as well as most of the Selkirk gabbro samples. It displays chondrite-normalized REE patterns with prominent positive Eu anomalies. The primitive mantle-normalized multi-element profiles exhibit negative Nb, Ti, Th, Hf and positive Sr and Eu anomalies. The Selkirk gabbro defines two groups on the basis of trace element abundances. One group resembles the mafic lavas of the Tati greenstone belt in terms of both compatible and incompatible trace element abundances. This group displays chondrite-normalized REE patterns similar to the Tati subgroup 2 mafic lavas. The patterns are slightly LREE-depleted with minor negative Eu anomalies. Their primitive mantle-normalized multi-element profiles are devoid of Ti and Nb anomalies. The second group of Selkirk gabbro has lower abundances of incompatible elements and possesses flat chondrite-normalized REE patterns with prominent Eu negative anomalies. This group show primitive mantle-normalized multi-element profiles marked by negative Th, Nb, P, Ti, Hf, Zr and positive Sr anomalies.

The incompatible element abundances of the diorite define two sub-groups. One sub-group which is enriched in incompatible elements corresponds to the low Mg# samples. It also displays LREE enriched chondrite-normalized REE patterns and primitive mantle-normalized multi-element profiles marked by negative Nb, Ti, P, Hf and positive Sr and Eu anomalies. The second sub-group exhibits near flat Chondrite-normalized REE patterns with prominent positive Eu anomalies. Its multi-element profiles, which are primitive mantle-normalized, show deep Nb, Th and P negative anomalies while Sr and Eu display prominent positive anomalies.

CHAPTER 7

Tectonic Settings

7.0 Introduction

Despite voluminous literature about the role of plate tectonics and nature of mantle convection during the early part of the Earth's history, the resolution of Archaean tectonics remains fuzzy. However, as more studies are carried out in Archaean terranes, consensus about Archaean tectonics appears to be gradually converging. There is for example now a recognition that the Neoarchaean tectonics may have been different from those in the Paleoarchaean (e.g. Martin et al., 2005). This is based on restricted occurrence of sanukitoids to the Neoarchaean period. The problem remains however, that this may just be preservation related. Sanukitoids are subduction-related rocks that occur in granite-greenstone terranes. Furthermore, there is also a recognition of compositional differences between the Neoarchaean and Mesoarchaean-Paleoarchaean TTGs. The Neoarchaean TTGs are characterised by more elevated Cr, Ni and Mg# (Rapp et al., 1999; Martin et al., 2005). This has been interpreted by many workers as an indication of interaction with the mantle wedge of subduction zones in their evolution.

Plate tectonics and plumes have been implicated in the formation of many Archaean greenstone belts (e.g. Dostal and Mueller, 1997; Hollings and Wyman, 1999; Hollings et al., 1999; Condie, 2005). However, the outstanding question is whether the tectonic processes that operated during the Archaean did so differently as compared to that of more modern times. Some recent studies suggest that Archaean greenstone belts were formed by processes and in tectonic settings analogous to those operating in the Phanerozoic (e.g. Sandeman et al., 2006; Smithies et al., 2005; Manya, 2004; Srivastava et al., 2004; Wang et al., 2004; Kampunzu et al., 2003). Additionally, geochemical comparisons between the Neoarchaean boninites (e.g. Kerrich et al., 1998) and adakites (e.g. Wang et al., 2004; Polat and Kerrich, 2001; Hollings and Kerrich, 2000) with their Cenozoic counterparts demonstrate that they are indistinguishable. This implies similar subduction zone processes operated in Archaean times and today. Furthermore, Mesoarchaean to Neoarchaean crustal horizontal shortening in the Neoarchaean (e.g. as detected on the Kaapvaal

Craton) resembles modern convergent collisional plate boundary processes (de Wit and Tinker, 2004).

Chemical compositions of volcanic and granitoid rocks of the Phanerozoic era are commonly used to extract information about their tectonic settings (e.g. Pearce and Cann, 1973; Pearce et al., 1984; Harris et al., 1986; Whalen et al., 1987; Eby, 1992; Rollinson, 1993; Pearce, 1996) because their variable chemical compositions are considered to emanate partly from plate tectonic processes (e.g. Ohta et al., 1996). Moreover, there are numerous chemical features of modern igneous rocks that can be interpreted directly in terms of plate tectonic processes. Nonetheless, there are still intense debates about the similar application to infer the tectonic settings of Archaean rocks. The contention is that due to high mantle temperature during the Archaean, the nature of mantle convection and hence plate tectonics might have been different from those of today. Chemical similarities between recent and ancient rock suites would then, of course, have to be explained as being due to different processes yielding similar chemical signatures. There is, however, a growing recognition of the relevance of tectonic discrimination diagrams in the construction of tectonomagmatic settings of Archaean magmatic rocks, provided they are supported with other geochemical information (e.g. Condie, 2005b). Here, I follow this line of enquiry.

7.1 Mafic lavas

Various tectonic discrimination diagrams for basaltic rocks have been published (see Rollinson, 1993 for overview). These are geochemical diagrams that define fields based on certain relatively immobile elements or element ratios that permit basalts of unknown origin to be assigned to its most probable tectonic setting of eruption. In this study, various tectonic discrimination diagrams have been tested to evaluate the tectonic setting of the mafic lavas from the Tati and Vumba greenstone belts (Fig. 7.1a-f). On the Ti-V diagram of Shervais (1982) the samples from both the Tati and Vumba greenstone belts plot in overlapping zones of volcanic arc basalt (VAB) and mid-ocean ridge basalt (MORB) as well as on the MORB + BAB (back-arc basalt) field. Ti and V are both transition elements but behave differently in silicate magmatic systems (Shervais, 1982). The fields in this Ti-V diagram are subdivided essentially according to Ti/V ratio. Mid-ocean ridge basalt (MORB) plots between Ti/V ratios of 20 and 50 though there is considerable overlap with the back-

arc basalt (BAB) field, whereas volcanic arc basalt (VAB) plots between Ti/V ratios of 10 and 25 with a small overlap onto the MORB field. The mafic lavas under investigation are characterised by a wide range of Ti/V ratio ranging between 10 and 35. To resolve the ambiguity, the samples were further plotted on Ti/V-Zr discrimination diagram of Gribble et al. (1996) that discriminates between MORB, BAB and VAB (Fig. 7.1b). The BAB field falls between, but overlaps with, the VAB and MORB fields. The majority of the mafic volcanic samples from the study area plot in the BAB field, with a few samples falling in the overlapping regions (Fig. 7.1).

On the Cr-Y diagram of Pearce (1983) the mafic lavas from the study area plot within the VAB field, with some samples falling in the overlapping region between VAB and MORB (Fig. 7.1c). This diagram discriminates effectively between MORB and VAB with only a small overlap between the two fields. However, great care is required when using binary discrimination diagrams involving high field strength elements (HFSE) versus compatible elements such as Ti,V and Cr because the position of a data point with respect to a field boundary can be affected by both dilution and concentration of immobile elements during alteration, and can also be significantly displaced from its true liquid composition by the presence of cumulate crystals (Pearce, 1996).

A ternary discrimination diagram based on the immobile HFSE elements Th-Ta-Hf (after Wood, 1980), is efficient at discriminating between MORB and VAB. The results suggest that the mafic lavas from the study area are volcanic arc tholeiites, except two samples from the Tati greenstone belt that straddle the enriched-MORB and within-plate tholeiites field boundary (Fig. 7.1d). Th/Ta ratio can be used to discriminate volcanic arc basalts from MORB and WPB. Most volcanic arc basalts have Th/Ta ratios greater than 3, whereas ocean plateau basalts and MORB possess Th/Ta ratios less than 3 (Condie, 1997). Samples of the mafic lavas from the Tati and Vumba greenstone belts are characterised by Th/Ta ratios that vary from 2.13 to 15.1, with only 2 samples recording value less than 3 (Table 6.1). Therefore, the Th/Yb versus Ta/Yb diagram of Pearce (1982) is employed for further verification of the tectonic setting for the mafic lavas from the two greenstone belts. This diagram uses Th/Yb and Ta/Yb ratios, which is basically Th/Ta, to distinguish subduction slab from mantle components. Yb is used as a normalizing factor to largely eliminate the effects of partial melting and fractional crystallization (Pearce, 1982). According to Pearce (1982), Yb is an effective normalizing factor since it does not participate in the enrichment

processes of Th and Ta. Vectors have been drawn on the diagram (Fig. 7.1e) to highlight the main components of variation. It has been demonstrated empirically (Pearce, 1983) that within-plate enrichment events increase Ta and Th equally, hence its vector has a slope of unity. Fluids off the slab during subduction affect the concentration of Th but not Ta. Hence, their vector is vertical. Finally, crustal contamination affects Th more than Ta, hence its vector is sub-vertical. As a result, MORB and within plate basalts plot within a well-defined band, while volcanic arc basalts and within plate basalts that have been extensively contaminated by continental crust are displaced to higher Th values. The mafic lavas from the greenstone belts in the study area are practically all displaced to relatively high Th values, which suggest that they are subduction related or within plate basalts that have been crustally contaminated. However, the within plate origin can be eliminated using the previous discrimination diagrams.

Condie (1997) also used the Nb content of oceanic basalts to discriminate between various tectonic settings. He proposed that MORB typically have lower Nb contents (< 3ppm) compared to ocean plateau basalts (OPB), which have >5 ppm Nb contents. The mafic lavas from the Tati and Vumba greenstone belts have Nb contents in the range of 1.43 to 4.68 ppm (average = 2.94 ppm) and 0.66 to 5.40 ppm (average = 2.91 ppm), respectively. This eliminates the mafic lavas from the two greenstone belts from any OPB origin. The La/Nb ratios in subduction related volcanic rocks is generally > 1.5, with an average of about 3. This contrast with low La/Nb ratios of hot spot and ocean ridge-derived rocks that have an average La/Nb ratio of about 1 (Rudnick, 1995). Condie (1999) suggested a La/Nb ratio of 1.4 as defining the boundary between arc-derived basalts, on one hand, and plateau and MORB, on the other. He argued that MORB and OPB have La/Nb < 1.4 whereas arc basalts possess La/Nb > 1.4. The Tati and Vumba mafic lavas display variable La/Nb ratios of 1.02 to 2.48 and 0.32 to 3.64, respectively. Thus, on this basis the mafic lavas from the Tati and Vumba exhibit a mixture of MORB and Arc basalt La/Nb ratios. A mixture of MORB and Arc basalt geochemical affinities is well known in back-arc basins (e.g. Hawkins et al., 1990; Gribble et al., 1996).

Volcanic arc basalts can be subdivided into oceanic arcs, where only oceanic crust is involved in arc construction (e.g. West Pacific-like), and arcs build on continental lithosphere, at active continental margins (e.g. Andean-like). Pearce (1983) noted that most basalts from active

continental margins have Ta/Yb ratios greater than 0.1, whereas oceanic arc basalts have ratios less than 0.1. The mafic lavas from the Tati and Vumba belts are characterised by Ta/Yb ratios varying from 0.01 to 0.15, which is indicative of both oceanic and continental margin type arcs. A more efficient discriminating diagram for this purpose is the Zr/Y versus Zr diagram of Pearce (1983), presented as Figure 7.1f. Continental margin arc basalts plot with higher Zr/Y and Zr than the oceanic basalts. Practically all the samples of mafic lavas from the study area plot in the continental arc field, with half of the samples straddling the overlapping region. This set of data therefore essentially favours a marginal back-arc origin for the mafic lavas from the Tati and Vumba greenstone belts.

Based on the evidence presented above (Figs. 7.1b & e), it is concluded that the mafic lavas from Tati greenstone belt represent a marginal back-arc basin similar to the island arc marginal back-arc basins of the Cenozoic western Pacific Ocean. Geochemical compositional characteristics of the erupted lavas in some back-arc basins are known to vary greatly from MORB-like dominated sequences to arc-like (e.g. Gribble et al., 1996). Chondrite normalized REE and primitive mantle normalized profiles presented in chapter 6, clearly reveal three distinct subgroups within the mafic lavas of each of the Tati and Vumba greenstone belts. One subgroup from the two greenstone belts resembles arc-like mafic lavas of modern oceanic and continental margins (e.g. Pearce, 1982; Gribble et al., 1996; Elliot et at., 1997). The mafic lavas also contain a second subgroup of tholeiitic basalt that exhibits variable, flat mildly LREE depleted patterns with no or with minor Nb anomalies in multi-element plots. Basaltic rocks that display similar geochemical characteristics are found along the mid-ocean ridges of the world (e.g. Pearce, 1996; Gribble et al., 1996). The third minor subgroup from the Tati greenstone belt have elevated LREE but low $(Th/La)_N$, a feature observed in continental- or back-arc or arc-rift basalt (Dostal and Muller, 1998; Hollings and Kerrich, 2000; Sandeman et al., 2006).

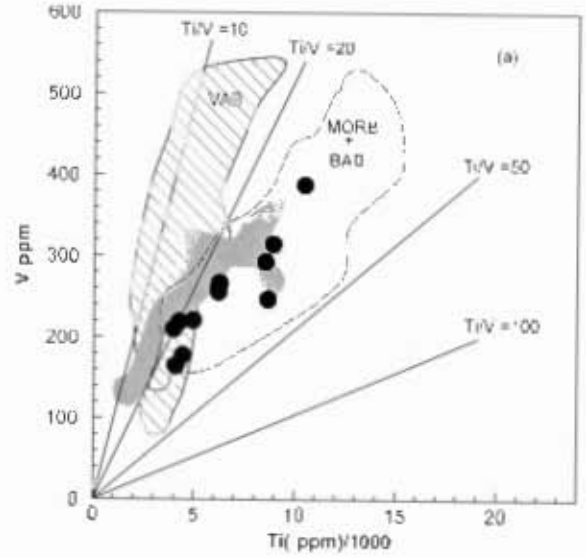

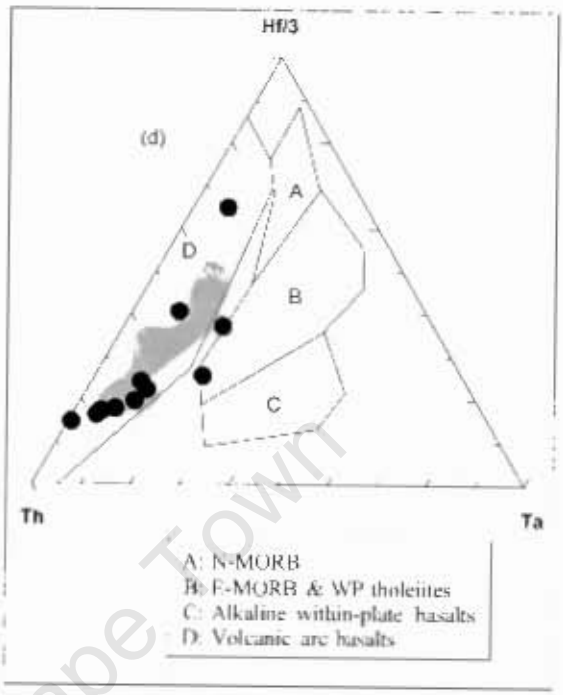

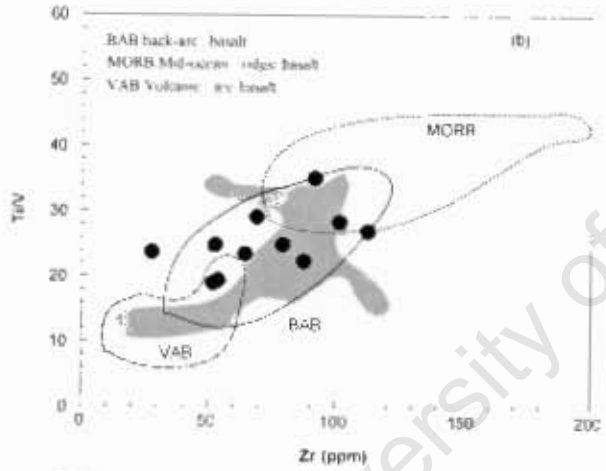

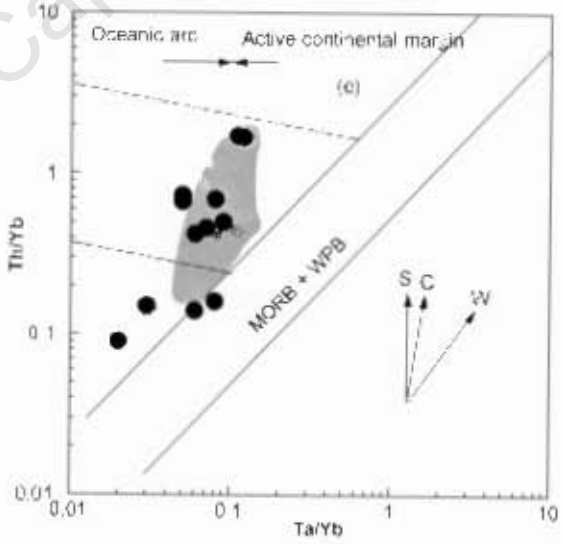

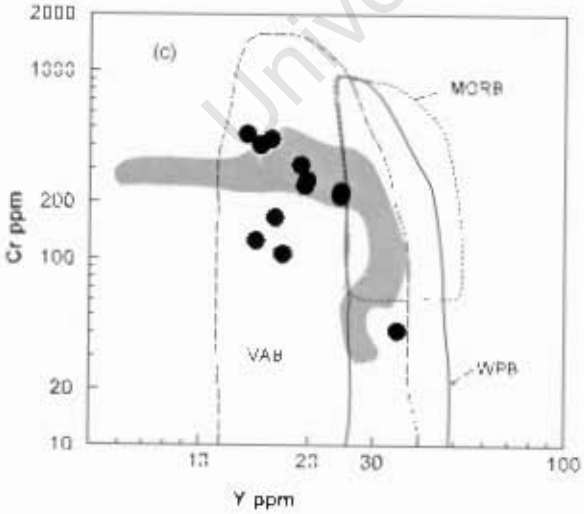

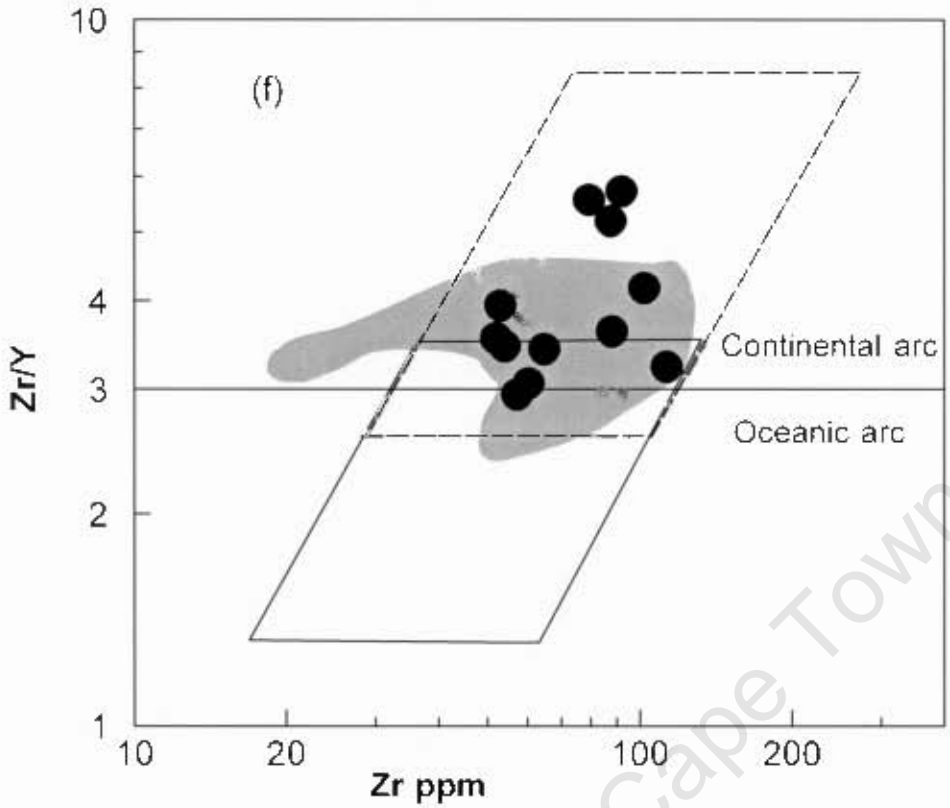

Fig. 7.1: Trace element discrimination diagrams for the mafic lavas from the Francistown Granite-Greenstone Complex. (a) Ti-V diagram of Shervais (1982). (b) Ti/V-Zr diagram after Gribble et al. (1996). (c) Cr-Y diagram of Pearce (1983). (d) Th-Hf-Ta diagram of Wood (1980). (e) Th/Yb-Ta/Yb diagram of Pearce (1982). (f) Zr/Y-Zr diagram of Pearce (1983). BAB = back-arc basalt; MORB = mid ocean ridge basalt; VAB = volcanic arc basalt; WPB = within plate basalt; s-subduction component; c-crustal component; w-within mantle. Grey fields represent samples from the Vumba greenstone belt.

7.2 Felsic lavas

Studies of geochemical characteristics of intermediate to felsic intrusive rocks from a range of tectonic settings revealed that certain trace elements are capable of discriminating the tectonic settings in which the magma was emplaced (Pearce et al., 1984; Harris et al., 1986). Though the diagrams were originally designed for intrusive granitic rocks, they are also applicable to felsic lavas (extrusive equivalents of the granitoids). On the Nb-Y diagram of Pearce et al. (1984), all the felsic lavas from the Tati and Vumba greenstone belts plot in the ambiguous field of volcanic arc and syn-collision granitoids (Fig. 7.2a). According to the Ta-Yb diagram of Pearce et al. (1984) presented as Figure 7.2b, the felsic lavas from the study area are similar to volcanic arc granitoids. Notably, volcanic arc and post-collision granitoids cannot be distinguished from each other based on the Nb-Y and Ta-Yb tectonic diagrams of Pearce et al. (1984). According to Harris et al. (1986),

post-collision granitoids that show many geochemical similarities with volcanic arc granitoids, however, can be distinguished from volcanic arc granites by their higher ratios of Ta/Hf. Felsic lavas from the Tati and Vumba greenstone belts are characterised by greatly overlapping Ta/Hf ratios ranging between 0.05 and 0.19 (Table 6.2), which is much lower than that for post-collision granitoids (Harris et al., 1986). Consequently, on the Hf-Ta-Rb discrimination diagram of Harris et al. (1986), the felsic lavas plot outside the post-collision granitoids field (Fig. 7.2c).

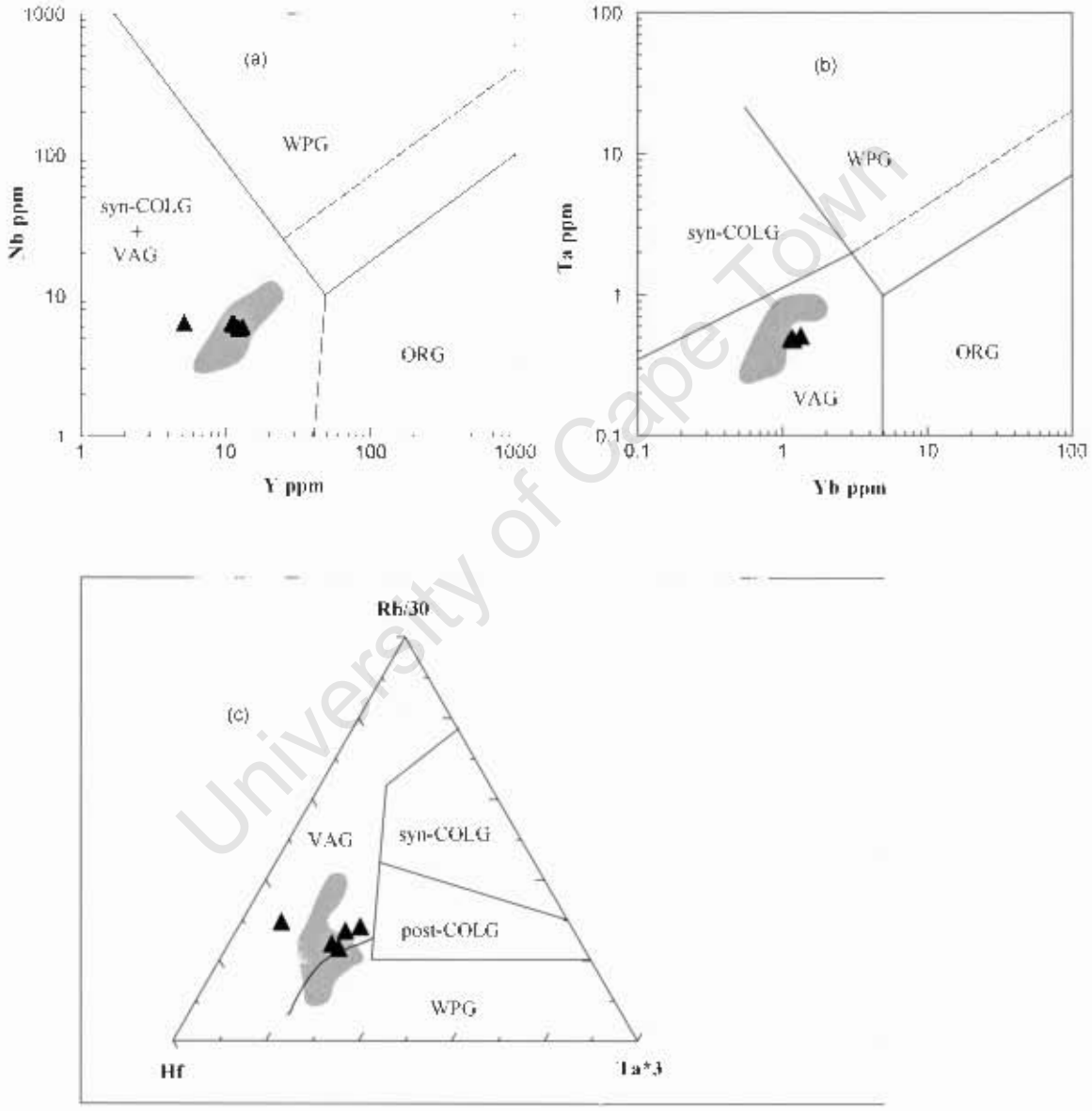

Fig. 7.2: Trace element discrimination diagrams for the felsic lavas from the greenstone belts of the Francistown Granite-Greenstone Complex. (a) Nb-Y and (b) Ta-Yb discrimination diagrams of Pearce et al. (1984). (c) Hf-Ta-Rb discrimination diagram of Harris et al. (1986). WPG = within plate granites; ORG = ocean ridge granites; VAG = volcanic arc granites; syn-COLG = syn-collision granites; post-COLG = post-collision granites. Grey fields represents samples from the Vumba granite-greenstone terrain

7.3 Gabbros, Diorite, Serpentinite and Metapyroxenite

The tectonic setting of the gabbro, diorite, serpentinite and metapyroxenite can be inferred from their trace element characteristics, for instance, from their primitive mantle-normalized diagrams, elemental composition and inter-element ratios. Mafic magmas generated in a convergent margin are characterised by enrichment of the large ion lithophile elements (LILE) over REE, and of LREE relative to P and HFSE (Hollings and Kerrich, 2004). The LILE and LREE enrichment are the subduction-derived components, whereas HFSE are inherited from the mantle (Pearce and Peate, 1995; Hawkesworth et al., 1993). Therefore, HFSE have been used to constrain the composition and enrichment or depletion history of the subarc mantle (Pearce et al., 2000). The composition and inter-elemental ratios for magmatic arc rocks emanate from three main processes; (1) mantle wedge enriched by sediments recycled into the mantle along subducting slabs, (2) mantle wedge enriched by fluids from the dehydration of a subducting slab and (3) subarc mantle enrichment by slab-derived melts (Pearce and Peate, 1995; Sajona et al., 2000). Primitive mantle-normalized multi-element profiles for the gabbro, diorite, serpentinite and metapyroxenite from the study area are all characterised by negative Nb anomalies (chapter 6), which is a characteristic feature of modern normal arc igneous rocks (Pearce and Peate, 1995; Sajona et al., 1996; 2000).

7.4 Granitoids

Granitoids from the Tati granite-greenstone terrane, together with granitoids from the Vumba granite-greenstone terrane presented here for comparison, plot entirely in the volcanic arc granitoids (VAG) and syn-collision granitoids (syn-COLG) field on the Nb-Y tectonic discrimination diagram of Pearce et al. (1984). The trondhjemite and monzogranite from the Tati terrane are exceptions in that these tend to straddle the boundary between the within-plate granitoids (WPG) and VAG + syn-COLG fields. On the Ta-Yb diagram of Pearce et al. (1984), presented as Figure 7.3, all, except one, of the data points representing granitoids from the Tati granite-greenstone terrane plot in the volcanic arc field. The exception being a sample of a tonalite-trondhjemite from the Tati pluton, which plots along the boundary of VAG and syn-COLG. Similarly, granitoids from the Vumba granite-greenstone terrain plot in the VAG field, except the granodiorite samples from the Mashawe pluton that fall along the boundary of syn-COLG and VAG fields. Since the Nb-Y and Ta-Yb discrimination diagrams of Pearce et al. (1984) cannot separate post-collision granitoids

from VAG, the Hf-Ta-Rb diagram of Harris et al. (1986) has been used to test for this (Fig. 7.3c). All, except two, of the data points representing granitoids from the Tati terrain plot in the VAG field of the Hf-Ta-Rb diagram of Harris et al. (1986). The exceptions are samples from the Tati pluton tonalite-trondhjemite (ZBT-32) and a tonalite-trondhjemite dyke (ZBT-36) which plot in the post-collision granitoids and within-plate granitoids fields, respectively. As for the Vumba granitoids, all the samples plot in the VAG field except the granodiorite samples from the Mashawe pluton, which resemble the post-collision granitoids in the Hf-Ta-Rb diagram of Harris et al. (1986). Since Rb is known to be a mobile element under hydrothermal and low-grade metamorphism (Pearce, 1996; Rollinson, 1993), the results of the Hf-Ta-Rb diagram need to be treated with caution or must be supported by other information. Post-collision granitoids can be distinguished from volcanic arc granitoids based on their higher Ta/Hf ratio (Harris et al., 1986), since these 2 are immobile high field strength elements (HFSE). The Tati granitoids display variable Ta/Hf ratios that range from 0.03 to 0.16, except two outlier samples ZBT-36 (Felsic dyke at Phoenix) and ZBT-32 (Tati pluton) that have 0.29 and 0.40 Ta/Hf ratios, respectively (Table 6.5). In comparison, the Vumba granitoids exhibit Ta/Hf ratios varying between 0.05 and 0.17, with exception of the samples from the Mashawe pluton which are characterised by high Ta/Hf ratios (0.41 – 0.31) (Appendix B). The Ta/Hf ratios recorded in the granitoids are consistent with the results of Hf-Ta-Rb diagram of Harris et al. (1986). This substantiates their sign as volcanic arc granitoids.

The prevalence of arc affinities for the felsic lavas, mafic intrusions and granitoids from the Tati and Vumba granite-greenstone terranes suggests a convergent margin tectonic setting. However, the mafic lavas in these greenstone belts represent a back-arc basin or Arc setting. Therefore, the spatial association of broadly contemporary rocks of back-arc and convergent margin settings suggests that there was a geodynamic relationship between the back-arc basin development and the convergent margin. The back-arc basin could have been initiated in response to upwelling asthenosphere in the hinterland of a subduction system due to slab rollback (e.g. Condie, 2005). Noteworthy, is the absence of diorite and trondhjemites as well as the prevalence of granodiorite in the Vumba area, which is the opposite case in the Tati terrain. This is attributed to a more complex subduction zone environment similar to the Andean margin with a back-arc development.

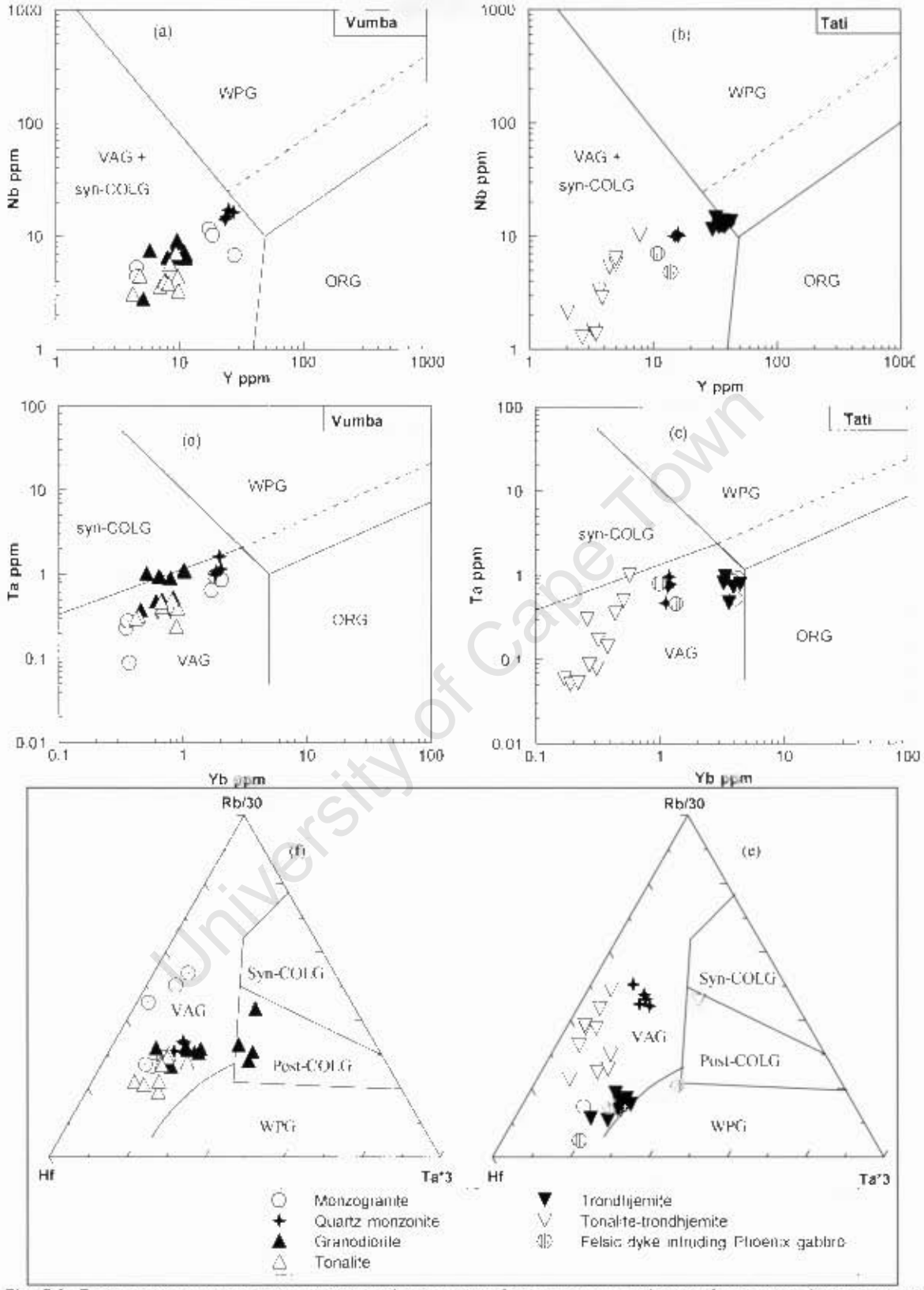

Fig. 7.3: Trace element discrimination diagrams for granitoids from Francistown Granite-Greenstone Complex. (a-b) Nb-Y and (c-d) Ta-Yb diagrams of Pearce et al. (1984). (e-f) Hf-Ta-Rb diagram of Harris et al. (1986). WPG = within plate granites; VAG = volcanic arc granites; syn-COLG = syn-collision granites; post-COLG = post-collision granites.

CHAPTER 8

ISOTOPE GEOCHEMISTRY

8.0 Introduction

This chapter presents both radiogenic and stable isotopes for a variety of rocks from the Francistown Granite-Greenstone Complex. Radiogenic isotopes that were analysed are whole-rock Sr, Nd and Pb. The Sr, Nd and Pb isotopic compositions were determined using a VG Sector thermal ionisation mass spectrometer at the University of Cape Town. The effects of fractionation during Sr and Nd isotope analyses were corrected for by normalizing to $^{87}Sr/^{88}Sr = 0.1194$ and $^{146}Nd/^{144}Nd = 0.7219$, respectively. Over the period of the analyses, NBS 987 (international standard for quality control) gave a value of 0.710253 ± 0.000008 (1σ). The mean $^{87}Sr/^{86}Sr$ value of internal standard MLW 03 was 0.706658, with a 1σ reproducibility of 0.000008 (n=7). Analysis of the La Jolla standard during the period of data collection yielded a value of $^{143}Nd/^{144}Nd$ = 0.511830 ± 0.000005 (1σ). The mean value for the internal reference standard SLH 9 during the period of measurement (reproducibility) was 0.512191 ± 0.000006 (1σ; n=5). Pb isotope ratios were corrected for fractionation by applying a discriminating factor determined by multiple analyses of NBS SRM 981 (n=8). The overall correction factor was about 0.10% $a.m.u^{-1}$. For all Pb isotope measurements 2σ in-run error are less than ±0.015 for $^{206}Pb/^{204}Pb$ and $^{207}Pb/^{204}Pb$ and less than ±0.028 for $^{208}Pb/^{204}Pb$. During the period of these analyses blank levels were very low, and no corrections were needed. In case of the stable isotopes, Oxygen isotope ratios were measured in quartz obtained from the granitoids and pyroxene in the case of gabbroic and dioritic rocks, using a Thermo Finnigan Delta ^{Plus}XP mass spectrometer housed in the Archaeology department, University of Cape Town. All the details on procedures and techniques are documented in Appendix B.

8.1 Background

Radiogenic isotope ratios are commonly used in geochemistry as petrogenetic tracers, yielding information on time-integrated elemental fractionation through processes of melting, crystallization, metamorphism, metasomatism and crustal contamination (Dickin, 2005). The isotope ratios of

elements such as Sr, Nd and Pb are subdivided into ranges that characterize different sources potentially involved in producing magmas. Over geological time, depleted mantle attained high $^{143}Nd/^{144}Nd$ (from high $^{147}Sm/^{144}Nd$) and low $^{87}Sr/^{86}Sr$ (from low $^{87}Rb/^{86}Sr$). On the other hand ancient continental crust acquired low $^{143}Nd/^{144}Nd$ and high $^{87}Sr/^{86}Sr$, reflecting long-term incompatible element enrichment. Between these two extreme sources lie a range of mantle isotope compositions, representing end-members with different enrichments at different times, corresponding to long-term mantle convection and recycling processes, such as melt extraction and lithospheric recycling (e.g. Davidson et al., 2007). Because the radiogenic isotopic ratios of Sr, Nd and Pb are not fractionated by processes of melting and crystallization (Dickin, 2005; Faure 1998), they have become a commonly used tool to fingerprint source contributions in magmatic rocks.

The results of Sr isotope are not always easy to interpret in Archaean rocks because both Rb and Sr are relatively mobile elements that are readily disturbed by secondary processes, particularly when applied to studies of ancient metamorphic terrains such as the Francistown Granite-Greenstone Complex.

The Nd isotopic composition of an igneous rock at the time of formation (initial isotopic composition) can be calculated if the age of the rock is known. This initial isotopic composition can be compared with the isotopic composition of the chondritic bulk earth at the same time, using the epsilon notation (ε_{Nd}) with values that range from positive to negative. The epsilon Nd of an igneous rock sample at the time of its formation, denoted $\varepsilon_{Nd}(t)$, where t is the age of the sample, is calculated by comparing the initial $^{143}Nd/^{144}Nd$ of the rock with the isotopic composition of a chondritic bulk earth at that time as shown in equation (Eq**1**).

$$\varepsilon_{Nd}(t) = \left\{ \frac{^{143}Nd/^{144}Nd_{sample}(t)}{^{143}Nd/^{144}Nd_{BE}(t)} - 1 \right\} \times 10^4 \qquad \textbf{Eq. (1)}$$

Positive initial ε_{Nd} value for igneous rock implies that the magma was derived from a source with greater Sm/Nd than the bulk Earth (BE), such as a depleted mantle source region. A negative initial ε_{Nd} value implies a magma source with lower Sm/Nd ratio than BE, such as an enriched mantle source, or an ancient crustal source (Rollinson, 1993). Thus initial ε_{Nd} values can be used

to test for crustal contamination of mantle-derived magmatic rocks, and characterise source regions of magmas.

Nd isotopic data can also be used to calculate model age of rocks. A model age is the time when the initial $^{143}Nd/^{144}Nd$ of the rock sample equals that of its depleted mantle source (Dickin, 2005; Rollinson, 1993). Such model ages are also referred to as depleted mantle model ages, denoted T_{DM} (e.g. the time of depletion). There are several different depleted mantle evolution models used in calculating the Nd T_{DM} (e.g. Dickin, 2005). Widely applied models are those of DePaolo (1981) and Goldstein et al. (1984). These two models differ. The Goldstein et al. (1984) model is linear between ε_{Nd} ~+10 today and ε_{Nd} ~0 at 4.6 Ga, while the DePaolo model is a quadratic equation Eq. (2) that defines a convex upward depleted mantle evolution curve. An alternative depleted mantle evolution model to that of DePaolo (1981) was proposed by Nagler and Kramers (1998). The Nagler and Kramers (1998) model is defined in Eq. (3).

$$\varepsilon_{Nd} = 0.25t^2 - 3t + 8.5 \qquad \textbf{Eq. (2)}$$

$$\varepsilon_{Nd}(T) = 0.164T^3 - 0.566T^2 - 2.79T + 10.4 \qquad \textbf{Eq. (3)}$$

Pb isotope systematics are more complex than the Sr and Nd isotopes. The complexity emanates from the fact that ^{238}U, ^{235}U and ^{232}Th undergo alpha decay through separate series of intermediate radioactive daughters to stable ^{206}Pb, ^{207}Pb and ^{208}Pb, respectively (Dickin, 2005; Faure, 1998). Pb isotope data are reported relative to ^{204}Pb, which is the only non-radiogenic stable Pb isotope. Lead is an incompatible element, but to a lesser extent than Th and U (Stacy and Kramer, 1975). Thus the U/Pb and Th/Pb values of unaltered magmatic rocks will normally be higher than those of the sources from which they were derived. The enrichment of U, Th and Pb in the continental crust relative to the upper mantle, along with the generally high U/Pb and Th/Pb ratios of fractionated upper continental crust, make Pb isotopes a sensitive indicator for crustal contamination of mantle derived rocks (Kramers and Tolstikhin, 1997).

Oxygen isotopes provide a way of distinguishing between rocks formed in equilibrium with the mantle and those which formed from the continental crust (Criss, 1999). Therefore, they are a valuable indicator of surface processes and a useful tracer of rocks that had contact with the Earth's surface at some point. Additionally, oxygen isotopes can be applied in investigation of

crustal contamination of mantle-derived magmatic rocks. The oxygen isotope ratio $^{18}O/^{16}O$ is measured relative to concentrations in Standard Mean Ocean Water (SMOW) and expressed in parts per mil (‰). This ratio is expressed as a δ value which is calculated as shown in equation Eq.4 below.

$$\delta^{18}O‰ = \frac{[^{18}O/^{16}O\ (sample) - {}^{18}O/^{16}O\ (standard)]}{^{18}O/^{16}O\ (standard)} \times 1000 \qquad \textbf{Eq. (4)}$$

8.2 Data presentation

8.2.1. Sr, Nd and Pb isotope data for the mafic lavas

Six representative mafic volcanic rock samples from the Tati and Vumba greenstone belts were analyzed for their Sr and Nd isotope composition. Initial Sr and Nd isotope ratio for each sample has been calculated from measured $^{87}Sr/^{86}Sr$, $^{143}Nd/^{144}Nd$, the calculated $^{87}Rb/^{86}Sr$ and $^{147}Sm/^{144}Nd$ ratios, and the absolute geologic age of the rock. For the Vumba mafic lavas, the absolute age was inferred from precisely determined U-Pb age on zircons of 2696 ± 5.6 Ma (this study) obtained from the intercalating felsic lavas. In case of the Tati mafic lavas, the minimum absolute age was deduced from the overlying andesitic lava which was precisely dated using U-Pb in zircons at 2737 ± 2 Ma (this study). Two samples of the mafic lavas were analysed for Pb isotope compositions, one from each greenstone belt. The data are presented in Table 8.1.

Initial $^{87}Sr/^{86}Sr$ for the mafic lavas from the Vumba and Tati greenstone belts range from 0.700903 ± 8 to 0.702807 ± 8 and 0.702236 ± 10 to 0.702696 ± 9, respectively (Table 8.1). The Tati mafic lava initial ratios fall within the wider range of the Vumba mafic lavas. However, sample ZBT-54 from the Tati belt displays anomalous initial $^{87}Sr/^{86}Sr$ ratio of 0.695338 (lower than BABI) and very low Sr (12.4 ppm) abundance, which suggests that Sr isotopic system in these mafic lavas has been variably disturbed. On a $^{87}Sr/^{86}Sr$ versus 1/Sr diagram (Fig. 8.1a), the mafic lavas from both belts do not indicate any equivocal relationship between their initial Sr isotopes and the inverse of the Sr abundances as would be expected for mantle-derived samples that experienced some crustal contamination.

Table 8.1: Whole rock Sr, Nd and Pb isotope analyses of the mafic lavas from the Vumba and Tati greenstone belts. Subscripts: i = initial; o = present.

Sample	ZBV-13	ZBV-182	ZBV-185	ZBT-51	ZBT-54	ZBT-46
Location	Vumba greenstone belt			Tati greenstone belt		
U-Pb age (Ma)	2733	2733	2733	2737	2737	2737
Rb (ppm)	0.91	2.30	21.4	3.27	1.27	0.70
Sr (ppm)	137	146	128	170	12.4	92.4
$^{87}Rb/^{86}Sr$	0.019221	0.045581	0.484642	0.055665	0.296471	0.021922
$(^{87}Sr/^{86}86)_{measured}$	0.703567	0.702707	0.721491	0.704439	0.707070	0.703563
1σ error	± 8	± 8	± 8	±10	± 8	± 9
$(^{87}Sr/^{86}86)_i$	0.702807	0.700903	0.702577	0.702236	**0.695338**	0.702696
Sm (ppm)	1.53	2.78	3.98	4.10	2.36	1.70
Nd (ppm)	5.60	8.72	13.6	12.5	10.2	6.10
$^{147}Sm/^{144}Nd$	0.165026	0.192862	0.176777	0.198285	0.139833	0.168455
$(^{143}Nd/^{144}Nd)_{measured}$	0.511939	0.512644	0.512656	0.512739	0.511597	0.512239
1 σ error	±12	± 5	±10	±10	± 6	± 5
$(^{143}Nd/^{144}Nd)_i$	0.508962	0.509166	0.509467	0.509163	0.509068	0.509201
ε_{Nd} (o)	-13.64	0.12	0.34	1.98	-20.32	-7.78
ε_{Nd} (i)	-2.52	0.53	7.40	1.61	-0.26	2.35
$f^{Sm/Nd}$	-0.16	-0.02	-0.10	0.01	-0.29	-0.14
$^{206}Pb/^{204}Pb$	20.38	-	-	-	20.88	-
$^{207}Pb/^{204}Pb$	16.08	-	-	-	16.38	-
$^{208}Pb/^{204}Pb$	39.59	-	-	-	39.81	-

The samples of the mafic lavas from the Vumba greenstone belt yielded a wide variation in initial Nd isotope ratios ($^{143}Nd/^{144}Nd$ = 0.508962 – 0.509467; Table 8.1 and Fig. 8.1b). The initial $^{143}Nd/^{144}Nd$ values exhibit noticeable co-variation with the inverse of the Nd (1/Nd) concentration (Fig. 8.1b), which suggests involvement of crustal contamination. The ε_{Nd} values of the mafic lavas, which were calculated at 2700 Ma, range broadly from -2.5 to +7.4. However, the high positive value is suspect because of secondary processes as evidenced by its high $^{147}Sm/^{144}Nd$ ratio (0.1929). The ε_{Nd} value for depleted mantle at 2700 Ma calculated according to the model of DePaolo (1981) is +2.2. Notably, the LREE enriched sub-group 1 (refer to chapter 6) sample yielded a negative ε_{Nd} value of -2.5, whereas the sub-group 2 (refer to chapter 6) samples that are unfractionated (flat REE) and slightly LREE depleted, record ε_{Nd} values of +0.5. This is consistent with variable enrichment of the source or contamination of the magma. However, caution needs to be exercised when interpreting results based on a small number of samples.

The initial $^{143}Nd/^{144}Nd$ ratios for the mafic lavas from the samples of Tati greenstone belt range from 0.509068 to 0.509201 with ε_{Nd} values varying between -0.3 and +2.4 (Table 8.1). The ε_{Nd} values have been calculated at 2737 Ma. It is worth noting that the ε_{Nd} value of -0.3 has been recorded from the sub-group 1 sample which is a LREE enriched sub-group (see chapter 6). Sub-group 2 (flat REE) samples yielded variable positive ε_{Nd} values averaging +2.0, which is marginally lower than that for depleted mantle (+2.2) at 2737 Ma according to the model of DePaolo (1981). The initial Nd and Sr ratios of the mafic lavas from the Tati and Vumba greenstone belts do not reflect any obvious relationship on variation diagram involving initial Nd versus initial Sr values (Fig. 8.1c).

Two samples of mafic lavas from the two greenstone belts were analysed for the Pb isotopes and their results are recorded in Table 8.1. The representative sample of the Vumba mafic lava has Pb isotope ratios of 20.28, 16.08 and 39.59 for $^{206}Pb/^{204}Pb$, $^{207}Pb/^{204}Pb$ and $^{208}Pb/^{204}Pb$, respectively. These ratios are comparable (though slightly lower) to the Pb isotope ratios of the single analysed Tati mafic lava, which are 20.88, 16.38 and 39.81 for $^{206}Pb/^{204}Pb$, $^{207}Pb/^{204}Pb$ and $^{208}Pb/^{204}Pb$, respectively.

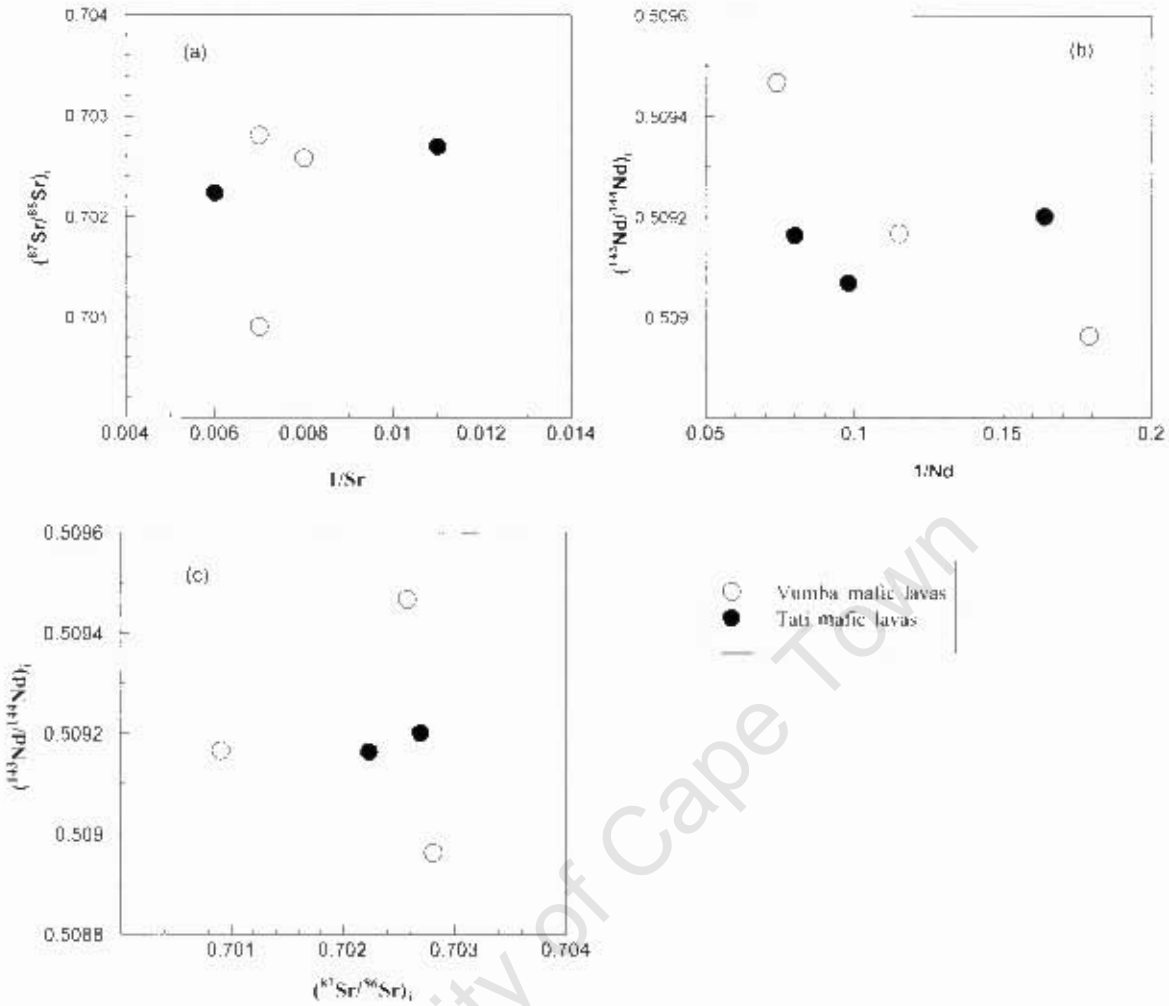

Fig. 8.1: Variations in Sr and Nd isotope compositions in the mafic lavas from the Tati and Vumba greenstone belts.

8.2.2. Sr, Nd and Pb isotope data for the felsic lavas

Three samples from the Vumba felsic lavas and one sample from the Tati felsic lavas were analysed for Sr and Nd isotopes, and the results are recorded in Table 8.2. The Vumba felsic lavas have initial $^{87}Sr/^{86}Sr$ values of 0.69745 to 0.70070 whereas the sample from the Tati felsic lavas yielded a value of 0.70083. The value of 0.69745 which was measured on one Vumba felsic lava indicates that the Sr isotope system was not a closed one. Notably, from Figure 8.2 the felsic lavas exhibit lower initial $^{87}Sr/^{86}Sr$ values than those recorded in the spatial associated mafic lavas, which could be further evidence that the Sr isotope system was not closed.

Table 8.2: Whole rock Sr, Nd and Pb isotope analyses of the felsic lavas from the Vumba and Tati greenstone belts. Subscripts: i = initial; o = present calculated.

Sample	ZBV-173	ZBV-166	ZBV-156	ZBT-43
Location	Vumba greenstone belt			Tati greenstone belt
U-Pb age (Ma)	2700	2700	2700	2735
Rb (ppm)	51.6	18.7	55.2	41.1
Sr (ppm)	83.6	281	347	179
$^{87}Rb/^{86}Sr$	1.797330	0.192659	0.461000	0.665938
$(^{87}Sr/^{86}86)_{measured}$	0.767593	0.708323	0.718548	0.726823
1σ error	± 9	± 9	±8	± 9
$(^{87}Sr/^{86}86)_i$	**0.697452**	0.700700	0.700558	0.700834
Sm (ppm)	3.09	2.40	3.59	2.96
Nd (ppm)	18.2	12.9	21.4	15.5
$^{147}Sm/^{144}Nd$	0.102595	0.112427	0.101372	0.115404
$(^{143}Nd/^{144}Nd)_{measured}$	0.511018	0.511104	0.511006	0.511216
1σ error	± 6	± 5	± 4	±12
$(^{143}Nd/^{144}Nd)_i$	0.509193	0.509101	0.509203	0.509129
ε_{Nd} (o)	-31.61	-29.93	-31.83	-27.74
ε_{Nd} (i)	1.15	-0.65	1.36	0.94
$f^{Sm/Nd}$	-0.48	-0.43	-0.48	-0.41
$^{206}Pb/^{204}Pb$	-	17.72	17.83	20.11
$^{207}Pb/^{204}Pb$	-	15.53	15.65	16.10
$^{208}Pb/^{204}Pb$	-	37.50	37.84	40.30

The initial $^{143}Nd/^{144}Nd$ values for the Vumba felsic lavas vary between 0.509101 and 0.509203, and the representative sample of the Tati felsic lavas records a ratio of 0.509129 (Table 8.2). These initial Nd isotope values versus the inverse of Nd concentration are presented on a variation diagram (Fig. 8.2a) together with the data from the mafic lavas indicated for comparison. It is clear from the variation diagram (Fig. 8.2a) that the initial Nd isotopes of the felsic lavas and mafic lavas from the two greenstone belts are similar. The variation plot of initial Nd versus initial Sr isotope for the felsic and mafic lavas, however, reveal no obvious relationship between the two isotopes (Fig. 8.2b). Additionally, it is apparent from the Fig. 8.2b that the felsic lavas have lower initial Sr isotope values than the mafic lavas.

The initial ε_{Nd} values for the Vumba felsic lavas calculated at 2700 Ma range from -0.65 to +1.36 (Table 8.2) with an average value of +0.6. This value is lower than the depleted mantle value at

2700 Ma which is +2.2 (model of DePaolo, 1981). The representative sample of the Tati felsic lavas recorded an initial ε_{Nd} value of +0.9, calculated at 2735 Ma.

Pb isotope analyses were determined from three felsic samples, two from the Vumba and one from the Tati greenstone belts. The Vumba felsic lavas are less radiogenic (average $^{206}Pb/^{204}Pb$ = 17.78, $^{207}Pb/^{204}Pb$ = 15.59 and $^{208}Pb/^{204}Pb$ = 37.62; Table 8.2) than the associated mafic lavas. The Tati felsic lava has more radiogenic Pb isotope ratios ($^{206}Pb/^{204}Pb$ = 20.11, $^{207}Pb/^{204}Pb$ = 16.10 and $^{208}Pb/^{204}Pb$ = 40.30), similar to that of the Tati mafic lavas.

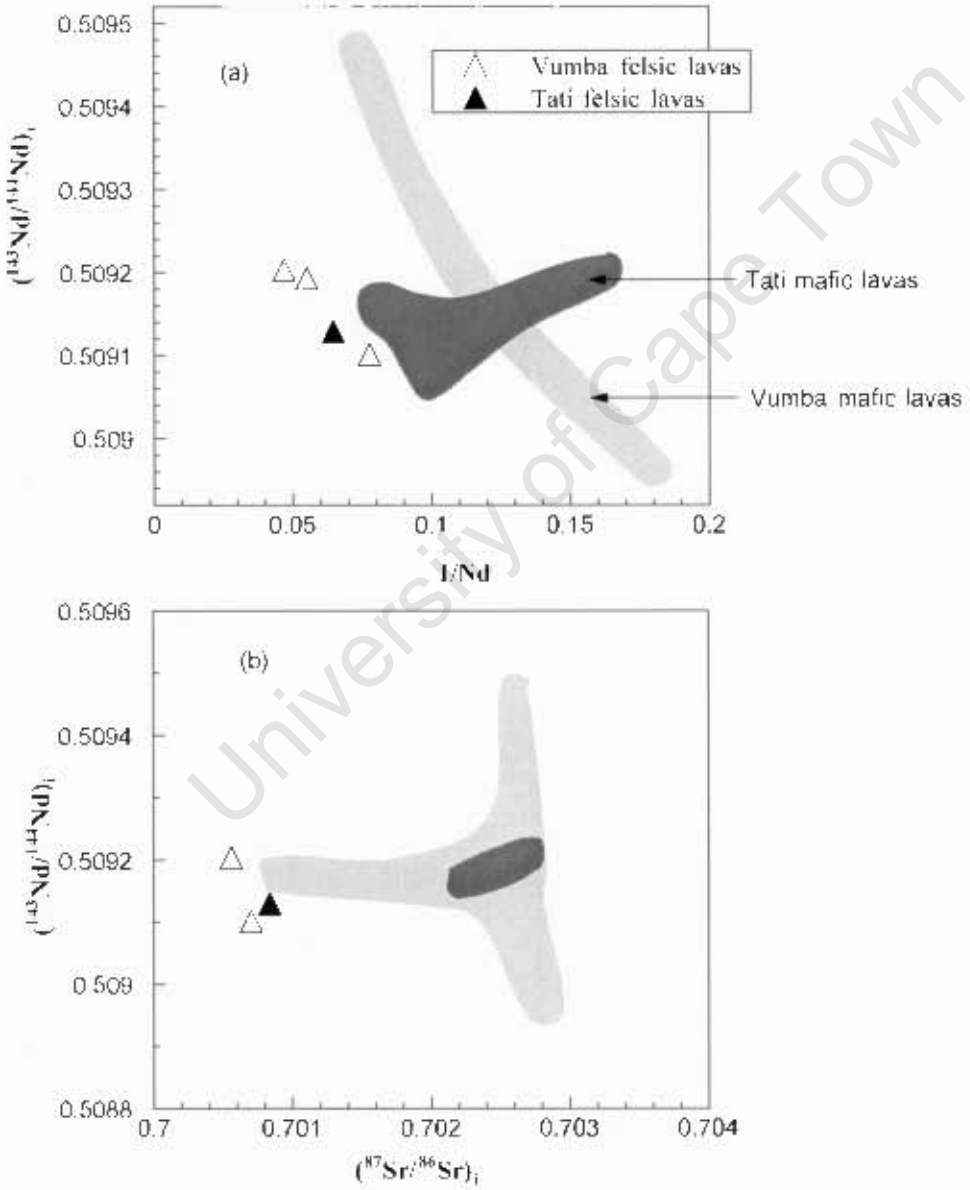

Fig. 8.2: Variations in Sr and Nd isotope compositions in the felsic lavas from the Tati and Vumba greenstone belts. Shaded areas represent compositions of mafic lavas included for comparison.

8.2.3. Sr, Nd and Pb isotope data for the serpentinite, metapyroxenite, gabbro and diorite

Sr, Nd and Pb isotope analyses of the serpentinite, metapyroxenite, gabbro and diorite units from the Francistown Granite-Greenstone Complex are recorded in Table 8.3. The serpentinite has a very high initial Sr isotope value of 0.733564, which falls outside the expected range for mantle Sr isotope ratios. The metapyroxenite sample has initial Sr isotope value of 0.702244. A representative sample of the Phoenix gabbro recorded an initial Sr isotope value of 0.701315 which overlaps the initial Sr ratios of the Selkirk gabbro (0.701311 to 0.702133; Table 8.3). Notably, the sub-group 1 gabbro of Selkirk has higher initial Sr isotope ratio than the sub-group 2 that has initial $^{87}Sr/^{86}Sr$ values comparable to those of the Phoenix gabbro. The Initial $^{87}Sr/^{86}Sr$ value for the sub-group 1 Selkirk gabbro is comparable with that of the metapyroxenite. The diorite samples yielded restricted initial $^{87}Sr/^{86}Sr$ values that range from 0.701230 to 0.701462 (Table 8.3).

Table 8.3: Whole rock Sr, Nd and Pb isotope analyses of the serpentinite, metapyroxenite, gabbro and diorite from the Francistown Arc Complex. Subscripts: i = initial; o = present.

Sample	ZBV-192	ZBV-194	ZBT-39	ZBT-67	ZBT-75	ZBT-24	ZBT-18
Location	Serpentinite	Metapyroxenite	Gabbro (Phoenix)	Gabbro (Selkirk)		Diorite	
U-Pb age (Ma)	2.73	2.73	2.73	2.73	2.73	2.72	2.72
Rb (ppm)	0.50	0.97	3.27	1.96	1.69	0.86	9.85
Sr (ppm)	2.90	41.8	88.0	108	88.4	167	158
$^{87}Rb/^{86}Sr$	0.501362	0.067159	0.107548	0.052518	0.055320	0.014899	0.180482
$(^{87}Sr/^{86}86)_m$	0.753404	0.704901	0.705571	0.704211	0.703500	0.702052	0.708372
1σ error	±13	± 8	±10	± 8	± 8	±11	±10
$(^{87}Sr/^{86}86)_i$	0.733564	0.702244	0.701315	0.702133	0.701311	0.701462	0.701230
Sm (ppm)	0.56	1.60	0.39	2.47	0.60	0.47	1.33
Nd (ppm)	1.65	6.00	1.11	7.57	1.76	1.55	5.71
$^{147}Sm/^{144}Nd$	0.206621	0.161595	0.212919	0.197254	0.206093	0.181738	0.140779
$(^{143}Nd/^{144}Nd)_m$	0.512376	0.512330	0.512200	0.512826	0.512822	0.512487	0.511832
1 σ error	±17	±18	± 5	± 5	±11	±10	± 23
$(^{143}Nd/^{144}Nd)_i$	0.508649	0.509415	0.508384	0.509291	0.509129	0.509230	0.509309
ε_{Nd} (o)	-5.12	-6.01	-8.55	3.66	3.59	-2.94	-15.73
ε_{Nd} (i)	-8.67	6.38	-13.7	4.11	0.93	4.46	2.92
$f^{Sm/Nd}$	0.05	-0.18	0.08	0.00	0.05	-0.08	-0.28
$^{206}Pb/^{204}Pb$	13.72	-	14.30	13.94	18.08	14.98	17.82
$^{207}Pb/^{204}Pb$	14.85	-	14.94	15.03	15.83	15.23	15.69
$^{208}Pb/^{204}Pb$	33.72	-	33.99	34.10	36.42	34.61	37.80

The initial Nd isotope value for the serpentinite is 0.508649 with initial ε_{Nd} value of -8.67 (Table 8.3). The metapyroxenite has an initial Nd isotope value of 0.509415 corresponding to initial ε_{Nd}

value of +6.38. The initial ε_{Nd} values for both serpentinite and metapyroxenite were calculated at 2700 Ma and are lower and higher, respectively, than the depleted mantle value at 2700 Ma, which is +2.2 (calculated using model of DePaolo, 1981).

The Phoenix gabbro has low initial Nd isotope and a very low initial ε_{Nd} value of -13.7, well outside the expected ε_{Nd} range of the mantle at 2700 Ma. The Selkirk gabbro has variable initial Nd isotope values from 0.509129 to 0.509291 corresponding to ε_{Nd} values of +0.93 to +4.11 (average = +2.5). Notably, the sub-group 1 Selkirk gabbro exhibits higher ε_{Nd} ratios than sub-group 2. The diorite unit within the same area has variable initial Nd isotope values, ranging from 0.509230 to 0.509309, with initial ε_{Nd} values ranging from +2.92 to +4.46 (average = +3.7; Table 8.3). The higher initial ε_{Nd} value corresponds to the diorites of sub-group 2 (unfractionated REE). The initial ε_{Nd} values for gabbros and diorite were calculated at 2737 and 2716 Ma, respectively. The ε_{Nd} values for the Selkirk gabbro and diorite are slightly higher than the values of the depleted mantle calculated at 2737 and 2716 Ma, respectively, which is +2.2 (model of DePaolo, 1981). The Sr and Nd initial isotopes for the serpentinite, metapyroxenite, gabbros and diorite are presented on variation diagrams in Figure 8.3 with the initial ratios for the mafic lavas indicated for comparison. It is apparent from the variation diagram (Fig. 8.3) that the initial Nd isotopes of the mafic lavas are comparable to those of the diorite, Selkirk gabbro and metapyroxenite.

The representative sample of serpentinite has less radiogenic Pb isotopes ($^{206}Pb/^{204}Pb$ = 13.72, $^{207}Pb/^{204}Pb$ = 14.85 and $^{208}Pb/^{204}Pb$ = 33.72; Table 8.3) comparable with those of the Phoenix gabbro ($^{206}Pb/^{204}Pb$ = 14.30, $^{207}Pb/^{204}Pb$ = 14.94 and $^{208}Pb/^{204}Pb$ = 33.99). The Selkirk gabbro is characterised by less radiogenic to radiogenic Pb isotope composition ($^{206}Pb/^{204}Pb$ = 13.94-18.08, $^{207}Pb/^{204}Pb$ = 15.03-15.83 and $^{208}Pb/^{204}Pb$ = 34.10-36.42; Table 8.3). The LREE enriched sub-group sample of the Selkirk gabbro exhibits less radiogenic Pb isotope composition than the sub-group 2 which comprise trace element depleted samples with high Mg#. The diorite unit displays variable Pb isotope composition from less to radiogenic ($^{206}Pb/^{204}Pb$ = 14.98-17.98, $^{207}Pb/^{204}Pb$ = 15.23-15.69 and $^{208}Pb/^{204}Pb$ = 34.61-37-80; Table 8.3) with the sub-group 1, which is composed of LREE enriched samples, displaying more radiogenic Pb isotope than the sub-group 2 diorite samples.

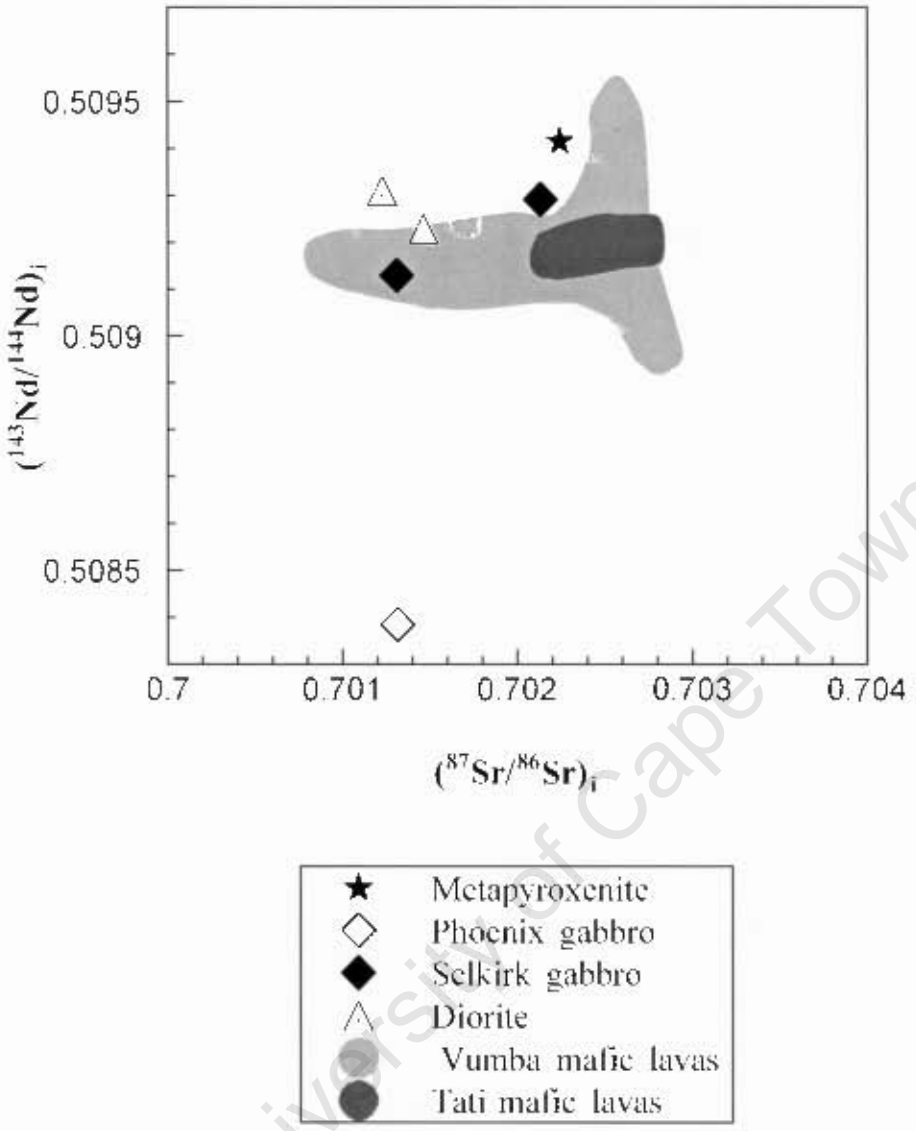

Fig. 8.3: Variations in initial Sr and Nd isotope compositions in the serpentinite, metapyroxenite, gabbro and diorite from the Francistown Granite-Greenstone Complex. Shaded areas represent compositions of mafic lavas included for comparison.

8.2.4 Sr, Nd and Pb isotope data for the granitoids

Analyses of Sr, Nd and Pb isotopes for a variety of granitoids from the Vumba and the Tati granite-greenstone terrains are recorded in Table 8.4

Table 8.4: Whole rock Sr, Nd and Pb isotope analyses of a variety of granitoids from the Francistown Granite-Greenstone Complex. Subscripts: i = initial; o = present. Abbreviation: Trondhje = trondhjemite.

Sample	ZBV-69	ZBV-74	ZBT-6	ZBV-83	ZBT-4	ZBV-78	ZBV-80	ZBV-91	ZBV-97	ZBT-10
Rock type	Monzogranite			Quartz monzonite		Granodiorite				Trondhje
Location	Vumba		Tati	Vumba	Tati	Vumba				Tati
U-Pb age (Ma)	2647	2647	2715	2690	2734	2686	2686	2686	2686	2716
Rb (ppm)	404	139	52.3	180	212	69.9	74.5	84.6	115	41.2
Sr (ppm)	187	216	99.7	535	586	673	459	136	275	83.5
$^{87}Rb/^{86}Sr$	6.300806	1.869078	1.524843	0.470382	1.050935	0.300810	0.470382	1.811525	1.211923	1.435033
$(^{87}Sr/^{86}86)_m$	0.788446	0.770731	0.749628	0.718915	0.743037	0.712441	0.718915	0.768262	0.745542	0.755081
1σ error	± 8	± 9	± 9	± 9	±14	±13	± 9	± 9	±10	± 9
$(^{87}Sr/^{86}86)_i$	0.547108	0.699140	0.691222	0.699781	0.702117	0.700746	0.700627	0.697834	0.698425	0.699205
Sm (ppm)	18.3	2.96	6.14	12.0	8.03	7.31	4.26	2.98	5.76	5.98
Nd (ppm)	106	21.8	31.6	74.6	54.3	52.0	25.9	15.5	36.3	31.3
$^{147}Sm/^{144}Nd$	0.103860	0.082044	0.117422	0.097285	0.089369	0.084942	0.099391	0.112675	0.095882	0.115445
$(^{143}Nd/^{144}Nd)_m$	0.511052	0.510762	0.511286	0.511027	0.510833	0.510718	0.510984	0.511220	0.510865	0.510828
1 σ error	± 6	± 5	± 5	± 6	± 5	± 7	± 5	± 5	± 5	± 5
$(^{143}Nd/^{144}Nd)_i$	0.509238	0.509329	0.509272	0.509297	0.509222	0.509235	0.509248	0.509223	0.509166	0.508740
ε_{Nd} (o)	-30.94	-36.60	-26.38	-31.42	-25.42	-37.45	-32.27	-27.66	-34.59	-35.32
ε_{Nd} (i)	0.69	2.48	0.15	2.94	0.36	1.62	1.88	1.40	0.27	-7.35
$f^{Sm/Nd}$	-0.47	-0.58	-0.40	-0.51	-0.55	-0.57	-0.49	-0.43	-0.51	-0.41
$^{206}Pb/^{204}Pb$	23.98	21.51	41.89	22.95	24.41	16.54	19.64	26.77	22.14	80.48
$^{207}Pb/^{204}Pb$	16.72	16.29	19.27	16.52	16.74	15.38	15.90	17.30	16.34	27.26
$^{208}Pb/^{204}Pb$	62.33	40.26	62.65	43.13	42.93	38.09	40.36	39.39	47.57	102.85

Table 8.4: Continued

Sample	ZBV-144	ZBV-09	ZBV-133	ZBT-36	ZBT-29	ZBT-33	ZBT-30	ZBT-77	ZBT-80
Rock type	Tonalite			Tonalite-trondhjemite					
Location	Vumba			Phoenix	Tati Pluton			Sekukwe Pluton	
U-Pb age (Ma)	2690	2690	2690	2700	2670	2670	2670	2734	2734
Rb (ppm)	69.4	58.9	54.4	11.0	42.0	69.9	45.6	51.9	42.0
Sr (ppm)	195	405	371	119	284	266	204	394	414
$^{87}Rb/^{86}Sr$	1.033629	0.421431	0.424481	0.267691	0.428546	0.762327	0.648550	0.381564	0.293814
$(^{87}Sr/^{86}Sr)_m$	0.740750	0.717964	0.717188	0.711482	0.717982	0.729180	0.730660	0.713993	0.712291
1 σerror	± 9	± 9	± 8	± 8	± 9	± 9	± 9	±13	±10
$(^{87}Sr/^{86}Sr)_i$	0.700504	0.701554	0.700660	0.701059	0.701295	**0.699497**	0.705407	**0.699136**	0.700851
Sm (ppm)	4.79	3.22	2.10	3.51	2.35	1.42	0.74	0.56	1.45
Nd (ppm)	33.6	24.1	12.7	19.4	16.3	8.46	5.97	2.07	10.0
$^{147}Sm/^{144}Nd$	0.086138	0.080731	0.099919	0.109334	0.087113	0.101429	0.074901	0.163531	0.087617
$(^{143}Nd/^{144}Nd)_m$	0.510617	0.510634	0.510970	0.511140	0.510671	0.511050	0.510960	0.512400	0.510831
1 σerror	± 6	± 9	± 5	± 5	± 6	±14	± 6	± 6	± 5
$(^{143}Nd/^{144}Nd)_i$	0.509088	0.509201	0.509197	0.509163	0.509096	0.509216	0.509606	0.509451	0.509247
εNd(o)	-39.43	-39.10	-32.54	-29.22	-38.37	-30.98	-32.73	-4.64	-35.24
εNd(i)	-1.16	1.06	0.98	0.58	-1.44	0.91	7.57	7.08	3.08
$f^{Sm/Nd}$	-0.56	-0.59	-0.49	-0.44	-0.56	-0.48	-0.62	-0.17	-0.55
$^{206}Pb/^{204}Pb$	-	24.68	21.16	21.92	16.14	19.80	16.25	16.52	15.72
$^{207}Pb/^{204}Pb$	-	17.26	16.22	16.34	15.28	15.98	15.38	15.59	15.20
$^{208}Pb/^{204}Pb$	-	45.36	39.05	42.37	41.00	36.05	35.13	35.18	35.34

Despite having highly radiogenic Sr isotope composition (0.749628 – 0.788446; Table 8.4) the granitoids generally record very low initial Sr isotope analyses that are even outside the expected mantle Sr isotope range. This suggests that the Rb-Sr isotope system in the granitoids has been too perturbed in general to yield any reliable information.

In terms of the Nd isotope data, the representative monzogranite samples in the Francistown Granite-Greenstone Complex have ε_{Nd} values in the region of +0.2 to +2.5 (Table 8.4). The monzogranite sample from the Tati terrain yielded a relatively lower ε_{Nd} value (+0.15) compared to the monzogranite from the Vumba granite-greenstone terrain that recorded ε_{Nd} values raging from +0.7 to +2.5. The ε_{Nd} values were calculated at 2650 and 2715 Ma for the Vumba and Tati monzogranites, respectively. The obtained ε_{Nd} values are less than those of the depleted mantle which at 2650 and 2715 Ma are +2.3 and +2.2, respectively (model of DePaolo, 1981).

Samples of the quartz monzonite from the Vumba and Tati terrains recorded initial Nd isotope values of 0.509297 and 0.509222 respectively (Table 8.4). Their ε_{Nd} values calculated at estimated

crystallization ages for the Vumba (2690 Ma) and Tati (2734 Ma) quartz monzonite are +2.9 and +0.4, respectively. The ε_{Nd} value for the Vumba quartz monzonite is slightly higher than the value of the depleted mantle calculated at 2690 Ma which is around +2.2 (model of DePaolo, 1981) whereas the quartz monzonite from the Tati terrain have a lower ε_{Nd} value.

The granodiorite samples analysed for Nd isotope composition were collected from four separate localities namely, the Vumba stock, Sechele stock, Mashawe pluton and the Kalakamati pluton, which all outcrop in the Vumba granite-greenstone terrain. Samples from the Mashawe pluton, Vumba and Sechele stocks have recorded similar initial Nd isotope values that yielded ε_{Nd} values that range from +1.4 and +1.9 (Table 8.4). The Kalakamati pluton sample yield a slightly lower value of +0.3. These values were calculated at 2686 Ma, and they are lower than that for depleted mantle, which at 2686 Ma is about +2.2.

The samples of tonalite from the Vumba granite-greenstone terrain analyzed for Nd isotope composition reflected variable ε_{Nd} values that range from -1.2 to +1.1, although two of the three samples recorded +1.0 and +1.1. The ε_{Nd} values were calculated at the crystallization age of the tonalite (2690 Ma).

A representative sample of trondhjemite from the Tati granite-greenstone terrain recorded the lowest (amongst the granitoids) initial Nd isotope composition of 0.508740, which corresponds to ε_{Nd} value of -7.4 calculated at the trondhjemite crystallization age of 2716 Ma. The tonalite-trondhjemite dyke sample yields an ε_{Nd} value of +0.6 calculated at the dyke's crystallization age of 2700 Ma.

The tonalite-trondhjemite from the Tati and Sekukwe plutons yielded a wide range of ε_{Nd} values (Table 8.4). The ε_{Nd} values for the three samples from the Tati pluton calculated at crystallization age of 2670 Ma vary between -1.4 to +7.6, although two of the three values are -1.4 and +0.9. Two samples from the Sekukwe pluton, which has a crystallization age of 2734 Ma, recorded ε_{Nd} values of +3.1 and +7.1. The ε_{Nd} values for the Sekukwe tonalite-trondhjemite are higher than that for depleted mantle, which at 2734 Ma is about +2.2 (model of DePaolo, 1981).

Pb isotope analyses for the monzogranite from the Vumba granite-greenstone terrain reflect radiogenic Pb composition of $^{206}Pb/^{204}Pb$ = 23.89-21.51, $^{207}Pb/^{204}Pb$ = 16.72-16.29 and $^{208}Pb/^{204}Pb$ = 62.33-40.26; Table 8.4). The two samples which represent the inner and outer phases of the Domboshaba Granite exhibit a conspicuous difference in composition of $^{208}Pb/^{204}Pb$ the inner phase has a higher $^{208}Pb/^{204}Pb$ value. The Tati monzogranite is more radiogenic ($^{206}Pb/^{204}Pb$ = 41.89, $^{207}Pb/^{204}Pb$ = 19.27 and $^{208}Pb/^{204}Pb$ = 62.65) than the Vumba monzogranite. The representative quartz monzonite samples from the two granite-greenstone terrain recorded comparable Pb isotope compositions (see Table 8.4) which are radiogenic and similar to that of the outer phase of the Domboshaba monzogranite.

Four representative samples of the granodiorite collected from isolated plutons exhibit different Pb isotope composition that vary from less radiogenic to highly radiogenic. The least radiogenic sample is the one collected from the Vumba stock (ZBV78), which has $^{206}Pb/^{204}Pb$ = 16.54, $^{207}Pb/^{204}Pb$ = 16.74 and $^{208}Pb/^{204}Pb$ = 38.09. The Sechele stock sample (ZBV80) is slightly more radiogenic than the Vumba stock as evidenced by the ratios $^{206}Pb/^{204}Pb$ = 19.64, $^{207}Pb/^{204}Pb$ = 15.90 and $^{208}Pb/^{204}Pb$ = 40.36. Samples from the Mashawe (ZBV91) and Kalakamati (ZBV97) Plutons recorded $^{206}Pb/^{204}Pb$ ratios of 26.77 and 22.14, respectively, which indicate that they are more radiogenic than the Vumba and Sechele stocks. Notably, the Pb isotope composition of the Kalakamati (granodiorite) is comparable with that of the contiguous quartz monzonite (ZBV83) unit in the Vumba area (see Pb isotope results of samples ZBV97 and ZBV83 in Table 8.4).

A representative sample of the trondhjemite (ZBT10) has a Pb isotope signature distinct from the rest of the granitoids in the Vumba and Tati granite-greenstone terrains. The sample is extremely radiogenic with $^{206}Pb/^{204}Pb$ and $^{207}Pb/^{204}Pb$ recording values of 80.48 and 27.26, respectively. $^{208}Pb/^{204}Pb$ recorded a value of 102.85. This possibly indicates the fractionation of feldspars during formation of the trondhjemite.

Two samples of the tonalite unit from the Vumba area were analysed for the Pb isotope composition and they recorded variable radiogenic values of 24.68 and 21.16 for $^{206}Pb/^{204}Pb$. The $^{207}Pb/^{204}Pb$ and $^{208}Pb/^{204}Pb$ ratios range from 16.22 to 17.26 and 39.05 to 45.36 respectively. A sample from a felsic dyke intruding the Phoenix gabbro has $^{206}Pb/^{204}Pb$, $^{207}Pb/^{204}Pb$ and

$^{208}Pb/^{204}Pb$ ratios 21.92, 16.34 and 42.37 respectively. These ratios are comparable with those of sample ZBV133 of the tonalite stated above.

Five samples of tonalite-trondhjemite from the Tati and Sekukwe plutons analysed for Pb isotope composition have recorded variable and generally less radiogenic $^{206}Pb/^{204}Pb$ values of 15.72 to 19.80, although three of the five samples cluster between 16.14 and 16.52. $^{207}Pb/^{204}Pb$ has a restricted range of 15.20 to 15.98 (average of 15.49). The samples from the Tati pluton display heterogeneous $^{208}Pb/^{204}Pb$ composition that range from 35.13 to 41.00.

Variation diagrams of the Pb isotopes measured from the mafic and felsic rocks of the Vumba and Tati granite-greenstone terrains are presented in Figure 8.4. It can be seen from the variation diagrams (Fig. 8.4a&c) that the $^{207}Pb/^{204}Pb$ and $^{208}Pb/^{204}Pb$ versus $^{206}Pb/^{204}Pb$ for mafic rocks from the two granite-greenstone terrains of the Francistown Granite-Greenstone Complex form tight linear arrays, plotting along the 2700 Ma reference isochron. Samples from a single source and of approximately the same age should plot on a tight array in the $^{207}Pb/^{204}Pb$ versus $^{206}Pb/^{204}Pb$ diagram. Figures 8.4a & b suggests that the felsic and mafic lavas and intrusives from the Vumba and Tati terrains are essentially, all derived from the same source type. If there was source- or crustal contamination, the array would be fuzzy because of assimilation of material with high $^{207}Pb/^{204}Pb$. Oldest crust often has elevated $^{207}Pb/^{204}Pb$ ratios at given $^{206}Pb/^{204}Pb$. If there was a significant contamination by much older crust, the felsic lavas from the two belts would show it most and their array would be offset above that of the mafic rocks.

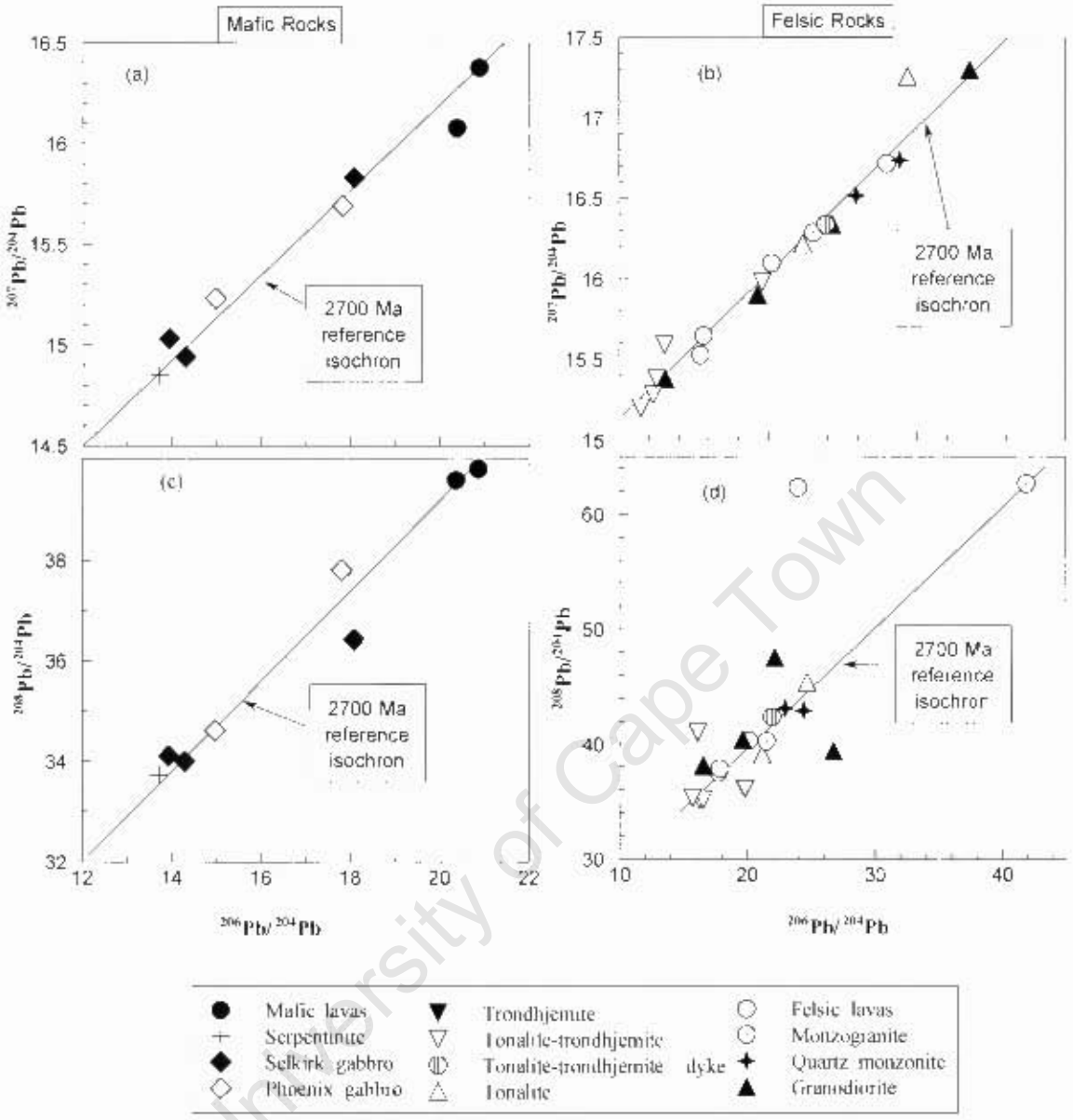

Fig. 8.4: Variation plots of $^{207}Pb/^{204}Pb$ and $^{208}Pb/^{204}Pb$ versus $^{206}Pb/^{204}Pb$ composition for whole-rock samples of igneous rocks from the Francistown Granite-Greenstone Complex. Note the scatter of the felsic rocks on the plot of $^{208}Pb/^{204}Pb$ versus $^{206}Pb/^{204}Pb$ (Fig. 8.4d). The isochron is within the framework of the Stacey and Kramers (1975) model of Pb isotopic evolution.

8.2.5 Oxygen isotope data for gabbro, diorite and granitoids

In this study, $\delta^{18}O‰$ measurements on quartz and pyroxene were obtained from the gabbro, diorite and granitoid units of the Francistown Granite-Greenstone Complex. A total of 16 samples was analysed for $\delta^{18}O$ values and the results are presented in Table 8.5. Reproducibility for repeated measurements of each standard was about ±0.1‰ (2σ).

Table 8.5: O isotope data of gabbro, diorite and granitoids from the Francistown Granite-Greenstone Complex.

Sample No.	Terrain	Locality	Rock type	Mineral	$\delta^{18}O$‰
ZBT39	Tati	Phoenix	Gabbro	Pyroxene	5.5
ZBT40	Tati	Phoenix	Gabbro	Pyroxene	5.5
ZBT18	Tati	Francistown	Diorite	Pyroxene	8.3
ZBT24	Tati	Francistown	Diorite	Pyroxene	7.1
ZBV83	Vumba	Kalakamati	Quartz Monzonite	Quartz	10.0
ZBT6	Tati	Francistown	Monzogranite	Quartz	10.1
ZBV69	Vumba	Domboshaba	Monzogranite	Quartz	9.0
ZBV91	Vumba	Mashawe Pluton	Granodiorite	Quartz	9.0
ZBT10	Tati	Francistown	Trondhjemite	Quartz	9.6
ZBT15	Tati	Francistown	Trondhjemite	Quartz	8.7
ZBV09	Vumba	Maebe	Tonalite	Quartz	12.1
ZBT30	Tati	Tati Pluton	Tonalite-trondhjemite	Quartz	9.5
ZBT33	Tati	Tati Pluton	Tonalite-trondhjemite	Quartz	9.1
ZBT77	Tati	Sekukwe Pluton	Tonalite-trondhjemite	Quartz	8.6
ZBT80	Tati	Sekukwe Pluton	Tonalite-trondhjemite	Quartz	9.0
ZBT36	Tati	Phoenix Gabbro	Tonalite-trondhjemite	Quartz	10.6

The Phoenix Gabbro unit yielded pyroxene $\delta^{18}O$ value of +5.5‰ which permit a direct mantle-derived origin without any crustal involvement, since the mantle has a $\delta^{18}O$ value of 5.3 ± 0.3‰ (Valley et al., 1998). Pyroxene $\delta^{18}O$ values that range from +7.1 to +8.3‰ (Table 8.5) were obtained from the diorite unit. Notably, the LREE enriched diorite sample recorded a higher $\delta^{18}O$ value (+8.3‰) than the non-fractionated REE sample that yielded $\delta^{18}O$ value of +7.1‰.

Monzogranite samples recorded quartz $\delta^{18}O$ values that vary from 9.0 to 10.1‰ with the sample from the Tati granite-greenstone terrain yielding the highest value. Granodiorite sample recorded similar quartz $\delta^{18}O$ value of +9.0‰ as the monzogranite. The quartz monzonite from the Vumba terrain has recorded quartz $\delta^{18}O$ value of +10.0‰ which marginally exceed those of the monzogranite and granodiorite within the same terrain. All these values fall within the $\delta^{18}O$ range of I-type granites. Only Maebe Tonalite sample, which recorded a high quartz $\delta^{18}O$ value of +12.1‰, falls within the range of S-type granite $\delta^{18}O$ values.

The trondhjemite unit in the Tati terrain have recorded variable quartz $\delta^{18}O$ values of +9.6 and +8.7‰. These values are lower than the value yielded by the monzogranite sample within the Tati terrain. A sample from the tonalite-trondhjemite dykes recorded a quartz $\delta^{18}O$ value of 10.6‰, which is higher than those recorded in the monzogranite and trondhjemite units. The tonalite-trondhjemite samples from the Tati and Sekukwe plutons have yielded slightly different quartz $\delta^{18}O$ values of +9.5 to +9.1‰ and +9.0 to +8.6 ‰, respectively. All these quartz $\delta^{18}O$ values fall within the range of the I-type granites $\delta^{18}O$ values.

8.3 Summary of isotope data

Mafic lavas from the Vumba greenstone belt indicate a rather heterogeneous Nd isotopic composition with initial ε_{Nd} values ranging from -2.5 to +0.5. The negative ε_{Nd} value corresponds to the LREE enriched subgroup sample, while the positive ε_{Nd} value has been recorded from the subgroup 2 samples that display unfractionated REE patterns. These ε_{Nd} values are lower than that for depleted mantle, which at 2700 Ma was about +2.2 (model of DePaolo, 1981). The Tati mafic lavas have varying Nd isotopic compositions with ε_{Nd} values of -0.3 to +2.4. Similarly, the negative ε_{Nd} value corresponds to the LREE enriched subgroup sample (see chapter 6).

Felsic lavas from the Vumba greenstone belt have variable ε_{Nd} values that range between -0.7 and +1.4 which is higher than those of the mafic lavas. In the Tati greenstone belt, the felsic lavas recorded an initial ε_{Nd} value of +0.9. All these ε_{Nd} values are lower than that of corresponding depleted mantle values calculated according to the model of DePaolo (1981).

The Phoenix gabbro in the Tati greenstone belt has recorded a mantle $\delta^{18}O$ value of +5.5‰ despite of a highly unradiogenic ε_{Nd} value of -13.7. Because of the very low Sm and Nd concentrations in Phoenix gabbro, this ε_{Nd} value is suspect. Selkirk gabbro has variable Nd isotopic composition with ε_{Nd} values of +4.1 and +0.9. The Sr isotopic values from both gabbros are of mantle values. The Serpentinite unit in the Vumba greenstone belt has both Sr and Nd isotopic compositions of non-mantle composition. It has anomalously low Rb, Sr, Sm and Nd concentrations and therefore is a suspect for secondary alteration.

The diorite unit in the Francistown Granite-Greenstone Complex records Sr and Nd isotopic initial compositions of mantle values, but non-mantle $\delta^{18}O$ values of +7.1 and +8.3. The granitoids from

the Vumba terrain display positive ε_{Nd} values that range from +0.2 to +2.9 except one sample from the tonalite that has an ε_{Nd} value of -1.2, along with quartz $\delta^{18}O$ value of +12.1. The other granitoids have mineral quartz $\delta^{18}O$ values that vary between +9.0 and +10.0‰.

Granitoids from the Tati granite-greenstone terrain are generally characterised by variable ε_{Nd} values which range from -1.4 to +3.1, though there are some outliers with more radiogenic ε_{Nd} values of +7.1 and +7.6. These outliers have very low Sm and Nd concentrations which are suspects of secondary processes. The mineral quartz $\delta^{18}O$ values vary between +8.6 and 10.1‰.

CHAPTER 9

Petrogenesis of the mafic and felsic lavas of the Tati and Vumba greenstone belts

This chapter aims at discussing the main geochemical characteristics, sources and petrogenesis of the Tati and Vumba greenstone belts assemblages. The rock assemblages include the mafic lavas, ultramafic-mafic intrusions and felsic lavas.

9.1 Mafic lavas

9.1.1 Main geochemical characteristics

Mafic lavas from the Tati greenstone belt are dominated by both tholeiitic and calc-alkaline iron rich basalts that display low Mg#. Additionally, the mafic lavas exhibit low compatible trace element abundances that are indicative of non-primary magma composition. The chondrite normalized REE and primitive mantle normalized multielement plots (Sun and McDonough, 1989) presented in chapter 6 (Fig. 6.4 & 6.5), reveal three distinct subgroups within the mafic lavas. They exhibit comparable HREE abundances but variable LREE enrichment and HFSE depletion amongst the subgroups. The predominant subgroup 1 comprises basalt with calc alkaline affinities and moderately elevated LREE patterns similar to arc basalts of modern oceanic arc setting (Pearce, 1982). Subgroup 2 is composed of tholeiitic MORB-like basalt, which exhibits flat, mildly LREE depleted patterns and lack of significant HFSE depletion. The calc-alkaline basalt of subgroup 3 is least represented in the Tati greenstone belt and it is characterised by elevated LREE and prominent HFSE depletion, a feature observed in basaltic rocks of modern continental margins (Pearce, 1982; Elliot et al., 1997; Gribble et al., 1996).

The mafic lavas from the Vumba greenstone belt exhibit tholeiitic to calc-alkaline affinities and iron enrichment. Their compatible trace element and MgO concentrations are not consistent with them being primary melts. Chondrite normalized REE patterns and primitive mantle multielement plot (Sun and McDonough, 1989) also define three distinct subgroups of mafic lavas within the Vumba greenstone belt, but these subgroups are not identical to the subgroups of the mafic lavas in the

Tati greenstone belt. It is noteworthy to mention that geochronological data (chapter 4) reveal that the Tati and Vumba greenstone belts are not contemporaneous. The subgroup 1 comprises calc-alkaline basalt that is characterised by elevated LREE pattern and HFSE negative anomalies. This subgroup possesses comparable HREE abundance with the subgroup 2 that comprises tholeiitic to calc-alkaline basalts with minor LREE enrichment or depletion. Subgroup 2 mafic lavas most closely resemble modern back-arc basin basalts that are generated through partial melting of depleted asthenosphere with addition of a minor crustal component via subduction processes (Saunders and Tarney, 1991; Pearce et al., 1994). The third subgroup 3 constitutes a minor component and is made of calc-alkaline basalt characterised by flat REE patterns, low abundance of REE and prominent HFSE negative anomalies, like modern back-arc basin basalts (e.g. Fretzdorff et al., 2002).

9.1.2 Petrogenesis

9.1.2.1 Contamination

In order to assess the role played by crustal assimilation in the evolution of the three subgroups of mafic lavas in the Tati and Vumba greenstone belts, plots of Th/Nb versus La/Nb (Figs. 9.1 & 9.3) are presented. La/Nb and Th/Nb ratios are very sensitive to the interaction of basaltic magma with continental crustal material hence effective in monitoring crustal contamination of mantle-derived mafic lavas (e.g. Elliot et al., 1997). This stems from relative depletion in Nb and enrichment in light REE and Th of continental crust compared to the upper mantle (Pearce, 1996). Variation in the ratios Th/Nb and La/Nb outline the differences in crustal or subduction zone input into the derivative magmas. This diagram demonstrate that the subgroup 1 has variable elevated Th/Nb and La/Nb ratios similar to back-arc basin-like mantle melts that exhibits evidence of either crustal contamination and/or addition of crustal components through subduction processes (Fig. 9.1). In contrast, the subgroup 2 mafic lavas possess low Th/Nb and La/Nb ratios similar to modern OIB- and/or MORB-like mantle melts (Elliot et al., 1997). Mafic lavas such as normal-MORB, which are devoid of crustal contamination, possess low La/Nb and Th/Nb ratios of 1.07 and 0.05, respectively (Smithies et al., 2005). The subgroup 3 mafic lavas exhibit higher Th/Nb and La/Nb than the subgroups 1 and 2, suggesting that they may represent a MORB-like basalt that interacted with upper crust or subduction component. However, geochemistry alone cannot be used to identify tectonic settings unequivocally.

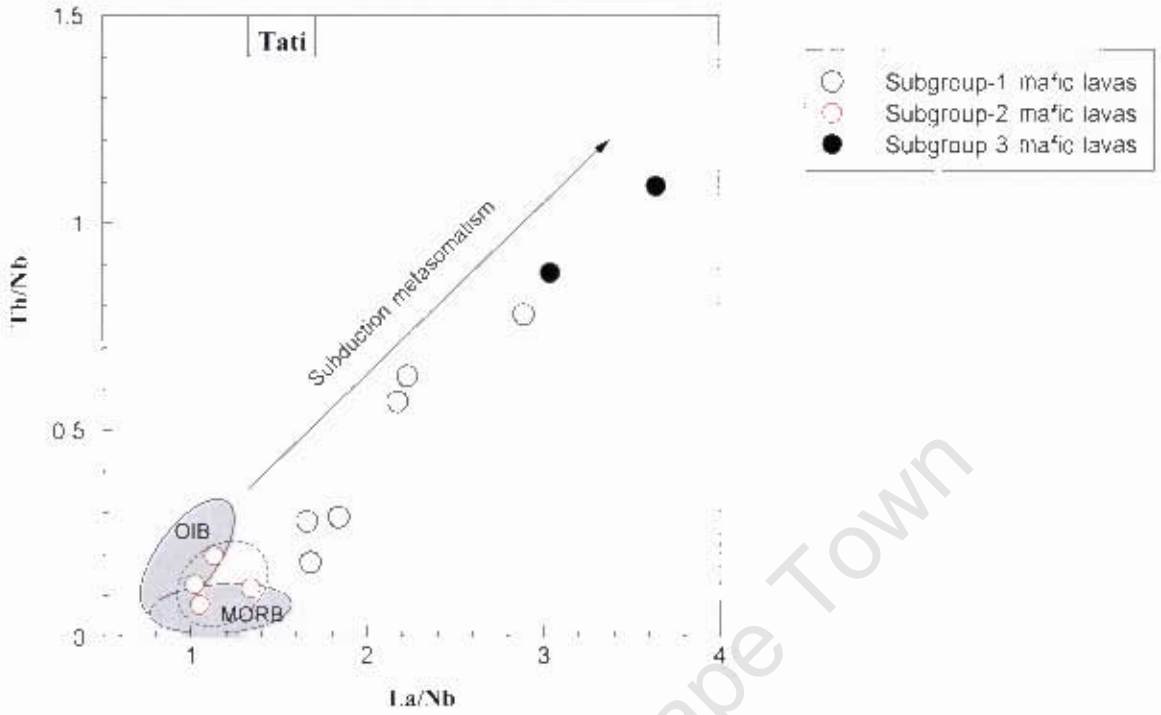

Fig. 9.1: Th/Nb versus La/Nb for the mafic lavas from the Tati greenstone belt. Ocean island basalt (OIB) and mid-ocean ridge basalt (MORB) fields are from Elliot et al. (1997). The subduction metasomatism vector is schematic.

High ratios of light rare earth elements to high field strength elements (e.g. La/Nb) in mafic igneous rocks can be indicative of crustal contamination of the source mantle (endogenic contamination) or mantle derived magma that has assimilated crust (exogenic contamination). Pearce (1983) and Pearce and Peate (1995) have demonstrated that the geochemical contribution of mantle versus subduction component as well as crustal component during arc basalt petrogenesis can be discriminated using the plot of Th/Yb versus Ta/Yb. It has been recognized that basaltic magmas derived from the mantle asthenosphere commonly referred to as depleted MORB mantle (DMM), mantle plume or fractionation products of these sources, all fall within a diagonal mantle array defined by constant Th/Ta ratios in the Th/Yb versus Ta/Yb diagram (Fig. 9.2). Subduction and crustal contamination generally impose a higher Th contents than Ta and Yb. Therefore, partial melting of mantle source regions that have been metasomatized through subduction processes will produce rocks that exhibit high Th/Yb ratio relative to Ta/Yb. Similarly, rocks derived from DMM source and assimilate continental crust will possess elevated Th/Yb ratio and relatively higher Ta/Yb ratio than lavas from subduction metasomatized mantle sources (refer to the vector inset in Fig. 9.2; Pearce, 1983). A plot of the three subgroups in Fig. 9.2 clearly outline the distinction of

subduction component between the subgroup 1 and 2, with subgroup 2 exhibiting only a minor subduction component. This is consistent with the results of Th/Nb versus La/Nb diagram (Fig. 9.1). The subgroup 3 straddles the boundary of mantle derived melts that involved subduction and crustal components. In view of the similarities in HREE abundances between the three subgroups, it is suggested that three subgroups were derived from the same source that was variable metasomatized by subduction processes. The subgroup 3 most likely reflects the effects of subduction sediments rather than continental crust.

Crustal contamination of mantle-derived rocks can also be evaluated through their radiogenic isotope composition, since the upper mantle and continental crust have different and distinct isotopic ratios. Such isotopic ratios include Sr, Nd and Pb. These isotopic ratios, therefore, provide a useful tool in ascertaining whether magmas generated from the upper mantle have interacted with material from the continental crust. The continental crust possesses elevated Sr, Pb and low Nd initial ratios compared to the upper mantle (e.g. Faure, 1998). The observed Sr isotope composition of the mafic lavas from the Tati greenstone belt has been variably disturbed by deformation hence cannot provide unequivocal evidence on contamination process (refer to chapter 8). Sample ZBT-46, a representative of subgroup 1 (IAB-type), yielded a positive εNd value of 2.35. This value is comparable with that of the contemporaneous depleted mantle, which argues against interaction with old crustal material. This is in accord with the results of incompatible trace element ratios (Fig. 9.1) that indicate the samples of subgroup 1 mafic lavas were derived from subduction metasomatized mantle source and underwent differentiation process as evidenced by high Th/Nb ratio. This is so because low Nb is inherent in the subduction zone magma generation process, and high Th is an equally inherent result of magma differentiation, hence high Th/Nb ratio.

A representative sample from the Tati subgroup 2 mafic lavas (MORB-type) recorded a positive initial εNd value of 1.61, which suggests that the subgroup 2 mafic lavas interacted with old crustal material. This is in spite of its low Th/Nb and La/Nb ratios comparable to those of the OIB/MORB that suggest no crustal involvement. The subgroup 3 representative sample (ZBT-54) recorded a negative initial εNd value of -0.26, which is consistent with the evidence of crustal involvement from the Th/Nb and La/Nb ratios. Additionally, the Pb isotope analysis was conducted on one sample (ZBT-54) of subgroup 3 and it recorded highly radiogenic Pb isotopes, which is in accord with the

evidences derived from Nd isotope data and incompatible trace element ratios that support significant interaction with old crustal material.

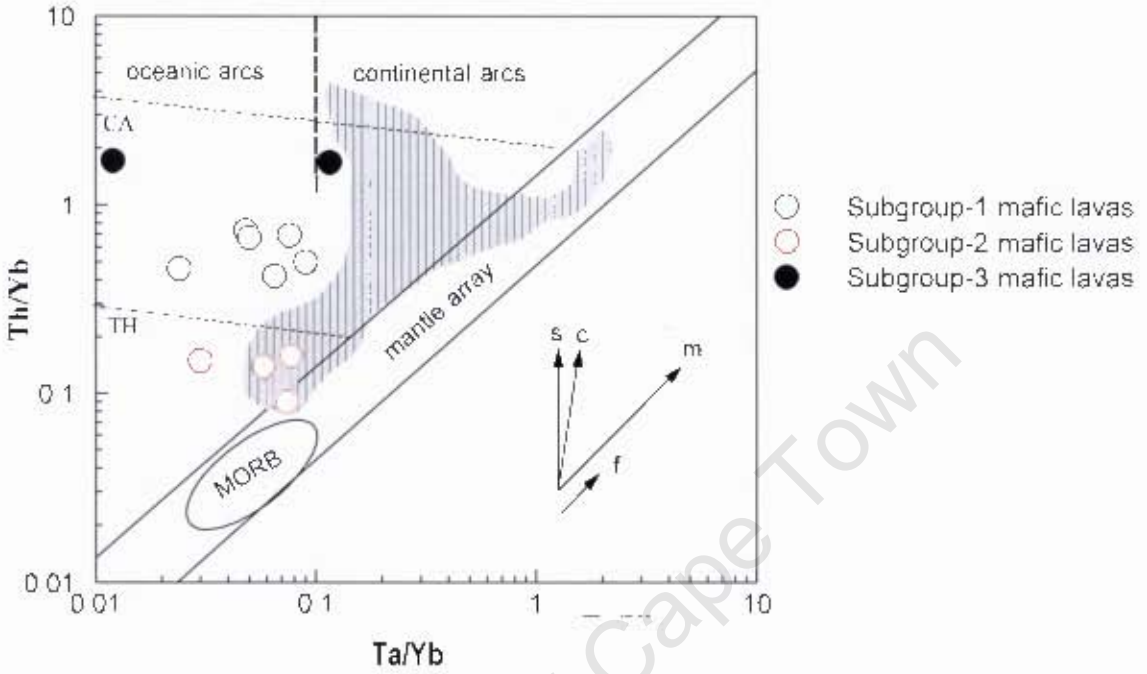

Fig. 9.2: Th/Yb versus Ta/Yb log-log diagram (after Pearce, 1983) for mafic lavas from the Tati greenstone belt. Mid-ocean ridge basalt (MORB) field is from Elliot et al. (1997). Shaded area represents basalts from the Sea of Japan (after Pouclet et al., 1994). Inset is a vector diagram illustrating effects of subduction (s), crustal assimilation (c), mantle (m) and fractionation (f). Abbreviations: TH-Tholeiite, CA-calc alkaline.

The mafic lavas from the Vumba greenstone belt display a more complex pattern when plotted on the Th/Nb versus La/Nb diagram (Fig. 9.3) than the mafic lavas from the Tati greenstone belt. For instance the subgroup 1 mafic lavas exhibit elevated Th/Nb and moderate La/Nb ratios that form a distinct trend from the remainder of the subgroups. This subgroup possesses Th/Yb and Ta/Yb ratios similar to calc-alkaline volcanic rocks of continental arcs (cf. Pearce, 1982; Fig. 9.4). The subgroup 2 mafic lavas, though variably mildly enriched in Th and La, are most similar to modern OIB-like melts in terms of Th/Nb and La/Nb ratios (Fig. 9.3; Eiliot et al., 1997). However, all the subgroup 2 samples plot above the mantle array in Fig. 9.4, displaying Th/Yb and Ta/Yb ratios similar to tholeiitic and calc-alkaline volcanic rocks of oceanic arcs. Similarly, the subgroup 3 displays elevated Th/Nb and La/Nb ratios that lie along the same variation trend with the subgroup 2 samples in Fig. 9.3. This subgroup exhibits Th/Yb ratio comparable with calc-alkaline oceanic arc basalts (Fig. 9.4). Based on the above observations and comparable HREE abundances of the

subgroups 1 and 2 mafic lavas, the displaced variation trends in the Th/Nb versus La/Nb diagram are interpreted as evidence of different types of contamination. Due to elevated Th/Nb ratio, exogenic contamination (crustal assimilation) is envisaged for the subgroup 1 variation trend in Fig. 9.3 whereas endogenic contamination (subduction metasomatism) is inferred for the variation trend displayed by subgroups 2 and 3.

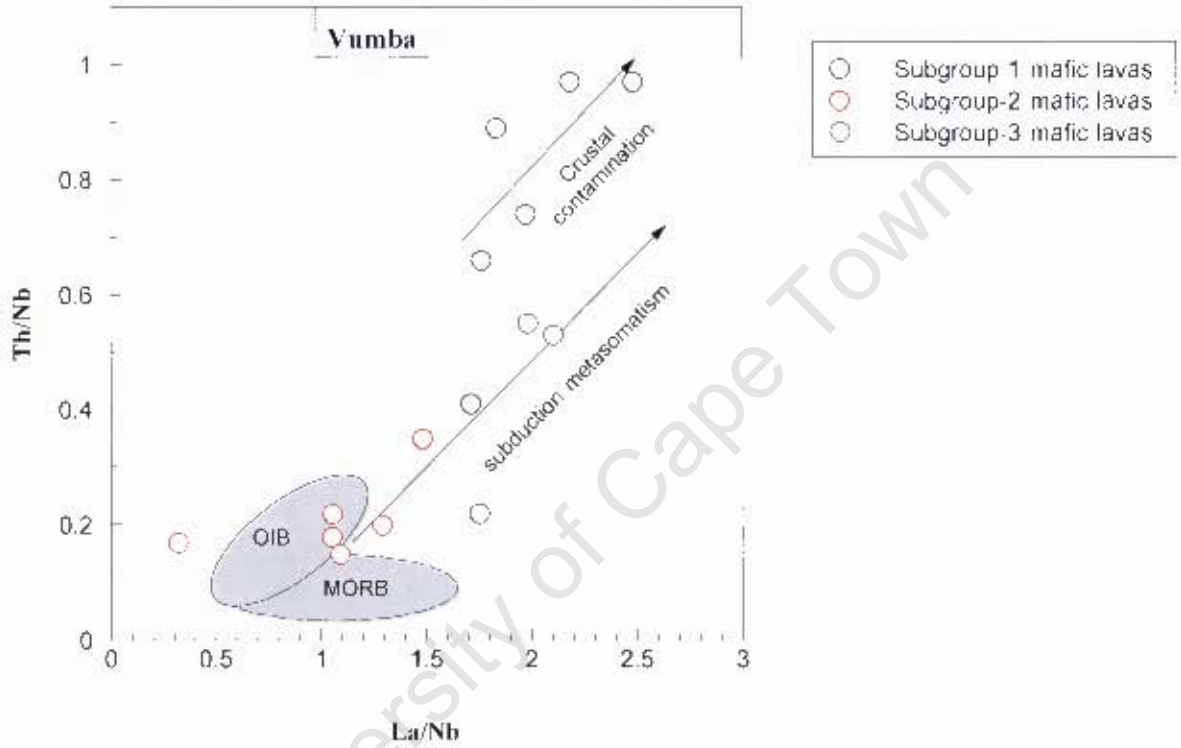

Fig. 9.3: Th/Nb versus La/Nb for the mafic lavas from the Vumba greenstone belt. Ocean island basalt (OIB) and mid-ocean ridge basalt (MORB) fields are from Elliot et al. (1997).

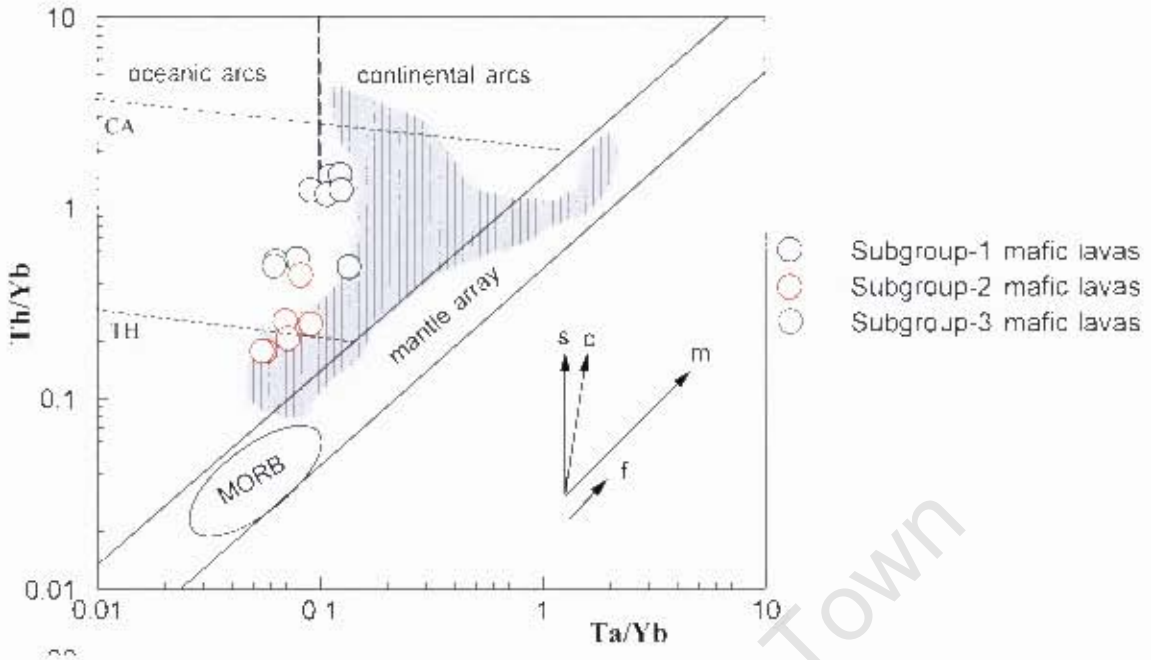

Fig. 9.4: Th/Yb versus Ta/Yb log-log diagram (after Pearce, 1983) for mafic lavas from the Vumba greenstone bel Mid-ocean ridge basalt (MORB) field is from Elliot et al. (1997). Shaded area represents basalts from the Sea of Japan (after Pouclet et al., 1994). inset is a vector diagram illustrating effects of subduction (s), crustal assimilation (c), mantle (m) and fractionation (f). Abbreviations: TH-Tholeiite; CA-calc alkaline.

The Vumba mafic lavas display significant variation in radiogenic Sr and Nd isotopic ratios. The initial εNd values recorded in three samples broadly range between -2.52 and +7.40. Sample ZBV-13, which is a representative of the LREE enriched samples of subgroup1 mafic lavas. yield a highly negative initial εNd value of -2.52 suggesting interaction with old crustal material. However, this result is inconsistent with the Pb isotope result. Pb isotope results are in agreement with the evidence revealed by the Th/Nb and La/Nb ratios. The large negative initial εNd value is probably an artifact of later Sm-Nd resetting during metamorphic events (e.g. Moorbath et al., 1997). Two samples (ZBV-182 and ZBV-185) from the subgroup 2 mafic lavas record positive initial εNd values of 7.40 and 0.53 respectively. Sample ZBV-185 possesses Th/Nb and La/Nb ratios that are indistinguishable from those of the OIB, suggesting little or no interaction with continental crust. In contrast, the low εNd value suggests interaction with older crustal material. Sample ZBV-182 records an anomalously high initial εNd value of +7.40 despite its higher Th/Nb and La/Nb ratios than those of sample ZBV-185. This contradicting result is further evidence that Sm-Nd resetting occurred during metamorphic events.

To resolve the paradoxical evidences of crustal contamination revealed by the initial εNd values versus ratios of the incompatible trace elements, the initial εNd values were plotted versus chondrite normalized Th/Nb ratios (Sandeman et al., 2006; Fig. 9.5). In this diagram, the Th_N/Nb_N ratio is utilized as a proxy for the extent of crustal contamination in mantle-derived rocks as well as the nature of the contaminant crust. Continental crust is known to be enriched in Th and depleted in Nb, hence high Th/Nb ratio (Sandeman et al., 2006). In contrast, the oceanic crust is characterized by low Th and high Nb, thus low Th/Nb ratio. Lower crust has similar Th/Nb ratios as the oceanic crust (Elliot et al., 1997). Therefore, assimilation of young juvenile continental crust by a mantle derived magma will result in the magma acquiring high Th/Nb ratio, and preserving the initial εNd value of the contemporary depleted mantle. By contrast assimilation of an old continental crust by a mantle-derived magma will result in the magma acquiring high Th/Nb ratio and lower initial εNd value than the contemporaneous depleted mantle. Moreover, assimilation of young oceanic crust by a mantle-derived magma will have no effect on both the Th/Nb ratio and initial εNd value of the magma resulting in the mafic rock maintaining low Th/Nb and high positive initial εNd value corresponding to that of the contemporary depleted mantle. Interaction of mantle-derived magma with an old oceanic crust or old lower crust will only disturb the εNd value causing the rock to acquire lower initial εNd value than the contemporary depleted mantle while it maintains a low Th/Nb ratio.

From the above, it follows that sample ZBT-46 (subgroup 1), which recorded high positive initial εNd value and elevated Th/Nb ratio corresponds to a mafic magma that interacted with young juvenile continental crustal material (Fig. 9.5). The representative sample ZBT-51 of subgroup 2 has a low positive εNd value and a low Th/Nb ratio that resembles mantle-derived rock that interacted with old oceanic crust or lower crust. However, existence of old oceanic crust is highly unlikely during the Archaean (e.g. Abbot et al., 1994). Lastly, subgroup 3 representative sample ZBT-54 resembles a mafic rock that interacted with old upper crustal material or subducted sediments derived from such old continental crust. The interaction with subduction sediments is more appealing than the interaction with old upper crust because there is no evidence of very old upper crust preserved in the Francistown Granite-Greenstone Complex, except an inherited zircon found in the Matsiloje pluton that has a crystallization age of 2911 Ma. It is quite possible that the inherited zircon could have been part of subduction sediments. Furthermore, no xenocrystic zircons

were found in the dated samples of felsic and andesitic lavas in the Tati area. Xenocrystic zircons were only found in an amphibolitic xenolith in the Vumba area. Nonetheless, the zircons yielded a U-Pb age of 2733 Ma, which would indicate interaction with continental material younger than the age of the Tati greenstone belt. Therefore, old crustal material could have been incorporated into subducted sediments derived from old crustal material formed elsewhere in the older granite-greenstone terrains in the Zimbabwe Craton. The very high εNd value for sample ZBV-185 is a very improbable result since it fits none of the likely scenarios in Figure 9.5. The representative subgroup 1 mafic lavas sample (ZBV-182) from the Vumba greenstone belt corresponds to a mantle-derived magma that interacted with old crustal material or subducted sediments derived from such crust (Fig. 9.5). On the other hand subgroup 2 representative sample ZBV-13 plot in the field of mantle-derived rocks that interacted with old lower crust or sediments.

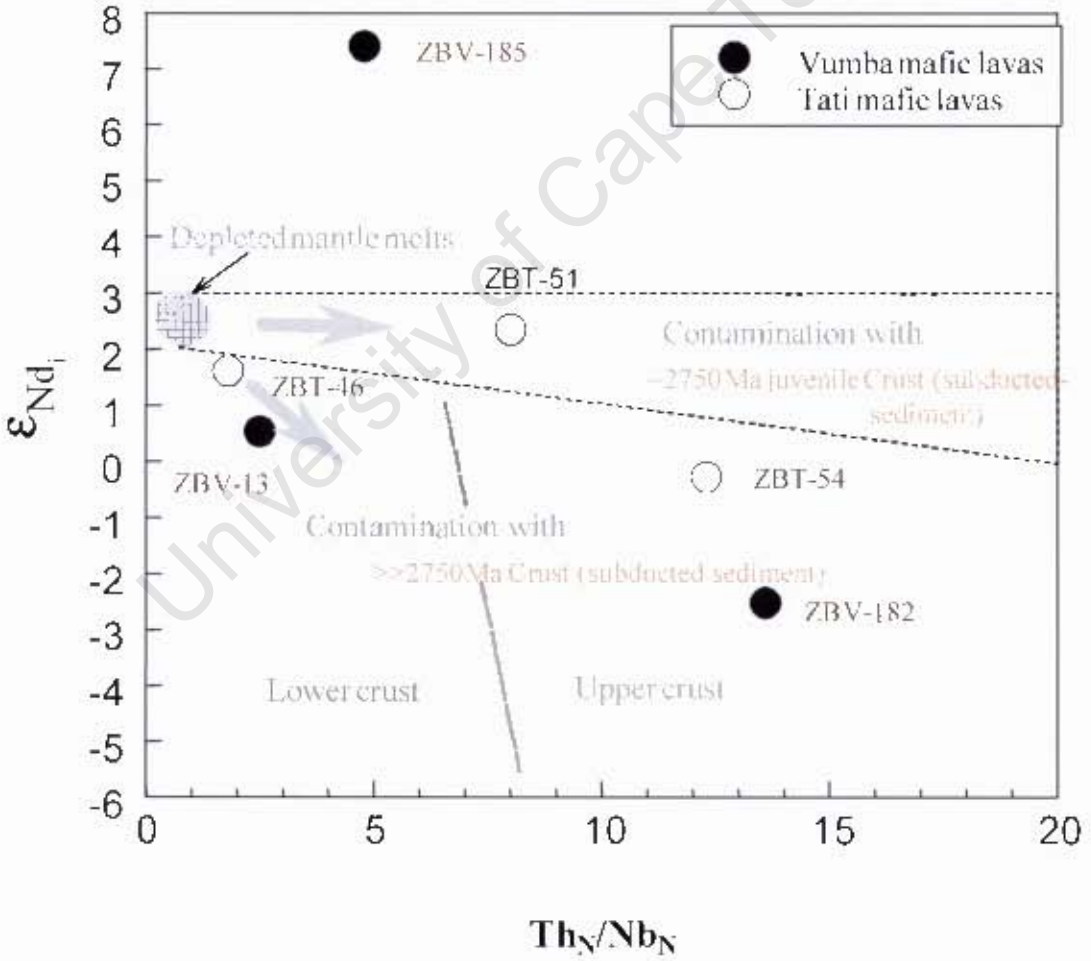

Fig. 9.5: Plot of initial εNd (t) versus Th_N/Nb_N (chondrite normalizing values are from Wood et al., 1979) for mafic lavas from the Tati and Vumba greenstone belts to illustrate probable sources of contamination. The diagram is after Sardeman et al. (2006).

9.1.2.2 Crystal fractionation

Non-primary magma Mg# coupled with low compatible trace element abundances displayed by mafic lavas from the study area demonstrates that the lavas evolved through differentiation processes. The differentiation of igneous rocks from primary magmas to non-primary magmas is commonly explained by crystal fractionation processes such as equilibrium crystallization, fractional crystallization and crystal accumulation. The Mg# of primary melts is estimated on the basis of equilibrium distribution of Fe and Mg between mantle olivine and melt to fall within the range 0.68 to 0.75 (Frey et al., 1978). Tholeiitic mafic lavas from the Tati greenstone belt are characterised by non-primary magma Mg# that range from 0.45 to 0.67. Ni and Cr are compatible trace elements with respect to olivine and Cr-spinel, respectively, which are early crystallizing phases in basic magmas. Therefore, basic magmas that have experienced olivine fractionation will be depleted in Ni and Cr. Clague and Frey (1982) have estimated the concentration of Ni in primary magmas to be in the range of 200 to 450 ppm. Furthermore, it has been realized that primary magmas are characterised by Ni/MgO ratio between 23 and 39 (Hart and Davis, 1978). Any basic lava with Mg# less than 0.68 is considered non primary but evolved. Magnesium numbers and Ni and Cr contents of the mafic lavas from the Tati and Vumba greenstone belts are mostly too low for them to be primary melts, with a few exception from the Vumba greenstone belt that have high Mg#s, Ni and Cr contents (Table 9.1). One sample (ZBV-13) from the Vumba greenstone area yielded a Mg# of 0.68, but with too low Ni, Cr and MgO contents (Table 9.1) to be a primary melt. The higher Mg# for samples ZBV-147 and ZBV-199 from the Vumba greenstone possibly reveals the effects of olivine accumulation. A summary of the mafic lavas samples that exhibit relatively the least differentiated or the most primitive character is presented in Table 9.1. Major and trace elements geochemical variations of the mafic lavas presented in chapters 5 and 6, respectively, suggest fractionation of an assemblage including olivine, clinopyroxene, titano-magnetite and apatite phases. Variable depletion of the elements Sr and Eu relative to other incompatible elements in multi-element and REE profiles, respectively, suggests effects of plagioclase fractionation.

Table 9.1: Selected samples of mafic lavas from the Tati and Vumba that exhibit relatively less evolved or most primitive composition.

	Tati			Vumba			
Sample	ZBT-46	ZBT-48	ZBT-53	ZBV-13	ZBV-185	ZBV-197	ZBV-199
Mg#	0.67	0.66	0.63	0.68	0.57	0.78	0.78
MgO wt.%	8.82	8.61	8.99	6.54	7.3	8.56	8.19
Cr ppm	460	404	315	261	332	272	301
Ni ppm	112	147	169	101	229	264	236
Ni/MgO	13	17	19	15	31	31	29

The normal procedure is to correct the composition of major elements for olivine fractionation. This can be achieved by adding back equilibrium olivine into least evolved lavas compositions in small increments until the lavas attain Mg# that is in equilibrium with the olivine composition. In case of samples that exhibit higher Mg# than the primary magma, small subtractions of olivine is conducted in steps until the Mg# is in equilibrium with the olivine within that of primary magma. To achieve this, knowledge of the composition of olivine phenocrysts that were in equilibrium with the primary magma of the lavas is necessary. Roeder and Emslie (1970) formulated an empirical equation guiding the partition coefficient of Mg and Fe between olivine and melt under equilibrium condition; $K_d^{Fe\text{-}Mg} = (FeO/MgO)^{olivine} / (FeO/MgO)^{melt} = 0.3$. With the help of this equation the composition of the primary magma in equilibrium with the olivine can be worked out once the composition of the olivine is known. In this study no mineral chemistry was conducted, hence the process of correcting major and trace elements compositions for fractionation is outside the scope of this thesis. Moreover, most of the minerals found in the mafic lavas under investigation are now not of magmatic origin but were generated during subsequent metamorphic history. Therefore their composition cannot be utilized in retracing the magmatic history of mafic lavas.

It has been revealed in the previous sections that the samples of subgroup 2 mafic lavas from the Tati greenstone belt did not suffer any significant crustal contamination and the HFSE, REE and some compatible trace elements were not perturbed by secondary processes. Interestingly, the Mg# and the contents of Ni and Cr in the subgroup 2 mafic lavas are indistinguishable from those of subgroups 1 and 3 that do show evidence of crustal contamination. This observation suggests that

contamination processes did not have significant effects on the abundances of compatible trace elements in the Tati greenstone belt. Similarly, the samples of subgroup 2 mafic lavas from the Vumba greenstone belt are considered less contaminated (at least by continental crust) on the basis of evidence from incompatible trace element ratios and εNd data presented above. Nevertheless, the Mg# and the contents of Ni and Cr in this subgroup are indistinguishable from those of the other subgroups that possess evidence of crustal contamination. Thus the distribution of the compatible trace elements cannot be attributed to crustal contamination or alteration processes. Therefore, the compatible elements are suitable for use in the evaluation of the effects of fractional crystallization process in the evolution of the mafic lavas from the Tati and Vumba greenstone belts.

In order to evaluate the role played by fractional crystallization process in the evolution of the mafic lavas from the Tati and Vumba greenstone belts, Ni versus Zr contents were plotted in Fig. 9.6 together with a vector diagram to model the concentrations of Ni and Zr in a basaltic melt that is experiencing differentiation. Zr is selected as a fractionation index because it is incompatible during differentiation of mafic lavas and highly immobile during alteration (e.g. Pearce, 1982). Additionally, Zr abundances in the mafic lavas under investigation do not define the three subgroups like other incompatible elements such as Th and La, which implies that it was not significantly affected by contamination scenarios. Theoretical crystallization trends are displayed in this plot for fractionating mineral or mineral assemblages for comparison with the observed trends in the mafic lavas. The direction of the lines shows the compositional change in the residual liquid when the specified mineral or mineral assemblage is removed during fractional crystallization. The theoretical fractionation vectors were calculated from the Rayleigh fractionation equation Eq. 9.1 given below. The fractionation trends are shown for 10, 30, 50 and 70% fractional crystallization. Theoretical vectors drawn predict that for a basic magma, fractionation of minerals such as olivine and clinopyroxene will deplete the residual liquid in Ni and enrich it in Zr. They also predict that fractional crystallization of plagioclase will leave a residual liquid enriched in both Ni and Zr.

$$C_L / C_o = F^{(D-1)} \qquad \text{(Eq. 9.1)}$$

Where

C_L = Concentration of the element in the remaining liquid

C_o = Initial concentration of a trace element in the parental melt

F = weight proportion of residual melt, i.e. degree of crystallization

D = bulk partition coefficient of the fractionation assemblage during crystal fractionation.

The mineral/melt partition coefficients (D) for Ni and Zr used in the calculation of the theoretical concentration values were obtained from Rollinson (1993). Table 9.2 presents the partition coefficients of various minerals that were used for modelling the distribution of Ni and Zr concentrations in basic magmas. The Ni versus Zr data for the mafic lavas from the Tati greenstone belt follow a distinct decreasing trend, which can be explained by fractional crystallization of an assemblage comprised of olivine, clinopyroxene and plagioclase according to the theoretical Rayleigh vectors (Fig. 9.6a). By comparison, the Ni and Zr contents for the mafic lavas from the Vumba greenstone belt display two separate parallel trends that are shallower than that of the Tati mafic lavas. Moreover, it can be observed from Fig. 9.5b that the subgroup 2 mafic lavas samples define a separate trend from the trend of subgroups 1 and 3 samples, although the trends are sub-parallel. According to the theoretical Rayleigh vectors, the trends can be explained by clinopyroxene crystallization. However, the samples of subgroup 2 exhibit a lower trend corresponding to lower initial concentration of Ni and Zr than samples of subgroups 1 and 3. These two parallel trends are interpreted as evidence for fractionation of similar phase or phases from parental melts with different initial compositions. This suggests that the subgroups 1 and 2 probably evolved from distinct parental magmas. The variation in initial compositions could emanate from partial melting a heterogeneous mantle source or different degrees of partial melting of a homogeneous source. The samples from subgroups 2 and 3 mafic lavas display overlapping Ni contents but different Zr concentrations. This could be reflecting the effects of fractional crystallization or partial melting processes. For the investigation of the effect of fractional crystallization process, knowledge of the composition of the primary melt is necessary. Previous studies (e.g. Minster et al., 1977) constrained the concentration of Ni in a primary basaltic magma between 280 and 450 ppm. In the theoretical vector modelling, the initial concentration for Ni and Zr were taken as 400 and 11.2 ppm respectively. The 11.2 ppm concentration of Zr is hypothetical and was assumed on the basis of the Zr abundance in primitive mantle (Sun and McDonough, 1989).

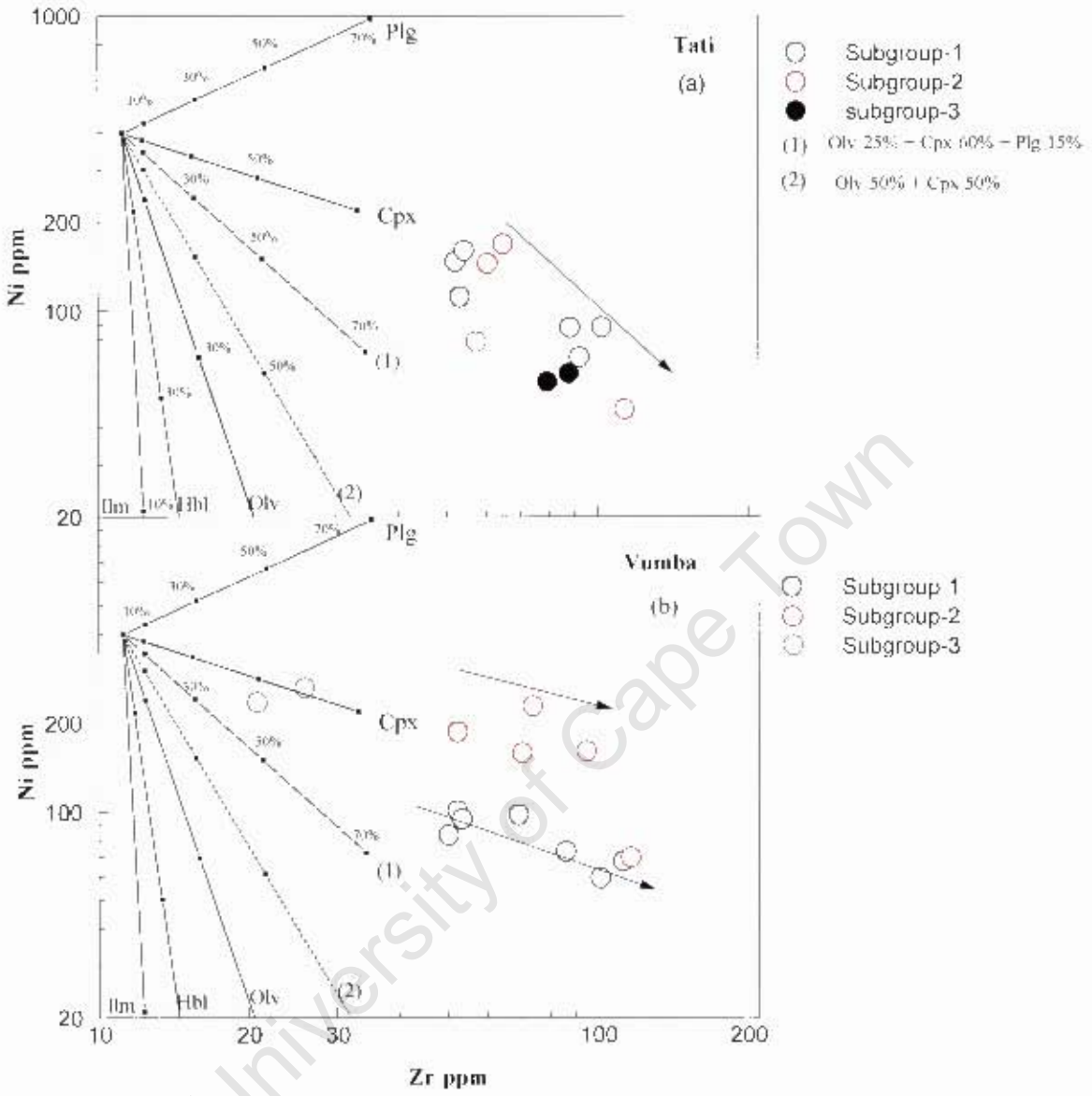

Fig. 9.6: Ni against Zr log-log diagram for the (a) Tati mafic lavas and the (b) Vumba mafic lavas. Theoretical Rayleigh fractionation vectors modelled for crystallization of individual minerals and mineral assemblages are indicated.

Table 9.2: Mineral-melt distribution coefficients for Ni and Zr used in the calculation of theoretical Rayleigh vector. The values were obtained from Rollinson (1993).

Composition	Element	Olivine	Clinopyroxene	Plagioclase	Hornblende	Ilmenite
Basic	Ni	5.9	1.5	0.26	6.8	29
	Zr	0.012	0.1	0.048	0.5	0.1

9.1.2.3 Partial melting

Mafic lavas are considered to be produced by partial melting of mantle peridotite, which is mainly composed of olivine, orthopyroxene, and clinopyroxene at upper mantle pressures, but the Al-phase changes from plagioclase to spinel to garnet with increasing pressure or depth (e.g. Kinzler, 1997). In order to probe the source region of the mafic lavas, it is necessary to establish the composition of the primary magma. Primary magmas are defined as the original melts that have compositions that have not been modified by processes such as crystal fractionation and crustal assimilation of country rock since they accumulated from their source region. The geochemical criterion that is commonly utilized to distinguish between primary and non-primary melt compositions in mafic lavas involves the Mg# and the concentrations of some compatible trace elements such as Ni and Cr as stated earlier.

Several hypothetical models describing melting processes within the Earth's interior have been published (see Rollinson, 1993; Shaw, 2006 for an overview). The models explain the theoretical behaviour of trace elements during partial melting through numerical analysis. This involves parameterising the source concentration of the trace element, modal mineralogy of the source, the melt mode of the source minerals, partition coefficient for the elements between the minerals and melt, and degree of partial melting.

Complications caused by post-melting processes, such as crustal contamination, crystal fractionation, alteration and metamorphism can render numerical modelling of the trace element signature of the source region for mafic lavas difficult. In this study REEs mafic lavas is preferred, using a forward modelling approach because of their consistent behaviour as a group during magmatic processes, as well as their immobility during low grade metamorphic conditions. The modeling utilizes the non-modal batch melting equation and REE partition coefficients of Shaw (2006) shown below, and in Table 9.3, respectively. Partial melting was modelled for both spinel-lherzolite and garnet-lherzolite source composition. The modal mineralogy and melt mode of the sources used in the calculation of the melt curves are presented in Table 9.4. Three reference mantle compositions have been tested in this study: the primitive mantle (PM) that represents the

mantle composition prior to MORB formation and depletion (Sun and McDonough, 1989); and the depleted MORB mantle (DMM) proposed by McKenzie and O'Nions (1991).

$$C_L = \frac{C_o}{D_o + F(1-P)} \qquad \text{(Eq. 9.2)}$$

Where

C_L = concentration of trace element in the melt

C_o = concentration of trace element in the original source

F = weight proportion of melted material, i.e. degree of partial melting

D_o = bulk partition coefficient of trace element calculated from the proportions of the minerals in the initial source

$= \Sigma X_o D_o$

P = bulk partition coefficient of trace element of trace element calculated from the proportions in which the minerals enter the melt

$= \Sigma p X_p$

Xo = proportion of mineral in the initial source (starting mode)

p = proportion in which mineral enters melt (melting mode)

K_d = mineral-melt partition coefficient

Table 9.3: Partition coefficients for REE during partial melting of a mantle source. The coefficients are from a compilation of Shaw (2006).

Element	Olivine	Orthopyroxene	Clinopyroxene	Spinel	Garnet	Amphibole	Plagioclase
La	0.000053	0.0004	0.0536	0.00002	0.001	0.12	0.0348
Ce	0.000105	0.001	0.0858	0.00003	0.004	0.18	0.0278
Pr	0.000251	0.002	0.137	0.0001	0.02	0.3	0.022
Nd	0.000398	0.0041	0.1873	0.0002	0.057	0.45	0.0179
Sm	0.0007	0.006	0.291	0.0004	0.14	0.6	0.0132
Eu	0.0008	0.01	0.329	0.0006	0.26	0.7	0.3
Gd	0.0015	0.012	0.367	0.0009	0.498	0.7	0.0125
Tb	0.0021	0.016	0.405	0.0012	0.75	0.66	0.0116
Dy	0.0027	0.02	0.442	0.0015	1.06	0.63	0.0112
Ho	0.005	0.026	0.415	0.0023	1.53	0.6	0.0114
Er	0.01	0.033	0.387	0.003	2.0	0.58	0.0116
Tm	0.016	0.045	0.409	0.0038	3.0	0.55	0.014
Yb	0.027	0.055	0.43	0.0045	4.03	0.53	0.016
Lu	0.03	0.07	0.433	0.0053	5.5	0.51	0.018

The results of modelling are presented in Figs. 9.7 and 9.8, where they are firstly examined in terms of the concentration of highly incompatible La and relatively less incompatible Sm. Neither of these two elements is significantly affected by partial melting of mantle source with variable Al-phases (e.g. garnet or spinel). This is evidenced by the parallel modelled curves of partial melting garnet- and spinel-lherzolite mantle sources (Fig. 9.7a & Fig. 9.8a). However, the La/Sm ratios of mantle-derived magmas may not be simply a function of their source composition but also a variety of magmatic and post-magmatic processes (Sylvester et al., 1997). Basalts in greenstone belts with sub-chondritic to chondritic La/Sm ratios are thought to have been derived from mantle sources with similarly low ratios. The LREE enriched basalts could have been derived from mantle sources that are LREE enriched. Alternatively, basalts with super-chondritic La/Sm ratios could have been derived from the depleted to chondritic sources, but then were subsequently contaminated by continental crust during their ascent to the surface. Therefore, it is quite difficult to determine how much of an enrichment in La/Sm ratio of a basalt is due to crustal contamination and how much is an inherited characteristic of its source mantle. Nevertheless, these elements can provide useful information on the bulk chemical composition of the source, particularly for samples that have not been significantly affected by contamination processes or when considered in conjunction with other geochemical evidences for crustal contamination.

Table 9.4: Starting and melt modes used in partial melting modelling.

	Spinel-lherzolite		Garnet-lherzolite	
Minerals	starting mode X_o	melt mode P	starting mode X_o	melt mode P
Olivine	0.53	0.06	0.60	0.03
Orthopyroxene	0.27	0.18	0.20	0.16
Clinopyroxene	0.17	0.65	0.10	0.72
Spinel	0.03	0.11	-	-
Garnet	-	-	0.10	0.09

Sources: Walter (1998), Kinzler (1997).

The mafic lavas from the Tati greenstone belt possess La concentrations and La/Sm ratios greater than those that could be generated by direct partial melting of DMM (Fig. 9.7a). The best-fit partial melting curve drawn for the mafic rocks from the Tati greenstone belt suggests that a mantle source with similar composition to the Phoenix gabbro is required to produce the mafic lavas and the Selkirk gabbro. The three subgroups of the mafic lavas follow the same melting curve, suggesting derivation from the same source but affected by variable degrees of partial melting or crustal contamination. Since it has been demonstrated in the previous section (9.1.2) that the subgroups 1 and 3 have been contaminated it is, therefore, probable that all the subgroups were generated by similar degrees of partial melting. The subgroup 2 mafic lavas and some samples from the Selkirk gabbro straddle the best–fit melting curve between the 20 and 10% divisions suggesting 20 to 10 % degrees of partial melting. The group of gabbro samples that plot at higher degrees of partial melting, display cumulus textures in thin sections.

In order to constrain the mineralogy of the source of the mafic lavas, their Sm/Yb ratio was plotted against Sm concentrations in Fig. 9.7b. Yb is a compatible element with garnet but not with spinel, hence the Sm/Yb ratio is useful in distinguishing garnet-lherzolite derived rocks from those of spinel-lherzolite source. It can be observed from Fig. 9.7b that the mafic rocks from the Tati greenstone belt plot along the spinel-lherzolite melting trend suggesting that they were derived from depth within the spinel stability field. This is consistent with high contents of HREE and their flat patterns.

The mafic and ultramafic rocks from the Vumba greenstone belt are presented in similar diagrams in Fig. 9.8a & b. It can be observed Fig. 9.8 that the composition of both the mafic and ultramafic rocks from the Vumba greenstone belt can be best explained by partial melting of a mantle spinel-lherzolite source.

In summary the results of partial melting modelling of REE indicate that both the Vumba and Tati mafic lavas were generated at relatively shallow depths at pressures within the spinel stability field (outside the garnet stability field).

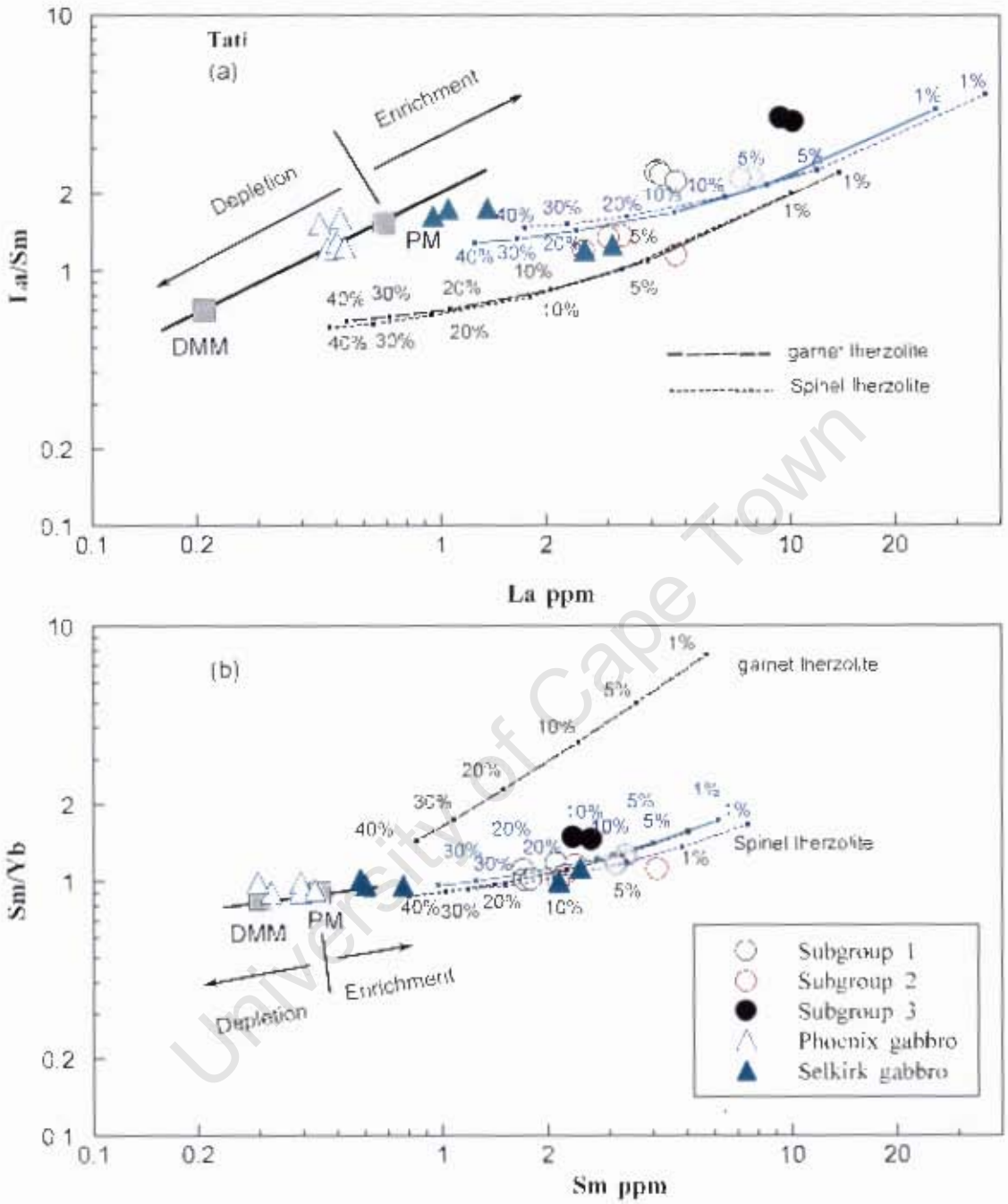

Fig: 9.7. Plot of mafic lavas from the Tati greenstone belt on diagrams: (a) La/Sm versus La and (b) Sm/Yb versus Sm showing melt curves obtained using non-modal batch melting equation of Shaw (2006). Black, blue and magenta coloured curves correspond to DMM, PM and mantle source similar to the Phoenix gabbro composition, respectively. The marks on each curve correspond to degrees of partial melting for a given source mantle. Depleted mid ocean ridge basalt mantle (DMM) source composition is from McKenzie and O'Nions (1991). Primitive mantle (PM) composition is from Sun and McDonough (1989).

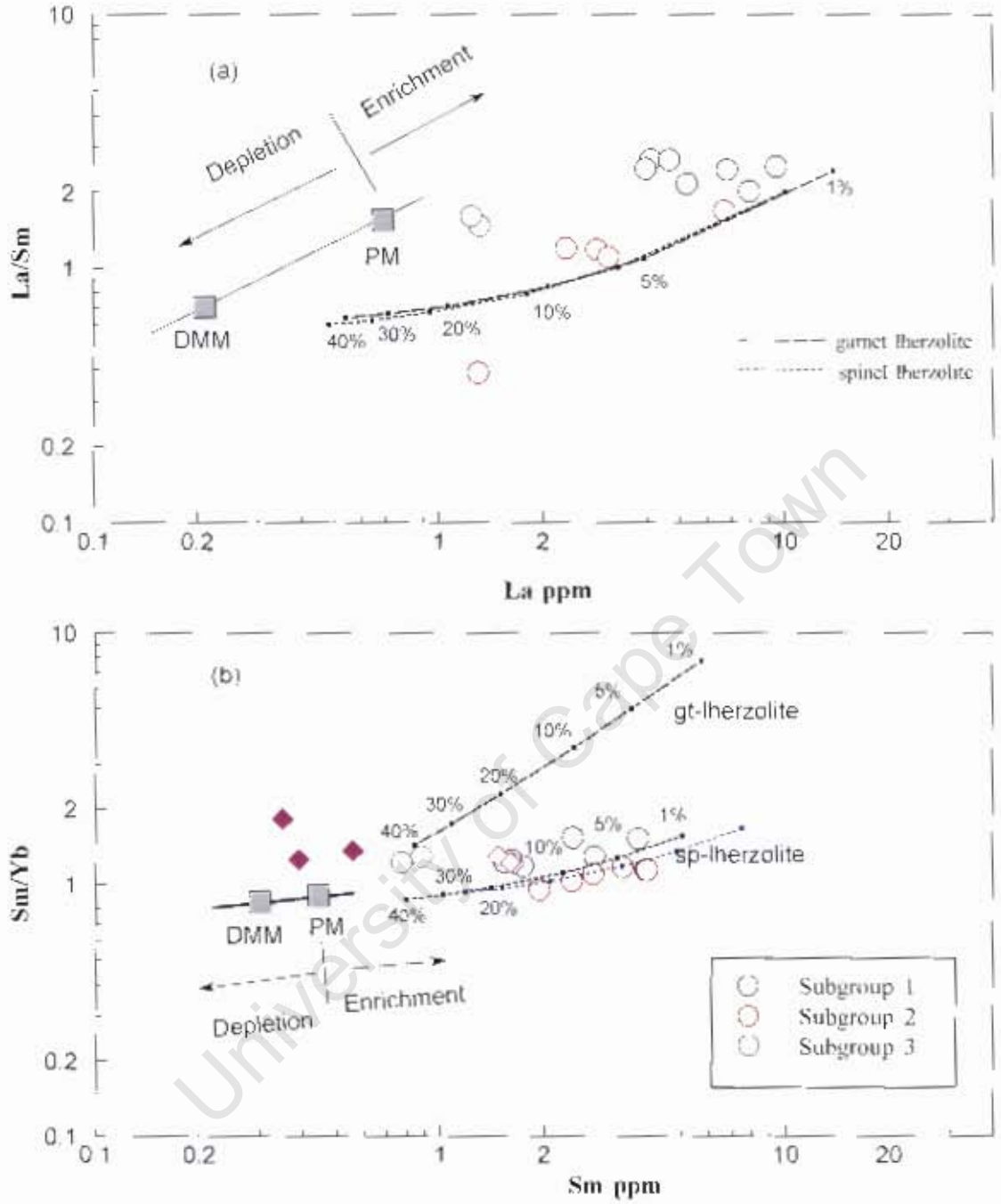

Fig. 9.8: Plot of mafic lavas from the Vumba greenstone belt on diagrams. (a) La/Sm versus La and (b) Sm/Yb versus Sm showing melt curves obtained using non-modal batch melting equation of Shaw (2006). Black and blue coloured melting curves correspond to DMM and PM sources, respectively. The marks on each curve correspond to degrees of partial melting for a given source mantle. Depleted mid ocean ridge basalt mantle (DMM) source composition is from McKenzie and O'Nions (1991). Primitive mantle (PM) composition is from Sun and McDonough (1989).

9.1.3 Source region

Several mantle components have been defined in young basalts using radiogenic isotope ratios. However, many of the radiogenic isotopes, such as Sr and Pb are vulnerable to remobilization during secondary processes hence are difficult to apply to Archaean basalts for similar definitions. Mantle components in Archaean basalts are best defined by immobile incompatible element ratios (e.g. Kerrich et al., 1999; Polat et al., 1999; Condie, 2003; 2005b; Sandeman et al., 2004; 2006). The ratios of incompatible elements do not change with time like the radiogenic isotope ratios.

In view of the similarity of partition coefficients of Nb, Th and LREE during mantle melting, they are unlikely to be fractionated from one another during relatively high degrees of partial melting involved in the genesis of tholeiitic mafic lavas (Sun and McDonough, 1989). Therefore, they are expected to reflect the respective source ratios. Th and LREE are fractionated from Nb during subduction process since they are preferentially transferred to the subarc mantle from the subducting slab while Nb is retained in the residual slab (Pearce and Peate, 1995; Polat et al., 1999). This results in the subarc mantle acquiring high Th/Nb and Ce/Nb ratios. The source of MORB is a depleted mantle characterised by relatively low Th/Nb but high Ce/Nb ratios (Polat et al., 1999).

In an attempt to elaborate on the potential mantle sources for the mafic lavas of the Tati and Vumba greenstone belts, the analyses of mafic lavas are plotted in a Ce/Nb versus Th/Nb diagram (after Saunders and Tarney, 1991) in Figure 9.9. These ratios have been successfully used to identify the characteristics of the different mantle sources that contribute to basaltic magmatism in oceanic basins (Saunders et al., 1988). The Th-Nb-Ce systematics of oceanic basalts have been described in terms of mixing between a depleted MORB source mantle (DMM), a recycled residual slab component (RSC) processed via the subduction zone, and a recycled subduction component (SDC) complementing recycled residual slab material (Fig. 9.8). The incompatible trace element ratio Ce/Nb is useful in discriminating between variations in the incompatible element enrichment of the mantle source and less so to the amount of crustal input (e.g. Sandeman et al., 2006). In contrast, variation in the ratio Th/Nb reveals differences in the crustal or subduction zone input into the derivative magmas. In a Ce/Nb versus Th/Nb diagram, all the mafic lavas from the Tati area overlaps with the field for basalts from the Sea of Japan, which is a continental back arc basin

associated with subduction zone. The Sea of Japan contains stretched continental crust with which the magma could have interacted.

Samples of subgroup 2 mafic lavas from the Tati greenstone belt plot between the normal mid ocean ridge basalt (N-MORB) and BABB fields, suggesting a DMM-like source. One sample of this subgroup plots within the N-MORB field. This subgroup possesses Th/Ce <0.1 and display features closely comparable to modern MORB, such as low Th and Ce contents (e.g. Elliot et al., 1997; Pearce, 1996). This is compatible with the lack of prominent Nb anomalies in the multielement profiles of the subgroup-2 mafic lavas. Some preserved pillow structures and the presence of banded iron formation in the Tati greenstone belt suggest a subaqueous depositional environment. The subgroup 3 samples have elevated LREE and variable negative HFSE anomalies, which is characteristic of arc mafic lavas of modern continental margins (e.g. Pearce, 1982; Elliot et al., 1997; Gribble et al., 1996). This group possesses high Ce/Nb (6.4-7.6) and Th/Ce ratios (>0.1). It has been shown by Hawkesworth et al. (1997) that sections of the Lesser Antilles arc (Caribbean) contaminated with sediments melts possess higher Th/Ce ratios (>0.1) than sections derived from mantle wedge metasomatized by slab dehydration fluids. Therefore, the subgroup 3 samples could represent magma generated from a sub-arc mantle source that has been metasomatized by subduction derived sediment melts. This is consistent with the initial εNd value of -0.26, which suggests interaction with old upper continental crust material. It has already been shown in the previous sections that the subgroups 1, 2 and 3 have subduction, MORB and continental arc affinities, respectively. Collectively, this suggests that the three subgroups of mafic lavas from the Tati greenstone belt were generated from heterogeneously metasomatized sub-arc mantle in a back-arc environment within oceanic crust near a continental margin (e.g. the Sea of Japan).

The Vumba mafic lavas subgroups presented in Fig. 9.9b show that subgroup 1, which is LREE enriched, mostly has high Th/Ce ratios exceeding 0.1 comparable with upper continental crust values. This is in line with the initial εNd data that advocates for significant involvement of upper continental crust in their evolution. The Th/Nb and Ce/Nb relationship of the subgroup 2 mafic lavas resembles that of Mariana back-arc basalts and Broken Ridge Ocean Plateau (Fig. 9.9b). The field for BROP and Mariana BABB lies between that of the MORB and arc basalts suggesting a mixture of DMM and subduction component sources. However, there is no other supporting evidence for an

ocean plateau origin in the Vumba mafic lavas. According to Mahoney et al. (1995) the BROP basalts are characterized by fractionated REE and radiogenic isotopes that show evidence of continental crust contamination. In contrast to the BROP basalts, the subgroup 2 mafic lavas from the Vumba greenstone belt exhibit flat to slightly LREE depleted patterns and positive εNd values, which suggests that interaction with continental crust was not significant. The Mariana BABB represents rocks derived from a mixture of SDC and DMM source (Gribble et al., 1996). Moreover, they possess flat REE patterns (Gribble et al., 1996) similar to the subgroup 2 mafic lavas, which mean the mafic lavas resemble more closely the BABB than the BROP. The subgroup 3 mafic lavas exhibit Ce/Nb and Th/Nb composition directly comparable to the Mariana arc, which formed from a mantle source dominated by SDC. This is in accord with the Ta/Yb ratio that resembles those of arc magmatism in Fig. 9.4 (Pearce, 1982). Furthermore, the subgroup 3 mafic lavas overlap with the field of basalts from the Sea of Japan, which is a typical example of a modern back-arc basin associated with continental rift near a continental margin. Collectively, all the three subgroups of the mafic lavas in the Vumba greenstone belt exhibit geochemical signatures of DMM, SDC + DMM and continental crust + SDC + DMM sources, which leads to the suggestion of a heterogeneous mantle source for the mafic lavas in a subduction back-arc basin setting.

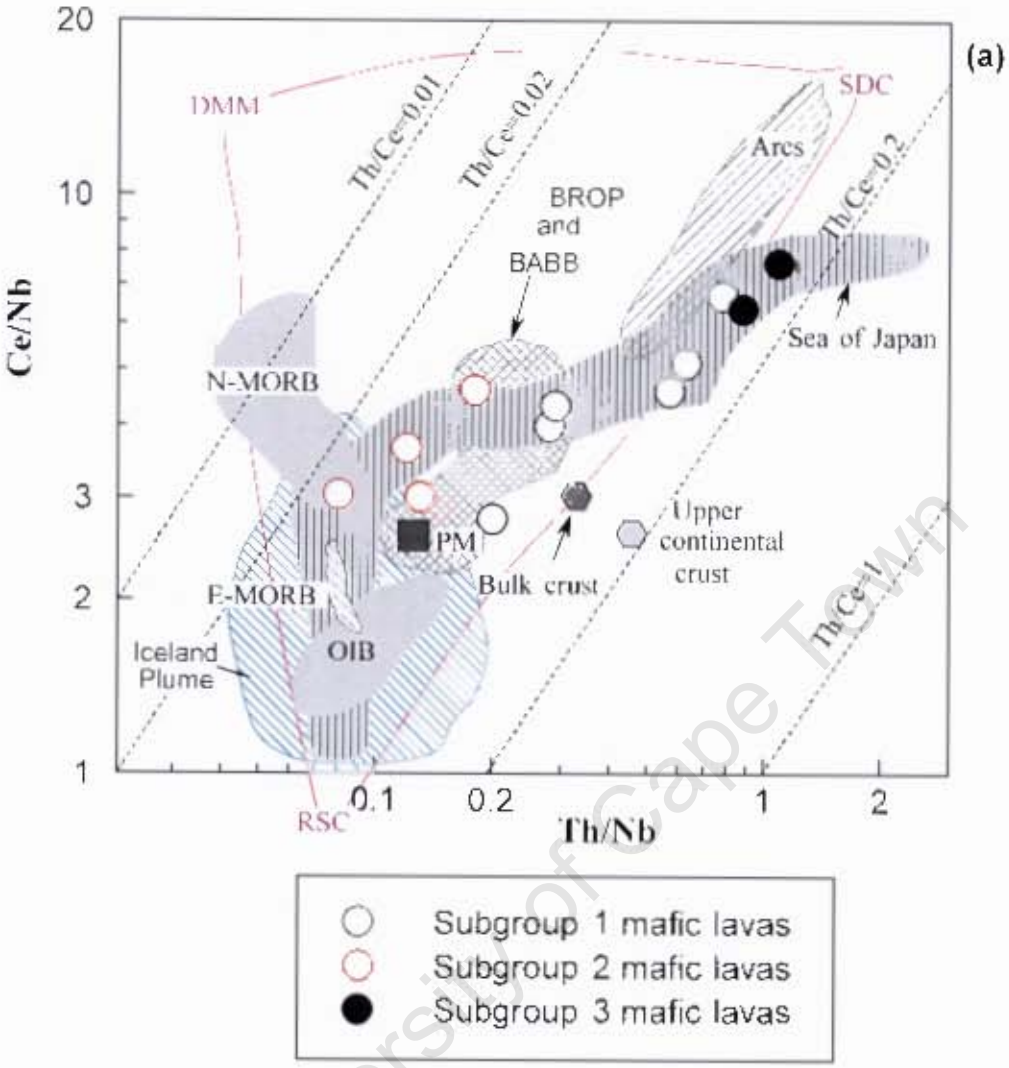

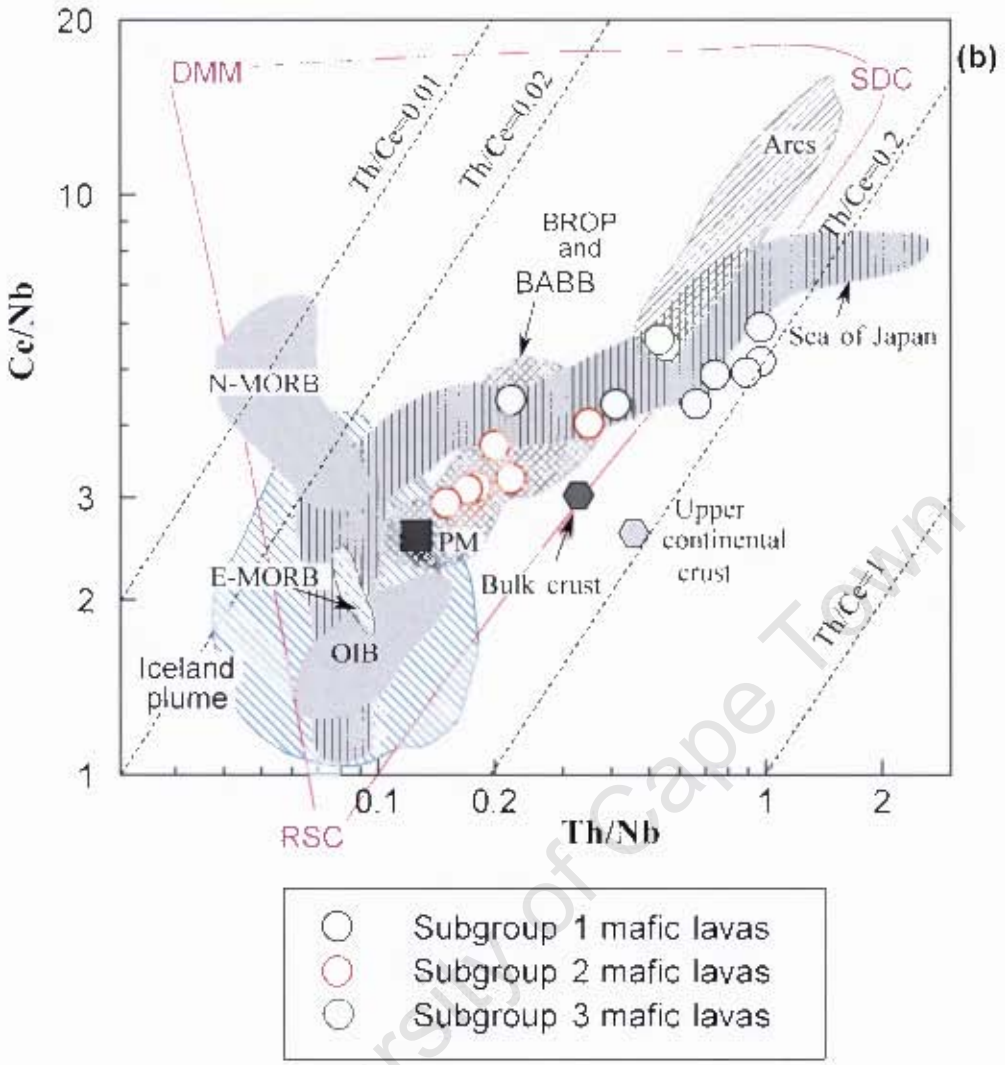

Fig. 9.9: Plot of the mafic lavas from (a) Tati and (b) Vumba greenstone belts on the Ce/Nb versus Th/Nb diagram (after Saunders et al., 1988), which is showing the various mantle components: depleted MORB mantle (DMM)-source of mid ocean ridge basalt; residual slab component (RSC); and subduction derived component (SDC). The following fields are shown for comparison: normal ocean ridge basalt (N-MORB), enriched mid ocean ridge basalt (E-MORB), ocean island basalt (OIB), primordial mantle (PM), Broken Ridge Ocean Plateau (BROP), Back Arc Basin Basalts (BABB)from Marianas Trough, celand plume basalts, basalts from the Sea of Japan and Marianas arc basalts. The fields were adopted from Kerrich et al. (1999), Polat et al., 1999 and Sandeman et al. (2006).

9.2 Felsic lavas

9.2.1 Main geochemical characteristics

Felsic lavas from both the Tati and Vumba greenstone belts are dacitic in composition. They are characterised by > 15 wt% Al_2O_3, low Y (13.1-5.20 ppm) and low Yb (0.55-1.19) concentrations, high La/Yb_n and Zr/Sm (55-115) ratios. Similar geochemical features are observed in modern rocks

termed adakites (e.g. Drummond and Defant, 1990). A summary of the dacite's geochemical characteristics is presented in Table 9.5 together with the main geochemical features of Cenozoic adakites presented for comparison purpose. Adakites are believed to be volcanic rocks formed by partial melting of young and relatively hot subducting oceanic slab at high pressure in Cenozoic convergent margins (e.g. Drummond and Defant, 1990; Martin, 1999). However, a few adakites of Archaean age have been reported in Archaean terranes such as the Wutai greenstone belt in the North China Craton (Wang et al., 2004), and the Birch-Uchi and Wawa greenstone belts (Hollings and Kerrich, 2000; Polat and Kerrich, 2002) in the Superior Province. The felsic volcanic rocks in the Tati and Vumba greenstone belts conform to most of the compositional criteria for Cenozoic adakites, with exception of chemical parameters involving Sr (Table 9.5). Sr is known to be a mobile element under metamorphic conditions, which the felsic volcanic rocks from the two greenstone belts have been subjected to. This is supported by the evaluation of trace element mobility test presented in chapter 6, which revealed that Sr concentration in the volcanic lavas has been disturbed as evidenced by its low correlation coefficient. However, the felsic volcanic rocks from the Tati greenstone belt exhibit more elevated Ni and Cr concentrations compared to the Cenozoic adakites and the felsic lavas from the Vumba greenstone belt. This can be accounted for by variable interaction between siliceous slab melts and the peridotitic mantle wedge (e.g. Rapp et al., 1999).

Table 9.5: Comparison of geochemical features of the felsic lavas from the Tati and Vumba greenstone belts, NE Botswana, with the main geochemical characteristics of adakites as defined by Martin et al. (2005).

Chemical parameter	Tati felsic lavas	Vumba felsic lavas	Adakite
SiO_2 (wt.%)	64 - 68	61 - 76	>56
Mg# - average	0.41	0.54	~0.51
Ni (ppm) - average	47	19	~24
Cr (ppm) - average	103	31	~36
Sr (ppm)	50 - 179	31 - 531	>400
Y (ppm)	5 - 13	7 - 21	<18
Sr/Y	8 - 15	3 - 40	>40
REE $(La/Yb)_N$	13 - 10	36 - 10	>10
Yb (ppm)	0.6 - 1.3	0.6 - 1.7	< 1.8

Moreover, the felsic volcanic rocks from the Tati and Vumba greenstone belts exhibit similar chondrite normalized REE patterns to those of Cenozoic adakites and other Archaean adakites (Figs. 9.10 and 9.11). It can be seen from Fig. 9.10a that the Tati dacite's REE patterns are virtually indistinguishable from the average Cenozoic and Wawa greenstone belt adakites whilst the REE patterns for the Vumba dacite resembles those of adakites from Birch-Uchi and Wutai greenstone belts (Fig. 9.10b and Fig. 9.11b). These similarities of the Cenozoic and Archaean adakites with the felsic volcanic rocks from the Tati and Vumba greenstone belts of the Francistown Granite-Greenstone Complex suggest that the felsic volcanic rocks are adakites.

Recent investigations on Cenozoic adakites defined two sub-types on the basis of silica abundance amongst other compositional factors (e.g. Martin et al., 2005). A high SiO_2 adakite has ≥56 wt.% SiO_2 and its primary source is believed to represent subducted oceanic crust whose resulting melts assimilated some peridotite as it ascends through the mantle wedge. In contrast, low-SiO_2 adakite contain <56 wt.% SiO_2 and is generated from mantle peridotite that has been metasomatized by slab-melts (Martin et al., 2005). It is evident that the two types of modern adakites are fundamentally different in terms of petrogenesis and sources. The only unifying petrogenetic factor between the two types of adakite is that they are both directly or indirectly linked to slab-melts. The high SiO_2 type is the one considered analogous to the Archaean adakite whilst the low SiO_2 adakite is petrogenetically similar to a group of rocks called Archaean sanukitoids (cf. Stern et al., 1989).

Nevertheless, the genesis of silica-rich magmas found in association with mafic volcanic rocks remains controversial. Different models have been proposed: extensive simple fractional crystallization of basaltic magmas (e.g. Cameron et al., 1980), and partial melting of a mafic crustal source (e.g. Graham et al., 1992). The possibility that the silica-rich magmas are products of extensive fractional crystallization can be ruled out on the basis of initial Sr-Nd and Pb isotope ratios. Silica-rich magmas derived from basaltic magmas should yield initial isotope ratios similar to those of the source of basaltic magmas. Additionally, chondrite-normalized REE patterns can be used to distinguish felsic magmas that have experienced extensive crystal fractionation from those that are closer to "primary magmas". During fractional crystallization, total REE concentrations generally increase, and the shape of REE patterns does not change basically, except for Eu anomalies (Takagi et al., 1999).

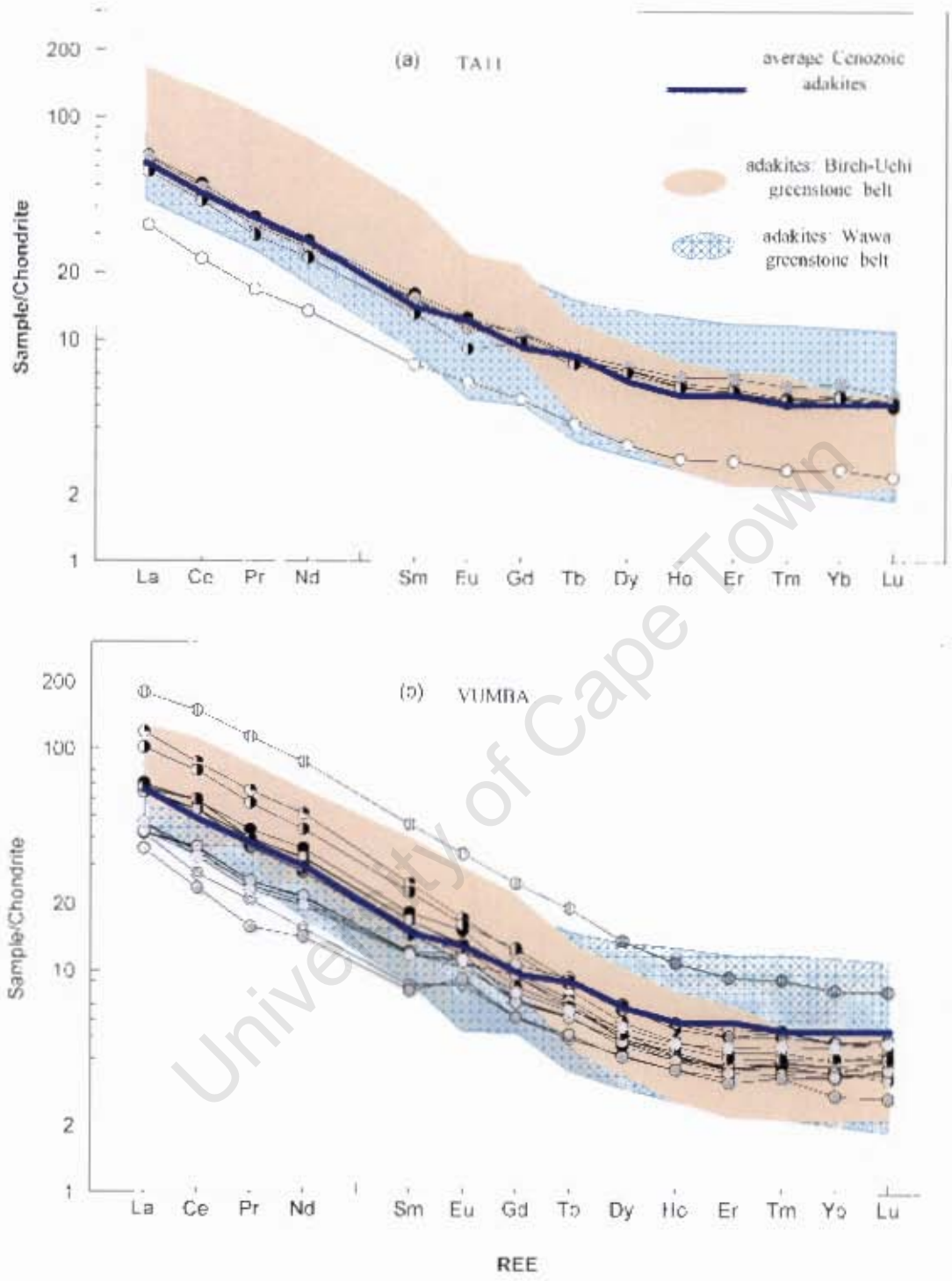

Fig. 9.10: Plots of REE patterns of adakites from the (a) Tati and (b) Vumba greenstone belts compared with the average Cenozoic adakites (from Drummond et al., 1996) and Neoarchaean adakites from the Wawa and Birch-Uchi greenstone belts in Superior province. The data for the Birch-Uchi and Wawa greenstone belts are from Hollings and Kerrich, 2000; Polat and Kerrich, 2002 respectively.

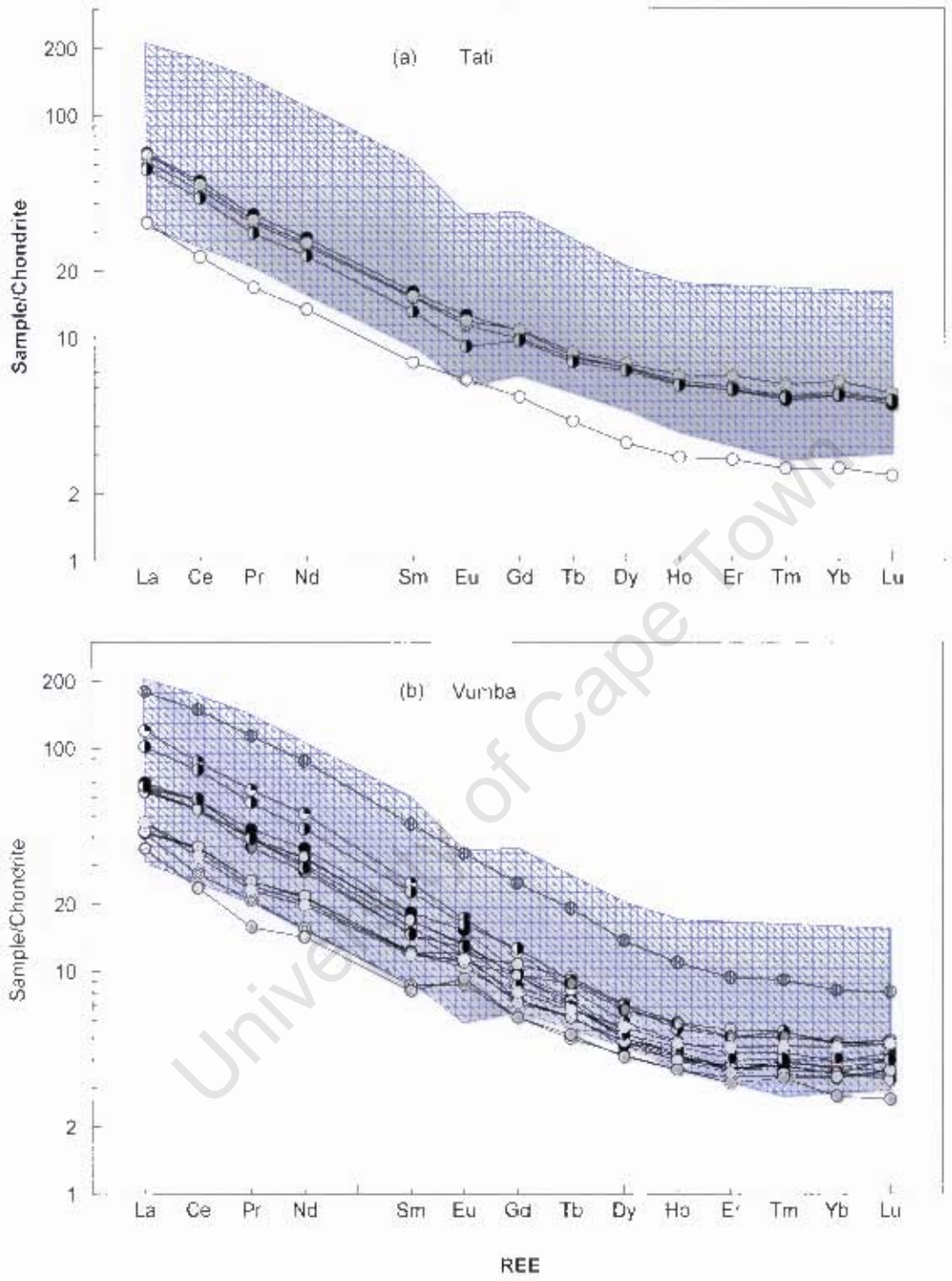

Fig. 9.11: Plots of REE patterns of adakites from the (a) Tati and (b) Vumba greenstone belts compared with the Neoarchaean adakites from the Wutai greenstone belt in North China Craton. The data for the Wutai greenstone belts are from Wang et al. (2004).

9.2.2 Petrogenesis

Removal of sub-aluminous minerals such as hornblende and garnet either as restite or during early high-pressure crystallization of melts are known to produce the high-Al, low Yb and Y compositions (Drummond et al., 1996). The possibility that the felsic volcanic rocks in the Tati and Vumba greenstone belts are products of extensive fractional crystallization of a basaltic magma is not supported by the initial Sr-Nd and Pb isotope ratios. The dissimilarity of initial Sr-Nd and Pb isotope ratios between the felsic volcanic rocks and coeval mafic lavas in these greenstone belts cannot be explained by simple fractional crystallization. Additionally, the chondrite-normalized REE patterns for the felsic volcanic rocks are highly fractionated and dissimilar from those of the mafic lavas. During fractional crystallization, total REE concentrations generally increase, and the shape of REE patterns do not change drastically. In the Vumba and Tati volcanic rocks, no systematic increase of total REE from mafic to felsic volcanic rocks is observed. Therefore, these suggest that fractional crystallization is an unlikely process for the formation of the felsic volcanic rocks in the Tati and Vumba greenstone belt. The REE patterns of the felsic volcanic rocks, however, resemble those of typical tonalite-trondhjemite-dacite (TTD) series magmas (Figs. 9.10 & 9.11; Defant et al., 1991). Additionally, the compositional similarity of these volcanic rocks with the modern adakites suggests that the Tati and Vumba felsic volcanics are slab-melts. This implies a mafic crustal source similar to MORB. Therefore, in an attempt to elaborate on the petrogenetic processes and sources involved in the genesis of the dacitic lavas from the Tati and Vumba greenstone belts, modeling partial melting a basic crustal source comparable to the average composition of subgroup 2 basalt (MORB-like basalt; section 9.1) is adopted here. The subgroup 2 mafic lavas from both greenstone belts have REE compositions similar to the average Archaean mafic composite (Table 9.5; Drummond and Defant, 1990). It is noteworthy that when oceanic crust is subducted, the tholeiitic MORB is converted to amphibolite through garnet amphibolite to eclogite with increasing depth (e.g. Sorensen, 1988).

In equilibrium batch melting, the magma generated by partial melting remains in equilibrium with the residual material until it is separated by buoyancy-driven segregation processes. Different types of residual assemblages will have different signatures on the resultant melt (e.g. Martin, 1987). REEs are preferred for partial melting modeling of the felsic lavas due to their consistent behaviour under magmatic processes. The equation (Eq. 9.2) of Shaw (2006; explained in the previous

section 9.1.2.3) that defines the behaviour of trace elements under equilibrium batch melting conditions, was applied. The mineral-melt partition coefficients, and starting and melt modes are given in Tables 9.6 and 9.7, respectively. A source of basaltic tholeiite composition was modelled at 10% degrees partial melting assuming a residue of amphibolite, garnet amphibolite with 5% modal garnet, garnet amphibolite with 25% modal garnet, and amphibole-bearing eclogite compositions. Compositions of REEs for the modelled melts were calculated for a range of potential residual assemblages and compared with the actual REE patterns of representative samples from the analytical data obtained from the Vumba and Tati felsic lavas (Fig. 9.12). It can be seen from Fig. 9.12 that the REE patterns for the felsic volcanics from the Tati and Vumba greenstone belts closely match those of model melts generated from garnet-bearing (5 modal % garnet) amphibolite.

Table 9.6: Source composition and partition coefficients used in batch melting model for the dacitic lavas. Partition coefficients (kd) are from Martin (1987). Archaean mafic composite data is from Drummond and Defant (1990).

REE	Tati ave. tholeiite (ppm)	Archaean Mafic Composite (ppm)	Vumba ave. tholeiite (ppm)	Cpx (Kd)	Hnbl (Kd)	Plg (Kd)	Gart (Kd)
La	3.67	3.6	3.26	0.1	0.2	0.13	0.04
Ce	10.43	9.2	11.21	0.2	0.3	0.11	0.08
Nd	9.00	6.6	9.37	0.4	0.8	0.07	0.20
Sm	2.91	2.0	2.90	0.6	1.1	0.05	1.00
Eu	1.02	0.73	1.02	0.6	1.3	1.30	0.98
Gd	3.96	2.6	3.86	0.7	1.8	0.004	3.8
Tb	0.66	-	0.69	0.7	2.0	0.037	7.5
Dy	4.49	3.1	4.32	0.7	2.0	0.031	11.0
Er	2.78	2.0	2.60	0.6	1.9	0.026	16.0
Yb	2.62	1.9	2.65	0.6	1.7	0.024	21.0
Lu	0.38	0.31	0.44	0.6	1.5	0.023	21.0

Table 9.7: Hypothetical starting and melt modes used in batch melting model for the dacitic lavas.

Minerals	Amphibolite		Garnet (5%)-amphibolite		Garnet (25%)-amphibolite		Eclogite	
	Start mode	melt mode	Start mode	melt mode	Start mode	melt mode	Start mode	melt mode
	X_o	p	X_o	p	X_o	p	X_o	p
Cpx	0.05	0.01	0.10	0.09	0.05	0.05	0.45	0.30
Hnbl	0.65	0.55	0.55	0.50	0.50	0.50	0.15	0.50
Plg	0.30	0.44	0.30	0.40	0.15	0.25	0	-
Gart	0	-	0.05	0.01	0.25	0.20	0.40	0.20

Abbreviation: Cpx-clinopyroxene, Hnbl-hornblende, Plg-plagioclase and Gart-garnet.

The distinctive REE compositions of felsic volcanic rocks from the Tati and Vumba greenstone belts in terms of the chondrite normalized La_N/Yb_N and Yb_N values are presented in Fig. 9.13. Modelled melting curves from Drummond and Defant (1990) for a MORB source, with Yb_N = 12.5 and La_N/Yb_N = 1, are superimposed on this figure. The melting curves correspond to melts that were in

equilibrium with amphibolite, garnet-bearing (10 modal % garnet) amphibolite, garnet-bearing (25 modal % garnet) amphibolite and amphibole-bearing eclogite residual assemblages. The REE modelling suggests that the felsic volcanic rocks in the Tati and Vumba greenstone belts were generated from partial melting of a garnetiferous amphibolite source. These results corroborate the results of Fig. 9.12 that show the entire spectrum of REE. From Figure 9.13, it can be suggested that the felsic volcanic rocks from the Vumba belt were derived from a more garnet-rich source than that of the Tati felsic volcanics.

The results of four felsic volcanic samples analysed for Sm/Nd isotopic composition are summarized in Table 9.8. One sample (ZBT-43) from the Tati greenstone belt records a positive εNd value of 0.94, suggesting that the felsic volcanics were generated from melting young juvenile mafic crust. The three samples from the Vumba greenstone belt have variable εNd values from 1.33 to -0.69 suggesting young juvenile crustal source that possibly interacted with minor enriched crustal material. This is consistent with the results of the associated mafic lavas whose Nd isotopic data indicate interaction with old crustal material. The positive εNd values imply that the time between the generation of the mafic source material from the mantle, and partial melting of that mafic source to form the felsic volcanics was short. The Tati and Vumba felsic volcanic rocks were extruded at 2735 and 2696 Ma, respectively. So this is useful as it can be used to calculate the age of the subducting slab.

Table 9.8: Summary of Nd isotopic data for felsic volcanic rocks from the Tati and Vumba greenstone belts.

Sample	Measured $^{143}Nd/^{144}Nd$	**2 σ error**	Measured $^{147}Sm/^{144}Nd$	U-Pb age (Ma)	Initial εNd	Sm (ppm)	Nd (ppm)	DePaolo T_{DM} (Ga)
Tati								
ZBT-43	0.511216	±12	0.1154	2735	0.94	2.96	15.5	2.98
Vumba								
ZBV-173	0.511018	± 6	0.1026	2696	1.12	3.09	18.2	2.91
ZBV-166	0.511104	± 5	0.1124	2696	-0.69	2.40	12.9	3.06
ZBV-156	0.511006	± 4	0.1014	2696	1.33	3.59	21.4	2.89

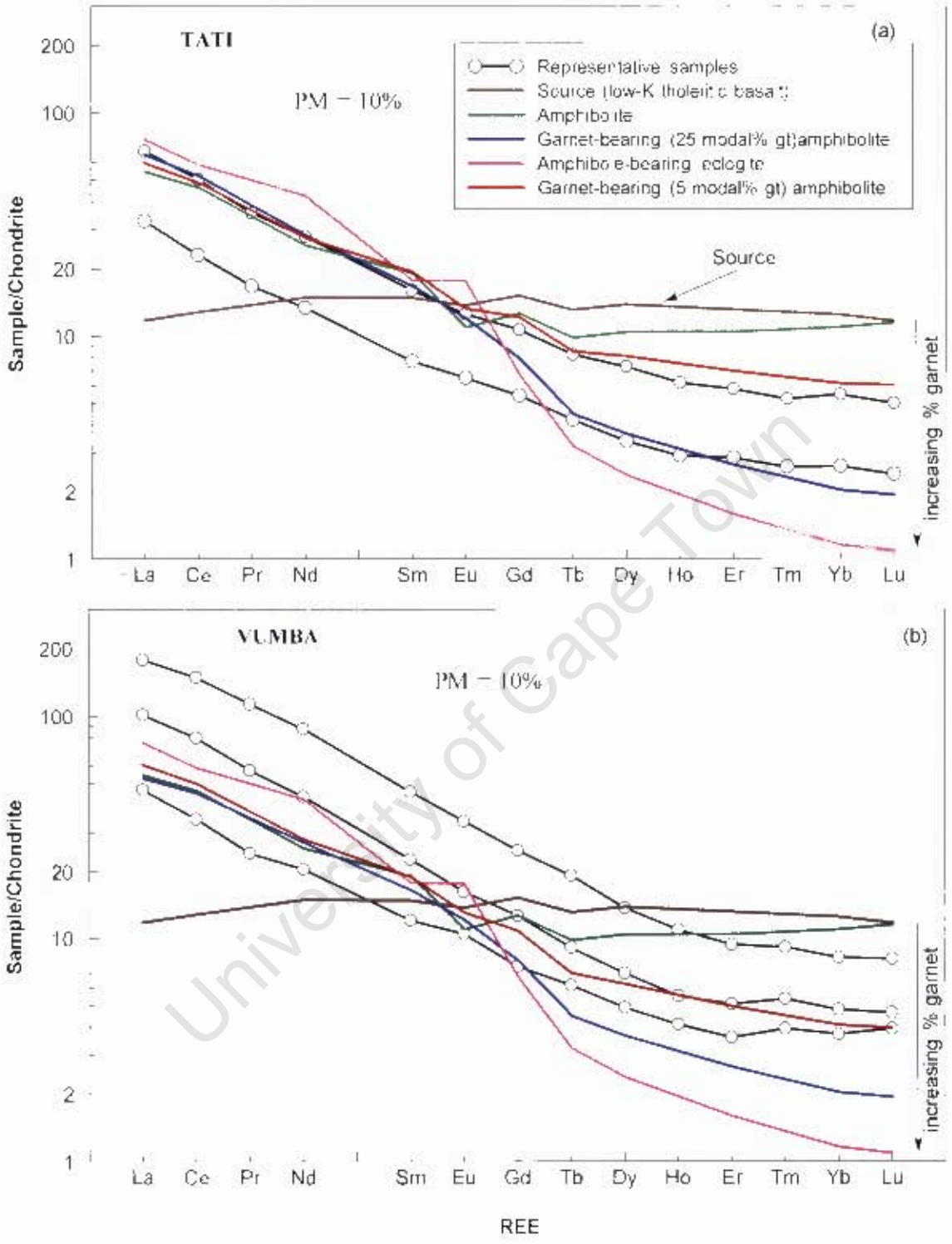

Fig. 9.12: Chondrite normalized (Sun and McDonough, 1989) REE patterns for the (a) Tati and (b) Vumba felsic lavas compared with fields defined by 10% batch melting of a low-K tholeiitic basalt source. The calculated patterns for batch melting are for potential sources containing amphibolite, garnet-bearing (5 modal % garnet) amphibolite, garnet-bearing (25 modal % garnet) amphibolite and amphibole-bearing eclogite residues (modelled after Martin, 1987). PM=partial melting.

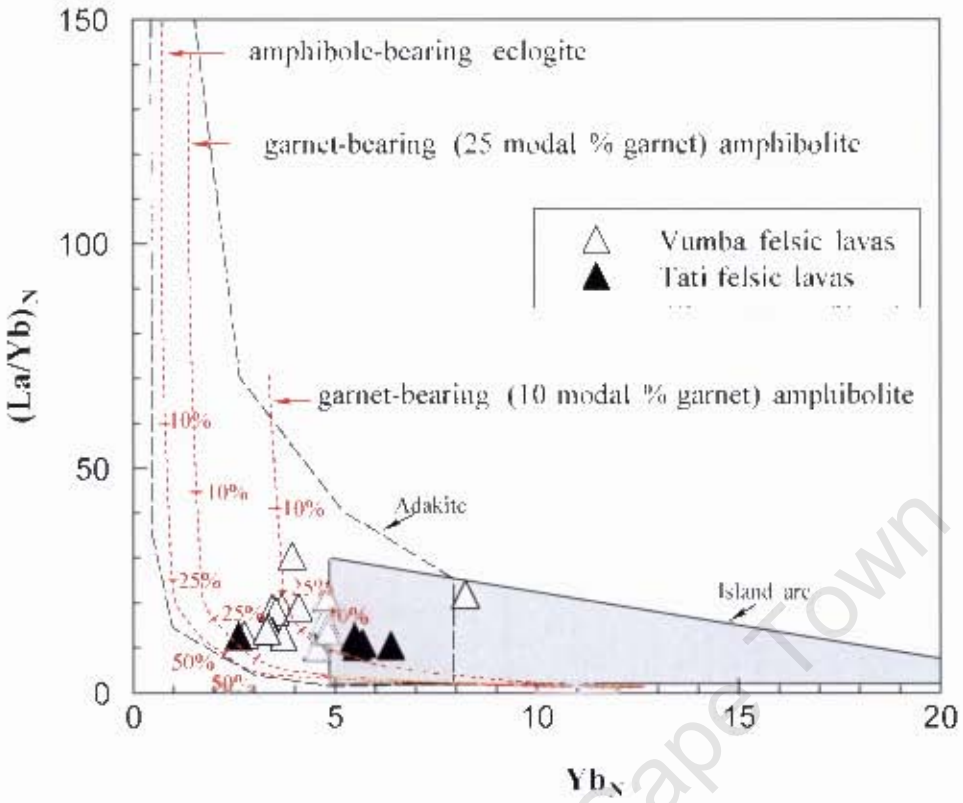

Fig. 9.13: Chondrite-normalized $(La/Yb)_N$ versus Yb_N diagram modified after Drummond and Defant (1990). Data from felsic lavas from the Tati and the Vumba greenstone belts are superimposed on the melting curves. The three partial melting curves are displayed and assume a MORB source having $Yb_N = 12.5$ and $(La/Yb)_N = 1$. The partial melting curves represent garnet-bearing (10 modal% garnet) amphibolite, garnet-bearing (25 modal% garnet) amphibolite and amphibole-bearing eclogite restites. Percent partial melt values are indicated on each of the curves.

CHAPTER 10

Petrogenesis of the granitoids

10.0 Introduction

Neoarchaean granitoids that are mainly dominated by tonalite, trondhjemite and granodiorite composition (TTG) are considered analogues of high-SiO_2 adakites (Martin et al., 2005), although this is not universally accepted (e.g. Condie, 2005a; Whalen et al., 2002; Smithies, 2000). Non-subduction models such as melting of underplated basaltic crust, the lower crust and the basal sections of thick oceanic plateaus (Condie, 2005a; Rollinson and Tarney, 2005; Whalen et al., 2002) have been proposed as alternative models for the formation of Neoarchaean TTGs. Condie (2005a) contends that TTGs can be generated from any tectonic setting in which stable hornblende eclogite is formed and subjected to temperatures of 700 to 800 °C. Recent studies (e.g. Martin et al., 2005; Condie 2005b) indicate that the Neoarchaean TTGs possess some geochemical features that are distinct from their early Archaean counterparts. This has been interpreted as an indication of change in tectonic regime during the Archaean. According to Martin et al (2005) Neoarchaean TTGs exhibit geochemical attributes that involve mantle in their petrogenesis. Such geochemical features include relatively high Mg#, Ni and Cr contents. The Dacites and TTGs in the study area overlap in age.

10.1 Main geochemical characteristics

The main geochemical characteristics that have some implications on the petrogenesis of the granitoids from the Francistown Granite-Greenstone Complex are presented in Table 10.1, where they are compared with the average composition of the Neoarchaean TTGs.

Previous geochemical investigation (Kampunzu et al., 2003) of plutonic rocks within the Tati terrain described the NE and SW tonalite-trondhjemites as low-Al and high-Al TTG subsuites, respectively. However, the data from this study shows that both the NE and SW tonalite-trondhjemites have high-Al type (cf. Barker, 1979) characteristics. The minor tonalite-trondhjemite dykes display low-Al affinities with an average Yb concentration of 1.15 ppm. Nonetheless, all the tonalite-trondhjemite units have an I-type affinity.

Table 10.1: Summary of the main geochemical characteristics of the granitoids in the Tati and Vumba granite-greenstone terrains.

	TATI						VUMBA				
Chemical Parameters	Quartz Monzonite	NE Tonalite-trondhjemite	SW Tonalite-trondhjemite	Tonalite-trondhjemite dyke	Trondhjemite	Monzogranite	Quartz Monzonite	Tonalite	Granodiorite	Monzogranite	Neoarchaean TTG
Age (Ma)	(2732)	2732	2673	2703	2715.9	2716	(2690)	2690	2686	2647	-
SiO_2 wt.%	62.9 - 64.2	67.3 - 72.0	69.4.5 - 74.7	72.3 - 75.7	71.5 - 75.7	72.3 - 76.2	59.8 - 66.3	67.3 - 72.3	66.5 - 75.7	63.1 - 73.5	> 64
ASI	0.93 - 1.02	1.00 - 1.03	1.00 - 1.06	1.02 - 1.08	0.92 - 1.09	0.99 - 1.06	0.84 - 0.90	0.98 - 1.02	0.98 - 1.08	1.00 - 1.08	-
Al_2O_3 wt.%	17.7 - 16.5	17.4 - 16.2	16.0 - 13.6	14.5 - 12.6	12.4 - 11.8	12.1 - 11.9	16.1 - 15.4	16.6 - 15.0	16.2 - 14.3	18.6 - 13.7	15.5 ± 0.75
K_2O/Na_2O	0.87 - 0.98	0.91 - 0.31	0.22 - 1.41	0.10 - 0.37	0.26 - 0.44	2.07 - 2.47	1.15 - 1.41	0.30 - 0.45	0.58 - 1.09	1.09 - 1.80	0.51 ± 0.24
Mg#	0.49 - 0.51	0.44 - 0.47	0.30 - 0.38	0.31 - 0.44	0.06 - 0.12	0.03 - 0.06	0.50 - 0.55	0.36 - 0.42	0.20 - 0.47	0.23 - 0.32	46.2 ± 6.7
Nb/Ta	21.0 - 10.4	23.8 - 9.6	21.1 - 10.2	10.5 - 8.7	22.2 -14.1	25.5 - 14.8	14.3 - 10.5	14.4 - 10.7	14.6 - 6.3	14.4 - 10.7	-
Zr/Hf	49 - 41	56 - 49	89 - 34	54 - 38	63 - 42	48 - 43	42 - 38	42 - 37	40 - 30	42 - 37	-
Zr/Sm	32 - 30	198 - 70	463 - 75	59 - 58	58 - 36	62 - 44	35 - 30	77 - 51	48 - 27	77 - 51	20 - 200
Cr (ppm)	33 - 27	14 - 8	15 - 6	13 - 10	12 - 6	12 - 7	74 - 47	33 - 15	31 - 13	24 - 9	35 ± 26
Ni (ppm)	39 - 23	7 - 5	7 - 4	68 - 6	4 - 3	4 - 3	-	-	-	-	22 ± 13
Cr/Ni	1.3 - 1.1	2.7 - 1.3	2.7 - 1.4	1.7 - 0.2	3.3 - 1.8	3.3 - 2.1	-	-	-	-	-
Sr (ppm)	622 - 570	484 - 381	305 - 108	133 - 119	113 - 64	100 - 95	548 - 383	405 - 195	673 - 135	313 - 187	515 ± 127
Y (ppm)	14.1 - 13.1	3.0 - 1.6	6.3 - 1.8	12.9 - 8.8	36.6 - 27.6	36.4 - 33.0	27.4 - 23.4	9.8 - 4.2	11.3 - 5.1	27.8 - 4.5	9.1 ± 5.4
Sr/Y	~42	234 - 142	115 - 17	15 - 9	~3	~3	22 - 15	91 - 21	60 - 12	52 - 7	89 ± 49
Yb (ppm)	1.20 -1.12	0.31 - 0.19	0.57 - 0.17	1.36 - 0.99	4.44 - 3.27	4.24 - 3.89	2.03 - 1.84	0.91 - 0.42	1.04 - 0.46	2.05 - 0.35	0.71 ± 0.41
$(La/Yb)_N$	44 - 38	37 - 5	62 - 12	40 - 38	10 - 3	7 - 5	37 - 28	51 - 8	95 - 11	94 - 26	36 ± 24
Eu/Eu*	0.81 - 0.77	2.1 - 1.1	2.3 - 1.1	0.88 - 0.77	0.74 - 0.53	0.60 - 0.57	0.71 - 0.56	2.08 - 0.80	1.24 - 0.77	1.77 - 0.66	-
$\delta^{18}O$ ‰	+8.0	+9.0 - +8.6	+9.5 - +9.1	+10.6	+9.6 - +8.7	+10.1	+10.0	+12.1	+9.0	+9.0	-
εNd	0.36	7.08 - +3.08	7.57 - -1.44	0.58	-7.35	0.15	2.91	1.06 - -1.16	1.88 - +0.27	2.48 - +0.69	-
$^{206}Pb/^{204}Pb$	24.41	16.52-15.72	19.80-16.14	21.92	80.48	41.89	22.95	24.68-21.16	26.77-16.54	23.98-21.51	-
$^{207}Pb/^{204}Pb$	16.74	15.59-15.20	15.98-15.28	16.34	27.26	19.27	16.52	17.26-16.22	17.30-15.38	16.72-16.29	-
$^{208}Pb/^{204}Pb$	42.93	35.18-35.34	41.00-35.13	42.37	102.85	62.65	43.13	45.36-39.05	47.57-38.09	62.33-40.26	-

Sources for Neoarchaean TTG composition: Condie, 2005a, Martin et al., 2005.

The granitoids from the Tati granite-greenstone terrain display different Sr, Cr and Y concentrations and different Sr/Y and Cr/Y ratios (Table 10.1). High Sr/Y ratios and low Y contents are generally regarded as characteristics of adakites and often interpreted as a product of high-pressure partial melting of a mafic garnet-bearing source origin (e.g. Martin, 1987; Drummond and Defant, 1990). Several studies have shown that the stability of plagioclase is strongly dependent on pressure (e.g. Martin, 1987; Drummond and Defant, 1990; Martin et al., 2005), which follows that the Sr concentrations in the granitoids have implications for both the source composition and pressure conditions under which partial melting took place. Y and Cr are highly compatible in garnet with partition coefficients of 3.08 and 13.0 (e.g. Martin, 1987; Shaw, 2006), respectively, so that the presence of garnet in the residue will result in Y and Cr depleted melt. On the other hand garnet has low partition coefficient for Sr (D^{Sr}_{gt} = 0.0065; Shaw, 2006; Green, 2006). Thus the presence of residual garnet during partial melting, any source of granitoids would fractionate Y and Cr from Sr, resulting in high Sr/Y and low Cr/Y ratio melts. Y and Cr are incompatible in plagioclase with partition coefficients of 0.0115 and 0.04 (Shaw, 2006), respectively. It has been established that garnet has a high mineral-melt partition coefficient for Yb (HREE) and a low partition coefficient for La (LREE), which renders it an effective phase for fractionation of REEs. All the tonalite-trondhjemite units in the study area are characterised by fractionated REE patterns with depleted HREE. This suggests residual garnet in their source. However, most granitoids in the Tati and Vumba granite-greenstone terrains show negative Sr anomalies in the multielement plots, which suggest fractionation of plagioclase during evolution of their magmas by fractional crystallization processes.

The relationships between Sr/Y and Cr/Y versus Y for the granitoids within the Francistown Granite-Greenstone Complex are presented in Fig. 10.1. This plot has been widely applied to discriminate between classical island arc granitoids and adakites (e.g. Drummond and Defant, 1990; Rapp, 1997; Whalen et al., 1999). It is evident from Fig 10.1 that all the tonalite-trondhjemite units and quartz monzonite are comparable to adakites and likely had garnet in their source. Even though all the tonalite-trondhjemite units occupy the adakites field, they exhibit distinct positions that make a decreasing trend of Sr/Y against increasing Y content. Similar trends can be caused by variable degree of partial melting in the presence of garnet (e.g. Rapp, 1997) or by fractional

crystallization process involving plagioclase fractionation. When melting a garnet-bearing source, the content of Y in the resulting melt would increase with the degree of partial melting since more garnet is melted to release Y into the melt. This leads to a decrease in Sr/Y ratio. Similarly when a melt is going under fractional crystallization involving fractionation of plagioclase, it would remove Sr from the melt, leading to decrease in Sr/Y ratio. However, if this trend is at all related to variable degree of partial melting, it is suppose to reflect a positive trend in a plot of Cr/Y versus Y (Rapp, 1997; Fig. 10.1b) because both Cr and Y contents should increase with increasing degree of partial melting. Since Cr is more compatible in garnet than Y, a steep positive trend is anticipated. The diagrams in Fig. 10.1 demonstrate that the tonalite-trondhjemite from the Sekukwe pluton, the Tati pluton and the tonalite-trondhjemite dykes maintain similar positions in both diagrams, which is incompatible with increasing degree of melting. Based on the Fig. 10.1, it is not possible to rule out the possibility that the granitoid melts were produced by fractional crystallization. The differences in the tonalite-trondhjemite units within the Tati granite-greenstone terrain is compatible with the geochronology data, which reflected that the three units belong to different magmatic events hence high possibility of different petrogenetic conditions.

The quartz monzonite unit from the Tati terrain possesses higher Sr, Y and lower SiO_2 contents than the tonalite-trondhjemite units (Table 10.1). Additionally, the quartz monzonite display higher concentrations of Cr and Ni as well as higher Mg# than the tonalite-trondhjemite units in the same area. Nonetheless, it possesses fractionated REE patterns similar to those of the tonalite-trondhjemites, although is more enriched in LREE abundances. It is important to note that the quartz monzonite occurs contiguous to the Sekukwe tonalite-trondhjemite pluton, which lead some previous workers (e.g. Key et al., 1976) to suggest that the two units must be genetically related. Experimental studies on the petrogenesis of TTGs have revealed that interaction of melts derived from subducting slab with peridotite within the mantle wedge can significantly modify Cr, Ni, MgO and SiO_2 content of the melt resulting in the melt acquiring high Cr, Ni, Mg# and low SiO_2 values (e.g. Rapp et al., 1999). Furthermore, these studies demonstrated that in addition to modification, the melt is also consumed during the interaction process. According to Rapp et al. (1999), the degree of modification is dependent on the volume ratio of the melt to peridotite. Small volume ratio of the melt to peridotite is vulnerable to the effects of modification. Therefore, the difference between the quartz monzonite and the tonalite-trondhjemite could be reflecting the differences in

degree of peridotite interaction with their parental melts, which is dependent on the volume of the primary melts. The quartz monzonite covers a small area, which suggests their primary magma was small in term of volume hence low volume ratio of the melt to peridotitic mantle. Tonalite-trondhjemite forms large plutons implying voluminous primary melt, which is less vulnerable to peridotite assimilation.

The purely trondhjemite unit is quite distinct from the tonalite-trondhjemite and quartz monzonite units in terms of geochemical characteristics (Table 10.1). It is a low-Al type (cf. Barker, 1979) with low Sr and high Y concentrations, which suggest the presence and absence, respectively, of plagioclase and garnet phases in the residual source, i.e. low pressure petrogenetic conditions. Additionally, the trondhjemite samples display REE patterns that have prominent negative Eu anomalies, flat HREE with high contents (Yb > 3 ppm) and moderately enriched LREE. Their multielement profiles exhibit a pronounced Sr trough, which is consistent with plagioclase fractionation during the petrogenesis or presence of residual plagioclase in the source. Unlike the tonalite-trondhjemite units, the trondhjemite's multielement profiles are devoid of a prominent positive Pb anomaly, which is one of the defining geochemical characteristics of subduction-related magmas. Furthermore, the trondhjemite unit is characterised by very low contents of Cr (<12 ppm), Ni (~4 ppm) and low values of Mg# (0.12 to 0.06) that are all below those of Neoarchaean high-Al TTGs (Table 10.1). This does not favour any possibility of mantle peridotite interaction with its parental magma. All these geochemical characteristics, clearly suggest that the petrogenetic history of the trondhjemite unit is distinct from that of the tonalite-trondhjemite and the quartz monzonite units. In Fig. 10.1a, the trondhjemite plot in the field of classic island arc granitoids, which is compatible with an origin through melting outside the garnet stability field, i.e. under low pressure conditions.

The monzogranite unit in the Tati granite-greenstone terrain resembles the trondhjemite unit in terms of geochemical parameters presented in Table 10.1 suggesting common petrogenetic bond between the two units. The only parameter that distinguishes between the two units is the K_2O/Na_2O ratio. The monzogranite possesses higher K_2O/Na_2O (2.07-2.47) than the trondhjemite, which exhibits low ratios ranging from 0.26 to 0.44. In terms of Sr/Y and Cr/Y versus Y plot, the two units are indistinguishable (Fig. 10.1). Moreover, geochronological data from this study

(chapter 4) shows that the monzogranite and trondhjemite units are contemporaneous, which is consistent with them forming from a common source.

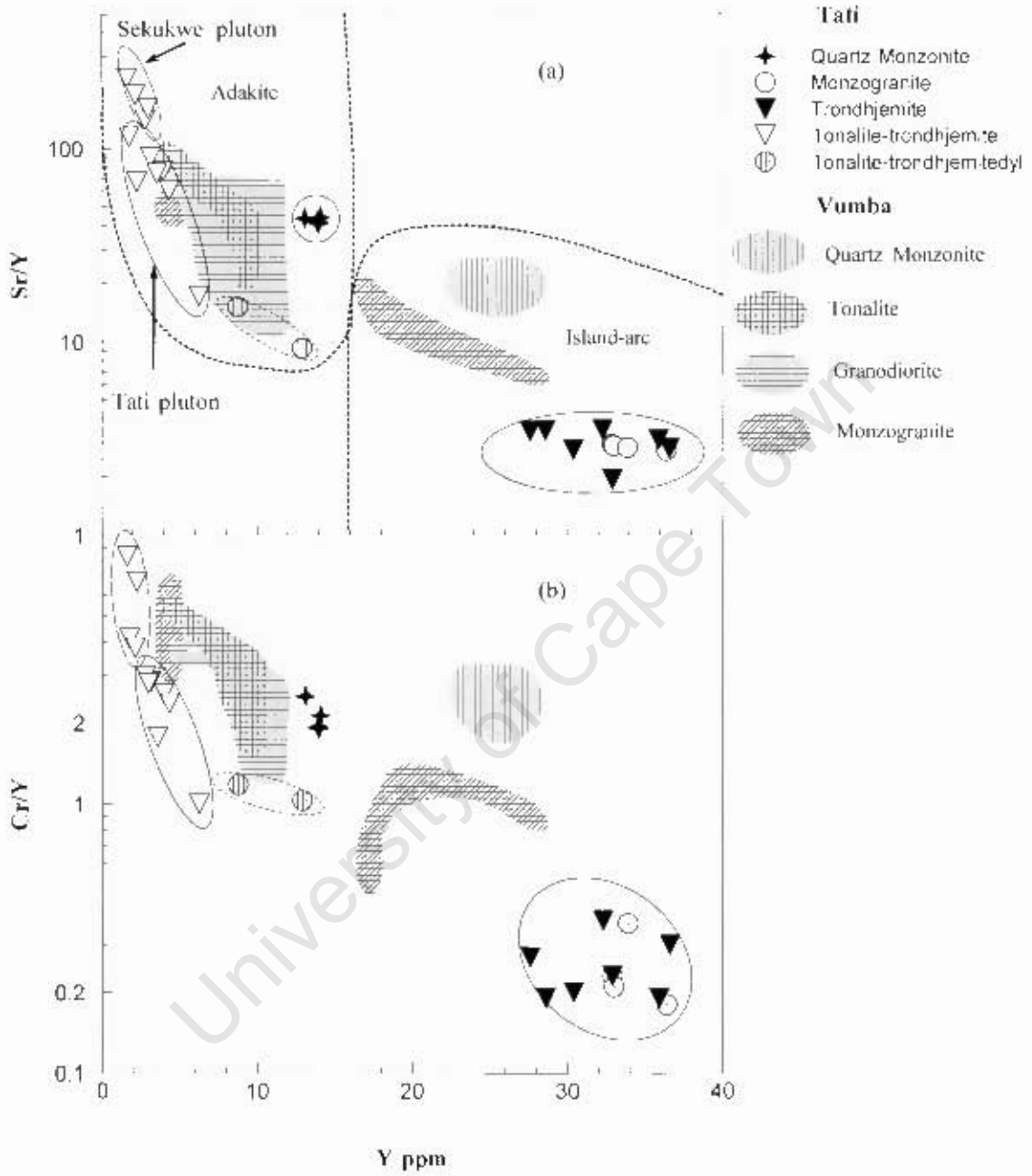

Fig. 10.1: Plot of (a) Sr/Y versus Y and (b) Cr/Y versus Y for the granitoids from the Tati granite-greenstone terrain. The granitoids from the Vumba granite-greenstone terrain are shown. Fields for adakites and island arc rocks are after Drummond and Defant (1990)

The granitoids from the Vumba granite-greenstone terrain display distinct pattern on plots of Sr/Y and Cr/Y versus Y contents compared to the Tati granitoids (Fig. 10.1) suggesting the differences of petrogenetic conditions. Tonalite, granodiorite and samples from the outer phase of the

monzogranite display high Sr/Y and Cr/Y ratios and low Y contents which are comparable with those of the Neoarchaean high-Al TTGs and high-SiO_2 adakites that, in turn, are linked to relative high pressure conditions of origin. The quartz monzonite and the monzogranite samples from the inner monzogranite possess Sr/Y ratios and Y contents that correspond to classic island arc rocks (Fig. 10.1a). However, some of the geochemical attributes of the quartz monzonite and the inner monzogranite in the Vumba area fall between those of the low-SiO_2 adakites (sanukitoids) and high-SiO_2 adakites (cf. Martin et al., 2005). For instance the Ni, Cr contents and Mg# for the quartz monzonite are higher than those of the high-Al Archaean TTGs but lower than those of sanukitoids and low-SiO_2 adakites. Furthermore, the quartz monzonite contains elevated Ba and Sr contents corresponding to those of sanukitoids (Table 10.1). It is also metaluminous and K-rich whilst the remainder of the granitoids is weakly peraluminous and medium-K (except monzogranite). All these geochemical features suggest a petrogenetic history distinct from the granitoid units in the Vumba area.

10.2 Petrogenesis

To evaluate the petrogenetic histories of the granitoids from the Francistown Granite-Greenstone Complex, REE abundances were utilized in a forward partial melting model testing different potential sources implicated by the geochemical data discussed above. The same equation of Shaw (2006; see section 9.1.2.3) was used, with the mineral-melt partition coefficients, and starting and melt modes, as presented in Tables 9.6 and 9.7 (see chapter 9), respectively. The Archaean tonalite-trondhjemite-granodiorite (TTG) association is often considered as products of partial melting of subducted slabs or oceanic plateaus or root zones of volcanic arcs (e.g. Condie, 2005b; Martin et al., 2005). In this study a mafic source of basaltic low-K tholeiite composition was modelled at different degrees of partial melting, assuming a residue of amphibolite, garnet amphibolite with 5% modal garnet, garnet amphibolite with 25% modal garnet and eclogite compositions. Only the results of the degrees of partial melting that are comparable or near comparable with the analytical data are shown on the diagrams. Compositions of REEs for the modelled melts were calculated for a range of potential residual assemblages and compared with the actual REE patterns of the granitoids from the Francistown Granite-Greenstone Complex (Figs. 10.2 to 10.5).

10.2.1 Tati Granitoids

The comparisons of Chondrite-normalized REE patterns for the Tati granitoids with the calculated REE compositions (Fig. 10.2) suggest different sources and conditions for the granitoids, which is consistent with different emplacement ages. For instance the origin of the quartz monzonite cannot be explained by partial melting of a mafic source under different pressure conditions alone (Fig. 10.2a). A model involving very low degree of partial melting of a mafic source, where a restite with about 10% garnet is left behind, followed by subsequent LREE enrichment process, or otherwise a LREE enriched mafic source is required to explain the origin of the quartz monzonite. As for the origin of the Sekukwe high-Al tonalite-trondhjemite a model encompassing partial melting of a mafic source at relatively high pressure where residual material containing about 25 modal% garnet, coupled with subsequent fractional crystallization process involving hornblende, is most likely. The tonalite-trondhjemite dykes's origin can be explained by low degree partial melting of a mafic source with residue containing about 10 modal% garnet. A similar model with a garnetiferous amphibolite containing between 10 and 25 modal% garnet, coupled with fractional crystallization of phases involving hornblende, illmenite and accessory allanite can be invoked to explain the origin of the Tati pluton tonalite-trondhjemite. The trondhjemite and monzogranite chondrite-normalized REE patterns are similar to the calculated REE patterns of a partially melted mafic source with an amphibolite residue. Experimental studies of TTG generation have revealed that hydrated mafic sources at lower pressure tend to produce more trondhjemitic melts (e.g. Rapp et al., 1999). This implies the possible source of the trondhjemite is a hydrated basaltic crust.

Further petrogenetic information on the Tati granitoids is revealed by plotting their chondrite-normalized La/Yb ratios versus Yb contents (Fig. 10.3). Calculated partial melting model curves for a MORB source with different residual assemblages are superimposed on the diagram for comparison with the analytical data from the Tati granitoids. Fields of adakites and island arc rocks from Drummond and Defant (1990) are also superimposed on the diagram. On this diagram the granitoids clearly form different clusters suggesting different petrogenetic conditions. Nonetheless, the results corroborate those of calculated REE profiles to a large extent.

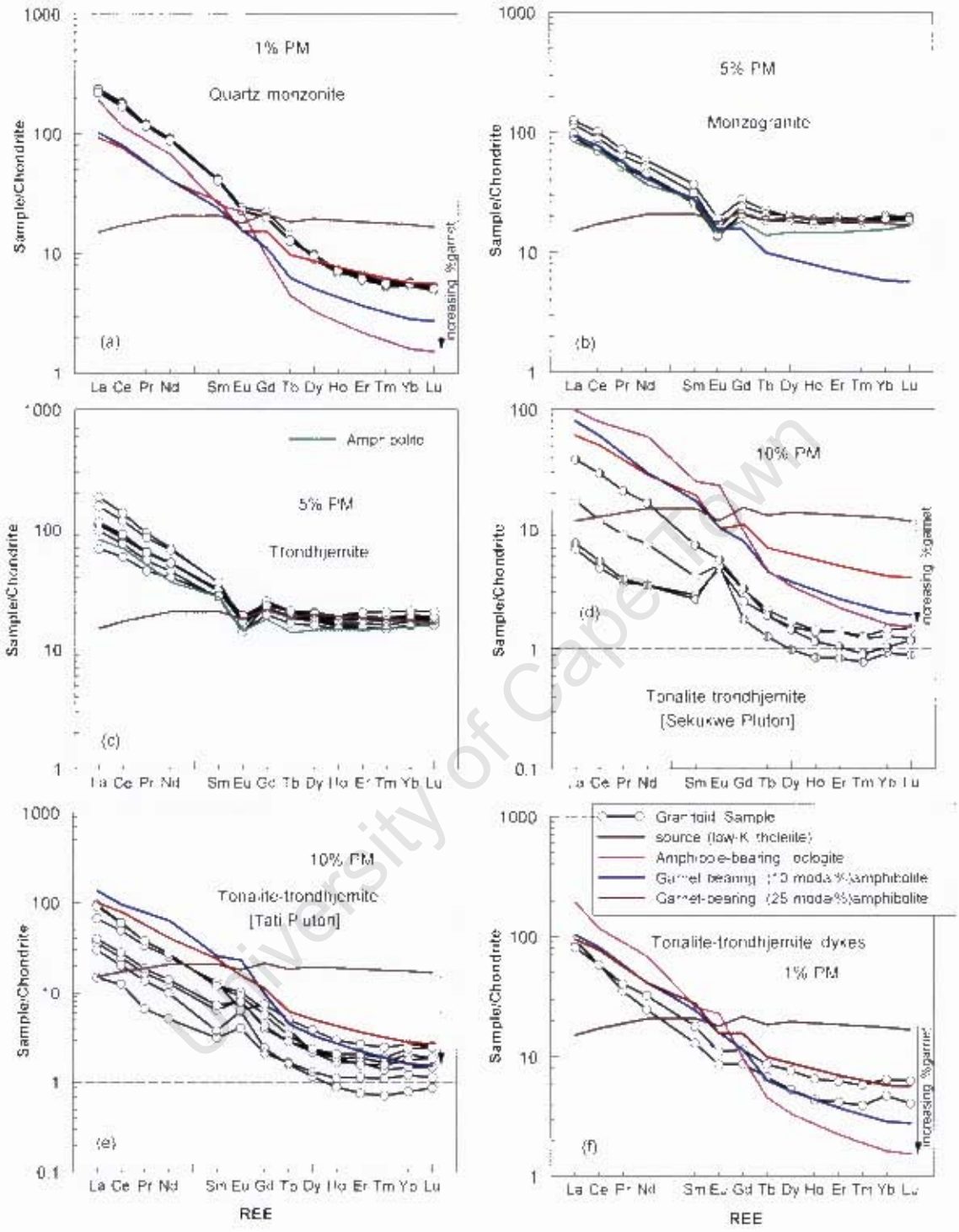

Fig. 10.2: Chondrite normalized (Sun and McDonough, 1989) REE patterns for the Tati granitoids compared with fields defined by various degree (%) batch melting of a low-K tholeiitic basalt source. The calculated patterns for batch melting are for potential mafic sources containing amphibolite garnet-bearing (10 modal%) amphibolite, garnet-bearing (25 modal%) amphibolite and amphibole-bearing eclogite residues (modelled after Martin, 1987). PM=partial melting.

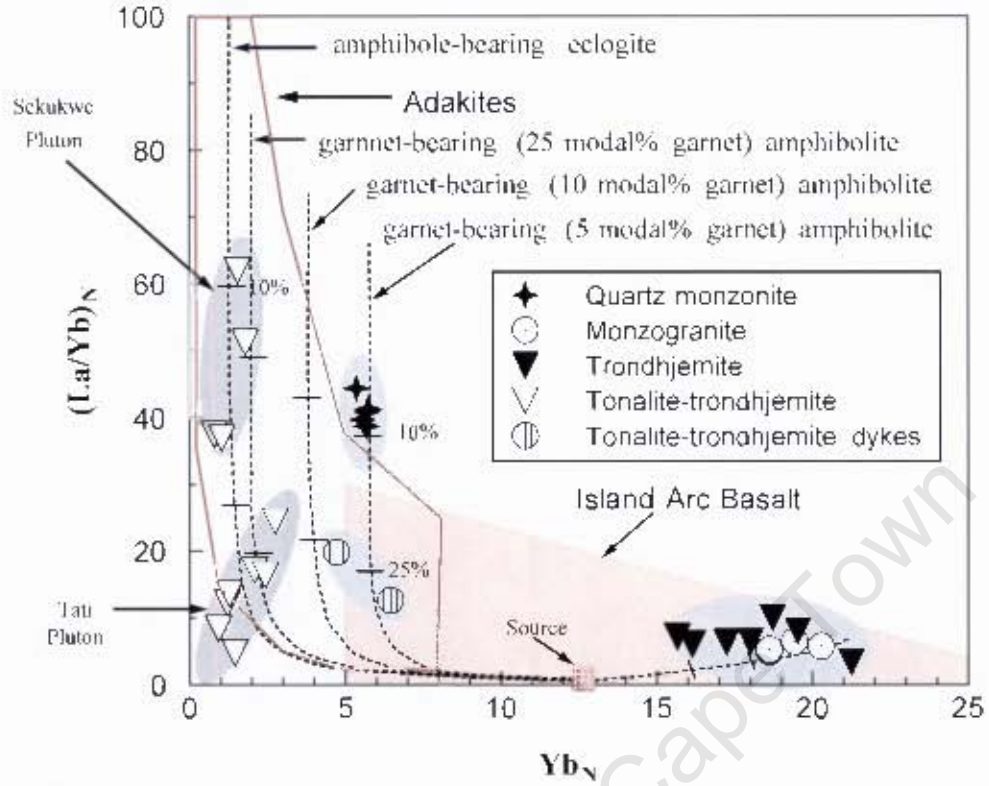

Fig. 10.3: Chondrite-normalized Yb_N versus $(La/Yb)_N$ diagram modified after Drummond and Defant (1990) showing granitoid data from the Tati granite-greenstone terrain, with superimposed melting curves. The five partial melting curves are displayed and assume a MORB source with $Yb_N = 12.5$ and $(La/Yb)_N = 1$. The partial melting curves represent garnet-bearing (10 modal% garnet) amphibolite, garnet-bearing (25 modal% garnet) amphibolite and amphibole-bearing eclogite restites. 10 and 25% degrees of partial melting are indicated on each of the curves.

The trondhjemite and the monzogranite data cluster on the calculated melting curve corresponding to partial melting of a MORB source at relative low pressure outside stability field of garnet. The quartz monzonite falls along calculated curve of a MORB source with an amphibolite restite bearing 5 modal% garnet. The tonalite-trondhjemite from the Sekukwe and Tati plutons straddle the melting curves of amphibole-bearing eclogite and garnet-bearing (25 modal% garnet) amphibolite residues. However, the Tati pluton tonalite-trondhjemite corresponds to higher degree partial melting than the Sekukwe tonalite-trondhjemite. Tonalite-trondhjemite dyke samples cluster around melting curves of a source with 5 to 10 modal% garnet in an amphibolite residue.

10.2.2 Vumba granitoids

Comparison of the calculated REE patterns from a theoretical tholeiitic basalt source and the chondrite-normalized REE analytical data from the Vumba granitoids is presented in Fig. 10.5 to establish the possible sources of the granitoids. The tonalite and granodiorite as well as the outer

phase of the monzogranite units have REE patterns that are close to those of a melt from a basaltic source with a garnetiferous amphibolite residue containing between 10 and 25% modal garnet. The quartz monzonite and the inner phase of the monzogranite display chondrite-normalized patterns which are more enriched in REE abundances than the modelled curves. This implies that their sources were somehow different from the rest of the granitoids as the results cannot be linked to a mafic source alone. Further analyses of the possible sources of the Vumba granitoids is presented in Fig. 10.5, where modelled melting curves for a MORB source with various restite compositions are superimposed on the diagram of chondrite-normalized La/Yb versus Yb concentration. The granodiorite, tonalite and some monzogranite samples cluster between the modelled curves that correspond to 10 to 25% degree partial melting of a mafic source with a restite containing between 10 and 25% modal garnet. Samples of quartz monzonite and inner monzogranite correspond to none of the modelled melting curves and plot both outside the adakite and island arc fields.

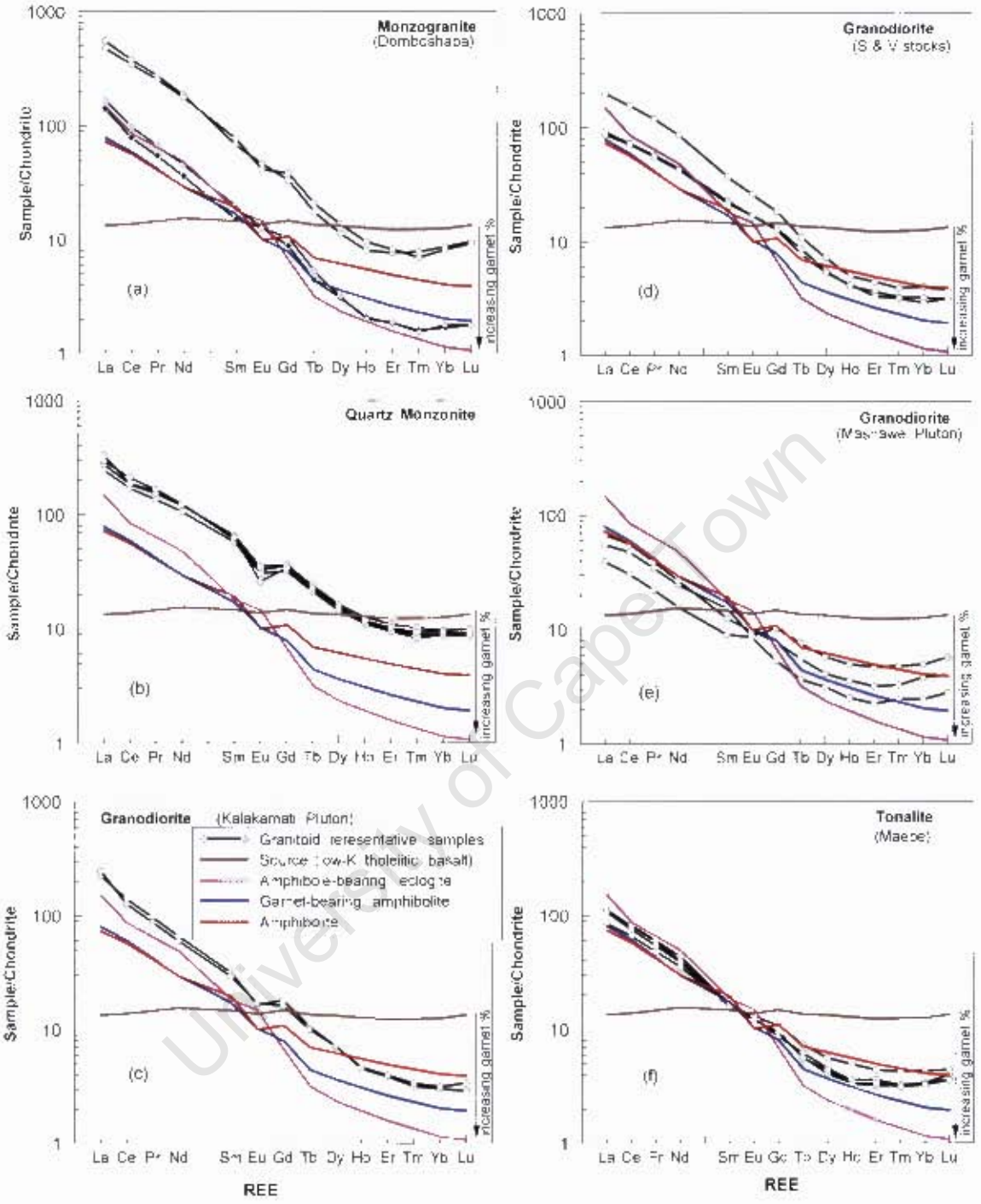

Fig. 10.4: Chondrite normalized (Sun and McDonough, 1989) REE patterns for the Vumba granitoids compared with fields defined by 10% batch melting of a low-K tholeiitic basalt source. The calculated patterns for batch melting are for potential mafic sources containing amphibolite, garnet-bearing (10 modal %) amphibolite, garnet-bearing (25 modal %) amphibolite and amphibole-bearing eclogite residues (modelled after Martin, 1987). PM=partial melting.

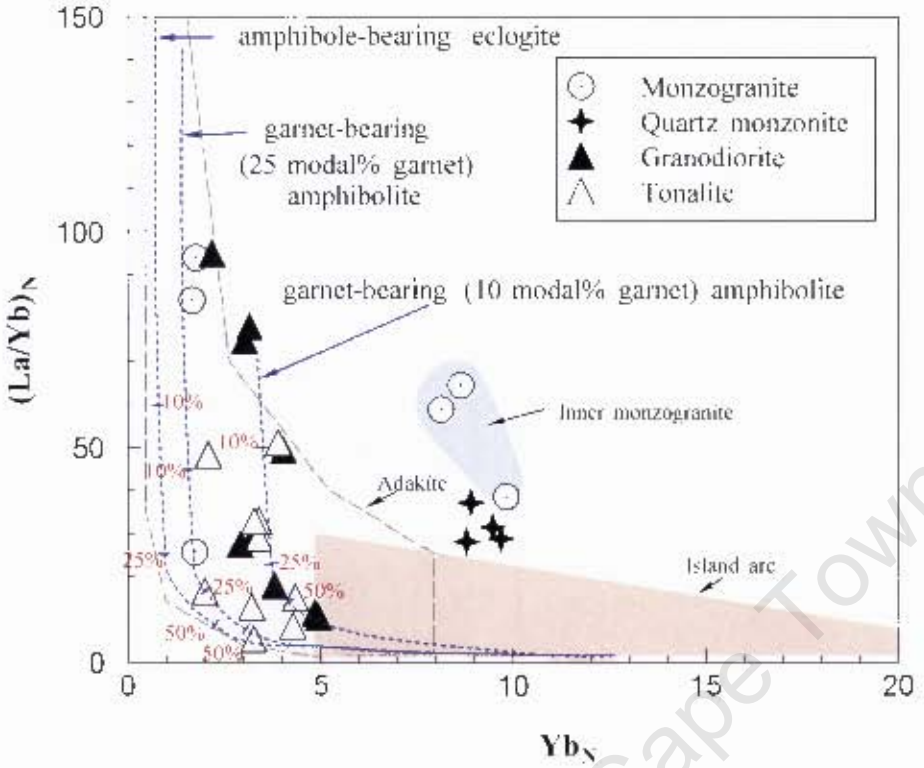

Fig. 10.5: Chondrite-normalized Yb_N versus $(La/Yb)_N$ diagram modified after Drummond and Defant (1990) showing granitoid data from the Vumba granite-greenstone terrain, and superimposed melting curves. Three partial melting curves are displayed and assume a MORB source with Yb_N = 12.5 and $(La/Yb)_N$ = 1. The partial melting curves represent 10% garnet amphibolite, 25% garnet amphibolite and eclogite restites. Percent partial melt values (in red) are indicated on each of the curves.

10.2.3 Implications of isotopic data on the nature of source regions

In Fig. 10.6 the initial εNd values for the various granitoids from the Tati area are plotted against their crystallization ages. Time-age corrected εNd values for the plutons from the monzogranite, NE tonalite-trondhjemite and SW tonalite-trondhjemite units from a previous study (Zhai et al., 2006) are also included in Fig. 10.6, and the data are comparable with the current data obtained from this study. The majority of the data for the tonalite-trondhjemite plot between the CHUR and depleted mantle (DM) model curve of DePaolo (1981) suggesting that they are either juvenile granitoids (at that time) that interacted with minor old crustal material or they are derivatives of young juvenile crust. Modelling of compositional sources for all the granitoids in the Tati granite-greenstone terrain suggests basic crustal sources partial melted under different pressure and temperature conditions. Thus the positive initial εNd values are consistent with derivatives of young juvenile crust. The tonalite-trondhjemite samples analysed for Pb isotopic recorded highly

radiogenic to moderately radiogenic compositions, (Table 10.1) in the range of 24.41 to 15.72 ($^{206}Pb/^{204}Pb$). This is consistent with a feldspar fractionation during the origin of tonalite-trondhjemite. The plot of 207Pb/204Pb versus 206Pb/204Pb both the volcanics and granitoids suggest similar sources for these rocks. Moreover, the O isotopic data acquired from the selected samples' quartz grains that yielded values that are characteristic for I-type granitoids (8.6 to 10.6 ‰).

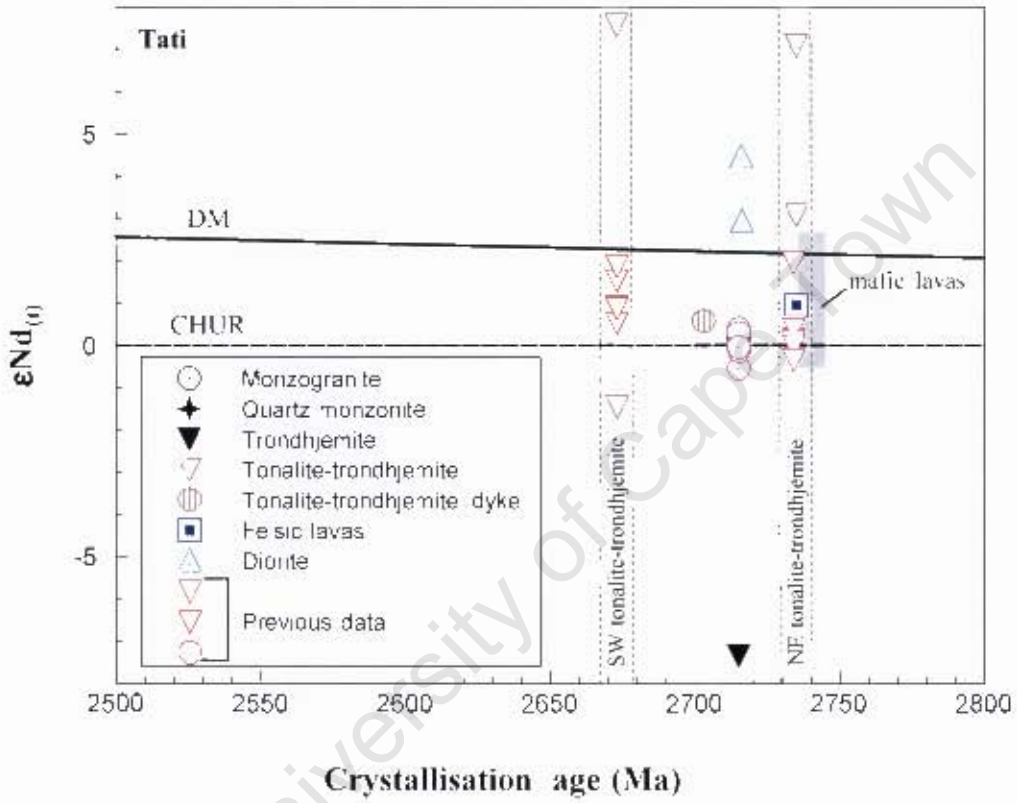

Fig. 10.6: Plot of initial epsilon values versus crystallization age for the granitoids from the Tati granite-greenstone terrain

One sample of the trondhjemite analysed for Sm/Nd isotopic composition recorded a very low Nd epsilon value of -7.25, which suggests an enriched source like an old crust. The same sample yielded anomalously high Pb isotopic composition ($^{206}Pb/^{204}Pb$ ratio of 80.48), which could be explained by open-system geochemical processes that either allowed Pb to escape or was related to the addition of U into the system (e.g. altered basalt of oceanic crust; de Wit et al., 1987). Moreover, the O isotopic data measured from quartz grains recorded a value of 10.1‰, which corroborates the results of Nd and Pb isotopic composition. A hydrothermally altered basaltic

source is compatible with the above-discussed observations. The isotope data support the trace element data discussed above in relation to the source.

The initial εNd values for the Vumba granitoids are plotted against the crystallization ages in Fig. 10.7. All the analysed samples show positive initial εNd values, except one sample from the tonalite unit, suggesting either juvenile origin or source. The tonalite sample that recorded a negative initial εNd value of -1.20 possibly demonstrates that some older crustal component was involved in their petrogenesis. It has a T_{DM} of 2927 Ma, while the other samples from the tonalite unit that have recorded positive initial εNd values exhibit 2800 Ma as the T_{DM}. The same sample yielded a quartz $\sigma^{18}O$ value of 12.1‰, which is a typical range for granitoids of sedimentary origin (e.g. Rollinson, 1993). The tonalite unit also exhibits highly radiogenic Pb isotopic composition, which is further evidence of crustal involvement in its origin.

Four samples of the granodiorite unit recorded positive initial εNd values ranging from 0.33 to 1.95. This suggests that the granodiorite unit was generated from a source that had short crustal residence time. The Nd model ages (according to DePaolo, 1981) calculated from the initial εNd values vary from 2720 to 2827 Ma, which is ~40-150 Ma older than the crystallization age of 2686 ± 6 Ma. The quartz monzonite unit in the Vumba area forms a single body intruded into the mafic lavas. One sample analysed for Sm/Nd isotopic composition yielded a positive initial εNd value of 2.91, which is comparable with that of the contemporaneous depleted mantle within margins of error. This suggests that the quartz monzonite is relatively juvenile. In addition the quartz monzonite is metaluminous with high compatible trace element concentration, low SiO_2 abundance, low Pb isotopic composition, relatively high Mg# and high contents of REE, all of which suggest involvement of the mantle components in the petrogenesis of the quartz monzonite. However, the O isotopic composition (quartz $\sigma^{18}O$ = +10.0‰) suggests a supracrustal input in the petrogenesis of the quartz monzonite. The seemingly paradoxical evidences can be explained by partial melting of a slab at depth within the asthenosphere to generate the quartz monzonitic melt. The monzogranite unit in the Vumba is composed of two phases; the inner granite and the outer granite phases, which show distinct Sm/Nd isotopic composition. The inner phase resembles the quartz monzonite and it has a positive initial εNd value corresponding to a depleted mantle source. Such mantle source origin for the quartz monzonite and the inner phase monzogranite is

supported by other geochemical attributes as its high compatible element content and high Mg#. Additionally, modelling of REE data reveals that their petrogenesis cannot be explained by melting a basic crustal source alone. The inner granite phase has a positive initial εNd value of 2.52, which is equivalent to the initial εNd value of a depleted mantle at 2650 Ma (the age of the monzogranite) demonstrating that it is relatively juvenile. The inner granite phase and the quartz monzonite falls in the island arc rock in the space of Sr/Y versus Y diagram, consistent with a mantle origin. On the other hand the outer granite phase records a low positive initial εNd value of 0.73 suggesting that it originated from a juvenile crustal source which had short residence time.

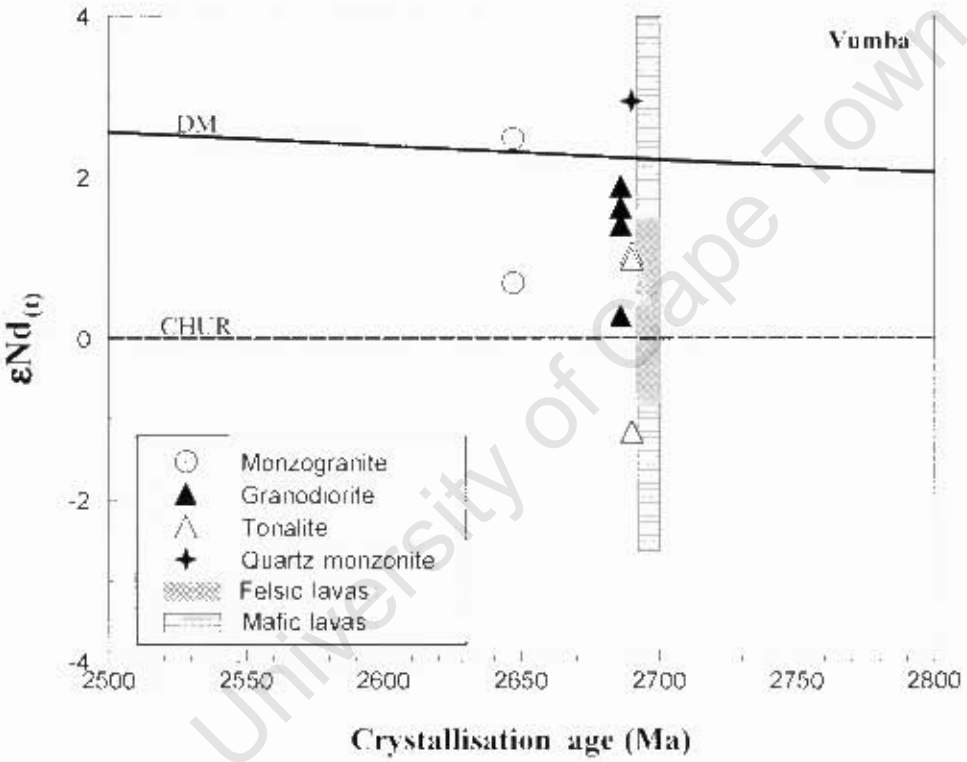

Fig. 10.7: Plot of epsilon values versus crystallization ages for plutonic and volcanic rocks from the Vumba granite-greenstone terrain.

10.2.4 Age of the granitoids sources

In order to evaluate the crustal residence times of the granitoid sources, Nd isotopic data together with the crystallization ages were used to calculate model ages following DePaolo (1981). The monzogranite in the Tati granite-greenstone terrain display clustering of T_{MD} between 2810 and

2920 Ma (Fig. 10.8a). The crystallization age of the monzogranite is ca. ~2715 Ma, thus they were derived from a source which had a crustal prehistory of ~100-200 Ma. Tonalite-trondhjemite units, which have different emplacement ages, exhibit a decreasing cluster of T_{MD} ages that seem to correspond to the crystallization ages (Fig. 10.8b). The SW tonalite-trondhjemite plutons, which were emplaced at ca. 2670 Ma, reveals T_{MD} ages between 2700 and 2820 Ma whilst the tonalite-trondhjemite dyke has a T_{MD} age of 2840 Ma (emplaced at 2703 Ma). The NE tonalite-trondhjemite plutons, which have crystallization age of ca. 2732 Ma, display older T_{MD} ages between 2860 and 2900 Ma. Petrogenetic analyses of the tonalite-trondhjemite units discussed in the above section suggest that they formed by anatexis of mafic source with residual garnet. The primitive mantle-normalized trace element patterns are characterized by negative Nb-Ta and Ti anomalies suggesting a subduction related signature or melting of crustal rocks that were formed along subduction zones. The T_{MD} ages of the NE tonalite-trondhjemite are consistent with the inherited zircon U-Pb date of 2911 Ma recorded from the Matsiloje pluton which is one of the NE tonalite-trondhjemite plutons.

Nd isotope evolution lines of tonalite, granodiorite and monzogranite from the Vumba granite-greenstone terrain overlap, and there is a clustering of T_{MD} between 2715 and 2910 Ma (Fig. 10.9). These ages cannot be distinguished from those displayed by the granitoids of the Tati granite-greenstone terrain. Collectively, the T_{MD} from the Tati and Vumba granite-greenstone terrains coincide with the formation age of the Belingwean Supergroup igneous rocks dated between 2.95 and 2.88Ga (Dirks and Jelsma, 2002). This implies that the Francistown Granite-Greenstone Complex is a relative juvenile Neoarchaean block that formed without major contribution from significantly older crustal material such as the 3.56 Ga gneisses from the Sebakwe proto-craton.

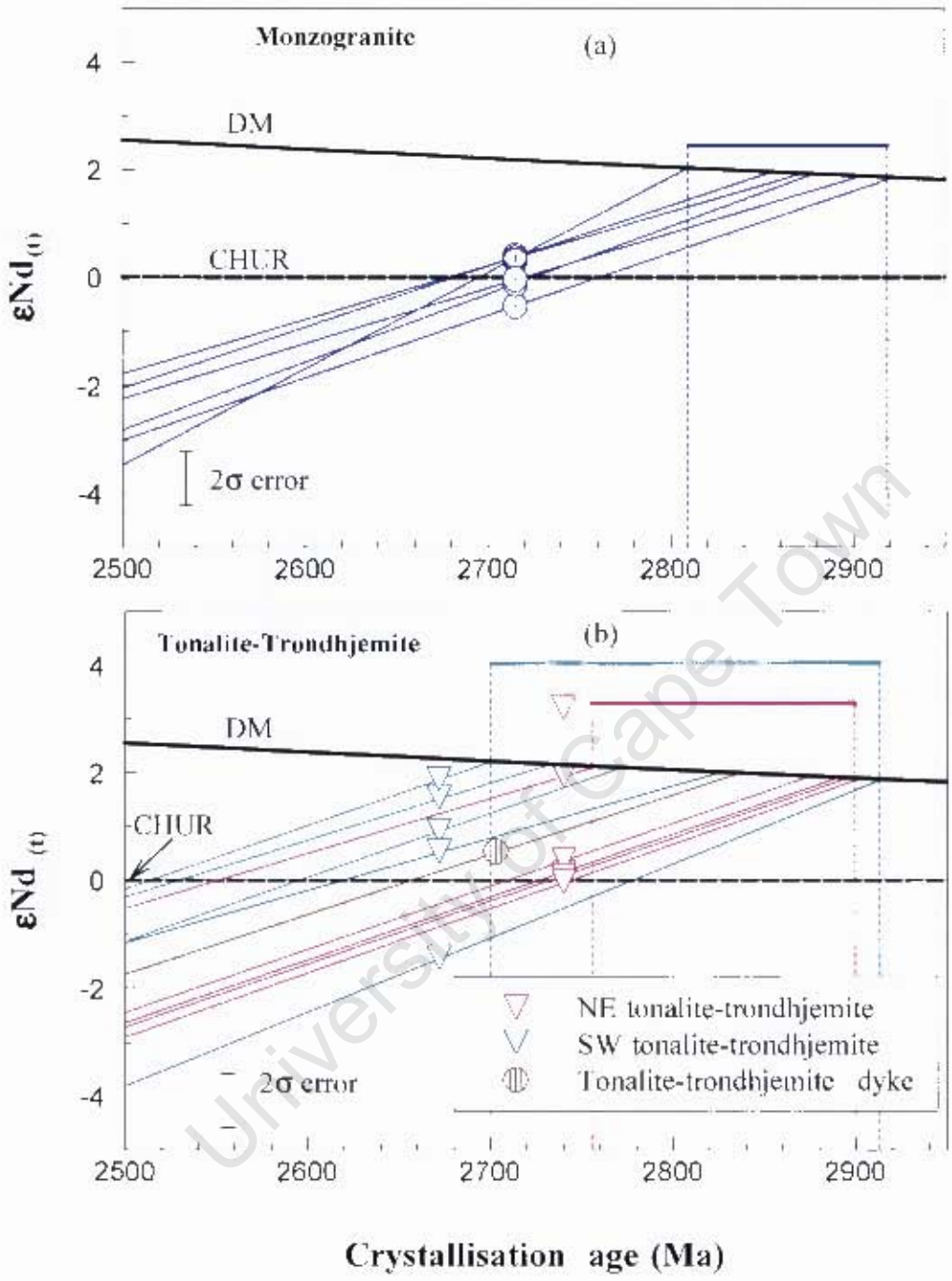

Fig. 10.8: Initial εNd versus crystalization age diagram for (a) monzogranite and (b) tonalite-trondhjemite samples from the Tati granite-greenstone terrain. DM and CHUR denote depleted mantle (after DePaolo, 1981) and chondritic uniform reservoir (after DePaolo and Wassenburg, 1976), respectively. Sloping lines are growth curves for each rock projected from measured values. They are single stage growth models for Sm/Nd ratio in each rock.

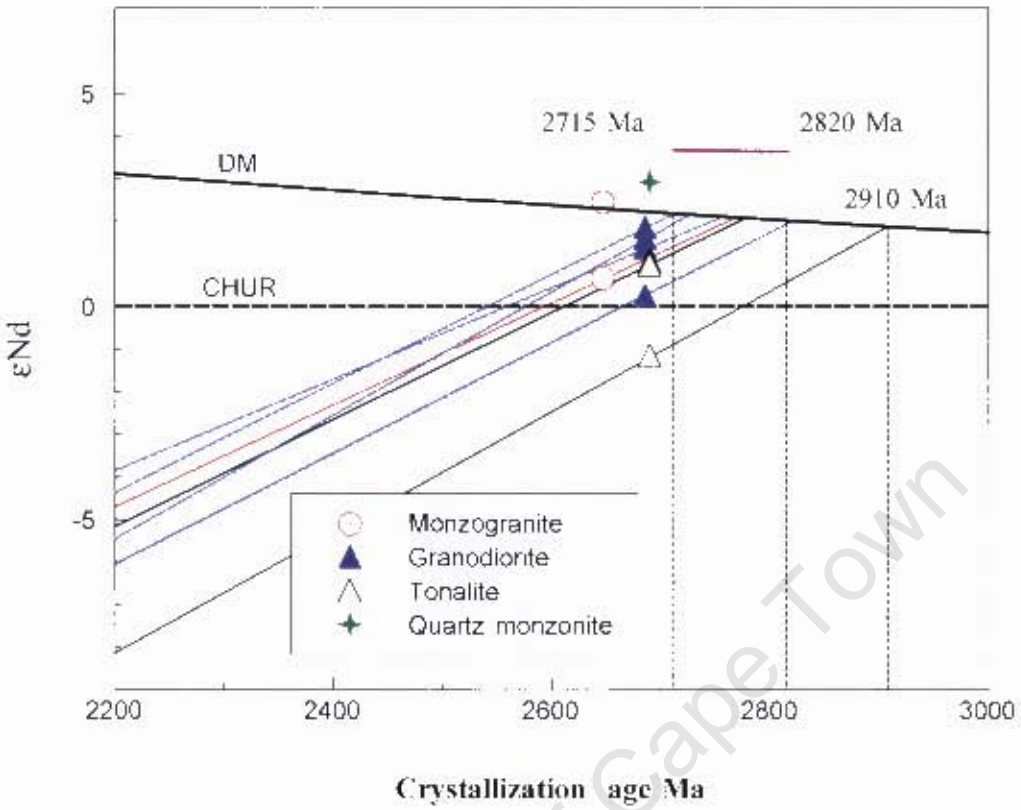

Fig. 10.9: Initial εNd versus crystallization age diagram for granitoids samples from the Vumba granite-greenstone terrain. DM and CHUR denote depleted mantle (after DePaolo, 1981) and chondritic uniform reservoir (after DePaolo and Wasserburg, 1976), respectively. Sloping lines are growth curves for each rock projected from measured values. They are single stage growth models for Sm/Nd ratio in each rock.

CHAPTER 11

Petrogenesis of the Diorite

11.0 Introduction

This chapter aims at discussing the main geochemical characteristics and petrogenesis of the diorite unit within the Francistown Granite-Greenstone Complex.

11.1 Main geochemical characteristics

The diorite in the Tati granite greenstone terrain was first described by Kampunzu et al. (2003) as an Archaean sanukitoid. The term Archaean sanukitoid was first introduced by Shirey and Hanson (1984) for Archaean andesites and diorites exposed in the Rainy River area within the Western Superior Province. These rocks possess geochemical characteristics similar to high-Mg andesites termed sanukites in the Setouchi area of Japan (Tatsumi and Ishizaka, 1982). According to Halla (2005) the term sanukitoid originally referred to all textural modifications of the sanukite magma type. However, there is considerable elasticity in the application of the term 'sanukitoid' in the literature. Currently, the name is applied to a broad range of rocks with diverse compositions and origins. For instance Stern et al. (1989) defined sanukitoids as primitive, intermediate igneous (intrusive and extrusive) rocks characterized with SiO_2 in the range of 55 to 60 wt.%, Mg# greater than 0.6, Ni and Cr contents exceeding 100 and 200 ppm, respectively, Ba and Sr concentration above 500 ppm each, K_2O content exceeding 1 wt.%, Rb/Sr ratios below 0.1, and strongly LREE enriched REE patterns with minor Eu anomalies. Many authors have applied the term Archaean sanukitoids to refer to suites of granitoids ranging from high-Mg diorite through granodiorite to granite (e.g. Stevenson et al., 1999; Halla, 2005). Others have used the term sanukitoid suite to collectively refer to diorites and gabbros (e.g. Da Silva Filho et al., 1993; Kampunzu et al., 2003). Recently, Halla (2005) adopted the term sanukitoid to describe charno-enderbites, which are high grade granitoids bearing orthopyroxene, in Finland. According to the International Union of Geological Sciences (IUGS) classification and glossary of terms of Le Maitre et al. (2002), sanukitoid is an Archaean high-Mg quartz monzodiorite and granodiorite or a plutonic equivalent of

sanukite. Therefore, there is a need to clarify the meaning of the term sanukitoid as used in the text. In this study the term is applied strictly to refer to calc-alkaline high-Mg diorite.

The Sanukitoids as loosely defined, have been recognized in many Archaean provinces (e.g. Shirey and Hanson, 1984; Stern and Hanson, 1991; Beakhouse et al, 1999; Stevenson et al., 1999; Smithies and Champion, 2000; Sarvothaman, 2001; Halla, 2002; Kampunzu et al., 2003; Moyen et al., 2003; Steenfelt et al., 2005) and occur in Archaean granite-greenstone terranes that were formed ca. 2.7 Ga, although the oldest known is ca. 2.95 Ga (Smithies and Champion, 2000). Lack of sanukitoids in the early Archaean leads some geoscientists to suggest that modern styles of tectonics started during the Neoarchaean, since the origin of sanukitoids is compared to those of adakites, which in turn are modern subduction-related lavas.

In the Tati granite-greenstone terrain the sanukitoid diorite occur as a single intrusion within the greenstone succession. A summary of the main geochemical characteristics of the sanukitoid diorite in the study area are presented in Table 11.1 where they are compared with the definition of sanukitoids as defined by Stern et al. (1989). As stated in the trace element geochemistry chapter (6), the sanukitoid diorite samples define two subgroups with distinct geochemical features. On the basis of low SiO_2 content of the sanukitoid diorite it is suggested here that the metasomatic component involved in its genesis was aqueous fluids and not a slab-melt. The metasomatism effect must have been volumetrically insignificant particularly for the source of subgroup 2 magma. Alternatively, the composition and the nature of metasomatising fluid was poor in alkalis and other incompatible elements. But the precise chemistry of slab melts and fluids is still highly debated. The involvement of a slab-melt in the genesis of the diorite is not favoured by many factors such as the low Sr/Y, La/Yb ratios and SiO_2 contents of the sanukitoid diorite samples. Experimental studies have shown that when sub-arc mantle is metasomatized by slab-fluids, the geochemical signature of the fluid is transferred to the future mantle source of the sanukitoid diorite (e.g. Rapp et al., 1999). Additionally, the Mg#s for the sanukitoid diorite are too high to be derived from a source with a significant contribution from a basaltic crustal source. The sanukitoid diorite in this study shows no resemblance of the slab-melt in terms of incompatible trace element ratios (Table 11.1), which negates any significant involvement of a slab-melt in metasomatising its source.

Table 11.1: Summary of geochemical characteristics of the sanukitoid diorite within the Francistown Granite-Greenstone Complex which are described as Archaean sanukitoids.

Chemical parameter	Diorite		Sanukitoids (Stern et al., 1989)
	Subgroup 1	Subgroup 2	
SiO_2 wt.%	51.4 - 50.0	49.8 - 49.4	55 - 60
Mg#	0.73 - 0.69	0.78 - 0.74	> 0.60
K_2O wt.%	0.55 - 0.29	0.17 - 0.05	> 1
Cr ppm	137 - 61	232 - 45	> 200
Ni ppm	168 - 131	204 - 92	> 100
Sr ppm	206 - 158	203 - 167	> 500
Ba ppm	93 - 48	70 - 22	> 500
Rb/Sr	0.13 - 0.03	0.02 - 0.01	< 0.1
Sr/Y	30 - 18	96 - 44	~50
$(La/Yb)_N$	3.3 - 2.9	2.5 - 1.3	65 - 19
$\delta^{18}O$ ‰	7.1	8.3	-
εNd	2.92	4.46	-
$^{206}Pb/^{204}Pb$	17.82	14.98	-
$^{207}Pb/^{204}Pb$	15.69	15.23	-
$^{208}Pb/^{204}Pb$	37.80	34.61	-

The Nd, Pb and O isotope data from the sanukitoid diorite present paradoxical evidence about its genesis (Table 11.1). For instance Nd isotope composition reflects a mantle origin, whereas high value of Pb isotopes ($^{206}Pb/^{204}Pb$) suggests significant crustal involvement in the origin of the sanukitoid diorite, particularly subgroup 1. However, in subduction systems, the over-enrichment of Pb in magmas is attributed to preferential transfer of Pb to the mantle-wedge from fluids emanating during dehydration of subducted slab, and from sediments that were derived from the continent (e.g. Scambelluri et al., 2001). These continental-derived sediments are known to add a considerable amount of radiogenic Pb to the overlying mantle-wedge (e.g. Elliot et al., 1997), which is then homogenized by effective mixing processes in subduction zones (Halla, 2005). This probably explains the paradoxical evidences from the Nd and Pb isotope data. The role of subduction-related fluids in the genesis of the sanukitoid diorite is also supported by the O isotope data. This study found that pyroxenes in the diorite from the Tati granite-greenstone terrain have elevated $\delta^{18}O$ values ranging from +7.1 to +8.3 ‰ that suggests an input from a high $\delta^{18}O$ source such as fluids from subducting oceanic crust and/or subducted sediments. Very similar $\delta^{18}O$ values have been reported from sanukitoids in Western Superior Province by Whalen et al. (2004). In

contrast to the sanukitoid diorite in Francistown Granite-Greenstone Complex, the Western Superior Province sanukitoids possess εNd values that support the involvement of crustal material.

11.2 Petrogenesis

Generally, the origin of sanukitoids is attributed to partial melting of metasomatized mantle wedge above subduction zones (e.g. Stern and Hanson, 1991). However, some workers have argued that the diorite end members are adakites (e.g. slab-derived melts) that subsequently assimilated peridotite during ascent through the mantle wedge (e.g. Yogodzinski et al., 1995). Experimental investigations (e.g. Rapp et al., 1999; Prouteau et al., 2001) on the interaction of felsic lavas and mantle peridotite reveal that both models are plausible in generating the sanukitoids. The determining factor is the volume ratio of slab-melt to peridotitic rock, which Rapp et al. (1999) referred to as 'effective ratio'. Furthermore, these studies discovered that during the interaction of the slab-melt and mantle peridotite, the slab-melt does not only assimilate mantle peridotite, it is also consumed by metasomatic reactions. In the case of a high effective ratio, some of the melt remains from the metasomatic reactions and assimilation process that subsequently form the sanukitoids. In contrast, when the effective ratio is low, all the melt is consumed by metasomatic reactions leaving a mantle peridotite that is slab-melt metasomatized. Subsequent partial melting of such mantle peridotite will give rise to sanukitoids characterised by some geochemical features similar to those of a slab-derived magma/melt. The sanukitoid diorite under investigation is compositionally heterogeneous, and form two distinct subgroups as mentioned earlier. The two subgroups plot in two distinct positions on a variation diagram of Th/Yb versus Yb (Fig. 11.1), which has been applied to test whether the variation between samples is due to fractional crystallization or partial melting processes (e.g. Manikyamba et al., 2004). Varied degrees of partial melting will generate samples with a positive slope, whereas fractional crystallization process will produce samples with flat trend, as indicated in the Fig. 11.1. This is because Yb is less incompatible than Th during melting, and both Th and Yb are incompatible to the common fractionating phases in a basaltic magma. Additionally, Th/Yb ratio can reflect the extent to which a source has been previously melted (depleted). Since Yb is less incompatible than Th during melting, the melt acquires a higher Th/Yb ratio, and the residual source a lower Th/Yb ratio with each successive

melting event. It is likely, therefore, that the source to subgroup 1 sanukitoid diorite was less depleted than the source for the subgroup 2 sanukitoid diorite

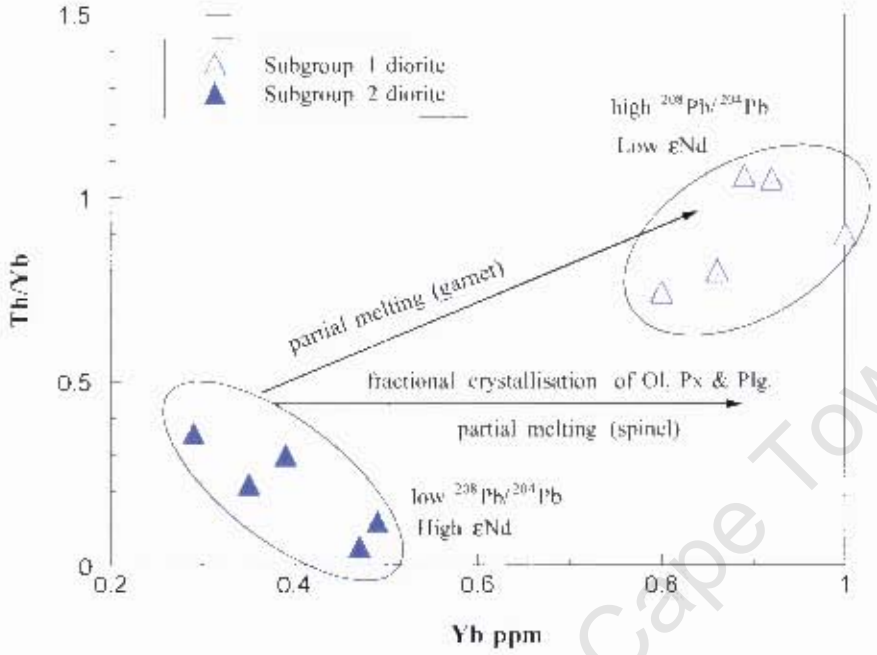

Fig. 11.1: P ot of Th/Yb versus Yb ppm for the sanukitoid diorite subgroups

It can be seen in the Fig 11.1 that neither partial melting nor fractional crystallization processes can explain the distinct subgroups of the diorite alone. The subgroup 2 samples exhibit a negative trend consistent with crustal contamination. However, Nd and Pb isotope data do not support a crustal contamination process in the petrogenesis of the subgroup 2 diorite, as evidenced by high positive Nd epsilon value of 4.46 and low initial Pb ratios (see Table 11.1). On the other hand O isotope composition of the subgroup 2 diorite suggests a non-mantle composition (8.3 ‰). This paradoxical evidence is interpreted as an indication of fluid metasomatism of the mantle that subsequently partially melted to produce the subgroup 2 diorite. In contrast, the subgroup 1 has relatively high SiO_2 content, low Mg#, high initial Pb isotope, low positive Nd epsilon value and high LREE abundances. All these observations suggest different source compositions for the two subgroups of the sanukitoids diorite.

Residual mineralogies and degrees of partial melting in the subarc mantle where the sanukitoids diorite was generated can be characterised using REE abundances and ratios. Incompatible Sm

abundance in sanukitoid diorite should constrain bulk source composition, because its concentration would not be controlled differently by spinel- and garnet-bearing source mineralogies (Green, 2006; Aldanmaz et al., 2000). Similarly, Sm/Yb ratios of sanukitoid diorite should be sensitive to source mineralogies because Yb is more compatible with garnet than spinel or clinopyroxene.

Partial melting of spinel-lherzolite produces magmas with Sm/Yb ratios similar to the source and Sm contents that decrease as melting increases (Aldanmaz et al., 2000). In contrast, magmas generated from small to moderate degrees of garnet lherzolite melting with residual garnet would have Sm/Yb ratios significantly higher than values in the mantle sources. It can be seen in Sm/Yb versus Sm plot (Fig. 11.2) that the composition of the subgroup 1 diorite can neither be explained by variable degrees of partial melting of a spinel- nor garnet-lherzolite sources. All the samples of subgroup 1 diorite are characterized by Sm/Yb ratios that fall between the garnet- and spinel-lherzolite melting trajectories, implying the presence of a garnet + spinel mineral assemblage in their source region. The subgroup 2 diorite samples have relatively lower Sm/Yb ratios than their subgroup 1 counterparts. Their Sm/Yb values are comparable to those of the primitive mantle (e.g. Sun and McDonough, 1989).

Since the origin of sanukitoids is linked to partial melting of metasomatized mantle wedge above subduction zones, it is anticipated that the source should be an enriched mantle. It can be seen from Fig. 11.2 that the subgroup 1 diorite had a mantle source more enriched in MREE and HREE than the PM, whereas the subgroup 2 diorite mantle source was similar to the PM in terms of the MREE and HREE compositions.

In conclusion the sanukitoid diorite from the Tati greenstone belt was most likely derived from a heterogeneous spinel-garnet lherzolitic mantle that probably originated through different previous degrees of melting associated with the genesis of magmas now represented by greenstone mafic lavas. In addition, isotope data suggests differential metasomatism of the mantle sources by fluids prior to partial melting to generate the sanukitoid diorite.

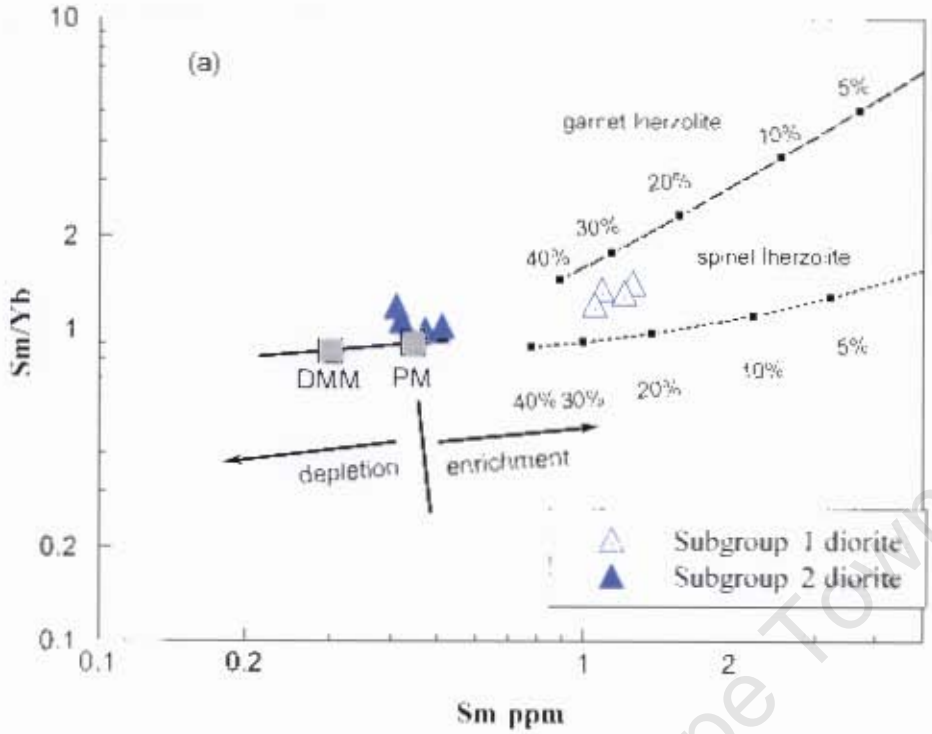

Fig. 11.2: Plot of sanukitoid diorite from the Tati greenstone belt on diagrams: (a) Sm/Yb versus Sm showing melting curves obtained using non-modal batch melting equation of Shaw (2006). Theoretical melting curves correspond to PM (primitive mantle) source. The same equation of Shaw (2006), partition coefficients, and starting and melt modes presented in section 9.1.2.3 of chapter 9 were adopted.

CHAPTER 12

Synthesis and conclusion for the evolution of the Francistown Granite-Greenstone Complex (FGGC)

Throughout this thesis various pieces of information regarding the age, source, petrogenesis and tectonomagmatic environments for the greenstone belts and associated granitoids in the Francistown Granite-Greenstone Complex (FGGC) have been presented. The aim of this chapter is to integrate all the available evidence from the various rock units investigated in an attempt to construct a robust geodynamic model for the formation of Francistown Granite-Greenstone Complex.

The two granite-greenstone terrains that constitute the FGGC are first treated independently to construct a geodynamic model for each terrain since it has emerged from this study that they have independent magmatic histories. Each model attempts to explore the temporal and possible genetic relationships between various rock types in each granite-greenstone terrain. Additionally, the working models should be compatible with petrogenetic models for the various rock assemblages in each terrain. Lastly, an integrated model to explain the relationship between the two granite-greenstone terrains is proposed.

12.1 Temporal and genetic relationships in granite-greenstone terrains

The felsic lavas in the greenstone belts of the Francistown Granite-Greenstone Complex occur in close spatial association with tholeiitic to calc-alkaline basalts. This is a common observation in many Archaean greenstone belts (e.g. Sandeman et al., 2006, 2004; Wang et al., 2005; Manya, 2004; Jelsma and Dirks, 2002; Polat and Kerrich, 2001; Hollings and Kerrich, 2000; Dostal and Muller, 1997; de Wit et al., 1987). Several models have been proposed to account for this close spatial association of the felsic and mafic lavas in different Archaean greenstone belts (e.g. Sylvester et al., 1997). One of the models considers the close spatial association of the felsic and mafic lavas as an indication that the two were derived from a single parental magma and are genetically related to each other by crystal fractionation processes. This model implies a common

source for the mafic and felsic lavas. The second model that has been proposed to explain the close spatial association of felsic and mafic lavas in Archaean greenstone belts perceives them as an outcome of two separate parental magmas derived from the mantle and crust, respectively, which shared the same magmatic plumbing system. The implication of this model is that the two lavas are not necessarily cogenetic. A third model invokes facies transitions between two concurrently erupting volcanoes from different sources, one mafic and the other felsic, separated by some unspecified distance leading to overlapping flows. In all these models the implication is that the felsic and mafic lavas in spatial association are contemporaneous. Fourth model embraces tectonic imbrication of felsic lavas from a distal setting tectonically thrust over unrelated mafic lavas (e.g. Jelsma and Dirks, 2000). In this model the volcanic lavas are not necessarily contemporaneous.

All the rocks in the Francistown Granite-Greenstone Complex have subduction tectonic setting in common. But the geodynamic details of this setting are what give rise to different and independently generated magmas.

12.1.1 Tati granite-greenstone terrain

Mafic and felsic lavas

In the Tati greenstone belt volcanic rocks consist of a bimodal suite of predominantly basalt and andesite together with volumetrically minor intercalated dacite. The possibility that the felsic magma was produced by fractional crystallization of basaltic magmas is not supported by Nd and Pb isotope data as well as trace element data. Moreover, geochronological data shows that there is a temporal relationship between the felsic and mafic lavas. The lavas were erupted ca. 2740 million years ago. Since the mafic lavas were derived from a mantle source that has been variable metasomatized by subducting slab dehydration fluids resulting in three types of basalts, which are intercalated by felsic lavas that were generated from subducting slab, it implies a convergent margin setting. Therefore, the temporal association of BABB-type, IAB-type, CAB-type and adakites found in the Tati greenstone belt can be accounted for by a supra-subduction back arc basin extension near a passive continental margin environment.

Plots of HFSE ratios of both mafic and felsic lavas reveal diverging trends that negate suggestions of a genetic relationship (Fig. 12.1). Incompatible trace element data reveal that the mafic lavas in

the Tati greenstone belt are comprises three subgroups that exhibit back arc basin basalt (BABB), island arc basalt (IAB) and continental arc basalt (CAB) geochemical characteristics. In contrast, the felsic lavas are most closely similar to Cenozoic adakites, suggesting that they are Archaean adakites (cf. Hollings and Kerrich, 2000). Additionally, petrogenetic interpretations suggest that the felsic lavas were derived from a mafic source within the garnet stability field, whereas the mafic lavas were generated from spinel lherzolite mantle with variable inputs of subduction component at depth outside the stability field of garnet. This suggests that the mafic and felsic lavas are tectonically arc related, but generated from different magma sources.

Mafic lavas and Gabbros

Though there is no absolute age information on the gabbroic intrusions in the Tati greenstone belt, field evidence suggests that they may be contemporaneous with the mafic lavas. In addition, plots of HFSE ratios for both the mafic lavas and gabbros exhibit a linear trend that passes through the origin (Fig. 12.1), which is suggestive of a common source through fractional crystallization. Such relationships are common for example Phanerozoic ophiolites and modern oceanic crust. This is compatible with the petrogenetic interpretation of the mafic lavas and gabbros, which also therefore suggests a direct genetic relationship between the two rock units (Fig. 9.7). Furthermore, petrographic analyses and geochemical data of the Phoenix gabbro indicate that this gabbro comprises cumulates, consistent with a feeder relationship between the gabbro and the mafic lavas in the Tati greenstone belt. The Selkirk gabbro displays two subgroups that resemble the Phoenix gabbro and the mafic lavas in terms of trace element compositional characteristics, respectively. Thin section examination of the Selkirk gabbro has revealed that it has two essential textures, granular and microgranular. The granular phase displays a cumulus texture and resembles the Phoenix gabbro to a large extent, while the microgranular phase exhibits a dolerite-like texture. Moreover, the microgranular gabbro exhibits incompatible trace element ratios that are indistinguishable from those of the mafic lavas (See chapter 6). In addition the Nd and Pb isotope data for the mafic lavas and the Selkirk gabbro are comparable. These suggest that the gabbro is hypabyssal, intruded at shallow level, consistent with the interpretation that it represents a transient chamber for magma of the greenstone mafic lavas implying a genetic relationship between the mafic lavas and the mafic intrusions.

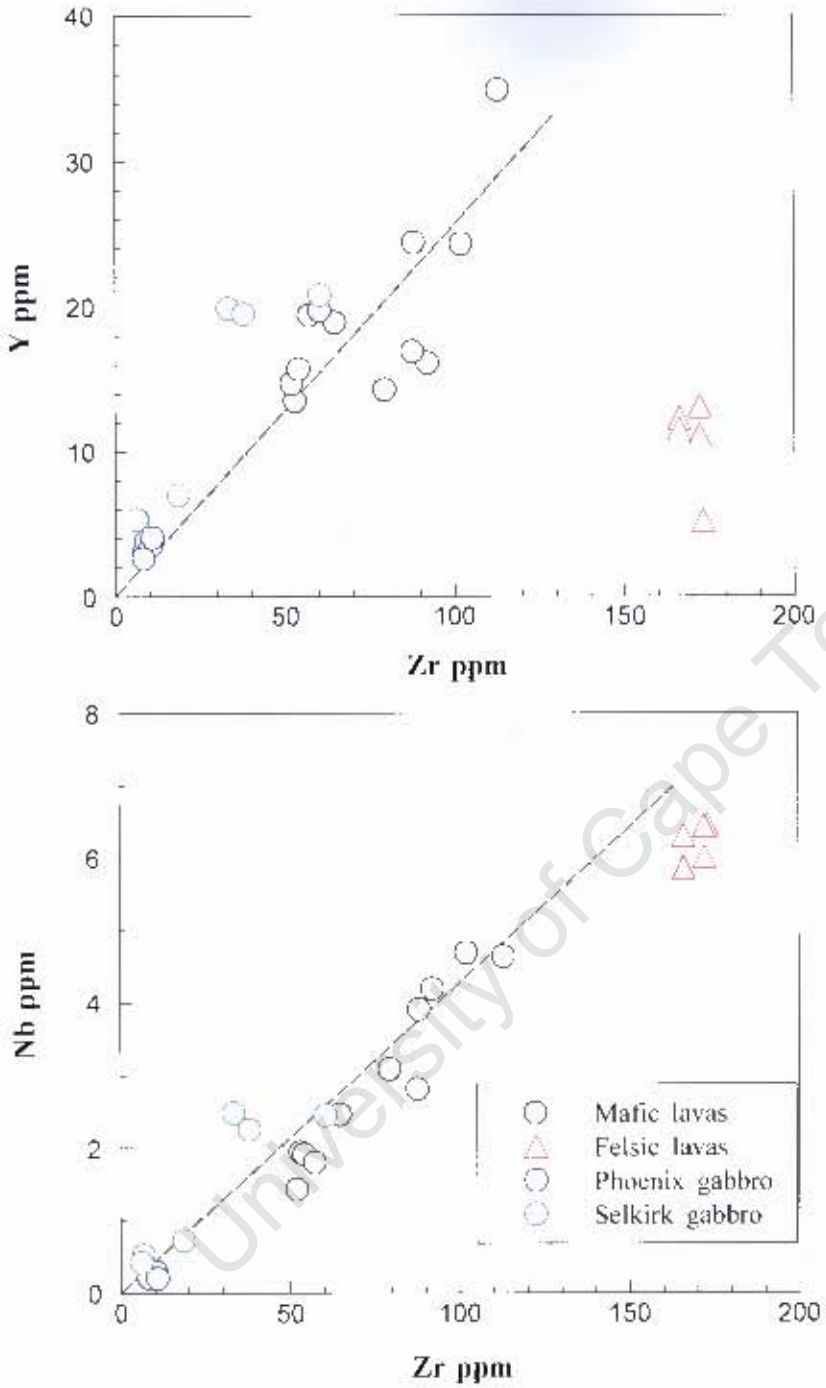

Fig. 12.1: Plot of HFSE for the mafic rocks and felsic lavas from the Tati granite-greenstone terrain, suggesting a cogenetic relationship between the mafic lavas and the gabbros through fractional crystallization. Such a simple relationship is not evident with the felsic volcanics

Felsic lavas and tonalite-trondhjemite

Felsic lavas in many greenstone belts are spatially associated with tonalite-trondhjemite granitoids that are contemporaneous and compositionally similar. Such granitoids have been interpreted as

plutonic equivalents of the felsic lavas representing "frozen" magma chambers from which the felsic lavas erupted (e.g. de Wit et al., 1987; Feng and Kerrich, 1992; Wilson et al., 1995; Sylvester et al., 1997). Although the felsic lavas and the NE tonalite-trondhjemite granitoids in the Tati granite-greenstone terrain are contemporaneous, they display some subtle geochemical differences. For instance the felsic lavas possess higher abundances of both HFSE and compatible trace elements than the tonalite-trondhjemite plutons. Additionally, the petrogenetic interpretations suggest that the felsic lavas were generated at a relatively shallow depth compared to the NE tonalite-trondhjemites. Nevertheless, Nd isotopic data suggest that these magmas have a common source. Therefore, the subtle chemical differences are most likely a reflection of the difference in petrogenetic conditions. The fact that the felsic lavas possess high contents of compatible elements suggests that its parental magma assimilated mantle peridotite with a small melt/rock volume ratio (e.g. Rapp et al., 1999). This is consistent with the low volume of the felsic lavas in the Tati terrain. It is here suggested, on the basis of petrogenetic interpretations, that the dacitic lavas was produced by partial melting of the subducting slab at the corner flow as a result of the rising asthenosphere above the subducting plate. The contemporaneous tonalite-trondhjemite plutons were probably generated by partial melting of this subducting slab at greater depth since their petrogenetic model suggests it must have been in equilibrium with a residual assemblage of garnetiferous amphibolite containing about 25% modal garnet to eclogite. Furthermore, the felsic lavas and their contemporary tonalite-trondhjemite unit exhibit comparable positive εNd values and coinciding T_{DM} ages, suggestive of a common source. The tonalite-trondhjemite dykes and the SW tonalite-trondhjemite plutons are ~ 30 to 60 Ma younger than the felsic lavas, so a genetic relationship is unlikely.

Trondhjemite, Diorite and Monzogranite

A genetic link has been inferred between sanukitoids and monzogranite magmatism in the Superior Province (e.g. Whalen et al., 2004). However, the sanukitoid diorite and the monzogranite in the Tati granite-greenstone terrain do not exhibit such a genetic relationship. Petrogenetic models presented in chapters 10 and 11 suggest that the diorite had a mantle source of spinel lherzolitic composition that interacted with subduction-derived fluids, while the monzogranite was most probably derived from an altered basaltic crust at shallower depth. The trondhjemite and the

monzogranite strongly resemble each other in virtually all geochemical characteristics except in their K_2O content, prompting suggestion that the two share a common source.

Although the sanukitoid diorite and the monzogranite, as well as the trondhjemite, do not have any genetic relationship, the three units have a temporal relationship. Moyen et al. (2001) proposed that sanukitoids and high-K granite magmatism share a unique temporal relationship in all Archaean cratons with the latter occurring shortly after the former. The sanukitoid diorite in the Tati granite-greenstone terrain is contemporaneous with the monzogranite and the trondhjemite. Moreover, the three units are also spatially associated. All these observations suggest a common source of heat for the generation of the sanukitoid diorite, trondhjemite and monzogranite. The three units were emplaced subsequent to the NE tonalite-trondhjemite plutons that are considered products of subducting slab melting. It is envisaged therefore that the sanukitoid diorite, trondhjemite and monzogranite magmatism may have been triggered by the slab break-off that in turn caused hot asthenosphere to rise and provide heat to the metasomatised mantle and the overlying basaltic crust at shallow depth.

Tonalite-trondhjemite, Trondhjemite, Diorite and Monzogranite

On the basis of close temporal association between tonalite-trondhjemite and sanukitoids in the Archaean terranes, some previous workers have suggested a subduction setting for these rocks. A common chronological sequence observed in the Archaean terrains is the emplacement of sanukitoid magmas after that of the tonalitic-trondhjemitic plutons (e.g. Smithies and Champion, 2000; Moyen et al., 2003; Bibikova et al., 2005; Käpyaho et al., 2006). In the Tati granite-greenstone terrain, the NE tonalite-trondhjemite is ~25 Ma older than the sanukitoid diorite that in turn is coeval with the trondhjemite and monzogranite units. However, the SW tonalite-trondhjemite granitoids are ~45 Ma younger than the sanukitoid diorite, trondhjemite and monzogranite. This implies a separate origin or at least melting event for the SW tonalite-trondhjemite from that of the sanukitoid diorite, trondhjemite and monzogranite. Subduction settings for sanukitoids have been proposed in terrains where they partly overlap in age with TTGs. The sanukitoids are envisaged to have been generated within a mantle wedge that has been metasomatised by slab-melts that also produced the TTGs (Moyen et al., 2003; Martin et al., 2005). In cases where there is significant time gap between the TTGs and sanukitoids, different

tectonic environments have been proposed. For example in Karelia Craton, Finland, where a time gap of about 100 Ma exists between the tonalite suite and sanukitoids, a subduction setting is proposed for the tonalite suite and the sanukitoids are related to a subsequent collision event. There is a smaller age difference of only ~25 Ma between the sanukitoid diorite and the older tonalite-trondhjemites in the Tati granite-greenstone terrain. This suggests that the two magmatic events probably were generated in the same tectonic environment. Petrogenetic interpretations and tectonic implications for the tonalite-trondhjemites in this area suggest that they were generated from slab-melts in a subduction environment. Additionally, the old tonalite-trondhjemites are temporally related as an arc-back arc basalt-adakite association. This suggests subduction coupled with a back-arc basin extension environment. The SW tonalite-trondhjemites, which are ~45 Ma younger than the sanukitoid diorite, also exhibit subduction geochemical affinities. Therefore, the sanukitoid diorite cannot be explained by a subsequent collision event. Delamination of the lithospheric mantle followed by decompression melting is here proposed as a more likely explanation for the sanukitoid diorite magmatism.

The sanukitoid diorite in the Tati granite-greenstone terrain is coeval, but not-cogenetic with the trondhjemite and monzogranite units. Neoarchaean K-rich magmatism is commonly modelled through melting of pre-existing TTG crustal material (e.g. Sylvester, 1994). However, petrogenetic modelling in this study reveals that melting of pre-existing TTG crustal source is not a viable model for the origin of the monzogranite in the Tati granite-greenstone terrain. The sanukitoids and high-K granites occur nearly coevally in the Superior Province (Whalen et al., 2004b) and in Finland (Karelia Craton). In both these terranes the temporal relationships between the sanukitoids and high-K granites are explained by invoking a hot asthenospheric magma that triggered the generation of sanukitoids and melting of the crust produce the more potassic magmas (Stevenson et al., 1999; Whalen et al., 2004b; Kovalenko et al., 2005). I suggest that either break-off of the subducting slab or detachment of underplated slab was a likely mechanism for the initiation of the sanukitoid diorite magmatism in the Tati granite-greenstone terrain. The same heat source that caused the sanukitoid diorite magmatism was also responsible for generating the trondhjemite and monzogranite magmas from underplated (or shallow subducting) basaltic crust. Basalt melting experiments have demonstrated that trondhjemitic melts are only generated when free water is available (Proutea et al., 2001). Thus the trondhjemite unit in the Tati granite-greenstone terrain

was generated from low pressure basic crust (50 km depth). Isotopic evidence suggests a hydrothermally altered, hydrous MORB-like source for the trondhjemite. This in turn implies subduction of oceanic crust affected by mid-ocean-ridge hydrothermal process. The monzogranite and trondhjemite share many compositional attributes which can be explained by derivation from similar sources. The tonalite-trondhjemite dykes that were subsequently emplaced may signify thermal relaxation following back-arc basin extensional collapse.

Subduction-accretion processes continued after the back-arc basin extensional collapse resulting in crustal thickening beneath the arc that eventually experienced melting to produce the SW tonalite-trondhjemites at ~2670 Ma. The continuation of subduction-accretion processes led to the closing of the Sea of Umtali (cf. Kusky, 1998) at ~2630 Ma, which is marked by syn-collision granitic augen gneiss.

12.1.2 Vumba granite-greenstone terrain

Mafic and felsic lavas

The Vumba greenstone belt displays bimodal volcanism, a feature which is commonly associated with continental rift settings and many young island arcs. In continental rifting, the mafic and felsic lavas are cogenetic and are related to each other by simple fractional crystallization process (e.g. Takagi et al., 1999). However, the mafic and felsic lavas from the Vumba greenstone belt display incompatible trace element ratios which are inconsistent with a genetic relationship by simple fractional crystallization processes. Fig. 12.2 a&b the HFSE clearly shows two distinct evolution trends for the mafic and felsic lavas. Additionally, REE patterns for the felsic lavas are fractionated and depleted in HREE compared to REE composition of the mafic lavas. This argues against any simple genetic link between the two by fractional crystallization process. Petrogenetic modelling of the mafic lavas suggests derivation from a depleted mantle spinel lherzolite source, whereas the felsic lavas appear to be derived by partial melting of a hydrated basaltic source. Geochronology data and field relationships indicate that the two lavas were erupted at ~2700 Ma. Although there is no apparent genetic relationship between the mafic and felsic lavas, a temporal relationship is clear. In view of the petrogenetic interpretations, tectonic settings, geochronological and field

relationship data, a back-arc basin setting related to subduction environment is envisaged to explain the temporal relationship between the Vumba mafic and felsic lavas.

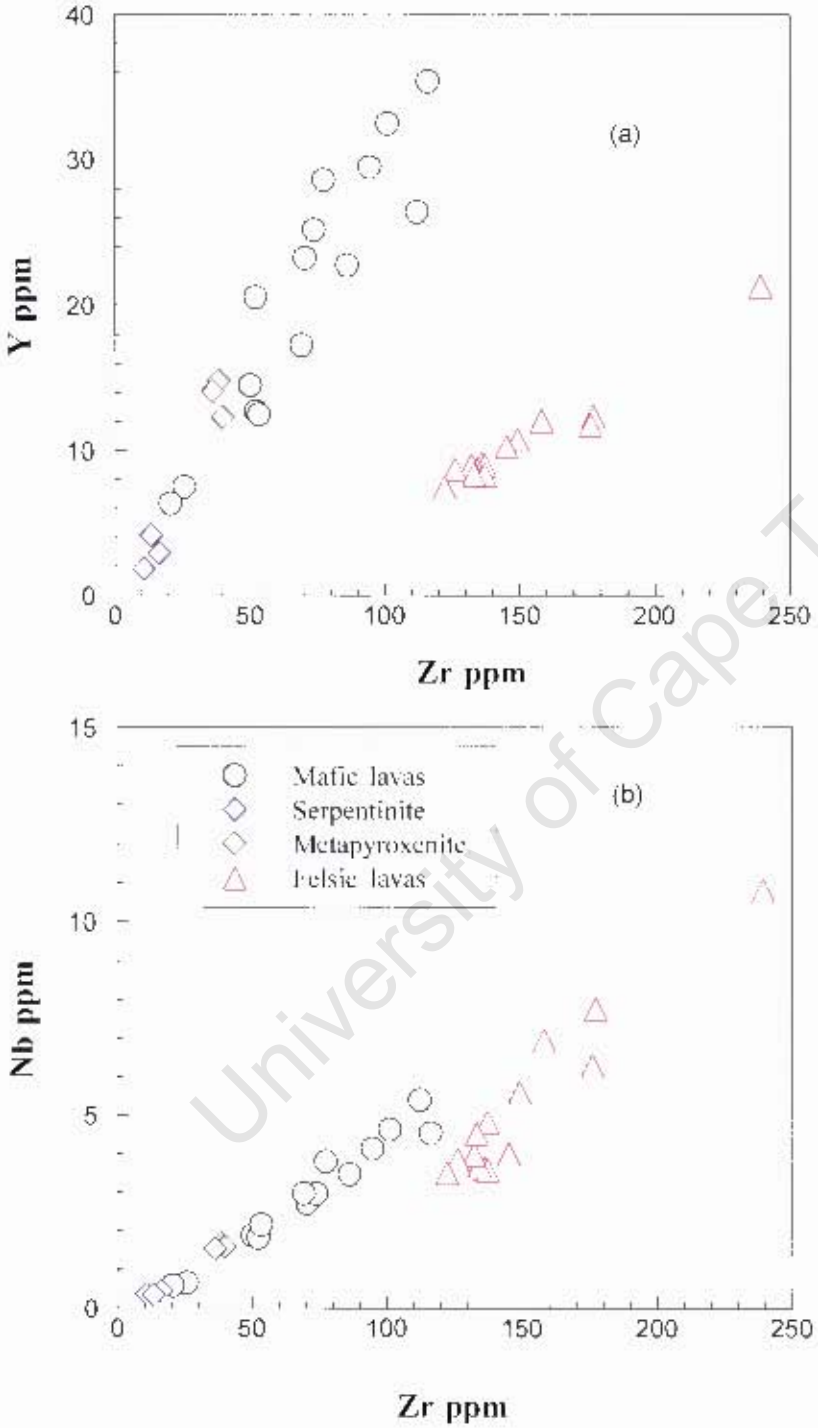

Fig. 12.2: Plot of HFSEs for the ultramafic -mafic rocks and felsic lavas from the Vumba granite-greenstone terrain. Note the cogenetic colinearity of the mafic to ultramafic rocks implicating a relationship through fractional crystallization distinct from that of the felsic lavas.

Mafic lavas and ultramafic intrusives

The ultramafic intrusives are considered cogenetic with the mafic lavas in most Archaean greenstone belts (e.g. Arndt et al., 1997). Geochronological data indicate that the ultramafic intrusives are at least older than 2696 ± 3 Ma as was constrained by a cross-cutting porphyritic quartz diorite dyke, whilst the age of the mafic lavas spatially associated with these ultramafic intrusives is at least 2696 ± 5 Ma, as was constrained by intercalated felsic lavas. On HFSE variation plots (Fig. 12.2) the mafic lavas and ultramafic intrusives exhibit a co-linear trend that goes through the origin suggesting that there is the likelihood of a feeder relationship between the ultramafic intrusives and the mafic lavas of the Vumba Mixed Volcanic Formation through fractional crystallization as is common in many ophiolites (Yildrid et al., 2005). This relationship is reminiscent of the Reliance komatiitic sill-flow complex in south central Zimbabwe Craton, which is made of sub-parallel dunite-peridotite and pyroxenite-gabbro units. This sill-flow complex is interpreted as subvolcanic phase of feeders of the komatiite and komatiitic basalts of the Reliance Formation in the Belingwe greenstone belt (e.g. Prendergast, 2004). The Reliance komatiites are associated also with the Zeederbergs basalts and they are considered to be derivatives of high- and low-degree partial melting, respectively (e.g. Bickle et al., 1993). In the Vumba greenstone belt the ultramafic intrusives comprise serpentinite and pyroxenite associated with gabbroic amphibolite. These units form sub-parallel rows of hills within the mafic lavas of the Vumba Mixed Volcanic Formation. The likelihood of a feeder relationship between the ultramafic intrusives and the mafic lavas from the Vumba Mixed Volcanic Formation is also supported by chemical coherency in calculated partial melting curves presented in chapter 9 (Fig. 9.6).

Felsic lavas and tonalite

Commonly, felsic lavas and tonalites in Archaean granite-greenstone terrain are treated as extrusive and intrusive equivalents. In the Vumba granite-greenstone terrain the felsic lavas (dacites) are slightly older in terms of absolute age, though the tonalite age is equivalent within the margin of error. Nonetheless, the two units show some geochemical variance which might indicate differences in their petrogenesis, although both the felsic lavas and the tonalite possess adakite affinities. Petrogenetic modelling suggests garnetiferous amphibolite as a potential source for both

the felsic lavas and the tonalite. This is supported by Nd isotopic compositions, which reveal comparable εNd values and T_{MD} ages (Fig. 12.3).

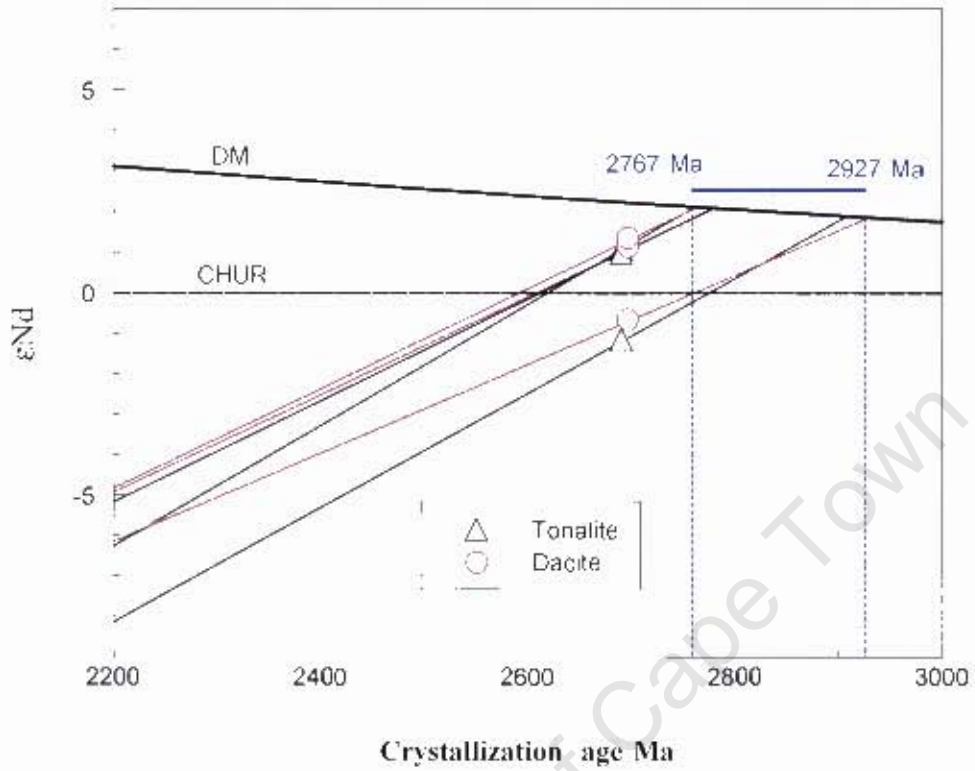

Fig. 12.3: εNd versus crystallization age diagram for tonalite and felsic lavas samples from the Vumba granite-greenstone terrain. DM and CHUR denote depleted mantle (after DePaolo, 1981) and chondritic uniform reservoir (after DePaolo and Wassenburg, 1976), respectively.

Tonalite, granodiorite, quartz monzonite and monzogranite

Although undated, the quartz monzonites, which intruded into the mafic lavas is suggested to be approximately contemporaneous with the 2690 Ma tonalite magmatism on the basis of field observations. The tonalite and granodiorite units are contemporaneous within margins of error. Notably the major element data for the Vumba granitoids displays coherent variation trends that suggest a petrogenetic relationship between the granitoids. Only the quartz-monzonite and the monzogranite samples from the inner phase deviate from these variation trends. Quantitative modelling of the Vumba granitoids suggests that tonalite and granodiorite parental melts were generated from the same source, but which was different from that of the contemporary quartz-monzonite. The young monzogranite possesses geochemical attributes that resemble those of the tonalite/granodiorite and quartz monzonite. This implies a heterogeneous source for the monzogranite, such as the pre-existing crust of quartz-monzonite-tonalite-granodiorite.

12.2 Geodynamic models

12.2.1 Tati granite-greenstone terrain

The development of the Tati granite-greenstone terrain was initiated ca. 2740 Ma along the convergent margin of the Zimbabwe craton and Limpopo Central Zone Block. It is envisaged that the Limpopo block was subducted beneath the margin of the Zimbabwe craton whose upper crust comprised mainly of the Belingwean and Lower Bulawayan Supergroups greenstones and associated granites at the time. The subducting slab released fluids which metasomatised the overlying mantle wedge. This induced volcanism of arc basalt and felsic lavas as well as the emplacement of the NE tonalite-trondhjemite plutons. The arc basalts were generated from the metasomatised mantle wedge, while the felsic lavas and the trondhjemite magmas formed from the subducting slab at different depths. Due to convection corner flow, possibly induced by slab retreat, a back-arc basin extension was initiated resulting in mafic volcanism of the back-arc basin basalt (BABB) type. Eventually the subducting slab broke off resulting in the rise of a hot asthenosphere that supplied a heat source to the depleted metasomatised mantle and the overlying mafic crust to generate high-Mg diorite and the trondhjemite/monzogranite rocks. Following this magmatic event the back-arc basin extension collapsed. Thermal relaxation associated with the collapse of the back-arc basin extension, triggered partial melting of the lower crust to generate the tonalite-trondhjemite dykes that intruded the Phoenix Gabbro. Accretion of the Limpopo Central Zone plate to Zimbabwe craton plate continued resulting in thickening of the crust below the arc. Eventually the over thickened crust partial melted to produce the tonalite-trondhjemite plutons that are confined to the SW of the greenstone belt. This event took place about 2670 Ma ago. The final collision of the Zimbabwe craton and the Kaapvaal craton occurred at 2630 Ma resulting in emplacement of syn-collision granitic augen gneiss within the collision zone. A summary of the geodynamic model for the formation of the Tati granite-greenstone terrain is presented in a schematic diagram below (Fig. 12.4).

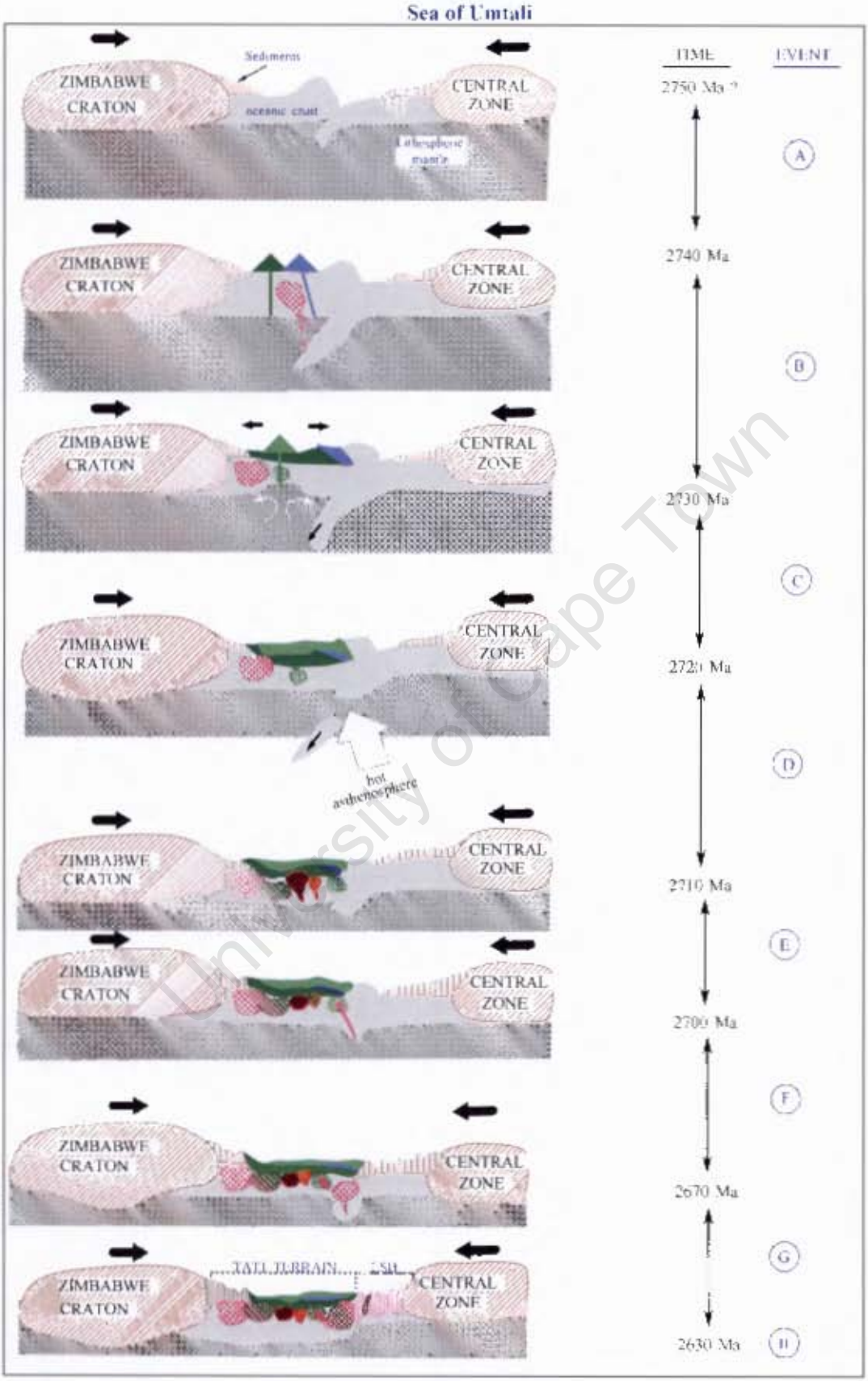

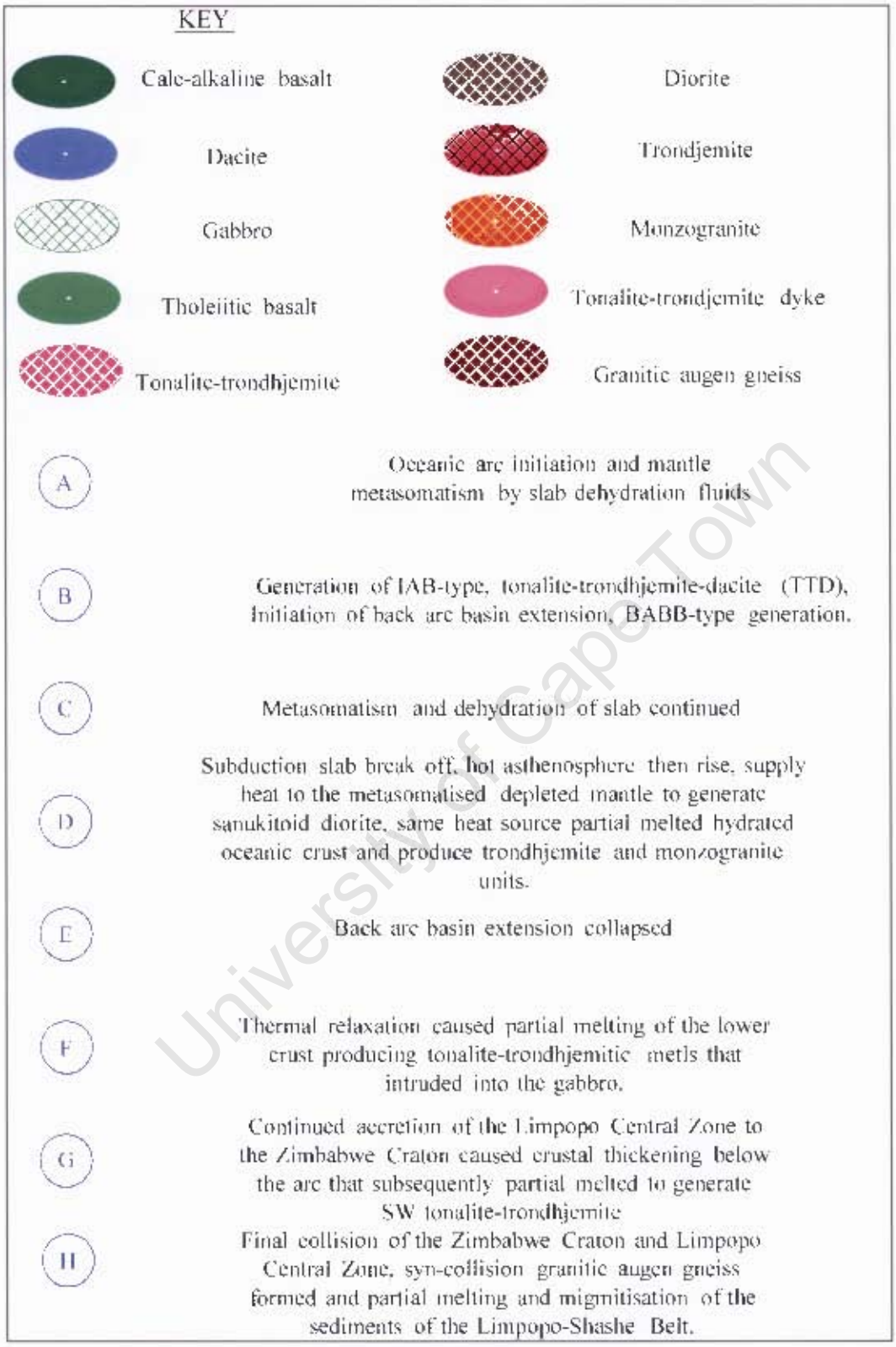

Fig. 12.4: A Schematic diagram illustrating the proposed geodynamic model of the evolution of the Tati granite-greenstone terrain.

12.2.2 Vumba granite-greenstone terrain

Mafic volcanic rocks in the Vumba greenstone belt display continental margin arc and back arc basin affinities similar to those of modern back-arc marginal basins such as the Sea of Japan in the western Pacific Ocean (Fig. 12.5). These volcanic rocks were formed at ~2700 Ma. Nd isotopic composition analysis performed on the two samples yielded positive and negative initial εNd values of +0.60 and -3.40. The sample that recorded a positive initial εNd value (ZBV-185) belongs to the tholeiitic basalt subgroup, which forms the top formation (Vumba Upper Mafic formation). By contrast, sample ZBV-13 exhibits a negative initial εNd value and is a calc-alkaline basalt that forms the basal mafic formation (Vumba Mixed Volcanic formation). The low positive initial εNd value of this tholeiitic basalt reflects minor endogenic contamination with old lower crust. Noteworthy, the tholeiitic basalt subgroup exhibits back-arc basin basalt (BABB) geochemical affinities. On the other hand the calc-alkaline subgroup's negative initial εNd value indicates significant exogenic contamination with old evolved crustal material. This is consistent with its continental arc affinity (See Fig. 12.5). The mafic lavas are intercalated with ca. 2696 Ma adakites, which were generated from a thickened volcanic arc root. Geochronological, geochemical and Nd isotopic data suggest that these adakites are extrusive equivalents of the Maebe tonalite that flanks the western margin of the Vumba greenstone belt. Both the adakites and the tonalite record mostly positive initial εNd values and few small negative values. The positive initial εNd values range between +0.94 and +1.33, which suggests the source was juvenile and it had short crustal residence. However, the negative initial εNd values of 0.69 and 1.20 suggest that some older component could have been present in their source. The two samples that record negative initial εNd values have Nd model ages (after DePaolo, 1981) between 2900 and 2927 Ma whereas the remainder of the samples exhibits an average T_{DM} of 2770 Ma. Moreover, sample ZBV-144 from the tonalite, which record a negative εNd value of 1.20, yielded a high quartz $\delta^{18}O$ isotope value of 12.1‰. This value is typical for S-type granitoids (Rollinson, 1993). Petrogenetic analyses suggest that the tonalite and adakites were generated from a basic crustal source similar to a subducting slab. Therefore, the sedimentary origin signatures can possibly be subduction sediments. The T_{DM} of ~2910 Ma is comparable with the 2911 Ma inherited zircon age recorded in the Matsiloje pluton in the Tati greenstone area.

The granodiorite plutons in the Vumba terrain are coeval within margins of error with the tonalite suggesting the same source of heat for their magma generation. Petrogenetic analyses indicate that the granodiorite was derived from a basic crustal source similar to a thickened underplated lower crust below the arc. The source is indistinguishable from that of the penecontemporaneous tonalite suggesting a common source. This is consistent with the coherent trends of major and trace element composition in variation diagrams. Quartz-monzonite is distinct from the granodiorite and tonalite in terms of geochemical attributes. It is most likely contemporaneous with the tonalite but with different source origin involving mantle component. In view of all the geochemical features of the quartz-monzonite, partial melting of a delaminated slab within the asthenospheric mantle is invoked for the generation of this quartz-monzonite magmatism. Monzogranite marks the last magmatic event in the Vumba granite-greenstone terrain. It is texturally and compositionally heterogeneous, and posses geochemical attributes comparable to those of the tonalite-granodiorite and the quartz-monzonite. This suggests partial melting of pre-existing tonalite-granodiorite-quartz monzonite crust. The monzogranite magmatism that marked the finale stabilization of the Francistown Granite-Greenstone Complex is related to the thermal relaxation. A schematic diagram that summarizes the geodynamic model for the evolution of the Vumba granite-greenstone terrain is presented as Fig. 12.5.

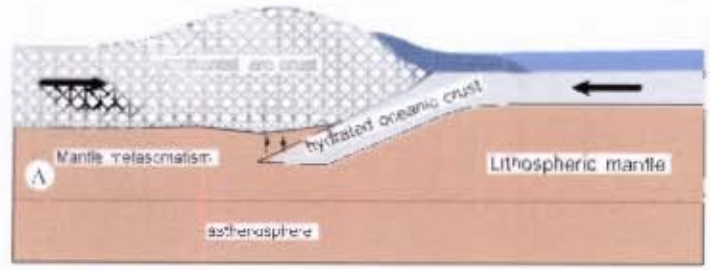

TIME: pre 2700 Ma

EVENT: Flat Subduction of oceanic crust

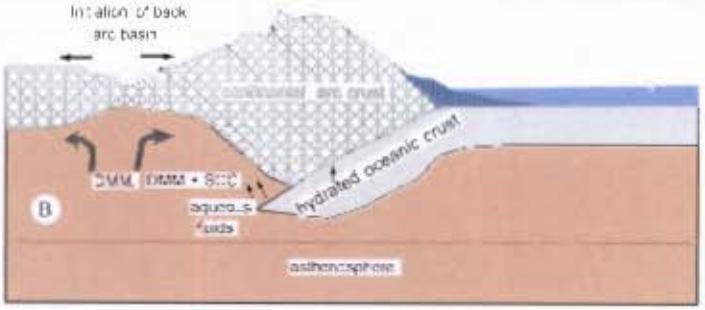

ca~2700 Ma

Crustal thickening underplating of basaitic crust and initiation of back arc extension

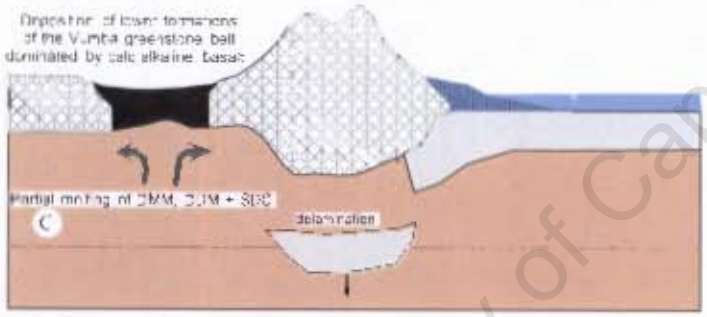

2700 Ma

delamination of overthickened crust & eruption of lower mafic Formations

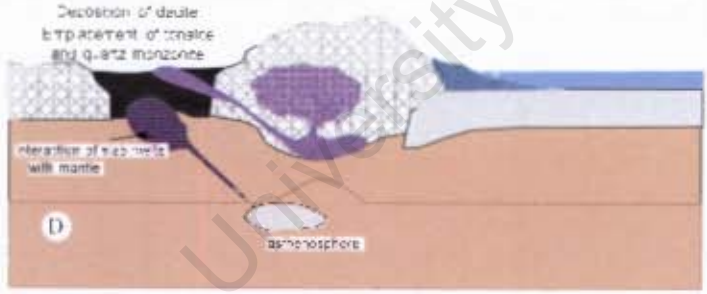

ca~2695 Ma

Partial melting of lower crust & underplated mafic crust to generate dacite & tonalite

Partial melting of delaminated mafic crust to generate quartz monzonite

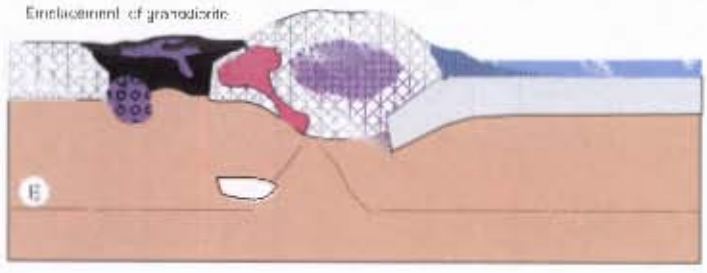

ca~2686 Ma

Partial melting of relatively shallow lower crust to generate granodiorite

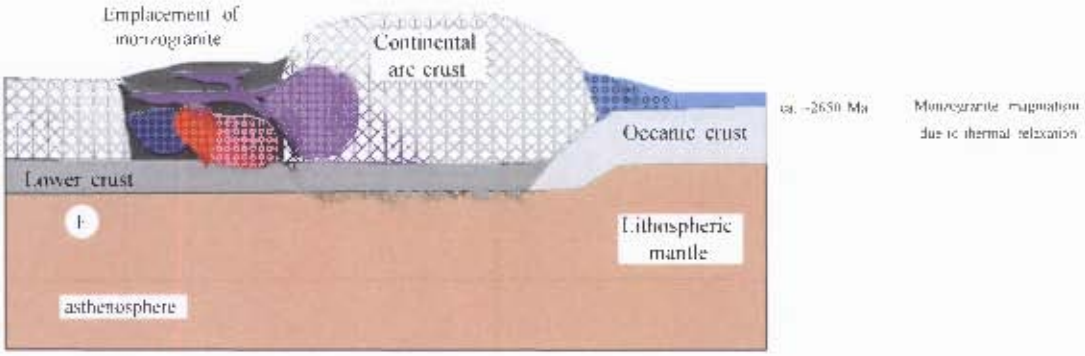

Fig. 12.5: A Schematic diagram illustrating the proposed geodynamic model of the evolution of the Vumba granite-greenstone terrain.

12.3 Geodynamic model for the evolution of the Francistown Granite-Greenstone Complex

Geochronological data from this study clearly dismiss the notion that the Vumba and Tati granite-greenstone terrains are contemporaneous and tectonically related. It emerged from this study that the Tati greenstone belt is ~40 Ma older than the Vumba greenstone belt, which strongly argues against any suggestion that portrays the two belts as a dismembered single greenstone belt, though the ranges of Sr, Nd and Pb isotopic data from their mafic lavas obtained from this study, overlap such that they cannot be distinguished on the basis of isotopic composition. It appears that the Tati and Vumba mafic lavas were derived from similar or perhaps identical mantle source

material. However, subtle differences in Nd isotopic composition do exist between the Tati and Vumba mafic lavas, which appear to reflect varying proportions of crustal involvement. These observations argue for a tectonic setting along a similar evolving convergent margin. The two greenstone belts might therefore be tectonically related through evolution of the margin.

Model ages calculated with respect to a depleted mantle source for the felsic lavas and granitoids from both the Tati and Vumba granite-greenstone terrains are indistinguishable. This suggests that the rocks from the two granite-greenstone terrains were formed along the margin of a single crustal block, most likely constituted by the Belingwean and Lower Bulawayan Supergroups greenstones.

It is important to understand when and how the Tati and Vumba granite-greenstone terrains became neighbours. From the geochronological data presented in chapter 4, it is apparent that magmatism in the Tati terrain was active from circa 2740 to 2701 Ma. The Vumba terrain did not yet exist at this time. In contrast, from 2700 to 2680 Ma the Vumba terrain was particularly active, during which time magmatism in the Tati terrain was dormant. Moreover, there is no indication of the effects of these magmatic events in the Tati area which raises questions about the juxtaposition of the two terrains. Therefore, the two terrains could not have been recording the same tectonic regime. The inheritance of 2733 ± 5 Ma zircons by the Vumba mafic volcanics suggests that the Vumba granite-greenstone terrain was built on the margin of the Tati granite-greenstone terrain or an equivalent terrain. At 2672 Ma, magmatism resumed in the Tati area and produced the SW tonalite-trondhjemite plutons, confined to the southwestern margin of the Tati greenstone belt. This magmatic event is related to the closure of the Limpopo Ocean and it has no traces in the Vumba area.

The Vumba greenstone belt represents a back-arc setting (localized extension) that developed on the same crustal block as the Tati greenstone belt, but its initiation commenced at a different time probably related to the subduction associated with the Shashe belt. This poses a challenge to the suggestion that the Limpopo and Shashe belts belong to the same orogenic belt (e.g. Ranganai et al., 2002).

In summary, the Nd isotope ratios determined on the variety of rocks analysed give the general impression that the Francistown Granite-Greenstone Complex is a Neoarchaean crustal block that formed from major recycling of pre-existing mafic crust with a short residence time. No evidence of significantly older crustal material such as the 3.56 Ga gneisses from the Sebakwe proto-craton is available. It is most probable that the current wide spread paragneiss of the Francistown Granite-Greenstone Complex represents sediments that were eroded from the felsic volcanic and plutonic (TTG) rocks of the Belingwean and Lower Bulawayan Supergroups greenstones that were deposited between 2.90 and 2.88 Ga and 2.83 and 2.79 Ga (Jelsma and Dirks, 2002), respectively. One sample from the paragneiss unit yielded poor quality zircons that gave poorly constrained metamorphic age of 2750 ± 100 Ma. Litherland (1975) and Key (1976) suggested that the paragneiss unit represent felsic volcanic components of the Tati and Vumba greenstone belts that were highly deformed. The distribution pattern of the paragneiss and the relationship with other igneous rocks as well as its deformation state do not favour this suggestion. The suggestion that the paragneiss unit could represent sediments that were derived from juvenile volcanic arc rocks with minor contribution from the Belingwean and Lower Bulawayan Supergroups felsic rocks is compatible with the proposed geodynamic model for the development of the Francistown Granite-Greenstone Complex.

Implication of the proposed geodynamic model for the evolution of the Zimbabwe craton

Previous studies on the evolution of the Zimbabwe craton have revealed that clastic sedimentation along the western and southern margin of the Sebakwe proto-craton occurred between 3.10 and 2.95 Ma (e.g. Dirks and Jelsma, 2002). This period does not overlap the model ages recorded in the granitoids of the Francistown Granite-Greenstone Complex along the southwestern margin. Rifting of the proto-craton is considered to have been initiated at 2.90 Ga resulting in the deposition of the Belingwean Supergroup greenstones between 2.90 and 2.88 Ga (Jelsma and Dirks, 2002). Incidentally, the age of the Belingwean Supergroup greenstones as well as those of the Lower Bulawayan Supergroup greenstones coincide with T_{DM} ages from the granitoids of the Francistown Granite-Greenstone Complex. This implies that the Belingwean Supergroup greenstones most likely extended as far as the southwestern margin of the Zimbabwe craton implying that 2.90 - 2.80 Ga was an extensive period of crustal growth in the Zimbabwe craton. The absence of the Chilimanzi granite suites equivalents in the southwestern margin of the

Zimbabwe craton is an indication that the region stabilized earlier than the interior of the craton. I propose with certain ambivalence that the Francistown Granite-Greenstone Complex is a large arc complex which also encompasses the Matsitama greenstone belt on the western side of the Vumba greenstone belt. This belt has been identified by Majaule et al. (1997) as a back-arc. Further delineation of the extent of the Francistown Granite-Greenstone Complex requires extensive sampling of the wide spread paragneiss unit for Sm-Nd isotope studies, and its precise age determination will undoubtedly refine the geodynamic model of the Francistown Granite-Greenstone Complex and the crustal growth history of the Zimbabwe craton in the NE Botswana.

LIST OF CITED REFERENCES

Abbott D., Burges L., Lonhi J., and Smith W. H. F. (1994) An empirical thermal history of the Earth's upper mantle. *Journal of Geophysical Research* **99**, 13835-13850.

Ayer J., Amelin Y., Corfu F., Kamo S., Ketchum J., Kwok K., and Trowell N. (2002) Evolution of the southern Abitibi greenstone belt based on U-Pb geochronology: autochthonous volcanic construction followed by plutonism, regional deformation and sedimentation. *Precambrian Research* **115**(1-4), 63-95.

Bagai Z. (2000) Geochemical and geochronological investigations of the Vumba granite-greenstone terrain of NE Botswana. MSc, University of Durham.

Bagai Z., Armstrong R. A., and Kampunzu A. B. (2002) U-Pb single zircon geochronology of granitoids in the Vumba granite-greenstone terrain (NE Botswana): implications for the Archaean Zimbabwe craton. *Precambrian Research* **118**, 149-168.

Ballard S. and Pollack H. N. (1987) Diversion of Heat by Archean Cratons - a Model for Southern-Africa. *Earth and Planetary Science Letters* **85**(1-3), 253-264.

Barker F. (1979) Trondhjemites, dacites and related rocks. In *Trondjemite. Definition, environment and hypothesis of origin.* (ed. F. Barker), pp. 1-12. Elselvier.

Beakhouse G. P., Heaman L. M., and Creaser R. A. (1999) Geochemical and U-Pb zircon geochronological contraints on the development of a Late Archean greenstone belt at Birch Lake, Superior Province, Canada. *Precambrian Research* **97**(1-2), 77-97.

Bibikova E. V., Petrova A., and Claesson S. (2005) The temporal evolution of sanukitoids in the Karelian Craton, Baltic Shield: an ion microprobe U-Th-Pb isotopic study of zircons. *Lithos* **79**(1-2), 129-145.

Bickle M. J., Arndt N. T., Nisbet E. G., Orpen J. L., Martin A., Keays R. R., and Renner R. (1993) Geochemistry of the igneous rocks of the Belingwe greenstone belt: alteration, contamination and petrogenesis. In *Geological Society of Zimbabwe Special Publication*, Vol. 2 (ed. M. J. Bickle and E. G. Nisbet), pp. 175-214.

Blake T. S., Buick R., Brown S. J. A., and Barley M. E. (2004) Geochronology of a Late Archaean flood basalt province in the Pilbara Craton, Australia: constraints on basin evolution, volcanic and sedimentary accumulation, and continental drift rates. *Precambrian Research* **133**(3-4), 143-173.

Bleeker W. (2003) The late Archean record: a puzzle in ca. 35 pieces. *Lithos* **71**(2-4), 99-134.

Blenkinsop T. G., Fedo C. M., Bickle M. J., Eriksson K. A., Martin A., Nisbet E. G., and Wilson J. F. (1993) Ensialic Origin for the Ngezi Group, Belingwe Greenstone-Belt, Zimbabwe. *Geology* **21**(12), 1135-1138.

Blenkinsop T. G., Martin A., Jelsma H. A., and Vinyu M. L. (1997) The Zimbabwe Craton. In *Greenstone Belts* (ed. M. J. de Wit and L. D. Ashwal), pp. 567-580. Oxford University Press.

Blichert-Toft J., Albarede F., Rosing M., Frei R., and Bridgwater D. (1999) The Nd and Hf isotopic evolution of the mantle through the Archean. Results from the Isua supracrustals, Greenland, and from the Birimian terranes of West Africa. *Geochimica et Cosmochica Acta* **63**, 3901-3914.

Bowring S. A. and Housh T. (1995) The Earth Early Evolution. *Science* **269**(5230), 1535-1540.

Bowring S. A. and Williams I. S. (1999) Priscoan (4.00 - 4.03 Ga) orthogneisses from northwestern canada. *Contribution to mineralogy and petrology* **134**, 3-16.

Burke K. (1997) Forword. In *Greenstone Belts* (ed. M. J. De Wit and L. D. Ashwal). Oxford University press.

Cambell I. H., Griffiths R. W., and Hill R. I. (1989) Melting in an Archaean mantle plume: heads it's basalt, tails it's komatiites. *Nature* **89**, 697-699.

Cann J. R. (1970) Upward Movement of Granitic Magma. *Geological Magazine* **107**(4), 335-&.

Carney J. N., Aldiss, D.T., Lock, N.P. (1994) The Geology of Botswana. Bulletin 37. Geological Survey Department, Government Printer, Gaborone.

Cavosie A. J., Valley J. W., and Wilde S. A. (2005) Magmatic delta O-18 in 4400-3900 Ma detrital zircons: A record of the alteration and recycling of crust in the Early Archean. *Earth and Planetary Science Letters* **235**(3-4), 663-681.

Chappell B. W. and White A. J. R. (1992) I-Type and S-Type Granites in the Lachlan Fold Belt, pp. 1-26.

Cheney E. S. (1996) Sequence stratigraphy and plate tectonic significance of the Transvaal succession of southern Africa and its equivalent in Western Australia. *Precambrian Research* **79**(1-2), 3-24.

Clague D. A. and Frey F. A. (1982) Petrology and Trace-Element Geochemistry of the Honolulu Volcanics, Oahu - Implications for the Oceanic Mantle Below Hawaii. *Journal of Petrology* **23**(3), 447-504.

Condie K. C. (1997) Contrasting sources for upper and lower continental crust: the greenstone connection. *Journal of Geology* **105**, 729-736.

Condie K. C. (1999) Mafic crustal xenoliths and the origin of the lower continental crust. *Lithos* **46**(1), 95-101.

Condie K. C. (2003) Incompatible element ratios in oceanic basalts and komatiites: Tracking deep mantle sources and continental growth rates with time. *Geochemistry Geophysics Geosystems* **4**.

Condie K. C. (2005a) TTGs and adakites: are they both slab melts? *Lithos* **80**, 33-44.

Condie K. C. (2005b) *Earth as an Evolving Planetary System*. Elsevier Academic Press.

Coward M. P., James, P.R. (1974) The deformation patterns of two Archaean greenstone belts in Rhodesia and Botswana. *Precambrian Research* **1**, 235-258.

Criss R. E. (1999) *Principles of stable isotope distribution.* Oxford University Press.

Crockett, R.N., Aldiss, D.T., and Key, R.M. (1974) Geological map of the Francistown area. Geological Survey of Botswana.

Cumming G. L. and Richards J. R. (1975) Ore Lead Isotope Ratios in a Continuously Changing Earth. *Earth and Planetary Science Letters* **28**(2), 155-171.

Davidson J. P., Morgan D. J., Charlier B. L. A., Harlou R., and Hora J. M. (2007) Microsampling and Isotopic Analysis of Igneous Rocks: Implications for the study of magmatic systems. *Annual Reviews of Earth and Plantary Sciences* **35**, 273-311.

Davies G. F. (1993) Cooling the Core and Mantle by Plume and Plate Flows. *Geophysical Journal International* **115**(1), 132-146.

Davis W. J., Hanmer S., and Sandeman H. A. (2004) Temporal evolution of the Neoarchaean Central Hearne supracrustal belt: rapid generation of juvenile crust in a suprasubduction zone setting. *Precambrian Research* **134**, 85-112.

Davis W. J., Jones A. G., Bleeker W., and Grutter H. (2003) Lithosphere development in the Slave craton: a linked crustal and mantle perspective. *Lithos* **71**(2-4), 575-589.

De Ronde C. E. J. and de Wit M. J. (1994) Tectonic history of the Barberton greenstone belt, South Africa: 490 million years of Archaean crustal evolution. *Tectonics* **13**, 983-1005.

de Wit M. J. (1998) On Archaean granites, greenstones, cratons and tectonics: does the evidence demand a verdict? *Precambrian Research* **91**, 181-226.

de Wit M. J. and Ashwal L. D. (1997) *Greenstone Belts.* Claredon Press.

de Wit M. J. and Hynes A. (1995) The onset of interaction between the hydrosphere and oceanic crust, and the origin of the first continental lithosphere. In *Early Precambrian Processes*, Vol. 95 (ed. M. P. Coward and A. C. Ries), pp. 1.9. Geological Society Special Publications.

de Wit M. J. and Tinker J. (2004) Crustal structures across the central Kaapvaal Craton from deep-seismic reflection data. *South African Journal of Geology* **107**, 185-206.

de Wit M. J., Armstrong R. A., Rodger J. H., and Wilson A. H. (1987) Felsic igneous rocks within the 3.3 to 3.5 Ga Barberton Greenstone Belt: High crustal level equivalents of the surrounding tonalite-trondhjemite terrain, emplaced during thrusting. *Tectonics* **6**(5), 529-549.

de Wit M. J., Richardson S. H., and Ashwal L. D. (2004) Kaapvaal Craton special volume-An introduction. *South African Journal of Geology* **107**, 1-6.

de Wit M. J., Roering C., Hart R. J., Armstrong R. A., De Ronde C. E. J., Green R. W. E., Tredoux M., Peberdy E., and Hart R. A. (1992) Formation of an Archaean continent. *Nature* **357**, 553-562.

DePaolo D. J. (1981) Neodymium Isotopes in the Colorado Front Range and Crust-Mantle Evolution in the Proterozoic. *Nature* **291**(5812), 193-196.

DePaolo D. J. and Wasserberg G. J. (1976) Nd isotopic variation and petrogenetic models. *Geophysical Research Letters* **3**, 249-252.

Dickin A. P. (2005) *Radiogenic Isotope Geology.* Cambridge University Press.

Dirks P. H. G. M. and Jelsma H. A. (2002) Crust-mantle decoupling and the growth of the Archaean Zimbabwe craton. *Journal od African Earth Sciences* **34**, 157-166.

Dodson M. H., Compston W., Williams I. S., and Wilson J. F. (1988) A search for ancient detrital zircons in Zimbabwean sediments. *Journal of Geological Society of London* **145**, 977-983.

Dostal J. and Mueller W. U. (1997) Komatiite flooding of a rifted Archean rhyolitic arc complex: Geochemical signature and tectonic significance of the Stoughton-Roquemaure Group, Abitibi Greenstone Belt, Canada. *Journal of Geology* **105**(5), 545-563.

Drummond M. S. and Defant M. J. (1990) A model for trondhjemite-tonalite-dacite genesis and crustal growth via slab melting: Archaean to modern comparisons. *Journal of Geophysical Research* **95B**, 21503-21521.

Drummond M. S., Defant M. J., and Kepezhinskas P. K. (1996) Petrogenesis of slab-derived trondhjemite-tonalite-dacite/adakite magmas, pp. 205-215.

Eby G. N. (1992) Chemical Subdivision of the a-Type Granitoids - Petrogenetic and Tectonic Implications. *Geology* **20**(7), 641-644.

Eglington B. M. and Armstrong R. A. (2004) The Kaapvaal Craton and adjacent orogens, southern Africa: a geochronological database and overview of the geological development of the craton. *South African Journal of Geology* **107**, 13-32.

Elliott T., Plank T., Zindler A., White W., and Bourdon B. (1997) Element transport from slab to volcanic front at the Mariana arc. *Journal of Geophysical Research-Solid Earth* **102**(B7), 14991-15019.

Faure G. (1998) *Principles and Applications of Geochemistry.* Prentice Hall, Englewood Cliffs,.

Feng R. and Kerrich R. (1992) Geochemical Evolution of Granitoids from the Archean Abitibi Southern Volcanic Zone and the Pontiac Subprovince, Superior Province, Canada - Implications for Tectonic History and Source Regions. *Chemical Geology* **98**(1-2), 23-70.

Fouch M. J., James D. E., Vanecar J. C., van der Lee S., and Group K. S. (2004) Mantle seismic structure beneath the Kaapvaal and Zimbabwe Cratons. *South African Journal of Geology* **107**, 33-44.

Frei R. and Jensen B. K. (2003) Re-Os, Sm-Nd isotope- and REE systematics on ultramafic rocks and pillow basalts from the Earth's oldest oceanic crustal fragments (Isua Supracrustal Belt and Ujaragssuit nunat area, W Greenland). *Chemical Geology* **196**(1-4), 163-191.

Frey F. A., Green D. H., and Roy S. D. (1978) Integrated Models of Basalt Petrogenesis - Study of Quartz Tholeiites to Olivine Melilities from South Eastern Australia Utilizing Geochemical and Experimental Petrological Data. *Journal of Petrology* **19**(3), 463-513.

Gill J. (1981) *Orogenic andesites and plate tectonics*. Springer-Verlag.

Goldstein S. L., Onions R. K., and Hamilton P. J. (1984) A Sm-Nd Isotopic Study of Atmospheric Dusts and Particulates from Major River Systems. *Earth and Planetary Science Letters* **70**(2), 221-236.

Goodwin A. M. (1996) *Principles of Precambrian Geology*. Academic Press.

Green N. L. (2006) Influence of slab thermal structure on basalt source regions and melting conditions: REE and HFSE contraints from the Garbaldi volcanic belt, northern Cascadia subduction system. *Lthos* **87**, 23-49.

Gribble R. F., Stern R. J., Bloomer S. H., Stuben D., Ohearn T., and Newman S. (1996) MORB mantle and subduction components interact to generate basalts in the southern Mariana Trough back-arc basin. *Geochimica Et Cosmochimica Acta* **60**(12), 2153-2166.

Halla J. (2005) Late Archean high-Mg granitoids (sanukitoids) in the southern Karelian domain, eastern Finland: Pb and Nd iostopic constraints on crust-mantle interactions. *Lithos* **79**, 161-178.

Hamilton W. B. (1998) Archaean magmatism and deformation were not products of plate tectonics. *Precambrian Research* **91**, 143-179.

Harris N. B. W., Pearce J. A., and Tindle A. G. (1986) Geochemical characteristics of collision-zone magmatism. In *Collision Tectonics*, Vol. Geological Society Special Publication No. 19 (ed. M. P. Coward and A. C. Ries), pp. 61-81. Blackwell Scientific Publications.

Hart S. R. and Davis K. E. (1978) Nickel Partitioning between Olivine and Silicate Melt. *Earth and Planetary Science Letters* **40**(2), 203-219.

Hawkesworth C. J., Gallagher K., Hergt J. M., and McDermott F. (1993) Mantle and Slab Contributions in Arc Magmas. *Annual Review of Earth and Planetary Sciences* **21**, 175-204.

Hawkesworth C., Turner S., Peate D., McDermott F., and vanCalsteren P. (1997) Elemental U and Th variations in island arc rocks: Implications for U-series isotopes. *Chemical Geology* **139**(1-4), 207-221.

Hawkins J. W., Lonsdale P. F., Macdougall J. D., and Volpe A. M. (1990) Petrology of the Axial Ridge of the Mariana Trough Backarc Spreading Center. *Earth and Planetary Science Letters* **100**(1-3), 226-250.

Herrington R. J. (1995) Late Archaean structure and gold mineralisation in the Kadoma region of the Midlands greenstone belt, Zimbabwe. In *Early Precambrian Processes*, Vol. 95 (ed. M. P. Coward and A. C. Ries), pp. 173-191. Geological Society Special Publications.

Hofmann A., Dirks P., Jelsma H. A., and Matura N. (2003) A tectonic origin for ironstone horizons in the Zimbabwe craton and their significance for greenstone belt geology. *Journal of the Geological Society* **160**, 83-97.

Hollings P. and Kerrich R. (2000) An Archean arc basalt-Nb-enriched basalt-adakite association: the 2.7 Ga Confederation assemblage of the Birch-Uchi greenstone belt, Superior Province. *Contributions to Mineralogy and Petrology* **139**(2), 208-226.

Hollings P. and Kerrich R. (2004) Geochemical systematics of tholeiites from the 2.86 Ga Pickle Crow Assemblage, northwestern Ontario: arc basalts with positive and negative Nb-Hf anomalies. *Precambrian Research* **134**, 1-20.

Hollings P. and Wyman D. (1999) Trace element and Sm-Nd sytematics of volcanic and intrusive rocks from the 3 Ga Lumby Lake Greenstone belt, Superior Province: evidence for Archaen plume-arc interaction. *Lithos* **46**, 189-213.

Hollings P., Wyman D., and Kerrich R. (1999) Komatiite-basalt-rhyolite volcanic associations in Northern Superior Province greenstone belts: significance of plume-arc interaction in the generation of the proto continental Superior Province. *Lithos* **46**, 137-161.

Holzer L., Frei R., Barton J. M., and Kramers J. D. (1998) Unraveling the record of successive high grade events in the Central Zone of the Limpopo Belt using Pb single phase dating of metamorphic minerals. *Precambrian Research* **87**(1-2), 87-115.

Horstwood M. S. A., Nesbitt R. W., Noble R. S., and Wilson J. F. (1999) U-Pb zircon evidence for an extensive early Archaean craton in Zimbabwe: a reassessment of the timing of craton formation, stabilization and growth. *Geology* **27**, 707-710.

Jackson M. (1981) The Geology of the Penhalonga Area. Unpublished report for Falconbridge Explorations Botswana.

Jacobsen S. B. and Wasserburg G. J. (1980) Sm-Nd Isotopic Evolution of Chondrites. *Earth and Planetary Science Letters* **50**(1), 139-155.

James D. E., Fouch M. J., VanDecar J. C., and van der Lee S. (2001) Tectospheric structure beneath southern Africa. *Geophysical Research Letters* **28**(13), 2485-2488.

Jelsma H. A. and Dirks P. H. G. M. (2000) Tectonic evolution of a greenstone sequence in northern Zimbabwe: sequential early stacking and pluton diapirism. *Tectonics* **19**, 135-152.

Jelsma H. A. and Dirks P. H. G. M. (2002) Neoarchaean tectonic evolution of the Zimbabwe craton. In *The Early Earth: Physical, chemical and biological development.*, Vol. 199 (ed. C. M. R. Fowler, C. J. Ebinger, and C. J. Hawkesworth), pp. 183-211. Special Publications Geological Society London.

Jelsma H. A., Vinyu M. L., Valbracht P. J., Davies G. R., Wijbrans J. R., and Verdurmen E. A. T. (1996) Constraints on Archaean crustal evolution of the Zimbabwe craton: a U-Pb zircon, Sm-Nd and Pb-Pb whole-rock isotope study. *Contribution to mineralogy and petrology* **124**, 55-70.

Jochum K. P., Arndt N. T., and Hofmann A. W. (1991) Nb-Th-La in Komatiites and Basalts - Constraints on Komatiite Petrogenesis and Mantle Evolution. *Earth and Planetary Science Letters* **107**(2), 272-289.

Johnson M. (1986) The Phoenix Deposit. . In Mineral Deposits of South Africa (ed. Anhauser).

Jones A. G., Lezaeta P., Ferguson I. J., Chave A. D., Evans R. L., Garcia X., and Spratt J. (2003) The electrical structure of the Slave craton. *Lithos* **71**(2-4), 505-527.

Kampunzu A. B., Tombale A. R., Zhai M., Bagai Z., Majaule T., and Modisi M. P. (2003) Major and trace element geochemistry of plutonic rocks from Francistown, NE Botswana: evidence for a Neoarchaean continental active margin in the Zimbabwe craton. *Lithos* **71**, 431-460.

Kapyaho A., Manttari I., and Huhma H. (2006) Growth of Archaean crust in the Kuhmo district, eastern Finland: U-Pb and Sm-Nd isotope constraints on plutonic rocks. *Precambrian Research* **146**, 95-119.

Karsten J. L., Klein E. M., and Sherman S. B. (1996) Subduction zone geochemical characteristics in ocean ridge basalts from the southern Chile Ridge: Implications of modern ridge subduction systems for the Archean. *Lithos* **37**(2-3), 143-161.

Katongo C., Koller F., Kloetzli U., Koeberl C., Tembo F., and De Waele B. (2004) Petrography, geochemistry, and geochronology of granitoid rocks in the Neoproterozoic-Paleozoic Lufilian-Zambezi belt, Zambia: Implications for tectonic setting and regional correlation. *Journal of African Earth Sciences* **40**(5), 219-244.

Kerrich R., Polat A., Wyman D., and Hollings P. (1999) Trace element systematics of Mg-, to Fe-tholeiitic basalt suites of the Superior Province: implications for Archean mantle reservoirs and greenstone belt genesis. *Lithos* **46**(1), 163-187.

Kerrich R., Wyman D., Fan J., and Bleeker W. (1998) Boninite series: low Ti-tholeiite associations from the 2.7 Ga Abitibi greenstone belt. *Earth and Planetary Science Letters* **164**(1-2), 303-316.

Key R. M. (1976) The geology of the area around Francistown and Phikwe, Northeast and Central Districts, Botswana. Geological Survey of Botswana District Memoir.

Key R. M., Litherland M., and Hepworth J. V. (1976) The evolution of the Archaean crust of northeastern Botswana. *Precambrian Research* **3**, 375-413.

King S. D. (2005) Archaean cratons and mantle dynamics. *Earth Planetary Science Letters* **234**, 1-14.

Kinzler R. J. (1997) Melting of mantle peridotite at pressures approaching the spinel to garnet transition: Application to mid-ocean ridge basalt petrogenesis. *Journal of Geophysical Research-Solid Earth* **102**(B1), 853-874.

Komiya T., Maruyama S., Masunda T., Nohda S., Hayashi M., and Okamoto K. (1999) Plate Tectonics at 3.8 - 3.7 Ga: Field Evidence from the Isua Accretionary Complex, Southern West Greenland. *The Journal of Geology* **139**, 75-110.

Kovalenko A., Clemens J. D., and Savatenkov V. (2005) Petrogenetic constraints for the genesis of Archaean sanukitoid suites: geochemistry and isotopic evidence from Karelia, Baltic Shield. *Lithos* **79**(1-2), 147-160.

Kramers J. D. and Tolstikhin I. N. (1997) Two terrestrial lead isotope paradoxes, forward transport modelling, core formation and the history of the continental crust. *Chemical Geology* **139**(1-4), 75-110.

Kroner A. (1991) Tectonic Evolution in the Archean and Proterozoic. *Tectonophysics* **187**(4), 393-410.

Kroner A., Jaeckel P., Brandl G., Nemchin A. A., and Pidgeon R. T. (1999) Single zircon ages for granitoid gneisses in the Central Zone of the Limpopo Belt, Southern Africa and geodynamic significance. *Precambrian Research* **93**(4), 299-337.

Kusky T. M. (1998) Tectonic setting and terrane accretion of the Archaean Zimbabwe craton. *Geology* **26**, 163-166.

Kusky T. M. and Kidd W. S. F. (1992) Remnants of an Archean Oceanic Plateau, Belingwe Greenstone-Belt, Zimbabwe. *Geology* **20**(1), 43-46.

Le Maitre R. W., Streckeisen A., Zanettin B., Le Bas M. J., Bonin B., Bateman P., Bellien G., Dudek A., Efremova S., Keller J., Lameyre J., Sabine P. A., Schmid R., Sbrensen H., and Woolley A. R. (2002) *Igneous Rocks: A Classification and Glossary of terms: Recommendations of*

the International Union of Geological Sciences. Subcommission on the Systematics of Igneous Rocks, 2nd ed. Cambridge University Press.

Litherland M. (1975) The geology of the area around Maitengwe, Sebina and Tshesebe, Northeast and Central Districts, Botswana. District Memoir No: 2. Geological Survey of Botswana.

Luas B. and Hawkesworth C. J. (1994) The generation of continental crust: an integrated study of crust forming processes in the Archaean of Zimbabwe. *Journal of Petrology* **35**, 43-93.

Ludtke G., Mosigi, B., Zeil, P. (1989) Mineral Exploration in the Vumba Schist Belt of Northeast Botswana. Final Report., pp. 93. BGR, Archive No: 105549.

Ludwig K. R. (2003) Isoplot/Ex rev. 3.00. Special publication No.4. Berkeley Geochrononlogy Centre.

Maas R., Kinny P. D., Williams I. S., Froude D. O., and Compston W. (1992) The Earths Oldest Known Crust - a Geochronological and Geochemical Study of 3900-4200 Ma Old Detrital Zircons from Mt Narryer and Jack Hills, Western-Australia. *Geochimica Et Cosmochimica Acta* **56**(3), 1281-1300.

Mahoney J. J., Jones W. B., Frey F. A., Salters V. J. M., Pyle D. G., and Davies H. L. (1995) Geochemical Characteristics of Lavas from Broken Ridge, the Naturaliste Plateau and Southernmost Kerguelen Plateau - Cretaceous Plateau Volcanism in the Southeast Indian-Ocean. *Chemical Geology* **120**(3-4), 315-345.

Majaule T., Hall R. P., and Hughes D. J. (1997) Geochemistry of mafic and ultramafic igneous rocks of the Matsitama supracrustal belt, northeastern Botswana - provenance implications. *South African Journal of Geology* **100**(2), 169-179.

Manikyamba C., Kerrich R., Naqvi S. M., and Mohan M. R. (2004) Geochemical systematic basalts from the 2.7 Ga Ramagiri-Hungund Composite greenstone belt, Dharwar craton. *Precambrian Research* **134**, 21-39.

Manya S. (2004) Geochemistry and petrogenesis of volcanic rocks of the Neoarchaean Sukumaland Greenstone Belt, northwestern Tanzania. *Journal of African Earth Sciences* **40**, 269-279.

Mapeo R. B. M., Armstrong R. A., Kampunzu A. B., and Ramokate L. V. (2004) SHRIMP U-Pb zircon ages of granitoids from the western domain of the Kaapvaal Craton, southern Botswana: implications for crustal evolution. *South African Journal of Geology* **107**, 159-172.

Martin H. (1987) Petrogenesis of Archaean Trondhjemites, Tonalites, and Granodiorites from EasternFinland: Major and Trace Element Geochemistry. *Journal of Petrology* **28**, 921-953.

Martin H. (1999) Adakitic magmas: modern analogues of Archaean granitoids. *Lithos* **46**, 411-429.

Martin H., Smithies R. H., Rapp R., Moyen J.-F., and Champion D. (2005) An overview of adakite, tonalite-trondhjemite-granodiorite (TTG), and sanukitoid: relationships and some implications for crustal evolution. *Lithos* **79**, 1-24.

McCourt S., Kampunzu A. B., Armstrong R. A., and Bagai Z. (2004) The crustal architecture of Archaean Terranes in north-eastern Botswana. *South African Journal of Geology* **107**, 147-158.

McDonough W. F. and Sun S.-S. (1995) Composition of the Earth. *Chemical Geology* **120**, 223-253.

McKenzie D. (1984) The Generation and Compaction of Partially Molten Rock. *Journal of Petrology* **25**(3), 713-765.

McKenzie D. P. and O'Nions R. K. (1991) Partial melt distribution from inversion of rare earth element concentrations. *Journal of Petrology* **32**, 1021-1091.

Middlemost E. A. K. (1989) Iron Oxidation Ratios, Norms and the Classification of Volcanic-Rocks. *Chemical Geology* **77**(1), 19-26.

Minster J. F., Minster J. B., Treuil M., and Allegre C. J. (1977) Systematic Use of Trace-Elements in Igneous Processes .2. Inverse Problem of Fractional Crystallization Process in Volcanic Suites. *Contributions to Mineralogy and Petrology* **61**(1), 49-77.

Miyashiro A. (1974) Volcanic rock series in island arcs and active continental margins. *American Journal of Science* **274**, 317-327.

Mojzsis S. J., Harrison T. M., and Pidgeon R. T. (2001) Oxygen-isotope evidence from ancient zircons for liquid water at the Earth's surface 4,300 Myr ago. *Nature* **409**, 178.

Mortimer G., McCulloch M. T., Kinsley L., and Esat T. (2002) High precision U-234-Th-230 dating using MC-ICPMS. *Geochimica Et Cosmochimica Acta* **66**(15A), A527-A527.

Mosigi B. (1987) Geochemical and geological investigations in the Vumba Belt, NE Botswana., University of Leicester.

Moyen J. F., Martin H., and Jayananda M. (2001) Multi-element geochemical modelling of crust-mantle interactions during late-Archaean crustal growth: the Closepet granite (South India). *Precambrian Research* **112**(1-2), 87-105.

Moyen J. F., Nedelec A., Martin H., and Jayananda M. (2003) Syntectonic granite emplacement at different structural levels: the Closepet granite, South India. *Journal of Structural Geology* **25**(4), 611-631.

Nagler E. G., Kramers J. D., Kamber B. S., Frei R., and Prendergast M. D. A. (1997) Growth of subcontinental lithospheric mantle beneath Zimbabwe started at or before 3.8 Ga; Re-Os study on chromites. *Geology* **25**, 983-986.

Nagler T. F. and Kramers J. D. (1998) Nd isotopic evolution of the upper mantle during the Precambrian: models, data and the uncertainty of both. *Precambrian Research* **91**(3-4), 233-252.

Nisbet E. G. and Fowler C. M. R. (1983) Model for Archean Plate-Tectonics. *Geology* **11**(7), 376-379.

Nisbet E. G., Cheadle M. J., Arndt N. T., and Bickle M. J. (1993) Constraining the potential temperature of the Archaean mantle: A review of the evidence from komatiites. *Lithos* **30**, 291-307.

Ohta H., Maruyama S., Takahashi E., Watanabe Y., and Kato Y. (1996) Field occurrence, geochemistry and petrogenesis of the Archaean Mid-Oceanic Ridge Basalts (AMORBs) of the Cleaverville area, Pilbara craton, Western Australia. *Lithos* **37**, 199-221.

Park R. G. (1997) Early Precambrian plate tectonics. *South African Journal of Geology* **100**, 23-35.

Parman S. W., Grove T. L., Dann J. C., and de Wit M. J. (2004) A subduction origin for komatiites and cratonic lithospheric mantle. *South African Journal of Geology* **107**, 107-118.

Pearce J. A. (1982) Trace element characteristics of lavas from destructive plate boundaries. In *Andesites* (ed. R. S. Thorpe), pp. 525-548. Wiley.

Pearce J. A. (1983) Role of the sub-continental lithosphere in magma genesis at active continental margins. In *Continental basalts and mantle xenoliths* (ed. C. J. Hawkesworth and M. J. Norry), pp. 230-249. Shiva.

Pearce J. A. (1996) A user's guide to basalt discrimination diagrams. In: Trace element geochemistry of volcanic rocks; applications for massive sulphide exploration. Short Course Notes. *Geological Association of Canada* **12**, 79-113.

Pearce J. A. and Cann J. R. (1973) Tectonic Setting of Basic Volcanic-Rocks Determined Using Trace-Element Analyses. *Earth and Planetary Science Letters* **19**(2), 290-300.

Pearce J. A. and Peate D. W. (1995) Tectonic Implications of the Composition of Volcanic Arc Magmas. *Annual Review of Earth and Planetary Sciences* **23**, 251-285.

Pearce J. A., Barker P. F., Edwards S. J., Parkinson I. J., and Leat P. T. (2000) Geochemistry and tectonic significance of peridotites from the South Sandwich arc-basin system, South Atlantic. *Contributions to Mineralogy and Petrology* **139**(1), 36-53.

Pearce J. A., Ernewein M., Bloomer S. H., Parson L. M., Murton B. J., and Johnson L. E. (1994) Geochemistry of Lau Basin volcanic rocks: influence of ridge segmentation and arc proximity. In *Volcanism Associated with Extension at Consuming Plate Margins.*, Vol. 81 (ed. J. L. Smellie), pp. 53-75. Geological Society Special Publication.

Pearce J. A., Harris N. B. W., and Tindle A. G. (1984) Trace element discrimination diagrams for the tectonic interpretation of granitic rocks. *Journal of Petrology* **25**, 957-983.

Pecerillo A. and Taylor S. R. (1976) Geochemistry of Eocene calc-alkaline volcanic rocks from the Kastamonu area, northern Turkey. *Contribution to mineralogy and petrology* **58**, 63-81.

Percival J. A., Roering C., Van Reenen D. D., and Smit C. A. (1997) Tectonic evolution of associated greenstone belts and high-grade terrains. In *Greenstone Belts* (ed. M. J. de Wit and L. D. Ashwal), pp. 398-420. Oxford University Press.

Pidgeon R. T. (1992) Recrystallization of Oscillatory Zoned Zircon - Some Geochronological and Petrological Implications. *Contributions to Mineralogy and Petrology* **110**(4), 463-472.

Polat A. and Kerrich R. (2000) Archaean greenstone belt magmatism and the continental growth-mantle evolution connection: constraints from Th-U-Nb-LREE sytematics of 2.7 Ga Wawa Subprovince, Superior Province, Canada. *Earth Planetary Science Letters* **175**, 41-54.

Polat A. and Kerrich R. (2002) Nd-isotope systematics of approximately 2.7 Ga adakites, magnesian andesites, and arc basalts, Superior province for shallow crustal recycling at Archaean subduction zones. *Earth Planetary Science Letters* **202**, 345-360.

Polat A., Kerrich R., and Wyman D. A. (1999) Geochemical diversity in oceanic komatiites and basalts from the late Archaean Wawa greenstone belts, Superior Province, Canada: trace element and Nd Isotope evidence for a heterogeneous mantle. *Precambrian Research* **94**, 139-173.

Pollack H. N. (1997) Thermal characteristics of the Archaean. In *Greenstone Belts* (ed. M. J. de Wit and L. D. Ashwal), pp. 223-232. Oxford University Press.

Pouclet A., Lee J., Vidal P., Cousens B., and Bellon H. (1994) Cretaceous to Cenozoic volcanism in South Korea and in the Sea of Japan: magmatic constraints on the opening of back-arc basin. In *Volcanism Associated with Extension at Consuming Plate Margins.*, Vol. 81 (ed. J. L. Smellie), pp. 169-191. Geological Society Spcecial Publication.

Prendergast M. D. (2004) The Bulawayan Supergroup: a late Archaean passive margin-related large igneous province in the Zimbabwe craton. *Journal of the Geological Society* **161**, 431-445.

Prouteau G., Scaillet B., Pichavant M., and Maury R. (2001) Evidence for mantle metasomatism by hydrous silicic melts derived from subducted oceanic crust. *Nature* **410**(6825), 197-200.

Puchtel I. S., Arndt N. T., Hofmann A. W., Haase K. M., Kroner A., Kulikov V. S., Kulikova V. V., Garbe-Schonberg C. D., and Nemchin A. A. (1998) Petrology of mafic lavas within the Onega plateau, central Karelia: evidence for 2.0 Ga plume-related continental crustal growth in the Baltic Shield. *Contributions to Mineralogy and Petrology* **130**(2), 134-153.

Rammlmair D. (1986) Ultrabasic rocks in the Vumba Schist Belt. BGR interim report. Hannover.

Ranganai R. T., Kampunzu A. B., Atekwana E. A., Paya B. K., King J. G., Koosimile D. I., and Steller E. H. (2002) Gravity evidence for a larger Limpopo Belt in southern Africa and geodynamic implications. *Geophysical Research Letters* **149**, F9-F14.

Rapp R. P. (1997) Heterogeneous source for Archaean granitoids: experimental and geochemical evidence. In *Greenstone Belts.* (ed. M. J. de wit and L. D. Ashwal), pp. 267-279. Oxford University Press.

Rapp R. P., Shimizu N., Norman M. D., and Applegate G. S. (1999) Reaction between slab melts and peridotite in the mantle wedge: experimental constraints at 3.8 GPa. *Chemical Geology* **160**, 335-356.

Richardson S. H., Gurney J. J., Erlank A. J., and Harris J. W. (1984) Origin of Diamonds in Old Enriched Mantle. *Nature* **310**(5974), 198-202.

Ridley, J.R., Vearncombe, J.R., and Jelsma, H.A. (1997) Relations between greenstone belts and associated granitoids. In: de Wit, M.J., Ashwal, L.D., (eds), *Greenstone belts*. Oxford University Press, pp. 376-397.

Roeder P. L. and Emslie R. F. (1970) Olivine-Liquid Equilibrium. *Contributions to Mineralogy and Petrology* **29**(4), 275-&.

Rollinson H. and Martin H. (2005) Geodynamic controls on adakite, TTG and sanukitoid genesis: implications for models of crust formation. *Lithos* **79**(Special issue), ix - xii.

Rollinson H. R. (1993) *Using Geochemical Data: Evaluation, Presentation, Interpretation*. Longman.

Rubatto D. and Herman J. (2003) Zircon formation during fluid circulation in eclogites (Monviso, Western Alps): implications for Zr and Hf budget in subduction zones. *Geochimica et Cosmochica Acta* **67**(12), 2173-2187.

Rudnick R. L. (1995) Making Continental-Crust. *Nature* **378**(6557), 571-578.

Sajona F. G., Maury R. C., Pubellier M., Leterrier J., Bellon H., and Cotton J. (2000) Magmatic source enrichment by slab-derived melts in a young post-collision setting, central Mindanao (Philippines). *Lithos* **54**, 173-206.

Sandeman H. A., Hanmer S., Davis W. J., Ryan J. J., and Peterson T. D. (2004a) Neoarchaean volcanic rocks, Central Hearne supracrustal belt, Western Churchill Province, Canada: geochemical and isotopic evidence supporting intra-oceanic, supra-subduction zone extension. *Precambrian Research* **134**, 113-141.

Sandeman H. A., Hanmer S., Davis W. J., Ryan J. J., and Peterson T. D. (2004b) Whole-rock and Nd isotopic geochemistry of Neoarchaean granitoids and their bearing on the evolution of the Central Hearne supracrustal belt, Western Churchill Province, Canada. *Precambrian Research* **134**, 143-167.

Sandeman H. A., Hanmer S., Tella S., Armitage A. A., Davis W. J., and Ryan J. J. (2006) Petrogenesis of Neoarchaean volcanic rocks of the MacQuoid supracrustal belt: A back-arc setting for the northwestern Hearne subdomain, western Churchill Province, Canada. *Precambrian Research* **144**(1-2), 140-165.

Sarvothaman H. (2001) Archaean high-Mg granitoids of mantle origin in the Eastern Dharwar craton of Andhra Pradesh. *Journal of Geological Society of India* **58**(3), 261-268.

Saunders A. and Tarney J. (1991) Back-arc basins. In *Oceanic Basalt* (ed. P. A. Floyd), pp. 219-(MAJAULE et al., 1997)263. Blackie and Sons.

Scambelluri M., Rampone E., and Piccardo G. B. (2001) Fluid and element cycling in subducted serpentinite: A trace element study of the Erro-Tobbio high-pressure ultramifites (Western alps, NW Italy).

Schmitz M. D., Bowring S. A., de Wit M. J., and Gartz V. (2004) Subduction and terrane collision stabilize the western Kaapvaal craton tectosphere 2.9 billion years ago. *Earth and Planetary Science Letters* **222**(2), 363-376.

Schmitz M. D., Vervoort J. D., Bowring S. A., and Patchett P. J. (2002) Decoupling of the Lu-Hf and Sm-Nd isotopic systems in granulitic lower crust beneath southern Africa. *Geochimica Et Cosmochimica Acta* **66**(15A), A682-A682.

Shaw D. M. (2006) *Trace elements in Magmas*. Cambridge University Press.

Shervais J. W. (1982) Ti-V plots and the petrogenesis of modern and ophiolitic lavas. *Earth Planetary Science Letters* **59**, 101-118.

Shirey S. B. and Hanson G. N. (1984) Mantle-Derived Archean Monozodiorites and Trachyandesites. *Nature* **310**(5974), 222-224.

Shirey S. B., Harris J. W., Richardson S. H., Fouch M., James D. E., Cartigny P., Deines P., and Viljoen F. (2003) Regional patterns in the paragenesis and age of inclusions in diamond, diamond composition, and the lithospheric seismic structure of Southern Africa. *Lithos* **71**(2-4), 243-258.

Shirey S. B., Richardson S. H., and Harris J. W. (2004) Age, paragneiss and composition of diamonds and evolution of the Precambrian mantle lithosphere of southern Africa. *South African Journal of Geology* **107**, 91-106.

Siegfried P. R. (1999) The Selkirk Formation-An Archaean Tonalitic Granite or Volcanic Pile? *Botswana Journal of Earth Sciences* **4**, 34-38.

Silver P. G., Fouch M. J., Gao S. S., Schmitz M., and Group K. S. (2004) Seismic anisotropy, mantle fabric, and the magmatic evolution of Precambrian southern Africa. *South African Journal of Geology* **107**, 45-58.

Smith A. D. and Lewis C. (1999) The planet beyond the plume hypothesis. *Earth-Science Reviews* **48**, 135-183.

Smithies R. H. (2000) The Archaean tonalite-trondhjemite-granodiorite (TTG) series is not an analogue of Cenozoic adakite. *Earth Planetary Science Letters* **182**, 115-125.

Smithies R. H. and Champion D. C. (2000) The Archaean high-Mg diorite suite: links to tonalite-trondhjemite-granodiorite magmatism and implications for early Archaean crustal growth. *Journal of Petrology* **41**, 1653-1671.

Smithies R. H., Champion D. C., Van Kranendonk M. J., Howard H. M., and Hickman A. H. (2005a) Modern-style subduction processes in the Mesoarchaean: geochemical evidence from the 3.12 Ga Whundo intra-oceanic arc. *Earth Planetary Science Letters* **231**, 221-237.

Smithies R. H., Van Kranendonk M. J., and Champion D. C. (2005b) It started with a plume - early Archaean basaltic proto-continental crust. *Earth Planetary Science Letters* **238**, 284-297.

Sorensen S. S. (1988) Petrology of amphibolite-facies mafic and ultramafic rocks from the Catalina Schist, southern California: metasomatism and migmitisation in a subduction zone metamorphic setting. *Metamorphic Geology* **6**, 405-435.

Srivastava R. K., Singh R. K., and Verma S. P. (2004) Neoarchaean mafic volcanic rocks from the southern Bastar greenstone belt, Central India: petrological and tectonic significance. *Precambrian Research* **131**, 305-322.

Stacey J. S. a. K., J.D. (1975) Approximation of terrestrial lead evolution by a two-stage model. *Earth Planetary Science Letters* **26**, 207-221.

Stankiewicz J., Chevrot S., van der Hilst R. D., and de Wit M. J. (2002) Crustal thickness, discontinuity depth, and upper mantle structure beneath southern Africa: constraints from body wave conversions. *Physics of the Earth and Planetary Interiors* **130**(3-4), 235-251.

Steenfelt A., Garde A. A., and Moyen J. F. (2005) Mantle wedge involvement in the petrogenesis of Archaean grey gneisses in West Greenland. *Lithos* **79**, 207-228.

Stern R. A. and Hanson G. N. (1991) Archaean high-Mg granodiorite: a derivative of light Rare Earth element-enriched monzodiorite of Mantle origin. *Journal of Petrology* **32**, 201-238.

Stern R. A., Hanson G. N., and Shirey S. B. (1989) Petrogenesis of mantle-derived, LILE-enriched Archaean monzodiorite and trachyandesites (sanukitoids) in southern Superior Province. *Canadian Journal of Earth Sciences* **26**, 1688-1712.

Stern R. J. (2002) Crustal evolution in the East African Orogen: a neodymium isotopic perspective. *Journal of African Earth Sciences* **34**(3-4), 109-117.

Stevenson R., Henry P., and Gariepy C. (1999) Assimilation-fractional crystallisation origin of Archaean Sanukitoid Suites: Western Superior Province, Canada. *Precambrian Research* **96**, 83-99.

Sun S. S. and McDonough W. F. (1989) Chemical and Isotopic systematics of oceanic basalts: implications for mantle composition and processes. In *Magmatism in Ocean Basins.*, Vol. 42 (ed. A. D. Sounders and M. J. Norry), pp. 313-345. Geological Society Special Publication.

Tatsumi Y. and Ishizaka K. (1982) Origin of high-magnesian andesites in the Setouchi volcanic belt. southwest Japan: petrographical and chemical characteristics. *Earth and Planetary Science Letters* **60**(2), 293-304.

Tera F. and Wasserburg G. J. (1972) U-Th-Pb Systematics in Lunar Highland Samples from Luna-20 and Apollo-16 Missions. *Earth and Planetary Science Letters* **17**(1), 36-51.

Treloar P. J. and Blenkinsop T. G. (1995) Archaean deformation patterns in Zimbabwe: true indicators of Tibetan-style crustal extrusion or not? In *Early Precambrian Processes*, Vol. 95 (ed. M. P. Coward and A. C. Ries), pp. 87-108. Geological Societry Special Publications.

Walter M. J. (1998) Melting of garnet peridotite and the origin of komatiite and depleted lithosphere. *Journal of Petrology* **39**(1), 29-60.

Wang Z., Wilde S. A., Wang K., and Yu L. (2004) A MORB-arc basalt-adakite association in the 2.5 Ga Wutai greenstone belt: late Archean magmatism and crustal growth in the North China Craton. *Precambrian Research* **131**, 323-343.

Wetherill G. W. (1956) An interpretation of the Rhodesia and Witwatersrand age patterns. *Geochimica et Cosmochica Acta* **9**, 290.

Whalen J. B., Currie K. L., and Chappell B. W. (1987) A-Type Granites - Geochemical Characteristics, Discrimination and Petrogenesis. *Contributions to Mineralogy and Petrology* **95**(4), 407-419.

Whalen J. B., McNicoll V. J., Galley A. G., and Longstaffe F. J. (2004a) Tectonic and metallogenic importance of an Archaean composite high- and low-Al tonalite suite, Western Superior Province, Canada. *Precambrian Research* **132**, 275-301.

Whalen J. B., Percival J. A., McNicoll V. J., and Longstaffe F. J. (2004b) Geochemical and isotopic (Nd-O) evidence bearing on the origin of late- to post-orogenic high-K granitoids in the Western Superior Province: implications for late Archaean tectonomagmatic processes. *Precambrian Research* **132**, 303-326.

Whalen J. B., Percival J. A., McNicoll V. J., and Longstaffe F. J. (2002) A mainly crustal origin for tonalitic granitoid rocks, Superior province, Canada: implications for Late Archaean tectonomagmatic processes. *Journal of Petrology* **43**, 1551-1570.

Wilde S. A., Valley J. W., Peck W. H., and Graham C. M. (2001) Evidence from detrital zircons for the existence of continental crust and oceans on the Earth 4.4 Gry ago. *Nature* **409**, 175-178.

Williams H., Hoffman P. F., Lewry J. F., Monger J. W. H., and Rivers T. (1991) Anatomy of North-America - Thematic Geologic Portrayals of the Continent. *Tectonophysics* **187**(1-3), 117-134.

Williams I. S. and Claesson S. (1987) Isotopic Evidence for the Precambrian Provenance and Caledonian Metamorphism of High-Grade Paragneisses from the Seve Nappes, Scandinavian Caledonides .2. Ion Microprobe Zircon U-Th-Pb. *Contributions to Mineralogy and Petrology* **97**(2), 205-217.

Wilson J. F., Nesbitt R. W., and Fanning C. M. (1995) Zircon geochronology of Archaean felsic sequences in the Zimbabwe craton: a revision of greenstone stratigraphy and a model for crustal growth. In *Early Precambrian Processes*, Vol. 95 (ed. M. P. Coward and A. C. Ries), pp. 109-126. Geological Society of London Special Publication.

Winchester J. A. and Floyd P. A. (1977) Geochemical discrimination of different magma series and their differentiation products using immobile elements. *Chemical Geology* **20**, 325-343.

Windley B. F. (1998) Tectonic development of early Precambrian orogens. *Memoirs of National Institute of Polar Research Special Issue* **53**, 8-38.

Wood D. A. (1980) The application of a Th-Hf-Ta diagram to problems of tectonomagmatic classification and to establishing the nature of crustal contamination of basaltic lavas of the British Tertiary volcanic province. *Earth Planetary Science Letters* **50**, 11-30.

Wood D. A., Joron J. L., Treuil M., Norry M., and Tarney J. (1979) Elemental and Sr Isotope Variations in Basic Lavas from Iceland and the Surrounding Ocean-Floor - Nature of Mantle Source Inhomogeneities. *Contributions to Mineralogy and Petrology* **70**(3), 319-339.

Wyman D. A. and Kerrich R. (2002) Formation of Archaean continental lithospheric roots the role of mantle plumes. *Geology* **30**, 543-546.

Yogodzinski G. M., Kay R. W., Volynets O. N., Koloskov A. V., and Kay S. M. (1995) Magnesian andesite in the western Aleutian Komandorsky region - implications for slab melting and processes in the mantle wedge. *Geological Society of American Bulletin* **107**(5), 505-519.

APPENDIX A: PETROGRAPHIC ANALYSES

Table A.1 Mafic Metavolcanics

Sample No.	Sample Location Coordinates (GPS)	Texture	Mode	Description	Rock name
ZBT-46	*Latitude: 21 08 495* *Longitude: 27 27 441*	Fine grained intergranular to porphyroblastic	30% Plagioclase 69% Hornblende 1% Fe-Ti oxide & quartz	Prismatic plagioclase within amphibole-dominated matrix that gives the sample a porphyritic texture. Randomly oriented albite & carlsbad twinned plagioclase display rare sericitisation. Hornblende has variable grain size <0.1 mm, and show parallel orientation.	Porphyritic amphibolite
ZBT-47	*Latitude: 21 08 509* *Longitude: 27 27 465*	Medium-grained intergranular	20% Plagioclase 79% Hornblende 1% Quartz & Fe-Ti oxide	Amphibole aggregates of acicular crystals pseudomorphing clinopyroxene. Anhedral untwinned plagioclase tend to occur between aggregated amphiboles and they both show preferred orientation	amphibolite
ZBT-48	*Latitude: 21 09 936* *Longitude: 27 28 953*	Fine-grained Schistose	30% Plagioclase 70% Hornblende Quartz, epidote & Fe-Ti oxide in trace proportions	Fine prismatic hornblende with subhedral to anhedral habit and fine lath-shaped plagioclase with combined carlsbad and albite twinning display a preferred direction. Locally extensive sericitisation of plagioclase.	Amphibolite Schist
ZBT-49	*Latitude: 21 09 195* *Longitude: 27 28 379*	Fine-grained Intergranoblastic	30% Plagioclase 69% Hornblende 1% Quartz & Fe-Ti oxide	Fine plagioclase laths display both random and parallel orientation. Albite and carlsbad twinning present. Hornblende shows a hexagonal shape with equilibrium boundaries. Locally, form aggregates with general orientation.	amphibolite
ZBT-50	*Latitude: 21 09 247* *Longitude: 27 28 510*	Fine-grained Basaltic	35% Plagioclase 65% Hornblende	Anhedral plagioclase associated with equant euhedral to subhedral amphibole with equilibrium grain contacts. Plagioclase display lack of twinning and rare sericitisation.	Fine amphibolite
ZBT-51	*Latitude: 21 09 287* *Longitude: 27 28 779*	Fine-grained Schistose	80% Hornblende 10% Plagioclase 9% Quartz 1% Fe-Ti oxide	Amphibole display acicular to prismatic habit. It is aligned in a preferred orientation. Untwinned anhedral plagioclase <0.1 mm interlocked with anhedral quartz of similar grain size aligned parallel to the amphibole.	Amphibolite Schist
ZBT-52	*Latitude: 21 12 592* *Longitude: 27 30 495*	Fine-grained Schistose	75% Hornblende 20% Plagioclase 5% Quartz <1% Fe-Ti oxide	Acicular to prismatic habit, mostly altered with weak pale green to pale yellow pleochroism hornblende. Display preferred orientation. <0.1 mm untwinned plagioclase interlocked with quartz of similar grain size. They show recrystallisation texture – straight grain boundaries with triple point junction at 120°.	Amphibolite schist

ZBT-53	*Latitude: 21 12 694* *Longitude: 27 30 438*	Medium-grained	80% Hornblende 20% Plagioclase + quartz < 1% Fe-Ti oxide	Anhedral skeletal hornblende poikilitically enclosing fine anhedral quartz. Variable grain size (3 – 0.5 mm). Plagioclase is anhedral without twinning and is mostly interlocked with quartz sandwiched between larger grains of hornblende. Under high magnification plagioclase and quartz segregates display recrystallisation texture.	Medium-grained amphibolite
ZBT-54	*Latitude: 21 13 011* *Longitude: 27 30 208*	Medium-fine grained Porphyroblastic	75% Hornblende 24% Quartz + Plagioclase 1% Fe-Ti oxide	Skeletal anhedral with variable grain size (2.5-1 mm) hornblende mostly poikilitically enclosing fine grains of quartz. They exhibit preferred orientation. Untwinned plagioclase + quartz mostly form segregates sandwiched between hornblende grains. The segregate display recrystallisation texture as evidence by straight boundaries with triple point junction at 120°. Fe-Ti oxide is common and shows even distribution.	Medium-grained amphibolite
ZBT-55	*Latitude: 21 13 092* *Longitude: 27 30 135*	Medium-grained	60% Hornblende 35% Plagioclase 5% Calcite <1% Fe-Ti oxide	Prismatic, anhedral with mild pale-green to green pleochroism hornblende. Variable grain sizes (3-0.1mm). In most places appears fragmented and intermingled with calcite and Fe-Ti oxide possible reflecting alteration product. Locally amphibole pseudomorphes the clinopyroxene. Plagioclase forms subhedral thin tabular crystals that are partially to wholly enclosed by clinopyroxene pseudomorphing hornblende. Plagioclase displays a combination of carlsbad and albite twinning whose extinction angles recorded An content between 60 and 68%, implying laboradoritic composition. Quartz is rare in this thin section. Secondary calcite and Fe-Ti oxide are common.	Medium-grained amphibolite
ZBT-56	*Latitude: 21 13 417* *Longitude: 27 29 859*	Medium-grained	60% Hornblende 30% Plagioclase 5% Quartz Accessory calcite + Fe-Ti oxide	This thin section display hornblende, plagioclase and quartz grains which resembles those described in thin section ZBT-54. The only difference is that this thin section contains secondary calcite, which displays even distribution.	Medium-grained amphibolite

ZBT-57	*Latitude: 21 13 786* *Longitude: 27 29 700*	Fine-grained Basaltic	79% Hornblende 20% Plagioclase 1% Quartz	Fine anhedral acicular to prismatic crystals with random orientation-hornblende. Plagioclase crystals are fine lath-shaped with mostly combined carlsbad and albite twinning. They are randomly oriented. Quartz form fine anhedral grains which are sporadically distributed. Fe-Ti oxide is a common accessory phase.	Basaltic amphibolite
ZBT-58	*Latitude: 21 13 297* *Longitude: 27 29 921*	Fine-grained Basaltic	80% Hornblende 18% Plagioclase <1% Biotite <1% Quartz 2% Calcite	Hornblende forms fine acicular to equant grains with random orientation. Acicular plagioclase platy crystals with carlsbad and albite twinning are randomly distributed. Sporadic biotite tabular crystals occur in association with rare anhedral quartz and secondary calcite. Calcite locally forms segregates that reveal straight grain boundaries with triple point junctions at 120°.	Basaltic amphibolite
ZBT-59	*Latitude: 21 12 748* *Longitude: 27 30 378*	Fine-grained Basaltic	79% Hornblende 20% Plagioclase 1% Quartz	Description similar to sample ZBT-57 above.	Basaltic amphibolite
ZBT-60	*Latitude: 21 12 632* *Longitude: 27 30 383*	Medium-grained	60% Hornblende 35% Plagioclase 5% Calcite <1% Fe-Ti oxide	Prismatic, anhedral with mild pale-green to green pleochroism hornblende. Variable grain sizes (3-1mm). In most places appear fragmented and intermingled with calcite and Fe-Ti oxide possible reflecting alteration product. Locally amphibole pseudomorphed the clinopyroxene. Plagioclase forms subhedral thin tabular crystals which are partially to whole enclosed by clinopyroxene pseudomorphing hornblende. Plagioclase displays a combination of carlsbad and albite twinning. Quartz is rare in this thin section. Secondary calcite and Fe-Ti oxide are common.	Medium-grained amphibolite
ZBT-61	*Latitude: 21 11 409* *Longitude: 27 30 730*	Medium-grained	80% Hornblende 20% Plagioclase + quartz < 1% Fe-Ti oxide	Anhedral skeletal hornblende poikilitically enclosing fine anhedral quartz. Variable grain size (3 – 0.5 mm). Plagioclase is anhedral with no twinning mostly interlocked with quartz sandwiched between larger grains of hornblende. Under high magnification plagioclase and quartz segregates display recrystallisation texture.	Medium-grained amphibolite
ZBT-62	*Latitude: 21 11 694* *Longitude: 27 30 540*	Medium-grained	75% Hornblende 25% Plagioclase + quartz < 1% Fe-Ti oxide	Amphibole display acicular to prismatic habit. It is aligned in a preferred orientation. Untwinned anhedral plagioclase <0.1 mm interlocked with anhedral quartz of similar grain size.	Medium-grained amphibolite

Table A.2 Felsic Metavolcanics

Sample No.	Sample Location Coordinates (GPS)	Texture	Mode	Description	Rock name
ZBT-41	*Latitude: 21 14 759* *Longitude: 27 34 194*	Fine grained	70% Feldspar + quartz 15% Biotite 10% Muscovite 5% Hornblende	Untwinned fine equant grains interlocked with quartz grains of similar sizes and habit. The feldspar and quartz grains contact each other with 120° dihedral angles. Muscovite and biotite form fine acicular grains defining prominent foliation. Hornblende forms sporadic medium-size crystals with anhedral habit. Hornblende crystals are randomly oriented.	Hornblende-muscovite-biotite dacite
ZBT-42	*Latitude: 21 14 754* *Longitude: 27 34 248*	Fine grained	75% Feldspar-quartz 10% Biotite 10% Muscovite 5% Hornblende	Fine untwinned feldspar grains interlocked with anhedral quartz of similar grain sizes. Both minerals exhibit straight grain boundaries with common 120° triple point junction. Biotite and muscovite form acicular grains which are oriented in a preferred direction. These micas are secondary phases. Hornblende displays anhedral tabular grains relatively coarser than the micas. It occurs sporadically.	Hornblende bearing dacite
ZBT-43	*Latitude: 21 14 710* *Longitude: 27 34 241*	Fine grained	75% Feldspar + quartz 10% Biotite 5% Hornblende 10% Calcite <1% Fe-Ti Oxide	Fine equant grains of untwinned feldspar with regular grain boundaries against equant quartz of similar grain size. They show a recrystallisation texture defined by straight boundaries with triple point junctions at 120°. Biotite forms acicular to tabular grains with a general preferred orientation. Anhedral hornblende grains associated with biotite show signs of alteration to biotite. Fe-Ti oxide is mostly associated with hornblende and biotite possible a product of break down of hornblende to biotite. Secondary calcite display uniform equant grains that are evenly distributed. The grains have regular boundaries.	Carbonatised hornblende-biotite Dacite
ZBT-44	*Latitude: 21 14 689* *Longitude: 27 34 209*	Fine grained	80% Feldspar + quartz 15% Biotite 5% Muscovite <1% Fe-Ti Oxide, epidote	Anhedral fine feldspars showing lack of twinning are interlocked with relatively coarser grains of anhedral quartz. The grain contacts are sutured and quartz displays undulose extinction. Fine biotite grains have tabular to acicular habit and it is commonly associated with epidote. Muscovite forms relatively coarser grains with subhedral habit. Fe-Ti oxide occurs in accessory amounts.	Muscovite-biotite Dacite

ZBT-45	*Latitude: 21 14 663* *Longitude: 27 38 185*	Fine grained	75% Feldspar + quartz 15% Biotite 10% Hornblende <1% Muscovite , Fe-Ti oxide	Fine grains of untwinned feldspars and interlocked quartz grains with similar grain sizes. Under high magnification the grains display a recrystallisation texture where grains have regular grain boundaries with triple point junction at 120°. Mostly fine tabular biotite crystals exhibit a preferred orientation and even distribution. In local places it is associated with fine acicular hornblende. Muscovite forms fine anhedral grains in accessory proportion. Fe-Ti oxide is a common accessory phase.	Hornblende-biotite Dacite

Table A.3 Diorite

Sample No.	Sample Location Coordinates (GPS)	Texture	Mode	Description	Rock name
ZBT-17	*Latitude: 21 07 011* *Longitude: 27 30 249*	Granular Sub-ophitic common	53% hornblende + Clinopyroxene 45% Plagioclase 2% Quartz	Anhedral hornblende pseudomorphed clinopyroxene. Display local chloritisation. Grain size range between 5 and 2 mm. Plagioclase exhibit subhedral 5 mm to <1mm grains with combined carlsbad and multiple albite twinning. Some grains display mild to extensive sericitisation. Quartz form anhedral fine (<1mm) sporadic grains.	Diorite
ZBT-18	*Latitude: 21 07 001* *Longitude: 27 30 235*	Granular Sub-ophitic common	55% hornblende + Clinopyroxene 40% Plagioclase 3% Quartz	Subhedral to anhedral hornblende and clinopyroxene grains with mostly 5 to 3 mm length. Most clinopyroxene has been replaced by hornblende. Plagioclase grains are subhedral with combined carlsbad and albite multiple twinning that yielded anorthite content of 42 to 48% indicating andesinic plagioclase. Grain size vary between 5 and 1mm. Sericitisation is mild. Quartz is fine (<1 mm), anhedral and occurs sporadically.	Diorite
ZBT-19	*Latitude: 21 07 000* *Longitude: 27 30 217*	Granular Sub-ophitic common	55% hornblende + clinopyroxene 45% Plagioclase Accessory quartz	Subhedral plagioclase with combined albite and carlsbad twinning showing general preferred orientation. Grain size variable (4-1 mm long). Plagioclase crystals are mildly sericitised. Hornblende and clinopyroxene display subhedral to anhedral habit. They are randomly oriented. Most clinopyroxene have been replaced by hornblende.	Diorite
ZBT-20	*Latitude: 21 07 021* *Longitude: 27 30 237*	Granular	65% hornblende + clinopyroxene 35% Plagioclase	The thin section is dominated by hornblende, which display wide range of grain size (5 1 mm long). All the grains are anhedral. Clinopyroxene has been pseudomorphed by hornblende. Plagioclase form fine crystals that are sandwiched between the relatively coarse hornblende crystals. They show albite twinning and sporadic sericitised grains.	Diorite
ZBT-21	*Latitude: 21 07 017* *Longitude: 27 30 177*	Granular	50% hornblende + clinopyroxene 50% Plagioclase	Clear granular texture with fresh subhedral plagioclase laths locally segregated between hornblende crystals. These segregations show a general preferred direction. The plagioclase show both albite and carlsbad twinning.	Diorite

ZBT-22	*Latitude: 21 07 365* *Longitude: 27 30 959*	Granular	60% Plagioclase 30% Hornblende 10% Clinopyroxene	Subhedral plagioclase interlocked with anhedral hornblende crystals that display regular grain boundaries. Hornblende is unevenly distributed resulting in other sections of the thin section to be purely made of plagioclase. Clinopyroxene has been mostly pseudomorphed by hornblende as evidenced by most hornblende grains that display relicts of clinopyroxene. Plagioclase display simple, multiple and combined carlsbad-albite twinning. Few plagioclase grains are mildly sericitised.	Diorite
ZBT-23	*Latitude: 21 07 393* *Longitude: 27 31 474*	Granular	60% Hornblende + clinopyroxene 35% Plagioclase 5% Quartz	The sample exhibits advanced pseudomorphism of clinopyroxenes by hornblende. Plagioclase crystals are extensively sericitised. Quartz forms sporadic anhedral grains with mild undulatory extinction.	Diorite
ZBT-24	*Latitude: 21 07 343* *Longitude: 27 31 428*	Granular	55% Plagioclase 30% Clinopyroxene 5% Orthopyroxene 10% Amphibole accessory quartz	Orthopyroxene forms anhedral fine equant (0.5 mm) grains with thin alteration rim around the margin. Clinopyroxene display subhedral habit and variable grain size up to 2 mm long. Few clinopyroxene grains are altering to hornblende. Primary hornblende forms anhedral grains with smooth boundaries. Plagioclase display subhedral habit and combination of albite and carlsbad twinning. The grains range between 4 and 1 mm in length. It is sericitisation free. Quartz forms fine sporadic anhedral grains with smooth boundaries and faint wavy extinction.	Diorite
ZBT-25	*Latitude: 21 06 650* *Longitude: 27 32 163*	Granular Cumulate	60% Plagioclase 30% Clinopyroxene 10% hornblende Quartz is accessory	Uneven distribution of plagioclase and mafic phases is evident. Plagioclase forms bundles of subhedral laths with a preferred direction. Plagioclase grains vary in size between 5 and 3 mm long. They exhibit both albite and carlsbad type of twinning. Clinopyroxene forms aggregates of medium-size subhedral to anhedral crystals that are clearly pseudomorphed by hornblende. Primary hornblende forms anhedral crystals that show stronger pleochroism than the secondary grains that replaced clinopyroxene.	Diorite

ZBT-26	*Latitude: 21 06 517* *Longitude: 27 32 236*	Granular	55% Plagioclase 30% Clinopyroxene 10% hornblende 5% orthopyroxene	Plagioclase forms subhedral fine lath-shaped grains that are mildly sericitised. The grain size vary in length from 1.5 to 0.5 mm. Plagioclase commonly display combined carlsbad and albite twinning. Clinopyroxene display relatively coarse grains partially pseudomorphed by hornblende (grain size range between 2.5 and 1 mm). Primary hornblende forms anhedral grains that are relatively fine than the secondary hornblende and they display a stronger pleochroism. Orthopyroxene is less common and it occurs as anhedral sub-rounded grains with altered margins.	Diorite

Table A.4a Gabbro (Phoenix Mine)

Sample No.	Sample Location Coordinates (GPS)	Texture	Mode	Description	Rock name
ZBT-37	*Latitude: 21 13 400* *Longitude: 27 46 376*	Granular Cumulate	65% Clinopyroxene + hornblende 35% Plagioclase	Predominantly anhedral clinopyroxene partially altered to hornblende. Epidote, chlorite, and calcite are recognizable amongst the alteration products. Ophitic texture is preserved in most instances. Plagioclase laths with anhedral to subhedral habit are mildly sericitised. Locally, plagioclase is enclosed within the partially altered clinopyroxenes. The grain size is variable up to 2.5mm long. Simple twinning by plagioclase is common.	Melagabbro
ZBT-38	*Latitude: 21 13 400* *Longitude: 27 46 376*	Granular Cumulate	70% Clinopyroxene + hornblende 30% Plagioclase	This thin section display similar features as the above sample ZBT-37, except that is has higher proportion of clinopyroxene which has been replaced by hornblende.	Melagabbro
ZBT-39	*Latitude: 21 13 400* *Longitude: 27 46 376*	Granular Cumulate	60% Plagioclase 40% Clinopyroxene + hornblende	Predominantly plagioclase laths with euhedral to subhedral habit, variable grain length (up to 3.5mm). They display albite, carlsbad and a combination of albite-carlsbad twinning. Fine plagioclase laths are partially to wholly enclosed within the coarse augitic clinopyroxene. Clinopyroxene form anhedral grains which mostly display alteration to clinoamphibole. Chlorite and epidote are common in the alteration product. Augitic clinopyroxene has variable grain size up to 4 mm. The distribution of plagioclase and clinopyroxene are uneven.	leucogabbro
ZBT-40	*Latitude: 21 13 400* *Longitude: 27 46 376*	Granular Cumulate	55% Clinopyroxene + hornblende 45% Plagioclase	Plagioclase and clinopyroxene show similar features as in the above thin section ZBT-39 except that this thin section display lower modal content of plagioclase than mafic phases. Clinopyroxene grain size varies up to 5mm and it poikilitically enclose the fine plagioclase laths. The distribution of both plagioclase and mafic phases is uneven.	Melagabbro
ZBT-81	*Latitude: 21 13 400* *Longitude: 27 46 376*	Granular Cumulate	55% Plagioclase 45% Clinopyroxene + hornblende	Plagioclase form euhedral to subhedral grains which vary in size up to 3mm long and 1mm wide. It displays simple twinning, and An content based on extinction angles range from 58 to 64. Clinopyroxene is partially altered to clinoamphibole. Chlorite and epidote are commonly in association of the clinopyroxene and	Leucogabbro

hornblende. Ophitic and sub-ophitic textures are ubiquitous. Primary hornblende (3mm) occurs sporadically.

Table A.4b Gabbro (Selkirk Mine)

Sample No.	Sample Location Coordinates (GPS)	Texture	Mode	Description	Rock name
ZBT-63	*Latitude: 21 18 793* *Longitude: 27 43 543*	-	-	Despite fresh-looking hand specimen the thin section is completely altered. No petrographic analyses can be made.	Metagabbro
ZBT-64	*Latitude: 21 18 793* *Longitude: 27 43 543*	-	-	The thin section is extensively hydrothermally altered. Poorly preserved aggregates of clinoamphibole and pyroxene.	Metagabbro
ZBT-65	*Latitude: 21 18 793* *Longitude: 27 43 543*	-	-	Extensively altered with calcite anhedral grains dominating the slide. No meaningful petrographic analyses can be made from the thin section.	Metagabbro
ZBT-66	*Latitude: 21 18 793* *Longitude: 27 43 543*	-	-	Too altered to make meaningful petrographic analysis	Metagabbro
ZBT-67	*Latitude: 21 18 793* *Longitude: 27 43 543*	Granular	65% Clinopyroxene 30% Plagioclase 5% Opaque minerals	Subhedral augite crystal associated with plagioclase laths of similar grain size (5-2 mm long). Plagioclase show combined albite-carlsbad twinning with mild sericitisation. Opaque minerals are common.	Melagabbro
ZBT-68	*Latitude: 21 18 793* *Longitude: 27 43 543*	-	-	Extensive hydrothermal alteration obliterated the primary petrographic features of the rock. The slide is dominated by secondary calcite and opaque minerals.	Metagabbro carbonated
ZBT-69	*Latitude: 21 18 793* *Longitude: 27 43 543*	-	-	Highly altered thin section dominated by secondary calcite and dolomite grains. It can be mistaken for a carbonate rock.	Carbonated metagabbro
ZBT-70	*Latitude: 21 18 793* *Longitude: 27 43 543*	-	-	Extensively altered thin section with abundant opaque minerals, most probable sulphides.	Metagabbro
ZBT-71	*Latitude: 21 18 793* *Longitude: 27 43 543*	Granular	65% Clinopyroxene 30% Plagioclase 5% Opaque minerals	Subhedral augite crystal associated with plagioclase laths of similar grain size (5-2 mm long). Plagioclase show combined albite-carlsbad twinning with mild sericitisation. Opaque minerals are common.	Melagabbro

ZBT-72	*Latitude: 21 18 793* *Longitude: 27 43 543*	-	-	Too altered to for any meaningful petrographic analysis to be made.	Metagabbro
ZBT-73	*Latitude: 21 18 793* *Longitude: 27 43 543*	-	-	Extensively altered with abundant secondary calcite and opaque minerals.	Metagabbro
ZBT-74	*Latitude: 21 18 793* *Longitude: 27 43 543*	Medium grained Granular	50% Clinopyroxene 25% Hornblende 20% Plagioclase 5% Opaque minerals	Forms anhedral to subhedral grains partially pseudomorphed by clinoamphibole. The grain size varies widely from 2mm to 0.5 mm. Hornblende forms relatively fine grains with anhedral to subhedral habit. They are near equant with two sets of cleavage while the grains that pseudomorphed clinopyroxene are tabular with one set of cleavage. Plagioclase grains are extensively altered.	Melagabbro
ZBT-75	*Latitude: 21 18 793* *Longitude: 27 43 543*	-	-	Extensive hydrothermal alteration affected this sample rendering it difficult to identify its constituents. Opaque minerals are prevalent.	Metagabbro
ZBT-76	*Latitude: 21 18 793* *Longitude: 27 43 543*	-	-	Thin section is too hydrothermally altered for a meaningful petrographic analysis.	Metagabbro

Table B.5 Quartz Monzonite

Sample No.	Sample Location Coordinates (GPS)	Texture	Mode	Description	Rock name
ZBT-1	*Latitude: 21 09 024* *Longitude: 27 28 062*	Granular	50% Alkali feldspar 10% Plagioclase 15% Quartz 15% Hornblende 10% Biotite	Alkali feldspars form two groups of grain size. Relatively large grains vary between 1 mm and 4 mm, and are made of anhedral grains with irregular grain boundaries. These large grains give the rock a porphyritic tendency. Alkali feldspars are in the form of perthite, microcline and orthoclase. Perthite is predominant. Fine grains (<< 0.1 mm) are interlocked with similar grain size equant quartz grains. They display straight contacts typical for recrystallisation texture. Myrmekite is sporadic. Hornblende forms anhedral skeletal (1-2mm) grains peppered with quartz inclusions. It displays yellow to green pleochroism. Biotite tend to form segregates composed of fine (< 0.1mm) anhedral grains with uneven distribution. Accessory phases are epidote, apatite and sphene.	Biotite-hornblende quartz monzonite
ZBT-2	*Latitude: 21 09 113* *Longitude: 27 28 210*	Granular	50% Alkali feldspars 10% Plagioclase 20% Hornblende 10% Biotite	Alkali feldspar display two grain sizes as above. Plagioclase displays carlsbad, albite and combined carlsbad and albite twining. It forms relatively large grains (1.5-3mm). Most quartz grains equant and are < 0.1mm and they show recrystallisation texture with equilibrium boundaries. Anhedral hornblende is associated with biotite and epidote. Locally displays biotite psuedomorphosed to hornblende. Biotite forms aggregates with a broad preferred orientation. Apatite, epidote and sphene form the accessories.	Biotite-hornblende quartz monzonite
ZBT-3	*Latitude: 21 09 267* *Longitude: 27 28 373*	Granular	50% Alkali feldspars 15% Plagioclase 10% Quartz 20% Hornblende 5% Biotite	Microcline common amongst the alkali feldspars. Similar grain size as above thin sections. Plagioclase is similar to the above sample. Quartz forms fine mosaic of recrystallisation texture. Hornblende locally associated with biotite, epidote and iron oxide. It replaces biotite in some places. Myrmekite is ubiquitous. Chlorite occurs as accessory phase.	Biotite-hornblende quartz monzonite
ZBT-4	*Latitude: 21 09 331* *Longitude: 27 28 371*	Granular	50% Alkali feldspars 20% Plagioclase 10% Quartz 15% Hornblende	Alkali feldspars like in previous slides display two types of grain size. Plagioclase display anhedral large grains (1.5-3mm) with carlsbad, albite and a combination of twining with mild sericitisation. Hornblende forms 1-0.8 mm long	Biotite-hornblende quartz monzonite

			5% Biotite	anhedral grains associated with biotite and epidote. Locally biotite has been psuedomorphosed to hornblende. Quartz forms very fine grains (<0.1mm) displaying recrystallisation texture or annealing texture. Myrmekite is ubiquitous. Sphene with euhedral to subhedral habit occurs in accessory amount.	
ZBT-5	*Latitude: 21 09 393* *Longitude: 27 28 442*	Granular	45% Alkali feldspars 15% Plagioclase 25% Hornblende 15% Biotite	Similar to the above sample. Accessories include epidote, sphene and apatite.	Biotite-hornblende quartz monzonite

Table B.6a Monzogranite

Sample No.	Sample Location Coordinates (GPS)	Texture	Mode	Description	Rock name
ZBT-6	*Latitude: 21 09 157* *Longitude: 27 30 331*	Granular Granophyric	50% Alkali feldspar 10% Plagioclase 35% Quartz 5% Biotite	Feldspars are extensively sericitised despite fresh looking hand specimen. Locally plagioclase exhibits poorly preserved carlsbad twining. Alteration hinders any detailed analysis on the feldspars. It evident that feldspar grain sizes are in the 1-3mm range. Granophyric texture is common. Quartz is anhedral and displays similar grain size (1-3mm) to feldspars. It has normal extinction and locally fractured. Biotite is extensively chloritised with few relicts in local places which survived the chloritisation. Altered biotite straddles the boundaries of quartz. Euhedral zircon is a common accessory phase as well as the iron oxide and epidote.	Leucocratic biotite Granite
ZBT-7	*Latitude: 21 09 145* *Longitude: 27 30 303*	Granular Granophyric	60% Feldspars 35% Quartz 5% Mafic phases (Epidote + chlorite)	Feldspars are extensively sericitised with higher degree of alteration along grain boundaries. Quartz displays same characteristics as in the above sample. Scarce hornblende extensively altered to amorphous chlorite, epidote and iron oxide is present. Zircon as common accessory phase.	Leucocratic Granite
ZBT-8	*Latitude: 21 09 133* *Longitude: 27 30 274*	Granular	60% Feldspars 35% Quartz 5% Mafic phases (Epidote + chlorite)	Similar to the above sample	Leucocratic Granite
ZBT-9	*Latitude: 21 09 211* *Longitude: 27 30 297*	Granular	60% Feldspars 35% Quartz 5% (Epidote + Chlorite)	Feldspars extensively altered with the alteration more severe along the periphery than the interior. Few carlsbad twining preserved. Quartz tends to form aggregates which display normal extinction. It unevenly distributed. Grain size range between 1mm and 3 mm. Epidote and chlorite are both secondary minerals and constitute the mafic phases.	Leucocratic Granite

Table B.6b Granite from Phoenix Mine (intruding the gabbro)

Sample No.	Sample Location Coordinates (GPS)	Texture	Mode	Description	Rock name
ZBT-35	*Latitude: 21 13 400* *Longitude: 27 46 376*	Granular	70% Feldspar 25% Quartz 5% Biotite	Extensively to mildly sericitised feldspars with anhedral habit, ≤ 1.5 mm grain size. Quartz shows anhedral habit, undulatory extinction, irregular grain contacts and ≤ 1mm. Biotite partially replaced by chlorite is anhedral with ≤ 0.5 mm. Secondary muscovite present in accessory amount. Other accessory phases include epidote and chlorite.	Biotite Tonalite
ZBT-36	*Latitude: 21 13 400* *Longitude: 27 46 376*	Granular Medium grained	70% Feldspars 25% Quartz 5% Biotite	Feldspars display sericitised cores, albite twinning obscured by sericitisation and variable grain size up to 4 mm. Quartz is anhedral with wavy extinction, sutured grain boundaries, variable grain size ≤4mm. Anhedral chloritised biotite mostly ≤ 0.5mm in size. Accessory phases include epidote, zircon and chlorite.	Biotite Tonalite

Table B.7 Trondhjemite

Sample No.	Sample Location Coordinates (GPS)	Texture	Mode	Description	Rock name
ZBT-10	*Latitude: 21 08 777* *Longitude: 27 30 371*	Granular	35% Quartz 35% Plagioclase 15% Alkali feldspar 10% Biotite 5% Muscovite	Quartz and feldspars display variable grain sizes from 1 to 4 mm. Alkali feldspar is orthoclase. Plagioclase is mainly albatic. Quartz with mild wavy extinction and irregular grain contacts. Biotite fine grains (< 0.1 mm) occur with feldspars uneven distribution. Locally form aggregates contain randomly oriented anhedral biotite grains. Muscovite occurs inside plagioclase associated with biotite. Form fine (< 0.1 mm) xenomorphic grains. Accessory phases include epidote and calcite both occur with feldspars.	Muscovite-biotite trondhjemite
ZBT-11	*Latitude: 21 09 201* *Longitude: 27 30 820*	Granular	10% Calcite 40% Plagioclase 10% Alkali feldspar 30% Quartz 5% Biotite 5% Muscovite	Subhedral calcite grains ranging from 2 to 5 mm. Straight grain contacts between calcite grains. Calcite not evenly distributed.	Calcite rich muscovite-biotite trondhjemite
ZBT-12	*Latitude: 21 09 949* *Longitude: 27 31 162*	Granular	35% Plagioclase 35% Quartz 15% Alkali feldspars 10% Biotite 10% Muscovite 2% Calcite	Feldspars are peppered by fine xenomorphic biotite and muscovite grains. Biotite display uneven distribution by locally forming segregates. Plagioclase, alkali feldspars and quartz mainly have similar range of grain sizes (1-3mm). Quartz anhedral grains have wavy extinction and sutured grain boundaries. Iron oxide associated with biotite is a common accessory phase.	Muscovite-biotite trondhjemite
ZBT-13	*Latitude: 21 10 043* *Longitude: 27 31 463*	Granular	35% Plagioclase 35% Quartz 15% Alkali feldspars 10% Biotite 5% Muscovite	Feldspars display similar features as above. Quartz is highly strained with sutures and strong undulatory extinction. Fine (<0.05mm) quartz have unfixed mutual boundaries possibly an indication of annealing. Calcite is rare and iron oxide is common.	Muscovite-biotite trondhjemite
ZBT-14	*Latitude: 21 10 093* *Longitude: 27 31 610*	Granular	35% Plagioclase 35% Quartz 15% Alkali feldspars 5% Biotite 5% Muscovite	Feldspars and quartz display similar features as in the above thin sections. Plagioclase display albite twining. Biotite and muscovite sprinkled on feldspars. They show similar features as in the previous thin sections. Calcite is rare and iron oxide is associated with biotite aggregates.	Muscovite-biotite trondhjemite

ZBT-15	*Latitude: 21 10 445* *Longitude: 27 31 448*	Granular	35% Plagioclase 35% Quartz 15% Alkali feldspars 10% Biotite 5% Muscovite	Quartz forms anhedral medium size (2-4 mm) grains with fine quartz grains occupying their margins. Mildly sericitised anhedral plagioclase grains (2-4mm) are peppered with fine (0.05mm) xenomorphic biotite and muscovite grains. Quartz clusters are mica free. Iron oxide is commonly associated with biotite. Zircon present in accessory amount.	Muscovite-biotite trondhjemite
ZBT-16	*Latitude: 21 11 004* *Longitude: 27 32 094*	Granular	35% Plagioclase 35% Quartz 15% Alkali feldspars 10% Biotite 5% Muscovite	Feldspars, quartz, biotite and muscovite display similar features as in the above described samples. Alkali feldspar mainly occurs in the form of perthite.	Muscovite-biotite trondhjemite

Table B.8a Tonalite-Trondhjemite (Tati Pluton)

Sample No.	Sample Location Coordinates (GPS)	Texture	Mode	Description	Rock name
ZBT-28	*Latitude: 21 16 526* *Longitude: 27 30 946*	Granular	40% Plagioclase 15% Alkali feldspar 35%Quartz 5% Biotite	Feldspars display a range of grain size (0.5 – 2mm) with anhedral habit. They are slightly sericitised. Plagioclase grains possess albite twining. Alkali feldspars occur as orthoclase and sporadic microcline. Quartz forms displays smooth to irregular grain boundaries. Its grain size is variable mostly range between 0.5 and 2 mm. quartz grains are highly strained with undulatory extinction. In local places it forms streaks curling around feldspars. Biotite occurs along grain contacts of feldspars and quartz. It is anhedral with grain size ranging from 0.2 to 0.8 mm). Locally associated with epidote.	Biotite tonalite
ZBT-29	*Latitude: 21 16 604* *Longitude: 27 31 058*	Granular	40% Plagioclase 20% Alkali feldspars 30% Quartz 8% biotite 2% Muscovite	Feldspars display similar range of grain sizes as above. Alkali feldspar is mainly orthoclase with anhedral habit. Plagioclase is anhedral with albite twining. Quartz has two groups of grain sizes; large grains (1-3 mm) which are interlocked with feldspars. They have strong undulatory extinction. Fine (<0.05mm) grains form streaks which are curled around the feldspars and larger quartz grains. This type of grains is dominant and it displays normal extinction. They have irregular mutual grain contacts. Biotite form fine (0.1-0.9mm) grains which are associated with epidote. They are confined to boundaries of large grains of feldspars and quartz. Locally they run parallel to the quartz streaks and show signs of deformation by being folded around the large grains of feldspars. Muscovite with anhedral habit and fine grain size is confined along grain boundaries together with biotite.	Biotite tonalite
ZBT-30	*Latitude: 21 16 607* *Longitude: 27 31 249*	Granular Granoblastic	35% Plagioclase 30% Alkali feldspars 30% Quartz 5% biotite	Feldspars and quartz display similar features as in the above thin section. Quartz streaks are more prevalent in this slide and more deformed. Under high magnification the streaks reveal equant quartz and untwined feldspar grains with polygonal shape meeting at triple point junction. Quartz is dominating the mosaic. Locally, granoblastic texture is conspicuous with feldspars and quartz displaying equilibrium contact boundaries. Biotite is relatively scarce and it appears altered to epidote and iron oxide. Muscovite occurs as a secondary phase.	Biotite granodiorite

ZBT-31	*Latitude: 21 16 322* *Longitude: 27 31 505*	Granular Microgranular	40% Alkali feldspars 25% Plagioclase 30% Quartz 5% Biotite + muscovite	Alkali feldspars occur as microcline, perthite and orthoclase. They show anhedral habit and a range of grain sizes (0.5-2mm). Plagioclase with similar grain size display albite twining. Quartz has fine and large grains show gradational contacts which are sutured. The texture is heterogeneous, locally, fine grains of quartz, biotite and muscovite show microgranular texture. No streaks observed in this slide. Biotite shows random orientation. Iron oxide and zircon are accessory phases.	Leucocratic monzogranite
ZBT-32	*Latitude: 21 16 329* *Longitude: 27 30 848*	Granular	35% Plagioclase 10% Alkali feldspars 30% Quartz 25% Biotite	Feldspars are anhedral and have similar range of grain size as above sample. Plagioclase with faint albite twinning is prevalent. Alkali feldspars display albite and pericline twinning. Quartz display similar features as in thin section ZBT-30. Common streaky quartz and biotite winding around large grains of feldspars. Muscovite is secondary.	Biotite trondhjemite
ZBT-33	*Latitude: 21 16 496* *Longitude: 27 30 321*	Granular	35% Quartz 20% Biotite 40% Plagioclase 5% Alkali feldspar	Anhedral quartz show variable grain size reaching up to 3mm long and 1 mm across. It is highly strained with wavy extinction and irregular boundaries. Streaks of quartz are rare. Fine (<0.1mm) xenomorphic grains of biotite displaying random distribution. Locally, squeezed along coarse feldspar and quartz boundaries. In some places it is curved (deformed) along the margins of feldspars. Epidote occurs mostly in association with biotite. Muscovite occurs in accessory amount also in association with biotite. Up to 3mm long plagioclase grains with simple albite twinning is prevalent. The albite twinning is faint hence difficult to use in the determination of determination of plagioclase composition. Very few grains of feldspars display microcline and pericline twinning. Few more feldspar grains show lack of twinning. Apatite is an accessory phase present.	Biotite trondhjemite
ZBT-34	*Latitude: 21 15 803* *Longitude: 27 29 315*	Granular	30% Quartz 15% Biotite 45% Plagioclase 10% Alkali feldspar	Plagioclase feldspars are dominant with anhedral grain size reaching up to 3mm. They have faint simple albite twinning. They show anhedral habit. Microcline with cross-hatched twinning occurs sporadically. It grain size reach up to 2mm. Few feldspar grains display lack of twinning and have been treated as orthoclase. Quartz shows variable grain size up to 2mm. It is anhedral, strained with undulatory extinction and irregular grain boundaries. Biotite forms fine anhedral grains with a broad preferred orientation. Epidote occurs sporadically in association with biotite and iron oxide.	Biotite tonalite

Table B.8b Tonalite-Trondhjemite (Sekukwe Pluton)

Sample No.	Sample Location Coordinates (GPS)	Texture	Mode	Description	Rock name
ZBT-77	*Latitude: 20 54 573* *Longitude: 27 36 860*	Granular cumulate	60% Plagioclase 15% Alkali feldspar 24% Quartz 1% Accessories	Feldspars are mildly sericitised, display subhedral habit and wide range of grain size (1-5mm). Plagioclase shows simple albite twinning while alkali feldspars display cross-hatched twinning. Quartz display similar grain size range, regular grain contact with feldspars, mild undulatory extinction and is evenly distributed. Chlorite appears to have pseudomorphed biotite occur in accessory amount as well as muscovite, calcite and Fe-Ti oxide.	Leucocratic tonalite
ZBT-78	*Latitude: 20 54 479* *Longitude: 27 36 796*	Granular cumulate	60% Plagioclase 10% Alkali feldspar 30% Quartz	Feldspars and quartz exhibit similar grain size as above thin section. They have equilibrium contact boundaries. A thin alteration rim around feldspars render them appear sub-rounded. Coarse crystals of alkali-feldspar show micro-perthitic texture. Myrmekite texture is ubiquitous. Partially chloritised biotite occurs in accessory proportion as well as calcite, muscovite and Fe-Ti oxide.	Leucocratic trondhjemite
ZBT-79	*Latitude: 21 00 950* *Longitude: 27 35 265*	Granular cumulate	55% Plagioclase 12% Alkali feldspar 25% Quartz 3% Biotite	Feldspars are mildly to extensively sericitised enclosed by a thin alteration rim. Myrmekite is common along plagioclase crystal margins. Fine (≤ 0.1mm) amorphous biotite mostly chloritised straddle the boundaries between feldspars and quartz crystals. Quartz similar grain size as above is strained and fractured with irregular grain boundaries. Epidote is secondary and is in accessory amount.	Leucocratic tonalite
ZBT-80	*Latitude: 21 00 648* *Longitude: 27 35 232*	Granular Cumulate	60% Plagioclase 10% Alkali feldspar 30% Quartz	Both quartz and feldspars display similar range of grain size (1-5 mm). They both show a thin rim of alteration around the grain margins. Plagioclase locally display zonation exploited by sericitisation. Locally plagioclase shows myrmekite texture along the periphery. The texture resembles a cumulate.	Leucocratic tonalite

APPENDIX B: ANALYTICAL PROCEDURES

ANALYTICAL PROCEDURES

1. X-RAY FLOURESCENCE ANALYSES

Sample preparation

Whole rock samples were prepared for analysis by initially splitting the rock samples into 1-2 cm blocks using a hydraulic splitter and crushing the resultant fragments in a jaw crusher. 80g of the crushed sample was then milled to approximately 400 mesh in a carbon steel mortar placed within a Sieb Techniek mill run for two minutes. The apparatus were pre-contaminated with the sample to minimize inter-sample contamination.

The sample powders were then roasted at 1000 °C in an oven to remove molecular and at 110 °C to get rid of surface water before being combined with a LiT (lithium tetraborate)-LiM (lithium metaborate) flux (57:43) in the proportion 0.7g of sample to 6g of flux. A few drops of LiBr were added to act as a releasing agent. The mixture was then fused into a glass disc using a Claisse fusion machine.

Analysis

The analysis was carried out on a Phillips PW1480 wavelength dispersive X-Ray spectrometer with a dual target Mo/Sc X-Ray tube. All measurements were made with the tube at 50 kV and 50 mA. The analytical conditions for the major elements are given in the Table B1.1. Analytical conditions are also described by Willis (1999). Fusion disks made up with 100% Johnson Matthey Specpure SiO_2 were used as blanks for all elements except Si, for which fusion disks made of Johnson Matthey Specpure Fe_2O_3 and $CaCO_3$ were used. Intensity data were collected using Phillips X40 software on a Pentium Celeron 333mHz PC. Data reduction was done off-line using Phillips software for major elements and internally developed software for trace elements. All peaks were corrected for background, and spectral overlap corrections were made for Br on Al, Cr on Mn, Al and Ca on Mg and Mg on Ca and Na.

The samples were analysed for the following major element oxides: SiO_2, TiO_2, Al_2O_3, Fe_2O_3, MnO, MgO, CaO, Na_2O, K_2O, P_2O_5, SO_3, NiO and Cr_2O_3. Duplicates were randomly inserted into the run to test the precision of the analysis.

Table B1.1 XRF instrumental set-up for major element analytical runs at UCT.

Element/line	collimator	Crystal	Detector	PHS Lwl-Upl	Counting Time (s)	Conc. Range**	RMS	L-limit determ*	No. of STDs
NiKα	F	LiF(220)	FS	22 70	100	0 – 0.48	0.003	0.004	11
FeKα	F	LiF(220)	FL	16 68	100	0 – 17	0.069	0.019	20
MnKα	F	LiF(220)	FL	15 66	100	0 – 0.27	0.004	0.014	22
CrKα	F	LiF(220)	FL	14 70	100	0 – 3.5	0.011	0.008	11
TiKα	F	LiF(220)	FL	32 68	100	0 – 3.9	0.022	0.023	22
CaKα	F	LiF(220)	FL	30 76	100	0 – 77	0.102	0.004	21
K Kα	F	LiF(220)	FL	32 74	100	0 – 15.5	0.037	0.003	21
S Kα	C	GE(111)	FL	32 74	100	0 – 53.5	0.112	0.100	11
P Kα	C	GE(111)	FL	34 74	100	0 – 3.4	0.011	0.008	16
SiKα	C	PE(002)	FL	26 80	100	0 – 100	0.215	0.052	20
AlKα	C	PE(002)	FL	26 80	100	0 – 100	0.084	0.074	21
MgKα	F	PX-1	FL	36 68	100	0 – 85	0.141	0.102	20
NaKα	F	PX-1	FL	30 78	100	0 – 9.1	0.065	0.17	12

** all concentrations expressed as wt. % oxide: S as SO_3

* = 10 x lower limit of detection, expressed as wt. % oxide

$$RMS = \sqrt{\{(1/n-k)\ \Sigma\ (Conc._{given} - Conc._{calc})\}}$$

Where

n = no. of standards

k = no. of calibration coefficients, i.e. 2, the slope and intercept of the calibration line.

$Conc._{given}$ = recommended concentration for an element in a standard

$Conc._{calc}$ = concentration of an element calculated from the best-fit calibration line

2. INDUCTIVELY-COUPLED PLASMA MASS SPECTROMETRY (ICP-MS)

Sample Preparation

50 mg of each sample powder (preparation described under XRF analyses) was first placed in a Teflon beaker with approximately 4ml of HF/HNO_3 stock solution (4:1). The lids on the beakers were then closed and the samples were left to stand for 48 hours on a hot plate set at 50-60°C. The samples were then allowed to evaporate to complete dryness before 2ml of 2-bottled concentrated HNO_3 was added to them. The sample solutions were then returned to the hotplate and allowed to evaporate to complete dryness at approximately 75°C. Another 2ml of concentrated HNO_3 was then added to the samples and the lids were returned to the beakers and the samples were allowed to dissolve overnight. Finally, the samples were allowed to evaporate to complete dryness at 75°C for a second time.

The dry sample was dissolved in 4ml of an internal standard stock solution (5%HNO_3 + 10 ppb In, Re, Rh, Bi). The dissolved samples were each transferred to a 50ml centrifuge tube and the volume was made up to 50ml with the internal standard stock solution. This solution represented a 1000-fold dilution of the original solid sample. The solution was ready for analyses and further dilutions.

Analysis

The trace element contents of the samples were determined on a Perkin Elmer/SCIEX ELAN 6000 inductively-coupled, argon plasma, quadrupole mass spectrometer, with the instrumental settings listed in Table B1.2 below.

Table B1.2 Instrumental settings for trace element analyses using the ICP-MS

Nebuliser Gas Flow:	0.86 L/min
Main Gas Flow:	15 L/min
Auxillary Gas Flow:	0.75 L/min
ICP RF Forward Power:	1100W
Instrument Sensitivity:	300 000 cps (10 ppb Rh)
Autolens Setting	
Lens Voltage	^{9}Be 7.6 V
	^{59}Co 8.2 V
	^{115}I 9.0 V
Analyses:	
Analytical time per sample:	50s (20 sweeps/3 replicates)
Dwell Time:	35-50 milliseconds
Internal Standard:	^{115}I, ^{187}Re

3. RADIOGENIC ISOTOPES (Sr, Nd and Pb) ANALYTICAL PROCEDURE

3.1 Dissolution of samples

The Sr, Nd and Pb isotopic compositions of selected rock samples from the Francistown Granite-Greenstone Complex were determined in the radiogenic isotope facility of the Department of Geological Sciences, UCT using a VG sector 54 seven-collector thermal ionization mass spectrometer (TIMS).

3.2 Sr & Nd isotopes - sample dissolution

The technique followed for the chemical separation of the elements of interest started by weighing out approximately 100mg of powdered sample and transfer it into labeled Teflon beakers. This was followed by addition of 4-5ml of 4:1 HF/HNO_3 to the sample. The Teflon beaker was closed and placed on a heating block for approximately 2 nights at 75°C to dissolve. After ascertaining that the sample has dissolved it was uncovered to allow it to evaporate to dryness. The covers (lids) were left to dry on the side. Once the samples were dry, the inside of the lids were rinsed with 6.2M HCl and transferred into their respective beakers. Then the inside of the beakers were rinsed down with 6.2M HCl up to the ~5ml mark. The samples were evaporated to dryness. This was to ensure that the HNO_3 is removed. Addition of the 6.2M HCl was repeated and the sample evaporated to dryness. Samples were removed from the heating block and allowed to cool down. Using a pipette 1ml of 2.5M HCl was added to the samples and allowed to dissolve in a fume cupboard. 0.5ml of 2.5M HCl was added to samples with low Sr, Nd concentration. The solutions were transferred to labeled centrifuge tubes which were then placed into a centrifuge machine for 20 minutes at the speed of 4 x 1000 rpm for removal of particulates. At this stage the samples are ready for separation using the ion-exchange primary columns.

3.3 Column chemistry using cation exchange resin

Strontium collection

Using a pipette 0.5 ml of sample solution was loaded in each column. After addition of various volumes of HCl the Sr fraction was eventually collected in 15 ml Teflon beakers. A few drops of

2B HNO_3 were added to Sr fractions and the samples were allowed to go to dryness. Addition of few drops of 2B HNO_3 was repeated and the samples were allowed to go to dryness again. At this stage the samples were ready for loading onto degassed single Ta filaments which will eventually be loaded into the mass spectrometer.

Sr loading onto Ta filaments

On a piece of parafilm a drop of nitric acid and a drop of phosphoric acid were mixed up. Using a pipette 1µl of the mixture was transferred into the sample beaker and mixed with the sample aliquot. The mixture was homogenized by a pipette tip before loaded onto a single Ta filament. Mass fractionation for Sr analyses was monitored by measuring non-radiogenic $^{86}Sr/^{88}Sr$ (= 0.1194) isotope and corrections were made to ratios of $^{87}Sr/^{86}Sr$ in the unknowns by normalizing with the $^{86}Sr/^{88}Sr$ fractionation factor.

3.4 Pb isotope- sample dissolution

The process started by weighing 0.4g rock powder for samples that contained more than 10 ppm Pb. For samples containing 10 ppm or less Pb, 0.5g of rock powder was weighed and transferred into a Teflon beaker. Then about 7 ml of 4:1 mixture of HF (hydrofluoric acid) and HNO_3 (nitric acid) was added to the weighed sample. The beaker was closed with the lid and left on a hotplate for at least 48 hours or until properly dissolved. After the samples had completely dissolved, the lid was removed and the solutions were evaporated to dryness in a clean-air box at temperatures of ~100 °C. Then about 4 ml of 6.2N HCl was added to the samples, sealed and left on the hotplate for a few hours to dissolve. Once dissolved, the lids were removed and samples dried down. This was followed by addition of approximately 1.5 ml of 0.5N HBr (hydrobromic acid) into the sample and left to stand until the sample went into solution. At this stage the sample was ready for column chemistry separation.

Column preparation

The small Teflon columns were thoroughly cleaned in 6N HCl and distilled water before placed in the column stand. Ion exchange resin (200-400 mesh AGI-8X BIO-RAD anion resin) was added to the neck of the column and then washed with distilled water so that it compacts correctly to the correct level. The columns were then cleaned by filling them with the 0.5N HBr

and distilled water. This was followed by addition of 1ml of 0.5N HNO_3 and H_2O consecutively. Before adding the sample onto the columns, the columns were preconditioned with 1 ml of 0.5N HBr. 1 ml of sample solution was pipetted into the ion exchange column. The solution into the resin was washed three times by 0.7 ml of 0.5N HBr. The Pb was collected from three 0.7 ml washes of 0.5N HNO_3 into a 5 ml square Savillex Teflon beaker. The eluted sample was dried down in the clean air box. A drop of H_3PO_4 was added to the sample before drying it. At this stage the dry sample is ready for loading onto a Re filament for mass spectrometric analysis.

Sample loading for the mass spectrometer

The sample was firstly mixed with 1 drop of the H_3PO_4 and 3 drops of HNO_3. A 4 µl silica gel solution was loaded onto a Re single filament and dried down at 1.0A. Subsequently the sample was loaded onto the silica gel bed and dried down slowly at 0.8A. When just dry the current was taken up steadily until a dull glow appeared. Once a dull glow appeared the current was brought down immediately to zero. After the samples were loaded onto the filament they were placed into the turret and eventually loaded into the mass spectrometer for analyses. In order to compensate for the effects of mass fractionation in Pb analyses, standards were analysed many times so that the fractionation factors could be calculated. The final analyses of Pb in the samples were normalized by calculated fractionation factors.

4. STABLE ISOTOPES

Sample preparation

Jaw-crushed whole rock samples were sieved to obtain -60 to -40 mesh size fractions which were washed by tap water to get rid of dust. The sample fractions were dried in an oven at 110 °C. The individual grains were handpicked with the use of a binocular microscope. For felsic granitoids quartz grains were handpicked and pyroxenes were handpicked in the case of gabbro and diorite. The separated minerals were then cleaned using HF/HNO_3 and distilled water. To avoid loosing sample due to dissolution in HF/HNO_3, $^2/_3$ of distilled water was added to $^1/_3$ of HF/HNO_3 into the samples in Teflon beakers and then placed on a hot plate for ~10

minutes. This was followed by thorough rinsing with tap water. The samples were left in an oven at 50 °C to dry completely and subsequently clean pure quartz grains were easily handpicked under a binocular microscope. Separated pure grains were crushed to a fine powder in an agate mortar and pestle and dried at 50 °C for 48 hours before analysis.

Oxygen-extraction technique

The oxygen was extracted from the mineral separates using the silicate stable isotope oxygen-extraction line facility in the Department of Geological Sciences at the University of Cape Town. Samples were loaded into nickel reaction vessels and degassed at 200 °C for 4 hours. The samples (10 mg) were reacted with ClF_3 following the procedure outlined by Borthwick and Harmon (1982). All of the separates were reacted at 550 °C overnight. Ten samples were loaded for every run of which two were the internal standards of MQ (Murchison Line quartz vein). The raw values of MQ are used to directly recalculate the sample values relative to Standard Mean Ocean Water (SMOW) assuming the value of MQ to be 10.10. The extracted oxygen was converted to CO_2 with a heated carbon rod and later analysed for the $^{18}O/^{16}O$ ratio using the dual inlet gas-source spectrometer (MAT252). Nearly all of the standard analyses were run in duplicate or triplicate. The average difference in the $\delta^{18}O$ value for rerun samples was below 0.5‰ for quartz and below 0.3‰ for pyroxene analyses. Data are reported in the standard δ notation relative to SMOW.

APPENDIX C: PEARSON-PRODUCT COEFFICIENT
AND
CORRELATION OF XRF-ICP MASS SPECTROMETRS TRACE
ELEMENT DATA